Axisymmetric Instabilities in Stellar and Planetary Magnetohydrodynamics

Alexander Kimbley

School of Mathematics

University of Leeds

A thesis submitted for the degree of

Doctor of Philosophy

24th June 2024

For
Ruth & Neil,
Carol,
Hector & Jasper

Acknowledgements

First and foremost, I would like to thank my supervisors, Stephen Griffiths and David Hughes, for your exceptional guidance, support and patience. It has been a pleasure to have known you both over these many years. I could not have asked for a better pair of supervisors, and I will sincerely miss our meetings.

I would like to express my appreciation to my examiners Andrew Gilbert and Rainer Hollerbach for their time and efforts in examining my thesis.

I would also like to thank my friends and colleagues, Rob Dymott, Joseph Elmes, Luke Gostelow, Sam Myers, Nils de Vries, and Muyang Zhang. It is remarkable how much inspiration and knowledge can be shared over a game of chess, a cup of coffee, or across a desk.

To my parents, Jacqueline and Jared, I am incredibly grateful for your unconditional devotion and sacrifices, before and throughout my PhD. Dad, I must also thank you for all the games of squash — they made excellent counting practice!

Last, but certainly not least, I would like to thank my partner, and companion, Katie Dinsdale, whose love and unwavering encouragement has driven me throughout the entirety of my PhD. You were here from my first day, and are here on my last — this achievement is as much yours as it is mine.

Abstract

The large-scale circulations of many geophysical and astrophysical bodies are dominated by parallel flows. It is natural to enquire about the stability of these flows, and how they depend upon background rotation, shear and stratification. In the terrestrial atmosphere, inertial instabilities may result and are most likely to occur close to the equator. We therefore investigate whether corresponding instabilities may occur in stellar and planetary atmospheres, where large-scale magnetic fields may have significant dynamical effects; in particular, we focus on applications to the solar tachocline, and the upper atmospheres of Hot Jupiters.

We investigate the axisymmetric linear stability of various parallel flows with latitudinal shear in the presence of background rotation, stratification and magnetic field. Using the Boussinesq and magnetohydrostatic approximations, we derive general stability criteria and growth rate bounds, taking account of the magnetic field. We show that sufficiently strong magnetic field stabilises the system.

We show that a uniform shear flow on an f-plane allows magnetically modified inertial instabilities and purely magnetic instabilities to occur, the latter being analogous to magnetorotational instabilities in limiting cases. Allowing for non-zero kinematic viscosity, thermal diffusivity and magnetic diffusivity leads to several steady and oscillatory stability criteria. We categorise various double-diffusive instabilities, some of which occur at vertical wavenumbers that would otherwise be stable in the ideal regime.

We also consider the nonlinear evolution of a hyperbolic shear layer at mid-latitudes to understand the effect of a locally unstable region, the entire time evolution of the nonlinear instability, the redistribution of vorticity and the resulting change to the mean flow. The redistribution of vorticity is most substantial in the hydrodynamically stable regime.

Finally we consider the stability of a jet profile on an equatorial β-plane, which admits localised solutions about a central latitude. For the ideal case, instabilities can occur at any vertical wavenumber given sufficiently weak magnetic field; the most unstable modes are found to occur for infinite vertical wavenumbers. In the presence of diffusion, instabilities are constrained to finite vertical wavenumbers and are often purely magnetic, occurring in the hydrodynamically stable regime.

Contents

List of Figures

List of Tables

Chapter 1

Introduction

1.1 Zonal Jets in Stellar and Planetary Atmospheres

The large-scale circulations of many geophysical and astrophysical bodies are dominated by parallel flows. Examples include the zonal jets of stellar and planetary atmospheres and interiors, and the approximately circular flow in accretion discs. It is thus natural to enquire about the stability of these flows, and how it depends upon background rotation, shear, stratification and, if present, magnetic field. This may be important for constraining the possible flow configurations (e.g., jet strength and location) or for understanding the development of turbulence. There is, for example, a long-standing interest in understanding the possible role of turbulence in angular momentum redistribution in accretion discs (e.g., Kuiper, 1941; Lynden-Bell & Pringle, 1974; Balbus & Hawley, 1991). More recently, observations of certain exoplanetary atmospheres, so-called Hot Jupiters, have revealed the existence of unexpectedly strong equatorial jets that apparently flow close to the speed of sound (e.g., Showman *et al.*, 2013; Heng & Showman, 2015).

In this thesis we will be considering the effect of magnetic field on axisymmetric instabilities in planetary atmospheres and stellar interiors. In Cartesian geometry, we consider the linear and nonlinear evolution of axisymmetric instabilities in the presence of vertical magnetic field in a planetary configuration, where background rotation (f-plane or equatorial β-plane), uniform vertical density stratification, uniform diffusion, and the magnetohydrostatic (thin layer) approximation are considered. The magnetohydrostatic approximation makes the analysis distinct from previous studies, and allows us to investigate the large scale dynamics of stellar and planetary atmospheres. In this chapter we introduce a selection of astrophysical bodies relevant to this system, inertial instability and the magnetorotational instability. We also introduce a number of other instabilities that illustrate mechanisms relevant in the thesis. Finally, we discuss the aims and outline of the thesis.

1.1.1 The Solar Tachocline

An astrophysical body that hosts a large scale magnetic field is the star of our solar system — the Sun. The internal structure of the Sun consists of three main regions: the core ($R < 0.2R_\odot$),
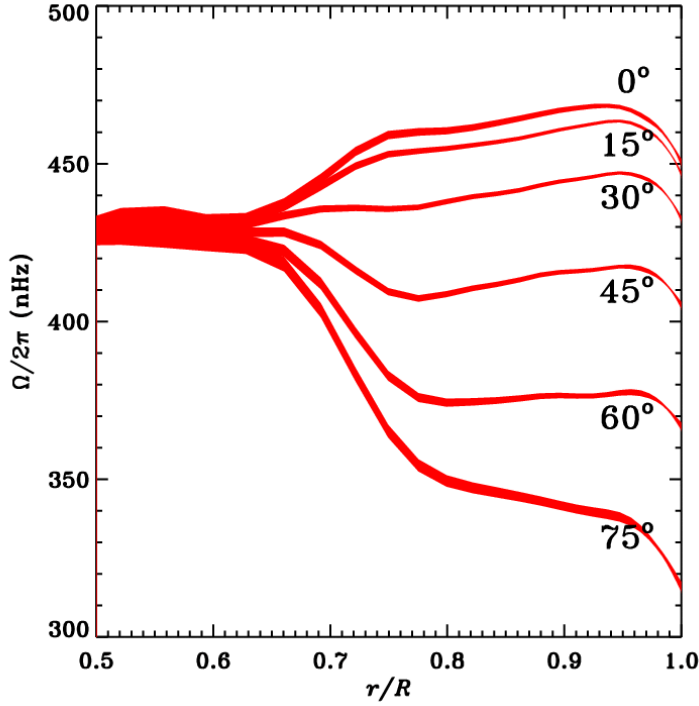
Figure 1.1: Helioseismological measurements of the internal angular velocity of the Sun at a number of given latitudes against the relative radius. Image credit: NSO/GONG.

the radiative zone ($0.2R_\odot < R < 0.7R_\odot$) and the convective zone ($R > 0.7R_\odot$), where the solar radius is $R_\odot = 7.0 \times 10^8$m. Helioseismology (a method that measures oscillations of the Sun caused by sound waves) indicates that the radiative zone rotates as a solid body (Gough, 2007, Chapter 1), while the external convective zone exhibits differential rotation, as illustrated in figure 1.1. The abrupt disparity between rotation profiles gives rise to a thin interface layer, approximately $2 - 5\%$ of the solar radius in depth, with strong latitudinal and vertical shear — it is known as the solar tachocline. The tachocline plays a crucial role in the transport of energy, mass and magnetic field throughout the Sun, and is thought to be primarily responsible for the solar dynamo (Gough, 2007, Chapter 1). The strong latitudinal shear of the solar tachocline may give rise to numerous instabilities that are likely to depend on the magnetic field, the strength of which, in the solar tachocline, is thought to be in the range 10^3G to 10^5G (Gough, 2007; Hughes *et al.*, 2007). It is apparent from figure 1.1 that the shear of the solar tachocline becomes more extreme at larger latitudes. It is important to note that the angular velocity increases with increasing radius in the near equatorial regions (i.e., latitudes less than $30°$) and decreases with increasing radius for larger latitudes.

1.1.2 Jupiter

The gas giant Jupiter, which rotates with angular velocity $\Omega \approx 1.76 \times 10^{-4}$s^{-1}, exhibits approximately axisymmetric zonal flows throughout its upper atmosphere, with surface winds exceeding
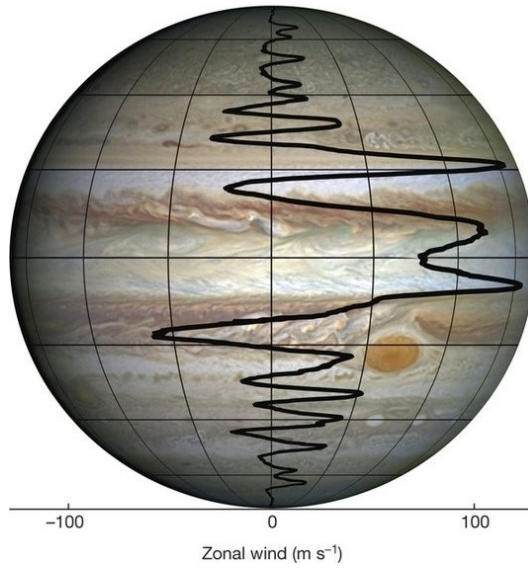
Figure 1.2: The surface zonal flow of Jupiter, the magnitude of which is illustrated by the thick black line, as a function of latitude. This was measured during Juno's third perijove pass on the 11th of December 2016 (Tollefson *et al.*, 2017). The image of Jupiter was taken by the Hubble Wide Field Camera in 2014. Image Credit: Kaspi *et al.* (2018).

100ms^{-1} (Tollefson *et al.*, 2017; Kaspi *et al.*, 2018; Read, 2024). There is a strong eastward equatorial jet which extends $\sim 15°$ into the northern and southern hemispheres and is flanked by numerous prograde and retrograde jets with varying speed and width, as illustrated in figure 1.2.

The depth of these jets has been a long-standing question (e.g., Vasavada & Showman, 2005); however, in recent years, there has been significant development on this topic due to the recent Juno missions (Iess *et al.*, 2018). Kaspi *et al.* (2018) suggest that the jets extend to $0.96R_j$ before rapidly decaying to $\simeq 1\%$ of their surface amplitude, where $R_j = 69911\text{km}$ is the radius of Jupiter (i.e., the jets extends $\simeq 3000\text{km}$ into the planet's atmosphere). The reason for this rapid decay is still under debate, but may be due to a number of factors, including the existence of a stably stratified layer from $0.8R_j$ or $0.9R_j$ to $0.92R_j$ (Debras & Chabrier, 2019; Gastine & Wicht, 2021) or Lorentz forces (Christensen *et al.*, 2020).Naturally, the strength of these Lorentz forces will depend on Jupiter's magnetic field, which is the strongest of all the planets in the solar system (Connerney, 1993). The predominantly dipolar field is generated in the electrically conducting "dynamo region", where the atmosphere is composed primarily of metallic hydrogen. The upper limit of this region occurs at $\simeq 0.85R_j$ (French *et al.*, 2012; Iess *et al.*, 2018), above which the conductivity rapidly falls to zero since Jupiter's upper atmosphere is composed primarily of molecular hydrogen (Guillot *et al.*, 2004). The fall in conductivity also leads to a rapid decay in magnetic field strength. Indeed, the maximum field strength decreases by approximately 75% from about 80G at $R = 0.85R_j$ to about 22.5G at $R = 1.0R_j$ (Connerney *et al.*, 2022). However, these maxima occur in localised regions of magnetic flux that extend throughout Jupiter's outer atmosphere; the average field strength at the surface is 4.1G (Connerney *et al.*, 2022).

1.1.3 Hot Jupiters

Hot Jupiters are gas-type exoplanets that are somewhat similar physically to Jupiter. Their radii range from $0.50R_J$ to $2.0R_J$, while their masses range from $0.36M_J$ to $11.8M_J$, where $M_J = 1.9 \times 10^{27}$kg is the mass of Jupiter (Winn *et al.*, 2010; Demory & Seager, 2011). Whilst Hot Jupiters are considered gas-giants, they have some distinctive characteristics compared with Jupiter.

Many Hot Jupiters have unusually low mean densities. For example, Mandushev *et al.* (2007) observed a Hot Jupiter with mean density 222kgm^{-3}; in comparison, Jupiter's mean density is 1330kgm^{-3}. This occurs as Hot Jupiters seem to have much larger radii than their mass dictates. Although high levels of irradiation are thought to be responsible for the inflated radii, the mechanism for this is still under debate (Heng & Showman, 2015).

The orbital periods of Hot Jupiters can range from 1.3 to 111 Earth days (Winn *et al.*, 2010); however, observations suggest that they are usually less than 10 Earth days (Berrier & Sellwood, 2015). The short orbital periods of Hot Jupiters coincide with small distances from their host stars, the typical distance being ~ 0.1AU.

Hot Jupiters are also typically tidally locked (Heng & Showman, 2015), with one side always facing its host star. Thus, assuming orbital periods $T < 10$ Earth days, we can estimate that their angular velocity $\Omega = 2\pi/T > 7.3 \times 10^{-6}$s^{-1}. However, we note that tides may drive planets away from synchronous rotation (Showman & Guillot, 2002; Correia *et al.*, 2003; Grießmeier *et al.*, 2004).

The close proximity and tidal locking leads to atmospheric temperatures of ~ 1000K to 3000K (Mayor & Queloz, 1995), which can ionise the planetary atmospheres and therefore allow large-scale magnetic fields to develop and influence atmospheric dynamics. The magnetic field strength of Hot Jupiters is somewhat uncertain. However, Yadav & Thorngren (2017) estimate the surface magnetic field strength of several Hot Jupiters from 10G to 120G, consistent with observations of the release of magnetic energy in four planet-star interactions, indicating field strengths from 20G to 120G (Cauley *et al.*, 2019).

Given a Hot Jupiter is tidally locked, intense stellar radiation on the permanent dayside may drive strong zonal flows that redistribute heat to the permanent nightside (Heng & Showman, 2015). Indeed, observations of Hot Jupiters have revealed the existence of unexpectedly strong (eastward) equatorial jets that apparently flow close to the speed of sound (e.g., Showman *et al.*, 2013; Heng & Showman, 2015); these were also predicted by dynamical models (Cooper & Showman, 2005; Rauscher & Menou, 2010). However, more recent observations found evidence of westward travelling jets (Armstrong *et al.*, 2016; Dang *et al.*, 2018). It is suspected that strong magnetic fields are largely responsible for the jet reversals. This is supported by three dimensional magnetohydrodynamic (MHD) numerical models of Rogers & Komacek (2014) and Rogers (2017); the first predicted these reversals, while the second showed moderate dipolar magnetic field strength could drive the inferred reversals on Hot Jupiter HAT-P-7b. Using shallow water MHD models, Hindle *et al.* (2019) and Hindle *et al.* (2021) further constrained the strength of magnetic field and explored mechanisms for such reversals.

1.2   Hydrodynamic and Inertial Instabilities

In this thesis we consider parallel flows $U(y)$ that exhibit latitudinal shear, from which numerous instabilities may result. In particular, we are interested in inertial instability which is axisymmetric in its purest form. Thus, we will assume axisymmetry to investigate inertial instability and ensure that numerous unstable modes will not occur simultaneously and compete with one-another, which would significantly complicate our analysis. However, since we are considering flows in a planetary configuration, in the following subsection we provide some examples of hydrodynamic instabilities, which are not necessarily driven by parallel flows $U(y)$, to illustrate the various effects of rotation, stratification and shear. This has the benefit of introducing concepts and mechanisms that are being neglected, and to understand what other instabilities may occur in observations and experiments.

1.2.1   Inviscid Instabilities in Rotating Planets

There are numerous hydrodynamic instabilities present in geophysical and astrophysical bodies. Shear flow instabilities of a flow $U(y)\hat{\mathbf{e}}_{\mathbf{x}}$ are among the simplest we can consider. Many important results have been derived within this system, such as Rayleigh's inflexion point criterion, Fjørtoft's theorem and Howard's semi-circle theorem (e.g., Rayleigh, 1880; Kuo, 1949; Drazin & Reid, 2004, and references therein). The study of parallel shear flows may be extended by considering the influence of rotation. For example, Watson (1980) studied, in spherical geometry, a two-dimensional shear instability in differentially rotating stars. He derived a necessary condition for stability, governed by the ratio between the angular velocities at the pole and equator.

We can also consider the influence of stable stratification on parallel flows with vertical shear $U(z)\hat{\mathbf{e}}_{\mathbf{x}}$, with buoyancy frequency N, where instability occurs if the Richardson number Ri $= N^2/U'^2 < 1/4$. This instability may be observed in a variety of geophysical flows, but is most commonly observed as waves on the surfaces of water and clouds. Incorporating rotation into the vertically sheared and stably stratified system, baroclinic instability can occur, a process by which perturbations draw energy from the potential energy of the mean flow. The instability can be observed in the mid-latitude of Earth's atmosphere and has been subject to numerous studies since the initial theoretical studies of Charney (1947) and Eady (1949). For example, the Eady model considers motions on the f-plane, where the Coriolis parameter f is constant, between two flat rigid horizontal surfaces, with vertical length scale H, and assumes the vertical shear satisfies a thermal wind balance. Instability occurs if $L_D(k^2 + l^2)^{1/2} < 2.399$, where k and l are the along-stream and cross-stream wavenumbers, respectively, and $L_D = NH/f$ is the Rossby radius of deformation (Eady, 1949).

1.2.2   Axisymmetric Inertial Instabilities

Another distinct, purely hydrodynamic instability is the so-called inertial instability, which will be a considerable part of this study; it is local and axisymmetric in nature. Inertial instability was

first studied in cylindrical geometry by Rayleigh (1917), who considered an inviscid axisymmetric swirling flow, with angular velocity Ω as a function of the radial coordinate R. Rayleigh showed that instability is possible energetically only if the magnitude of $R^2\Omega$ (which is proportional to the angular momentum) decreases with increasing radius in some region of the flow. Often known as the Rayleigh criterion, a necessary condition for instability is that the Rayleigh discriminant

$$\Phi = \frac{1}{R^3}\frac{d(R^2\Omega)^2}{dR} < 0, \tag{1.1}$$

somewhere in the flow. Rayleigh derived the criterion (1.1) by using an energy argument to consider the fluid exchange between two rings of equal volume, while assuming that their angular momentum must be conserved. If the rings are within a domain where $\Phi > 0$, the total kinetic energy of the system must increase, implying stability. Any resulting instability is driven by an imbalance between the radial pressure gradient and the centrifugal force, manifesting itself in overturning motions in the (R, z) plane. Synge (1933) later showed that the criterion (1.1) is both a sufficient and necessary condition for instability.

To enquire if analogous instabilities can be realised on rotating spherical planets and stars, we consider Cartesian geometry rather than the full complexity of spherical geometry. The equivalent necessary and sufficient condition to (1.1), in Cartesian geometry, for inviscid and axisymmetric instability is that $fQ < 0$, where $Q = f - U'$ is the absolute vorticity (or potential vorticity) and $U(y)$ is a parallel shear flow with latitudinal shear (see Appendix A for derivation). In cylindrical geometry, Ooyama (1966) considered baroclinic circular vortices in an axisymmetric, inviscid and incompressible fluid without boundaries, deriving a necessary and sufficient condition for the stability of these vortices. Ooyama (1966) also predicted that inertial instability is manifested as overturning motions in the meridional plane (analogous to the overturning motions of centrifugal instability in the (R, z)-plane), and is primarily constrained to the local region where the total vorticity fQ is negative.

Equatorial β-plane

The studies of inertial instabilities did not address the equatorial regime until, crucially, Dunkerton (1981) realised that $fQ > 0$ is easily violated near the equator since the Coriolis effect becomes small. This is illustrated in figure 1.3, which is a contour plot of the potential vorticity in the northern hemisphere. Black patches indicate negative potential vorticity (so that $fQ < 0$ in the northern hemisphere); indeed, it is clear that these regions of negative potential vorticity are more prominent near the equator, but can occasionally occur in the tropics. Dunkerton (1981) considered the inertial instabilities of a zonal flow $U(y) = \Lambda_0 y$, with constant shear Λ_0, on the equatorial β-plane, with Coriolis parameter $f = \beta y$, where β is the planetary vorticity gradient, in a stratified and diffusive system. The hydrostatic (thin layer) approximation was also assumed to be valid so that the vertical momentum equation reduces to a balance between the pressure gradient and the buoyancy term; the approximation is valid provided the horizontal lengthscale is much larger than
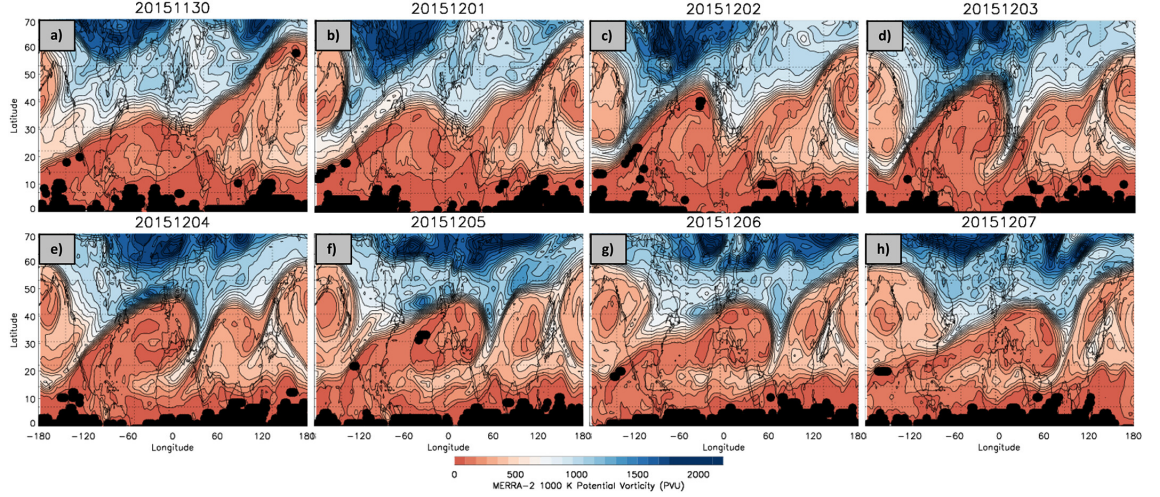
Figure 1.3: Northern hemisphere Mercator maps of MERRA-2 potential vorticity in the upper stratosphere (at height $\approx$ 35km) from a) November 30th to h) December 7th 2015. Black dots indicate negative potential vorticity and therefore conditions suitable for inertial instability. Blue and red shaded sections represent high and low levels of potential vorticity. Image credit: Harvey & Knox (2019).

the vertical lengthscale. In the inviscid case, with uniform shear and uniform buoyancy frequency N, axisymmetric instability on the equatorial β-plane occurs if

$$s^2 = \frac{\Lambda_0^2}{4} - \frac{(2n+1)N\beta}{|k|} > 0,$$

(1.2)

where s, k and n are the growth rate, vertical wavenumber and eigenvalue, respectively. Note that $n = 0$ gives the most unstable mode. Equation (1.2) shows that the fastest growing mode occurs as $k \to \infty$ (i.e., the most unstable mode occurs on vanishingly small vertical scales), which is physically undesirable. Thus, the effects of diffusion, in particular vertical diffusion, will be important in constraining vertical wavenumbers to finite values to make the model physically realisable.

Dunkerton (1981) also considered the role of kinematic viscosity ν and thermal diffusion κ, with their ratio, the Prandtl number $Pr = \nu/\kappa$, set to unity. The marginally stable shear becomes $|\Lambda_0| = 2\sqrt{5}\nu^{\frac{1}{5}} (N\beta/4)^{2/5}$ and the maximum growth rate occurs at $|k_c|^5 = N\beta/(4\nu^2)$. Dunkerton (1982) later considered the system with $Pr \neq 1$, where several steady and oscillatory stability results were derived.

As Dunkerton predicted, inertial instabilities were later observed in the equatorial atmosphere (e.g., Hayashi *et al.*, 1998; Knox, 2003) and ocean (e.g., Richards & Edwards, 2003; d'Orgeville *et al.*, 2004). Using data from more recent satellite observations of an inertial instability, Rapp *et al.* (2018) contour daily-mean temperature perturbations in the northern and southern hemispheres on the 3rd December 2015, given in figure 1.4. The temperature perturbations illustrate the typical "pancake structure" of inertial instability in the upper stratosphere and lower mesosphere with thin modes spanning from the equator to mid-latitudes (at $50°$) with a vertical lengthscale of

mean(90W-45E), dT [K], 3. Dec. 2015
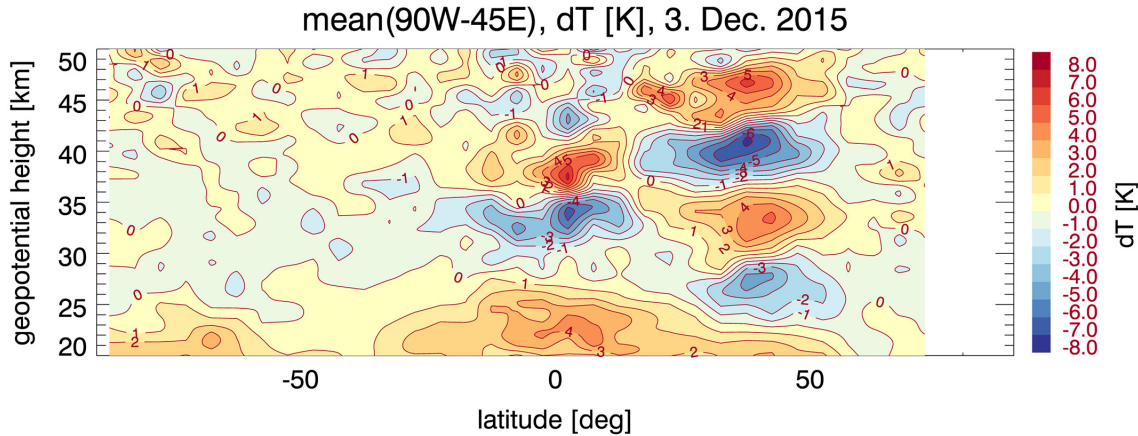
Figure 1.4: Daily-mean temperature perturbations for the longitudinal range $90°$W to $45°$E on the 3rd December. The temperature perturbations are based on METOP-A and METOP-B GPS radio occultation data. Image Credit: Rapp *et al.* (2018).

$O(10\mathrm{km})$ and latitudinal lengthscale of $O(1000\mathrm{km})$. This agrees with prior observations of inertial instability in the upper stratosphere and lower mesosphere (e.g., Hayashi *et al.*, 1998; Knox, 2003). The inertial instability event depicted by the temperature perturbations in figure 1.4 also coincides with negative potential vorticity seen in figure 1.3 at an altitude of $35\mathrm{km}$. These observations are non-axisymmetric, but are often interpreted in terms of axisymmetric theory owing to the large longitudinal scales (e.g., figure 1.3 considers the mean temperature perturbations from $90°W$ to $45°E$).

It is also natural to look at the nonlinear evolution of inertial instability, and, for example, investigate the mean flow change. Griffiths (2003a,b) further extended the analysis of equatorial inertial instabilities to the nonlinear regime. Under the hydrostatic approximation, Griffiths (2003a,b) considered an axisymmetric stably stratified fluid with constant buoyancy frequency N on the equatorial β-plane with uniform shear Λ_0 and Prandtl number unity. Specifically, Griffiths (2003a) studied the interactions between inertial instability and the mean flow. The weakly nonlinear regime is considered, deriving equations for the amplitude of the most unstable mode, and for the mean flow change; the numerical simulations agree with these analytical predictions. In the moderately diffusive regime, the numerical simulations show that the action of instability on the mean flow creates a latitudinal region in which fQ is homogenized to a small negative value. Interestingly, the vertical scale of the weakly nonlinear regime agrees with observations of inertial instability in the terrestrial equatorial atmosphere, where the vertical lengthscale is expected to be about $10\mathrm{km}$ (Hitchman *et al.*, 1987; Hayashi *et al.*, 1998; Smith & Riese, 1999). However, the weakly nonlinear regime required unrealistically large vertical diffusion, and thus the inertial instabilities of the equatorial atmosphere must be described by the moderately nonlinear simulations that predict a vertical lengthscale of $1\mathrm{km}$. Clearly, for the moderately diffusive case, the vertical scale structure is an order of magnitude smaller than those of observed inertial instabilities.

A possible mechanism to compensate for this discrepancy is suggested in Griffiths (2003b);

it is dependent on a secondary Kelvin-Helmholtz instability that develops during the evolution of the inertial instability. By considering the redistribution of vorticity over the evolution, Griffiths (2003b) also further investigates the difference between the dynamics and mean flow change of the weakly nonlinear and strongly nonlinear regimes. The evolution in both regimes redistribute vorticity over a latitudinal region in order to stabilise the flow. The dynamics of the weakly non-linear regime are driven only by the need to reduce the maximum value of $(-fQ)$ slightly, since vertical diffusion can stabilise regions with $fQ < 0$ to a certain degree; however, the dynamics of the strongly nonlinear regime are driven by the need to reduce the maximum of $(-fQ)$ to a very small value throughout the domain to stabilise the flow.

Moving back to linear stability theory, Griffiths (2008a) then considered a rotating, stably stratified flow $U(y)\mathbf{e}_x$ with arbitrary horizontal cross-stream shear $U'(y)$ and uniform buoyancy frequency N in the context of linear normal modes. For axisymmetric disturbances the perturbed cross stream velocity v is governed by the equation

$$\hat{v}'' - \frac{k^2}{N^2}(s^2 + fQ)\hat{v} = 0. \tag{1.3}$$

Equation (1.3) allows for the derivation of an analytical expression known as the near-inertial limit solution, which gives approximations as the vertical wavenumber $|k| \to \infty$ for the discrete eigenvalues and eigenmodes of the system, localised around the minimum of fQ, $\bar{y}$ say. Indeed, by taking the latitudinal lengthscale

$$L = \left(\frac{2N^2}{k^2\overline{(fQ)''}}\right)^{1/4}, \tag{1.4}$$

the following equation for the growth rate was obtained

$$s^2 = -\overline{fQ} - \frac{(2n+1)N}{|k|}\left(\frac{\overline{(fQ)''}}{2}\right)^{1/2}, \tag{1.5}$$

where the overbar denotes evaluation at $\bar{y}$. By decreasing $|k|$, the near-inertial balance is broken by an increasing cross-stream pressure gradient that, in turn, reduces the growth rate of the inertial instabilities and renders them stable at some critical $|k|$. Taking the zonal flow $U(y) = \Lambda_0 y$ (with constant shear Λ_0) on an equatorial β-plane ($f = \beta y$) reduces (1.5) to (1.2) of Dunkerton (1981).

Many studies of inertial instability consider the hydrostatic approximation (e.g., Dunkerton, 1981; Griffiths, 2008a) and therefore, by necessity of energy conservation, the traditional approximation must be employed (i.e., terms that deflect fluid vertically in full Coriolis force are neglected). However, it is well known that the validity of the approximation comes into question at the equator. This is a point of interest as we will employ the magnetohydrostatic approximation (a magnetic analogue of the hydrostatic approximation) throughout the thesis, including the analysis of flows on an equatorial β-plane. Griffiths (2008a) discusses the validity of the traditional approximation on an equatorial β-plane; in particular, it is noted that the approximation may break down when the vertical wavenumber $k \to \infty$. Physically, this is not the case for inertial instability, where observations suggest structures stretching thousands of kilometres (e.g., Hayashi *et al.*,

1998; Knox, 2003) as illustrated in figure 1.4. However, mathematically, it may be of interest to consider the full Coriolis force. Indeed, Kloosterziel *et al.* (2017) considers how the full Coriolis force affects the axisymmetric inertial instabilities of an oceanic Gaussian jet on the equatorial β-plane in the absence of stratification through the use of numerical simulations. There are a number of significant differences to the system under the traditional approximation. For example, the growth rate is found to approach the inviscid maximum growth rate with correction $Re^{-1/4}$ as the Reynolds number Re (the ratio of inertial forces to viscous forces) tends to infinity; under the traditional approximation, the maximum inviscid growth rate is attained with correction $Re^{-1/3}$ as $Re \to \infty$.

f-plane

Thus far we have primarily discussed inertial instabilities in reference to the equatorial atmosphere. However, in the thesis, we will also consider instabilities at mid-latitudes; we therefore discuss analysis of inertial instabilities on an f-plane, where the Coriolis parameter f takes a constant value. Note that the following results are non-hydrostatic, and therefore do not directly relate to the results of this thesis, but give insight into inertial instabilities at mid-latitudes.

Kloosterziel & Carnevale (2008) investigated linear inertial instabilities on an f-plane for varying Prandtl number with particular focus on the vertical scale selection (as in Griffiths, 2003a, for the equatorial β-plane). Kloosterziel & Carnevale (2008) considered a non-hydrostatic, stratified fluid with constant buoyancy frequency N on an f-plane with uniform shear Λ_0, and, after seeking axisymmetric normal mode solutions in the absence of diffusion, they derived the following equation for the growth rate squared:

$$s^2 = -\frac{k^2 fQ + l^2 N^2}{l^2 + k^2}, \tag{1.6}$$

where l is the cross-stream wavenumber. Equation (1.6) was also previously derived by Hoskins (1974). Thus, for any l, if $fQ < 0$, there is instability if $|k| > N|l|/|fQ|^{1/2}$ and the growth rate approaches the inviscid maximum growth rate $|fQ|^{1/2}$ as the vertical scale becomes infinitesimally small (i.e., $|k| \to \infty$). Note once again that, physically, vanishing vertical scales are implausible, and thus diffusion must be considered to make the model viable. Kloosterziel & Carnevale (2008) then derived numerous conditions for steady and oscillatory stability with $Pr \neq 1$, which are noted to be qualitatively the same as for the equatorial β-plane case in Dunkerton (1981) and Griffiths (2003a). However, in the limit of large Reynolds number for $Pr = 1$, the vertical scale selection and maximum growth rate are found to be significantly different to the results of Dunkerton (1981) and Griffiths (2003a). That is, in the limit of large Reynolds number, Kloosterziel & Carnevale (2008) find that the vertical wavenumber that generates the maximum growth rate, $k_{\max}$ say, scales with $(N^2 Re)^{1/4}$ on the f-plane, while Griffiths (2003a) finds that $k_{\max} \sim (NRe)^{1/3}$ on the equatorial β-plane. Similarly, the correction to the maximum growth rate on the f-plane scales with $(N^2/Re)^{1/2}$ (Kloosterziel & Carnevale, 2008), while on the equatorial β-plane the correction to the growth rate scales with $(N^2/Re)^{1/3}$ (Griffiths, 2003a). This difference hinges on

normal mode solutions of the equatorial β-plane which depend upon the value of $\overline{(fQ)''}$. These decay exponentially with $|y|$ and become ever more confined to the region about the minimum of fQ. Indeed, this constraint on the modes does not occur if fQ is constant (as on the f-plane for uniform shear) since $(fQ)'' = 0$. For $Pr \neq 1$, steady instabilities occur for $Pr < 1.44$, while for $Pr > 1.44$ it is possible for oscillatory instabilities to occur; the fastest growing modes are found to be steady given sufficiently large Re. In the limit of large Reynolds number, the maximum growth rate and scale selection are found to be the same as for $Pr = 1$.

Kloosterziel *et al.* (2007b) discussed the nonlinear saturation of inertial instability in a rotating shear flow, focusing on how inertial instability redistributes absolute linear momentum $M(y) = U(y) - fy$ until the instability is neutralised. Based on total momentum conservation, it is predicted that an inertially unstable flow evolves so that dM/dy becomes zero over a latitudinal range. Thus, in the region of constant M, M_c say, the predicted equilibrated velocity is $u(y) = M_c + fy$, while the initial velocity remains unchanged outside of this region (i.e., $u(y) = U(y)$). Kloosterziel *et al.* (2007b) note that setting $M = M_c$ is equivalent to setting $Q = 0$; however, only the condition on the total momentum conservation allows the boundaries of the latitudinal region to be determined. The prediction is shown to be valid for a number of flows, increasing in accuracy as the Reynolds number Re increases. It is noted that the range of y in which the instability is neutralised is generally greater than the initially unstable region. Further to this investigation of predicting the evolution of the mean flow, Kloosterziel *et al.* (2015) consider the saturation of inertial instability for a number of flow profiles on the equatorial β-plane. However, the constraint on the conservation of angular momentum is not always sufficient to predict the equilibrium flow; the equilibrium momentum M_c must first be determined through numerical simulations so that the condition on the total angular momentum may be used.

1.2.3 Double-diffusive Instabilities

In this subsection we discuss the Goldreich–Schubert–Fricke (GSF) instability, which is an important mechanism in the transfer of angular momentum in planets and stars (Goldreich & Schubert, 1967; Fricke, 1968), and depends upon distinct magnitudes of kinematic viscosity ν and thermal diffusion κ. Note that the instability results from vertical shear (which we will not consider in this thesis) rather than latitudinal shear; however, the instability illustrates an important mechanism present in our analysis. The instability is essentially an axisymmetric instability enabled by the role of thermal diffusion. That is, given a flow with $fQ < 0$ (which is unstable by (1.1)) that has been stabilised by pressure gradients due to the effects of buoyancy (in a stably stratified fluid), then sufficiently strong thermal diffusion will nullify the stabilising role of stratification and allow the flow to be come unstable. Although Goldreich & Schubert (1967) and Fricke (1968) do not consider Cartesian geometry, we illustrate the instability for longitudinal coordinate x, latitudinal y and local vertical z (see also Barker *et al.*, 2019, for a similar argument). First, we note that the angular velocity $\Omega(R)$ can be decomposed into uniform rotation $2\mathbf{\Omega} = (0, f, 0)$ plus a linear radial (local vertical) shear flow $\mathbf{u} = -U_z z \mathbf{e}_x$. Thus, seeking axisymmetric normal mode solutions of

the vertical shear flow in the presence of uniform vertical buoyancy frequency N, we can obtain the following criteria for instability:

$$f\hat{Q} + \frac{f^2 N^2}{4}Pr < 0, \tag{1.7}$$

where we define $\hat{Q} = f - U_z$. In contrast to the previous definition of fQ, since the rotation is aligned about the planetary axis rather than the local vertical, the absolute vorticity appears in a slightly different form. However, it is important to note that throughout the thesis the absolute vorticity will strictly be defined as $Q = f - U'$, where f is the Coriolis parameter with rotation aligned about the local vertical and U' is the latitudinal derivative of a parallel flow $U(y)$. In the absence of diffusion, stability is guaranteed if the Solberg–Høiland criterion $f\hat{Q} + f^2 N^2/4 > 0$ is satisfied. Hence, thermal diffusion can allow instability to occur even though the Solberg–Høiland criterion is satisfied. Specifically, the GSF instability operates when $Pr < 1$, $N^2 > 0$ and $f\hat{Q} < 0$. Recently, the GSF instability has been investigated as a mechanism to transport angular momentum in the radiation zones of stars via the use of 3D numerical simulations at both the equator and mid-latitudes (e.g., Barker *et al.*, 2019, 2020; Dymott *et al.*, 2023).

1.2.4 Non-axisymmetric Instabilities

In this thesis we consider only axisymmetric flows (so that inertial instability may occur in isolation without competition from other instabilities); however, it is still of importance to be aware of non-axisymmetric instabilities that can occur. We therefore discuss non-axisymmetric inertial instability theory, inertial instabilities in experiments, and the strato-rotational instability.

Non-axisymmetric Inertial Instabilities

There have been many studies regarding non-axisymmetric inertial instabilities (e.g., Dunkerton, 1983, 1993; Clark & Haynes, 1996; Griffiths, 2008a). Focusing on Griffiths (2008a), non-axisymmetric solutions are derived in the near inertial limit ($|k| \to \infty$) with small along-stream wavenumber m, which illustrates how the non-axisymmetric solutions smoothly transition to the axisymmetric solutions; this confirms that the $m \neq 0$ instabilities can clearly be regarded as inertial instabilities. It was found that as the m increases, the stabilising effect from the cross-stream pressure gradient increases, yielding a critical m, m_c say, for which no inertial instability can occur. Thus, provided $|k|$ is sufficiently large and $0 < m < m_c$, the solutions may be classified as inertial instabilities. However, if $k \to 0$ with $0 < m < m_c$, the solutions can no longer be classified as inertial instabilities. Note that Griffiths (2008a) illustrates these general criteria for a shear layer on an f-plane and a uniform flow profile on an equatorial β-plane.

In regard to the physical application of the non-axisymmetric analysis, vanishing vertical scales of symmetric theory cannot occur in reality and, thus, a finite scale is chosen by a combination of vertical diffusion and nonlinear effects (Dunkerton, 1981; Griffiths, 2003b); hence, it is possible that these non-axisymmetric instabilities become important when $|k|$ is sufficiently

small. Griffiths (2003b) suggests that the larger vertical structure of equatorial cells found in the numerical simulations when $|k| = O(1)$ are indicative of a underlying Kelvin-wave instability, which are likely to play a much more significant role at smaller vertical wavenumbers.

Experiments

Here we consider non-axisymmetric inertial instabilities found in experiments and provide an example of how they compete with other growing modes.

The inertial instabilities studied by Rayleigh (1917) and Synge (1933) were concerned with cylindrical geometry, as realised in the famous experiments of Taylor (1923), who considered a viscous and rotating system, which is now known as the Taylor-Couette flow. The system consists of fluid between two tall concentric cylinders with different radii, where the cylinders are rotated at distinct angular velocities to stimulate the flow. The system exhibits axisymmetric inertial instability if $\mu < \eta$, where μ is the ratio of the angular momentum of the outer cylinder to the angular momentum of the inner cylinder and η is the ratio of the radius of the inner cylinder to the radius of the outer cylinder. The unstratified system is known to be stable for $\mu \geq \eta^2$ (by substituting $\Omega(R)$ for the Couette flow in (1.1)), which includes the domain of Keplerian flows such as accretion discs). Indeed, in the limit of large Reynolds number (where viscous forces are small) the stability boundary converges to the Rayleigh line, corresponding to the condition for stability (1.1).

In more recent experimental studies, the evolution of non-axisymmetric inertial instabilities and barotropic instabilities are investigated (see review by Carnevale *et al.*, 2016, and references therin). In a similar configuration to the Taylor-Couette flow, a column is inserted into a rotating cylinder that is filled with water; the column is then rotated anticyclonically (opposite direction to the tank) and then raised out of the cylinder, leaving behind an anticyclonic vortex. Kloosterziel & Van Heijst (1991) observed that after the column was raised, a turbulent motion followed throughout the vortex, which then separated into two dipolar vortices that drifted further away as they became more two dimensional.

The three dimensional unstratified numerical simulations of Orlandi & Carnevale (1999) could capture all of the phenomena seen in experiments. Indeed, Orlandi & Carnevale (1999) concluded that inertial instability was responsible for the initial turbulent stage, which, in turn, through the redistribution of angular momentum, increases the horizontal velocity gradients in the flow, which then allows barotropic instability to occur, forming the drifting dipolar vorticies. How inertial instability affected the evolving flow was found to be highly dependent on the initial distribution of vorticity, and thus, it was of interest to predict the evolution and final equilibrium state of the flow from the initial distribution. Indeed, in the axisymmetric numerical simulations, Kloosterziel *et al.* (2007a) showed that, in the large Reynolds number limit, the evolution and final stage of the flow could be predicted from the initial distribution by considering the conservation of total absolute angular momentum (analogous to Kloosterziel *et al.*, 2007b). This was extended to the fully three dimensional system in Carnevale *et al.* (2016), which was found to accurately predict

the evolution of inertial and barotropic instability. Here, we note that it is also possible for inertial instability and barotropic instability to compete (if the initial distribution allows for this), since the growth rates of both modes are comparable (e.g., Orlandi & Carnevale, 1999; Gallaire & Chomaz, 2003); the instabilities have also been shown to occur simultaneously in experiments (e.g., Kloosterziel, 1990; Afanasyev & Peltier, 1998).

The Strato-Rotational Instability

Kushner *et al.* (1998) discussed the existence of a Kelvin wave instability in an inviscid, stratified semi-geostrophic channel flow with constant shear and rotation. Kelvin waves are transverse waves that travel alongside a boundary, driven by the combination of stratification and rotation. Subsequently, Yavneh *et al.* (2001) extended these results by considering the same system, but configured between two concentric cylinders (i.e., an idealised Taylor-Couette flow). They discovered that inertially stable flows could be destabilised by vertical stratification; the instability is now known as the Strato-Rotational Instability and crucially depends upon along-stream variation (non-axisymmetric). Provided the Froude number $Fr = |\Omega|/N \ll 1$, the sufficient condition for instability is that

$$\frac{d\Omega^2}{dR} < 0,$$

(1.8)

somewhere in the flow. Yavneh *et al.* (2001) concluded that the instability was driven by shear-modified Kelvin waves.

1.3 Magnetic and Magnetorotational Instabilities

In contrast to the terrestrial atmosphere, the atmospheres of most astrophysical bodies are electrically conducting. Thus, not only rotation, shear and stratification are of importance, but magnetic field may also play a significant role. Magnetic fields can influence hydrodynamic shear instabilities in a variety of ways. Instabilities can be completely altered, suppressed or even created from hydrodynamically stable systems.

1.3.1 Ideal Instabilities in Astrophysical Bodies

Motivated by the radial and latitudinal shear of the solar tachocline, Hughes & Tobias (2001) considered the influence of magnetic field on hydrodynamic shear flow instabilities (see also, for example, Kent, 1968; Hunt, 1966; Adam, 1980; Cally, 1983). They found that aligned magnetic field modifies the Howard (1961) hydrodynamic semi-circle theorem, leading to stability criteria rather than just bounds on unstable eigenvalues. Aligned magnetic field has a stabilising effect on the unstable hydrodynamic system, whereby sufficiently large magnetic field would completely stabilise the instability.

Conversely, magnetic field may lead to the destabilisation of rotating shear flows that are stable in the purely hydrodynamic regime. One example of hydrodynamically stable flows being

destabilised by magnetic field is found in application to accretion discs. Accretion discs are rotating structures formed about (usually massive) rotating astrophysical bodies due to the competing gravitational and centrifugal forces; that is, the latter inhibits matter from falling directly onto the massive central body. Indeed, some of the most intriguing accretion discs are those centered about galactic nuclei and quasars, both of which are likely ionised and can therefore support large scale magnetic fields. Accretion discs have been at the centre of many studies (e.g., Kuiper, 1941; Shakura & Sunyaev, 1973; Lynden-Bell & Pringle, 1974; Balbus & Hawley, 1991); in particular, it is of interest to explain the inferred rate of accretion (made from observations of their luminosity), which may only be explained by the existence of turbulence within the system. The rate of accretion cannot be explained by hydrodynamic models; indeed, accretions discs exhibit Keplerian rotation profiles, $\Omega = R^{-3/2}$, which are inertially stable to axisymmetric perturbations by (1.1) of Rayleigh (1917). The role of kinematic viscosity is also not sufficient to explain the inferred rate of accretion (Spitzer, 2006). Thus, it is of interest to find mechanisms that allow accretion discs to exhibit instability within inertially stable flows.

Throughout the thesis we will derive results in Cartesian geometry; however it is important, for comparison, to consider results in cylindrical geometry. Indeed, the main body of work we will be considering is related to the magnetorotational instability, which was first discovered in the context of accretion discs, which are naturally modelled in cylindrical coordinates. Experiments are also conducted in Taylor-Couette flow (Taylor, 1923) to verify these theoretical results. We therefore review instabilities that may occur in accretion discs, with particular focus on those that illustrate mechanisms discussed in the thesis.

1.3.2 Axisymmetric Instabilities

We now consider axisymmetric magnetic instabilities; in particular, since we will be considering inertial instabilities in the presence of vertical magnetic field (in Cartesian geometry), we will focus on magnetic instabilities that are generated by axial magnetic field.

Axial Magnetic Field

Chandrasekhar (1960) considered an axisymmetric, rotating, ideal and unstratified flow between two concentric cylinders with a constant axial magnetic field B_z. The governing equation for the perturbed radial velocity u_R becomes

$$(s^2 + \Omega_A^2)DD_* u_R - k^2 \left(s^2 + \Phi + \Omega_A^2 - \frac{4\Omega^2 \Omega_A^2}{s^2 + \Omega_A^2} \right) u_R = 0, \tag{1.9}$$

where the Rayleigh discriminant Φ is given by (1.1), $D_* = d/dR + 1/R$, k is the vertical wavenumber, s is the growth rate, $\Omega_A^2 = k^2 B_z^2/(\mu_0 \rho)$ is the Alfvén frequency squared, ρ is the density and μ_0 is the permeability of free space. Equation (1.9) is the cylindrical, non-hydrostatic and magnetic analogue of (1.3). Chandrasekhar (1960) found, via an integral argument, that in the limit of weak magnetic field strength a necessary condition for instability is that the angular

speed, $|\Omega|$, is a monotonically decreasing function of R. Chandrasekhar (1960) also found that magnetic field of sufficient strength will stabilise any instance of destabilising angular velocity gradient. It is noted that the instability condition on the angular velocity does not reduce to (1.1) in the limit of weak magnetic field. The condition for instability was also derived by Velikhov (1959), who considered how axial magnetic field affects an ideal rotating flow between two cylinders. This discovery made by Velikhov (1959) and Chandrasekhar (1960) is now known as the magnetorotational instability (MRI).

Motivated by the inferred angular momentum transport found in accretion discs, Balbus & Hawley (1991) revisited the problem studied by Chandrasekhar (1960) and Velikhov (1959). Balbus & Hawley (1991) considered axisymmetric disturbances of an unstratified, incompressible, ideal shear flow in a rotating thin disc with weak constant axial magnetic field B_z. They derived the following dispersion relation:

$$s^4 + s^2(\Phi + 2k^2v_A^2) + k^2v_A^2 \left(k^2v_A^2 + \frac{d\Omega^2}{d\ln R} \right) = 0, \tag{1.10}$$

where $v_A^2 = B_z^2/(\mu_0\rho)$ is the Alfvén velocity squared. From (1.10), Balbus & Hawley (1991) derived the necessary and sufficient criterion for instability, that

$$k^2v_A^2 < -\frac{d\Omega^2}{d\ln R}, \tag{1.11}$$

somewhere in the flow. Thus, a necessary criterion for instability is that the angular velocity decreases with increasing radius somewhere in the flow; this is a less stringent condition than the Rayleigh criterion (1.1), which, for instability, requires that the angular momentum $R^2\Omega$ decreases with increasing radius somewhere in the flow. Thus, Balbus & Hawley (1991) showed that weak axial magnetic field allows instability to occur within hydrodynamically stable regimes (i.e., flows that are stable by (1.1)); in particular, an accretion disc with a hydrodynamically stable Keplerian rotation profile could be unstable in the presence of weak axial magnetic field. Thus, the MRI provides a mechanism for which turbulence may arise in accretion discs, possibly explaining the observed rates of accretion.

If (1.11) is satisfied, then the system is unstable with maximum growth rate

$$|s_{\max}| = \frac{1}{2} \left| \frac{d\Omega}{d\ln R} \right|, \tag{1.12}$$

occurring at

$$(k^2v_A^2)_{\max} = -\left(\frac{1}{4} + \frac{\Phi}{16\Omega^2} \right) \frac{d\Omega^2}{d\ln R}. \tag{1.13}$$

For a Keplerian orbit, (1.12) implies the growth rate is $3\Omega/4$. It is noted that this is a huge growth rate, which, left unchecked, results in an amplification of energy of more than 10^4 per orbit.

Interestingly, (1.10) can also be derived in the presence of weak azimuthal field (as well as axial); however, this generalisation does not alter the eigenvalue relation (1.10). This is a consequence of the weak field assumption, which, by definition, requires that the Alfvén velocity is much smaller than the sound speed and local rotational velocity. Thus, even though the azimuthal

field grows with the instability, it does so while still satisfying the conditions on the Alfvén velocity; the axial field still has a dynamical impact due to the angular velocity gradient. We see azimuthal field play a crucial role in an instability in a following subsection, where there is no prior assumption of weak field.

We also note that (1.10) can be derived by considering the local behaviour of (1.9). However, Knobloch (1992) suggested that because of this locality, expression (1.10) was erroneous, arguing that the instability should be considered as a global shear instability instead. On account of this, he argued that azimuthal field did in fact play an important role in the instability. Gammie & Balbus (1994) argued that Knobloch neglected terms in his analysis, as he did not consider a rotationally supported thin disc as Balbus and Hawley did.

Further to this, Balbus & Hawley (1991) investigated the axisymmetric disturbances of an ideal shear flow under the Boussinesq approximation, in the presence of axial magnetic field as well as both radial and axial stratification. For a weakly magnetised disc, the following condition guarantees stability:

$$k^4 v_A^4 + k^2 v_A^2 \left(N^2 + \frac{d\Omega^2}{d\ln R} \right) + N_z^2 \frac{d\Omega^2}{d\ln R} > 0, \qquad (1.14)$$

where $N = N_R + N_z$ and N_z, is equivalent to the Brunt–Väisälä frequency, while N_R can be considered to be a radial analogue of N_z. The condition (1.14) holds for all vertical wavenumbers provided

$$\frac{d\Omega^2}{dR} > 0. \qquad (1.15)$$

We discussed this condition following equation (1.11).

Following the discovery of the magnetorotational instability, many studies investigated the role of magnetic field in accretion discs. For example, the nonlinear evolution of the MRI is investigated in Hawley & Balbus (1991, 1992). They consider a compressible Keplerian flow in the presence of weak axial magnetic field. The most important dynamical effect is the redistribution of angular momentum, which radially disperses the magnetic field, leading to stabilisation. The redistribution of angular momentum throughout the instability supports the conjecture that the MRI provides a mechanism to explain the inferred rate of accretion in astrophysical discs. It is noted that the numerical simulations limit the magnetic Reynolds number Rm (the ratio of advection due the magnetic field to magnetic diffusivity), implying that stabilisation is significantly harder to attain in accretion discs, where Rm is orders of magnitude greater. However, this discrepancy may be resolved by considering the effects of axial stratification which reduces the initial linear growth and therefore contributes to the nonlinear evolution and stabilisation.

There have also been many studies that investigate the role of the magnetorotational instability in stellar interiors. For example, Menou *et al.* (2004) considered the local axisymmetric stability (with adiabatic perturbations) of a magnetised rotating flow with angular velocity $\Omega(R, z)$ in the presence of stable stratification, kinematic viscosity ν, thermal diffusion κ, and magnetic diffusivity η. Menou *et al.* (2004) note that the system is a magnetised generalisation of the Goldreich-Schubert-Fricke (GSF) instability (Goldreich & Schubert, 1967; Fricke, 1968), which requires

kinematic viscosity and thermal diffusion to operate. Menou *et al.* (2004) derived a quintic dispersion relation which we will not give here; however, we discuss an analogue of the equation in Chapter 4. Numerous necessary conditions for stability are derived from the quintic in the perfectly conducting limit $\eta \to 0$ and the inviscid limit $\nu \to 0$; no necessary conditions are derived in the triply diffusive system. Indeed, in the perfectly conducting limit (which is found to be the closest analogue of Goldreich & Schubert, 1967; Fricke, 1968) a subset of the necessary conditions for stability are that

$$\frac{\partial \Omega^2}{\partial \ln R} > 0, \tag{1.16}$$

and

$$\left(R \frac{\partial \Omega^2}{dz} \right)^2 < 0, \tag{1.17}$$

where the latter implies that marginal stability is possible only if Ω is independent of z. These conditions are valid for finite ν and κ only. The condition (1.16) corresponds to (1.15); however, it is important to note the condition still holds in the diffusive system. In the inviscid limit, a subset of the necessary conditions for stability is that (1.17) holds (once again) and that $N^2 > 0$. Interestingly, the conditions (1.16) and (1.17) are independent of diffusive parameters; however, this also implies that they may not hold when all diffusivites are non-zero. Menou *et al.* (2004) discuss the applications to the Sun's radiative zone, where it is hypothesised that the combination of magnetic field and multi-diffusive modes will destabilise any small instances of negative differential rotation (that would otherwise be stable in strongly stratified atmospheres and interiors). Thus, as any instances of negative differential rotation are neutralised, the Sun's upper radiative zone is forced into near solid body rotation (which is inferred from helioseismological observations, e.g., Schou *et al.*, 1998).

There have also been many studies investigating the role of the magnetorotational instability (MRI) in the solar tachocline, where the MRI is thought to be limited by the effect of strong stable stratification (Ogilvie, 2007). However, Parfrey & Menou (2007) suggest that the MRI can occur at latitudes above $37°$ since the magnitude of the negative angular velocity gradients (as illustrated by figure 1.1) in combination with triple diffusive effects (Menou *et al.*, 2004) is just sufficient to overcome the strong stratification. Parfrey & Menou (2007) hypothesised that the turbulence generated by the MRI prevents solar dynamo action in these regions, consistent with the observations of sunspots that are restricted to the equatorial region.

Azimuthal Magnetic Field

Azimuthal magnetic field may also allow instability to occur in inertially stable flows. Michael (1954) showed that azimuthal magnetic field B_ϕ altered the Rayleigh criterion (1.1), deriving the necessary and sufficient criterion for axisymmetric instability, that

$$\frac{1}{R^3} \frac{d(R^2\Omega)^2}{dR} - \frac{R}{\mu_0 \rho} \frac{d}{dR} \left(\frac{B_\phi}{R} \right)^2 < 0 \tag{1.18}$$

18

somewhere in the flow, which clearly reduces to (1.1) in the absence of field. In the absence of angular velocity, the condition (1.18) implies that stability is guaranteed if

$$\frac{d}{dR}\left(\frac{B_\phi}{R}\right)^2 < 0 \tag{1.19}$$

everywhere in the flow. Condition (1.19) has also been derived by Velikhov (1959) and Vandakurov (1972). Equation (1.19) shows that an azimuthal magnetic field of the form $B_\phi \propto R^{n+1}$ is unstable if $n > 0$. Thus, condition (1.18) guarantees that the combination of inertially stable flows and flows that are stable by (1.19) are stable. Similarly, (1.18) also guarantees that the combination of inertially unstable flows and flows that are unstable by (1.19) are unstable. However, if any combination of stable or unstable flows is present, then the stability of the system depends on the magnitude of each effect. In contrast to Balbus & Hawley (1991), azimuthal field plays a dynamical role in this system since it is not assumed to be weak.

Helical Magnetic Field

Axial and azimuthal fields can both destabilise hydrodynamic systems; thus, it is natural to consider the effects of helical magnetic field (the combination of axial and azimuthal magnetic field). Chandrasekhar (1960) showed that in the absence of angular velocity an axial field B_z of sufficient strength would suppress any axisymmetric instability driven by an azimuthal field B_ϕ. He derived the following necessary and sufficient condition for stability:

$$IB_z^2 > \int \frac{\zeta_R^2}{R^2}\frac{d}{dR}(RB_\phi)^2 dR, \tag{1.20}$$

where $I > 0$ and ζ_R is a radial eigenfunction. Thus, (1.20) allows us to obtain the sufficient condition for stability that

$$\frac{d}{dR}(RB_\phi)^2 < 0, \tag{1.21}$$

everywhere in the flow. Thus, azimuthal magnetic field of the form $B_\phi \propto R^n$, with $n < 1$, guarantees stability. Howard & Gupta (1962) extended the study of Chandrasekhar (1960) by including the effects of differential rotation alongside helical magnetic field. They derived a necessary condition for instability, that

$$R\frac{d\Omega^2}{dR} - \frac{1}{\mu_0\rho R^3}\frac{d}{dR}(RB_\phi)^2 > 0 \tag{1.22}$$

is violated somewhere in the flow.

More recently, Mamatsashvili *et al.* (2019) investigated the axisymmetric instabilities of a rotating flow with increasing angular velocity (stable to the MRI) in the presence of helical magnetic field. The so-called type 2 super-helical magnetorotational instability can occur only provided the magnetic Prandtl number $Pm = \nu/\eta$ is not too close to unity. Indeed, the instability can occur at small or large Pm and is applicable to the equatorial region of the solar tachocline, which is thought to be stable to the MRI and type 1 super-helical MRI, the latter being another type of helical field instability which requires a flow with much steeper increasing angular velocity. The timescale of the linear growth rate of the type 2 super-helical MRI is of similar order to the solar

cycle period, suggesting the instability may influence the dynamical and magnetic activity of the equatorial region.

1.3.3 Non-axisymmetric Instabilities

We reiterate that this thesis will consider only axisymmetric flows; however, it is still of importance to be aware of some non-axisymmetric instabilities that may occur outside of our system. Here, we briefly discuss non-axisymmetric instabilities that can occur in magnetohydrodynamic theory and experiment.

Non-axisymmetric Magnetorotational Instabilities

After the discovery of the axisymmetric magnetorotational instability, Balbus & Hawley (1992) extended the analysis to consider the non-axisymmetric model. In cylindrical geometry, Balbus & Hawley (1992) consider an adiabatic thin disc under the Boussinesq approximation with radial angular velocity $\Omega(R)$ in the presence of weak magnetic field of arbitrary local geometry (i.e., $\mathbf{B} = (B_R, B_\phi, B_z)$). It is found that azimuthal field does not affect the fundamental mechanism of the axisymmetric or non-axisymmetric disturbances. The weakly non-axisymmetric disturbances (i.e., when azimuthal wavenumber $w_\phi = 1$) smoothly transition to the axisymmetric case, where the presence of axial magnetic field ensures growth rates comparable to the axisymmetric theory; for large azimuthal wavenumbers, the disturbances have a much smaller growth rate. In the absence of axial field, purely azimuthal field is found to produce a much smaller growth rate (approximately one order of magnitude smaller). This is in contrast to the axisymmetric case, where azimuthal field alone cannot generate an instability due to the nature of the weak field assumption.

Furthermore, there are numerous other non-axisymmetric magnetohydrodynamic instabilities. For example, Tayler (1957) and Vandakurov (1972) extended condition (1.18) to a non-axisymmetric system, by considering a stationary flow in a vertically unbounded cylinder. It was shown that a sufficient condition for stability is that the azimuthal wavenumber is greater than or equal to two. However, if the azimuthal wavenumber is unity, the necessary and sufficient condition for instability becomes

$$\frac{d}{dR}(RB_\phi^2) > 0, \tag{1.23}$$

implying azimuthal magnetic field of the form $B_\phi \propto R^{n/2}$, with $n < 1$, guarantees stability.

Experiments

Following the discoveries of Balbus & Hawley (1991), many studies have taken place that incorporate axial, azimuthal and helical field, particularly in one of the most important paradigms of fluid dynamics which we have already introduced, the Taylor-Couette flow. In experiments there are many ways to configure the field (strength and orientation), flow (respective cylinder speeds) and fluid (see, for example, the recent review Rüdiger *et al.*, 2018). We note that the standard MRI is difficult to observe experimentally since sufficiently large magnetic Reynolds numbers are

difficult to attain because of the high levels of magnetic diffusivity in the liquid metals used for experiments. However, the helical MRI, which can be observed experimentally (Stefani *et al.*, 2006), requires much smaller magnetic Reynolds and Hartmann numbers to operate, the latter being the ratio of magnetic forces to viscous forces. Indeed, for Reynolds numbers of $O(10^3)$ and Hartmann numbers of order $O(10)$, helical magnetic field is shown to destabilise centrifugally stable flows (i.e., stable by (1.1)).

1.4 Aims of the Thesis

Inertial instabilities in the terrestrial atmosphere are well understood (e.g., Dunkerton, 1981, 1982, 1983; Griffiths, 2003a,b, 2008a). The instabilities have been observed in the equatorial atmosphere (e.g., Hayashi *et al.*, 1998; Knox, 2003) and ocean (e.g., Richards & Edwards, 2003; d'Orgeville *et al.*, 2004); sufficiently strong shear may also lead to inertial instabilities in the extratropics (e.g., Potylitsin & Peltier, 1998; Shen & Evans, 2002). Thus, it is natural to consider if corresponding instabilities may be realised in stellar and planetary atmospheres (e.g., the solar tachocline, Jupiter and Hot Jupiters), which are, in general, electrically conducting and can therefore support large-scale magnetic fields; indeed, magnetic fields can completely alter, suppress or generate new instabilities (from hydrodynamically stable systems). The Sun, Jupiter and Hot Jupiters provide a clear physical motivation to investigate inertial instabilities in presence of magnetic field, where large shears can be found in the solar tachocline, the zonal bands of Jupiter's upper atmosphere and the intense equatorial jets of Hot Jupiters.

Inertial instabilities are also a planetary analogue of centrifugal instabilities, which are often considered when discussing angular momentum redistribution in accretion discs (e.g., Kuiper, 1941; Shakura & Sunyaev, 1973; Balbus & Hawley, 1991). Thus, with a longstanding interest in this topic, there are many studies related to our research (e.g., Chandrasekhar, 1960; Balbus & Hawley, 1991; Menou *et al.*, 2004). For example, the MRI destabilises centrifugally (inertially) stable flows owing to weak axial magnetic field.

Hence, the aim of this thesis can be summarised into one key statement:

- We investigate if inertial instabilities may be realised in the presence of a vertical magnetic field in stellar and planetary atmospheres, where the effects of background rotation (f-plane or equatorial β-plane), uniform vertical density stratification, uniform vertical diffusion, and the magnetohydrostatic (thin layer) approximation will also be important. The magnetohydrostatic approximation makes the analysis distinct from previous studies, and allows us to investigate the large scale dynamics of stellar and planetary atmospheres.

However, this raises a number of questions:

- Is it possible for magnetic field to destabilise inertially stable flows in a planetary configuration?

- What role will vertical magnetic field play in the inertially unstable regime?

- Will one particular instability dominate the system?

- Can magnetic field further destabilise inertial instability?

- Is it possible that magnetic field will generate new modes, extending the instability domain?

- How will strong magnetic field affect inertially unstable modes?

• How will diffusion affect the system?

- How significantly will inertial and magnetic modes be altered by varying levels of kinematic viscosity, thermal conductivity and magnetic diffusion?

- Under what conditions could these instabilities occur in stellar and planetary atmospheres?

Thus, we choose to consider inertial instabilities in Cartesian geometry and in the presence of vertical magnetic field. Using Cartesian co-ordinates, we study the linear and nonlinear stability of a steady flow, arbitrarily sheared in the horizontal cross-stream direction, in the presence of background rotation, vertical density stratification, vertical magnetic field and diffusion. We seek axisymmetric solutions since it allows us to isolate the effects of pure inertial instability from other possible instabilities that may occur. Under the formulation we derive conditions on the growth rate for arbitrary Coriolis parameter $f(y)$, shear $U'(y)$ and vertical magnetic field $B(y)$. We consider simplified regimes on the f-plane and equatorial β-plane, where we implement uniform shear, shear layers and jets where appropriate; we also incorporate uniform vertical magnetic field B_0 so that analytical progress is possible. We later investigate the effects of diffusion on the system by varying the Prandtl $Pr = \nu/\kappa$ and magnetic Prandtl number $Pm = \nu/\eta$, where ν is the kinematic viscosity, κ is the thermal conductivity and η is the magnetic diffusivity. We also consider the nonlinear evolution of inertial instabilities for a hyperbolic shear profile on a f-plane.

1.5 Outline of the Thesis

In Chapter 2 we derive the equations of motion under various simplifying assumptions, including the magnetohydrostatic approximation (thin layer approximation in the presence of magnetic field), which reduces the vertical momentum equation to a balance between the magnetic pressure and buoyancy. We linearise about the basic state, which allows us to derive a second order ordinary differential equation (ODE) that forms the basis for all subsequent chapters (Chapter 5 also contains nonlinear results). A condition on the validity of the magnetohydrostatic approximation is derived from the ODE; it does not extend trivially from the hydrostatic approximation. A table of estimated parameters, in the Earth's upper stratosphere and lower mesosphere, the solar tachocline and the upper atmospheres of Jupiter and Hot Jupiters, is then provided. Finally, we derive a series of growth rate bounds and stability criteria for an ideal fluid, invoking instabilities generated by weak axial magnetic field (e.g., Velikhov, 1959; Chandrasekhar, 1960; Balbus & Hawley, 1991).

In Chapter 3 we consider the ideal linear stability of a parallel flow with uniform latitudinal shear on an f-plane. Uniform vertical magnetic field strength is now considered in this and all subsequent chapters. The formalisation admits sinusoidal modes in latitude y and height z, where we first discuss the inertial and magnetically modified waves within the system, finding links to the hydromagnetic-inertial waves found in Acheson & Hide (1973), who considered applications to the Earth's core. Turning our interest primarily to the unstable modes, we derive stability criteria, analytically determine the maximum growth rate, and consider the effects of stratification and magnetic field. The analogies to the magnetorotational instability (MRI) of Balbus & Hawley (1991) are discussed. We also consider the dynamical balances of our system in numerous parameter regimes.

In Chapter 4 we extend the linear stability analysis of Chapter 3 to the diffusive system, where we consider the effects of kinematic viscosity, thermal diffusion and magnetic diffusivity. First, we consider the hydrodynamic regime, deriving sufficient and necessary conditions for steady and oscillatory stability. Analogies to the Goldreich-Schubert-Fricke (GSF) instability (Goldreich & Schubert, 1967; Fricke, 1968) are discussed. In the magnetohydrodynamic regime we derive a quintic polynomial for the growth rate. A non-magnetohydrostatic and cylindrical analogue to the quintic can be found in Menou *et al.* (2004); however, the generalisation does not allow for the derivation of many results found in our analysis. We find a necessary and sufficient condition for steady stability (provided the mode is magnetic) independent of wavenumbers. We then consider various constraints on the Prandtl and magnetic Prandtl numbers (e.g., $Pr = \nu/\kappa = Pm = \nu/\eta \neq 1$ or $Pr \ll Pm \ll 1$).

In Chapter 5, we consider the ideal linear stability of a hyperbolic shear layer on an f-plane in the presence of uniform vertical magnetic field strength, which admits localised modes. The linear analysis follows the same structure as Chapter 3. The nonlinear evolution of the system is investigated via numerical simulations with $Pr = 1$. We focus on the mean flow change and the redistribution of the absolute vorticity fQ throughout the latitudinal domain. The most significant redistribution of vorticity and mean flow changes are found to occur in the inertially stable regime, even in the presence of relatively weak magnetic field.

In Chapter 6, we consider the ideal linear stability of a parallel flow with uniform latitudinal shear on an equatorial β-plane in the presence of uniform vertical magnetic field strength. This case is of particular interest given the previous hydrodynamic analysis of this system on an equatorial β-plane (e.g., Dunkerton, 1981, 1982; Griffiths, 2003a,b). We derive a parabolic cylinder equation, which can be solved analytically to yield an eigenvalue relation (reducing to (1.2) of Dunkerton, 1981, in the absence of magnetic field). We discuss inertial and hydromagnetic waves and investigate the unstable domain, deriving asymptotic expansions in the weak and strong field limits. Dynamical balances are then considered in numerous parameter regimes. A jet profile is then considered so that the shear is no longer uniform and unbounded; there are significant changes to the unstable domain.

Chapter 7 extends the linear stability analysis of the jet profile in Chapter 6 to the diffusive regime, where we consider the effects of kinematic viscosity, thermal diffusion and magnetic diffusivity. We follow the structure of Chapter 4; however, on the equatorial β-plane, stability criteria are significantly harder to derive. First, we consider the hydrodynamic regime, which is closely related to the studies of Dunkerton (1982) and Griffiths (2003a, 2008a). We then focus on the magnetohydrodynamic case, where we consider when the magnetic Prandtl number $Pm = \nu/\eta$ or the Prandtl number are unity, when they are equal and when $Pr \ll Pm \ll 1$.

The thesis will end with Chapter 8, where we discuss our results and possible further work.

Chapter 2

The Governing Equations and General Theorems

2.1 Introduction

In this chapter, we provide the framework for which the linear and nonlinear inertial instabilities of stellar and planetary atmospheres are modelled throughout the thesis. This can be split into three main sections: our model and the equations of motion, linearisation of these equations about the basic state, which yields our governing equation, and, finally, general theorems regarding conditions for linear stability, and bounds on the growth rate. Since the thesis contains primarily linear results, we do not further describe the nonlinear framework beyond the equations of motion and their corresponding energetics until Chapter 5.

To derive our equations of motion, we first introduce the magnetohydrodynamic equations for an ideal gas (e.g., Priest, 2012) and seek to simplify these under a number of approximations. Under the planar (Cartesian), Boussinesq, hydrostatic, traditional and axisymmetric approximations, the magnetohydrodynamic equations reduce to the equations of motion that will be used within this thesis. Many of these approximations are typical in geophysical fluid dynamics (see, Salmon, 1998; Vallis, 2017); however, some do not trivially extend to the magnetohydrodynamic regime. In particular, we take care when discussing the magnetic analogues of the Boussinesq and hydrostatic approximations. Throughout the thesis we will be well within the restrictions of these approximations; however, in certain cases, we will approach limits that push the validity of some of these approximations, which we will discuss on a case by case basis.

Under our equations of motion, we then introduce the basic state: a zonal flow $\mathbf{u} = U(y)\mathbf{e}_x$ in the presence of background rotation $f = f(y)$ and vertical field $\mathbf{B} = B_3(y)\mathbf{e}_z$, where x, y and z are the longitudinal, latitudinal and vertical coordinates (with corresponding velocities u, v, w and fields B_x, B_y and B_z). We also include an along-stream field as a part of the basic state however, due to axisymmetry it has no dynamical effect on our system. Linearising about the basic state and seeking normal mode solutions yields a second order ordinary differential equation for the perturbed cross-stream velocity, which is the basis for all linear results throughout

the thesis. The equation is derived with a magnetohydrostatic switch that allows us to easily derive a condition for regarding the use of the magnetohydrostatic approximation, building on the discussion surrounding its validity in Section 2.2. The content of the thesis however will be entirely magnetohydrostatic, except one small excerpt in Chapter 3.

The governing equation allows for the derivation of numerous stability criteria and growth rate bounds for an ideal fluid. These are derived for both the hydrodynamic and magnetohydrodynamic systems, linking to previous results (e.g., Rayleigh, 1917; Chandrasekhar, 1960; Balbus & Hawley, 1991; Griffiths, 2008a). Recalling that the condition $fQ = f(f - U') < 0$ on the absolute vorticity is the Cartesian equivalent of the condition on the Rayleigh Criterion (1.1), we find that the magnetohydrodynamic criteria for stability is found to be less constricting than this hydrodynamic condition on fQ. Indeed, vertical magnetic field allows instability to occur within inertially stable regimes ($fQ > 0$) provided that anti-cyclonic shear is present somewhere in the system ($U'f > 0$). The bound on the growth rate is also found to be less constricting in comparison to the hydrodynamic case.

Finally, we provide a list of parameters (e.g., buoyancy frequency, angular velocity and field strength) for the Earth's lower mesosphere and upper stratosphere (where inertial instability is most likely to occur in the terrestrial atmosphere), the solar tachocline as well as the upper atmospheres of Jupiter and Hot Jupiters. The table includes parameters relevant to both mid-latitude and equatorial atmospheres. We will refer back to these parameters throughout the thesis to give insight in various regimes.

2.2 Approximations to the Magnetohydrodynamic Equations

In standard notation, the magnetohydrodynamic equations for a perfect gas in a rotating system with velocity $\mathbf{u}$, magnetic field $\mathbf{B}$, angular velocity $\mathbf{\Omega}$, density ρ, temperature T and gas pressure p (e.g., Priest, 2012), are

$$\rho \left(\frac{D\mathbf{u}}{Dt} + 2\mathbf{\Omega} \times \mathbf{u} \right) = -\nabla\Pi - \rho\mathbf{g} + \frac{1}{\mu_0}(\mathbf{B} \cdot \nabla)\mathbf{B} + \nabla \cdot \tau, \tag{2.1}$$

$$\frac{D\rho}{Dt} + \rho\nabla \cdot \mathbf{u} = 0, \tag{2.2}$$

$$\rho c_P \frac{DT}{Dt} - \frac{Dp}{Dt} = K\nabla^2 T + \frac{\eta}{\mu_0}(\nabla \times \mathbf{B})^2 + \Phi, \tag{2.3}$$

$$p = R\rho T, \tag{2.4}$$

$$\frac{\partial \mathbf{B}}{\partial t} + (\mathbf{u} \cdot \nabla)\mathbf{B} = (\mathbf{B} \cdot \nabla)\mathbf{u} - (\nabla \cdot \mathbf{u})\mathbf{B} + \eta\nabla^2\mathbf{B}, \tag{2.5}$$

$$\nabla \cdot \mathbf{B} = 0, \tag{2.6}$$

where $\mathbf{e}_z$ is a unit vector in the vertical direction and $\Pi = p + |B|^2/2\mu_0$ is the total pressure. The viscous stress tensor τ and viscous heating $\mathbf{\Phi}$ are given by

$$\tau_{ij} = \mu\left(\partial_i u_j + \partial_j u_i - \frac{2}{3}\delta_{ij}\partial_k u_k\right), \qquad \Phi = \tau_{ij}\partial_i u_j. \tag{2.7}$$

We take the gravitational acceleration g, permeability of free space μ_0, dynamic viscosity μ, thermal conductivity K, magnetic diffusivity η, specific heat at constant volume c_v, specific heat at constant pressure c_p and the gas constant $R = c_p - c_v$ to be uniform.

In order to investigate the inertial instabilities of stellar and planetary atmospheres we simplify the equations (2.1)-(2.6) under various approximations in the following subsections.

2.2.1 The Planar Approximation

In general, it is natural to model planets and stellar interiors with spherical coordinates, where the entire atmospheric domain can be described by the coordinate system. However, this is not always desirable as we may only want to model a specific phenomenon local to one region of the stellar interior or planetary atmosphere, where the added complexity of spherical coordinates is not necessary. Indeed, many waves and instabilities occur in local regions of atmospheres and stellar interiors, including inertial instability. Hence, since we expect the latitudinal lengthscale of inertial instabilities to be much less than the radius of the stellar or planetary atmosphere under consideration, we may neglect the curvature of the star or planet and in turn model the fluid with a local Cartesian system. In the thesis x, y and z are our longitudinal, latitudinal and vertical coordinates. Throughout the thesis we will be well within the restrictions of the planar approximation; however, in certain cases, we will approach limits that push its validity, in particular, when modes become wide (i.e., for modes with large latitudinal lengthscales).

2.2.2 Boussinesq Approximation

The next approximation to the equations (2.1)-(2.6) we will consider is the Boussinesq approximation; initially, we discuss the approximation in the absence of magnetic field (i.e., $\mathbf{B} = \mathbf{0}$), and then extend the discussion to incorporate magnetic field.

The Boussinesq approximation (Boussinesq, 1903) is valid provided the vertical lengthscale of the flow is much less than the scale height of any thermodynamic quantity, and the perturbations in density, temperature and pressure that are induced by the fluid flow do not exceed, in order of magnitude, the total background values of these quantities (e.g., density perturbations $\tilde{\rho}$ are much less than the reference density $\bar{\rho}$ so that $|\tilde{\rho}| \ll \bar{\rho}$). Many geophysical flows are Boussinesq, where the approximation allow us to simplify the full Navier-Stokes equations (equations (2.1)-(2.6) in the absence of magnetic field), as shown in Spiegel & Veronis (1960) and Salmon (1998). Under the Boussinesq approximation, the conservation of mass equation (2.2) reduces to $\nabla \cdot \mathbf{u} = 0$ at leading order, which is the condition for incompressible flow (even though the flow itself could be compressible if so desired). It follows that $\nabla \cdot \tau$ reduces to $\mu \nabla^2 \mathbf{u}$ at leading order, and that Φ, in the thermodynamic equation (2.9), may be neglected. Furthermore, we may neglect density variations except in the buoyancy term of the equation of motion (i.e., we may write ρ as the reference density $\bar{\rho}$ in equation (2.1), except in the $\rho \mathbf{g}$ term). Finally, perturbations in density that are induced by motion result primarily from thermal (as opposed to pressure) effects; thus, density perturbations are directly proportional to perturbations in temperature. Hence, by perturbing the

thermodynamic equation (2.3) such that p, ρ and T take the form $q = \bar{q} + q_0(z) + \tilde{q}$, with reference state $\bar{q}$, initial background state $q_0(z)$ and perturbation $\tilde{q}$, we obtain

$$\left(\frac{D\tilde{\rho}}{Dt} + \tilde{w}\frac{d\rho_0}{dz} \right) - \frac{\rho c_v}{p c_p}\left(\frac{D\tilde{p}}{Dt} + \tilde{w}\frac{dp_0}{dz} \right) = \frac{K}{c_p \bar{\rho}}\nabla^2 \tilde{\rho}, \tag{2.8}$$

where have written $\bar{\rho}\tilde{T} = -\bar{T}\tilde{\rho}$, and used the ideal gas law on the first and final terms of (2.3). Then, following Salmon (1998), we may neglect $D\tilde{p}/Dt$ provided the flow is hydrostatic (or, more generally, provided buoyancy effects are at least comparable with those of inertia). Thus, using the vertical component of (2.1) in the absence of motion, so that $dp_0/dz = -(\bar{\rho} + \rho_0)g$, we obtain

$$\frac{D\tilde{\rho}}{Dt} - \tilde{w}\frac{\bar{\rho}N^2(z)}{g} = \kappa\nabla^2\tilde{\rho}, \tag{2.9}$$

where κ is the thermal diffusivity and

$$N^2(z) = -\frac{g}{\bar{\rho}}\left(\frac{d\rho_0}{dz} + \frac{(\bar{\rho} + \rho_0)g}{c^2} \right) \tag{2.10}$$

is the squared Brunt-Väisälä frequency and $c^2 = \bar{p}c_p/c_v\bar{\rho}$.

We want to ensure the validity of the Boussinesq approximation in the presence of magnetic field. There are numerous studies on this delicate topic, and following these we will incorporate magnetic field in to the Boussinesq equations in the standard manner (e.g., Chandrasekhar, 1961; Proctor & Weiss, 1982) — the so-called equations of Boussinesq magnetoconvection. Indeed, magnetic field does not have any bearing on the thermodynamics of the system so that density perturbations are still proportional to those of temperature. We may also neglect Ohmic heating so that the thermodynamic equation (2.3) still reduces to (2.9) in the presence of magnetic field. We note that under this variation of the approximation the effects of magnetic buoyancy are no longer present. Incorporating magnetic buoyancy into the Boussinesq approximation is described by Spiegel & Weiss (1982), Bowker *et al.* (2014) and Wilczyński *et al.* (2022).

2.2.3 Magnetohydrostatic Approximation

Many geophysical flows have a small aspect ratio; that is, the horizontal lengthscale L is much larger than the vertical lengthscale H. This allows for the derivation, via a simple scaling argument (e.g., Vallis, 2017) of the hydrostatic approximation; it is an asymptotic model for the Navier-Stokes equations, where the vertical momentum equation reduces to a balance between the pressure gradient and gravitational forces. In the terrestrial atmosphere, the approximation is widely used in meteorology and oceanography. In particular, observations of inertial instabilities in the equatorial stratosphere and mesosphere with a vertical wavelength of $\sim 10\text{km}$ and latitudinal lengthscale of about $\sim 30°$ (into the winter hemisphere) or, equivalently, $\sim 3000\text{km}$ (Hitchman *et al.*, 1987; Hayashi *et al.*, 1998; Smith & Riese, 1999). Thus, since the latitudinal lengthscale is two orders of magnitude larger than the vertical lengthscale, we can certainly justify the use of the hydrostatic approximation when investigating inertial instability in the terrestrial atmosphere.

We want to ensure the validity of the hydrostatic approximation in the presence of magnetic field. That is, given that a magnetohydrodynamic flow has a small aspect ratio, is it possible to show that the vertical momentum equation reduces to a balance between the magnetic pressure gradient and gravitational forces, and if any additional assumptions are required. Thus, we consider the perturbed quantities of (2.5) under the Boussinesq approximation (after dropping the tildes introduced previously for perturbed quantities):

$$\bar{\rho}\left(\frac{Dw}{Dt} - 2\Omega u \cos\theta\right) = -\frac{\partial\Pi}{\partial z} - \rho g + \frac{1}{\mu_0}(\mathbf{B}\cdot\nabla)b_z + \mu\nabla^2 w, \tag{2.11}$$

where θ is the latitude, b_z is the z component of the perturbed magnetic field, and each term is of the following order

$$O\left(\frac{\bar{\rho}W}{T}\right) \quad O\left(\frac{\bar{\rho}\hat{\Omega}LW}{H}\right) \quad O\left(\frac{\hat{\Pi}}{H}\right) \quad O\left(\hat{\rho}g\right) \quad O\left(\frac{\hat{B}_z^2}{\mu_0 H}\right) \quad O\left(\frac{\mu W}{H^2}\right),$$

respectively. Here, L, H, $\hat{\Omega}$ and T are the horizontal lengthscale (in the longitudinal and latitudinal directions), vertical lengthscale, rotation frequency and timescale of the fluid motion, respectively. The quantities W, $\hat{\Pi}$ and $\hat{B}_z$ are the characteristic perturbations of vertical velocity, total pressure and vertical magnetic field, respectively. We have used the incompressibility and magnetic sinusoidal condition in (2.2.3) to write the horizontal velocities and fields in terms of their respective vertical components (e.g., $\nabla\cdot\mathbf{u} = 0$ implies $U \sim V \sim LW/H$, where U and V are the characteristic perturbed longitudinal and vertical velocities).

In the horizontal momentum equations (2.1) we scale the acceleration, advection, rotation, pressure and diffusive terms with the Lorentz force, arguing that the Lorentz force must be a part of the leading order balance to be dynamically significant. If this was not the case, given a small aspect ratio, (2.11) would reduce to the hydrostatic balance (cf. Vallis, 2017). By denoting $\Gamma \sim \hat{B}_z^2/\mu_0 H$, it follows that $T^{-1} \sim \Gamma/\bar{\rho}W$, $\hat{\Omega} \sim \Gamma/\bar{\rho}W$, $\hat{\Pi} \sim \Gamma L^2/H$, and $\mu \sim \Gamma H^2/W$. Note that, aside from the pressure gradient, the corresponding terms would be trivially negligible in (2.11) if they were not a part of the leading order balance (i.e., the scalings give the maximum value of each quantity given magnetic field is dynamically significant).

Hence, the vertical acceleration, Coriolis, pressure, Lorentz, and diffusive terms in equation (2.11) have the following ordering

$$\bar{\rho}\frac{Dw}{Dt} \sim \Gamma, \quad 2\bar{\rho}\Omega u \cos\theta \sim \frac{L}{H}\Gamma, \quad \frac{\partial\Pi}{\partial z} \sim \frac{L^2}{H^2}\Gamma, \quad \frac{1}{\mu_0}(\mathbf{B}\cdot\nabla)B_z \sim \Gamma \text{ and } \mu\nabla^2 w \sim \Gamma. \tag{2.12}$$

Thus, if we now assume a small aspect ratio, so that $H/L \ll 1$, it follows that all terms except the buoyancy term in (2.11) are at least of order L/H smaller than the pressure gradient and are therefore negligible. This yields a balance between the pressure gradient and buoyancy term to leading order in equation (2.11) — the so-called magnetohydrostatic balance.

However, crucially, the total pressure may not necessarily scale with the Lorentz force in the horizontal momentum equations (2.1), perhaps interfering with the magnetohydrostatic balance.

Note that under this assumption $\Pi/H \ll \Gamma L^2/H^2$, and thus (2.11) may still reduce to magneto-hydrostatic balance since the second order term in (2.12)) is $O(L\Gamma/H)$. Hence, for the magneto-hydrostatic approximation to be valid, we require $L\Gamma/H \ll \hat{\rho}g \; (\sim \hat{\Pi}/H)$. Scaling ρ via the thermodynamic equation (2.9) under the Boussinesq approximation, it follows that $\hat{\rho}g \sim \bar{\rho}^2 \bar{N}^2 W^2/\hat{\Gamma}$, where $\bar{N}$ is the scale of the buoyancy frequency (2.10). Thus, the condition $L\Gamma/H \ll \hat{\rho}g$ implies that $\bar{\rho}^2 \bar{N}^2 W^2 H/L \gg \Gamma^2 = \hat{B}_z^4/H^2\mu_0^2$, and we therefore require that the magnetic field cannot be too strong for the magnetohydrostatic approximation to remain valid.

Hence, under the assumptions that the aspect ratio is small, and the magnetic field strength is not too strong, it follows that the vertical momentum equation (2.11) reduces to the magnetohydrostatic balance. This is consistent with the assumptions used to derive the magnetohydrostatic approximation in Deluca & Gilman (1986) and Gilman (2000).

We can also derive an alternative assumption to that of a small aspect ratio. To illustrate this, we assume that the magnetohydrostatic approximation is valid, and scale ρ via the thermodynamic equation (2.9), so that for the pressure gradient to scale with the buoyancy term in (2.11), we require $L^2/H^2 \sim \bar{N}^2 T^2$. Hence, assuming a small aspect ratio ($H/L \ll 1$) is equivalent to taking $\bar{N}^2 T^2 \gg 1$, and one could therefore derive the magnetohydrostatic approximation from the latter (instead of assuming $H/L \ll 1$). The condition $\bar{N}^2 T^2 \gg 1$ is seen later when deriving a condition from our governing equation to determine the validity of the magnetohydrostatic approximation; it is then used on a case by case basis throughout the thesis to ensure that the size of the neglected terms in (2.11) remain negligible compared to the pressure gradient and buoyancy term.

2.2.4 The Coriolis Parameter and the Traditional Approximation

The planar approximation and the use of the Cartesian system have consequences for how we consider rotation. Given that a planet or star rotates at an angular velocity Ω, then at a given latitude θ, its components are $\boldsymbol{\Omega} = (0, \Omega\cos\theta, \Omega\sin\theta)$. To simplify our argument, we assume the geocentric and geodetic latitudes are equal (i.e., the normal to the surface at the latitude we are considering passes through the centre of the planet or star). Thus, the Coriolis acceleration is $2\boldsymbol{\Omega} \times \mathbf{u} = 2\Omega(w\cos\theta - v\sin\theta, u\sin\theta, -u\cos\theta)$. This is the full form of the Coriolis acceleration in the Cartesian model; however, in many cases we can simplify this to $2\boldsymbol{\Omega} \times \mathbf{u} = 2\Omega(-v\sin\theta, u\sin\theta, 0)$ — the so-called traditional approximation. It is useful to write the Coriolis acceleration in terms of the Coriolis parameter $f = 2\Omega\sin\theta_0$, yielding $2\boldsymbol{\Omega} \times \mathbf{u} = (-fv, fu, 0)$.

The traditional approximation is widely used in the study of the terrestrial atmosphere and oceans. That is, the cosine terms in full Coriolis acceleration are neglected (i.e., vertical induced motions from the Coriolis force are neglected). The approximation is justified via the assumption that the depth of the layer of atmosphere (or ocean) is small compared to the radius of the planet. For inertial instability in the terrestrial atmosphere, which occurs in the upper stratosphere and lower mesosphere with a vertical lengthscale ~ 10km, this condition is certainly satisfied since the radius of Earth is $6,371$km. Thus, the horizontal motion of fluid must be much more significant than that of the vertical, implying that the cosine components of the full Coriolis acceleration are

negligible. Indeed, we can immediately neglect $w \cos \theta$ in the x component of $2\mathbf{\Omega} \times \mathbf{u}$ since $w \sim Hv/L$ with $H/L \ll 1$. Similarly, we may neglect $-u \cos \theta$ since it is negligible in comparison to the dominant terms in the vertical momentum equation (see Tritton, 2012, for a similar derivation).

Note that under the traditional approximation the condition on the magnetic field strength not being too strong for the magnetohydrostatic approximation to be valid reduces to $\bar{\rho}^2 \bar{N}^2 W^2 \gg \Gamma^2 = \hat{B}_z^4 / H^2 \mu_0^2$ since the second order term in (2.11) becomes $O(\Gamma)$ rather than $O(\Gamma L/H)$. We will later derive an analogous condition in a following subsection.

Alternatively, we note that under the magnetohydrostatic approximation we must also take the traditional approximation. Indeed, the magnetohydrostatic approximation implies that we must neglect the cosine term in the x component of $2\mathbf{\Omega} \times \mathbf{u}$ since $w \sim Hv/L$ with $H/L \ll 1$; furthermore, to conserve the energy of the system, we must also neglect $-u \cos \theta$.

The use of the traditional approximation close to the equator is questionable (Veronis, 1968; Gerkema *et al.*, 2008) since the cosine term in the x component of $2\mathbf{\Omega} \times \mathbf{u}$ will be comparable to $w \sin \theta$ provided θ is sufficiently small. However, we may argue that the traditional approximation remains appropriate at the equator since stratification and kinematic viscosity dampen the vertical deflection of fluid by the Coriolis force. Further justification is found in Griffiths (2008a), where the traditional approximation is valid at the equator provided $f \ll N$, which is the case for geophysical flows. However, the approximation still breaks down as the horizontal lengthscale L approaches zero; this is only of mathematical significance (rather than physical) since the most unstable mode for inviscid inertial instability has latitudinal lengthscale $L \propto 1/H^{1/2}$ for vanishing vertical scales, thus satisfying the condition for validity.

Throughout the thesis we will use the f-plane and equatorial β-plane approximations, which are standard under the planar and traditional approximations (see Vallis, 2017). These are derived by Taylor expanding $\sin \theta$ about a given latitude θ_0.

2.2.5 Axisymmetric Assumption

The axisymmetric assumption may be applied when a given fluid flow is weakly dependent on a coordinate (i.e., the fluid flow is almost identical when this coordinate is varied). In our Cartesian system we assume an axisymmetric basic state and axisymmetric perturbations about it, both in the longitudinal direction x. Thus, we may neglect all derivatives with respect to longitude x, simplifying our governing equations (2.14)-(2.18). Physically, we may justify this choice of basic state since many astrophysical flows are approximately axisymmetric. Indeed, seismological observations suggest the latitudinal and vertical shear in the Solar tachocline varies weakly with longitude; Jupiter's surface jet streams are clearly approximately axisymmetric. Observations of Hot Jupiters also allow us to infer that their extreme equatorial jets can span the entire day-side of the planet, implying that the fluid flow varies slowly with longitude. In terms of inertial instabilities in the terrestrial atmosphere, observations suggest inertial instabilities are approximately axisymmetric (longitudinally) in nature (having small zonal wavenumbers) as seen in figure 1.4.

Regarding axisymmetric perturbations, the most unstable mode of inertial instabilities are axisymmetric provided the vertical wavenumber $k \to \infty$ (i.e., vanishing vertical scale) and the system is inviscid (Griffiths, 2008a). However, note that the most unstable inertial instability mode need not be axisymmetric in the presence of diffusion. Taking axisymmetric perturbations also allows us to study inertial instability without interference of competing modes such as the strato-rotational instability which may occur only in a non-axisymmetric system.

2.3   Equations of Motion and the Basic State

We consider a set of Cartesian coordinates, with horizontal along-stream coordinate x, cross-stream coordinate y and vertical-stream coordinate z, with corresponding velocity $\mathbf{u} = (u, v, w)$ and magnetic field $\mathbf{B} = (B_x, B_y, B_z)$. We examine an incompressible, axisymmetric and diffusive flow with basic state $\mathbf{u} = (U(y), 0, 0)$ and $\mathbf{B} = (B_1(y), 0, B_3(y))$. The choice of $\mathbf{B}$ is motivated from the studies discussed in Chapter 1; in particular, vertical magnetic field is shown to have significant dynamical effects. The choice of $\mathbf{u} = U(y)\mathbf{e}_x$ is motivated by the zonal jets found in many astrophysical bodies (e.g., Jupiter and Hot Jupiters). We also suppose the fluid is stratified and assume the Boussinesq approximation is valid, where the constant buoyancy frequency N is linked to the initial density stratification $\rho_0(z)$ and reference density $\bar{\rho}$ via

$$N^2 = -\frac{g}{\bar{\rho}}\frac{d\rho_0}{dz}, \tag{2.13}$$

where g is the gravitational acceleration. Hence, the magnetohydrodynamic equations for a perfect gas (2.1)-(2.6) reduce to:

$$\frac{Du}{Dt} - fv = \frac{1}{\mu_0\bar{\rho}}(\mathbf{B}\cdot\nabla)B_x + \nu\nabla^2 u, \tag{2.14}$$

$$\frac{Dv}{Dt} + fu = -\frac{1}{\bar{\rho}}\frac{\partial\Pi}{\partial y} + \frac{1}{\mu_0\bar{\rho}}(\mathbf{B}\cdot\nabla)B_y + \nu\nabla^2 v, \tag{2.15}$$

$$\frac{\partial\Pi}{\partial z} = -\rho g + \mathcal{H}\left(\frac{1}{\mu_0\bar{\rho}}(\mathbf{B}\cdot\nabla)B_z + \nu\nabla^2 w - \frac{Dw}{Dt}\right), \tag{2.16}$$

$$\frac{D\rho}{Dt} + w\frac{d\rho_0}{dz} = \kappa\nabla^2\rho, \ \nabla\cdot\mathbf{u} = 0, \tag{2.17}$$

$$\frac{\partial\mathbf{B}}{\partial t} + (\mathbf{u}\cdot\nabla)\mathbf{B} = (\mathbf{B}\cdot\nabla)\mathbf{u} + \eta\nabla^2\mathbf{B} \ \text{and} \ \nabla\cdot\mathbf{B} = 0, \tag{2.18}$$

where $f = f(y)$ is the Coriolis parameter due to background rotation, $\Pi(y, z, t)$ is the perturbed total pressure, $\rho(y, z, t)$ is the density perturbation, ν is the kinematic viscosity, η is the magnetic diffusivity, κ is the thermal conductivity. The parameter $\mathcal{H}$, which takes the value 0 or 1, acts as a switch to determine whether the system is magnetohydrostatic ($\mathcal{H} = 0$) or not ($\mathcal{H} = 1$). We will be primarily addressing the magnetohydrostatic system ($\mathcal{H} = 0$), thus, making an obvious connection to hydrostatic results for geophysical flows (Dunkerton, 1981, 1982; Griffiths, 2003a,b, 2008a). However, the validity of the magnetohydrostatic approximation does not trivially extend from the hydrostatic approximation, which is valid provided the horizontal lengthscale is much

larger than the vertical lengthscale (as is the case in planetary atmospheres). Therefore, we examine the validity of the approximation on a case by case basis; we will shortly derive a condition for the validity after linearising the system.

The basic state $\mathbf{u} = (U(y), 0, 0)$ and $\mathbf{B} = (B_1(y), 0, B_3(y))$ satisfies equations (2.14)-(2.18) provided that

$$f(y)U(y) = -\frac{1}{\bar{\rho}}\frac{\partial \Pi_0}{\partial y}, \qquad (2.19)$$

where is the basic state of the total pressure perturbation. Hence, the basic state is geostrophic balance in the latitudinal direction.

2.3.1 Energetics

The evolution of energy of the system (2.14) - (2.18) is of particular importance when considering the nonlinear evolution of the system in Chapter 5. The rate of change of the total energy E, the derivation of which is given in Appendix A, is given by

$$\frac{dE}{dt} = \frac{d}{dt}\int_V \left(\frac{1}{2}\bar{\rho}|\mathbf{u}|^2 + \frac{1}{2}\frac{g^2}{\bar{\rho}N^2}\rho^2 + \frac{1}{2\mu_0}|\mathbf{B}|^2\right)dV = -\mu\int_V |\omega|^2\,dV$$
$$- \frac{g^2\kappa}{\bar{\rho}N^2}\int_V |\nabla\rho|^2\,dV - \frac{1}{\sigma}\int_V |\mathbf{j}|^2 dV, \quad (2.20)$$

where $\omega = \nabla \times \mathbf{u}$ is the local vorticity, $\sigma = 1/\mu_0\eta$ is the electrical conductivity, $\mathbf{j} = \mu_0^{-1}(\nabla \times \mathbf{B})$ is the current. Note that in the derivation it is shown that the magnetic energy lost owing to the rate of working of the Lorentz force is balanced by the rate of kinetic energy gained from the working of the Lorentz force on the flow. We can also note that since the system is axisymmetric, the volume and surface integrals in equation (2.20) can be equivalently written as surface and line integrals, respectively.

2.4 Linearisation, Normal Modes and the Governing Equation

In general, the nonlinear equations (2.14)-(2.18) must be solved numerically in order to gain insight into the dynamical system. However, linear stability analysis allows us to neglect the nonlinear terms and progress analytically by considering small perturbations around the basic state. It is a fundamental tool for the investigation of geophysical and astrophysical flows; it allows us to determine stability criteria, maximum growth rates, the form of the disturbances as well as their role within the system. Indeed, most results in the thesis are derived using linear stability analysis.

Hence, we linearise the governing equations (2.14)-(2.18) via perturbations to the velocity, magnetic field, pressure and density, where we seek solutions of the following form:

$$(\tilde{\mathbf{u}}, \tilde{\mathbf{b}}, \tilde{\theta}, \tilde{\rho}) = \text{Re}\left((\hat{\mathbf{u}}(y), \hat{\mathbf{b}}(y), \hat{\theta}(y), \hat{\rho}(y))e^{ikz+st}\right), \qquad (2.21)$$

where $\tilde{\theta}$ is defined as the perturbation to the total pressure divided by the reference density $\bar{\rho}$, k is the vertical wavenumber and s is the growth rate. Under this formulation, (2.14)-(2.18) reduce to the following system of linear equations (where all superscripts have been dropped):

$$(s + \nu k^2)u - Qv = \frac{1}{\mu_0 \bar{\rho}} \left(\frac{dB_1}{dy} b_y + ik B_3 b_x \right), \quad (2.22)$$

$$(s + \nu k^2)v + fu = -\frac{d\theta}{dy} + \frac{ik B_3}{\mu_0 \bar{\rho}} b_y, \quad (2.23)$$

$$(s + \kappa k^2)\theta + \left(\frac{N^2}{k^2} + \frac{\mathcal{H}(s + \kappa k^2)}{k^2} \left(\frac{k^2 v_A^2}{s + \eta k^2} + s + \nu k^2 \right) \right) \frac{dv}{dy} = 0, \quad (2.24)$$

$$(s + \eta k^2)b_x + \frac{dB_1}{dy}v = \frac{dU}{dy} b_y + ik B_3 u, \quad (2.25)$$

$$(s + \eta k^2)b_y = ik B_3 v, \quad (2.26)$$

where b_x and b_y are the along-stream and cross-stream components of the magnetic field. Note that we neglected the horizontal component of the diffusive terms since a small aspect ratio (magnetohydrostatic approximation) implies $d^2/dy^2 \ll k^2$ as the latitudinal lengthscale is much larger than the vertical lengthscale. Recall that $Q = f - U'$ is the vorticity, where U' represents the y derivative of U. Equation (2.24) is derived from combining the z component of the momentum equation (2.16), the thermodynamic equation and the conservation of mass (2.17) as well as the definition of the buoyancy frequency (2.13). We later consider these equations (in various limits) when discussing dynamical balances.

Combining equations (2.22), (2.23), (2.24), (2.25) and (2.26) yields a second order governing equation for the perturbed cross-stream velocity, given by

$$\frac{(s + \eta k^2)}{(s + \kappa k^2)} \left(\frac{N^2}{k^2} + \frac{\mathcal{H}(s + \kappa k^2)}{k^2} \left(\frac{k^2 v_A^2}{s + \eta k^2} + s + \nu k^2 \right) \right) \frac{d^2 v}{dy^2} +$$
$$\left(\frac{k^2 v_A^2 U' f - fQ(s + \eta k^2)^2 - ((s + \nu k^2)(s + \eta k^2) + k^2 v_A^2)^2}{(s + \nu k^2)(s + \eta k^2) + k^2 v_A^2} \right) v = 0, \quad (2.27)$$

where $v_A^2(y) = B_3^2(y)/(\bar{\rho}\mu_0)$ is the square of the Alfvén wave speed. We suppose the flow is in a bounded domain, with the boundary conditions

$$v = 0 \text{ at } y = \pm y_b. \quad (2.28)$$

Clearly, the along-stream field does not affect the dynamics or stability of the flow, since the governing equation (2.27) is independent of $B_1(y)$. This is unlike the cylindrical problem, in which, as a consequence of field line curvature, azimuthal field can play an important role in axisymmetric systems (e.g., Michael, 1954; Vandakurov, 1972). This is also the case for the azimuthal component of helical field in axisymmetric flows; thus, instabilities that depend on both components of field in combination can not occur within our system.

We can see that making the magnetohydrostatic approximation (i.e., setting $\mathcal{H} = 0$ in (2.27)) will be valid provided that

$$\left| (s + \kappa k^2) \left(\frac{k^2 v_A^2}{s + \eta k^2} + s + \nu k^2 \right) \right| \ll N^2. \quad (2.29)$$

It is clear that if the hydrostatic approximation for $v_A = 0$ is valid ($|(s + \kappa k^2)(s + \nu k^2)| \ll N^2$), then we can not trivially deduce the validity of the magnetohydrostatic approximation. We have

already discussed this in (2.2.3) and shown that the magnetohydrostatic approximation is valid provided that the magnetic field is not too strong. Indeed, in the absence of diffusion (2.29) reduces $k^2 v_A^2 \ll N^2$ and requires that the magnetic field is not too strong. To ensure the validity of the approximation throughout the thesis the condition (2.29) will be checked on a case by case basis. For example, for inviscid inertial modes with $s^2/f^2 = O(1)$, (2.29) will be satisfied provided $f^2 \ll N^2$ (as is usually assumed in planetary atmospheres owing to the presence of thin strongly stratified flows) and $k^2 v_A^2 \ll N^2$. The latter condition implies that the magnetohydrostatic approximation may break down in the large field or large vertical wavenumber limit. However, linking to the vanishing vertical wavelength ($|k| \to \infty$) of the most unstable modes of inertial instabilities in inviscid systems (e.g., Dunkerton, 1981; Griffiths, 2008a), it is possible to satisfy $k^2 v_A^2 \ll N^2$ with $|k| \to \infty$ provided the field strength is sufficiently weak so that $v_A^2 \ll N^2/k^2$.

Assuming the flow is magnetohydrostatic (i.e., the condition (2.29) holds) the second order governing equation (2.27) reduces to

$$
\frac{N^2(s + \eta k^2)}{k^2(s + \kappa k^2)}((s + \nu k^2)(s + \eta k^2) + k^2 v_A^2)\frac{d^2 v}{dy^2} +
$$
$$
(k^2 v_A^2 U' f - fQ(s + \eta k^2)^2 - ((s + \nu k^2)(s + \eta k^2) + k^2 v_A^2)^2)v = 0. \quad (2.30)
$$

In the absence of magnetic field and diffusion, equation (2.30) reduces to equation (1.3) in Griffiths (2008a). The governing equations (2.27) and (2.30) taken with the boundary conditions (2.28) will form the basis of our linear results. We will apply (2.27) and (2.30) to problems on the f-plane and equatorial β-plane, using analytical and numerical methods to drive results regarding inertial, magnetic and hybrid instabilities that depend upon inertial and magnetic effects.

2.5 Stability Criteria for an Ideal Fluid

In this section, we derive a number of stability conditions and growth rate bounds for an ideal fluid with flow $U(y)$ and Coriolis parameter $f(y)$. To derive these results we consider the magnetohydrostatic ($\mathcal{H} = 0$) system only; the non-magnetohydrostatic system is used only for one small excerpt in Chapter 3, for which stability results are not required. Note that we still provide a non-magnetohydrostatic ideal governing equation to clearly illustrate the condition for magnetohydrostatic approximation to be valid. We initially derive solutions for magnetic field $B_3(y)$ that depends on latitude, before restricting attention to the case of uniform field B_0; the latter case allows for the derivation of a stronger stability condition.

In the absence of diffusion, the second order governing equation (2.27) reduces to

$$
(N^2 + \mathcal{H}(s^2 + k^2 v_A^2))\frac{d^2 v}{dy^2} - k^2 \left(s^2 + k^2 v_A^2 + fQ - \frac{k^2 v_A^2 f^2}{s^2 + k^2 v_A^2} \right) v = 0, \quad (2.31)
$$

from which it follows that the magnetohydrostatic approximation is valid provided that

$$
\left| s^2 + k^2 v_A^2 \right| \ll N^2. \quad (2.32)
$$

The second order governing equation (2.31) with $\mathcal{H} = 1$ (non-magnetohydrostatic) is the Cartesian analogue of (1.9) of Chandrasekhar (1960). Then, assuming (2.32) holds, (2.31) becomes

$$\frac{d^2 v}{dy^2} - \frac{k^2}{N^2}\left(s^2 + k^2 v_A^2 + fQ - \frac{k^2 v_A^2 f^2}{s^2 + k^2 v_A^2}\right) v = 0. \tag{2.33}$$

This is the ideal analogue of equation (2.30) and is thus the governing equation for all of our ideal results throughout the thesis, including the stability criteria derived in the following subsections.

2.5.1 Magnetic Field as a Function of Latitude

In the case for magnetic field depending upon latitude, equation (2.33) allows for the derivation of numerous stability conditions as well as a hydrodynamic and magnetohydrodynamic bound on the growth rate s.

First, we prove that s^2 must be real. Multiplying (2.33) by the complex conjugate of v, v^*, integrating over the domain and applying the boundary conditions (2.28) gives

$$\frac{N^2}{k^2}\int_{-y_b}^{+y_b}|v'|^2 dy + \int_{-y_b}^{+y_b}(s^2 + fQ + k^2 v_A^2)|v|^2 dy - \int_{-y_b}^{+y_b}\frac{k^2 v_A^2 f^2}{k^2 v_A^2 + s^2}|v|^2 dy = 0. \tag{2.34}$$

Then, the imaginary part of (2.34), after multiplying the numerator and denominator of the final term by $-(k^2 v_A^2 + s^{*2})$ becomes

$$\mathrm{Im}(s^2)\left(\int_{-y_b}^{+y_b}|v|^2 dy + \int_{-y_b}^{+y_b}\frac{k^2 v_A^2 f^2}{|k^2 v_A^2 + s^2|^2}|v|^2 dy\right) = 0. \tag{2.35}$$

Hence, as the quantity multiplying $\mathrm{Im}(s^2)$ in (2.35) is always positive, it follows that $\mathrm{Im}(s^2) = 0$. Therefore, in the absence of diffusion, unstable modes $(\mathrm{Re}(s) > 0)$ are not oscillatory.

We now derive hydrodynamic and magnetohydrodynamic bounds on the growth rate. These require conditions on the Coriolis parameter $f(y)$ and shear $U'(y)$ to be satisfied. Reconsidering (2.34), it follows that

$$s^2\int_{-y_b}^{+y_b}|v|^2 dy = \int_{-y_b}^{+y_b}\left(\frac{k^2 v_A^2 f^2}{k^2 v_A^2 + s^2} - k^2 v_A^2 - fQ\right)|v|^2 dy - \frac{N^2}{k^2}\int_{-y_b}^{+y_b}|v'|^2 dy. \tag{2.36}$$

Restricting ourselves first to the hydrodynamic case ($v_A = 0$), equation (2.36) reduces to

$$s^2\int_{-y_b}^{+y_b}|v|^2 dy = -\int_{-y_b}^{+y_b}fQ|v|^2 dy - \frac{N^2}{k^2}\int_{-y_b}^{+y_b}|v'|^2 dy, \tag{2.37}$$

so that the sufficient and necessary condition for hydrodynamic stability is that

$$\frac{N^2}{k^2}\int_{-y_b}^{+y_b}|v'|^2 dy + \int_{-y_b}^{+y_b}fQ|v|^2 dy > 0. \tag{2.38}$$

Thus, as the first term in (2.38) is always positive, it follows that if $fQ > 0$ everywhere in flow, then the hydrodynamic system is stable. Equivalently, a necessary condition for hydrodynamic instability is that $fQ < 0$ somewhere in the flow.

Therefore, assuming $fQ < 0$ somewhere in the flow (so that instability is possible) we reconsider equation (2.37) to derive a growth rate bound for the hydrodynamic system. Removing the negative definite term from (2.37) yields

$$s^2 \int_{-y_b}^{+y_b} |v|^2 dy < - \int_{-y_b}^{+y_b} fQ|v|^2 dy. \qquad (2.39)$$

Then, assuming $fQ < 0$ somewhere in the flow, it follows from (2.39) that any unstable mode (if one exists) obeys

$$s^2 < -\min(fQ), \qquad (2.40)$$

so that the growth rate squared must satisfy $s^2 < \max(-fQ)$ as seen previously in Griffiths (2008a).

In the magnetohydrodynamic regime, equation (2.36) does not reduce as easily as in the hydrodynamic case. This is due to the growth rate being contained within the denominator of the first term of the integrand on right hand side of (2.36). Writing $fQ = f^2 - U'f$ in (2.36), collecting the f^2 terms and then removing all negative definite terms from the right hand side of (2.36) yields

$$s^2 \int_{-y_b}^{+y_b} |v|^2 dy < \int_{-y_b}^{+y_b} \left(U'f - \frac{s^2 f^2}{k^2 v_A^2 + s^2} \right) |\hat{v}|^2 dy. \qquad (2.41)$$

Hence, on rearranging (2.41), we obtain

$$s^2 \int_{-y_b}^{+y_b} \left(1 + \frac{f^2}{k^2 v_A^2 + s^2} \right) |\hat{v}|^2 dy < \int_{-y_b}^{+y_b} U'f|\hat{v}|^2 dy. \qquad (2.42)$$

Thus, assuming the system is unstable so that $s^2 > 0$, we can divide (2.42) by the integral on the left hand side to obtain

$$s^2 < \int_{-y_b}^{+y_b} U'f|\hat{v}|^2 dy \left/ \int_{-y_b}^{+y_b} \left(1 + \frac{f^2}{k^2 v_A^2 + s^2} \right) |\hat{v}|^2 dy \right. . \qquad (2.43)$$

Hence, since the denominator on the right hand side of (2.43) is positive we can deduce, by contradiction, that the system is stable provided we have cyclonic shear ($U'f < 0$) everywhere. Therefore, a necessary condition for instability is that anti-cyclonic shear ($U'f > 0$) occurs somewhere in the flow.

Hence, given anti-cyclonic shear somewhere in the flow so that the assumption $s^2 > 0$ is satisfied, equation (2.43) implies

$$s^2 < \int_{-y_b}^{+y_b} U'f|\hat{v}|^2 dy \left/ \int_{-y_b}^{+y_b} |\hat{v}|^2 dy \right. . \qquad (2.44)$$

Therefore, given anti-cyclonic shear ($U'f > 0$) somewhere in the flow, then any unstable mode (if one exists) obeys

$$s^2 < \max(U'f). \qquad (2.45)$$

Comparing the MHD results to that of the hydrodynamic regime, we found that a necessary condition for instability in the MHD regime is that $U'f > 0$ somewhere in the domain, which is less restrictive than the necessary hydrodynamic condition for instability, that $fQ < 0$ somewhere

in domain. This becomes clear when writing $fQ = f^2 - U'f > -U'f$, which clearly implies that $U'f > 0$ is required for $fQ < 0$. Secondly, we have derived that the magnetohydrodynamic growth rate squared is bounded by the maximum of $U'f$, which is again a less restrictive condition than that of the hydrodynamic regime which bounds s^2 by the maximum of $-fQ$. Comparisons may be made with the magnetorotational instability (e.g., Velikhov, 1959; Chandrasekhar, 1960; Balbus & Hawley, 1991), where instabilities are generated by weak vertical field; indeed, the condition (2.45) is analogous to the maximum growth rate (1.12) of Balbus & Hawley (1991). However, one must note that the results of this section do not prove that an MRI occurs within the system, but, instead, allow for the existence of such an instability.

2.5.2 Uniform Magnetic Field

In this section we consider uniform vertical magnetic field $B_3 = B_0$. This allows for the derivation of a stronger condition for magnetohydrodynamic stability than in the previous section; it is both necessary and sufficient. Multiplying (2.34) by $s^2 + k^2 v_A^2$ (which is now constant) and rearranging gives

$$s^4 \int_{-y_b}^{+y_b} |v|^2 dy + s^2 \left(\frac{N^2}{k^2} \int_{-y_b}^{+y_b} |v'|^2 dy + 2k^2 v_A^2 \int_{-y_b}^{+y_b} |v|^2 dy + \int_{-y_b}^{+y_b} fQ|\hat{v}|^2 dy \right)$$
$$+ k^2 v_A^2 \left(\frac{N^2}{k^2} \int_{-y_b}^{+y_b} |v'|^2 dy + k^2 v_A^2 \int_{-y_b}^{+y_b} |v|^2 dy - \int_{-\infty}^{\infty} U'f|\hat{v}|^2 dy \right) = 0. \quad (2.46)$$

Thus, since (2.46) is a quadratic in s^2, which is real by (2.35), given a solution $v(y)$ that satisfies the ODE (2.33), there must be two values of s^2 provided $v_A \neq 0$. For stability we therefore require that both roots of (2.46) are negative. Both roots are negative if and only if the following two inequalities are satisfied:

$$\frac{N^2}{k^2} \int_{-y_b}^{+y_b} |v'|^2 dy + 2k^2 v_A^2 \int_{-y_b}^{+y_b} |v|^2 dy + \int_{-y_b}^{+y_b} fQ|\hat{v}|^2 dy > 0, \quad (2.47)$$

$$k^2 v_A^2 \left(\frac{N^2}{k^2} \int_{-y_b}^{+y_b} |v'|^2 dy + k^2 v_A^2 \int_{-y_b}^{+y_b} |v|^2 dy \right) > k^2 v_A^2 \int_{-y_b}^{+y_b} U'f|\hat{v}|^2 dy. \quad (2.48)$$

Using the definition for the absolute vorticity $Q = f - U'$, we can re-write (2.47) as

$$\int_{-y_b}^{+y_b} f^2|\hat{v}|^2 dy + \frac{N^2}{k^2} \int_{-y_b}^{+y_b} |v'|^2 dy + 2k^2 v_A^2 \int_{-y_b}^{+y_b} |v|^2 dy > \int_{-y_b}^{+y_b} U'f|\hat{v}|^2 dy. \quad (2.49)$$

Hence, if we assume that (2.48) holds and that the Alfvén wave speed is non-zero, we can substitute (2.48), after the division of $k^2 v_A^2$, into (2.49) to obtain

$$\int_{-y_b}^{+y_b} f^2|\hat{v}|^2 dy + k^2 v_A^2 \int_{-y_b}^{+y_b} |v|^2 dy > 0, \quad (2.50)$$

which trivially holds.

Therefore, if we assume (2.48) holds and that the Alfvén wave speed is non-zero, then (2.47) is trivially satisfied and we have real and negative s^2 if and only if

$$\frac{N^2}{k^2} \int_{-y_b}^{+y_b} |v'|^2 dy + \int_{-y_b}^{+y_b} (k^2 v_A^2 - U'f)|v|^2 dy > 0, \quad (2.51)$$

valid for a non-zero Alfvén wave speed (due to the division of $k^2 v_A^2$ in the derivation). Then, assuming the maximum of U' and f both take finite values, the condition (2.51) allows us to make a number of conclusions regarding the stability of the system. We find that any instance of instability, created by anti-cyclonic shear, can be stabilised by vertical field of sufficient strength (as in Chandrasekhar, 1960) or equivalently, for sufficiently large vertical wavenumber. This is in contrast to the hydrodynamic result (2.38) where large vertical wavenumber implies that $fQ > 0$ is a necessary and sufficient condition for stability. This also conflicts with the hydrodynamic results, where the most unstable mode occurs at infinitesimally small vertical scales ($k \rightarrow \infty$) (Dunkerton, 1981; Griffiths, 2008a). However, one could argue that the most unstable mode could still occur at vanishingly small scales provided we also have infinitesimally weak field such that $k^2 v_A^2 \sim U'f$. This is clearly consistent with the hydrodynamic result that the most unstable mode occurs for infinitesimally small scales, while invoking the weak field results of Balbus & Hawley (1991). We also note that, in the limit $k \rightarrow \infty$, the role of stratification is negligible (provided the integral on the left hand side of (2.51) is bounded); thus, yielding the necessary and sufficient condition for stability that $k^2 v_A^2 > U'f$ as $|k| \rightarrow \infty$. This is analogous to the criteria (1.11) of Balbus & Hawley (1991). We must recall that (2.51) is invalid in the absence of field ($v_A^2 = 0$) and instead take (2.47), or equivalently (2.38), as the necessary and sufficient condition for hydrodynamic stability.

2.6 Parameter Values in Geophysical and Astrophysical Bodies

To address possible physical applications of this research, we provide table 2.1, which consists of typical parameter values such as angular velocity, buoyancy frequency and magnetic field strength, found in the Solar tachocline, Jupiter's upper atmosphere and Hot Jupiters. For comparison, we also include typical values found in Earth's upper stratosphere and lower mesosphere (where inertial instability is most likely to occur). Parameters will be given that are relevant to both equatorial and mid-latitude regions. Throughout the thesis we will refer back to the parameters in table 2.1 to give insight into various regimes.

In the terrestrial atmosphere, inertial instability is known to occur in the lower mesosphere and upper stratosphere with a flow vertical wavelength ~ 10km and latitudinal lengthscale $L \sim$ 3000km (Hitchman *et al.*, 1987; Hayashi *et al.*, 1998; Smith & Riese, 1999); the instabilities could occur anywhere in the atmospheric layer given sufficiently strong shear (relative to stratification, etc.), yielding a layer depth $H_D \approx 50$km. Over this vertical range in the upper stratosphere and lower mesosphere, the density of the atmospheric layer ranges from $\bar{\rho} = 3.0 \times 10^{-3}$kgm^{-3} to 8.1×10^{-3}kgm^{-3}. Following Griffiths (2003a) on the estimate of a diffusive parameter in the equatorial stratosphere and mesosphere near solstice, we estimate the buoyancy frequency $N = 2.0 \times 10^{-2}$s^{-1} and kinematic viscosity $\nu = 1.5 \times 10^{-2}$m^{2}s^{-1}. Then, as the Prandtl number $Pr = \nu/\kappa \approx 0.7$ in the upper stratosphere and lower mesosphere, we estimate the thermal diffusivity $\kappa = 2.1 \times 10^{-2}$m^{2}s^{-1}. Hitchman *et al.* (1987) observed cross-equatorial shear $\Lambda_0 \in [3.5, 5.8] \times$

10^{-5}s^{-1} at 50km, increasing to $\Lambda_0 \in [4.6, 8.1] \times 10^{-5}\text{s}^{-1}$ at 70km. Hayashi *et al.* (1998) also indicated that inertial instability occurs when $\Lambda_0 \in [2.3, 4.6] \times 10^{-5}\text{s}^{-1}$. Thus, we take $\Lambda_0 \in [3, 6] \times 10^{-5}\text{s}^{-1}$. The radius and angular velocity of Earth are $R = 6.4 \times 10^3\text{km}$ and $\Omega = 7.3 \times 10^{-5}\text{s}^{-1}$, respectively. Thus, we can estimate the Rossby parameter $\beta = 2\Omega/R = 2.3 \times 10^{-11}\text{m}^{-1}\text{s}^{-1}$ and Coriolis parameter at mid-latitude $f = 2\Omega\sin(45°) \approx 1.0 \times 10^{-4}\text{s}^{-1}$.

For the Solar tachocline, we refer to Hughes *et al.* (2007) and references therein, noting that some parameters are estimated seismologically (Schou *et al.*, 1998), whereas others are inferred from the solar model presented in Christensen-Dalsgaard (2002). The parameters provided are estimates at $R = 0.7R_\odot$, where $R_\odot = 7.0 \times 10^5\text{km}$ is the approximate solar radius. The angular velocity at this radius is approximately $\Omega = 2.8 \times 10^{-6}\text{s}^{-1}$ at the equator and $\Omega = 2.7 \times 10^{-6}\text{s}^{-1}$ at mid-latitude (45°), as shown in figure 1.1. The angular velocity at this radius beneath the poles is $\Omega = 2.0 \times 10^{-6}\text{s}^{-1}$, provided Ω varies weakly with depth (Gough, 2007). Thus, the Rossby parameter is $\beta = 8.0 \times 10^{-15}\text{m}^{-1}\text{s}^{-1}$ and the Coriolis parameter at mid-latitude (45°) is $f = 3.8 \times 10^{-6}\text{s}^{-1}$. With the difference between angular velocity at the poles and equator being $\Delta\Omega = 8.0 \times 10^{-7}\text{s}^{-1}$ it follows that the average change in zonal velocity from equator to pole is $U_0 = \Delta\Omega R_\odot \approx 500\text{ms}^{-1}$. Thus, taking a latitudinal lengthscale equal to a third of the solar radius $L = 2.3 \times 10^8\text{m}$, we obtain the latitudinal shear $\Lambda = U_0/L = 2.1 \times 10^{-6}\text{s}^{-1}$. Observations of the solar tachocline show that the depth of the layer is no more than $0.05R_\odot$ (Christensen-Dalsgaard & Thompson, 2007), yielding $H_D = 0.05R_\odot = 3.5 \times 10^7\text{m}$. The density and buoyancy frequency across the layer are $\bar{\rho} = 210\text{kgm}^{-3}$. and $N = 8.0 \times 10^{-4}\text{s}^{-1}$, respectively (Gough, 2007). There is considerable uncertainty regarding the magnetic field strength in the solar tachocline (Gough, 2007), however, it is likely to be in the range $10^3\text{G} < B_0 < 10^5\text{G}$. The kinematic viscosity, thermal diffusion and magnetic diffusivity in the layer are $\nu = 2.7 \times 10^{-3}\text{m}^2\text{s}^{-1}, \kappa = 1.4 \times 10^3\text{m}^2\text{s}^{-1}$ and $\eta = 4.1 \times 10^{-2}\text{m}^2\text{s}^{-1}$ (Gough, 2007, Table 1.1).

We will now focus on the upper atmosphere of Jupiter; that is, $0.9R_j < R < R_j$, where $R_j = 7.0 \times 10^7\text{m}$ is the radius of Jupiter. Thus, we take the layer depth to be the extent of this region, yielding $H_D = 0.04R_j \approx 3000\text{km}$. The parameters will vary inside this region, however to simplify our argument while still capturing their ordering, we provide the value of these parameters at $0.98R_j$. To estimate the parameters we refer to French *et al.* (2012), Connerney *et al.* (2018), Gastine & Wicht (2021), and references therein, which include estimates from the data gathered by the Galileo and Juno missions. The density and buoyancy frequency are taken to be $\bar{\rho} = 84.8\text{kgm}^{-3}$ and $N = 5.0 \times 10^{-4}\text{s}^{-1}$ (Debras & Chabrier, 2019; Gastine & Wicht, 2021). We take the field strength to be $B_0 = 10\text{G}$ (Connerney *et al.*, 2018). French *et al.* (2012) state that the kinematic viscosity, thermal diffusion and magnetic diffusivity are $\nu = 3.9 \times 10^{-7}\text{m}^2\text{s}^{-1}$, $\kappa = 1.3 \times 10^{-6}\text{m}^2\text{s}^{-1}$ and $\eta = 2.3 \times 10^9\text{m}^2\text{s}^{-1}$. The zonal flows seen at the surface extend down to $R = 0.96R_j$; thus, the zonal velocity at $R = 0.98R_j$ may range from $U_0 = 10\text{s}^{-1}$ to $U_0 = 150\text{s}^{-1}$ as on the surface (Tollefson *et al.*, 2017; Kaspi *et al.*, 2018). Thus, taking $L = R_j/3 = 2.3 \times 10^7\text{m}$ we obtain a latitudinal shear from $\Lambda_0 = U_0/L = 4.3 \times 10^{-7}\text{ms}^{-1}$ to $6.5 \times 10^{-6}\text{s}^{-1}$. The angular

velocity of Jupiter is $\Omega \approx 1.8 \times 10^{-4} \text{s}^{-1}$, which allows us to estimate the Rossby parameter $\beta = 5.0 \times 10^{-12} \text{m}^{-1}\text{s}^{-1}$, and Coriolis parameter at mid-latitude (45°) $f = 2.5 \times 10^{-4} \text{s}^{-1}$.

Naturally, there are many uncertainties regarding parameter values of Hot Jupiters; however, through the radial velocity method (Hatzes, 2016), transit photometry (Deeg & Alonso, 2018) and other detection methods, we can infer numerous properties. The radial velocity method allows us to determine many properties regarding star-planet orbits, such as period and eccentricity, whereas transit photometry allows us to infer planet size, thermal radiation (of both planet and star) as well as the atmosphere circulation of Hot Jupiters (Showman *et al.*, 2013). Indeed, we can infer many physical characteristics of Hot Jupiters, but it is difficult to prescribe specific parameter values such as buoyancy frequency, kinematic viscosity, thermal diffusivity and magnetic diffusivity with a high degree of certainty. Thus, in table 2.1 we provide a range of typical parameter values in the upper atmospheres of Hot Jupiters (where the strong equatorial jets are present), taken from Showman *et al.* (2013), Heng & Showman (2015) and references therein; for less certain parameters we look to Jupiter as motivation for our estimates. The radii of Hot Jupiters range from $0.5R_j$ to $2.0R_j$ (Demory & Seager, 2011). Assuming that the Hot Jupiters under consideration are tidally locked and have orbital periods from 3 to 10 Earth days (which is typically the case (Winn *et al.*, 2010)), it follows that their angular velocity must be in the range $\Omega \in [7.3, 24] \times 10^{-6} \text{s}^{-1}$. Hence, we can estimate a range of Coriolis and Rossby parameters by taking the most extreme radii and angular velocities, yielding $f = [1.0, 3.4] \times 10^{-5} \text{s}^{-1}$ and $\beta = [1.0, 14] \times 10^{-13} \text{m}^{-1}\text{s}^{-1}$. Observations of Hot Jupiters have shown that many have inflated radii when compared to Jupiter, leading to unusually low mean densities $\bar{\rho} = 220 \text{kgm}^{-3}$ (Mandushev *et al.*, 2007); however, a mean density as large as $\bar{\rho} = 2100 \text{kgm}^{-3}$ has been observed (Espinoza *et al.*, 2017). We record both densities to give a reasonable interval, however note that we will generally take $\bar{\rho} = 500$–1000kgm^{-3} since we are concerned with the upper atmospheres of Hot Jupiters (where the strong equatorial jets are present). We take the buoyancy frequency as $N = 5.0 \times 10^{-3} \text{s}^{-1}$ (Tsai *et al.*, 2014); however, it is not unreasonable to consider smaller buoyancy frequencies as in Jupiter's upper atmosphere (i.e., $N = 5.0 \times 10^{-4} \text{s}^{-1}$). The magnetic field strengths of Hot Jupiters are largely uncertain; however, Yadav & Thorngren (2017) estimate the surface magnetic field strength of many Hot Jupiters to be in the range 10G to 250G. This agrees with the estimates made from the release of magnetic energy in star-planet interactions by Cauley *et al.* (2019), ranging from 20G to 120G. Observations and models of Hot Jupiters have also indicated the existence of strong equatorial jets that can flow close to the speed of sound (e.g., Showman *et al.*, 2013; Heng & Showman, 2015; Koll & Komacek, 2018); thus, we take a jet speed of $U_0 = 1000 \text{ms}^{-1}$ to $U_0 = 2000 \text{ms}^{-1}$. We take a latitudinal lengthscale equal to a third of planetary radius, yielding $L = [1.2, 4.6] \times 10^7 \text{m}$, thus giving latitudinal shear in the range $\Lambda_0 = U_0/L \in [2.1, 17] \times 10^{-5} \text{s}^{-1}$. For the remaining parameters, we take values from Jupiter: that is $H_D = 3.0 \times 10^6 \text{m}$, $\nu = 3.9 \times 10^{-7} \text{m}^2\text{s}^{-1}$, $\kappa = 1.3 \times 10^{-6} \text{m}^2\text{s}^{-1}$ and $\eta = 2.3 \times 10^9 \text{m}^2\text{s}^{-1}$.

	Earth	Solar Tachocline	Jupiter	Hot Jupiters
Radius (m)	6.4×10^6	$R_\odot = 7.0 \times 10^8$	$R_J = 7.0 \times 10^7$	$0.5R_J - 2.0R_J$
Angular Velocity Ω (s^{-1})	7.3×10^{-5}	2.8×10^{-6}	1.8×10^{-4}	$7.3 \times 10^{-6} - 2.4 \times 10^{-5}$
Coriolis Parameter f (s^{-1})	1.0×10^{-4}	3.8×10^{-6}	2.5×10^{-4}	$1.0 \times 10^{-5} - 3.4 \times 10^{-5}$
Rossby Parameter β (m^{-1}s^{-1})	2.3×10^{-11}	8.0×10^{-15}	5.0×10^{-12}	$1.0 \times 10^{-13} - 1.4 \times 10^{-12}$
Layer Depth H_D (m)	5.0×10^4	3.5×10^7	3.0×10^6	3.0×10^6
Density $\bar{\rho}$ (kg m^{-3})	$3.0 \times 10^{-3} - 8.1 \times 10^{-3}$	210	85	$220 - 2100$
Buoyancy Frequency N (s^{-1})	1.0×10^{-2}	8.0×10^{-4}	5.0×10^{-4}	$5.0 \times 10^{-4} - 5.0 \times 10^{-3}$
Zonal Velocity U_0 (ms^{-1})	$30 - 120$	500	$10 - 150$	$1000 - 2000$
Latitudinal Lengthscale L (m)	3.0×10^6	2.3×10^8	2.3×10^7	$1.2 \times 10^7 - 4.6 \times 10^7$
Latitudinal Shear Λ_0 (s^{-1})	$3.0 \times 10^{-5} - 6.0 \times 10^{-5}$	1.0×10^{-6}	$4.3 \times 10^{-7} - 6.5 \times 10^{-6}$	$2.1 \times 10^{-5} - 1.7 \times 10^{-4}$
Magnetic Field B_3 (G)	0	$1.0 \times 10^3 - 1.0 \times 10^5$	10	$10 - 250$
Kinematic Viscosity ν (m^{2}s^{-1})	1.5×10^{-2}	2.7×10^{-3}	3.9×10^{-7}	3.9×10^{-7}
Thermal Conductivity κ (m^{2}s^{-1})	2.1×10^{-2}	1.4×10^3	1.3×10^{-6}	1.3×10^{-6}
Magnetic Diffusivity η (m^{2}s^{-1})	0	4.1×10^{-2}	2.3×10^9	2.3×10^9

Table 2.1: Estimated parameter values in the Earth's upper stratosphere and lower mesosphere, the solar tachocline, and the upper atmospheres of Jupiter and Hot Jupiters.

Chapter 3

Waves and Instabilities for a Uniform Shear Flow at Mid-latitudes

3.1 Introduction

In this chapter we consider the linear stability of an ideal parallel flow $U(y) = \Lambda_0 y$ with uniform latitudinal shear $U'(y) = \Lambda_0$ on an f-plane in the presence of a uniform vertical magnetic field of strength $B_3(y) = B_0$. This is the simplest possible configuration to study the competition between inertial and magnetic modes. Indeed, since the Coriolis parameter, the magnetic field strength and shear are all constant the ideal governing equation (2.31) has constant coefficients and can therefore be solved analytically with solutions for the perturbed cross-stream velocity of the form $v \propto \exp(ily)$, where l is the cross-stream wavenumber.

We can further justify our model beyond the grounds of simplicity. First, if modes occur over a sufficiently small range of latitude, the magnitude of the Coriolis parameter will not vary significantly and thus can be approximated by some constant value f_0. This is known as the f-plane approximation and is often applied in geophysical systems (see, for example Vallis, 2017, for a derivation). Second, we have already seen in Section 1.3.2 that even a weak uniform axial magnetic field can significantly influence hydrodynamic flows (e.g., Balbus & Hawley, 1991; Menou *et al.*, 2004) and thus, we consider uniform (local) vertical magnetic field.

We begin the chapter with Section 3.2, in which we discuss the inertial and magnetically modified waves within the system. In order to do this without interference from the unstable modes, we make yet another simplification and consider the system in the absence of shear. This guarantees stability by condition (2.51), which implies there must be anti-cyclonic shear (i.e., $U'f > 0$) somewhere in the system for instability to occur. We begin the analysis by deriving a quadratic equation for the frequency squared ω^2, which still contains a magnetohydrostatic switch $\mathcal{H}$ (as the governing equation (2.31) did). We first consider the non-magnetohydrostatic system ($\mathcal{H} = 1$) in order to compare with the hydromagnetic-inertial waves found in Acheson & Hide (1973). Throughout the thesis we will confirm the validity of the magnetohydrostatic approximation by using the condition (2.29), particularly when considering asymptotic results. In the magnetohydrostatic system

43

($\mathcal{H} = 0$), we introduce our nondimensional parameters A and $\mathcal{L}$, which are a rescaled aspect ratio and Lehnert number, respectively. The latter is proportional to magnetic field strength. Note that, following Section 3.2, these parameters will be used alongside the Rossby number Λ throughout the instability analysis of Section 3.3 and Chapter 4. We recast the quadratic equation for the frequency squared in terms of the nondimensional parameters; the system yields inertia-gravity waves in the absence of magnetic field and inertial-Alfvén waves for vanishing aspect ratio. We categorise the waves of the weak and strong field limits as well as the limits of small and large aspect ratio. We then discuss the links between the magnetohydrostatic magnetic waves in the weak field limit to the non-magnetohydrostatic hydromagnetic-inertial waves as found in Acheson & Hide (1973). In the following instability analysis of Section 3.3, we discuss the magnetohydrostatic waves that occur outside of the unstable domain and in the presence of shear.

In section 3.3 we consider the sheared system so that instability may occur by the condition (2.51) since anti-cyclonic shear is now possible (i.e., $U'f > 0$ in some region of the flow). Note that all subsequent results throughout the thesis will be magnetohydrostatic ($\mathcal{H} = 0$). We derive stability criteria in terms of the nondimensional parameters A, $\mathcal{L}$ and Λ using condition (2.51). We then derive the maximum growth rate, which is analogous to (1.12) of Balbus & Hawley (1991) for $\Lambda < 2$. We consider the limit of large vertical wavenumber $|k|$, which yields an analogous approximation to the "thin disc" and weak field assumptions of Balbus & Hawley (1991). For $\Lambda > 2$, the maximum growth rate is that of the hydrodynamic system. We provide contours of the frequencies and growth rates of the system as a function of the aspect ratio A and Lehnert number $\mathcal{L}$. These are shown for three distinct Rossby numbers Λ. The contour plots motivate an asymptotic analysis of the weak field limit, where magnetically modified inertial instabilities are found alongside those that are purely magnetic. We discuss the inertial and magnetic waves that are also embodied by the weak field expansions.

The contours of the growth rate also motivate a physical discussion regarding the vertical scale selection of the instabilities in astrophysical bodies, such as those given in table 2.1. Motivated by the nature of the results, we investigate the small A limit of the system, where an analogue to the magnetorotational instability (MRI) of Balbus & Hawley (1991) is found.

In Section 3.4 we consider the dynamical balances of the unstable modes of our system. We investigate numerous parameter regimes, including the weak field limits of hydrodynamically unstable and stable regimes, the most unstable mode, as well as regimes of marginal stability. In particular, we categorise the magnetorotational instability (MRI) in our system, a "stratified" MRI and magnetically modified inertial instabilities. We also find an approximation to the dynamical balance of the most unstable mode.

3.2 Inertial and Magnetic Waves

In order to isolate ideal inertial and magnetic waves, we will first consider the system in the absence of shear ($\Lambda_0 = 0$), so that instability may no longer occur by the condition (2.51). Recall that

we are considering a uniform Coriolis parameter f_0 and uniform magnetic field strength $B_3 = B_0$ so that our ideal governing equation (2.31) has constant coefficients and may be solved analytically with solutions of the form $\hat{v} \propto e^{ily}$. We consider the governing equation (2.31) so that the parameter $\mathcal{H}$ allows for the derivation of some non-magnetohydrostatic results. Introducing the frequency $\omega = -is$, equation (2.31) reduces to the eigenvalue relation

$$(k^2 + \mathcal{H}l^2)(\omega^2 - k^2 v_A^2)^2 - (\omega^2 - k^2 v_A^2)(l^2 N^2 + k^2 f_0^2) - k^4 v_A^2 f_0^2 = 0. \qquad (3.1)$$

Expression (3.1) is quadratic in ω^2 and therefore gives the following solutions:

$$\omega_{\pm}^2 = k^2 v_A^2 + \frac{1}{2}\left(\frac{l^2 N^2 + k^2 f_0^2}{k^2 + \mathcal{H}l^2} \pm \left(\frac{(l^2 N^2 + k^2 f_0^2)^2}{(k^2 + \mathcal{H}l^2)^2} + \frac{4k^4 v_A^2 f_0^2}{k^2 + \mathcal{H}l^2} \right)^{\frac{1}{2}} \right). \qquad (3.2)$$

The eigenvalue relations (3.1) and (3.2) can describe waves in a number of regimes, including those that are magnetohydrostatic ($\mathcal{H} = 0$) and those that are not ($\mathcal{H} = 1$). We will discuss magnetohydrostatic waves in the following subsection and then provide a small discussion of the non-magnetohydrostatic waves found in Acheson & Hide (1973).

3.2.1 Magnetohydrostatic Waves

In the magnetohydrostatic case, which is the most relevant in planetary atmospheres and hence the focus of this study, we set $\mathcal{H} = 0$ in (3.1), yielding

$$\omega^4 - \omega^2 \left(\frac{l^2 N^2}{k^2} + 2k^2 v_A^2 + f_0^2 \right) + k^2 v_A^2 \left(\frac{l^2 N^2}{k^2} + k^2 v_A^2 \right) = 0. \qquad (3.3)$$

To simplify the analysis we define the nondimensional parameters

$$\hat{\omega} = \frac{\omega}{f_0}, \ A^2 = \frac{l^2 N^2}{k^2 f_0^2} \ \text{ and } \ \mathcal{L}^2 = \frac{k^2 v_A^2}{f_0^2}, \qquad (3.4)$$

where $1/f_0$ is the chosen timescale. The Lehnert number $\mathcal{L}$ is the ratio between the Alfvén frequency and rotation, and governs the relative magnetic field strength. The parameter A may be interpreted as a re-scaled aspect ratio. In planetary atmospheres, the aspect ratio is comparable with f_0/N and hence we may consider A of order unity. Indeed, we can estimate the value of A by recalling that the cross-stream wavenumber $l = 2\pi/\text{wavelength} = n/R$ (since the wavelength $= 2\pi R/n$), where R is the planetary radius and $n \in [1, 10]$ is the planetary wavenumber.

Mathematically, there are a number of ways to interpret the nondimensional parameters A and $\mathcal{L}$, with the only prior restriction being that $l^2/k^2 \ll 1$ (small aspect ratio). This requirement can be met by having vanishingly thin modes $|k| \to \infty$ or, equivalently, modes that extend infinitely in the latitudinal direction ($|l| \to 0$). If we consider vanishingly thin modes, A can remain order unity by supposing $l^2/k^2 \sim f_0^2/N^2$; the small and large A limits are attained by varying the relative size of l^2/k^2. The large $|k|$ limit also has implications for the Lehnert number. Indeed, we must take the weak field limit such that the Lehnert number is not too large (e.g., so that $\mathcal{L} = O(1)$

or $\mathcal{L} \ll 1$). The small and large Lehnert limits are then attained by considering smaller or larger field strengths relative to $f_0/|k|$. Alternatively, we can obtain a small aspect ratio with $|l| \to 0$. This has similar implications to A, where different limits are attained by varying $|l|/|k|$. There are, however, no implications on $\mathcal{L}$ in this case, which allows us to determine a vertical scale for the mode.

The nondimensionalisation (3.4) allow us to recast (3.3) in nondimensional form as

$$\hat{\omega}^4 - (A^2 + 2\mathcal{L}^2 + 1)\hat{\omega}^2 + \mathcal{L}^2(A^2 + \mathcal{L}^2) = 0. \tag{3.5}$$

The condition for magnetohydrostatic validity (2.32), recast in nondimensional form, becomes

$$|\hat{\omega}^2 - \mathcal{L}^2| \ll \frac{N^2}{f_0^2}, \tag{3.6}$$

which will be checked on a case by case basis. Note that N/f_0 is typically large in planetary atmospheres.

Solving (3.5) for the two real and non-negative roots $\hat{\omega}^2$ yields

$$2\hat{\omega}_\pm^2 = A^2 + 2\mathcal{L}^2 + 1 \pm \sqrt{(A^2 + 1)^2 + 4\mathcal{L}^2}. \tag{3.7}$$

In the absence of magnetic field, equation (3.7) describes only one mode (since $\omega_-^2 = 0$), which is an inertia-gravity wave, given by

$$\omega_+^2 = \frac{l^2 N^2}{k^2} + f_0^2. \tag{3.8}$$

Since we obtain only one mode in the absence of magnetic field, it implies the existence of a magnetic wave in the magnetohydrostatic system. Thus, we will examine the asymptotic limits of $\mathcal{L}$ in order to classify the behaviour of the waves. However, we also find that as cross-stream wavenumber $|l| \to 0$ ($A \to 0$), where the effects of stratification are negligible, that equation (3.7) still describes two modes. The modes are inertial-Alfvén waves with

$$2\omega_\pm^2 = 2k^2 v_A^2 + f_0^2 \pm \sqrt{f_0^2 + 4k^2 v_A^2}. \tag{3.9}$$

Thus, we will also examine the asymptotic behaviour of the parameter A in order to fully classify the waves of the system.

The solutions (3.7) of (3.5) allows us to obtain two plots, shown in figure 3.1, for $\hat{\omega}_+^2$ and $\hat{\omega}_-^2$ in $(\mathcal{L}, A)$ space. Note that the frequency of both waves increases as A and $\mathcal{L}$ are increased. However, $\hat{\omega}_-^2$ is quite insensitive to variations in the parameter A in the limit of weak magnetic field.

Limits in $\mathcal{L}$

We first restrict our attention to the small and large $\mathcal{L}$ regimes. In the weak field limit ($\mathcal{L} \ll 1$) with $A = O(1)$ the two modes described by equation (3.7) are

$$\hat{\omega}_+^2 = A^2 + 1 + \frac{A^2 + 2}{A^2 + 1}\mathcal{L}^2 + O(\mathcal{L}^4), \tag{3.10}$$
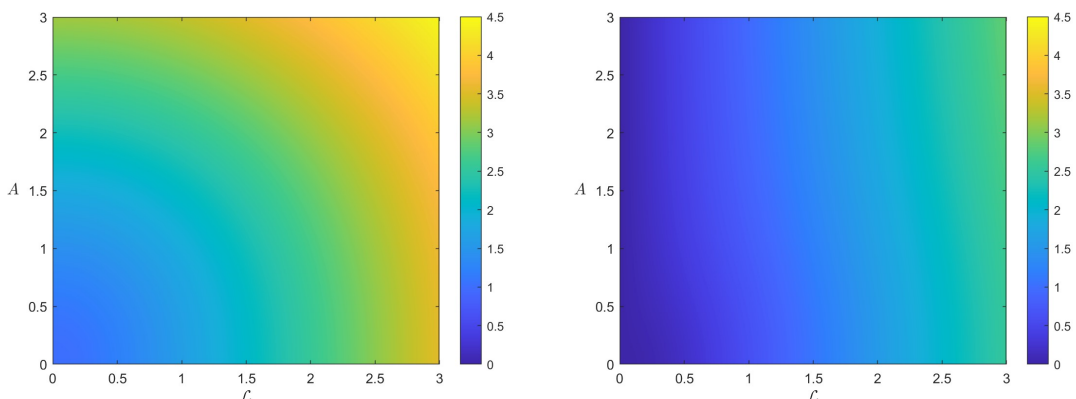
Figure 3.1: The frequencies $\hat{\omega}_+$ (left) and $\hat{\omega}_-$ (right) in $(\mathcal{L}, A)$ space. The maximum values of the frequencies are $\hat{\omega}_+ = 4.4532$ and $\hat{\omega}_- = 3.1623$.

and

$$\hat{\omega}_-^2 = \frac{A^2}{A^2 + 1}\mathcal{L}^2 + O(\mathcal{L}^4). \tag{3.11}$$

Here, as in Acheson & Hide (1973), at leading order we have an inertia-gravity wave (3.10) and a hydromagnetic-inertial wave (3.11). We will discuss the latter in relation to the non-magnetohydrostatic results of Acheson & Hide (1973) in more detail in the subsection 3.2.2. We can see that the hydromagnetic-inertial wave (3.11) will be insensitive to varying A, provided $A^2 \gg 1$, as seen in figure 3.1. Note that the expressions (3.10) and (3.11) remain valid with $A \gg 1$ (or $A \ll 1$) since $\mathcal{L}^2/(A^2 + 1)$ remains small.

The validity of the expansions under the magnetohydrostatic approximation can be ensured via (3.6). The first mode (3.10) is shown to be valid since it is given by $\hat{\omega}^2 = A^2$ at leading order, so that $|A^2 - \mathcal{L}^2| \approx A^2 = l^2 N^2/(k^2 f_0^2) \ll N^2/f_0^2$ since the aspect ratio is small and $N^2 \gg f_0^2$ in planetary atmospheres. The second mode (3.11) is valid since $\hat{\omega}_-^2 \propto \mathcal{L}^2 \ll 1$, so that $|\hat{\omega}^2 - \mathcal{L}^2| \propto \mathcal{L}^2 \ll N^2/f_0^2$.

Next we consider the large $\mathcal{L}$ limit, where the two modes described by equation (3.7) are given by

$$\hat{\omega}_\pm^2 = \mathcal{L}^2 \pm \mathcal{L} + \frac{A^2 + 1}{2} + O(\mathcal{L}^{-1}), \tag{3.12}$$

which correspond to Alfvén waves ($\omega^2 = k^2 v_A^2$) at leading order. The parameter A first appears at third order, implying that it does not have much dynamical effect on the magnetic modes, as can be seen in figure 3.1.

The validity of the expansions under the magnetohydrostatic approximation can be ensured via (3.6) provided $\mathcal{L}$ is not too large. Equation (3.12) implies $\hat{\omega}_\pm^2 = \mathcal{L}^2 \pm \mathcal{L}$ after neglecting smaller terms, so that $|\hat{\omega}_\pm^2 - \mathcal{L}^2| \propto |\mathcal{L}| \ll N^2/f_0^2$.

With the small and large limits of the parameter $\mathcal{L}$ described analytically, we can conclude that both modes, $\hat{\omega}_+^2$ and $\hat{\omega}_-^2$, transition to Alfvén waves from inertia-gravity waves and hydromagnetic-inertial waves, respectively, as $\mathcal{L}$ increases. To ensure the validity of the expansions and observe the transition, we plot the frequency $\hat{\omega}$, for each expansion, with the exact value of the roots (found
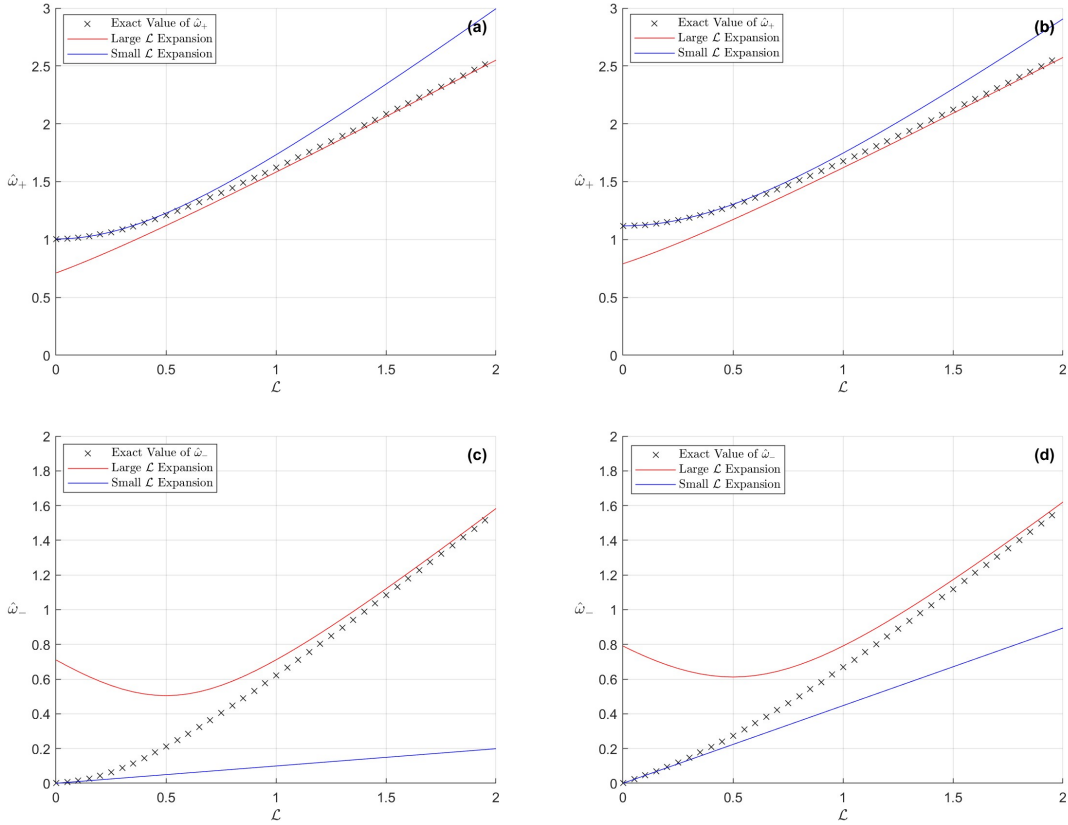
Figure 3.2: The asymptotic behaviour of $\hat{\omega}_+$ and $\hat{\omega}_-$ plotted with the exact value of the root against $\mathcal{L}$. Plots (**a**) and (**b**) correspond to $\hat{\omega}_+$ against $\mathcal{L}$ at $A = 0.1$ and $A = 0.5$, respectively. Plots (**c**) and (**d**) correspond to $\hat{\omega}_-$ against $\mathcal{L}$ at $A = 0.1$ and $A = 0.5$, respectively.

by solving (3.7)) against $\mathcal{L}$ in figure 3.2, for both $A = 0.1$ and $A = 0.5$. The figure shows that the small and large $\mathcal{L}$ expansions describe $\hat{\omega}_+^2$ with significantly greater accuracy than $\hat{\omega}_-^2$; in particular, the accuracy of the weak field expansion (3.11) is significantly worse than (3.10). We can also see that as we increase A, the weak field expansions remain accurate for significantly larger $\mathcal{L}$. Indeed, expansion (3.11) is sensitive to the parameter A; however, this persists only while $A = O(1)$ or smaller.

Limits in A

We now restrict our attention to the small and large A regimes. In the limit of large A, equation (3.7) implies the existence of two modes, given by

$$\hat{\omega}_+^2 = A^2 + (1 + \mathcal{L}^2) + \frac{\mathcal{L}^2}{A^2} + O(A^{-4}), \tag{3.13}$$

and

$$\hat{\omega}_-^2 = \mathcal{L}^2 - \frac{\mathcal{L}^2}{A^2} + O(A^{-4}). \tag{3.14}$$

The first wave, described by (3.13), is a gravity wave at leading order ($\omega^2 = l^2 N^2 / k^2$). The second wave, described by (3.14), is an Alfvén wave ($\omega^2 = k^2 v_A^2$) at leading order. Magnetic

field is still dominant in $\hat{\omega}_-^2$ within the large A limit, indicating that the effects of stratification are negligible (to $O(A^{-2})$) on the magnetic mode (at least while A is large).

The expansion (3.13) is ensured to be valid under the magnetohydrostatic approximation provided $|l|/|k| \ll 1$ since $\hat{\omega}_+^2 = A^2$ at leading order, so that $|\hat{\omega}_+^2 - \mathcal{L}^2| \approx A^2 = l^2 N^2/(k^2 f_0^2) \ll N^2/f_0^2$. Similarly, the second expansion (3.14) is valid, provided the magnetic field does not becomes too large, since $\hat{\omega}_-^2 \approx \mathcal{L}^2 - \mathcal{L}^2/A^2$, so that $|\hat{\omega}_-^2 - \mathcal{L}^2| \approx \mathcal{L}^2/A^2 \ll N^2/f_0^2$.

In the small A limit, equation (3.7) implies

$$\hat{\omega}_+^2 = \frac{2\mathcal{L}^2 + 1 + \sqrt{4\mathcal{L}^2 + 1}}{2} + \frac{1 + \sqrt{4\mathcal{L}^2 + 1}}{2\sqrt{4\mathcal{L}^2 + 1}} A^2 + O(A^4), \qquad (3.15)$$

and

$$\hat{\omega}_-^2 = \frac{2\mathcal{L}^2 + 1 - \sqrt{4\mathcal{L}^2 + 1}}{2} + \frac{\sqrt{4\mathcal{L}^2 + 1} - 1}{2\sqrt{4\mathcal{L}^2 + 1}} A^2 + O(A^4). \qquad (3.16)$$

The waves (3.15) and (3.16) correspond to inertial-Alfvén waves at leading order (in dimensional terms (3.15) and (3.16) depend upon both rotation and the Alfvén wave frequency). Thus, we have shown that by increasing the value of A, for fixed $\mathcal{L}$, that one of the inertial-Alfvén waves becomes inertial, while the other becomes Alfvénic.

The expansions (3.15) and (3.16) are valid under the magnetohydrostatic approximation since $|\hat{\omega}_\pm^2 - \mathcal{L}^2| \approx |1 \pm (4\mathcal{L}^2 + 1)^{1/2}|/2$ which is either of order unity or $O(\mathcal{L})$ and is therefore much less than N^2/f_0^2 (usually large in planetary atmospheres) provided $\mathcal{L}$ is not too large.

With the asymptotic behaviour of the parameter A fully defined, we can conclude that both modes $\hat{\omega}_+^2$ and $\hat{\omega}_-^2$ transition from inertial-Alfvén waves to inertia-gravity waves and Alfvén waves, respectively, as A increases. To ensure the accuracy of the expansions and observe this transition we plot the small and large A expansions of $\hat{\omega}$ with the exact value of the roots (from (3.7)) against A in figure 3.2, for both $\mathcal{L} = 0.1$ and $\mathcal{L} = 0.5$. Note that the small and large A expansions describe $\hat{\omega}_+^2$ with far greater accuracy than $\hat{\omega}_-^2$. We can also see that as we increase $\mathcal{L}$, the large A expansions require A of greater magnitude to describe the modes accurately; the accuracy of the small A expansions (3.15) and (3.16) also degrades.

3.2.2 Non-magnetohydrostatic Waves in the Weak Field Limit

We now address the non-magnetohydrostatic ($\mathcal{H} = 1$) waves of equation (3.2), which will allow us to draw links between the magnetohydrostatic waves in this system and the hydromagnetic-inertial waves of Acheson & Hide (1973), which are derived with application to the Earth's core.

In the absence of magnetic field, equation (3.2) describes only one mode (since $\omega_-^2 = 0$), which is an inertial wave, given by

$$\omega_+^2 = \frac{l^2 N^2 + k^2 f_0^2}{k^2 + l^2}. \qquad (3.17)$$

This implies the existence of a magnetic wave, as only the wave described by (3.17) exists in the absence of field. Thus, we examine the weak field regime of the system in order to see whether the wave described by ω_-^2 does in fact exhibit magnetic behaviour. It is worth noting that Acheson
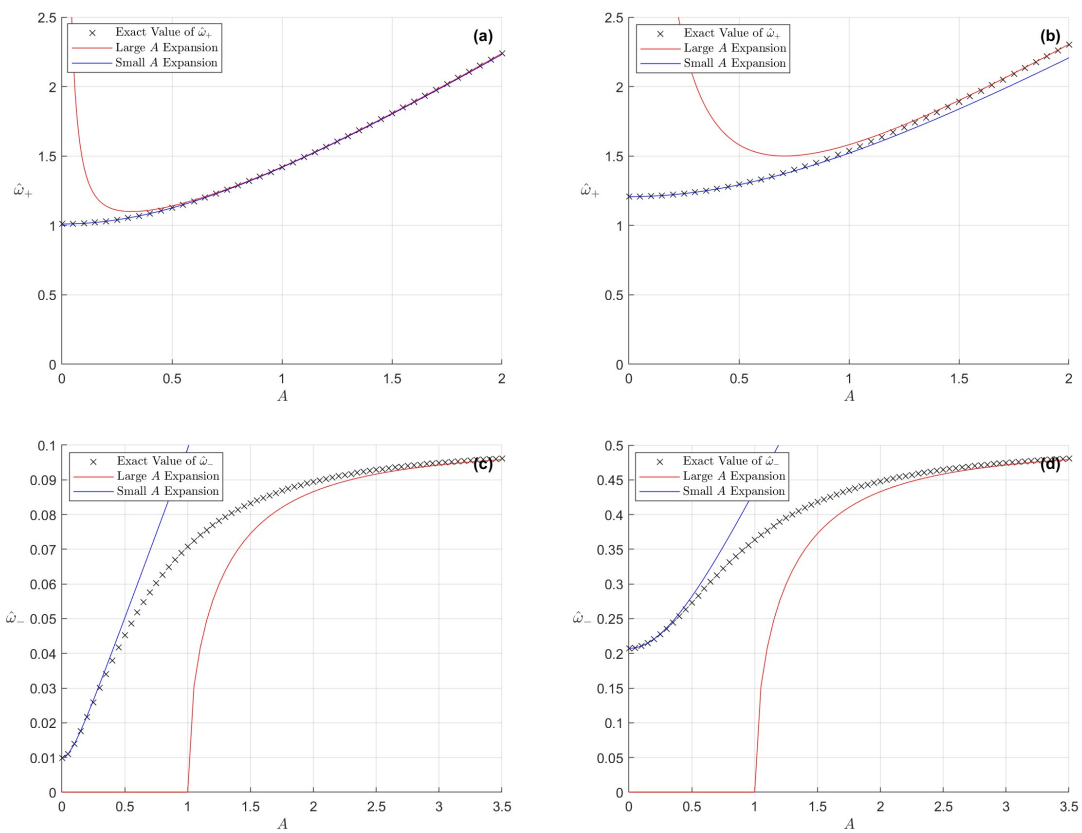
Figure 3.3: The asymptotic behaviour of $\hat{\omega}_+$ and $\hat{\omega}_-$ plotted with the exact value of the root against $\mathcal{L}$. Plots (**a**) and (**b**) correspond to $\hat{\omega}_+$ against A at $\mathcal{L} = 0.1$ and $\mathcal{L} = 0.5$, respectively. Plots (**c**) and (**d**) correspond to $\hat{\omega}_-$ against A at $\mathcal{L} = 0.1$ and $\mathcal{L} = 0.5$, respectively.

& Hide (1973) examined an unstratified ($N = 0$) and non-magnetohydrostatic ($\mathcal{H} = 1$) system in the weak field limit, where they found the existence of a "hydromagnetic-inertial" wave. Hence, if the wave exists, it is also of interest to see how the wave is modified by stratification and magnetohydrostatic affects.

The weak field limit of equation (3.2) allows us to obtain the mode

$$\omega_-^2 \approx \frac{l^2 N^2}{l^2 N^2 + k^2 f_0^2} k^2 v_A^2 + \frac{k^4 f_0^4 (k^2 + \mathcal{H} l^2)}{(l^2 N^2 + k^2 f_0^2)^3} k^4 v_A^4, \tag{3.18}$$

which is indeed dependent on magnetic field and will therefore be referred to as a hydromagnetic-inertial wave. The frequency of waves described by (3.18) crucially depends on whether the flow is stratified or not; for example, if $N \neq 0$, $\omega_-^2 \propto k^2 v_A^2$, while if $N = 0$, $\omega_-^2 \propto k^4 v_A^4$. Indeed, in the case $N = 0$ and $\mathcal{H} = 1$, the wave (3.18) reduces to

$$\omega_-^2 \approx \frac{(k^2 + l^2)}{k^2 f_0^2} k^4 v_A^4, \tag{3.19}$$

which is the hydromagnetic-inertial wave derived by Acheson & Hide (1973). However, since we are primarily concerned with planetary atmospheres, where the system is stratified ($N \neq 0$), we will consider (3.18), where the frequency of the wave scales with $|k| v_A$.

Recasting our weak field magnetic wave (3.11) in dimensional terms, we obtain

$$\omega_-^2 \approx \frac{\frac{l^2 N^2}{k^2}}{\frac{l^2 N^2}{k^2} + f_0^2} k^2 v_A^2, \tag{3.20}$$

which is the same as the leading order term of (3.18). Clearly, the frequency of the wave (3.20) scales with $|k| v_A$ at leading order, instead of $k^2 v_A^2$, as in equation (3.19). We also note that the change in scaling occurs for both the magnetohydrostatic and non-magnetohydrostatic system.

3.3   Uniform Shear Instabilities

In this section we again consider a uniform Coriolis parameter f_0 (f-plane approximation) and uniform field strength B_0. However, in contrast to the previous section, we now consider a magnetohydrostatic system only (in fact, this will be the case throughout the rest of the thesis). We will also consider a uniform parallel flow $U(y) = \Lambda_0 y$ with constant latitudinal shear Λ_0, so that instability is possible by condition (2.51) as the system can now exhibit anti-cyclonic shear (i.e., $U' f = \Lambda_0 f_0 > 0$). With this model, the governing equation (2.33) has constant coefficients and can therefore be solved analytically with solutions of the form $\hat{v} \propto e^{-ily}$, giving the eigenvalue relation:

$$s^4 + s^2 \left(\frac{l^2 N^2}{k^2} + 2 k^2 v_A^2 + f_0 Q_0 \right) + k^2 v_A^2 \left(\frac{l^2 N^2}{k^2} + k^2 v_A^2 - \Lambda_0 \right) = 0, \tag{3.21}$$

where the absolute vorticity $Q_0 = f_0 - \Lambda_0$ and Alfvén velocity squared $v_A^2 = B_0 / \sqrt{\rho \mu_0}$ are uniform.

First we recast the nondimensional parameters (3.4) alongside the Rossby number Λ :

$$S = \frac{s}{f_0}, \quad A^2 = \frac{l^2 N^2}{k^2 f_0^2}, \quad \mathcal{L}^2 = \frac{k^2 v_A^2}{f_0^2} \quad \text{and} \quad \Lambda = \frac{\Lambda_0}{f_0}, \tag{3.22}$$

where $1/f_0$ is the timescale, A is a rescaled aspect ratio and the $\mathcal{L}$ is the Lehnert number. In contrast to the previous section we are now considering the growth rate s (rather than the frequency) and now have the nondimensional parameter Λ since the shear is non-zero.

In nondimensional form, equation (3.21) becomes

$$S^4 + S^2 \left(A^2 + 2\mathcal{L}^2 + 1 - \Lambda \right) + \mathcal{L}^2 \left(A^2 + \mathcal{L}^2 - \Lambda \right) = 0, \tag{3.23}$$

which in the absence of the cross-stream wavenumber ($A = 0$) reduces to a Cartesian analogue of (1.10), as seen in Balbus & Hawley (1991). Indeed, an analogous form to (1.10) can also be attained by supposing we have a vanishing vertical scale $|k| \to \infty$ such that $A \ll 1$ and $\mathcal{L} = O(1)$. The requirement $\mathcal{L} = O(1)$ implies that $|k|v_A/f_0 \sim 1$ so that the Alfvén frequency $|k|v_A$ is small in comparison to the strength of rotation. This limit is analogous to taking the "thin disc" and weak field approximations as made by Balbus & Hawley (1991). However, as we have already discussed, having $|k| \gg 1$ does not necessarily ensure $A \ll 1$; thus, the aspect ratio and therefore the role of stratification may not be negligible. The large $|k|$ limit is also of interest when considering the hydrodynamic problem, where the most unstable mode in the absence of diffusion occurs on vanishingly small scales (e.g., Dunkerton, 1981; Griffiths, 2008a).

We may solve equation (3.23) for S^2, yielding two modes:

$$2S_\pm^2 = \Lambda - 1 - A^2 - 2\mathcal{L}^2 \pm \sqrt{(\Lambda - 1 - A^2)^2 + 4\mathcal{L}^2}, \tag{3.24}$$

where we note that the root S_- vanishes in the absence of magnetic field. Equation (3.24) has two distinct modes: the negative root, which is always stable, and the positive root, which is either stable or unstable, depending upon $A, \mathcal{L}$ and Λ. Note that, to determine that the negative root is always stable one can set $\Lambda - 1 - A^2 - 2\mathcal{L}^2 > 0$ and consider $S_-^2 > 0$, which leads to a contradiction (similarly, assuming $\Lambda - 1 - A^2 - 2\mathcal{L}^2 < 0$ implies $S_-^2 < 0$ trivially).

Since anti-cyclonic shear allows instability to occur, we will find, for each value Λ, the domain for which unstable modes can occur in $(\mathcal{L}, A)$ space, the growth rates of these modes and the values of $\mathcal{L}$ and A that yield the maximum growth rate.

3.3.1 Stability Criteria

We now find the values of $\mathcal{L}$ and A where instability can occur for each Λ by considering equation (3.24). To do this, we only consider the positive root of (3.24) since the negative root is always stable. Thus, by considering S_+^2, it follows that $\Lambda - 1 - A^2 - 2\mathcal{L}^2 > 0$ is a sufficient condition for instability. However, assuming $\Lambda - 1 - A^2 - 2\mathcal{L}^2 < 0$ and considering $S_+^2 > 0$, yields the requirement that $A^2 + \mathcal{L} < \Lambda$ for instability, which is a stronger condition than $\Lambda - 1 - A^2 - 2\mathcal{L}^2 >$

0. Hence, the condition implies that a necessary and sufficient condition for stability is that the following inequality is satisfied:

$$A^2 + \mathcal{L}^2 > \Lambda. \tag{3.25}$$

The condition (3.25) implies that instability occurs within a quarter-circle (since $\mathcal{L}, A > 0$) in the $(\mathcal{L}, A)$ plane, with radius $\sqrt{\Lambda}$. Instability occurs on the $\mathcal{L}$ axis ($A = 0$) if and only if $\mathcal{L}^2 < \Lambda$, implying that the $\mathcal{L}$ axis is unstable given non-negative Λ. Note that (3.25) is not valid in the hydrodynamic regime ($\mathcal{L} = 0$), owing to the division by $\mathcal{L}^2$ in the derivation. However, by setting $\mathcal{L} = 0$ in equation (3.24), it follows that the necessary and sufficient hydrodynamic condition for stability that $A^2 + 1 - \Lambda > 0$, where instability can occur only if $\Lambda > 1$. Thus, by considering (3.25) alongside the hydrodynamic condition for instability $A^2 + 1 - \Lambda > 0$, it follows that instability may occur in the magnetohydrodynamic regime for $\Lambda < 1$, while the system would otherwise be stable in the absence of magnetic field. Hence, we may have found an MRI within the system, as we might expect from the analogies between the eigenvalue relations (3.23) and expression (1.10) of Balbus & Hawley (1991).

Note that the condition (3.25) may have alternatively been derived from the stability condition (2.51); this is possible since the boundary conditions of (2.51) are either bounded (with $v = 0$), unbounded (with $v \to 0$), or periodic. In the first two cases, the boundary terms (after integration by parts) vanish, and in the third case they cancel. Recall that the condition (2.51) also required $v_A \neq 0$ (as equation (3.25) requires $\mathcal{L} \neq 0$).

3.3.2 The Maximum Growth Rate

We now focus on finding the most unstable mode of the system described by the parameters $\mathcal{L}, A$ and Λ. To do this, we differentiate S_+^2 with respect to A and $\mathcal{L}$, which allows us to derive the maximum and minimum values of S_+^2 and where they occur in $(\mathcal{L}, A)$-space.

We have to be careful about the interpretation of differentiating with respect A and $\mathcal{L}$ since the vertical wavenumber is contained within both nondimensional parameters. There are two options. First, we can consider the derivatives with respect to A as those of the cross-stream wavenumber l and interpret the $\mathcal{L}$ derivatives as those of the vertical wavenumber $|k|$. Second, we can consider derivatives of A as those of vertical wavenumber k and the $\mathcal{L}$ derivatives as those of the Lehnert number itself (i.e., the ratio of $|k|v_A$ and f_0).

By differentiating S_+^2 in equation (3.24) with respect to A and $\mathcal{L}$ it follows that when $\Lambda < 2$, the maximum growth rate is given by

$$S^2 = \frac{\Lambda^2}{4} \implies s^2 = \frac{\Lambda_0^2}{4}, \text{ occurring at } (A^2, \mathcal{L}^2) = (0, \frac{\Lambda}{4}(2 - \Lambda)). \tag{3.26}$$

When $\Lambda > 2$, the maximum growth rate is given by

$$S^2 = \Lambda - 1 \implies s^2 = -f_0 Q_0, \text{ occurring at } (A^2, \mathcal{L}^2) = (0, 0). \tag{3.27}$$

Equations (3.26) and (3.27) imply that the growth rate of the most unstable mode is dependent only on the shear of the system. The first and last equations in (3.26) are analogous to equations (1.12)

and (1.13) of Balbus & Hawley (1991). However, (3.27) is instead equivalent to the maximum hydrodynamic growth rate given by (2.40). Together, the equations imply that if the absolute vorticity $Q_0 = f_0 - \Lambda_0$ satisfies $Q_0 > -\Lambda_0/2$ (or equivalently $Q_0 > -f_0$) so that $\Lambda_0 < 2f_0$, then $\Lambda < 2$ and the most unstable mode is purely magnetic (requires $\mathcal{L} \neq 0$) and occurs when $A = 0$ and $\mathcal{L}^2 = \Lambda(2 - \Lambda)/4$. Thus, in dimensional terms, when $\Lambda < 2$ ($Q_0 > -\Lambda_0/2$), the most unstable mode occurs when $k^2 v_A^2 = (2f_0 - \Lambda_0)\Lambda_0/4$, with growth rate $\Lambda_0/2$. However, this also implies that once the absolute vorticity is sufficiently negative, such that $Q_0 < -\Lambda_0/2$, the most unstable mode occurs for vanishing aspect ratio in the absence of magnetic field, with growth rate $|f_0 Q_0|^{\frac{1}{2}}$.

We can interpret the maximum growth rate when $\Lambda < 2$, given by (3.26), as occurring when $k v_A / f_0 = O(1)$ as $|k| \to \infty$. We have already discussed how this interpretation links to both the weak field and thin disc approximations of Balbus & Hawley (1991) as well as the hydrodynamic results that the most unstable mode occurs on vanishingly thin scales (e.g., Dunkerton, 1981; Griffiths, 2008a). Alternatively, we could interpret that the maximum growth rate occurs at infinitesimal cross-stream wavenumber and critical vertical wavenumber $|k|^2_{\max} = \Lambda_0(2f_0 - \Lambda_0)/v_A^2$. The maximum growth rate in the case $\Lambda > 2$ can be interpreted to occur at vanishingly small aspect ratio and weak field strength such that $v_A \ll f_0/k$ (i.e., $\mathcal{L} = k v_A / f_0 \ll 1$).

3.3.3 The Stable and Unstable Modes in Parameter Space

We continue our analysis by providing plots of the stable and unstable modes, given in figure 3.4. The left hand plots of the figure show the frequency of the stable mode in $(\mathcal{L}, A)$-space. The right hand plots show the growth rate and frequency of the unstable mode in $(\mathcal{L}, A)$-space. Note that the stable mode and unstable mode have distinct colourbars. We include the condition (3.25) in the plots of the growth rate as a red line following the border of the unstable region to provide a clear bound where neutral stability is found. The dashed black lines are the hyperbolas given by $A = C/\mathcal{L} = lN v_A / f_0^2 \mathcal{L}$ for $C = 0.025 \cdot 2^j$, for $j = 0, 1, \ldots, 7$. The hyperbolas represent lines where the only parameter that varies is the vertical wavenumber (since C is not dependent on k). The solid black line traces the vertical wavenumbers that give the maximum growth rate for each C in the unstable domain. We will discuss the application of the hyperbolas in the following subsection 3.3.4.

Figure 3.4 for $\Lambda = 0.5$ illustrates a solely hydrodynamically stable regime since $\Lambda < 1$, allowing us to conclude that weak magnetic field destabilises the system. Figure 3.4 with $\Lambda = 1.5$ also shows both a hydrodynamically unstable regime, for $A = A_c < \sqrt{\Lambda - 1}$, and a stable regime for $A > A_c$. In both cases weak magnetic field, again destabilises the system, where this behaviour persists for $1 < \Lambda < 2$. We also find for $\Lambda = 2.5$ a hydrodynamically stable and unstable regime separated by some critical value A_c, where weak field clearly destabilises the system for $A > A_c$. However, the behaviour is less clear for $A < A_c$.
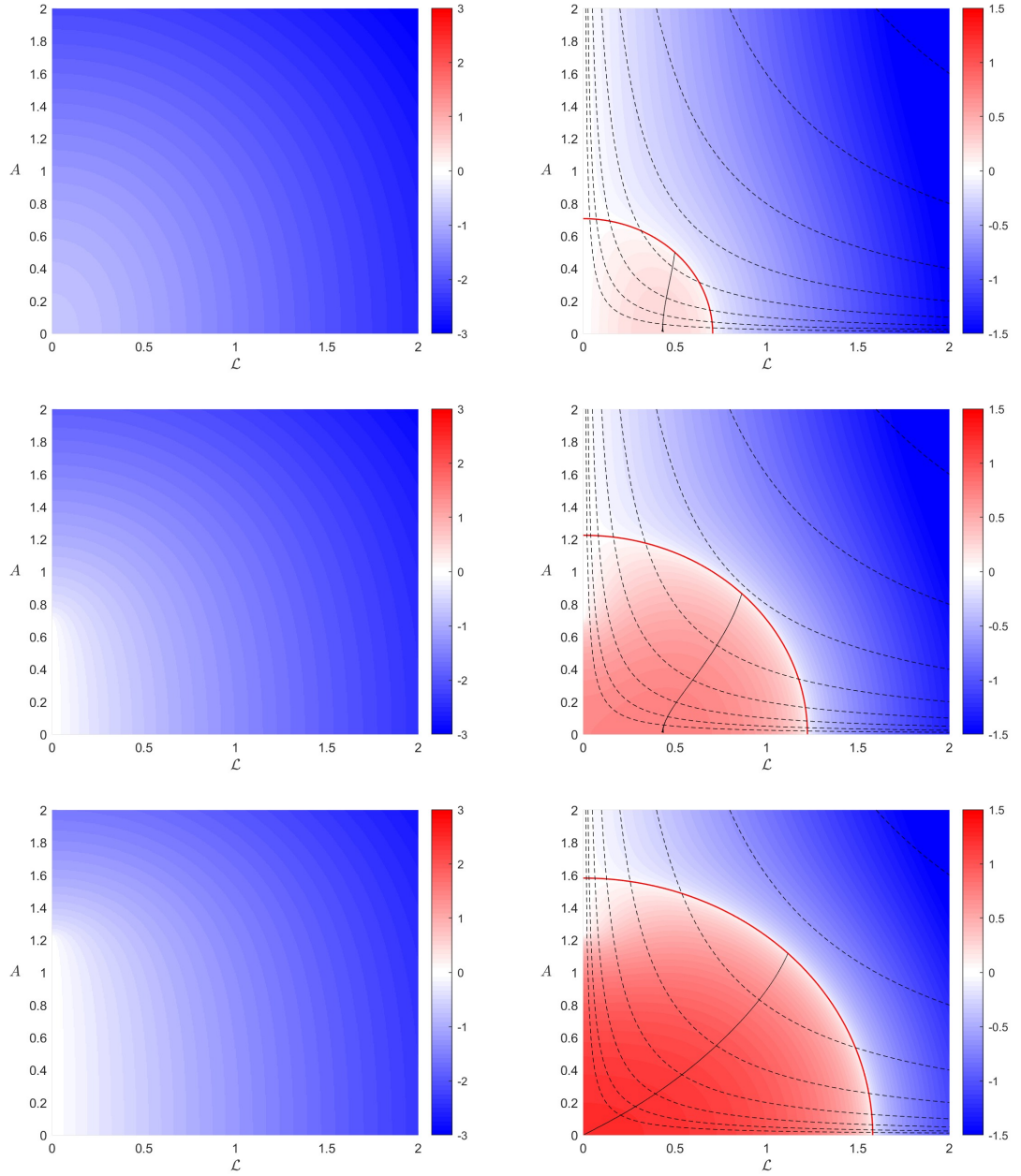
Figure 3.4: Contours of the frequencies of the stable modes (left) and the growth rates (and frequencies) of the unstable modes (right). The top row corresponds to the Rossby number $\Lambda = 0.5$, where the system is stable in the absence of magnetic field. The second and third rows correspond to the Rossby numbers $\Lambda = 1.5$ and $\Lambda = 2.5$, respectively; in these cases the A (hydrodynamic) axis is stable provided $A^2 > \Lambda - 1$. The red line is governed by (3.25) and separates the growth rate of the unstable region (red) from the frequency of the stable region (blue).

3.3.4 Scale Selection in Astrophysical Bodies

To estimate the vertical scales of the unstable modes and illustrate that these instabilities may occur in the astrophysical bodies listed in table 2.1, we focus our attention on the hyperbolas $A = \mathcal{L}/C$ in figure 3.4, where $C = lNv_A/f_0^2$. We do this by assuming the cross-stream wavenumber l is fixed and can be estimated by taking $l = 2\pi/L$, where L is the latitudinal lengthscale of the flow (as seen in table 2.1), so that the only parameter to vary in the system is the vertical wavenumber. This is physically reasonable since possible latitudinal lengthscales could be inferred from observations, while the vertical scales are somewhat harder to determine (e.g., there is still uncertainty regarding the depth of Jupiter's atmospheric jets; see Vasavada & Showman, 2005). Thus, we can estimate the value of C in the solar tachocline, and the upper atmospheres of Jupiter and Hot Jupiters, and depending on the resulting value of C and the Rossby number, we make use of equations (3.26) and (3.27) to obtain the Lehnert number (and therefore vertical wavenumber) that generates the maximum growth rate. Note that the values of the shear Λ_0 and f_0 will not be uniform in observations, however these are necessary (although limiting) requirements of the model. It is also a concern to discuss vertical scale selection in the absence of diffusion, where previous studies find that the maximum growth rate occurs at vanishingly small vertical scales (Dunkerton, 1981; Griffiths, 2003a); however, owing to the magnetic field, nondimensional parameter choice, and resulting condition for stability $A^2 + \mathcal{L}^2 > \Lambda$, given fixed l, N, v_A and f_0, then the vertical wavenumber is finite and bounded.

For the solar tachocline we take $L = 2.3 \times 10^8\text{m}$, $N = 8 \times 10^{-4}\text{s}^{-1}$, $\Omega = 2.8 \times 10^{-6}\text{s}^{-1}$ so that $f_0 = 2\Omega\sin(\pi/3) = 4.8 \times 10^{-6}\text{s}^{-1}$ and $\bar{\rho} = 210\text{kgm}^{-3}$ so that $v_A = B_0/\sqrt{\bar{\rho}\mu_0} = 6.2 - 620\text{ms}^{-1}$ since the field strength in the solar tachocline is likely to be $B_0 = 10^{-1} - 10\text{T}$. Together these give the range of values $C = O(1) - O(10^2)$.

For Jupiter's upper atmosphere, we take $L = 2.3 \times 10^7\text{m}$, $N = 5 \times 10^{-4}\text{s}^{-1}$, $f_0 = 2.5 \times 10^{-4}\text{s}^{-1}$, $\bar{\rho} = 85\text{kgm}^{-3}$ and $B_0 = 10^{-3}\text{T}$ so that $v_A = B_0/\sqrt{\bar{\rho}\mu_0} = 9.7 \times 10^{-2}\text{ms}^{-1}$. Together, these values give $C = O(10^{-4})$.

In Hot Jupiters, we take $L = 2.3 \times 10^7\text{m}$, $N = 5 \times 10^{-4}\text{s}^{-1}$, $f_0 = 3.4 \times 10^{-5}\text{s}^{-1}$, $\bar{\rho} = 10^3\text{kgm}^{-3}$ and $B_0 = 10^{-3} - 10^{-2}\text{T}$ so that $v_A = B_0/\sqrt{\bar{\rho}\mu_0} = 0.028 - 0.28\text{ms}^{-1}$. Together, these give the range of values $C = O(10^{-3}) - O(10^{-2})$.

Hence, for the upper atmospheres of Jupiter and Hot Jupiters, we expect C to be small, yielding a low lying hyperbola $A = C/\mathcal{L}$ so that the predicted maximum growth rate and the vertical scale for which it occurs are well estimated by (3.26) and (3.27). This is confirmed by figure 3.4, where the lowest lying hyperbola is $C = 0.025 \sim O(10^{-2})$ for reference. For the solar tachocline, $C = O(1)$. However, table 2.1 suggests the Rossby number $\Lambda = \Lambda_0/f_0 \approx 0.21$, where figure 3.4 (at a similar Rossby number) indicates that the vertical scale does not deviate too much from that of the predicted (3.26); the deviation also becomes smaller for yet smaller Rossby number Λ. Thus, we may use (3.26) and (3.27) to predict the vertical scales for the given C in the astrophysical bodies we are considering.

In the solar tachocline, the Rossby number $\Lambda \approx 0.21$ so that (3.26) is appropriate for estimating the vertical scale. Recasting (3.26) in dimensional terms and dividing by v_A^2/f_0^2, we obtain

$$k^2 = \frac{\Lambda_0}{4v_A^2}(2f_0 - \Lambda_0). \tag{3.28}$$

Taking the latitudinal shear $\Lambda_0 = 10^{-6}\text{s}^{-1}$ (from table 2.1) and $v_A = 6.2\text{ms}^{-1}$ (the lowest value for v_A), we obtain $k = 2.4 \times 10^{-7}\text{m}^{-1}$ as the estimate for the vertical wavenumber. This yields the vertical lengthscale $H = 2\pi/k = 2.6 \times 10^7\text{m}$. With the vertical extent of the solar tachocline being $3.5 \times 10^7\text{m}$, it would be more feasible to have a slightly smaller vertical scale; however, since $C = O(1)$ in this case, the vertical wavenumber that generates the most unstable mode (3.26) will be slightly larger (see solid black line in figure 3.4). The predicted vertical lengthscale in the Solar tachocline also allows us to calculate $A = NH/Lf_0 \sim O(10)$. This is at least an order of magnitude too large to remain accordant with the location of the maximum growth rate (3.26); however this is consistent in the sense that a larger vertical wavenumber would progress towards clarifying the discrepancy as $C = O(1)$ in this case so that the vertical wavenumber that generates the most unstable mode (3.26) will be slightly larger (see solid black line in figure 3.4).

In Jupiter's upper atmosphere we also expect the Rossby number $\Lambda < 1$, so that (3.26) is appropriate for estimating the vertical scale. Taking the latitudinal shear $\Lambda_0 = 4.3\times10^{-7}\text{s}^{-1}$ (from table 2.1) we obtain the following estimate for the vertical wavenumber: $k = 7.4 \times 10^{-5}\text{m}^{-1}$, using equation (3.28). This yields the vertical scale $H = 2\pi/k = 8.5 \times 10^4\text{m}$. This is physically reasonable when the depth of Jupiter's upper atmosphere is $3.0 \times 10^6\text{m}$. For this value of H we obtain the corresponding value $A = 7.4 \times 10^{-3}$. Hence, the parameters in table 2.1 are consistent with the predicted scale selection (3.26).

For Hot Jupiters we expect the Rossby number $\Lambda \in [0.5, 5]$ so that (3.26) and (3.27) may both be appropriate for estimating the vertical scale. First, taking the latitudinal shear $\Lambda_0 = 2.1 \times 10^{-5}\text{s}^{-1}$ (from table 2.1) the Rossby number is $\Lambda = 0.62$ so that (3.26) is relevant. We also take $v_A = 0.028\text{ms}^{-1}$. We obtain the following estimate for the vertical wavenumber: $k = 5.6 \times 10^{-4}\text{m}^{-1}$, using equation (3.28). This yields the vertical scale $H = 2\pi/k = 1.1 \times 10^4\text{m}$. This is physically reasonable when considering an atmospheric depth similar to that of Jupiter's upper atmosphere (i.e., $3.0 \times 10^6\text{m}$). For this value of H we obtain the corresponding value $A = 7.0\times10^{-3}$. Hence, the parameters in table 2.1 are consistent with the predicted scale selection (3.26).

If the latitudinal shear in Hot Jupiters is $\Lambda_0 = 1.7 \times 10^{-4}\text{s}^{-1}$ (from table 2.1), the Rossby number is $\Lambda = 5$ so that (3.27) is relevant. Taking $v_A = 0.028\text{ms}^{-1}$ we are free to take a vertical wavenumber as small as necessary to ensure $\mathcal{L} \ll 1$ as in (3.27). Taking a vertical wavenumber $k < 10^{-4}\text{m}^{-1}$ ensures that $\mathcal{L} = O(10^{-2})$ or smaller. Taking $k = 10^{-4}\text{s}^{-1}$ yields a vertical lengthscale $H = 6.3 \times 10^4\text{m}$, where the corresponding aspect ratio is $A = 0.04$. Hence, the parameters in table 2.1 are consistent with the predicted scale selection (3.27).

3.3.5   The Weak Field Limit

Figure 3.4 has shown that weak magnetic field induces instability within certain parameter regimes, including the hydrodynamically stable regime ($\Lambda < 1$). Naturally, we consider the weak field regime to categorise the behaviour of the system. For small $\mathcal{L}$, equation (3.23) implies that the roots take the form

$$S_H^2 = \Lambda - 1 - A^2 - \frac{\mathcal{L}^2(\Lambda - 2 - A^2)}{\Lambda - 1 - A^2} + O(\mathcal{L}^4), \tag{3.29}$$

$$S_M^2 = \frac{\mathcal{L}^2(A^2 - \Lambda)}{\Lambda - 1 - A^2} + \frac{\mathcal{L}^4}{(\Lambda - 1 - A^2)^3} + O(\mathcal{L}^6), \tag{3.30}$$

where (3.29) represents the hydrodynamic root $S_H^2 = \Lambda - 1 - A^2$, while (3.30) corresponds to the magnetic root $S_M^2 = 0$.

Clearly, the expansions (3.29) and (3.30) break down when $\Lambda - 1 - A^2 = O(\mathcal{L})$, since the leading and first order terms in $\mathcal{L}^2$ become comparable. We address this by supposing $\Lambda - 1 - A^2 = \alpha\mathcal{L}$ for some constant α of order unity, and substitute into (3.23) to derive the expression

$$S_B^2 = \frac{\alpha\mathcal{L}}{2} \pm \frac{\mathcal{L}}{2}\sqrt{\alpha^2 + 4} + O(\mathcal{L}^2), \tag{3.31}$$

where S_B^2 is the "breakdown" (or singular) root which is valid for $\Lambda - 1 - A^2$ sufficiently close to zero. The positive sign of (3.31) corresponds to unstable modes while the negative corresponds to stable modes. The expressions (3.29), (3.30) and (3.31) describe the weak field regime.

We will first address the use of the expressions (3.29), (3.30) and (3.31) in application to the unstable modes that are shown in figure 3.4. Together, the expansions (3.29), (3.30) and (3.31) indicate that if the flow is hydrodynamically stable ($\Lambda - 1 - A^2 < 0$), then the growth rate of the most unstable mode is given by S_M^2 (equation (3.30)). Thus, when the flow is hydrodynamically stable, the leading order term of equation (3.30) indicates that weak magnetic field increases the growth rate if $\Lambda - 1 < A^2 < \Lambda$ (and increases the frequency if $A^2 > \Lambda$). However, if the flow is hydrodynamically unstable ($\Lambda - 1 - A^2 > 0$), then the growth rate of the most unstable mode is given by S_H^2 (equation (3.29)). Thus, when the flow is hydrodynamically unstable, the second order term in equation (3.29) implies that if $\Lambda < 2$, then weak magnetic field increases the growth rate. Similarly, if $\Lambda > 2$, weak magnetic field increases the growth rate provided $\Lambda - 2 < A^2 < \Lambda - 1$, and stabilises if $A^2 < \Lambda - 2$.

The validity of expressions (3.29), (3.30) and (3.31) can be ensured under the magnetohydrostatic approximation by ensuring that the inequality (3.6) holds, which implies that we require $|S^2 + \mathcal{L}^2| \ll N^2/f_0^2$. The leading order term of equation (3.29) is proportional to $\Lambda - 1 - A^2 > 0$ so that (3.6) implies $|\Lambda - 1 - A^2 + \mathcal{L}^2| \approx |\Lambda - 1 - A^2| \ll N^2/f_0^2$ since $A^2 = l^2 N^2/k^2 f_0^2 \ll N^2/f_0^2$ as the aspect ratio is small. Similarly, equation (3.30) implies that $|S^2 + \mathcal{L}^2| = |\mathcal{L}^2(A^2 - 1 - \Lambda)^{-1}|$ for $A^2 - 1 - \Lambda > 0$. Thus, provided $\Lambda - 1 - A^2$ is not sufficiently close to zero it follows that $|S^2 + \mathcal{L}^2| \ll N^2/f_0^2$. Finally, equation (3.31) implies S_B^2 is $O(\mathcal{L})$ by construction and thus $|S^2 + \mathcal{L}^2| \propto |\mathcal{L}| \ll N^2/f_0^2$ as we are in the weak field limit.
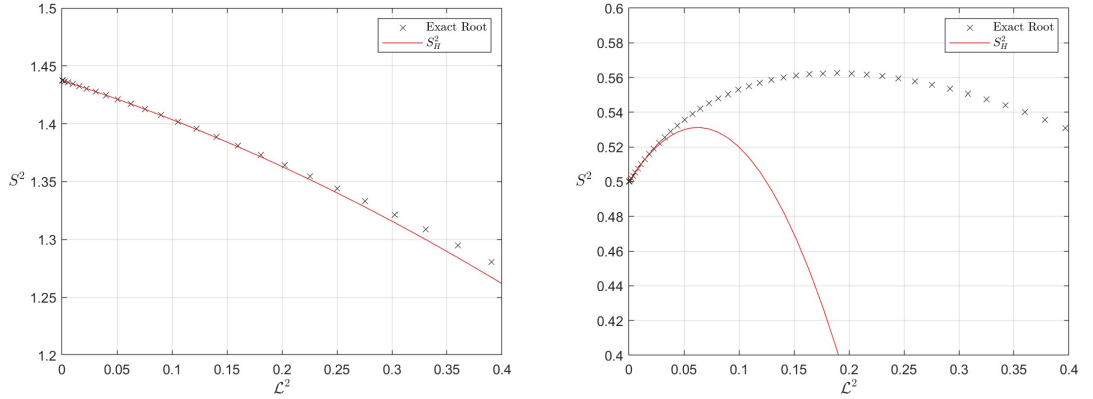
Figure 3.5: Growth rate squared against $\mathcal{L}^2$ in the hydrodynamically unstable regime ($\Lambda - 1 - A^2 > 0$) for $\Lambda = 2.5$ with $A = 0.25$ (left) and $A = 1$ (right). The red line shows the value S_H^2 of the weak field expansion (3.29) while the black is the exact solution (numerically determined from (3.24)).

In figures 3.5 and 3.6 we compare the weak field expansions (3.29) and (3.30) with the exact solution, plotting both against $\mathcal{L}^2$. These plots show various A with $\Lambda = 2.5$, where magnetic field can act to decrease or increase the growth rate as well as generating instability in the hydrodynamically stable regime.

Figure 3.5 illustrates the hydrodynamically unstable regime ($\Lambda - 1 - A^2 > 0$) and the expansion (3.29) at $A = 0.25$ and $A = 1$. We find that both expansions are accurate for weak field; however, for $A = 1$ the accuracy degrades much faster. This is due to the leading order term of (3.29) being larger for $A = 0.25$ so that the $O(\mathcal{L}^4)$ error is smaller. The plots confirm that weak field decreases the growth rate for $A < \sqrt{\Lambda - 2}$, while increasing the growth rate if $\sqrt{\Lambda - 2} < A < \sqrt{\Lambda - 1}$.

Figure 3.6 illustrates when $\Lambda - 1 - A^2 = O(\mathcal{L})$ with $\mathcal{L} \ll 1$ as well as the hydrodynamically stable regime ($\Lambda - 1 - A^2 < 0$). The figure illustrates the breakdown expansion (3.31) at $A = 1.2247$ and the expansion (3.30) at $A = 1$. The expansions are accurate for weak magnetic field. We can also see that magnetic field increases the growth rate in both cases, as predicted by (3.30) and (3.31).

We find that when $\Lambda - 1 - A^2$ is not close to zero, the singular expansion (3.31) still describes the exact root (3.24) in the weak field limit. The reason for this can be determined by taking the second order correction of (3.31), which to $O(\mathcal{L}^3)$ gives (3.24) in the small $\mathcal{L}$ limit. However, this does explain why the singular root (3.31) captures the weak field behaviour of any mode with $\Lambda - 1 - A^2 \neq 0$. To determine how the two roots of (3.31) link to (3.29) and (3.30) in the weak field limit, we consider the large $|\alpha|$ limit of (3.31) and compare with the small $|\alpha|$ limit of (3.29) and (3.30). Specifically, the positive root of (3.31) yields

$$\frac{S^2}{\mathcal{L}} \to \frac{\alpha + |\alpha|(1 + 2/\alpha^2 + \cdots)}{2} \sim \begin{cases} -1/\alpha & \alpha < 0, \\ \alpha & \alpha > 0, \end{cases} \quad \text{as } |\alpha| \to \infty. \quad (3.32)$$
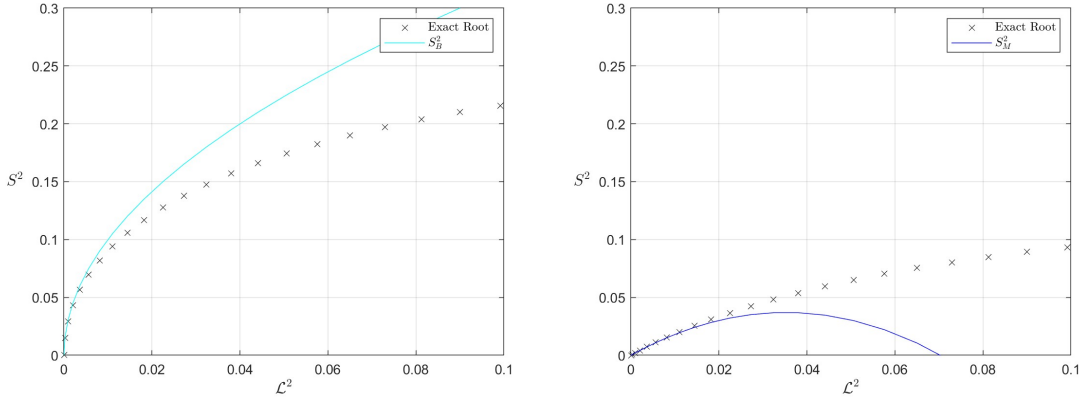
Figure 3.6: Growth rate squared against $\mathcal{L}^2$ in the hydrodynamically unstable regime ($\Lambda - 1 - A^2 > 0$) for $\Lambda = 2.5$ with $A = 1.2247$ (left) and $A = 1.35$ (right). The cyan line shows the value S_B^2 of the weak field singular expansion (3.31) while the black is the exact solution (numerically determined from (3.24)). The blue line shows the value S_M^2 of the weak field expansion (3.30).

Similarly, the negative root of (3.31) yields

$$\frac{S^2}{\mathcal{L}} \to \frac{\alpha - |\alpha|(1 + 2/\alpha^2 + \cdots)}{2} \sim \begin{cases} \alpha & \alpha < 0, \\ -1/\alpha & \alpha > 0, \end{cases} \quad \text{as } |\alpha| \to \infty. \tag{3.33}$$

We also find the the hydrodynamic root (3.29) yields

$$S^2 \sim \alpha \mathcal{L} \text{ as } \alpha \to 0, \tag{3.34}$$

while the magnetic root (3.30) yields

$$S^2 \sim \frac{\alpha \mathcal{L} - 1}{\alpha} \mathcal{L} \sim -\frac{\mathcal{L}}{\alpha} \text{ as } \alpha \to 0. \tag{3.35}$$

Thus, (3.32) shows that the +ve root in (3.31) becomes the hydrodynamic root (3.29) as $\alpha \to +\infty$ and the magnetic root (3.30) as $\alpha \to -\infty$ (or, the hydrodynamic root (3.29) becomes the magnetic root (3.30) as A decreases through $\Lambda - 1$). Likewise, (3.33) shows that the −ve root in (3.31) becomes the magnetic root (3.30) as $\alpha \to +\infty$ and the hydrodynamic root (3.29) as $\alpha \to -\infty$ (or, the hydrodynamic root (3.29) becomes the magnetic root (3.30) as A increases through $\Lambda - 1$). So the roots exchange identity as A passes through $\Lambda - 1$. The hydrodynamic mode is not a single entity that can be tracked through parameter space, and neither is the magnetic mode.

3.3.6 The Small Aspect Ratio Limit

After discussing the weak field limit it is natural to investigate the small A limit of (3.24). This limit can be attained by taking $|k| \to \infty$ with $\mathcal{L} = O(1)$, which, as previously mentioned, is equivalent to the weak field and "thin disc" approximations of Balbus & Hawley (1991). Equivalently, we can just take $|l| \to 0$ to ensure $A \ll 1$, which has no constraints on the field strength and vertical wavenumber. Note that mathematically these interpretations are satisfactory; however, physically, modes with infinite vertical wavenumbers or infinitesimal cross-stream wavenumbers are not feasible.
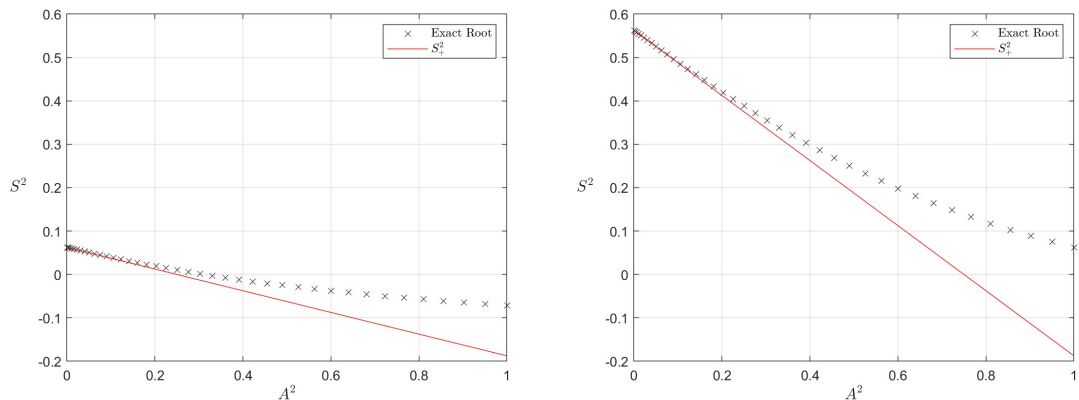
Figure 3.7: The positive (unstable) root S_+^2 of (3.36) plotted with the exact root against A^2 for $\Lambda = 0.5$ (left) and $\Lambda = 1.5$ (right), with $\mathcal{L} = (\Lambda(2 - \Lambda))^{1/2}/2 = \sqrt{3}/4$.

By supposing $A \ll 1$ in equation (3.24), we obtain

$$2S_\pm^2 \approx \Lambda - 1 - 2\mathcal{L}^2 \pm \sqrt{(\Lambda - 1)^2 + 4\mathcal{L}^2} + A^2 \left(-1 \pm \frac{\Lambda - 1}{\sqrt{(\Lambda - 1)^2 + 4\mathcal{L}^2}} \right). \qquad (3.36)$$

The leading order term of (3.36) is just (3.24) in the absence of A. For $\Lambda < 1$ (which is inertially stable since $\Lambda - 1 < 0$), the positive root of (3.36), when unstable, corresponds to the MRI of Balbus & Hawley (1991); the maximum growth rate and the vertical wavenumber at which it occurs are given by (3.26). In the regime $\Lambda > 1$, the $\mathcal{L}$ axis is inertially unstable and thus cannot be categorised as an MRI. The negative root of (3.36) is always stable and corresponds to a shear-modified analogue of the inertial-Alfvén wave (3.16) for $\mathcal{L} = O(1)$, and an Alfvén wave for $\mathcal{L} \gg 1$ at leading order. When the positive root of (3.36) is stable, we can describe the resulting waves in an analogous manner. For both roots of (3.36) we find that the second order term is always negative. Thus, if the system is unstable, an increasing aspect ratio reduces the growth rate, as stable stratification has more of an effect on the mode. If the system is stable, increasing the aspect ratio increases the frequency of the modes.

In figure 3.7, we compare the small A expansions (3.36) with the exact solution, plotting both against A^2. We plot the positive root of (3.36) with $\Lambda = 1.5$ and $\Lambda = 2.5$ for $\mathcal{L}^2 = \Lambda(2 - \Lambda) = 1/16$ (i.e., where the maximum growth rate occurs for $\Lambda = 0.5$ and $\Lambda = 1.5$). As predicted, increasing the aspect ratio decreases the growth rate of the positive root in (3.36).

3.3.7   The Weak Field and Small Aspect Ratio Limit

It is now natural to consider the dual limit of small A and small $\mathcal{L}$. To do this, we suppose that $k^2 v_A^2 f_0^{-2} \sim N^2 l^2 f_0^{-2} k^{-2} \ll 1$ so that A^2 and $\mathcal{L}^2$ are small and of comparable size. We can obtain this limit in a number of ways. For example, assuming f_0 fixed, we can suppose $|k| \to \infty$ such that $\mathcal{L} \sim A \ll 1$, again relating to the weak field and "thin disc" approximations of Balbus & Hawley (1991). We could also leave the vertical wavenumber unconstrained and suppose $|l| \to 0$ such that $\mathcal{L} \sim A \ll 1$ (i.e., weak magnetic field strength). We could also consider a rapidly
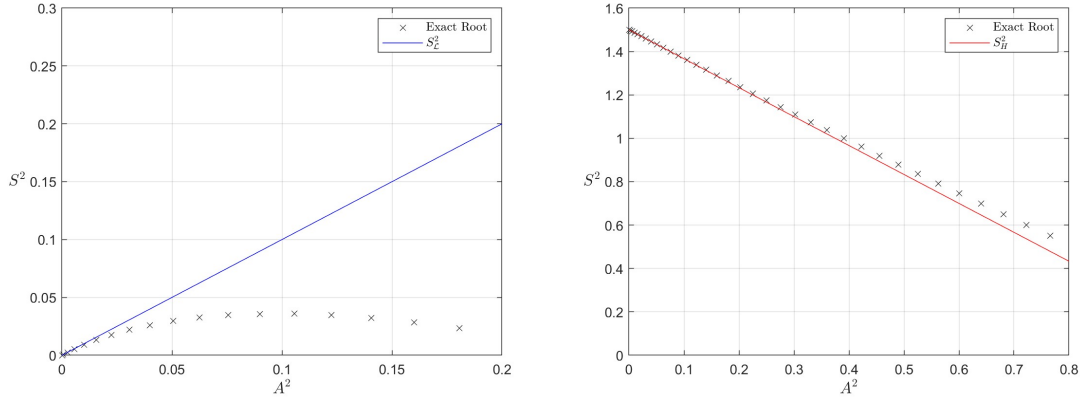
Figure 3.8: In the hydrodynamically stable regime, we plot (3.38) with the exact root against $A^2 = \mathcal{L}^2$ for $\Lambda = 0.5$ (left). In the hydrodynamically unstable regime, we plot (3.37) with the exact root against $A^2 = \mathcal{L}^2$ for $\Lambda = 2.5$ (right).

rotating astrophysical body that exhibits flows with strong latitudinal shear (e.g., Jupiter, or Hot Jupiters) such that $f_0 \sim \Lambda_0$ (so that S may remain order unity) and $\mathcal{L} \sim A \ll 1$. Visually, these limits can be thought of as a small increment from the origin along the line $A = \mathcal{L}$ in the plots of figure 3.4.

Hence, we consider equation (3.24) when $\mathcal{L}^2 \sim A^2 \ll 1$, which yields two modes. The first is a perturbation to the hydrodynamic mode, given by

$$S_H^2 \approx \Lambda - 1 - A^2 - \frac{2 - \Lambda}{1 - \Lambda}\mathcal{L}^2. \tag{3.37}$$

The second is a magnetic mode, given by

$$S_{\mathcal{L}}^2 \approx \frac{\Lambda}{1 - \Lambda}\mathcal{L}^2. \tag{3.38}$$

We could have alternatively derived (3.37) and (3.38) by considering the small A limit of (3.29) and (3.30) or the small $\mathcal{L}$ limit of (3.36). The modes (3.37) and (3.38) can be categorised in a similar manner to that of (3.29) and (3.30); that is, if the flow is hydrodynamically stable we take (3.38) to describe the most unstable mode. Similarly, if the flow is hydrodynamically unstable, (3.37) describes the most unstable mode. If the flow is hydrodynamically unstable ($A^2 < \Lambda - 1$) the magnetic perturbation in (3.37) is negative provided $1 < \Lambda < 2$ and positive otherwise. Again, increasing A acts either to decrease the growth rate of unstable modes or increase the frequency of stable modes.

We compare the small A and $\mathcal{L}$ expansions (3.37) and (3.38) with the exact solution, plotting both against $A^2 = \mathcal{L}^2$. In the hydrodynamically stable regime with $\Lambda = 0.5$, equation (3.38) remains accurate for a small interval of $A^2 = \mathcal{L}^2$. In the hydrodynamically unstable regime with $\Lambda = 2.5$, equation (3.37) remains accurate for a much larger interval of $A^2 = \mathcal{L}^2$. Indeed, the accuracy of (3.37) increases as we increase Λ, while the accuracy of (3.38) decreases as we increase Λ to 1.

3.4   Dynamical Balances

We now consider the dynamical balances of the system, giving physical insight into the instabilities present. This will allow us to determine the dominant terms in the perturbed equations of motion and understand the mechanisms that drive the instabilities in the various parameter regimes of figure 3.4.

We begin by recasting equations (2.22)-(2.26) in terms of the nondimensional parameters (3.22). We then investigate the dynamics of hydrodynamic inertial instabilities, confirming what drives the instability and role of the parameter A in the system. Naturally, this leads us to categorise magnetically modified inertial instabilities, illustrated by the small $\mathcal{L}$ limits of figure 3.4 for $\Lambda = 1.5$ and $\Lambda = 2.5$; we focus primarily on the effect of magnetic field and why this may either increase or decrease the growth rate. Next we consider the arguably simplest case of the purely magnetic instabilities found in figure 3.4; that is, the onset of the MRI found in the small $\mathcal{L}$ limit of figure 3.4 with $\Lambda = 0.5$ and $A \ll 1$. We focus on how weak magnetic field generates instability in a hydrodynamically stable regime. The next dynamical balance we consider is that of the most unstable mode with $\Lambda < 2$, given by (3.26) and seen in figure 3.4 with $\Lambda = 0.5$ or $\Lambda = 1.5$ (both with $A \ll 1$ and $\mathcal{L} = O(1)$). The case $\Lambda = 0.5$ naturally extends from the previous dynamical balance regarding the onset of the MRI; however, the case $\Lambda = 1.5$ is found to be a magnetically modified inertial instability. For $\Lambda > 2$ the most unstable mode occurs in the absence of magnetic field and is therefore described by the dynamical balance of hydrodynamic inertial instability. Next, we consider the instabilities found in the hydrodynamically stable regime with $A = O(1)$, which are found in figure 3.4 for all values of Λ; however, for $\Lambda > 1$ the instabilities occur only when $A^2 > \Lambda - 1$. Naturally, we also consider the dynamical balance as the unstable modes are about to be stabilised either by increasing $\mathcal{L}$ or A in figure 3.4. For completeness we also discuss the dynamical balance of the singular expansion (3.31) which is valid for $A^2 + 1 - \Lambda = O(\mathcal{L})$ with $\mathcal{L} \ll 1$. Then, finally, we discuss the dynamical balance of rapidly rotating instabilities which are otherwise concealed by the chosen timescale $1/f_0$ of the nondimensionalisation (3.22).

We now consider the perturbed equations (2.22), (2.23), (2.24), (2.25) and (2.26) in the absence of diffusion and under the magnetohydrostatic approximation ($\mathcal{H} = 0$). In the presence of uniform magnetic field strength B_0, uniform shear Λ_0 and uniform Coriolis parameter f_0, the equations have solutions of the form $v \propto \exp(i(ly + kz) + st)$. Thus, after neglecting B_1, since it does not affect the dynamics of the flow, equations (2.22)-(2.26) reduce to

$$ su - (f_0 - \Lambda_0)v = \frac{ikB_3}{\mu_0 \bar{\rho}}b_x, \;\; sv + f_0 u = -il\theta + \frac{ikB_3}{\mu_0 \bar{\rho}}b_y, \;\; s\theta = \frac{iN^2}{k}w, \;\; w + \frac{l}{k}v = 0, \;\; (3.39)$$

$$ sb_x = \Lambda_0 b_y + ikB_3 u, \;\; sb_y = ikB_3 v, \;\; sb_z = ikB_3 w, \;\; b_z + \frac{l}{k}b_y = 0, \qquad (3.40)$$

where the incompressibility and solenoidal conditions are also given. The horizontal momentum, thermodynamic and incompressibility equations are given by (3.39). The components of the induction equation and the solenoidal condition are given by (3.40).

It is now convenient to nondimensionalise equations (3.39) and (3.40) under the nondimensional parameters (3.22) with timescale $1/f_0$. The cross-stream and vertical lengthscales are given by $1/l$ and $1/k$, respectively. We nondimensionalise the horizontal velocities with the arbitrary constant V (with dimension of velocity). Via the incompressibility condition the appropriate nondimensionalisation for w is Vl/k. Hence, via the thermodynamic equation in (3.39), the total pressure θ scales with $N^2 l V/k^2 f_0$. We choose to nondimensionalise the cross-stream magnetic field with $V\sqrt{\mu_0\bar{\rho}}$ so that the solenoidal condition implies that the vertical magnetic field scales with $V\sqrt{\mu_0\bar{\rho}}l/k$. Thus, equations (3.39) and (3.40) become

$$Su - (1 - \Lambda)v = i\mathcal{L}b_x, \;\; Sv + u = -iA^2\theta + i\mathcal{L}b_y, \;\; S\theta = iw, \;\; w + v = 0, \tag{3.41}$$

$$Sb_x = \Lambda b_y + i\mathcal{L}u, \;\; Sb_y = i\mathcal{L}v, \;\; b_z + b_y = 0. \tag{3.42}$$

Note that we have dropped the vertical component of the induction equation from (3.42) as it is described by combining the cross-stream component of the induction equation and the solenoidal condition. Note that the imaginary unit i in (3.41) and (3.42) indicates that the quantities are out of phase. For example, in the cross-stream induction equation, v is out of phase with b_y; this is due to the $i\mathcal{L}v$ term originating from a partial derivative with respect to z of v (i.e., from $(\mathbf{B}\cdot\nabla)v$).

This nondimensionalisation allows us to easily investigate the dynamical balances in various limits of the system, which is now defined by the three parameters A, $\mathcal{L}$ and Λ.

3.4.1 Hydrodynamic Inertial Instabilities

We first consider the dynamic balance of hydrodynamic inertial instability (so that $\mathcal{L} = 0$), where equations (3.41) and (3.42) reduce to

$$Su = (1 - \Lambda)v, \;\; Sv + u = -iA^2 p, \;\; Sp = iw, \;\; w + v = 0, \tag{3.43}$$

where p is the hydrodynamic pressure. Equations (3.43) allow us to describe the mechanism of inertial instability in the absence of magnetic field; this will be useful when considering the effects of weak magnetic field in the inertially unstable regime. Note that the cross-stream pressure gradient can be neglected if $A^2 \ll S^2$. This can be seen by writing u and p in terms of v using the along-stream momentum equation, the thermodynamic equation, and the incompressibility constraint.

We can rewrite the cross-stream pressure gradient by combining the thermodynamic equation $Sp = iw$ and the incompressibility condition $v + w = 0$, yielding the equations

$$Su = (1 - \Lambda)v, \;\; Sv + u = -\frac{A^2}{S}v. \tag{3.44}$$

This allows us to see clearly that the cross-stream pressure gradient acts only to reduce the cross-stream acceleration. Equations (3.44) can be combined to yield $S^2 = \Lambda - 1 - A^2$, implying that an increasing aspect ratio reduces the growth rate of any unstable mode; this also implies that the cross-stream pressure gradient always acts to reduce the growth rate of any unstable mode.

The stabilising effect of the cross-stream pressure gradient was also noted by Dunkerton (1981), Stevens (1983) and Griffiths (2008a) for flows on an equatorial β-plane. Note that if $\Lambda - 1 - A^2 < 0$ the system is stable and the dynamical balances are described by those of gravity ($A \gg 1$), inertia ($A \ll 1$) and inertia-gravity waves ($A = O(1)$). If $\Lambda - 1 - A^2 > 0$ the system is inertially unstable.

To describe inertial instability in its simplest form we first neglect the cross-stream pressure gradient in (3.44). Thus, by taking $\Lambda > 1$ (so that the system is inertially unstable) we find, from the along-stream momentum equation, that a positive latitudinal displacement of fluid ($v > 0$) drives a negative longitudinal acceleration ($Su < 0$). The cross-stream momentum equation then implies that the longitudinal displacement of fluid (generated by the negative longitudinal acceleration) is deflected by the Coriolis force, generating a positive latitudinal acceleration ($Sv > 0$) and further displacement of fluid in the latitudinal direction. Thus, as a positive latitudinal displacement of fluid leads to further displacement, it follows that the process runs away.

Note that physically the horizontal motions described cannot continue indefinitely; this leads to an alternative interpretation of the system (which is physically viable), where overturning motions in the meridional plane (i.e., (y, z)-plane) are considered, as illustrated in figure 3.9. The overturning motions are analogous to those of centrifugal instability in the (R, z)-plane.

To understand the role of the aspect ratio A and why the perturbed cross-stream pressure gradient reduces the growth rate of inertial instabilities, we consider overturning motions in the meridional plane (i.e., (y, z)-plane). Consider the parcel of fluid in the bottom left corner of figure 3.9. The parcel is perturbed vertically so that denser fluid is transported up and the density of the atmosphere increases ($\delta\rho > 0$). This generates a negative vertical pressure gradient perturbation ($\partial(\delta p)/\partial z < 0$), made evident from the hydrostatic balance ($dp/dz = -\rho g$). The parcel then moves northward ($v > 0$), which, assuming instability, is supported by along-stream fluid travelling out of the page ($u < 0$) that is deflected northward ($v > 0$) by the Coriolis force. However, due to vertical motions, negative and positive cross-stream pressure gradients are created (see the parcels in the centre row of figure 3.9) that inhibit the cross-stream motions depending upon the value of the rescaled aspect ratio A. Naturally, if the aspect ratio A is small, then the ratio of the vertical lengthscale to the latitudinal lengthscale of the overturning cells is small; thus, even though $\partial_y(\delta p)$ is positive, it is also small and therefore has little dynamical effect. For increasing A, the magnitude of $\partial_y(\delta p)$ increases and thus the latitudinal pressure gradients inhibit cross-stream motions. For $A > \sqrt{\Lambda - 1} > 0$, the pressure gradient is strong enough to instead drive southward ($v < 0$) cross-stream motions, rendering the system stable as the runaway process discussed in the previous paragraph can not occur. Given $A < \sqrt{\Lambda - 1}$ the perturbed cross-stream motions are still positive and by the mechanism that occurs in the horizontal plane, which are discussed in the previous paragraph, are still (perhaps weakly) accelerated amplifying the overturning motions.
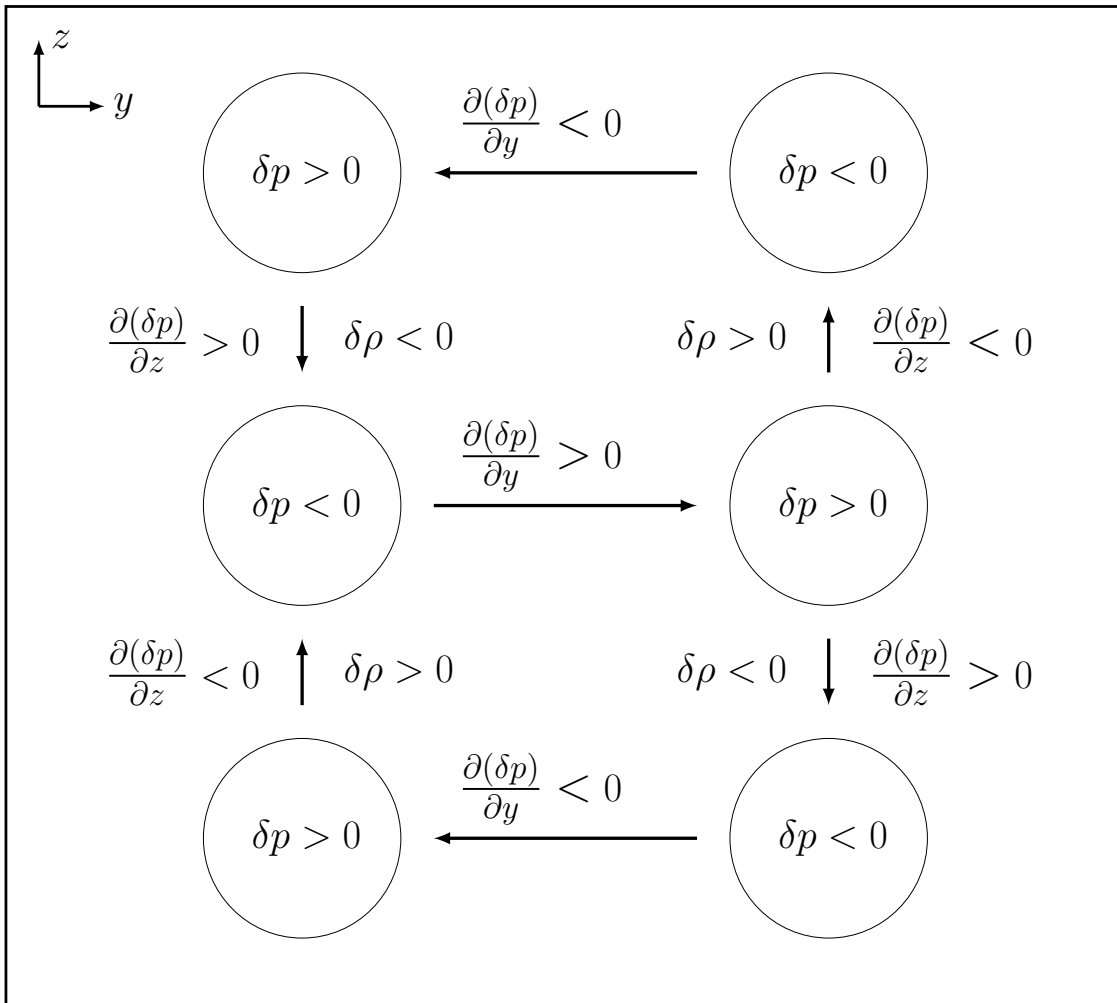
Figure 3.9: Illustration of the overturning motions of inertial instability for latitude y and height z. Arrows represent the direction of fluid motion. The quantities $\delta\rho$ and δp represent small variations in density and pressure. The quantities $\partial(\delta p)/\partial y$ and $\partial(\delta p)/\partial z$ are pressure gradients in the cross-stream and vertical directions.

3.4.2 Magnetically Modified Inertial Instabilities

We will now consider the magnetohydrodynamic dynamical balances of the numerous parameter regimes illustrated in figure 3.4. First, in this section, we consider the dynamical balance of the hydrodynamically unstable regime ($\Lambda - 1 - A^2 > 0$, so that Λ must be greater than 1) in the limit of weak magnetic field ($\mathcal{L} \ll 1$) with $A = O(1)$ and $S = O(1)$, corresponding to the small $\mathcal{L}$ limits of figure 3.4 with $\Lambda = 1.5$ and $\Lambda = 2.5$. This will allow us to describe the mechanisms that allow weak magnetic field to either increase or decrease the growth rate of the unstable hydrodynamic regime, as shown by the weak magnetic field expansion (3.29). In this regime, the cross-stream induction equation see (3.42) implies that $b_y \sim \mathcal{L}v$, while the momentum equations and along-stream induction equation allow us to deduce that $u \sim v$ and $b_x \sim \mathcal{L}v$. Hence, with these scalings, equations (3.41) and (3.42) reduce to

$$Su - (1 - \Lambda)v = 0, \ \ Sv + u = -iA^2\theta, \ \ Sb_x = \Lambda b_y + i\mathcal{L}u, \ \ Sb_y = i\mathcal{L}v. \tag{3.45}$$

The leading order dynamics of the instability remain the same as the hydrodynamic case (3.44); however, magnetic field must increase or decrease the growth rate of the already unstable modes via second order terms, as seen in the weak field expansion (3.29). Note that, if $A \ll S^2$, then the balance would only be altered by neglecting the cross-stream pressure gradient.

To address the second order feedback on the growth rate from the magnetic field we evaluate the Lorentz forces in terms of v. To do this, we substitute for b_y and u in the along-stream induction equation via the cross-stream induction equation and the leading order along-stream momentum balance. This yields $Sb_x = i\mathcal{L}\Lambda v/S + i\mathcal{L}(1 - \Lambda v)v/S = i\mathcal{L}v/S$ so that the along-stream Lorentz force $i\mathcal{L}b_x$ becomes $-\mathcal{L}^2v/S^2$. The cross-stream Lorentz force $i\mathcal{L}b_y$ can simply be re-written in terms of v by using the cross-stream induction equation, yielding $-\mathcal{L}^2v/S$. Thus, for weak magnetic field, the along-stream Lorentz force always acts to increase the growth rate (in comparison to the hydrodynamic case) since it takes the same sign as $(1 - \Lambda)v$ when $\Lambda > 1$. The cross-stream Lorentz force always acts to reduce the growth rate as it takes the same sign as the pressure gradient. Rewriting (3.45) to include the $O(\mathcal{L}^2)$ Lorentz forces yields

$$Su = -(\Lambda - 1)v - \frac{\mathcal{L}^2}{S^2}v, \ \ Sv + u = -\frac{A^2}{S}v - \frac{\mathcal{L}^2}{S}v, \ \ Sb_x = \Lambda b_y + i\mathcal{L}u, \ \ Sb_y = i\mathcal{L}v, \tag{3.46}$$

where the pressure gradient has been written in terms of v to show that it acts to reduce the growth rate. We can see that the along-stream Lorentz force increases the along-stream acceleration generated by the shear Λ dominating over the Coriolis force. This perturbation in the magnitude of the along-stream acceleration then affects the cross-stream momentum balance due to the Coriolis force deflecting the along-stream travelling fluid. Thus, we substitute the along-stream momentum equation into the cross-stream momentum equation for u and then compare the $O(\mathcal{L}^2)$ terms, yielding the following $O(\mathcal{L}^2)$ correction to the acceleration Sv :

$$(Sv)_{\text{correction}} = \frac{\mathcal{L}^2}{S^3}v - \frac{\mathcal{L}^2}{S}v, \tag{3.47}$$

where the first and second terms on the right hand side are contributions from the along-stream and cross-stream Lorentz forces, respectively. Assuming $v > 0$ without loss of generality, it is clear that the contribution from the along-stream Lorentz force acts to give a positive correction to the cross-stream acceleration and therefore increase the growth rate. In contrast, the contribution from the cross-stream Lorentz force acts to give a negative correction to the cross-stream acceleration and therefore decrease the growth rate.

It is thus not clear whether the combined effect of the along-stream and cross-stream Lorentz forces is to enhance or suppress the instability. However, the right hand side of (3.47) is positive if $S^2 < 1$, and hence, upon substituting the leading order solution for the growth rate (i.e., $S = \sqrt{\Lambda - 1 - A^2}$) into this condition, we find that the right hand side of (3.47) is positive if $A^2 > \Lambda - 2$ and negative if $A^2 < \Lambda - 2$. Thus, the correction increases the growth rate if $A^2 > \Lambda - 2$ and decreases the growth rate if $A^2 < \Lambda - 2$ (the first being true for all $\Lambda < 2$). This is consistent with the results of the weak field expansion upon the hydrodynamic mode (3.29). So the question of whether the Lorentz force is stabilising or destabilising turns out to be rather subtle, and depends upon the values of Λ and A.

There are a number of questions left to be answered. Why does the cross-stream Lorentz force always act to decrease the growth rate? Why does the along-stream Lorentz force always act to increase the growth rate? Why does the sign of $A - \Lambda + 2$ determine which Lorentz force is larger in magnitude? To help answer these questions we provide figure 3.10, where vertical magnetic field lines (in teal) have been overlayed on figure 3.9. Physically, the instability still manifests itself in overturning motions in the meridional plane and the process is described in an analogous manner to that of hydrodynamic inertial instability in section 3.4.1; however, magnetic field may amplify or inhibit this dynamical process.

First, we address the stabilising effect of the cross-stream Lorentz force. Figure 3.10 illustrates cross-stream motions interacting with vertical magnetic field lines; this creates a cross-stream magnetic field (see cross-stream induction equation). Then, as indicated by the teal arrows in figure 3.10, a magnetic tension is created that acts to restore the magnetic field lines to their original (vertical) position. The magnetised fluid also feels this restoring force, slowing the cross-stream motions, reducing the cross-stream acceleration.

Second, we address the destabilising nature of the along-stream Lorentz force by considering the along-stream induction equation. Again, figure 3.10 illustrates cross-stream motions interacting with vertical magnetic field lines; this creates a cross-stream magnetic field (see cross-stream induction equation). This cross-stream magnetic field is then sheared into the along-stream direction by the basic flow, generating an along-stream field (see Λb_y in the along-stream induction equation). The cross-stream velocity is also deflected by the Coriolis force and shear which generates a net along-stream acceleration (provided $\Lambda > 1$) opposite to the direction of the along-stream field generated by Λb_y. The along-stream velocity interacts with vertical magnetic field lines, which would generate an along-stream field in the same direction as the flow (see along-stream induction equation); however, the along-stream field generated through the Λb_y term leads
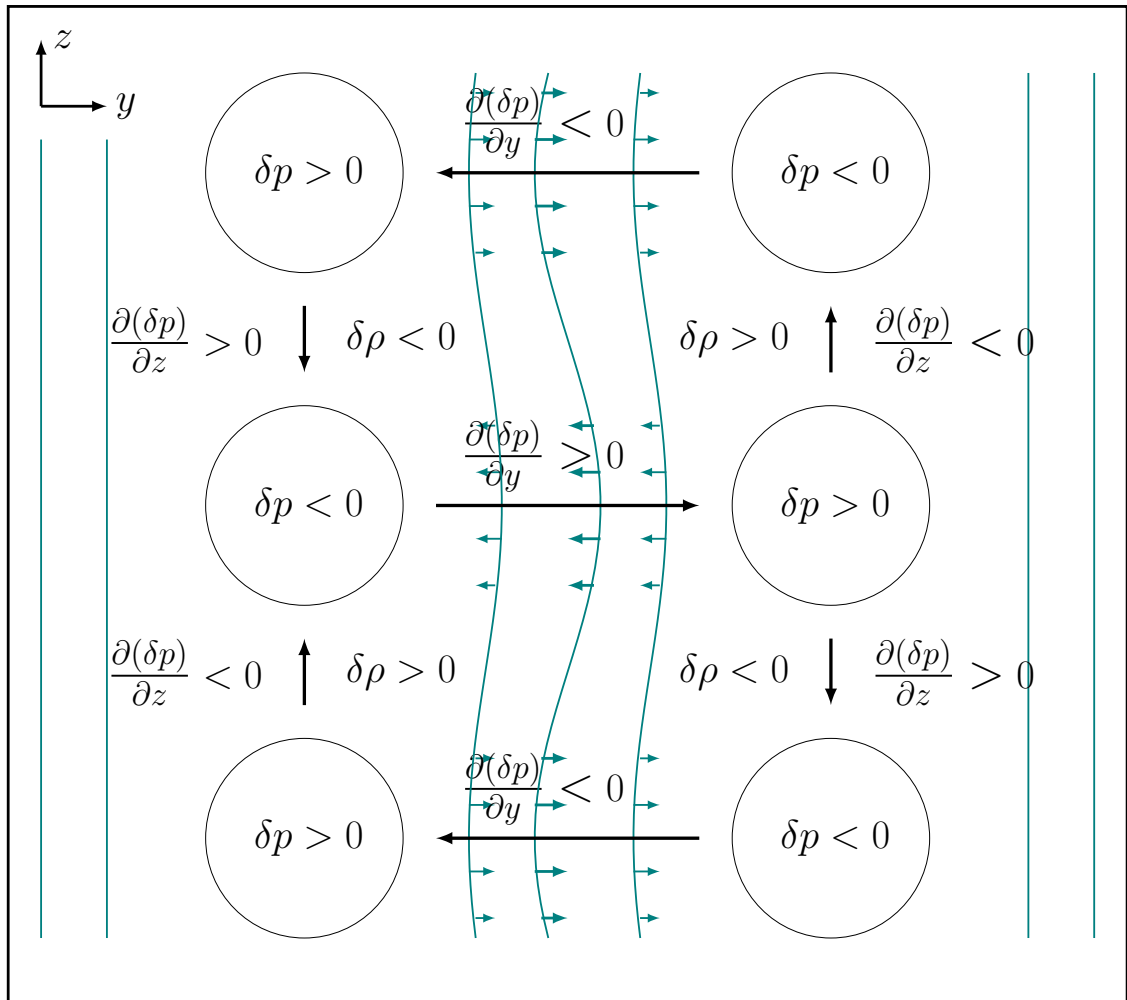
Figure 3.10: Illustration of the overturning motions of inertial instability for latitude y and vertical height z. Black arrows represent the direction of fluid motion. The quantities $\delta\rho$ and δp represent small variations in density and pressure. The quantities $\partial(\delta p)/\partial y$ and $\partial(\delta p)/\partial z$ are pressure gradients in the cross-stream and vertical directions. The teal lines represent magnetic field lines. In the absence of fluid motion, magnetic field lines are vertical; however, these may be bent due to the motion of electrically conducting fluid. This curvature generates magnetic tension, a force that acts to restore the magnetic field line to a vertical position.

to along-stream field magnetic field being generated in the opposite direction to the along-stream velocity.

Interestingly, we could simplify this description by interpreting that the only contribution to along-stream field generation is made by the Coriolis force deflecting cross-stream fluid in the along-stream direction. We see this since $\Lambda b_y = i\mathcal{L}\Lambda v/S$ (cross-stream induction) and $i\mathcal{L}u = i\mathcal{L}(1-\Lambda)v/S$ (along-stream momentum at leading order) have terms including the shear Λ which cancel so that the only term that remains is that originating from the Coriolis force.

The along-stream field generated in the opposite direction to the perturbation velocity u leads to a magnetic tension force that acts to increase the along-stream velocity; this is why the Lorentz force in the along-stream momentum equation takes the form $-\mathcal{L}^2 v/S^2$ in (3.46). Hence, since there is a greater along-stream velocity than in the hydrodynamic case, due to the Lorentz force acting with the shear term, there is also a greater cross-stream velocity owing to the Coriolis force deflecting along-stream motions. The cross-stream velocity is then sheared into the along-stream direction, and the process runs away.

Finally, we address why the sign of $A^2 - \Lambda + 2$ determines whether weak magnetic field increases or reduces the growth rate; indeed, if $S^2 - 1 = \Lambda - 2 - A^2 < 1$ then weak magnetic field increases the growth rate, while if $S^2 > 1$ weak magnetic field decreases the growth rate. We saw this condition in equation (3.47), where it is clear that the contribution to the cross-stream acceleration from the along-stream Lorentz force is a factor of S^2 smaller than the contribution from the cross-stream Lorentz force provided $S^2 > 1$. Thus, by considering that the overturning motions in figure 3.10 are more vigorous for modes with larger growth rates (i.e., $S^2 > 1$), it follows that a larger cross-stream field is generated, which, in turn, yields a larger cross-stream Lorentz force (which acts as a magnetic tension to reduce the cross-stream accelerations). This larger cross-stream Lorentz force then dominates over the magnetic contributions that are deflected from the along-stream Lorentz force by the Coriolis force, as seen in equation (3.47).

In terms of the parameter A, an increasing aspect ratio reduces the growth rate and therefore the speed of the overturning motions (since there is a larger cross-stream pressure gradient for modes with a larger aspect ratio, as we discussed in section 3.4.1). Thus, by increasing the aspect ratio, we reduce the magnitude of the cross-stream Lorentz force, which acts as tension to reduce the cross-stream motions. This leads to the correction (3.47) being positive, where weak magnetic field once again increases the growth rate. For example, if we consider figure 3.4 with $\Lambda = 2.5$, weak magnetic field is stabilising for $A < \Lambda - 2$ (as the expansion (3.29) shows). Then, as A increases beyond $A = \Lambda - 2$, weak magnetic field increases the growth rate instead.

3.4.3 The Onset of the Magnetorotational Instability

We now consider the simplest possible occurrence of the purely magnetic instabilities found in figure 3.4. That is, the limit of weak magnetic field with $A \ll 1$ of the hydrodynamically stable regime ($\Lambda < 1$), which is illustrated in figure 3.4 for $\Lambda = 0.5$.

We focus on the unstable magnetic mode (3.30) where $S \ll 1$ with $\mathcal{L} \ll 1$, in which the cross-stream induction equation in (3.42) implies $b_y \sim \mathcal{L}v/S$, where, as a result, the cross-stream momentum equation in (3.41) implies that $u \sim Sv$ or $u \sim \mathcal{L}^2 v/S$. In either case, the along-stream induction equation (3.42) shows that $S \sim \mathcal{L}$ and $i\mathcal{L}u$ to be negligible. Thus, $b_y \sim v, u \sim \mathcal{L}v$ and $b_x \sim v/\mathcal{L}$ in which case (3.41) and (3.42) reduce to

$$-(1-\Lambda)v = i\mathcal{L}b_x, \;\; Sb_x = \Lambda b_y, \;\; Sb_y = i\mathcal{L}v, \tag{3.48}$$

where the along-stream velocity u is prescribed by the cross-stream momentum equation

$$Sv + u = -iA^2\theta + i\mathcal{L}b_y. \tag{3.49}$$

Note that we still retain four equations for the four quantities u, v, b_x, and b_y (recalling that the thermodynamic equation allows us to write $\theta = -iv/S$); however, three of these decouple (shown in (3.48)), whilst the other prescribes the along-stream velocity u. The pressure gradient $iA^2\theta$ may be neglected if $A \ll \mathcal{L}$. This can be seen by comparing terms in (3.49) after combining the thermodynamic equation and incompressibility condition in (3.41) yielding $\theta = -iv/S$, and using the cross-stream induction equation to write $b_y = ilv/S$. The equations of (3.48) imply $S^2 = \mathcal{L}^2\Lambda/(1-\Lambda)$, in agreement with the leading order term in the weak field expansion (3.30) when $A \ll \mathcal{L} \ll 1$. This implies that the cross-stream momentum equation (3.49) does not play a role in the dynamical balance and only prescribes the along-stream velocity u. Note that usually a balance between the Coriolis and Lorentz force is defined as magnetostrophic; however, since the advection and Coriolis terms are always the same order of magnitude when $\Lambda = O(1)$ in this system, we assert that the along-stream momentum equation in (3.48) is in magnetostrophic balance. We do this as the balance is repeatedly observed in the analysis of this section, and later in Chapter 6.

To classify the dynamics of the hydrodynamically stable regime when $A \ll 1$ and $\Lambda < 1$ we consider a latitudinal displacement. The displacement yields a cross-stream velocity so that the cross-stream induction equation in (3.48) implies that an out of phase cross-stream magnetic field is generated due to field line stretching, as seen in figure 3.10. The cross-stream magnetic field is then sheared by the basic flow so that an along-stream field is generated (see along-stream induction equation in (3.48)). The along-stream field generates an along-stream Lorentz force, which is balanced by an increasing cross-stream flow (which is deflected in the along-stream direction by the basic flow and Coriolis force) so that the magnetostrophic balance is maintained. Thus, as the perturbed cross-stream velocity must increase to retain the balance, yet more cross-stream field is generated and the process runs away. This describes the magnetorotational instability, in which weak magnetic field generates instability within the hydrodynamically stable regime. The classical argument of Balbus & Hawley (1991) in which two parcels are tethered may also describe this process, where radial displacements are considered rather than latitudinal.

We now provide contour plots of the momentum equations as well as the along-stream induction equation using the nondimensional equations (3.41) and (3.42) to illustrate the dynamical
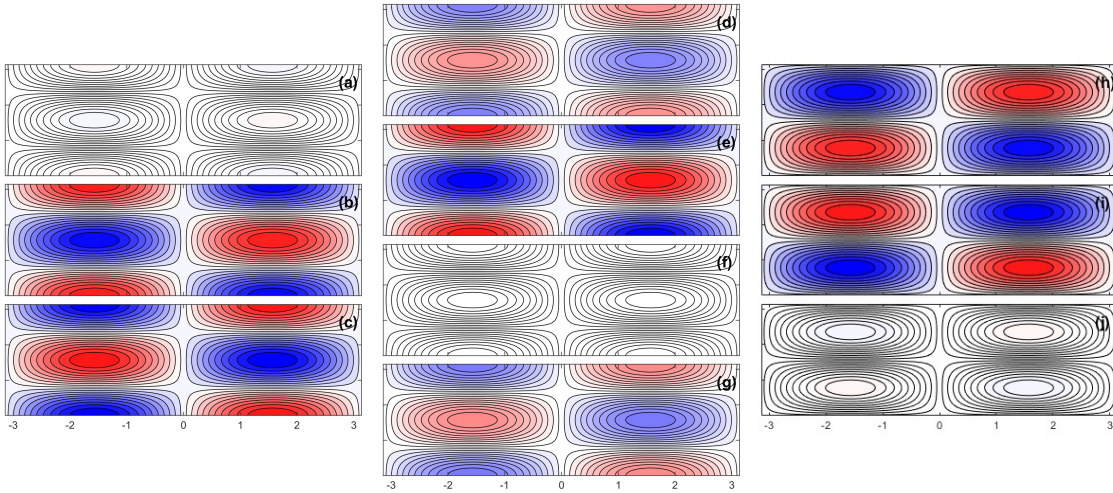
Figure 3.11: The dynamical balance of (3.48) at $A = 0.01$ and $\mathcal{L} = 0.1$ with $\Lambda = 0.5$, illustrating a magnetic perturbation from the hydrodynamic regime. This is the onset of the magnetorotational instability with growth rate $S = 0.096$. Plots (**a**), (**b**) and (**c**) show the along-stream acceleration, advection and Coriolis terms, and Lorentz force. Plots (**d**), (**e**), (**f**) and (**g**) show the cross-stream acceleration, Coriolis force, pressure gradient and Lorentz force. Plots (**h**), (**i**) and (**j**) show the along-stream field generation, advection and tension terms.

balance (3.48) in figure 3.11 for $\mathcal{L} = 0.1$ and $A = 0.01$ with $\Lambda = 0.5$. We find that the terms balance, as predicted by (3.48), showing that the along-stream magnetic field perturbation b_x is large enough to allow the Lorentz force in the along-stream momentum equation in (3.48) to generate a magnetostrophic balance in which there is no along-stream acceleration. This confirms that the cross-stream momentum equation does not affect the dynamical balance and only prescribes the along-stream velocity u.

3.4.4 The Most Unstable Modes

The most unstable mode in the hydrodynamically stable regime occurs when $A \ll 1$, with $\mathcal{L}^2 = \Lambda(2 - \Lambda)/4$; however, this criteria remains the same in the hydrodynamically unstable regime, provided $\Lambda < 2$ (see equation (3.26)). Note that, if $\Lambda > 2$, the most unstable mode is the hydrodynamic mode with $A \ll 1$, which is described by the dynamical balance (3.44).

Thus, for $\Lambda < 2$, it is convenient to address the hydrodynamically stable ($\Lambda < 1$) and unstable regimes ($\Lambda > 1$), where $A \ll 1, \mathcal{L} = O(1)$ and $S = O(1)$, as shown in figure 3.4 for $\Lambda = 0.5$ and $\Lambda = 1.5$. This regime may describe any unstable mode on the $\mathcal{L}$ axis, provided $\mathcal{L}$ is not small or sufficiently close to $\sqrt{\Lambda}$. Under the assumptions, the cross-stream induction equation in (3.42) implies that $b_y \sim v$, which we can deduce from the along-stream and cross-stream momentum equations in (3.41) and the along-stream induction equation in (3.42) that $b_x \sim u \sim v$. Hence, the balance is categorised by

$$Su - (1 - \Lambda)v = i\mathcal{L}b_x, \ \ Sv + u = i\mathcal{L}b_y, \ \ Sb_x = \Lambda b_y + i\mathcal{L}u, \ \ Sb_y = i\mathcal{L}v. \tag{3.50}$$
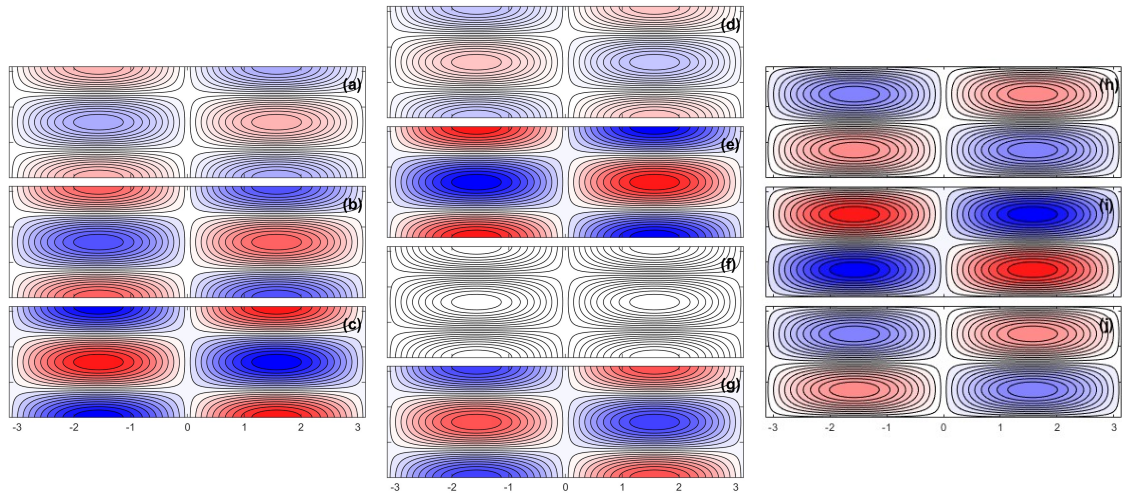
Figure 3.12: The dynamical balance of (3.50) at $A = 0.01$ and $\mathcal{L}^2 = \Lambda(2 - \Lambda)/4$ with $\Lambda = 0.5$, illustrating the most unstable mode of the MRI with growth rate $S = 0.250$. Plots (**a**), (**b**) and (**c**) show the along-stream acceleration, advection and Coriolis terms, and Lorentz force. Plots (**d**), (**e**), (**f**) and (**g**) show the cross-stream acceleration, Coriolis force, pressure gradient and Lorentz force. Plots (**h**), (**i**) and (**j**) show the along-stream field generation, advection and tension terms.

Under our assumptions the only simplification to the dynamical balance (3.50) from equations (3.41) and (3.42) is that the cross-stream pressure gradient may be neglected since $A \ll 1$ and therefore $A \ll \mathcal{L}$. This lack of simplification is made evident when combining the equations of (3.50), which yields the two modes (with A neglected) of equation (3.24), one of which is always stable. Thus, it may be possible to simplify the dynamical balance (3.50) further to describe the unstable mode only. We investigate this by providing contour plots of the momentum equations as well as the along-stream induction equation using the nondimensional equations (3.41) and (3.42). This will also allow us to determine which terms in each equation are stabilising or destabilising. Thus, we contour terms of (3.50) in figures 3.12 and 3.13 for $\Lambda = 0.5$ and 1.5, respectively, with $A = 0.01$ and $\mathcal{L}^2 = \Lambda(2 - \Lambda)/4$, in order to address the hydrodynamically stable and unstable regimes.

Figure 3.13 shows that the most unstable mode for $\Lambda = 1.5$ is a magnetically modified inertial instability rather than an MRI similar to that of figure 3.12 when $\Lambda = 0.5$. This is made evident by the contours of figure 3.13, where the along-stream acceleration (**a**), the along-stream advection and Coriolis (**b**), the cross-stream acceleration (**c**), and the cross-stream Coriolis force (**d**) are clearly the dominant terms in the along-stream and cross-stream momentum equations. Alone, these four terms describe the dynamical balance of (3.44), while the weak contributions from the Lorentz forces yield a balance similar to that of the dynamical balance of magnetically modified inertial instabilities (3.45).

The differences between figures 3.12 and 3.13 show that we must neglect different terms in each regime to reduce the dynamical balance (3.50) so that it describes the most unstable mode only. In figure 3.12, when $\Lambda = 0.5$, we can observe that the cross-stream momentum equation is
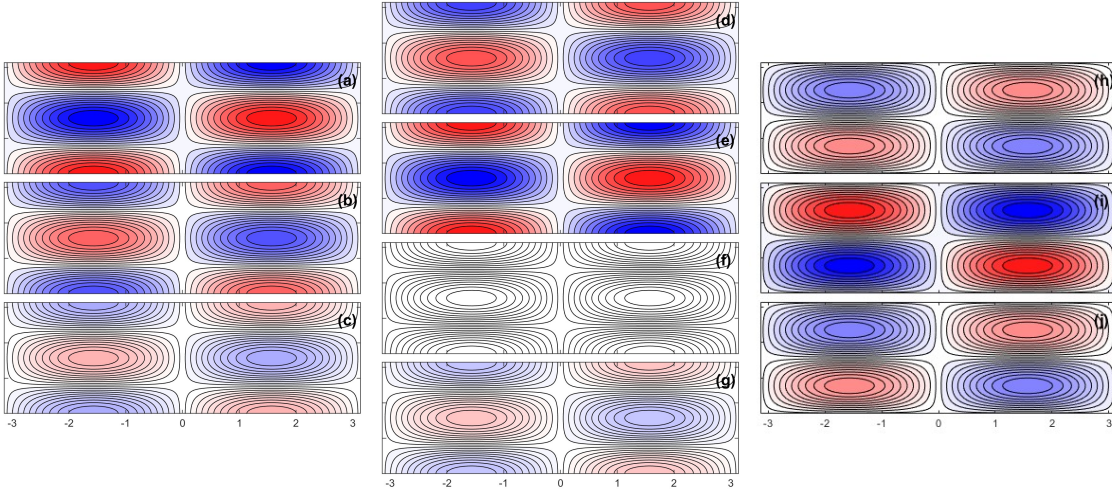
Figure 3.13: The dynamical balance of (3.50) at $A = 0.01$ and $\mathcal{L}^2 = \Lambda(2 - \Lambda)/4$ with $\Lambda = 1.5$, illustrating the most unstable mode of the inertially unstable regime for $1 < \Lambda < 2$ with growth rate $S = 0.750$. Panel layout as in figure 3.12.

approximately in a magnetostrophic balance, motivating us to neglect the cross-stream acceleration Sv. In so doing, the dynamical balance (3.50) may be solved for S, yielding

$$S^2 = \mathcal{L}^2 \frac{(\Lambda - \mathcal{L}^2)}{\mathcal{L}^2 + 1 - \Lambda}, \tag{3.51}$$

which reduces to the weak field expansion (3.30) in the small A limit and is unstable provided $\Lambda - 1 < \mathcal{L}^2 < \Lambda$.

Using a similar justification we may also neglect the along-stream acceleration Su or the $i\mathcal{L}u$ term in the along-stream induction equation alongside the cross-stream acceleration. First, if we neglect Su and Sv the dynamical balance (3.50) may be solved for S, yielding

$$S^2 = \mathcal{L}^2 \frac{(\Lambda - \mathcal{L}^2)}{1 - \Lambda}, \tag{3.52}$$

which reduces to the weak field expansion (3.30) in the small A limit and is unstable provided $\mathcal{L}^2 < \Lambda < 1$.

Neglecting Sv and $i\mathcal{L}u$, the dynamical balance (3.50) may be solved for S, yielding

$$S^2 = \mathcal{L}^2 \frac{\Lambda}{\mathcal{L}^2 + 1 - \Lambda}, \tag{3.53}$$

which reduces to the weak field expansion (3.30) in the small A limit and is unstable provided $\Lambda - 1 < \mathcal{L}^2$. Note that, on neglecting $i\mathcal{L}b_y$ and Su, we obtain the same expression (3.53).

Thus, to determine if neglecting these terms yields a reasonable approximation, we plot (3.51), (3.52) and (3.53) with the exact growth rate at $A = 0.01$ in figure 3.14 for $\Lambda = 0.25, \Lambda = 0.5$ and $\Lambda = 0.75$, respectively. The figures allow us to conclude that $Su, Sv, i\mathcal{L}b_y$ and $i\mathcal{L}u$ are all stabilising terms for $\Lambda < 1$ since neglecting them increases the growth rate of the system. We find that the accuracy of the approximations reduces as we increase Λ towards unity. We expect this since values of Λ greater than 1 make the $A \ll 1$ regime unstable to magnetically modified inertial
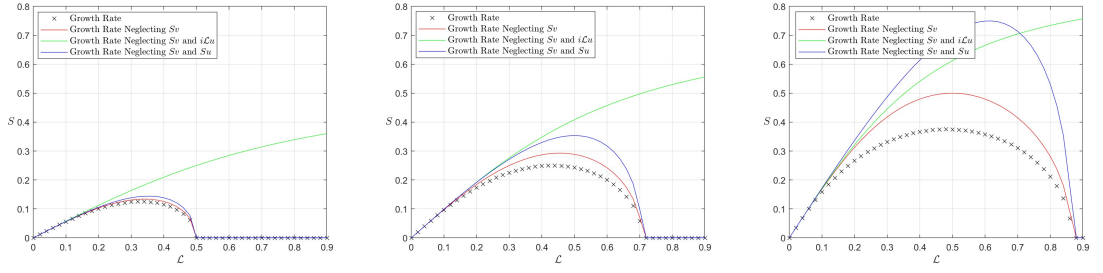
Figure 3.14: The exact growth rate plotted with the approximate growth rates (3.51), (3.52) and (3.53) with $A = 0.01$ for $\Lambda = 0.25, 0.5$ and 0.75, respectively.

instabilities, as seen in figure 3.13. Clearly, the approximation (3.51), where a magnetostrophic balance is taken in the cross-stream direction, is the most accurate for all values of Λ.

We can apply a similar method to figure 3.13, where the system is hydrodynamically unstable with $\Lambda = 1.5$. On inspection of figure 3.13 it is reasonable to neglect the along-stream or cross-stream Lorentz forces; neglecting both Lorentz forces yields hydrodynamic inertial instability, which has been previously categorised by the balance (3.44). However, neglecting one of the Lorentz forces yields a very inaccurate approximation. It is worth noting that for $2 > \Lambda > 1$, the along-stream advection term $(1 - \Lambda)v$ along with the along-stream and cross-stream accelerations Su and Sv are now destabilising. This is contrary to the case for $\Lambda < 1$. Thus, when $1 < \Lambda < 2$, the only stabilising terms are the cross-stream Lorentz force $i\mathcal{L}b_y$ and the $i\mathcal{L}u$ term in the along-stream induction equation, which is consistent with the analysis of the dynamical balances of magnetically modified inertial instabilities.

3.4.5 Stratified Magnetic Instabilities

We now discuss the dynamical balance of the hydrodynamically stable regime in the weak field limit ($\mathcal{L} \ll 1$) with $A = O(1)$ such that $A^2 + 1 - \Lambda > 0$. This allows us to investigate the hydrodynamic stable regimes ($A^2 > \Lambda - 1$) of figure 3.4 with $\Lambda > 1$. The assumptions also apply to figure 3.4 with $\Lambda = 0.5$, where the system is always hydrodynamically stable since $\Lambda < 1$. Again, we focus on the unstable modes so that $S \ll 1$ when $\mathcal{L} \ll 1$ and $A = O(1)$. Since $A = O(1)$, the pressure gradient will now play a significant role in the dynamical balance in comparison to (3.49).

Under the assumptions $S \ll 1$, $\mathcal{L} \ll 1$ and $A = O(1)$, the thermodynamic and incompressibility equations in (3.41) imply that $\theta \sim v/S$ in general, in which it follows from the incompressibility constraint that $u \sim v/S$ when $A = O(1)$. Once again, the cross-stream induction equation in (3.42) implies that $b_y \sim \mathcal{L}v/S$, from which it follows from the along-stream induction equation in (3.42) that $b_x \sim \mathcal{L}v/S^2$. Hence, after substituting the expressions for u and b_x into the along-stream momentum equation in (3.41) we find that $S \sim \mathcal{L}$. Thus, $b_y \sim v, u \sim v/\mathcal{L}$ and $b_x \sim v/\mathcal{L}$ so that equations (3.41) and (3.42) yield the following dynamical balance:

$$Su - (1 - \Lambda)v = i\mathcal{L}b_x, \quad u = -iA^2\theta, \quad Sb_x = \Lambda b_y + i\mathcal{L}u, \quad Sb_y = i\mathcal{L}v, \qquad (3.54)$$

where the pressure gradient is determined by the thermodynamic and incompressibility equations in (3.41), yielding $-iA^2\theta = -A^2v/S$. Thus, comparing (3.54) to (3.49) we can see that when $A = O(1)$, the pressure gradient and the along-stream velocity play a significant role in the dynamical balance. We can confirm this by combining the equations of (3.54), to obtain the leading order term of the weak field expansion (3.30), since the equations imply $S^2 = (\Lambda - A^2)\mathcal{L}^2/(A^2 + 1 - \Lambda)$.

We now provide contour plots of the momentum equations, as well as the along-stream induction equation using the nondimensional equations (3.41) and (3.42), to illustrate the dynamical balance (3.54) for various Λ and A with $\mathcal{L} = 0.1$. In figure 3.15 we plot the dynamical balance (3.54) for $\Lambda = 0.5$ with $A = 0.5$ illustrating a stratified analogue of the MRI on the f-plane. In particular, the analogy is made clear when comparing figure 3.15 with 3.12; the only difference is that the cross-stream Coriolis force is being balanced by the pressure gradient in figure 3.15 (geostrophic balance) rather than the Lorentz force (magnetostrophic balance) in figure 3.12. We also plot the dynamical balance (3.54) with $A = 0.5$ for $\Lambda = 1.5$ in figure 3.16, illustrating an analogous instability to that of figure 3.15; this similarity arises as both cases are hydrodynamically stable (i.e., $\Lambda - 1 - A^2 < 0$). We note that a very similar dynamical balance is also found to that of figure 3.12 with $\Lambda = 2.5$ for larger A (so that the system is hydrodynamically stable). Comparing figures 3.15 and 3.16, we find that the cross-stream momentum and along-stream induction equations are approximately identical, while the along-stream momentum equation of figure 3.16 differs from that of 3.15 as $(1 - \Lambda)$ has changed sign to act with the Lorentz force, thus driving a greater along-stream acceleration. Comparing figure 3.15 with figure 3.11 where $\Lambda = 0.5, \mathcal{L} = 0.1$ and $A = 0.01$, it is clear that the growth rate decreases when increasing A. This is due to the geostrophic balance in the cross-stream momentum equation in figure 3.15, which in turn dampens the along-stream field generation. This breaks the magnetostrophic balance in the along-stream momentum equation, generating an along-stream acceleration, which dampens the instability.

3.4.6 Stabilisation of the Unstable Mode

We now consider the dynamic balance when the magnetic field or pressure gradient is about to stabilise the system, that is, when $S \ll 1$, $A = O(1)$ and $\mathcal{L} = O(1)$. Under these assumptions, the cross-stream induction equation in (3.42) implies $b_y \sim v/S$, and thus the cross-stream momentum equation in (3.41) implies that $u \sim v/S$ since $\theta \sim v/S$. Then, the along-stream momentum equation in (3.41) implies that $b_x \sim v$ or smaller, so that the along-stream induction equation in (3.42) reduces to a relation between u and b_y. Thus, by combining the cross-stream momentum equation in (3.41) and the along-stream induction equation in (3.42) with the cross-stream induction equation it follows that $A^2 + \mathcal{L}^2 \sim \Lambda$ and $b_x \sim v$. Hence, the dynamical balance is given by

$$Su - (1 - \Lambda)v = i\mathcal{L}b_x, \quad u = -iA^2\theta + i\mathcal{L}b_y, \quad 0 = \Lambda b_y + i\mathcal{L}u, \quad Sb_y = i\mathcal{L}v, \qquad (3.55)$$
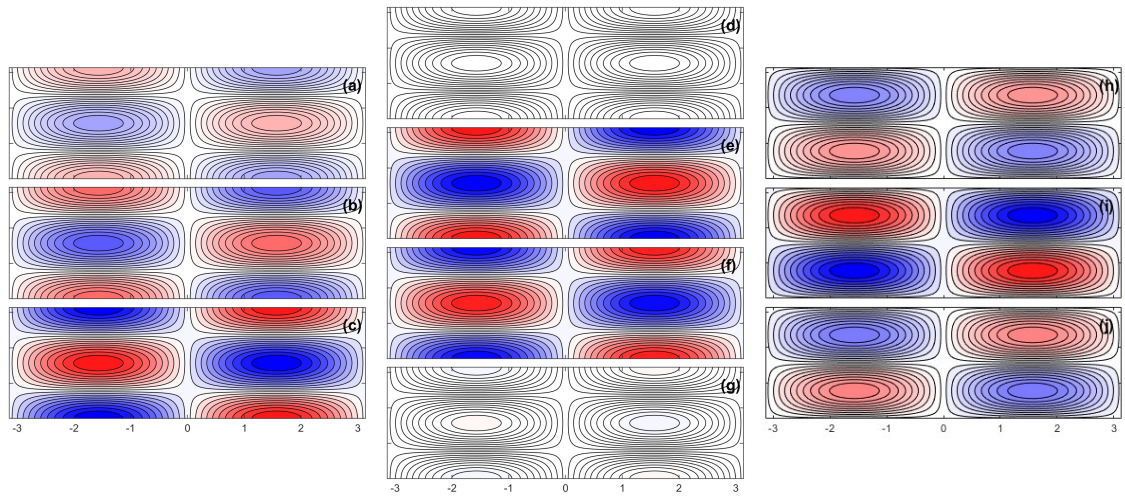
Figure 3.15: The dynamical balance of (3.54) at $A = 0.5$ and $\mathcal{L} = 0.1$ with $\Lambda = 0.5$, illustrating a stratified analogue of the MRI on the f-plane with growth rate $S = 0.056$. Panel layout as in figure 3.12.
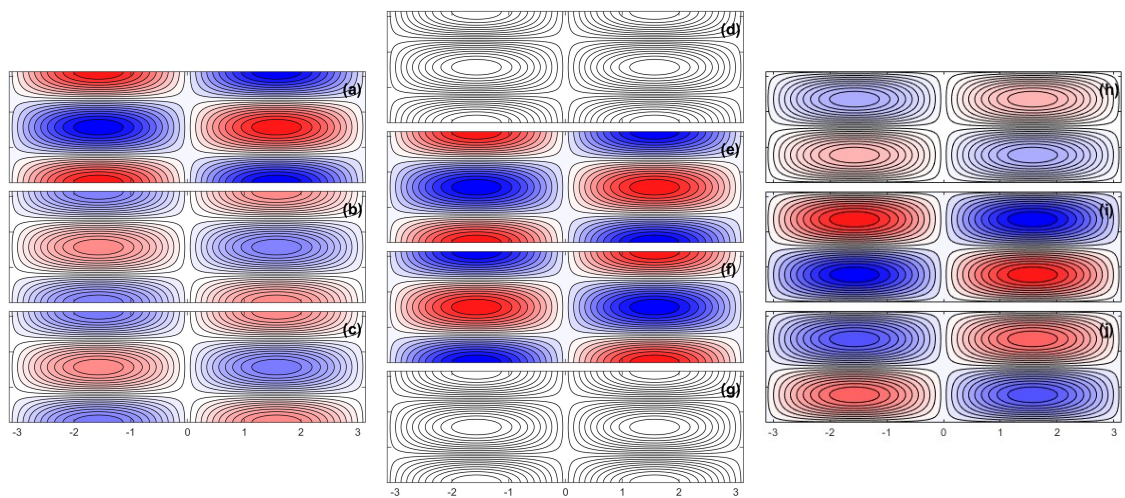
Figure 3.16: The dynamical balance of (3.54) at $A = 1$ and $\mathcal{L} = 0.1$ with $\Lambda = 1.5$, illustrating a stratified magnetic instability (similar to the stratified MRI of figure 3.15) with growth rate $S = 0.096$. Panel layout as in figure 3.12.
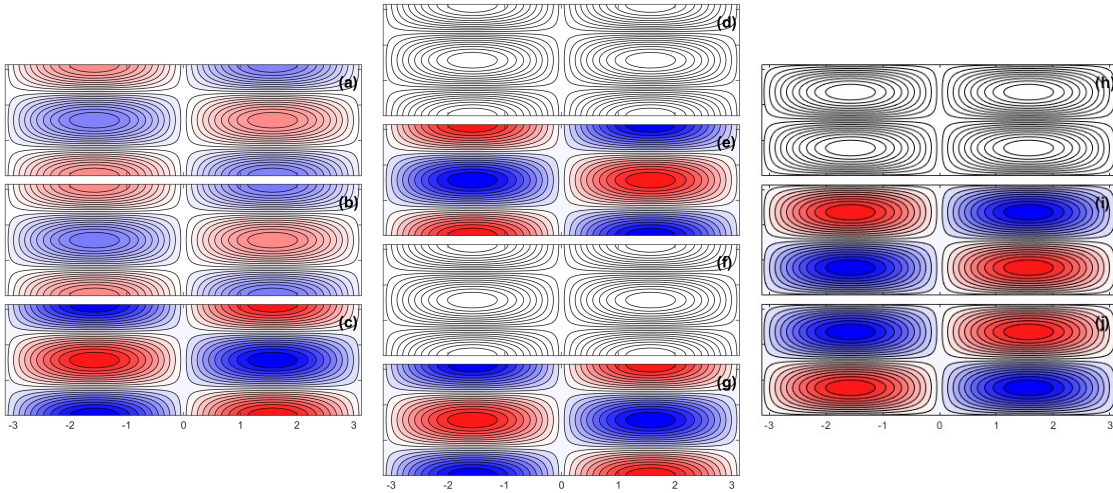
Figure 3.17: The dynamical balance of (3.55) at $A = 0.01$ and $\mathcal{L} = 0.7$ with $\Lambda = 0.5$, illustrating the stabilisation of the unstable mode on the f-plane in the hydrodynamically stable regime with growth rate $S = 0.057$. Panel layout as in figure 3.12.

in which b_x is prescribed by

$$Sb_x = \Lambda \hat{b}_y + i\mathcal{L}\hat{u}, \tag{3.56}$$

where $\hat{b}_y \sim Sv$ and $\hat{u} \sim Sv$ are the second order corrections for b_y and u, respectively. Under these assumptions, the equations of (3.55) describe the dynamical balance at leading order; however, we are required to retain the second order along-stream induction equation (3.56) to prescribe a value of b_x and ensure the equations of (3.55) are closed. Note that, if $A \ll 1$, then the pressure gradient can be neglected in the cross-stream momentum equation in (3.55) with no other change to the dynamical balance. The equations of (3.55) and (3.56) are in line with the previous results, where many stabilising terms are now dominating the dynamical balance. For example, $i\mathcal{L}u$ now balances Λb_y in the along-stream induction equation, inhibiting the generation of along-stream field.

We now provide contour plots of the momentum equations as well as the along-stream induction equation using the nondimensional equations (3.41) and (3.42) to illustrate the dynamical balance in figures 3.17 and 3.18 for $A = 0.01$ with $\Lambda = 0.5$ and $\Lambda = 1.5$, respectively. In both cases, we find that the terms balance, as predicted by (3.55), where the along-stream Lorentz force still plays a role in the along-stream momentum equation even when there is little generation of along-stream field via the along-stream induction equation in (3.55). Thus, since there is little generation of along-stream field, the destabilising mechanism of the along-stream Lorentz force is very weak so that the growth rate becomes very small.

3.4.7 The Singular Expansion

We have already discussed in section 3.3.5 that neither the hydrodynamically unstable mode nor the magnetic (hydrodynamically stable) mode are single entities that can be tracked through parameter space; instead we have a single stable mode and a single unstable mode; the nature of

78
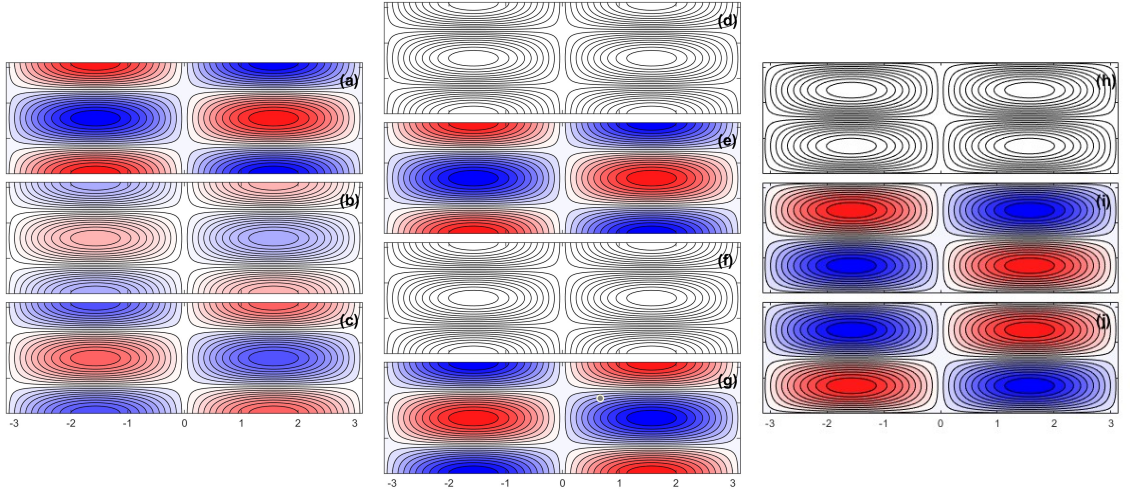
Figure 3.18: The dynamical balance of (3.55) at $A = 0.01$ and $\mathcal{L} = 1.22$ with $\Lambda = 1.5$, illustrating the stabilisation the unstable mode on the f-plane in the hydrodynamically unstable regime with growth rate $S = 0.083$. Panel layout as in figure 3.12.

the latter transitions from magnetically modified inertial instabilities to magnetic instabilities as we move through parameter space. An interesting transition occurs in the weak field limit as highlighted by the singular expansion (3.31) and the asymptotic analysis of (3.32)-(3.35).

Thus, we consider the dynamical balance when $\mathcal{L} \ll 1$ with $A^2 + 1 - \Lambda = \alpha\mathcal{L}$ for some constant α of order unity, where the singular expansion (3.31) implies that $S \sim \mathcal{L}^{1/2}$. Under these assumptions, equations (3.41) and (3.42) imply that $b_y \sim \mathcal{L}^{1/2}v, u \sim \mathcal{L}^{-1/2}v$ and $b_x \sim v$, so that the dynamical balance in the limit becomes

$$Su - (1 - \Lambda)v = 0, \ \ u = -iA^2\theta, \ \ Sb_x = \Lambda b_y + i\mathcal{L}u, \ \ Sb_y = i\mathcal{L}v, \tag{3.57}$$

which is purely hydrodynamic at leading order, representing a neutrally stable mode. However, upon writing $-iA^2\theta = -A^2v/S$ (as we have done previously) and substituting the cross-stream momentum equation into the along-stream momentum equation in (3.57) the leading order (hydrodynamic) terms cancel and the left hand side of the along-stream momentum equation reduces to $(\Lambda - 1 - A^2)v$, which is $O(\mathcal{L}v)$ and can therefore balance the along-stream Lorentz force. Similarly, by writing $-iA^2\theta = -A^2v/S$ and substituting the along-stream momentum equation into the cross-stream momentum equation in (3.57) yields $(1 - \Lambda + A^2)v = 0$, where the left hand side is $O(\mathcal{L}v)$ and is balanced by an $O(\mathcal{L}v)$ cross-stream acceleration and Lorentz force.

To confirm that the dynamical balance (3.57) describes the singular expansion (3.31), we evaluate the Lorentz forces in terms of v, yielding $i\mathcal{L}b_x = -\mathcal{L}^2(\Lambda - A^2)v/S^2$ and $i\mathcal{L}b_y = -\mathcal{L}^2v/S$. Then, upon substitution of the along-stream momentum equation into the cross-stream momentum equation in (3.57) and considering the $O(\mathcal{L})$ terms, we do indeed obtain the singular expansion (3.31). If we neglect the $O(\mathcal{L})$ cross-stream acceleration Sv, we obtain the magnetic expansion (3.29). Similarly, neglecting the correction $i\mathcal{L}b_x$, we obtain the leading order hydrodynamic growth rate.
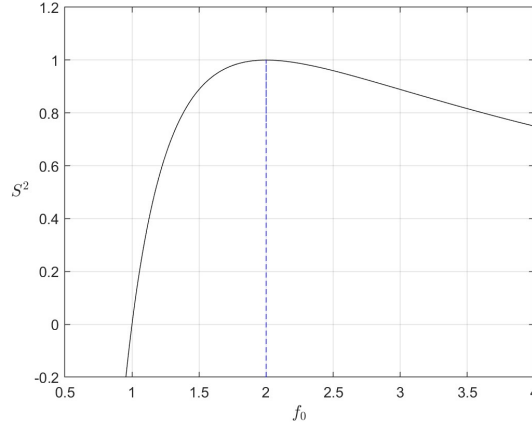
Figure 3.19: The growth rate squared plotted against the Coriolis parameter f_0. The maximum growth rate is attained for some value f_0 in the rapidly rotating limit.

Hence, the dynamical balance (3.57) describes the transition from the unstable magnetically modified inertial mode to the unstable magnetic mode (in the limit of weak magnetic field).

3.4.8 Rapidly Rotating Instabilities

Until now we have considered a fixed Coriolis parameter due to f_0 being the chosen timescale of the nondimensionalisation (3.4). However, it is possible to consider a rapidly rotating system, where to obtain instability we must suppose $f_0 \sim k^2 v_A^2 / \Lambda_0 \gg \Lambda_0$ (i.e., $1 \sim \mathcal{L}^2 / \Lambda \gg \Lambda$). This limit corresponds to the bottom left corner of figure 3.4, where the instability domain is much smaller (compressed in the bottom corner) since $\Lambda \ll 1$; however, instability is still possible provided $\mathcal{L}^2 < \Lambda \ll 1$. We must also consider the stability bound (3.25), which implies that we require $A^2 < \Lambda \ll 1$ for instability; thus, for instability to occur we require $l^2 N^2 / k^2 \ll f_0^2$.

First, to deduce the scaling of the growth rate when $f_0 \sim k^2 v_A^2 / \Lambda_0 \gg \Lambda_0$ we reconsider the dimensional quadratic equation (3.21) for the growth rate squared, from which we can immediately deduce that

$$s^2 (2k^2 v_A^2 + f_0 Q_0) + k^2 v_A^2 (k^2 v_A^2 - \Lambda_0 f_0) = 0, \tag{3.58}$$

with $s^2 \ll f_0^2$. Then, since $2k^2 v_A^2 \sim f_0 \Lambda_0 \ll f_0^2$ by assumption, it follows that

$$s^2 = \frac{k^2 v_A^2}{f_0^2} \left(\Lambda_0 f_0 - k^2 v_A^2 \right) \implies S^2 = \mathcal{L}^2 (\Lambda - \mathcal{L}^2). \tag{3.59}$$

Thus, there is instability provided $\mathcal{L}^2 < \Lambda$, which is consistent with the stability condition (3.25). Equation (3.59) implies that if $f_0 = 2k^2 v_A^2 / \Lambda_0$, then we will attain the maximum growth rate, which is consistent with (3.26) in the rapidly rotating limit. To illustrate this, we plot the growth rate squared against f_0 using (3.59) with $k^2 v_A^2 = 1$ and $\Lambda_0 = 1$ (arbitrary) in figure 3.19. Clearly, there is instability in this limit since $S > 0$, where $f_0 2k^2 v_A^2 / \Lambda_0 = 2$ yields the maximum growth rate.
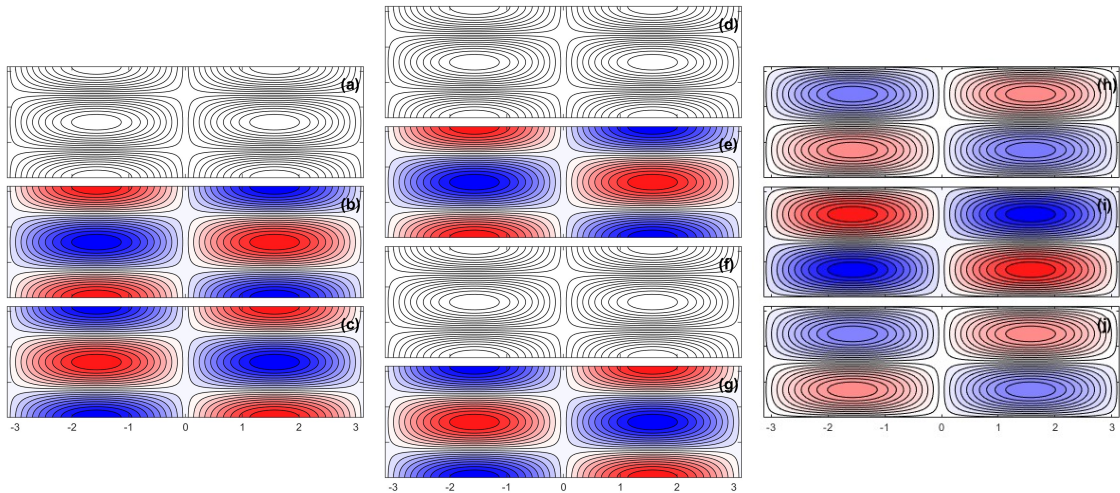
Figure 3.20: The dynamical balance of (3.48) at $A = 10^{-3}$ and $\mathcal{L} = 7 \times 10^{-2}$ with $\Lambda = 10^{-2}$, which illustrates the rapidly rotating instability with $f_0 \sim k^2 v_A^2/\Lambda_0$ and growth rate $S = 5 \times 10^{-3} \approx O(\Lambda)$. These parameters illustrate the maximum growth rate of the rapidly rotating and large field instability. Panel layout as in figure 3.12.

Equation (3.59) implies that the growth rate will be of order $\Lambda \sim \mathcal{L}^2$. Thus, if we now reconsider the dimensional equations (3.39) and (3.40) with $f_0 \sim k^2 v_A^2/\Lambda_0 \gg \Lambda_0$ and $s \ll f_0$, they reduce to

$$-f_0 v = \frac{ikB_3}{\mu_0 \bar{\rho}} b_x, \quad f_0 u = \frac{ikB_3}{\mu_0 \bar{\rho}} b_y, \quad sb_x = \Lambda_0 b_y + ikB_3 u, \quad sb_y = ikB_3 v, \tag{3.60}$$

which balance when $S^2 = \mathcal{L}^2(\mathcal{L}^2 - \Lambda)$, as predicted by (3.59). Hence, in the rapidly rotating limit, with $f_0 \sim k^2 v_A^2/\Lambda_0 \gg 1$, the system becomes magnetostrophic in the horizontal directions, while all terms in the induction equations are retained. We can also note that the balance (3.60) corresponds to the small Λ limit of (3.48) with $A \ll \mathcal{L}$, since $f_0 \sim k^2 v_A^2/\Lambda_0 \gg \lambda_0$ ensures $\mathcal{L} \ll 1$ and $\Lambda \ll 1$. Indeed, by considering the small Λ limit of (3.48) we obtain a magnetostrophic balance in the horizontal directions equivalent to that of (3.60). However, this also illustrates the rapidly rotating instability governed by (3.60) may also be attained with weak magnetic field and small shear such that $\mathcal{L}^2 \sim \Lambda$ (with f_0 fixed and not large).

We now provide contour plots of the momentum equations as well as the along-stream induction equation, using the nondimensional equations (3.41) and (3.42) to illustrate the dynamical balance (3.60) in figure 3.20 for $\mathcal{L} = 7 \times 10^{-2}$ and $A = 10^{-3}$ with $\Lambda = 10^{-2}$. These parameters ensure that $f_0 \sim k^2 v_A^2/\Lambda_0 \gg \Lambda_0$ since $\mathcal{L}^2 \sim \Lambda \ll 1$. Clearly, the horizontal momentum equations are in magnetostrophic balance, while the induction equations remain unchanged. By comparing figures 3.11 and 3.20, we can see that taking the small Λ limit of (3.48), such that $\mathcal{L}^2 \sim \Lambda$, allows the cross-stream momentum equation to play an important role in the instability. Similarly, we can see the stabilising role of $i\mathcal{L}u$ in the induction equation since the sheared cross-stream field Λb_y is now small.

3.5 Conclusions

In this chapter we have considered the linear stability of a uniform shear flow $U(y) = \Lambda_0 y$ in the presence of a uniform vertical magnetic field with Coriolis parameter f_0 (constant). The results of the chapter are clearly applicable to the mid-latitudinal regions of the solar tachocline and the flanks of the jets found in Jupiter's upper atmosphere. We may also use this system to model the latitudinal shear on the flanks of the strong equatorial jets found in the upper atmospheres of Hot Jupiters, which reach upwards of $30°$ in latitude (Heng & Showman, 2015).

In Section 3.2 we discuss inertial and magnetically modified waves in the absence of shear (so that there is no interference from unstable modes). We first introduce the nondimensional growth rate S (under the timescale $1/f_0$), re-scaled aspect ratio A and Lehnert number $\mathcal{L}$, where the latter is proportional to magnetic field strength. We categorise the behaviour of the two stable modes, finding that both are described by inertial-Alfvén waves in the small A limit and transition to inertia-gravity waves and Alfvén waves in the large A limit. In the large $\mathcal{L}$ limit the modes are described by Alfvén waves also; however, in the small $\mathcal{L}$ limit the modes are described by inertia-gravity waves and a hydromagnetic-inertial waves. An analogous wave to the latter is derived in a non-magnetohydrostatic and unstratified system in application to the Earth's core by Acheson & Hide (1973), leading us to determine that the frequency of the waves crucially depends upon whether the system is stratified or not. In the limit of weak magnetic field ($v_A \ll 1$) and in the absence of stratification, the frequency of the hydromagnetic-inertial wave scales with the Alfvén velocity squared, while in the presence of stratification the frequency scales with the Alfvén velocity v_A.

In section 3.3 we consider the sheared system so that instability is possible since anti-cyclonic shear may occur within the system. We also introduce the final nondimensional parameter of the chapter, given by Λ which may be interpreted as a Rossby number. We determine the condition for stability $A^2 + \mathcal{L}^2 > \Lambda$, given by (3.25), which implies that instability can occur in hydrodynamically stable regimes ($A^2 > \Lambda - 1$) provided $\mathcal{L}^2 \neq 0$ and sufficiently small. Indeed, we see that this is the case in figure 3.4, where the growth rate is contoured in $(\mathcal{L}, A)$-space for $\Lambda = 0.5, 1.5$ and 2.5, and explicitly showed instabilities in the hydrodynamically stable regime. We determined where the maximum growth rate occurred in $(\mathcal{L}, A)$-space for all $\Lambda > 0$, given by (3.26) and (3.27). For $\Lambda > 2$ the maximum growth rate is $\sqrt{\Lambda - 1}$ and occurs at $A = 0$ and $\mathcal{L}^2 = 0$ (hydrodynamic); for $\Lambda < 2$ the growth rate is $\Lambda/2$ and occurs at $A = 0$ and $\mathcal{L}^2 = \Lambda(2 - \Lambda)/4$. The latter corresponds to the maximum growth rate of the MRI and where it occurs in parameter space, as derived by Balbus & Hawley (1991). Indeed, we may interpret the maximum growth rate for $\Lambda < 2$ to occur as the vertical wavenumber $|k| \to \infty$ such that $\mathcal{L} = |k|v_A/f_0 = O(1)$, where as a result $A \propto 1/|k| \ll 1$; this is equivalent to the weak field and "thin disc" approximation made by Balbus & Hawley (1991).

Alternatively, to estimate the vertical scales of the unstable modes in the Solar tachocline, and the upper atmospheres of Jupiter and Hot Jupiters, we considered the hyperbolae $A = C/\mathcal{L} =$

$lNv_A/f_0^2\mathcal{L}$ shown in figure 3.4, where only the vertical wavenumber may vary. The hyperbolae required us to constrain the cross-stream wavenumber, which we argued is physically reasonable since possible latitudinal lengthscales could be inferred from observations. Thus, with the resulting estimate of C and the Rossby number Λ (using parameter values in table 2.1), we could obtain the value of $\mathcal{L}$ which generates the maximum growth rate from (3.26) and (3.27), and therefore estimate the vertical lengthscale of the modes. Note that (3.26) and (3.27) imply that the maximum growth rate of the system always occurs as $A \to 0$; thus, the vertical lengthscales estimated from (3.26) and (3.27) will be most accurate for a given astrophysical body which yields small values of C so that the hyperbolae $A = C/\mathcal{L} \ll 1$ with $\mathcal{L} = O(1)$. Also note that the values of the shear Λ_0 and Coriolis parameter f_0 used to estimate Λ will not be uniform in observations, however these are necessary (although limiting) requirements of the model.

In the solar tachocline we considered the Rossby number $\Lambda = 0.21$, so that the system is hydrodynamically stable. The resulting value of C is $O(1)$-$O(10^2)$, and the chosen vertical wavelength was estimated to be $H = 2.6 \times 10^7$m. With the vertical extent of the solar tachocline being $O(10^7\text{m})$, the estimated lengthscale is presumably too large. However, it must be noted that the consideration of diffusion will significantly alter the vertical lengthscale. Owing to the values of C, instabilities, if they occur, may be categorised as stratified magnetic instabilities, the dynamical balance of which we discussed in section 3.4.5.

In Jupiter's upper atmosphere we estimated $C = O(10^{-4})$ and $H = 8.5 \times 10^4$m with $\Lambda < 1$. In contrast to the solar tachocline this a much more reasonable estimate given that the depth of Jupiters atmosphere is $O(10^6\text{m})$. Since $C \ll 1$ it follows that instabilities, if they occur, may be described by the balance discussed in section 3.4.4, which can be considered to be analogous to the MRI.

In the upper atmospheres of Hot Jupiters the Rossby number may vary significantly owing to the strong equatorial jets. Thus, we consider $\Lambda = 0.62$ and $\Lambda = 5$ with $C = O(10^{-2})$ (estimated from parameters in table 2.1). In each case we estimated the vertical lengthscale H to be $O(10^4\text{m})$, which is physically reasonable. Instabilities, if they occur, for $\Lambda = 0.62$ will likely be analogous to those described in section 3.4.4 (and relate to the MRI), while those for $\Lambda = 0.62$ are categorised as inertial instabilities. However, given $1 < \Lambda < 2$, we may classify resulting unstable modes as magnetically modified inertial instabilities.

It is important to note that this problem of scale selection in this uniform shear framework is not straightforward, and we make progress by constraining the cross-stream wavenumber. However, this is artificial and thus motivates the more complex flows that have localised unstable regions, which we investigate in Chapters 5, 6, and 7. We find that in most cases the vertical lengthscales predicted by the system are appropriate in the astrophysical bodies we are considering.

In Section 3.4 we consider the dynamical balances of the various parameter regimes contained within the unstable regions of figure 3.4. We first categorise the dynamical balance of hydrodynamic inertial instability, given by equation (3.44). To do this, we considered overturning motions

in the meridional plane, which are illustrated in figure 3.9, and described the physical significance of the terms in (3.44) as well as the parameters Λ and A.

The first dynamical balance we considered in the magnetohydrodynamic regime were those of magnetically modified inertial instabilities (see the dynamical balances (3.45) and (3.46)), which are illustrated in figure 3.4 for $\Lambda = 1.5$ and $\Lambda = 2, 5$ (in the limit of small $\mathcal{L}$). We found that the cross-stream Lorentz force acts to decrease the growth rate, while the along-stream Lorentz force acts to increase the growth rate; the magnitude of each effect governs whether the correction to the growth rate is positive or negative, as seen in equation (3.47). If the growth rate $S > 1$, weak magnetic field decreases the growth rate, while if $S^2 < 1$, weak magnetic field increases the growth rate.

We then considered the onset of the magnetorotational instability in the hydrodynamically stable regime $\Lambda < 1$ with $A \ll 1$, corresponding to the limit of small $\mathcal{L}$ in figure 3.4 with $\Lambda = 0.5$. We found that weak magnetic field allowed instability to occur as the hydrodynamic inertial wave along-stream dynamical balance $(Su - (1 - \Lambda)v = 0)$ is broken as the Lorentz force now balances the Coriolis and shear term so that there is no along-stream acceleration at leading order (see equation (3.48)); the cross-stream momentum equation does not play a role in the dynamical balance and only prescribes the along-stream velocity u.

Next, we considered the dynamical balance of the most unstable mode for $\Lambda < 2$ (if $\Lambda > 2$ the most unstable mode is described by the dynamical balance of hydrodynamic inertial instability (3.43)), corresponding to the maximum growth rate on the $\mathcal{L}$ axis as illustrated in figure 3.4 for $\Lambda = 0.5$ and 1.5. We found subtly different balances between the $\Lambda = 0.5$ (hydrodynamically stable) and the $\Lambda = 1.5$ (hydrodynamically unstable) cases; even though all terms except the cross-stream pressure gradient played a role in each dynamical balance, the $\Lambda = 1.5$ dynamical balance was more dominated by inertial terms, while the $\Lambda = 0.5$ was more dominated by Lorentz forces (compare figures 3.12 and 3.13). For $\Lambda < 1$ we discussed a number of possible approximations to the dynamical balance, where we compared estimated and exact growth rates in figure 3.14.

The final balance we highlight is that of stratified magnetic instabilities, which are given by (3.54) and correspond to the hydrodynamically stable regions ($A^2 > \Lambda - 1$) of figure 3.4 (for $\Lambda < 1$, this is the entire unstable domain with $A = O(1)$). There is little difference in the dominant terms between the magnetic instabilities occurring for $A^2 > \Lambda - 1$ (with $\Lambda > 1$) and for $\Lambda < 1$ with $A = O(1)$ (compare figures 3.15 and 3.16), allowing us to conclude that the instabilities can both be interpreted as stratified magnetorotational instabilities.

In the following chapter we extend the analysis of Chapter 3 and investigate the role of kinematic viscosity ν, thermal diffusion κ and magnetic diffusivity η on the system we have considered.

Chapter 4

Diffusive Instabilities of a Uniform Shear Flow at Mid-latitudes

4.1 Introduction

In this chapter we extend the analysis of Chapter 3 by incorporating constant kinematic viscosity ν, thermal diffusion κ and magnetic diffusivity η. Hence, we consider the linear instability of the parallel flow $U(y) = \Lambda_0 y$ with uniform latitudinal shear $U'(y) = \Lambda_0$ on an f-plane in the presence of a uniform vertical magnetic field of strength $B_3(y) = B_0$. This is the simplest possible configuration to study the competition between inertial and magnetic modes in the presence of diffusion. Indeed, since the Coriolis parameter, the magnetic field strength, shear and diffusivites are all constant, the governing equation (2.30) has constant coefficients and can therefore be solved analytically with solutions for the perturbed quantities being of the form $v \propto \exp(ily)$, where l is the cross-stream wavenumber. The consideration of diffusion stabilises modes that occur at infinite vertical wavenumbers so that instabilities must occur with physically viable vertical scales.

In Chapter 1 we have already discussed a number of diffusive systems. Kloosterziel & Carnevale (2008) investigate how kinematic viscosity and thermal diffusion affect the scale selection of a hydrodynamic non-hydrostatic uniform shear flow on an f-plane. They derive stability bounds for steady and oscillatory modes when $Pr = \nu/\kappa \neq 1$; furthermore, they show that for $Pr = 1$, in the limit of large Reynolds number Re (ratio of inertial forces to viscous forces), the vertical wavenumber k that generates the maximum growth rate scales with $(N^2 Re)^{1/4}$. Albeit for the more complex hydrodynamic analysis on the equatorial β-plane, Dunkerton (1981), Dunkerton (1982), and Griffiths (2008b), also set out the problem of scale selection in a linear framework. For example, Dunkerton (1981) notes that it is necessary to consider diffusion in the system to obtain finite scales for the mode with the maximum growth rate, whereby taking $Pr = 1$ transforms the growth rate $s_D = s - \nu k^2$, where s is the inviscid growth rate, and therefore results in the maximum growth rate occurring at a finite scale.

An important hydrodynamic instability that is believed to be of importance regarding the angular momentum redistribution in planets and stars is the Goldreich-Schubert-Fricke (GSF) insta-

bility (Goldreich & Schubert, 1967; Fricke, 1968). In the terminology of our system, the GSF instability (which was originally derived in cylindrical coordinates) is essentially an axisymmetric inertial instability enabled by the role of thermal diffusion. That is, given a flow with $fQ < 0$ that has been stabilised by pressure gradients due to the effects of buoyancy (in a stably stratified fluid), then sufficiently strong thermal diffusion will nullify the stabilising role of stratification and allow the flow to become unstable. Menou *et al.* (2004) extend this analysis to the triple-diffusive magnetohydrodynamic regime, where the magnetic diffusivity also plays a role alongside the thermal conductivity and kinematic viscosity. Many necessary conditions for stability are derived in either the limit of zero kinematic viscosity or zero magnetic diffusivity. We will discuss the analogies to these studies in more detail throughout the Chapter.

In the triple-diffusive system, equation (2.30) reduces to a quintic equation for the growth rate. Interestingly, a non-magnetohydrostatic, cylindrical and adiabatic analogous quintic dispersion relation is found in Menou *et al.* (2004); however, the added complexity of their system complicates the stability analysis and does not allow for many of the derivations found in this analysis. The nondimensionalisation (3.22) is again used (i.e., the growth rate is a function of aspect ratio A, Lehnert number $\mathcal{L} \propto v_A$, Λ and the diffusive parameters) in order to relate the results of this chapter to the ideal results of Chapter 3. However, this choice has a number of consequences that we will discuss in detail in the following section. Given two natural choices of nondimensional diffusive parameters, we choose the parameters to be dependent on the cross-stream wavenumber, which must therefore be assumed constant (and prescribed from observations), so that only the vertical wavenumber may vary. This is equivalent to assuming the flow is confined to a channel of fixed latitudinal lengthscale L; we see why it is reasonable to confine the cross-stream wavenumber (so that the system is not free to choose any latitudinal lengthscale) in the following section.

The chosen nondimensionalisation leads to two main routes of analysis. The first aims to address what is the most unstable mode of a given astrophysical body (e.g., those seen in 2.1) and what the nature of that mode is (e.g., a magnetically modified inertial instability or a double diffusive instability); we do this by providing contours of the maximum growth rate in $(\mathcal{L}, A)$-space (as seen in figure 3.4 in Chapter 3) at fixed ν, κ and η. The second aims to address the specific role of ν, κ and η on the system; we do this by contouring the maximum growth rate as a function of two diffusive parameters, where, at each value of the two diffusive parameters, we have selected the A and $\mathcal{L}$ that maximises the growth rate.

Initially we consider the hydrodynamic regime, first with $Pr = 1$ and then with $Pr \neq 1$, establishing links to Kloosterziel & Carnevale (2008) and the GSF instability. Conditions for steady and oscillatory modes are derived. We contour the growth rate as a function of nondimensional kinematic viscosity and thermal conductivity, where in order to do this, we select the aspect ratio A that maximises the growth rate. We use this method repeatedly throughout the Chapter (in the magnetohydrodynamic regime we must also select the Lehnert number $\mathcal{L}$ that generates the maximum growth rate) so that we can focus primarily on the effects of diffusion on the most unstable mode.

In the magnetohydrodynamic regime we also derive a steady stability condition that is valid provided the system is only unstable to magnetic instabilities on the bound; if this is not the case, the hydrodynamic conditions of the hydrodynamic regime are used instead. We consider the case of $Pr = Pm = 1$, where $Pm = \nu/\eta$ is the magnetic Prandtl number, which can be described by a transformation from the ideal system of Chapter 3. Next, we consider the case of $Pr \neq 1$ with $Pm = 1$, which is an obvious extension to both the magnetohydrodynamic regime with $Pr = Pm = 1$ and the hydrodynamic regime with $Pr \neq 1$. We find links to the hydrodynamic GSF instability; however, magnetic field now modifies the instability provided the Rossby number Λ is not too large.

We also consider the case when $Pr = 1$ and $Pm \neq 1$. In this regime we find another double-diffusive instability which requires $\kappa \neq \eta$ and is also purely magnetic. To categorise the instability we investigate the limit of large Pm.

Next we consider the case when $Pr = Pm \neq 1$ (i.e., $\kappa = \eta$). In the limit of large κ and η, we obtain an analogous system to the hydrodynamic case with $Pr \neq 1$; indeed, instabilities may occur owing to the strong thermal diffusion. For large ν instability may occur only with magnetic field present and for sufficiently small η.

Finally, we consider the case where $Pr \ll Pm \ll 1$, such that $Pr = Pm^p$ for $p = 1.5$ and 3. This regime is found in the Solar tachocline (see table 2.1) or in Jupiter's interior, where the magnitude of η is not as extreme in comparison to its upper atmosphere. The most unstable modes under this formulation are dominated by (hydrodynamic) inertial modes. However, for $p = 3$, magnetic instabilities may occur, provided Pm is sufficiently large.

4.2 Formulation

We again consider uniform f, uniform shear Λ_0 and uniform magnetic field strength B_0. Then (2.30) has constant coefficients and may be solved analytically with solutions of the form $\hat{v} \propto e^{-ily}$, where l is the cross-stream wavenumber. We obtain the following quintic equation for the growth rate s :

$$\frac{N^2 l^2 (s + \eta k^2)}{k^2 (s + \kappa k^2)}((s + \nu k^2)(s + \eta k^2) + k^2 v_A^2) - k^2 v_A^2 U' f$$
$$+ fQ(s + \eta k^2)^2 + ((s + \nu k^2)(s + \eta k^2) + k^2 v_A^2)^2 = 0. \quad (4.1)$$

4.2.1 Nondimensionalisation

We use the same nondimensionalisation (3.22) as in Chapter 3, allowing us to easily compare to the ideal regime:

$$S = \frac{s}{f_0}, \;\; A^2 = \frac{l^2 N^2}{k^2 f_0^2}, \;\; \mathcal{L}^2 = \frac{k^2 v_A^2}{f_0^2} \;\; \text{and} \;\; \Lambda = \frac{\Lambda_0}{f_0}. \quad (4.2)$$

Reiterating Chapter 3, the chosen timescale is the Coriolis parameter $1/f_0$, the parameter S is the nondimensional growth rate, A is interpreted as a rescaled aspect ratio, $\mathcal{L}$ is the Lehnert number

(the ratio between magnetic field strength and rotation) and Λ may be interpreted as a Rossby number.

To nondimensionalise the diffusive parameters, we require a quantity with dimension involving length. This leaves us with a few (not necessarily obvious) choices; that is, the cross-stream wavenumber, the vertical wavenumber or the Alfven wave speed. Choosing the vertical wavenumber yields $\{\hat{\nu}, \hat{\kappa}, \hat{\eta}\} = k^2 \{\nu, \kappa, \eta\}/f_0$, and is equivalent to assuming the flow lies in the vertical channel of height $H = 2\pi/|k|$. As a result, the most unstable mode always occurs as $A \to 0^+$. This is because the cross-stream wavenumber is still free to choose an infinite lengthscale. To illustrate this, we consider the system with $\nu = \kappa$ and in the absence of magnetic field, in which the dispersion relation (4.1) reduces to

$$s = \sqrt{\Lambda_0 f_0 - f_0^2 - \frac{l^2 N^2}{k^2}} - \nu k^2. \tag{4.3}$$

Clearly, if one was a given an astrophysical body so that Λ_0, N and ν were given, and assume that the flow is contained within a vertical channel, then a minimum value that k can take is set, and discretizes it above that. Thus, in a vertical channel, the maximum growth rate of (4.3) occurs when $|l| \to 0$, yielding an infinite lengthscale. This is not desirable as a use of diffusion is to obtain physically reasonable scales; in addition, the role of l completely disappears from the problem, essentially yielding a one dimensional system.

Choosing the Alfven wave speed leads to the following nondimensional parameters $\{\tilde{\nu}, \tilde{\kappa}, \tilde{\eta}\} = f_0 \{\nu, \kappa, \eta\}/v_A^2$, and would not allow for a smooth comparison to the ideal system of Chapter 3 nor diffusive hydrodynamic results (e.g., Kloosterziel & Carnevale, 2008). This choice also still leads to the most unstable modes of the system occurring when $A \to 0^+$ owing to infinitesimal cross-stream wavenumbers being chosen as in the previous case.

Hence, we are left to nondimensionalise the diffusive parameters with the cross-stream wavenumber, yielding

$$\nu_0 = \frac{l^2 N^2 \nu}{f_0^3}, \quad \kappa_0 = \frac{l^2 N^2 \kappa}{f_0^3} \quad \text{and} \quad \eta_0 = \frac{l^2 N^2 \eta}{f_0^3}. \tag{4.4}$$

Thus, given an astrophysical body, where the values of f_0, N and ν can be inferred from observations, we assume that the flow is contained within a latitudinal channel with (latitudinal) lengthscale L, yielding a minimum value for the cross-stream wavenumber l. Further to this, we assume that the system takes this minimum value of l, then $l = 2\pi/L$, and the solutions of (2.30) take the form $v \propto \sin(2\pi y/L)$ rather than $\exp(ily)$. Under this formulation, the system can not choose an infinite (or infinitesimal) vertical (or latitudinal) scale to maximise the growth rate. Indeed, for example, given a flow in a latitudinal channel on astrophysical body so that $|l|, \Lambda_0, N$ and ν are fixed, then equation (4.3) predicts stability at large and small k, in turn yielding more physical relevant latitudinal and vertical lengthscales.
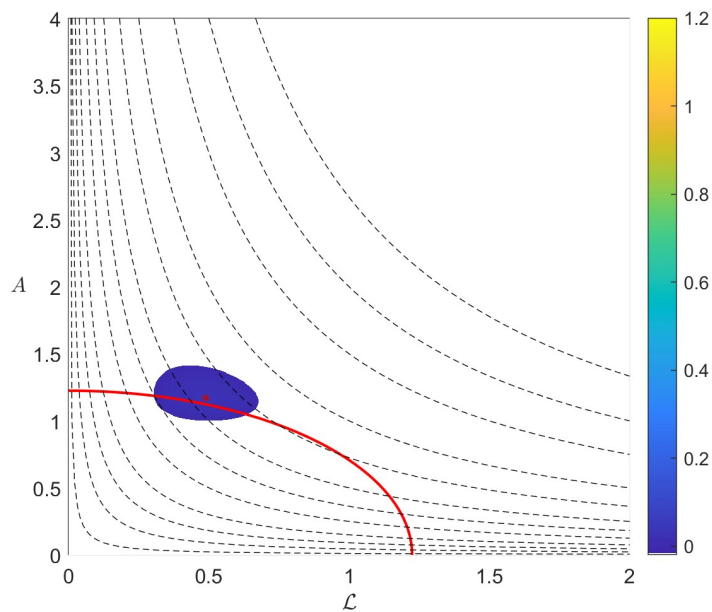
Figure 4.1: Contours of the maximum growth rate in $(\mathcal{L}, A)$-space with $\Lambda = 1.5$ and $\nu_0 = \eta_0 = 0.5$ and $\kappa_0 = 1$. The red line is the inviscid stability bound (3.25). The vertical wavenumber can only vary along hyperbolae $A\mathcal{L} = C$, with C constant. The location of the maximum growth rate is indicated by the red dot.

4.2.2 Consequences of the Nondimensionalisation

As we have already mentioned we will be analysing the system via two main routes of analysis. The first addresses what is the most unstable mode of a given astrophysical body (e.g., those seen in 2.1) and what the nature of that mode is (e.g., a magnetically modified inertial instability or a double diffusive instability); we do this in part by providing contours of the maximum growth rate in $(\mathcal{L}, A)$-space (as seen in figure 3.4 in Chapter 3) at fixed values of Λ, ν_0, κ_0 and η_0. For illustrative purposes, we provide figure 4.1, which is a contour of the nondimensional growth rate in $(\mathcal{L}, A)$-space plotted with $\nu_0 = \eta_0 = 0.5$, $\kappa_0 = 1$ and $\Lambda = 1.5$ (the growth rate can be numerically determined from a nondimensional analogue of (4.1)). The hyperbolae are given by $C = A\mathcal{L} = |l|Nv_A/f_0^2$, and are independent of vertical wavenumber; thus, increasing $\mathcal{L}$ such that $C = A\mathcal{L}$ increases the chosen vertical wavenumber. Hence, by considering a flow in a latitudinal channel on an astrophysical body and taking $l = 2\pi/L$, where L is the latitudinal scale of the channel, then the mode of interest lies on one of the hyperbolae $C = A\mathcal{L} = |l|Nv_A/f_0^2$ since we can infer (and fix) values of Λ_0, N and ν from observations. Thus, the chosen vertical scale is found by considering the point along the hyperbola that generates the maximum growth rate. Note that we can write $\nu_0 = A^2\mathcal{L} f_0\nu/v_A^2$ and thus, by prescribing a value of ν_0 we are considering the hyperbolae $A^2\mathcal{L} = \nu_0 v_A^2/f_0\nu = C$. Then, by considering a single astrophysical body we fix the remaining parameters of C yielding a single hyperbola in $(\mathcal{L}, A)$-space.

The second aim is to address the specific role of ν_0, κ_0 and η_0 on the system; we do this by contouring the maximum growth rate as a function of two diffusive parameters (e.g., (ν_0, κ_0)-

space with $\nu_0 = \eta_0$), where, at each value of the two diffusive parameters, we have selected the A and $\mathcal{L}$ that maximises the growth rate. It is useful to do this otherwise many plots with varying values of $\nu_0 = \eta_0$ and κ_0 (similar to figure 4.1) would need be analysed in order to categorise the behaviour of the diffusive parameters. This process allows us to consider the role of the diffusive parameters on the maximum growth rate only (illustrated by the red dot in figure 4.1) simplifying the analysis. Note that we consider the optimisation of A as that of the vertical wavenumber and the optimisation of the Lehnert number $\mathcal{L}$ as that of magnetic field strength.

Recasting equation (4.1) in terms of the nondimensional parameters (4.2) and (4.4) yields

$$A^2 \frac{S + \eta_0/A^2}{S + \kappa_0/A^2} \left(\left(S + \frac{\nu_0}{A^2} \right) \left(S + \frac{\eta_0}{A^2} \right) + \mathcal{L}^2 \right) - \mathcal{L}^2 \Lambda$$
$$+ (1 - \Lambda) \left(S + \frac{\eta_0}{A^2} \right)^2 + \left(\left(S + \frac{\nu_0}{A^2} \right) \left(S + \frac{\eta_0}{A^2} \right) + \mathcal{L}^2 \right)^2 = 0. \quad (4.5)$$

Equation (4.5) will be the basis for the entire chapter. However, it is useful to consider limiting cases when either Pr and Pm (or both) are unity.

4.2.3 Analogies to Previous Studies

Note that equation (4.5) is a particular (Cartesian and magnetohydrostatic) case of the quintic equation for the growth rate found in Menou *et al.* (2004), the (non-magnetohydrostatic) system of which we discussed in Chapter 1. Specifically, recall that Menou *et al.* (2004) considered, in cylindrical geometry, the local axisymmetric stability (with adiabatic perturbations) of a magnetised rotating flow with angular velocity $\Omega(R, z)$ in the presence of radial and axial stable stratification, kinematic viscosity ν, thermal conductivity κ, and magnetic diffusivity η. Thus, the study of Menou *et al.* (2004) also considers the role of vertical shear and axial stratification (analogous to latitudinal stratification here) and is therefore a generalisation of this system; the added complexity, however (particularly the non-magnetohydrostatic extension), makes the derivation of analytical results very difficult. The stability analysis of Menou *et al.* (2004) is therefore restricted to limiting cases, including, for example, the limit of zero kinematic viscosity and the limit of zero magnetic diffusivity. Here we are able to derive powerful stability criteria which do not require unrealistic additional assumptions such as vanishing kinematic viscosity or magnetic diffusivity.

In order to see the analogies with Menou *et al.* (2004), it is useful to recast the equation (4.5) explicitly as a quintic polynomial for the growth rate S. Indeed, after multiplying (4.5) by the factor $S + \kappa_0/A^2$, we obtain

$$S^5 + a_4 S^4 + a_3 S^3 + a_2 S^2 + a_1 S + a_0 = 0, \quad (4.6)$$

where the coefficients a_j are given by

$$a_4 = \frac{1}{A^2}(2\nu_0 + \kappa_0 + 2\eta_0), \quad (4.7a)$$

$$a_3 = \frac{1}{A^4}(A^4(A^2 + 2\mathcal{L}^2 + 1 - \Lambda) + (\nu_0 + \eta_0)^2 + 2(\nu_0\kappa_0 + \nu_0\eta_0 + \kappa_0\eta_0)), \quad (4.7b)$$

$$a_2 = \frac{1}{A^6}(A^6(\nu_0 + 2\eta_0) + A^4((\kappa_0 + 2\eta_0)(1 - \Lambda) + 2\mathcal{L}^2(\nu_0 + \kappa_0 + \eta_0)) +$$
$$\nu_0^2(\kappa_0 + 2\eta_0) + \eta_0^2(2\nu_0 + \kappa_0) + 4\nu_0\kappa_0\eta_0), \quad (4.7c)$$

$$a_1 = \frac{1}{A^8}(\mathcal{L}^2 A^8(\mathcal{L}^2 + A^2 - 1) + \eta_0(2\nu_0 + \eta_0)A^6 +$$
$$((\eta_0^2 + 2\kappa_0\eta_0)(1 - \Lambda) + 2\mathcal{L}^2(\nu_0(\kappa_0 + \eta_0) + \kappa_0\eta_0))A^4 +$$
$$\nu_0\eta_0(\nu_0(2\kappa_0 + \eta_0) + 2\kappa_0\eta_0)), \quad (4.7d)$$

$$a_0 = \frac{1}{A^{10}}(\mathcal{L}^2\eta_0 A^{10} + \kappa_0\mathcal{L}^2(\mathcal{L}^2 - \Lambda)A^8 + \nu_0\eta_0^2 A^6 + \kappa_0\eta_0(2\mathcal{L}^2\nu_0 + \eta_0(1 - \Lambda))A^4 + \nu_0^2\kappa_0\eta_0^2).$$
$$(4.7e)$$

The coefficients (4.7) of the quintic (4.6) are similar to those in the quintic equation of Menou *et al.* (2004). Indeed, by writing a_3 in dimensional terms, we obtain

$$\frac{l^2 N^2}{k^2} + 2k^2 v_A^2 + f_0(f_0 - \Lambda_0) + k^4 \nu^2 + \dots, \quad (4.8)$$

where we have multiplied by f_0^5 due to it being a common factor in (4.6). Then, by recognising that

$$l^2 N^2 \longrightarrow -k_Z^2 \left(\frac{1}{\gamma\rho} \frac{\partial}{\partial R} \left(P \frac{\partial}{\partial R} \ln(P\rho^{-\gamma}) \right) \right), \quad (4.9)$$

$$f_0(f_0 - \Lambda_0) \longrightarrow \frac{k_Z^2}{k_R^2 + k_Z^2} \frac{1}{R^3} \frac{\partial}{\partial R}(R^4\Omega^2), \quad (4.10)$$

$$k^2 \longrightarrow k_R^2 + k_Z^2, \quad (4.11)$$

with the latter implying that $k^2 v_A^2 \longrightarrow (\mathbf{k} \cdot \mathbf{v_A})^2$, the right hand terms are those that are found in the quintic equation of Menou *et al.* (2004). In order of appearance, k_Z is the vertical wavenumber, Z is the vertical coordinate, γ is the adiabatic index of the gas, R is the radial coordinate, $P \equiv P(R)$ is the pressure, $\rho \equiv \rho(R)$ is the density, k_R is the radial wavenumber, $\Omega \equiv \Omega(R)$ is the angular velocity and $\mathbf{k} = (k_R, 0, k_Z)$. The Alfvén velocity $\mathbf{v_A}$ is defined in terms of the basic state magnetic field of arbitrary geometry, which is assumed weak compared to both rotation and pressure gradients (so that it does not affect the basic state). We have neglected the Z dependence in the pressure, density and angular velocity of the Menou *et al.* (2004) system to make the analogy clearer.

We see that a number of differences exist between the two formulations. The transformations (4.9) and (4.11) are due to Menou *et al.* (2004) considering adiabatic perturbations and a non-magnetohydrostatic system, respectively. Naturally, there are also differences due to the contrast in coordinate systems; however, for example, as shown in Appendix A, there is direct analogy between fQ and the Rayleigh discriminant Φ, which is proportional to the right hand side of (4.10). Menou *et al.* (2004) also consider a weak uniform magnetic field with radial, azimuthal and vertical components; however, the vertical component is the only one necessary for instability.

Clearly, the system of Menou *et al.* (2004) is a generalisation of our system in this chapter. However, due to the added complexity of the system, the results obtained by Menou *et al.* (2004)

are obtained only for limiting regimes. For example, Menou *et al.* (2004) derive a number of necessary conditions for stability in the perfectly conducting regime ($\eta \to 0$) and the inviscid regime ($\nu \to 0$). By contrast, we derive distinct conditions that do not require any additional assumption on the kinematic viscosity, thermal conductivity or magnetic diffusivity.

4.3 Hydrodynamic Regime

It is natural to first consider the hydrodynamic system, where we determine under what conditions the system is unstable, the vertical wavenumber at which the growth rate is maximum and the influence of kinematic viscosity ν_0 and thermal conductivity κ_0.

On setting $\mathcal{L} = 0$ in (4.5), we obtain the following cubic equation for the growth rate S :

$$\frac{(S + \nu_0/A^2)}{(S + \kappa_0/A^2)} A^2 + 1 - \Lambda + (S + \nu_0/A^2)^2 = 0. \tag{4.12}$$

This equation is found in Dunkerton (1982), who derived marginal stability criteria for oscillatory modes (provided $Pr \neq 1$). We find this criteria and expand upon it in order to form a basis for our magnetohydrodynamic results. In general, equation (4.12) does not allow us to obtain an analytical expression for the growth rate and must be solved numerically. However, in the case where $Pr = 1$ such an expression can be obtained.

The results of Kloosterziel & Carnevale (2008), which we have already discussed in section 1.2.2, focus on the vertical scale selection in the limit of large Reynolds number and will also be closely related to this section.

4.3.1 $Pr = 1$

In the case of $Pr = 1$ equation (4.12) simplifies to

$$S = (\Lambda - 1 - A^2)^{\frac{1}{2}} - \frac{\nu_0}{A^2}. \tag{4.13}$$

We note that (4.13) implies that modes with large vertical wavenumber ($A \ll 1$) are stabilised since the diffusive term becomes large (which is always stabilising since $\partial_{\nu_0} S < 0$); this is in contrast to the inviscid case where the most unstable mode is found at infinite vertical wavenumber, and where stability occurs only if $A^2 > \Lambda - 1$. Thus, with $\nu_0 \neq 0$, instability (and therefore the maximum growth rate) must occur in a bounded region of A. We note that equation (4.13) may be obtained from the inviscid system by transforming the inviscid growth rate from S to $S + \nu_0/A^2$, so that the growth rate is ν_0/A^2 less than that of the inviscid system. Equation (4.13) also implies that $\Lambda > 1 + A^2$ is a necessary condition for instability since $A \neq 0$.

It is of interest to find the vertical wavenumber for which the maximum growth rate occurs for fixed Λ and ν_0. Thus, equivalently, we want to find the A, $A_{\max}$ say, for which the growth rate is maximised. We differentiate equation (4.13) with respect to A and set the derivative to zero, yielding

$$\frac{\partial S}{\partial A} = -A(\Lambda - 1 - A^2)^{-\frac{1}{2}} + 2\frac{\nu_0}{A^3} = 0 \implies A^4 = 2\nu_0(\Lambda - 1 - A^2)^{\frac{1}{2}}. \tag{4.14}$$

Hence, A_{max}^2 must satisfy the 4th degree polynomial:

$$A_{\mathrm{max}}^8 = 4\nu_0^2(\Lambda - 1 - A_{\mathrm{max}}^2). \tag{4.15}$$

The polynomial (4.15) does not allow us to derive a corresponding maximum growth rate $S_{\mathrm{max}} = S(A_{\mathrm{max}})$ for each A_{max} since the expression can not be solved analytically for A_{max}. However, provided $\nu_0 \ll 1$ (which is typically the case in planetary atmospheres) we may approximate A_{max}^2 by expanding in terms of ν_0 (cf. Griffiths, 2003a):

$$A_{\mathrm{max}}^2 = \sqrt{2}(\Lambda - 1)^{\frac{1}{4}}\nu_0^{\frac{1}{2}} - \frac{1}{2\sqrt{\Lambda - 1}}\nu_0 + O(\nu_0^{\frac{3}{2}}). \tag{4.16}$$

Hence, provided $\nu_0 \ll 1$, the dimensional vertical wavenumber that generates the maximum growth rate is given by

$$k_{\mathrm{max}}^2 \approx \frac{2(-f_0 Q_0)^{1/2} lN}{2\sqrt{2}(-f_0 Q_0)^{3/4}\nu^{1/2} - lN\nu}. \tag{4.17}$$

Note that the $lN\nu$ term in the denominator results from the second order term of (4.16). Indeed, without this second order term, equation (4.17) is analogous to the non-hydrostatic equation (4.11) of Kloosterziel & Carnevale (2008), which implies that the vertical wavenumber scales with $Re^{1/4}$ in the limit of large Reynolds number Re. To show that this is true for equation (4.17), we compare the acceleration and diffusive terms in the perturbed horizontal momentum equation (2.22). On taking the Coriolis parameter as the time scale for the growth rate, equation (2.22) implies that the $Re = f_0/\nu k^2$, which under the nondimensional parameters (4.4) becomes $Re = A^2/\nu_0$. Hence, we are in the limit of large Re provided $A^2 \gg \nu_0$. Indeed, equation (4.16), at leading order, implies $A_{\mathrm{max}}^2 \sim \nu_0^{1/2}$ and $Re = \sqrt{2}(\Lambda - 1)^{1/4}\nu_0^{-1/2}$ so that $Re \sim \nu_0^{-1/2} \gg 1$ provided $\Lambda = O(1)$.

There is no exact analogy between (4.11) of Kloosterziel & Carnevale (2008) and (4.17). This is due to us defining Re with the vertical lengthscale $H = 2\pi/k$, which is unavoidable since the horizontal component of diffusion is neglected owing to the hydrostatic approximation. By contrast, Kloosterziel & Carnevale (2008) define their Re in terms of the latitudinal lengthscale L (i.e., $Re = L^2\Lambda_0/\nu$) as the horizontal component of diffusion is not neglected as their system is non-hydrostatic. However, by introducing the nondimensional parameter $K = kH$, writing $H = 2\pi/k$ and using our nondimensional parameters (4.4), equation (4.17) implies $K^2 \propto ARe^{1/2}$.

The upper atmospheres of Hot Jupiters can be hydrodynamically unstable (i.e., $f_0 Q_0 < 0$) and thus, we can also use equation (4.17) to estimate the vertical lengthscale of the possible instabilities that can occur. Using the parameter values $l = 2\pi/L \approx 2.7 \times 10^{-7}\mathrm{m}^{-1}$, $f_0 = 3.4 \times 10^{-5}\mathrm{s}^{-1}$, $\Lambda_0 = 1.7 \times 10^{-4}\mathrm{s}^{-1}$, $N = 5 \times 10^{-4}\mathrm{s}^{-1}$ (which were also used in Section 3.3.4) and $\nu = 3.9 \times 10^{-7}\mathrm{m}^2\mathrm{s}^{-1}$ (from table 2.1), we obtain the estimate $k_{\mathrm{max}} = 4.3 \times 10^{-3}\mathrm{m}^{-1}$. Thus, we obtain the vertical lengthscale $H \approx 1.5 \times 10^3\mathrm{m}$.

Next, by substituting (4.16) into (4.13), we can also derive the corresponding maximum growth rate $S_{\mathrm{max}} = S(A_{\mathrm{max}})$ when $\nu_0 \ll 1$, in terms of Λ and ν_0 only:

$$S_{\mathrm{max}} = \sqrt{\Lambda - 1} - \frac{2}{\sqrt{2}}(\Lambda - 1)^{-\frac{1}{4}}\nu_0^{\frac{1}{2}} + O(\nu_0). \tag{4.18}$$

Thus, the maximum growth rate is the inviscid maximum growth rate $\sqrt{\Lambda - 1}$ dampened by a correction proportional to $\nu_0^{\frac{1}{2}}$. The correction becomes smaller as Λ increases, provided it is not too large (since the expansion will break down due to ν_0 appearing with $\sqrt{\Lambda - 1}$ in (4.16)). The correction to the maximum growth rate in (4.18) is consistent with Kloosterziel & Carnevale (2008), since the second order term may be re-written in the form $= 1/Re$ (since $Re = \sqrt{2}(\Lambda - 1)^{1/4}\nu_0^{-1/2}$).

To derive the marginal diffusion ν_0 at arbitrary A and Λ, for which no instability may occur if surpassed, we set $S = 0$ in equation (4.13):

$$\nu_0 = A^2(\Lambda - 1 - A^2)^{\frac{1}{2}} > 0. \tag{4.19}$$

Further to this, we can find the magnitude of diffusion ν_c (in terms of Λ only) for which no instability may occur if $\nu_0 > \nu_c$ for any A at fixed Λ. To do this, we simultaneously consider equations (4.14) and (4.19) which allows us to find the value of A, A_c say, where the final unstable mode yet to be stabilised occurs, given by

$$A_c = 2^{\frac{1}{6}}\nu_c^{\frac{1}{3}}. \tag{4.20}$$

Then, by substituting (4.20) into (4.19) for A, we obtain ν_c in terms of Λ only:

$$\nu_c = 2\left(\frac{\Lambda - 1}{3}\right)^{\frac{3}{2}}. \tag{4.21}$$

Thus, ν_c increases with Λ, scaling with $\Lambda^{\frac{3}{2}}$ in the large Λ limit. We also find that ν_c remains relatively small even for strong shears (e.g., $\Lambda = 4$); this justifies the approximation ($\nu_0 \ll 1$) used to derive $S_{\max}$ in (4.18).

We now determine an estimate for the bounded region in A where instability is possible for arbitrary ν_0 and Λ. To do this, we consider the small A and ν_0 limits of equation (4.19). Taking the small A limit of (4.19) implies that A must be greater than $\nu_0^{\frac{1}{2}}(\Lambda - 1)^{-\frac{1}{4}}$, forming a lower bound on the interval of A. To find the upper bound we must consider $\Lambda - 1 - A^2 \ll 1$ with $v_0 \ll 1$ in (4.19). Considering the small ν_0 limit of equation (4.19) with $A^2 = \Lambda - 1 + O(\nu_0)$ gives the approximate upper bound in A:

$$A = (\Lambda - 1)^{\frac{1}{2}} - \frac{1}{2(\Lambda - 1)^{\frac{5}{2}}}\nu_0^2 + O(\nu_0^4). \tag{4.22}$$

Hence, instability may occur if

$$\nu_0^{\frac{1}{2}}(\Lambda - 1)^{-\frac{1}{4}} < A < (\Lambda - 1)^{\frac{1}{2}} - \frac{1}{2(\Lambda - 1)^{\frac{5}{2}}}\nu_0^2. \tag{4.23}$$

Note that this interval in A is only approximate. We also note that ν_0 is likely to be small in stellar and planetary atmospheres, so that (4.23) may give a very accurate interval of unstable vertical wavenumbers.

We now provide a series of contour plots for the growth rate S in (A, ν_0)-space, which will illustrate the bounded region in A for which instability may occur, provided $\nu_0 < \nu_c$, alongside
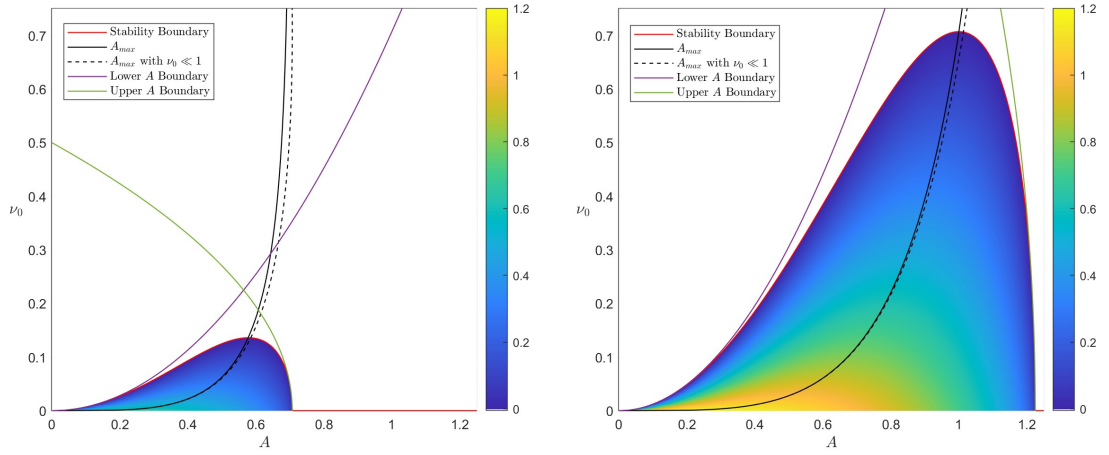
Figure 4.2: $Pr = 1$: The growth rate S plotted in (A, ν_0)-space with $\Lambda = 1.5$ (left) and $\Lambda = 2.5$ (right). The stability boundary (4.19) is shown in red. The solid and dashed black lines denote the $A_{\max}$ given by (4.15) and (4.16); the first is exact, while the latter is an approximation when $\nu_0 \ll 1$. The magenta and green lines are the lower and upper boundary in A, for which stability is guaranteed once surpassed, given by the approximate condition (4.23).

the maximum growth rate and the corresponding aspect ratio A at which it occurs for each ν_0. Thus, by solving equation (4.13) numerically, figure 4.2 shows the contour plots for $\Lambda = 1.5$ and $\Lambda = 2.5$. It is clear that the stability boundary estimates are accurate at small ν_0 and remain accurate as Λ increases; the upper boundary retains its accuracy even for $\nu_0 = O(1)$. Figure 4.2 allows us to confirm that increasing Λ increases the critical diffusion ν_c required for stability, as predicted from (4.21). Increasing Λ also increases the size of the bounded region in A as well as the maximum growth rate at each ν_0. We find that increasing A only increases the growth rate to some $A_{\max}$ (given by (4.16) when $\nu_0 \ll 1$), whereas increasing A further decreases the growth rate. Clearly, increasing ν_0 decreases the growth rate monotonically, as expected. We also find that increasing ν_0 increases the value of A at which the growth rate is maximum (the maximum of which decreases) and reduces the bounded region in A for which instability may occur.

To confirm the last of the analytical results, we plot the estimated $S_{\max}$ (4.18) with the exact maximum growth rate against ν_0 for various Λ in figure 4.3. Naturally, the small ν_0 expansion of $S_{\max}$ is accurate with $\nu_0 \ll 1$ and decays in accuracy as ν_0 increases. We find that increasing Λ allows the estimated $S_{\max}$ to remain accurate for larger ν_0. This is expected since the second order term of (4.18) becomes smaller as Λ increases.

4.3.2 $Pr \neq 1$

The case $Pr \neq 1$ is a natural extension to the case of $Pr = 1$ and allows us to consider the regime $Pr \ll 1$, which is typically the case in planetary atmospheres. We consider equation (4.12) and
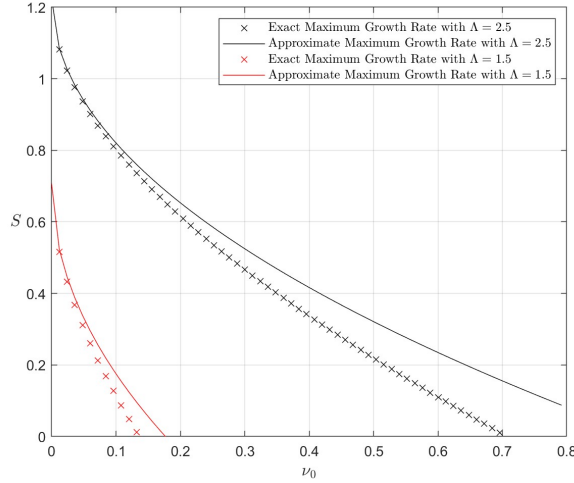
Figure 4.3: The exact maximum growth rate (4.13) plotted with the approximate $S_{\max}$ calculated from the small ν_0 expansion (4.18) for $\Lambda = 1.5$ and $\Lambda = 2.5$.

multiply by $(S + \kappa_0/A^2)$ to form the following cubic for the growth rate S :

$$
S^3 + \frac{1}{A^2}(\kappa_0 + 2\nu_0)S^2 + \frac{1}{A^4}(2\kappa_0\nu_0 + \nu_0^2 - A^4(\Lambda - 1 - A^2))S
$$
$$
+ \frac{1}{A^6}(\nu_0^2\kappa_0 + \nu_0 A^6 - (\Lambda - 1)\kappa_0 A^4) = 0. \quad (4.24)
$$

Since equation (4.24) is a cubic in S it may have three real roots, or one real root with a pair of complex conjugate roots. Thus, steady and oscillatory instabilities may occur (as commented on in Dunkerton, 1982).

To derive a condition for marginal oscillatory instability we substitute $S = iS_i$ and equate the real and complex parts. These coupled equations allow us to isolate and remove S_i from the system, yielding the condition for marginal oscillatory instability:

$$
(\kappa_0 + 2\nu_0)(2\kappa_0\nu_0 + \nu_0^2 - A^4(\Lambda - 1 - A^2)) = \nu_0^2\kappa_0 + \nu_0 A^6 - (\Lambda - 1)\kappa_0 A^4, \quad (4.25)
$$

provided $S_i^2 > 0$, which requires

$$
2\kappa_0\nu_0 + \nu_0^2 > A^4(\Lambda - 1 - A^2). \quad (4.26)
$$

Note that the condition (4.25) is the multiple of the coefficients of S^2 and S equal to the coefficient of S^0 in equation (4.24). Hence, if equation (4.25) is satisfied exactly, while (4.26) simultaneously holds, we have two marginal oscillatory modes.

We can also set $S = S_i = 0$ in equation (4.24), giving the criteria for marginal steady instability:

$$
\nu_0^2\kappa_0 + \nu_0 A^6 = (\Lambda - 1)\kappa_0 A^4. \quad (4.27)
$$

Note that equation (4.27), if satisfied, implies that at least one root of (4.24) exists and is marginally unstable. However, if oscillatory instability occurs, governed by equations (4.25) and (4.26), at fixed κ_0 and Λ say, then there may be unstable modes alongside the marginal mode on the

boundary (4.27). If there are no oscillatory instabilities, at fixed κ_0 and Λ say, then equation (4.27) describes the unstable boundary exactly.

There are numerous options to analyse (4.24) in order to investigate the effects that ν_0 and κ_0 have on the growth rate. For example, various contour plots of the maximum growth rate could be made in (ν_0, A) and (κ_0, A)-space for fixed κ_0 and ν_0, respectively. However, this method requires a complex selection of contour plots (at various Λ also) and is difficult to decipher as a whole. Thus, we solve for the maximum growth rate in (4.24) at each A, ν_0, and κ_0, then select the A, $A_{\max}$ say, that generates the maximum growth rate (i.e., $S_{\max} = S(A_{\max})$) for each ν_0 and κ_0; we then contour the growth rate S in (ν_0, κ_0)-space. To reiterate our discussion around the definition of our nondimensional parameters (4.2) and (4.4), we consider that the cross-stream wavenumber l is fixed (since it occurs in A, ν_0 and κ_0) and so the maximisation of the growth rate over A is considered an optimisation over the vertical wavenumber k only.

Oscillatory Stability Bounds Independent of A

Thus, since we are maximising the growth rate over A, we can do the same for the stability bounds (4.25) and (4.27), which will allow us to derive conditions that depend only on ν_0, κ_0 and Λ. Differentiating the condition for marginal oscillatory instability (4.25) with respect to A implies that the aspect ratio on the stability boundary must satisfy

$$A^2 = \frac{4}{3} \frac{(\Lambda - 1)\nu_0}{\kappa_0 + \nu_0}. \tag{4.28}$$

The aspect ratio required so that the pressure gradient can stabilise oscillatory modes increases with increasing Λ and ν_0 while it decreases with increasing κ_0.

Hence, if $S = S_r + iS_i$ with $S_r = 0$ and $S_i \neq 0$, then A must satisfy (4.28). We can substitute (4.28) into (4.25) in order to obtain the following necessary and sufficient condition for oscillatory stability which is independent of A:

$$\kappa_0 > \nu_0^{\frac{1}{2}} \left(\left(\frac{16}{27}\right)^{\frac{1}{4}} (\Lambda - 1)^{\frac{3}{4}} - \nu_0^{\frac{1}{2}} \right), \tag{4.29}$$

provided (4.26) is satisfied. That is, if (4.26) is not satisfied, then (4.29) is not a valid condition for stability. Note that differentiating (4.29) with respect to ν_0 implies $\kappa_0 \equiv \kappa_0(\nu_0)$ is maximised (i.e., the largest value at which marginal oscillatory instability can occur) at

$$\nu_0 = \left(\frac{\Lambda - 1}{3}\right)^{\frac{3}{2}}, \tag{4.30}$$

which increases with increasing Λ. Hence, after substituting (4.30) into (4.29) we obtain the value of κ_0 for which marginal oscillatory instability no longer occurs

$$\kappa_0 = \left(\frac{\Lambda - 1}{3}\right)^{\frac{3}{2}}, \tag{4.31}$$

which also increases with increasing Λ.

The bound (4.29) also allows us to derive the maximum value of ν_0 for which no oscillatory instability can occur:

$$\nu_0 > \frac{4}{3\sqrt{3}}(\Lambda - 1)^{\frac{3}{2}}. \tag{4.32}$$

Note that the conditions (4.29), (4.30) and (4.31) and (4.32) are valid only provided (4.26) holds.

Steady Stability Bounds Independent of A

We now derive the corresponding steady stability condition from the condition on $S = 0$ (4.27). Note that, the condition (4.27) only corresponds to a single root with $S = 0$; thus, it is possible for other roots to be unstable on the bound. We partially differentiate (4.27) with respect to A which, after some manipulation, implies that on the steady stability boundary the aspect ratio A must satisfy

$$A^2 = \frac{2(\Lambda - 1)\kappa_0}{3\nu_0}. \tag{4.33}$$

The aspect ratio required for stability increases with increasing κ_0 and decreases with increasing ν_0.

Thus, if $S = 0$ exactly (i.e., S has no complex part so the modes are steady), then A must satisfy (4.33). We can substitute (4.33) into (4.27) in order to obtain the following steady stability condition which is independent of A:

$$\kappa_0 < \frac{3\sqrt{3}\nu_0^2}{2(\Lambda - 1)^{3/2}}. \tag{4.34}$$

The stability bound (4.29) κ_0 cannot be maximised since it increases monotonically with increasing ν_0. However, this implies that for any given ν_0, instability is possible for sufficiently large κ_0. Likewise, at any κ_0 sufficiently large, ν_0 will stabilise the steady modes, where we require a larger value of ν_0 as Λ increases.

Exchanging Roots

We have already discussed that the stability bound (4.29) only defines a single marginally unstable root. Indeed, if $S = 0$ on the bound (4.29), there are two other possible roots where S may be positive. This becomes apparent when assuming (4.27) holds in the cubic for the growth rate (4.24), yielding

$$S^3 + \frac{1}{A^2}(\kappa_0 + 2\nu_0)S^2 + \frac{1}{A^4}(2\kappa_0\nu_0 + \nu_0^2 - A^4(\Lambda - 1 - A^2))S = 0. \tag{4.35}$$

Clearly, equation (4.35) has three roots, with one being $S = 0$. The other two roots are given by

$$2SA^2 = -(\kappa_0 + 2\nu_0) \pm \sqrt{(\kappa_0 + 2\nu_0)^2 - 4(2\kappa_0\nu_0 + \nu_0^2 - A^4(\Lambda - 1 - A^2))}, \tag{4.36}$$

where if the discriminant is negative, we have two stable oscillatory modes. However, if the discriminant is positive, it is possible that one mode of (4.36) is steady and unstable. Note that the latter part of the discriminant relates to the condition (4.26) on whether marginal oscillatory

instability can occur. Indeed, if (4.26) holds at fixed κ_0, so that oscillatory instability may occur at that κ_0, then the discriminant of (4.36) may be positive. However, the mode will always be guaranteed to be stable since the magnitude of the first term of (4.36) will be larger than that of the square-root term.

To see that other steady modes can occur outside of the stability bound (4.34), we substitute the value of A from (4.33) on the stability boundary into (4.36), yielding

$$2SA^2 = -(\kappa_0 + 2\nu_0) \pm \sqrt{(\kappa_0 + 2\nu_0)^2 - 8(2\kappa_0\nu_0 - \nu_0^2)}, \tag{4.37}$$

where we have made use of the stability boundary (4.34) to write κ_0 in terms of ν_0. Clearly, we have an unstable steady mode provided $2\kappa_0 < \nu_0$, illustrating that (4.29) is not necessarily a necessary and sufficient steady boundary if there are oscillatory modes that occur for $\nu_0^2 > 2(\Lambda - 1)^{3/2}k_0/3\sqrt{3}$ at fixed κ_0.

Necessary and Sufficient Conditions for Stability

We can derive a necessary and sufficient stability condition on all modes (i.e., steady and oscillatory); indeed, the stability bound (4.29) is both necessary and sufficient provided (4.26) is satisfied, while the bound (4.34) is necessary and sufficient if there are no oscillatory instabilities at a fixed κ_0. However, if we take the stability bounds (4.29) and (4.34) together they form the following sufficient and necessary condition for stability (including both steady and oscillatory modes):

$$\nu_0^{\frac{1}{2}} \left(\left(\frac{16}{27}\right)^{\frac{1}{4}} (\Lambda - 1)^{\frac{3}{4}} - \nu_0^{\frac{1}{2}} \right) < \kappa_0 < \frac{3\sqrt{3}\nu_0^2}{2(\Lambda - 1)^{3/2}}, \tag{4.38}$$

where, if either side of the inequality is violated, then instability (either steady or oscillatory) is guaranteed. This is a powerful condition as it requires no additional assumption and the stability bound is independent of the vertical wavenumber. Thus, given some astrophysical body, the parameters ν_0, κ_0 and Λ may be estimated so that (4.38) either implies that the system is stable or unstable.

It is possible for instability to occur regardless of the value of κ_0 if the right hand term is smaller than the left hand term of (4.38) since the inequality would never be satisfied. Thus, we set the left hand side equal to the right hand side of (4.38) which yields the following cubic in $\nu_0^{1/2}$:

$$\frac{3\sqrt{3}}{2(\Lambda - 1)^{3/2}}\nu_0^{\frac{3}{2}} + \nu_0^{\frac{1}{2}} - \left(\frac{16}{27}\right)^{\frac{1}{4}} (\Lambda - 1)^{\frac{3}{4}} = 0. \tag{4.39}$$

Equation (4.39) is a cubic with one real root for ν_0. We know this as the right hand term of (4.38) is a quadratic passing through $(\nu_0, \kappa_0) = (0, 0)$, while the left hand term of (4.38) is only valid for $\nu_0 > 0$ and is only positive for $\nu_0 < 4(\Lambda - 1)^{1/2}/3\sqrt{3}$ (i.e., one interval of ν_0). Equation (4.39) clearly cannot be satisfied for $\nu_0 < 0$, and thus, equation (4.39) has one real root with $\nu_0 > 0$. Hence, once this value is surpassed, then stability is possible since (4.38) can be satisfied. Note that for large ν_0 equation (4.39) cannot be satisfied with $\Lambda = O(1)$ or smaller (as we expect of

the astrophysical bodies in table 2.1), which implies that (4.38) can be satisfied so that stability is possible.

To make further progress, we assume $\Lambda = O(1)$ (which is reasonable in astrophysical planetary atmospheres, e.g., Hot Jupiters) and $\nu_0 \ll 1$ (which is again reasonable in planetary atmospheres). These assumptions allow us to justify neglecting the cubic term in $\nu_0^{1/2}$, yielding

$$\nu_0 \approx \frac{4}{\sqrt{27}}(\Lambda - 1)^{\frac{3}{2}}. \tag{4.40}$$

Therefore, if we observe an astrophysical body with $\nu_0 \ll 1$ and less than the value of ν_0 in equation (4.40), then we are guaranteed instability since (4.38) cannot be satisfied.

The stability bounds (4.38) and (4.40) are very useful in application to astrophysical bodies since there is no vertical wavenumber dependence. This allows a bound on κ_0 (equivalently ν_0 or Λ) to be formed using inferred values of our parameters from the astrophysical body. For example, using observed values for Hot Jupiters (found in the previous section and table 2.1), we estimate $\Lambda = 5$ and $\nu_0 = 10^{-13}$. This satisfies the criteria $\nu_0 \ll 1$ with $\Lambda = O(1)$ for (4.40) and, indeed, our observed ν_0 is smaller than the critical ν_0 in (4.40). Hence, (4.38) cannot be satisfied and instability is guaranteed. However, it is possible for the parameters in astrophysical bodies (even Hot Jupiters) to satisfy (4.38), implying stability. We also note that numerical simulations typically run with larger values of ν_0 ($\nu_0 = O(10)$ in large scale numerical models for Hot Jupiters, e.g., Rogers & Komacek, 2014) where (4.39) cannot be satisfied and so instabilities may be artificially suppressed.

The Maximum Growth Rate in (ν_0, κ_0)-space

We now provide contour plots of the maximum growth rate S (and its corresponding imaginary part) in (ν_0, κ_0)-space for $\Lambda = 1.5$ and $\Lambda = 2.5$ in figure 4.4. We determine the growth rate by arraying (4.24) over A, ν_0 and κ_0 at fixed Λ. Then, at each ν_0 and κ_0 we select the A that generates the maximum growth rate and also plot this value in (ν_0, κ_0)-space for the chosen Λ in figure 4.5. To determine the range of A that is required to maximise the growth rate at each ν_0 and κ_0, we undergo preliminary runs of the process described above with $A \in [0, A_+]$, iterating until the value A required is less than A_+. Note that, the maximisation of the growth rate over A can be interpreted as an optimisation over the vertical wavenumber k since the cross-stream wavenumber is assumed to be fixed (as discussed around (4.2) and (4.4) since ν_0 and κ_0 contain the cross-stream wavenumber). The bounds (4.29) and (4.34) form the necessary and sufficient boundary for stability (4.38). The intersection of (4.29) and (4.34) is given by (4.39), reducing to (4.40) provided $\nu_0 \ll 1$ at the point of intersection.

We find that increasing ν_0 always decreases the growth rate, while increasing κ_0 always increases the growth rate to the maximum growth rate of the inviscid hydrodynamic regime $\Lambda/2$. The maximum growth rate occurs in the limit $Pr \ll 1$ (which is typically the case in planetary atmospheres), and are therefore steady instabilities. In general, we find that sufficiently large κ_0 guarantees instability at any value of ν_0. Interestingly, at certain values of ν_0, increasing κ_0 first
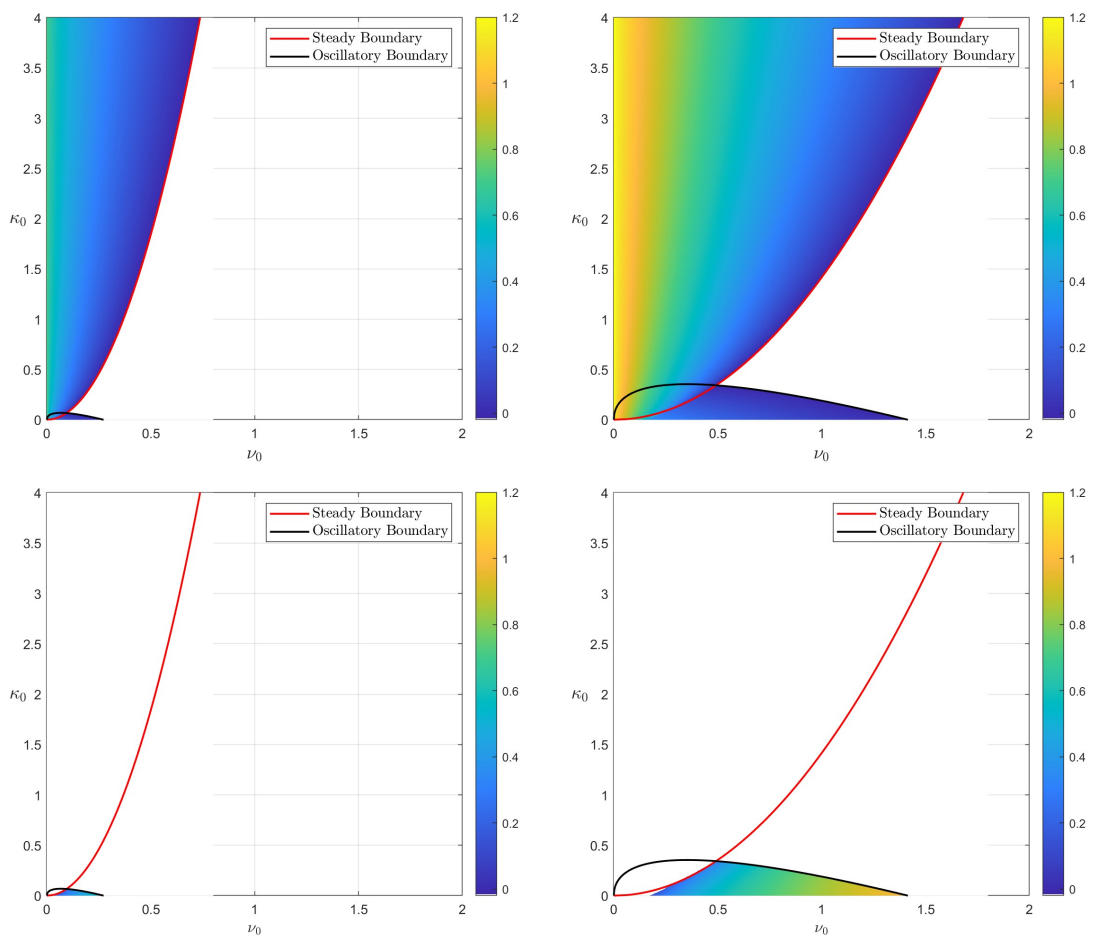
Figure 4.4: The maximum growth rate S (top) and corresponding imaginary part (below) in (ν_0, κ_0)-space with $\Lambda = 1.5$ (left) and $\Lambda = 2.5$ (right). The black oscillatory stability boundary is given by equation (4.29). The red stability boundary is given by equation (4.34).

stabilises the system and then generates instability once again. This is owing to the oscillatory instabilities that can occur only for sufficiently weak thermal diffusivity where buoyancy effects are still felt (i.e., increasing the magnitude of thermal diffusivity dampens buoyancy effects and stabilises oscillatory instabilities). This is confirmed by the corresponding imaginary part of the maximum growth rate in (ν_0, κ_0)-space in figure 4.4 for $\Lambda = 1.5$ and $\Lambda = 2.5$. We note that stability is guaranteed at any value of κ_0 given sufficiently large ν_0.

Figure 4.5 illustrates the corresponding aspect ratio in (ν_0, κ_0)-space that generates the maximum growth rate $S_{\max}$ (as found in figure 4.4) for $\Lambda = 1.5$ and $\Lambda = 2.5$. The values $\Lambda = 1.5$ and $\Lambda = 2.5$ are chosen so that comparisons can be made to figure 4.2. We find that increasing ν_0 or κ_0 increases the value of $A_{\max}$ (i.e., the critical vertical wavenumber at which the maximum growth rate occurs decreases). Modes with $Pr \ll 1$ have the largest vertical wavenumbers (small A). This is of interest as Pr is typically small in planetary atmospheres; the maximum growth rate of the hydrodynamic regime also occurs in the large vertical wavenumber limit (Griffiths, 2008a). The large κ_0 limit also shows that instability may now occur within the stable regime of the inviscid system. That is, instability may now occur for $A^2 > \Lambda - 1$. For example, at
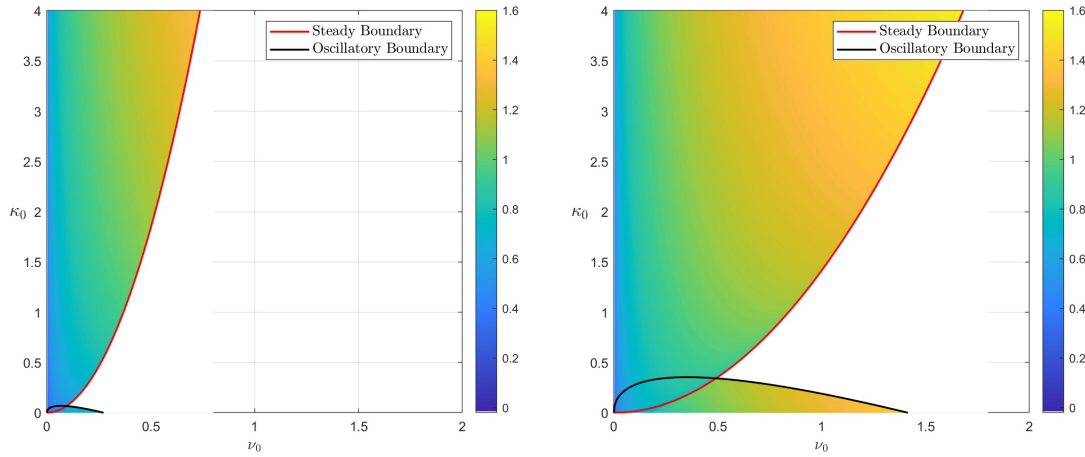
Figure 4.5: The $A_{\max}$ that generates the maximum growth rate $S_{\max}$ (as seen in figure 4.4) in (ν_0, κ_0)-space with $\Lambda = 1.5$ (left) and $\Lambda = 2.5$ (right). The black oscillatory stability boundary is given by equation (4.29). The red stability boundary is given by equation (4.34).

$\kappa_0 = 4$ and $\nu_0 = 1.5$ with $\Lambda = 2.5$, $A_{\max} \approx 1.5$ so that $A^2 = 2.25 > 1.5 = \Lambda - 1$. This is consistent with (4.33), which predicts that as the strength of thermal conductivity increases at a fixed ν_0, then larger A is required to stabilise the steady modes of the system. Thus, instability can occur at larger A which were stable in the ideal regime ($A > \sqrt{\Lambda - 1}$ gives stability). This is due to the pressure gradient (whose strength increases with increasing A) being damped by an increasing rate of thermal diffusion (κ_0 increasing). Note that these instabilities are much like the Goldreich-Schubert-Fricke (GSF) instability (Goldreich & Schubert, 1967; Fricke, 1968), where thermal diffusion counteracts the stabilising effect of the pressure gradient and allows instability to occur at larger A (which would otherwise by stable in the absence of diffusion).

Limit of Strong Thermal Diffusion

Motivated by the complex behaviour found in the limit of large thermal diffusion in figures 4.4 and 4.5, we investigate the large κ_0 limit of equation (4.20). However, we must also consider the asymptotic behaviour of the growth rate S and aspect ratio A since they also vary with κ_0, as seen in figures 4.4 and 4.5. First, we address the upper left section of figure 4.4 and suppose $\kappa_0 \gg 1$ with $S = S_0 + S_1 \kappa_0^{-\beta}$, where $S_0 = O(1)$, $S_1 = O(1)$, and $\beta = O(1)$ are yet to be determined. We also suppose that $A \sim \kappa_0^{1/8}$ (numerically determined) from which (4.20) yields:

$$S_{\kappa_1} = \sqrt{\Lambda - 1} - \frac{\nu_0}{A^2} - \frac{A^4}{2\kappa_0} + O(\kappa_0^{-1}). \tag{4.41}$$

Equation (4.41) is the growth rate (4.13), found for $Pr = 1$, in the absence of the $-A^2$ term (found within the square root) that acts to reduce the growth rate. This is expected in the large κ_0 limit since effects generated by the pressure (which is stabilising) will be negligible.

We now address the upper right section of figure 4.4 by supposing $A \sim \kappa_0^{\frac{1}{4}}$ and $\nu_0 \sim \kappa_0^{\frac{1}{2}}$ (inferred from the stability bound (4.34) with its corresponding value of A (4.33)) with $\kappa_0 \gg 1$,

102
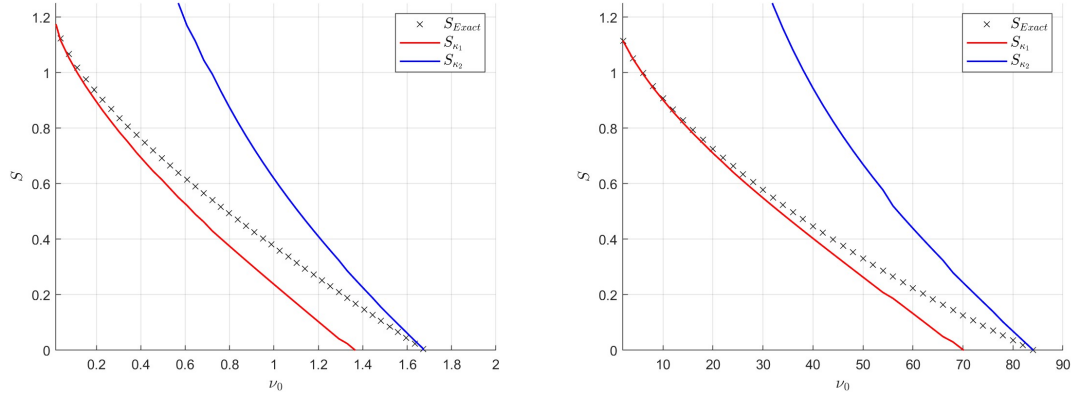
Figure 4.6: The exact growth rate (calculated from (4.20)) plotted with the large κ_0 expansions (4.41) and (4.42) (solid red and blue lines, respectively) at $\kappa_0 = 4$ and $\kappa_0 = 10^5$ for $\Lambda = 2.5$ against ν_0. Note that, in order to do this, at each ν_0 we select the A that generates the maximum growth rate.

in which case (4.20) yields:

$$S_{\kappa_2} = \frac{(\Lambda - 1)\kappa_0 A^4 - \nu_0^2 \kappa_0 - \nu_0 A^6}{A^2(2\kappa_0\nu_0 + A^6)} + \dots, \tag{4.42}$$

which has been derived from a quadratic in S, where we have taken the positive sign so that instability is possible (the negative sign guarantees the mode is stable).

To confirm the validity and assess the accuracy of the large κ_0 expansions (4.41) and (4.42), we plot them in figure 4.6 alongside the exact growth rate (calculated via (4.20)) at $\kappa_0 = 4$ and $\kappa_0 = 10^5$ for $\Lambda = 2.5$ against ν_0. Note that, in order to do this, at each ν_0 we select the A that generates the maximum growth rate so that S_{κ_i} is a function of ν_0 only (since $A = A(\nu_0)$). We observe that each expansion is accurate for some small interval of ν_0, capturing the behaviour of the unstable mode in their respective cases. We find that the accuracy of (4.41) improves as we increase κ_0 (as one would expect); however, (4.42) still only captures the unstable mode for a small region of ν_0 before stabilisation.

4.4 Magnetohydrodynamic Regime

We now consider the magnetohydrodynamic regime, where the magnetic diffusivity η must be considered alongside ν and κ. In the following subsections we consider $Pr = Pm = 1$, $Pr \neq 1$ and $Pm = 1$, $Pr = 1$ and $Pm \neq 0$ as well as $Pr \neq 0$ and $Pm \neq 0$. In the final case, we investigate the regime $Pr \ll Pm \ll 1$, which is typically the case in astrophysical objects. The cases prior remain useful for analytical progress, numerical simulations and physical understanding.

4.4.1 Formulation and Stability Bounds

We first derive stability bounds from equation (4.5). In the hydrodynamic regime we derived stability bounds independent of A, motivated by our analysis of the system (e.g., contouring the

maximum growth rate and the value of A at which occurs in (ν_0, κ_0)-space); however, we will later be maximising the growth rate over both A and the Lehnert number $\mathcal{L}$. Thus, we now derive stability bounds independent of A and $\mathcal{L}$.

In the magnetohydrodynamic regime we can only make analytic progress regarding the steady neutrally unstable mode (i.e., $a_0 = 0$ so that the quintic equation (4.6) yields an $S = 0$ root); it is impractical to analytically determine an oscillatory boundary (analogous to (4.25) of the hydrodynamic system) by the Routh-Hurwitz criteria (Routh, 1877; Hurwitz, 1895) owing to the six non-zero coefficients of (4.6). However, the hydrodynamic oscillatory condition (4.29) still may be used in certain cases (e.g., $Pr \neq 1$ and $Pm = 1$ with sufficiently large Λ). Thus, we proceed by deriving a steady stability boundary ($S = 0$) by differentiating (4.5) with respect to each A^2 and $\mathcal{L}^2$, then setting the derivatives and S to zero. Indeed, since equation (4.5) is a quintic polynomial in S, this process yields the A^2 and $\mathcal{L}^2$ derivatives of the coefficient of S^0 (since setting $S = \partial_{A^2} = \partial_{\mathcal{L}^2} = 0$ annihilates all other terms). That is, we obtain the A^2 and $\mathcal{L}^2$ derivatives of

$$\frac{A^2 \eta_0}{\kappa_0} \left(\frac{\nu_0 \eta_0}{A^4} + \mathcal{L}^2 \right) - \mathcal{L}^2 \Lambda + (1 - \Lambda) \frac{\eta_0^2}{A^4} + \left(\frac{\nu_0 \eta_0}{A^4} + \mathcal{L}^2 \right)^2 = 0, \tag{4.43}$$

which can be derived by setting $S = 0$ in the quintic polynomial (4.5). Note that, in general, the quintic equation (4.5) may have complex roots; however, the stability bound (4.43) applies only to steady modes.

To derive the steady stability boundary we differentiate (4.5) with respect to A^2 and $\mathcal{L}^2$. Hence, differentiating (4.43) with respect to $\mathcal{L}^2$ and setting $\partial_{\mathcal{L}} S = 0$, yields

$$2\mathcal{L}^2 = \Lambda - \frac{A^2 \eta_0}{\kappa_0} - \frac{2\nu_0 \eta_0}{A^4}. \tag{4.44}$$

Note that since $\mathcal{L}^2$ cannot be negative, equation (4.44) holds only if the right hand side is positive. If (4.44) implies that $\mathcal{L}^2 < 0$, which can not be the case, then the steady hydrodynamic bound (4.34) must be used with $\mathcal{L} = 0$.

Next, we differentiate (4.43) with respect to A^2, yielding

$$-\frac{\nu_0 \eta_0^2}{\kappa_0 A^4} + \frac{\eta_0 \mathcal{L}^2}{\kappa_0} + 2(\Lambda - 1)\frac{\eta_0^2}{A^6} - \frac{4\nu_0 \eta_0}{A^6} \left(\frac{\nu_0 \eta_0}{A^4} + \mathcal{L}^2 \right) = 0. \tag{4.45}$$

Substituting (4.44) into (4.45) yields an expression independent of $\mathcal{L}^2$, that is

$$\frac{\eta_0 \Lambda}{2\kappa_0} - \frac{A^2 \eta_0^2}{2\kappa_0^2} - \frac{2\Lambda \nu_0 \eta_0}{A^6} - 2(1 - \Lambda)\frac{\eta_0^2}{A^6} = 0. \tag{4.46}$$

Next, in order to derive a stability bound in terms of ν_0, κ_0, η_0 and Λ only, we substitute (4.44) and (4.46) into equation (4.43), yielding the following quadratic in A^2:

$$\Lambda^2 \kappa_0^2 + 2A^4 \eta_0^2 - 3\kappa_0 \eta_0 \Lambda A^2 = 0, \tag{4.47}$$

where, upon factorising (4.47), we obtain

$$\left(\Lambda - \frac{2A^2 \eta_0}{\kappa_0} \right) \left(\Lambda - \frac{A^2 \eta_0}{\kappa_0} \right) = 0. \tag{4.48}$$

Thus, A^2 can take two values. First, if $A^2 = \Lambda\kappa_0/\eta_0$, then the corresponding $\mathcal{L}^2$ calculated from (4.44) is negative. Thus, we must take the following value of A^2 and $\mathcal{L}^2$:

$$A^2 = \frac{\Lambda\kappa_0}{2\eta_0} \implies \mathcal{L}^2 = \frac{\Lambda}{4} - \frac{4\eta_0^3\nu_0}{\Lambda^2\kappa_0^2}, \tag{4.49}$$

where the latter is calculated by substituting $A^2 = \Lambda\kappa_0/2\eta_0$ into (4.44). The expression for $\mathcal{L}^2$ is valid only if $\Lambda^3\kappa_0^2 > 16\eta_0^3\nu_0$; if this is not the case, we take $\mathcal{L} = 0$ and the hydrodynamic steady stability bound (4.34). Equation (4.49) implies that on the steady stability bound the aspect ratio A increases with increasing κ_0 or Λ. This is reasonable as we expect that increasing κ_0 and Λ will increase the growth rate of unstable modes so that stronger buoyancy forces (via increasing A) are required in order to stabilise the system. The aspect ratio A also decreases with increasing magnetic diffusivity η_0. Indeed, the growth rate of unstable magnetic modes is already dampened (or stabilised) by magnetic diffusivity and therefore only weak buoyancy effects are required in order to stabilise the system. The expression for $\mathcal{L}$ in (4.49) is harder to interpret owing to the different possible scalings between Λ, ν_0, κ_0 and η_0. However, given that the value of the Lehnert number in (4.49) is positive, so that the marginally unstable modes are magnetic on the boundary, then the value of the Lehnert number increases with increasing Λ or κ_0 and decreases with increasing η_0 or ν_0.

Thus, when $\partial_{\mathcal{L}^2}S = \partial_{A^2}S = S = 0$ and the marginally unstable modes are magnetic, then the values of A^2 and $\mathcal{L}^2$ are given in (4.49). Substituting these values into equation (4.43) yields the following criteria for stability to steady modes:

$$\kappa_0^2 < \frac{64\eta_0^4}{\Lambda^4}\left(\frac{\nu_0\Lambda}{\eta_0} + (1 - \Lambda)\right), \tag{4.50}$$

provided $\Lambda^3\kappa_0^2 > 16\eta_0^3\nu_0$ (i.e., equation (4.49) is satisfied). If the condition (4.49) is not met, then $\mathcal{L} = 0$ and the steady hydrodynamic stability bound (4.34) is used. We will consider this on a case by case basis when considering different constraints on the Prandtl numbers (e.g., $Pr \neq 1$). Note that, if (4.50) is satisfied, then it is still possible for oscillatory instabilities to occur since (4.50) describes a boundary where $S \equiv 0$ (i.e., zero imaginary part). We also note that the bound (4.50) corresponds to $a_0 = 0$ and $S = 0$ in (4.6); however, equation (4.6) could also be satisfied with either four complex roots, two complex and two real roots, or four real roots, and thus, in certain cases, (4.50) may not be a necessary and sufficient condition for steady stability. We will address the use of (4.50) in numerous Prandtl numbers regimes.

Note that since we considering a flow with a fixed latitudinal lengthscale on an astrophysical body so that all parameters aside from the vertical wavenumber k are fixed, then we must consider a single hyperbola $A^2\mathcal{L}^2 = C$ in figure 4.1; then, writing $\mathcal{L}^2 = C/A^2$ in equation (4.43) yields a quartic in A^2, which gives the points at which the hyperbolae intersects with boundary of the unstable domain. For example, equation (4.43) would yield two distinct real roots (and two complex roots) if the hyperbola intersected the boundary of the unstable region in figure 4.1 at two distinct points; alternatively, equation (4.43) would yield a double real root (and two complex

roots) if the hyperbola intersected the unstable region once only (i.e., the hyperbolae that bound the region from above and below). Unfortunately, writing $\mathcal{L}^2 = C/A^2$ in equation (4.43) does not allow for any useful analytical progress to be made; however, the roots can be determined numerically. Further to this, note that the $(\mathcal{L}, A)$ given by (4.49) corresponds to the final unstable mode that is stabilised in the $(\mathcal{L}, A)$-space of figure 4.1 (e.g., owing to an increasing magnitude of kinematic viscosity ν_0 say). Thus, given contours of the maximum growth rate in diffusive space (e.g., (ν_0, κ_0)-space with $\nu_0 = \eta_0$) at fixed Λ, where A and $\mathcal{L}$ have been selected to maximise the growth rate, then (4.50) bounds the steady unstable modes.

4.4.2 $Pr = Pm = 1$

We first consider the simplest possible choice of Prandtl numbers, where both are unity. In this case, we write κ_0 and η_0 as ν_0 which allows us to recast equation (4.5) as

$$\left(S + \frac{\nu_0}{A^2}\right)^4 + \left(S + \frac{\nu_0}{A^2}\right)^2 \left(A^2 + 2\mathcal{L}^2 + 1 - \Lambda\right) + \mathcal{L}^2 \left(A^2 + \mathcal{L}^2 - \Lambda\right) = 0. \qquad (4.51)$$

Equation (4.51) reduces to its inviscid analogue (3.23) in the absence of diffusion. However, we can also obtain equation (4.51) from (3.23) via a transformation of the growth rate S to $S + \nu_0/A^2$. That is, for each point in $(\mathcal{L}, A)$-space we may obtain the growth rate when $\nu_0 \neq 0$ by subtracting ν_0/A^2 from the growth rate in the absence of diffusion. This transformation allows us to use numerous results from the inviscid case such as the weak field expansions (3.29) and (3.30) provided ν_0/A^2. The transformation also implies that oscillatory instabilities will not occur in this regime, and thus weakly unstable modes within the inviscid instability domain, given by (3.25), will be stabilised. Thus, the sufficient and necessary condition for stability (3.25) becomes a sufficient condition only.

Stability Conditions

It is of interest to find the critical diffusion, $\nu_0 = \nu_c$ say, for which no steady unstable modes exist (noting that there are only steady instabilities in the case $Pr = Pm = 1$). We obtain this value from the stability bounds (4.34) and (4.50), where the latter is used if $\mathcal{L} > 0$ in equation (4.49). Writing κ_0 and η_0 as ν_0 allows us to recast equation (4.49) as

$$\mathcal{L}^2 = \frac{\Lambda}{4} - \frac{4\nu_0^2}{\Lambda^2}. \qquad (4.52)$$

Hence, if ν_c required for stabilisation becomes too large, then $\mathcal{L}$ will not be positive on the boundary and the hydrodynamic critical diffusion must be calculated from (4.34).

In the cases where (4.52) does not predict a positive value for $\mathcal{L}$, we have the steady hydrodynamic stability bound (4.34) which implies that ν_c is given by

$$\nu_c = \frac{2(\Lambda - 1)^{3/2}}{3\sqrt{3}}. \qquad (4.53)$$

106

If equation (4.52) predicts a positive value for $\mathcal{L}$, we have the magnetic steady stability bound (4.34) which yields the critical diffusion:

$$\nu_c = \frac{\Lambda^2}{8}. \tag{4.54}$$

Note that the scaling between ν_c and Λ differs between the two cases (4.53) and (4.54).

To determine the value of $\nu_0 = \nu_c$ (or Λ) at which the stability bound shifts from (4.53) to (4.54) we substitute (4.54) into equation (4.52), yielding

$$\mathcal{L} > 0 \iff \nu_0 < 2, \text{ or equivalently, } \Lambda < 4. \tag{4.55}$$

Hence, provided $\Lambda < 4$, then the critical diffusion $\nu_c < 2$ and is predicted by the magnetic bound (4.54). If $\Lambda > 4$, then the critical diffusion $\nu_c > 4$ and is predicted by the hydrodynamic bound (4.53). Note that if either of the critical diffusions (4.53) or (4.54) are satisfied (when relevant), then the system is stable since oscillatory instability is not possible with $Pr = Pm = 1$.

The Growth Rate as a function of Lehnert Number and Aspect Ratio

We continue our analysis by providing contour plots of the growth rate (calculated numerically from (4.51)) in $(\mathcal{L}, A)$-space. Naturally, we are primarily concerned with the most unstable mode; however, it is also of interest to investigate the entire instability domain as nonlinear evolution may allow other modes to grow more rapidly. In planetary atmospheres, it is also possible that the flow interacts with waves of arbitrary vertical wavenumber, forcing modes to become unstable with a non-optimal aspect ratio (i.e., the vertical wavenumber is prescribed to the mode from the wave). Thus, modes with growth rate less than the maximum may also be relevant in understanding the dynamics of planetary atmospheres. Recall that if we are given a flow of latitudinal lengthscale L on an astrophysical body so that all parameters are fixed aside from the vertical wavenumber, then we must consider a single hyperbola in $(\mathcal{L}, A)$-space, where the vertical wavenumber only may vary as they are traversed.

In figures 4.7-4.9 we contour the growth rate (calculated numerically from (4.51)) in $(\mathcal{L}, A)$-space with $\Lambda = 0.5, 1.5$ and 2.5, respectively, for multiple ν_0. These are useful in order to compare the diffusive system with that of the ideal regime, where we also include the inviscid necessary and sufficient condition for stability (3.25), given by the solid red line. We also include dashed black lines that represent the hyperbolae $A\mathcal{L} = C$, where C incrementally doubles from $C = 0.025$ to $C = 3.2$; large vertical wavenumbers are found in the large $\mathcal{L}$ limit. The red dot represents the location of the most unstable mode in the domain.

Figure 4.7 indicates a solely hydrodynamically stable regime (since $\Lambda < 1$), allowing us to conclude that even weak magnetic field destabilises the system. Increasing ν_0 reduces the growth rate and stabilises the system at $\nu_0 = 0.03125$, as predicted by (4.54).

Figure 4.8 shows both a hydrodynamically unstable regime, for $A_- < A < A_+$, and a stable regime with $A < A_-$ or $A > A_+$, where A_- and A_+ are approximated by the hydrodynamic instability domain (4.23), which is valid for $\nu_0 \ll 1$. In both cases, weak field again destabilises
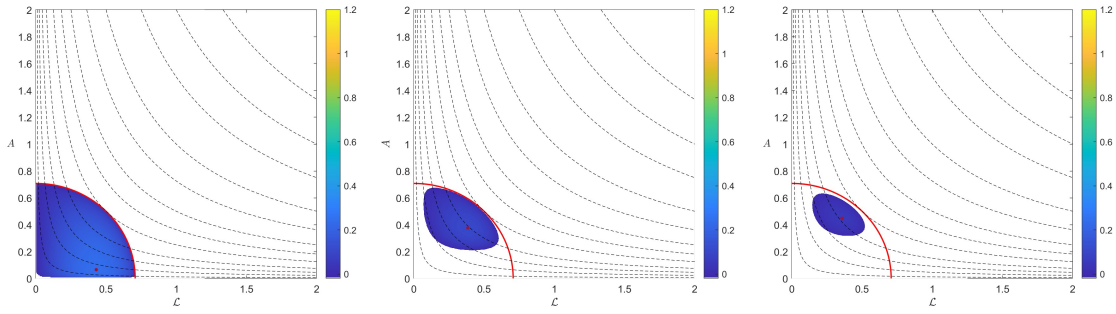
Figure 4.7: $Pr = Pm = 1$: The most unstable mode in $(\mathcal{L}, A)$-space with $\Lambda = 0.5$ for $\nu_0 = 10^{-5}$ (left), $\nu_0 = 0.01$ (centre) and $\nu_0 = 0.02$ (right). The red line is the inviscid stability bound (3.25).
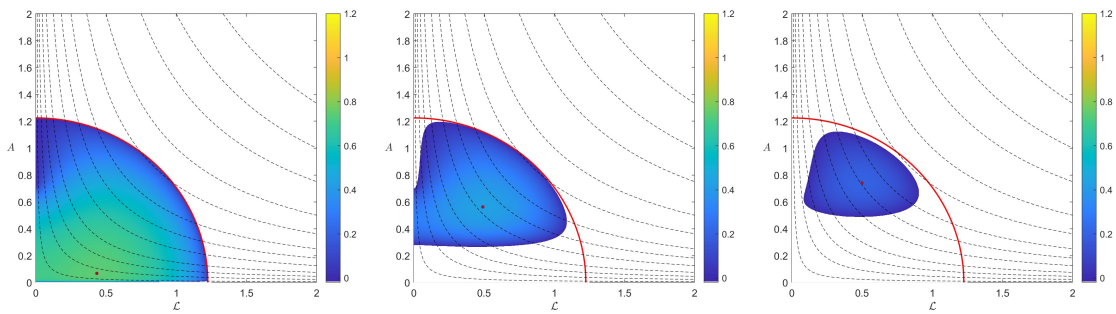
Figure 4.8: $Pr = Pm = 1$: The most unstable mode in $(\mathcal{L}, A)$-space with $\Lambda = 1.5$ for $\nu_0 = 10^{-5}$ (left), $\nu_0 = 0.05$ (centre) and $\nu_0 = 0.15$ (right). The red line is the inviscid stability bound (3.25).

the system as the maximum growth rate occurs with $\mathcal{L} \neq 0$, where this behaviour persists for $1 < \Lambda < 2$. We find that increasing ν_0 reduces the growth rate and stabilises the system at $\nu_0 = 0.28125$, as predicted by (4.54). The value of A, $A_{\max}$ say, where the maximum growth rate occurs, increases with increasing ν_0, while the corresponding $\mathcal{L}_{\max}$ is approximately constant.

Figure 4.9 once again shows a hydrodynamically stable and unstable regime, where weak field clearly allows instability to occur in the hydrodynamically stable regime. For sufficiently large ν_0 ($\nu_0 \approx 0.12$) the most unstable mode occurs at $\mathcal{L} \neq 0$. This is because the hydrodynamic modes dominate at larger Rossby number Λ but are damped by increasing kinematic viscosity, allowing magnetic modes to have larger growth rates in comparison to the hydrodynamic modes even while the magnitude of magnetic diffusivity is also increasing (since $\eta_0 = \nu_0$ for $Pm = 1$).

The Limit of Weak Magnetic Field

Figures 4.7-4.9 have shown that weak magnetic field induces instability within certain parameter regimes, including the entire unstable domain for $\Lambda < 1$ as this is hydrodynamically stable. Following the inviscid analysis we consider the weak field regime to categorise the behaviour of the system. To investigate the small $\mathcal{L}$ regime we can transform the ideal weak field expansions (3.29) and (3.30) by writing S as $S + \nu_0/A^2$ or, alternatively, consider the small $\mathcal{L}$ regime of equation
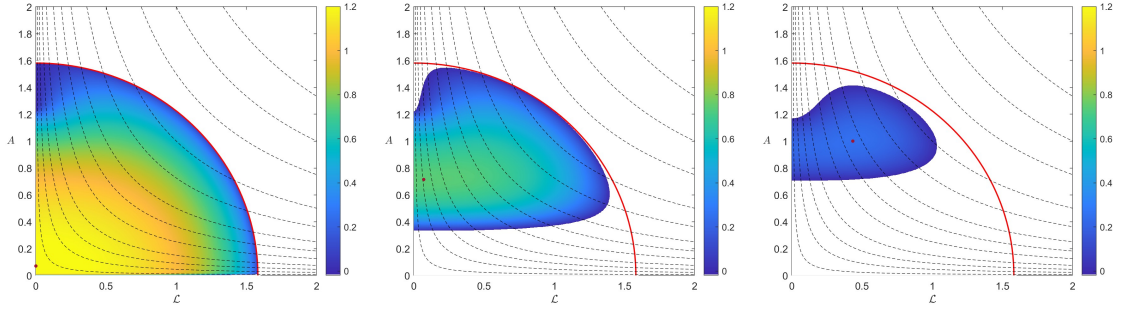
Figure 4.9: $Pr = Pm = 1$: The most unstable mode in $(\mathcal{L}, A)$-space with $\Lambda = 2.5$ for $\nu_0 = 10^{-5}$ (left), $\nu_0 = 0.013$ (centre) and $\nu_0 = 0.5$ (right). The red line is the inviscid stability bound (3.25).

(4.51). In either case, the growth rate for the modes scale as

$$S_H = (\Lambda - 1 - A^2)^{1/2} - \frac{\nu_0}{A^2} - \frac{\mathcal{L}^2(\Lambda - 2 - A^2)}{2(\Lambda - 1 - A^2)^{3/2}} + O(\mathcal{L}^4), \tag{4.56}$$

$$S_{\mathcal{L}} = \frac{\mathcal{L}(\Lambda - A^2)^{1/2}}{(A^2 - 1 - \Lambda)^{1/2}} - \frac{\nu_0}{A^2} - \frac{\mathcal{L}^3}{2(A^2 - 1 - \Lambda)^{5/2}(\Lambda - A^2)^{1/2}} + O(\mathcal{L}^5), \tag{4.57}$$

where S_H represents the hydrodynamic mode, while $S_{\mathcal{L}}$ corresponds to the magnetic root. Clearly, the expansions break down when $\Lambda - 1 - A^2$ is sufficiently close to zero, since the leading and first order terms in $\mathcal{L}$ become comparable. We address this regime by supposing that $\Lambda - 1 - A^2 = \alpha \mathcal{L}$ for some constant α, of order unity (or undergo the relevant transformation of (3.31)), and substitute into (4.51) to derive the expression

$$S_B = \left(\frac{\mathcal{L}}{2}\right)^{\frac{1}{2}} \left(\Lambda - 1 - A^2 + \sqrt{(\Lambda - 1 - A^2)^2 + 4}\right)^{\frac{1}{2}} - \frac{\nu_0}{A^2}, \tag{4.58}$$

valid for $\Lambda - 1 - A^2$ sufficiently close to zero. To derive (4.58) we took the positive sign of the square root as it describes the most unstable mode (the negative sign would guarantee stability).

Expressions (4.56), (4.57) and (4.58) completely describe the weak field regime. Together, they indicate that if the system is hydrodynamically stable, we must take $S_{\mathcal{L}}^2$ (equation (4.57)) to describe the most unstable mode. Thus, when the system is hydrodynamically stable, the first order term in $\mathcal{L}$ of equation (4.57) indicates that weak field is destabilising if $A^2 < \Lambda$, and stabilising otherwise.

If the system is hydrodynamically unstable, we take S_H^2 (equation (4.56)) to describe the most unstable mode. Thus, when the system is hydrodynamically unstable, the first order term in $\mathcal{L}$ of equation (4.56) indicates if $\Lambda < 2$, then weak field increases the growth rate. Similarly, if $\Lambda > 2$, weak field increases the growth rate provided $\Lambda - 2 < A^2 < \Lambda - 1$, and stabilises if $A^2 < \Lambda - 2$.

Note that in the case $Pr = Pm = 1$, the asymptotic expansions (4.56), (4.57) and (4.58) do not invalidate the magnetohydrostatic approximation since (2.29) reduces to $|(S + \nu_0/A^2)^2 + \mathcal{L}^2| \ll N^2/f_0^2$. Thus, (2.29) holds since we can exploit the transformation from the ideal regime $(S \to S + \nu_0/A^2)$ to consider the constraint. Hence, as in the ideal regime, provided $\mathcal{L}$ is not too large, then (4.56), (4.57) and (4.58) remain valid.
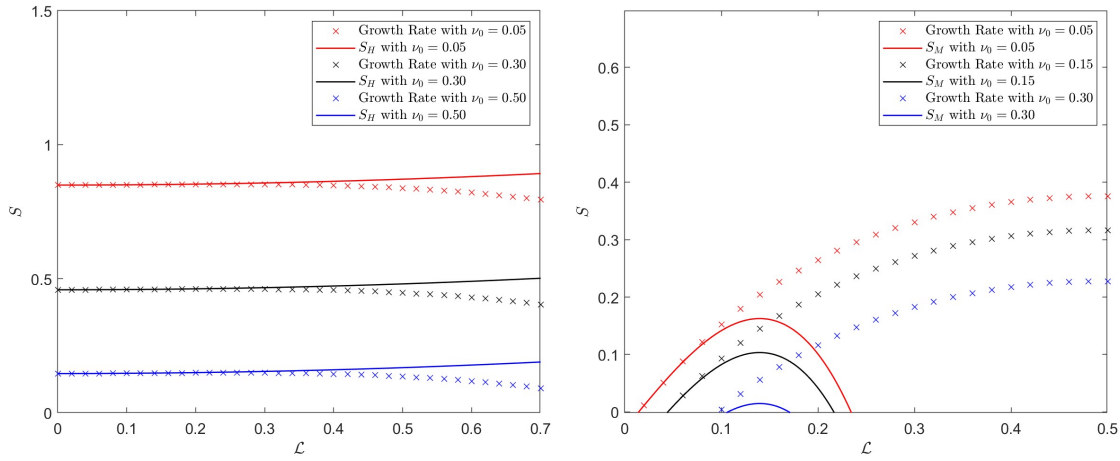
Figure 4.10: $Pr = Pm = 1$: The growth rate of the weak field expansions (4.56) at $A = 0.8$ (left) and (4.57) at $A = 1.3$ (right) are plotted against the exact growth rate for various ν_0 with $\Lambda = 2.5$.
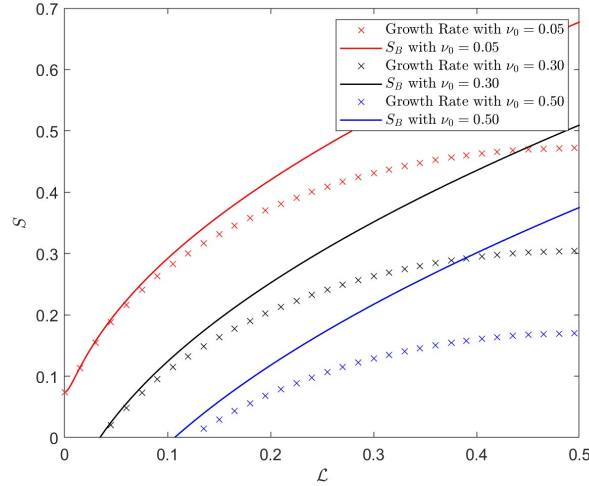
Figure 4.11: $Pr = Pm = 1$: The growth rate of the weak field singular expansion (4.58) at $A = 1.22$ is plotted against the exact growth rate for various ν_0 with $\Lambda = 2.5$.

In figures 4.10 and 4.11 we plot the weak field expansions (4.56), (4.57) and (4.58) with the exact solution (calculated numerically from (4.51)) against $\mathcal{L}$ to ensure their accuracy. These plots are made for various A and ν_0 with $\Lambda = 2.5$ (where all magnetic effects can be visualised). Note that the axis length and the magnitude of ν_0 are altered across the figures.

Figure 4.10 shows that the expansions (4.56) and (4.57) remain accurate under the transformation of the growth rate; however, we find that the magnetic expansion (4.57) becomes invalid when ν_0 becomes too large. This is due to the expansion transformation breaking down when $S \sim \nu_0/A^2$. The role of magnetic field on the system remains consistent with the expansions (4.56) and (4.57), where, for example, at $A = 1.3$, magnetic field increases the growth rate of the system. Figure 4.11 shows that the expansion (4.58) remains accurate under the transformation of the growth rate; however, we also find that the magnetic expansion becomes invalid when ν_0 becomes too large.

The Maximum Growth Rate as a Function of Diffusion

We will be maximising the growth rate over A and $\mathcal{L}$ at fixed ν_0 and Λ, where we once again reiterate that the cross-stream wavenumber is considered to be fixed (prescribed via our diffusive parameters). This allows us determine the role of diffusion on the most unstable mode of the system, and describe these results in a more rigorous and effective manner. However, it must be noted, it is difficult to interpret these results for given astrophysical bodies since v_A, ν_0, and therefore the cross-stream wavenumber, take fixed values (inferred from observations). This consequence arises because the maximisation over A must be interpreted as an optimisation over the vertical wavenumber k, while the maximisation over $\mathcal{L}$ must be interpreted as an optimisation over kv_A, where an optimal magnetic field strength is inferred (since k is already chosen via the optimisation of A) from the quantity kv_A (e.g., if k increases, but $\mathcal{L}$ remains constant, then v_A must decrease). Thus, since v_A must vary in magnitude, we cannot consider a single astrophysical body.

Having maximised the growth rate over the parameters $\mathcal{L}$ and A, we provide plots of the maximum growth rate, $\mathcal{L}_{\max}$, and $A_{\max}$ against ν_0 in figure 4.12, for $\Lambda = 0.5, 1.5$ and 2.5, where $\mathcal{L}_{\max}$ and $A_{\max}$ are the values of $\mathcal{L}$ and A that generate the maximum growth rate $S_{\max}$ (i.e., $S_{\max} = S(\mathcal{L}_{\max}, A_{\max})$). The black, red and blue crosses denote the maximum growth rate, $\mathcal{L}_{\max}$ and $A_{\max}$, respectively.

As ν_0 increases, the maximum growth rate monotonically decreases in all cases. For $\Lambda = 0.5$ and 1.5, the optimal Lehnert number $\mathcal{L}_{\max}$ does not vary much from $\mathcal{L} \approx 0.4$ as ν_0 increases. However, the aspect ratio A increases significantly as ν_0 increases, implying the vertical wavenumber is decreasing. Hence, for $\mathcal{L}$ to remain approximately fixed over the domain, the optimal magnetic field strength must be increasing to balance the decreasing vertical wavenumber. For $\Lambda = 2.5$, the aspect ratio A and Lehnert number $\mathcal{L}$ increase at approximately the same rate as ν_0 increases. Thus, vertical wavenumber must decrease with increasing ν_0 implying that the magnetic field strength must increase at faster rate. Figure 4.12 suggests that the magnetic field strength scales approximately with $1/k^2$. Hence, in all cases, as ν_0 increases, the maximum growth rate occurs at decreasing vertical wavenumber while the magnetic field strength increases at a rate such that $\mathcal{L}$ remains fixed or increases. Physically, as ν_0 increases, the most unstable mode must occur at larger A since kinematic viscosity stabilises modes with large vertical wavenumbers. The Lehnert number prefers to remain approximately constant and equal to 0.4 since this is close to the value that maximises the growth rate in the ideal regime (see equation (3.26)). Hence, as increasing strength of diffusion increases the aspect ratio of the most unstable mode, we require increasing field strength to obtain the maximum growth rate of the system.

4.4.3 $Pr \neq 1$, $Pm = 1$

In this section we consider the case where $Pr \neq 1$ and $Pm = 1$. Thus, $\nu_0 \neq \kappa_0$ with $\kappa_0 \neq 0$ and $\nu_0 = \eta_0$. This is a natural extension to the case $Pr = Pm = 1$ and allows us to make useful analogies to the hydrodynamic case described by (4.24) where $Pr \neq 1$.
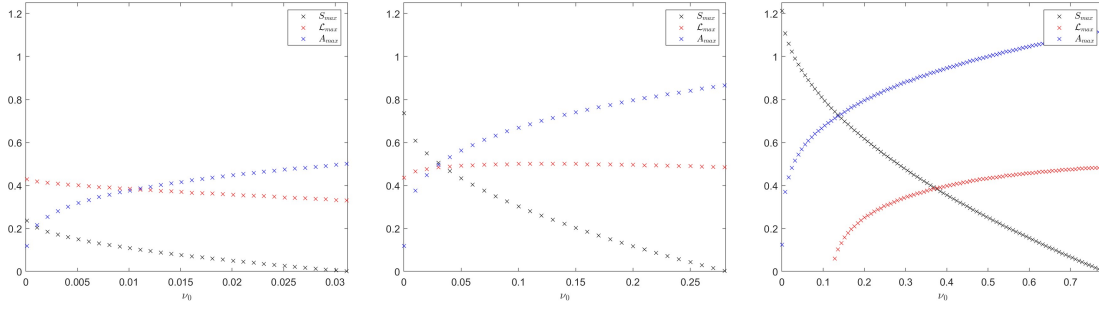
Figure 4.12: $Pr = Pm = 1$: Maximum growth rate $S_{\max} = S(A_{\max}, \mathcal{L}_{\max})$ plotted alongside $\mathcal{L}_{\max}$ and $A_{\max}$ against ν_0. The Rossby number $\Lambda = 0.5$ (left), 1.5 (centre) and 2.5 (right).

Formulation and Stability Bounds

Writing η_0 as ν_0 in (4.5) yields the following equation for the growth rate S :

$$A^2 \frac{S + \nu_0/A^2}{S + \kappa_0/A^2} \left(\left(S + \frac{\nu_0}{A^2}\right)^2 + \mathcal{L}^2 \right) - \mathcal{L}^2 \Lambda$$
$$+ (1 - \Lambda)\left(S + \frac{\nu_0}{A^2}\right)^2 + \left(\left(S + \frac{\nu_0}{A^2}\right)^2 + \mathcal{L}^2\right)^2 = 0. \quad (4.59)$$

We can set $S = 0$ in equation (4.59), giving the criterion for marginal steady instability in terms $A, \mathcal{L}, \nu_0$ and κ_0. However, since we are optimising the growth rate over A and $\mathcal{L}$, we can use the previously derived criterion (4.50) for marginal steady instability. Recall that this criterion only applies to steady instabilities (i.e., $S \equiv 0$) and therefore oscillatory instabilities may exist while the conditions are satisfied. Note that this criterion is only valid if (4.49) predicts $\mathcal{L} > 0$; otherwise the hydrodynamic bound (4.34) must be used. Hence, after writing η_0 as ν_0, we recast equation (4.49) as

$$\mathcal{L}^2 = \frac{\Lambda}{4} - \frac{4\nu_0^4}{\Lambda^2 \kappa_0^2}. \quad (4.60)$$

Equation (4.60) implies that the magnetic stability bound (4.50) is valid if $\Lambda^3 \kappa_0^2 > 16\nu_0^4$.

In the cases where (4.60) does not imply a positive value for $\mathcal{L}$, we have the hydrodynamic necessary and sufficient condition for steady stability (4.34), which we rewrite here for convenience:

$$\kappa_0 = \frac{3\sqrt{3}\nu_0^2}{2(\Lambda - 1)^{\frac{3}{2}}}. \quad (4.61)$$

In the cases where (4.60) predicts a positive value for $\mathcal{L}$, we have the magnetic necessary and sufficient steady stability condition (4.50) which we recast as follows:

$$\kappa_0 < \frac{8\nu_0^2}{\Lambda^2}. \quad (4.62)$$

Note that equations (4.61) and (4.62) only apply to one root and thus there may be other steady modes with $S > 0$ while these conditions are satisfied; we will address this using contours of the growth rate in (ν_0, κ_0)-space. The conditions (4.61) and (4.62) also only apply to steady

112

instabilities (i.e., $S \equiv 0$) and therefore oscillatory instabilities may exist while (4.61) and (4.62) are satisfied.

To determine the value of Λ (or equivalently a relation between ν_0 and κ_0) at which the stability bound shifts from (4.61) to (4.62) we substitute (4.62) into (4.60), yielding

$$\mathcal{L} > 0 \iff \Lambda < 4, \text{ or equivalently, } 2\kappa_0 > \nu_0^2. \tag{4.63}$$

Hence, provided $\Lambda < 4$, then the critical diffusion satisfies $2\kappa_0 > \nu_0^2$ and the relevant stability bound is given by equation (4.62). Otherwise (i.e., $\Lambda > 4$), stability is determined by the hydrodynamic bound (4.61). Note that if either of the stability bounds are satisfied (when relevant), then the system is only stable to steady instabilities (i.e., instabilities may still occur with a complex growth rate).

Now, (4.59) is a quintic in S and thus has some expression, by the Routh-Hurwitz theorem (Hurwitz, 1895; Routh, 1877), for marginal oscillatory instability. Unfortunately, the expression is extremely complex and cannot be easily derived or optimised over A and $\mathcal{L}$, and thus an analytical result of the oscillatory stability boundary can not be determined. However, the hydrodynamic condition (4.29) remains valid when $\Lambda > 2$ since the most unstable mode on the boundary is hydrodynamic. Hence, for $4 > \Lambda > 2$, equation (4.60) implies the use of (4.62) for which we obtain the necessary and sufficient condition for stability of all modes:

$$\nu_0^{\frac{1}{2}} \left(\left(\frac{16}{27} \right)^{\frac{1}{4}} (\Lambda - 1)^{\frac{3}{4}} - \nu_0^{\frac{1}{2}} \right) < \kappa_0 < \frac{8\nu_0^2}{\Lambda^2}. \tag{4.64}$$

If $\Lambda < 2$, the hydrodynamic oscillatory condition (4.34) becomes only a necessary condition for stability. Thus, equation (4.64) becomes a necessary condition for stability; however, the latter inequality ($\kappa_0 < 8\nu_0^2/\Lambda^2$) still remains necessary and sufficient. For $\Lambda > 4$, equation (4.60) implies the use of (4.61) for which we obtain the necessary and sufficient condition for stability of all modes:

$$\nu_0^{\frac{1}{2}} \left(\left(\frac{16}{27} \right)^{\frac{1}{4}} (\Lambda - 1)^{\frac{3}{4}} - \nu_0^{\frac{1}{2}} \right) < \kappa_0 < \frac{3\sqrt{3}\nu_0^2}{2(\Lambda - 1)^{\frac{3}{2}}}, \tag{4.65}$$

which is just the hydrodynamic condition (4.38). It may seem surprising that (4.65) is both necessary and sufficient in the MHD regime, however, the bound corresponds to the final modes that are stabilised, which are hydrodynamic for sufficiently large Λ. Note that we can once again derive a cubic in $\nu_0^{1/2}$ from (4.64); however, we can only make further analytical progress if $\nu_0 \ll 1$, which yields the same critical diffusion (4.40) as in the hydrodynamic case.

The Maximum Growth Rate as a Function of Aspect Ratio and Lehnert Number

Here we provide contour plots of the maximum growth rate S in $(\mathcal{L}, A)$-space in order to address what is the most unstable mode of a given astrophysical body (a single hyperbola) and what the nature of the mode is (e.g., magnetically modified inertial or double diffusive instability).

In figures 4.13 and 4.14 we therefore plot contours of the growth rate (calculated numerically from (4.59)) in $(\mathcal{L}, A)$-space, which are plotted with $\kappa_0 = 1$ for $\Lambda = 1.5$ and $\Lambda = 2.5$, respectively, and for $Pr = 0.01$ and $Pr = 0.5$.

We can see by comparing figure 4.13 to figure 4.8 at $\nu_0 = \kappa_0 = 0.05$ (so we are comparing figures with similar kinematic viscosity) that both the maximum growth rate increases as well as the size of the unstable domain for larger thermal conductivity (equivalently, smaller Pr). We can also see that for $Pr = 0.01$, instability can now occur for larger aspect ratios that are stable in the inviscid system, which is implied by the ideal necessary and sufficient condition for stability (3.25). This is similar to the double-diffusive GSF instability (Goldreich & Schubert, 1967; Fricke, 1968) and the triple-diffusive extension in Menou *et al.* (2004), where the stabilising effect of the pressure gradient (which increases for increasing A) is neutralised by thermal diffusion, allowing instability to occur at aspect ratios that would otherwise be stable in the absence of diffusion. We can see by increasing Pr and therefore the kinematic viscosity that the number of unstable modes decreases. Interestingly, the maximum growth rate occurs outside at a value of A that is stable in the ideal system for $Pr = 0.5$, indicating that the most unstable mode occurs at increasing values of A as Pr increases; the Lehnert number the generates the maximum growth rate is approximately constant and is close to the selected Lehnert number in the ideal regime (3.26). Note that an analogous plot for $\Lambda = 0.5$ shows the same effects, but has a much smaller range of unstable aspect ratios (and Lehnert numbers) and is stabilised for $Pr \approx 0.2$.

Figures 4.14 shows an analogous plot to figure 4.13 for $\Lambda = 2.5$, where inertial effects are more prominent. Indeed, we see that for $Pr = 0.01$, the maximum growth rate occurs on the hydrodynamic axis. However, as Pr increases, the most unstable mode is generated at an increasing Lehnert number. This is due to kinematic viscosity reducing the growth rate of the hydrodynamic inertial modes such that the magnetic growth rates become larger in comparison. We see that as Pr increases, $\mathcal{L}$ approaches the value which generates the maximum growth rate in the ideal regime (3.26). We also observe many of the effects described previously for figure 4.13.

The Maximum Growth Rate as a Function of Diffusivities

In figure 4.15, we provide contour plots of the maximum growth rate S and its corresponding imaginary part in (ν_0, κ_0)-space for $\Lambda = 0.5$, $\Lambda = 1.5$ and $\Lambda = 2.5$. We determine the growth rate via (4.59) for each $A, \mathcal{L}, \nu_0$ and κ_0 at fixed Λ. Then, for each ν_0 and κ_0, we select the values of A and $\mathcal{L}$ for which the growth rate is maximised and plot the maximum growth rate in (ν_0, κ_0)-space for the chosen Λ. Again, we note that the maximisation of the growth rate is one of the vertical wavenumber (via the aspect A) and the quantity kv_A (via the Lehnert number $\mathcal{L}$); the latter allows us to infer an optimal magnetic field strength as k is already chosen (via A). We note that the oscillatory hydrodynamic bound (4.34) is indeed only a necessary condition for stability for $\Lambda = 0.5$ and $\Lambda = 1.5$, while it is necessary and sufficient for $\Lambda = 2.5$.
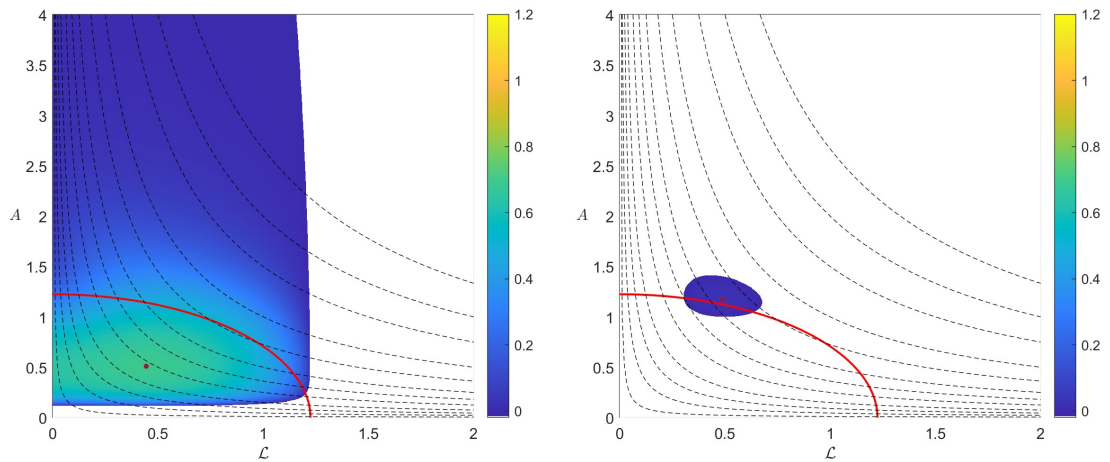
Figure 4.13: $Pr \neq 1$, $Pm = 1$: Growth rate in the $(\mathcal{L}, A)$-space with $\kappa_0 = 1$ and $\Lambda = 1.5$ for $Pr = 0.01$ (left) and $Pr = 0.5$ (right). The red line is the ideal necessary and sufficient boundary (3.25). The dashed black lines represent hyperbolae $A\mathcal{L} = C$, where C incrementally doubles from $C = 0.025$ to $C = 3.2$. The red dot represents the location of the most unstable mode.
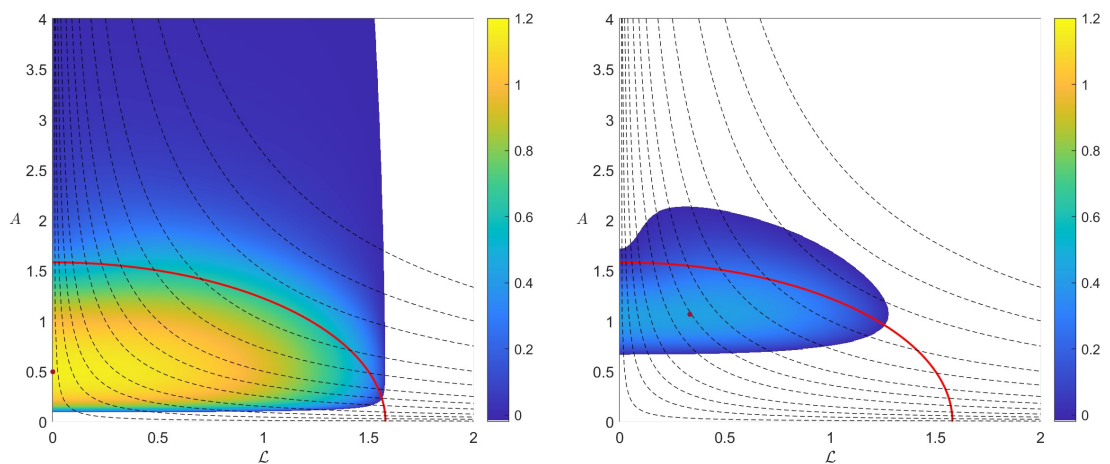
Figure 4.14: $Pr \neq 1$, $Pm = 1$: The maximum growth rate in $(\mathcal{L}, A)$-space with $\kappa_0 = 1$ and $\Lambda = 2.5$ for $Pr = 0.01$ (left) and $Pr = 0.5$ (right). The red line is the ideal necessary and sufficient boundary (3.25). The dashed black lines represent hyperbolae $A\mathcal{L} = C$, where C incrementally doubles from $C = 0.025$ to $C = 3.2$. The red dot represents the location of the most unstable mode.
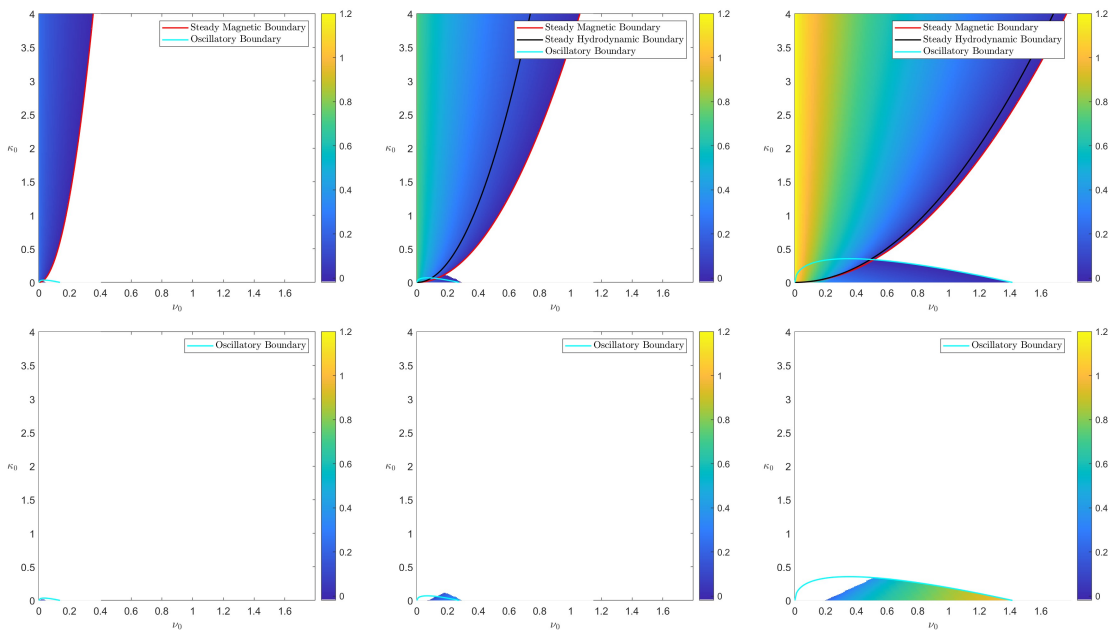
Figure 4.15: $Pr \neq 1$, $Pm = 1$: The maximum growth rate S and corresponding imaginary part (plotted below) in (ν_0, κ_0)-space with $\Lambda = 0.5$ (left), $\Lambda = 1.5$ (centre) and $\Lambda = 2.5$ (right). The black oscillatory stability boundary is described by equation (4.29). The red stability boundary is described by equation (4.62). Note that since $\Lambda < 4$, the use of the hydrodynamic boundary (4.61) is not necessary.

Immediately one can notice that the instability domain is extended when compared to the hydrodynamic regime since (4.29) is contained within the bound (4.62). This implies purely magnetic instabilities exist once (4.29) is surpassed; thus, magnetic field allows modes to remain unstable for larger ν_0 in comparison to the hydrodynamic case. We note the discrepancy between (4.29) and (4.62) decreases as we increase Λ, which is expected since (4.60) implies (4.29) replaces (4.62) at $\Lambda = 4$ as the necessary and sufficient steady stability bound.

It is clear that ν_0 always decreases the growth rate, while the behaviour of increasing κ_0 is more complex. If the system is unstable to oscillatory instabilities (where (4.15) exhibits complex growth rates), then increasing thermal diffusion decreases the growth rate until the system is stable or steady instabilities are induced. Oscillatory instabilities can occur only for sufficiently weak thermal diffusion where buoyancy effects are still felt (i.e., increasing the magnitude of thermal diffusivity dampens buoyancy effects). Increasing κ_0 further in the stable region eventually also induces steady instabilities. Thus, once the system exhibits unstable steady modes from sufficiently large κ_0, then increasing κ_0 further always increases the growth rate to the maximum of the inviscid hydrodynamic regime $\Lambda/2$. The maximum growth rates occur in the limit $Pr \ll 1$, which was the case in the hydrodynamic regime, as shown in figure 4.4. Thus, in stellar and planetary atmospheres, where typically $Pr \ll 1$, instabilities, if they occur, will be steady. In general, the system is unstable for sufficiently large κ_0 at any value of ν_0; also, stability is possible at any value of κ_0 given sufficiently large ν_0.

It is natural to plot the corresponding aspect ratio A and Lehnert number $\mathcal{L}$, $A_{\max}$ and $\mathcal{L}_{\max}$ say, in $(\nu_0 = \eta_0, \kappa_0)$-space that generate the maximum growth rate $S_{\max}$ found in figure 4.15. Thus, we plot the value of $A_{\max}$ and $\mathcal{L}_{\max}$ in (ν_0, κ_0)-space in figure 4.16 for $\Lambda = 0.5$, $\Lambda = 1.5$ and $\Lambda = 2.5$. The red line represents the steady magnetic stability bound (4.62), while the dashed red line represents the steady hydrodynamic stability bound (4.29). The black line represents the hydrodynamic oscillatory stability bound (4.34). Note that we will first focus only on the steady instabilities.

First, we comment on the discrepancy between the steady bounds (4.29) and (4.62). Clearly, as previously mentioned, purely magnetic instabilities occur once (4.29) is surpassed, where for $\Lambda = 0.5$ this is trivial as no hydrodynamic instabilities exist. However, for $\Lambda = 1.5$ and $\Lambda = 2.5$, the plots of the optimal Lehnert number imply that increasing magnetic field strength also increases the growth rate of hydrodynamically unstable modes since $\mathcal{L} \neq 0$ before (4.29) is surpassed. Thus, we obtain magnetic modified inertial instabilities in the diffusive regime similar to those described in the ideal dynamical balance (3.50) and represented in figure 3.13.

Figure 4.16 shows, for all Λ, that increasing ν_0 or κ_0 increases the value of $A_{\max}$ until stabilisation. Thus, the vertical wavenumber decreases with increasing ν_0 or κ_0. We note that modes with $Pr \ll 1$ have the smallest aspect ratio; this is of interest as Pr is typically small in planetary atmospheres. The maximum growth rate of the hydrodynamic regime also occurs in the large vertical wavenumber (i.e., small aspect ratio) limit (e.g., Griffiths, 2008a).

For $\Lambda = 0.5$ and $\Lambda = 1.5$, figure 4.16 also suggests that the optimal Lehnert number $\mathcal{L}$ that maximises the growth rate is again approximately constant over the domain, as seen previously in figure 4.12. Thus, as ν_0 or κ_0 increases, the vertical wavenumber of the most unstable mode decreases, while increasing magnetic field is required so that the Lehnert number remains constant.

For $\Lambda = 2.5$ the Lehnert number increases as ν_0 increases and decreases as κ_0 increases (note that we restrict $\mathcal{L}$ to be no less than 10^{-4} so that feasible vertical wavenumbers are chosen to fit planetary atmospheres). The Lehnert number decreases with increasing κ_0 as increasing thermal conductivity excites inertial modes until they obtain the maximum growth rate of the system $\Lambda/2$ so that magnetic field can only act to reduce the growth rate; thus, the modes choose a small Lehnert number. Inertial modes with large vertical wavenumber are stabilised as ν_0 increases, and the most unstable modes become magnetic. Since this occurs while the aspect ratio increases, it implies that the optimal magnetic field strength increases at a faster rate than for $\Lambda = 0.5$ or $\Lambda = 1.5$.

For $\Lambda = 0.5, 1.5$ and 2.5 we see that $\mathcal{L}_{\max}$ either remains constant or increases (for $\Lambda = 2.5$) with increasing ν_0. This is somewhat surprising since $\nu_0 = \eta_0$, where increasing η_0 would stabilise magnetic modes. For $\Lambda = 0.5$ and 1.5 this can be explained since the most unstable modes are magnetic with $\nu_0 = 0$, and thus, increasing $\nu_0 = \eta_0$ reduces the growth rate of the hydrodynamic and magnetohydrodynamic modes such that the most unstable mode occurs at the same Lehnert number. Interestingly, for $\Lambda = 0.5$ and 1.5, these values approximately coincide with the optimal Lehnert number of the ideal system (see equation 3.26). For $\Lambda = 2.5$ the most unstable mode
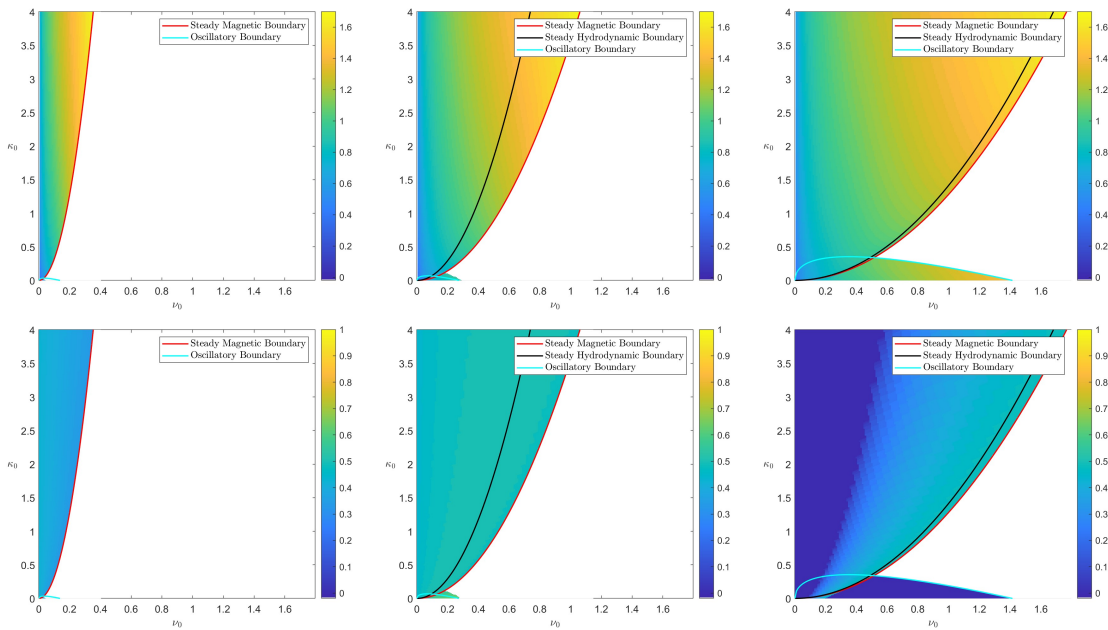
Figure 4.16: $Pr \neq 1$, $Pm = 1$: The value of $A_{\max}$ (top) and $\mathcal{L}_{\max}$ (bottom) in (ν_0, κ_0)-space for $\Lambda = 0.5$ (left), $\Lambda = 1.5$ (centre) and $\Lambda = 2.5$ (right). The black oscillatory stability boundary is described by equation (4.29). The red stability boundary is described by equation (4.62). Note that since $\Lambda < 4$, the hydrodynamic boundary (4.61) is not relevant.

is hydrodynamic with $\nu_0 = 0$, where upon increasing ν_0 to some critical value $\mathcal{L}_{\max}$ increases from zero. This implies that increasing $\nu_0 = \eta_0$ reduces the growth rate of the hydrodynamic and magnetohydrodynamic modes such that the kinematic viscosity reduces the growth rate of the hydrodynamic modes more significantly than magnetic diffusivity reduces the growth rate of the magnetohydrodynamic modes.

Clearly, as in the hydrodynamic case (see figure 4.5) we find that instability may occur within the stable regime of the inviscid system. That is, instability may now occur for $A^2 > \Lambda$. For example, at $\kappa_0 = 4$ and $\nu_0 = 1.6$ with $\Lambda = 2.5$, $A_{\max} \approx 1.7$ so that $A^2 \approx 2.9 > 2.5 = \Lambda$. This is consistent with (4.49) which predicts that as the strength of thermal conductivity increases at fixed ν_0, then larger A is required to stabilise the system. As for the hydrodynamic system, we may draw comparisons with the GSF instability (Fricke, 1968; Goldreich & Schubert, 1967) and the magnetic extension of Menou *et al.* (2004). For $\Lambda = 0.5$ and $\Lambda = 1.5$ the modes in this regime can be purely magnetic or magnetically modified inertial instabilities. In either case, we find that the modes that are stable in the absence of diffusion become unstable owing to thermal diffusion dampening the effects of buoyancy. Thus, instabilities can occur for $A^2 > \Lambda$. For $\Lambda = 2.5$ there are both hydrodynamic modes, where thermal diffusion enables instability (as previously discussed in section 4.3.2), and magnetically modified inertial instabilities.

4.4.4 $Pr = 1, Pm \neq 1$

We now extend the previous section by considering the case where $Pr = 1$ ($\nu_0 = \kappa_0$) while $Pm \neq 1$ ($\nu_0 \neq \eta_0$).

Formulation and Stability Bounds

Writing κ_0 as ν_0 allow us to rewrite the equation for the growth rate (4.5) as follows:

$$A^2 \frac{S + \eta_0/A^2}{S + \nu_0/A^2} \left(\left(S + \frac{\nu_0}{A^2} \right) \left(S + \frac{\eta_0}{A^2} \right) + \mathcal{L}^2 \right) - \mathcal{L}^2 \Lambda$$
$$+ (1 - \Lambda) \left(S + \frac{\eta_0}{A^2} \right)^2 + \left(\left(S + \frac{\nu_0}{A^2} \right) \left(S + \frac{\eta_0}{A^2} \right) + \mathcal{L}^2 \right)^2 = 0. \quad (4.66)$$

Once again we can set $S = 0$ in equation (4.66), yielding the criterion for marginal steady instability in terms $A, \mathcal{L}, \nu_0$ and κ_0. However, since we are maximising the growth rate over A and $\mathcal{L}$, we can use the previously derived stability criterion (4.50). However, this criterion is valid only if (4.49) predicts $\mathcal{L} > 0$; otherwise the hydrodynamic bound (4.34) must be used. Hence, after writing κ_0 as ν_0, we rewrite equation (4.49) as follows:

$$\mathcal{L}^2 = \frac{\Lambda}{4} - \frac{4\eta_0^3}{\Lambda^2 \nu_0}, \quad (4.67)$$

implying that η_0 cannot become too large compared with $\nu_0 = \kappa_0$. Physically, this is reasonable, as we expect large η_0 will suppress magnetic instabilities. Equation (4.67) therefore predicts that the magnetic stability bound (4.50) is valid if $\Lambda^3 \nu_0 > 16\eta_0^3$.

In the cases where (4.67) does not predict a positive value for $\mathcal{L}$, we have the steady hydrodynamic stability bound (4.34) which reduces to the critical diffusion:

$$\nu_0 = \frac{2(\Lambda - 1)^{3/2}}{3\sqrt{3}}. \quad (4.68)$$

In the cases where (4.67) predicts a positive value for $\mathcal{L}$, we have the steady magnetic stability bound (4.50), which we rewrite as a quadratic in ν_0 :

$$\nu_0^2 - \frac{64\eta_0^3}{\Lambda^3} \nu_0 + \frac{64\eta_0^4}{\Lambda^4}(\Lambda - 1) < 0, \quad (4.69)$$

with stability if the inequality is satisfied. Solving (4.69) for ν_0 gives the following condition for steady stability:

$$\frac{32\eta_0^3}{\Lambda^3} \left(1 - \sqrt{1 - \frac{\Lambda^2}{16\eta_0^2}(\Lambda - 1)} \right) < \nu_0 < \frac{32\eta_0^3}{\Lambda^3} \left(1 + \sqrt{1 - \frac{\Lambda^2}{16\eta_0^2}(\Lambda - 1)} \right), \quad (4.70)$$

where if $16\eta_0^2 < \Lambda^2(\Lambda - 1)$, equation (4.69) cannot be satisfied so that steady instability is guaranteed. Conditions (4.68) and (4.70) apply only to steady instabilities (i.e., $S \equiv 0$) and therefore oscillatory instabilities may exist while (4.68) and (4.70) are satisfied. Note that equations (4.68) and (4.70) are not necessarily necessary and sufficient conditions for all steady modes and only

applies to one root of (4.66) and thus, there may be other steady modes with $S > 0$. We will address this using contours of the growth rate in (ν_0, η_0)-space.

We now determine a relation between η_0 and Λ at which the stability bound shifts from (4.68) to (4.70). We substitute (4.70) into (4.68) which trivially yields $\mathcal{L} > 0$ if we take the positive sign of the square root; if we instead take the negative sign, then $\mathcal{L} > 0$ if and only if

$$\eta_0^2 < \frac{\Lambda^2(1 - \Lambda)}{7}. \tag{4.71}$$

Hence, the inequality with the positive square root in (4.70) is always valid regardless of the magnitude of ν_0, η_0 and Λ. However, the stability bound with negative square root in (4.70) is only valid if $\eta_0^2 < \Lambda^2(1 - \Lambda)/7$, otherwise the hydrodynamic stability bound (4.68) is used instead. Note that if either of the stability bounds are satisfied (when relevant), then the system is only stable to steady instabilities (i.e., instabilities may still occur with a complex growth rate).

The Maximum Growth Rate as a Function of Aspect Ratio and Lehnert Number

Once again we provide contour plots of the maximum growth rate S in $(\mathcal{L}, A)$-space in order to address what is the most unstable mode of a given astrophysical body (a single hyperbola) and what the nature of the mode is.

In figure 4.17 we therefore contour the growth rate (calculated numerically from (4.66)) in $(\mathcal{L}, A)$-space for $\Lambda = 1.5$. Note that in section 3.3.4 (using the parameters in table 2.1) we estimated that $C = A\mathcal{L}$ ranges from $O(10^{-4})$ to $O(10^{-2})$ in the upper atmospheres of Jupiter and Hot Jupiters, while ranging from $O(1)$ to $O(10^2)$ in the solar tachocline.

These plots illustrate two regimes, the left hand plot contains inertial and magnetically modified inertial instabilities, while the right hand plot contains purely magnetic instabilities. Together, they indicate that increasing the magnitude of ν_0 with κ_0 ($Pr = 1$) leads to the stabilisation of hydrodynamic modes, noting that we might expect thermal diffusion to allow hydrodynamic instabilities to still occur. Indeed, in the right hand plot, the hydrodynamic modes have been stabilised; however, owing to the distinct magnitudes of kinematic viscosity (and thermal conductivity since $\nu_0 = \kappa_0$) and magnetic diffusion, magnetic instabilities persist. The magnetic instabilities occur for values of A outside of the ideal unstable domain, implying that thermal diffusion plays a significant role in nullifying the stabilising role of the pressure gradient. Interestingly, the maximum growth rate now occurs outside of the ideal unstable domain. We also note that for all values of ν_0 and η_0 that allow instability to occur for $\Lambda = 0.5$ we obtain an analogous plot to that seen in the right hand panel; the only difference being that the unstable domain is much smaller owing to the smaller Rossby number.

In figure 4.18 we plot two contours of the growth rate in $(\mathcal{L}, A)$-space for $\Lambda = 2.5$. Generally, these plots are very similar to those seen in figure 4.17 for $\Lambda = 1.5$; however, we see that the growth rate of the hydrodynamic modes in the left hand plot is significantly larger. In both cases, the size of the domain containing unstable modes has increased; however, for $\nu_0 = 0.2$ and $\eta_0 = 2.0$, the unstable domain is completely altered owing to the oscillatory instabilities that can
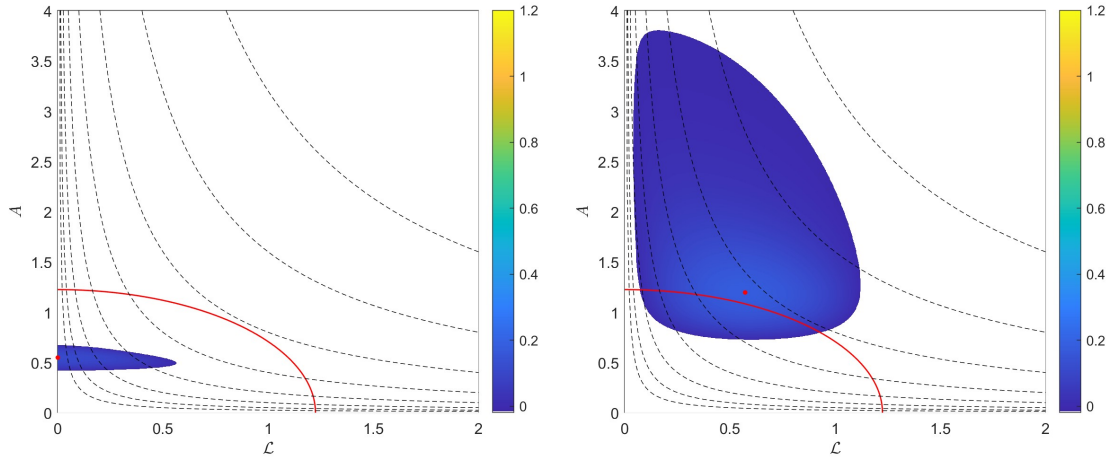
Figure 4.17: $Pr = 1$, $Pm \neq 1$: Growth rate in the $(\mathcal{L}, A)$-space for $\Lambda = 1.5$, with $\nu_0 = 0.1$ and $\eta_0 = 1.0$ ($Pm = 0.1$) in the left panel and with $\nu_0 = 1$ and $\eta_0 = 0.1$ ($Pm = 10$) in the right panel. The red line is the ideal necessary and sufficient boundary (3.25). The dashed black lines represent hyperbolae $A\mathcal{L} = C$, where C incrementally doubles from $C = 0.025$ to $C = 3.2$. The red dot indicates the location of the most unstable mode.

now occur for $\Lambda = 2.5$. To illustrate which of the modes are oscillatory, we provide figure 4.19 which contours the frequency (noting each oscillatory mode has a complex conjugate) in $(\mathcal{L}, A)$-space for $\Lambda = 2.5$ with $\nu_0 = 0.2$ and $\eta_0 = 2.0$.

The Maximum Growth Rate as a Function of Diffusivities

Once again we provide contour plots of the maximum growth rate S and the corresponding values of A and $\mathcal{L}$ it occurs at in (ν_0, η_0)-space for $\Lambda = 0.5, 1.5$ and $\Lambda = 2.5$ in figure 4.15 and figure 4.21, respectively.

The stability bounds clearly bound the region of instability accurately. The hydrodynamic bound (4.61) is clearly valid for $\eta_0^2 > \Lambda^2(1 - \Lambda)/7$, where only hydrodynamic instabilities are present due to the magnitude of the magnetic diffusion. The bounds of (4.70) are also accurate for $\eta_0^2 > \Lambda^2(1 - \Lambda)/7$. We also find that some oscillatory instabilities exist within the domain. However, they are confined to a small region in the corner of the unstable domain. We identify their existence for $\Lambda = 0.5$ and $\Lambda = 1.5$ only.

First, we see that the largest growth rates occur when $Pm \ll 1$. For $\Lambda < 1$, increasing the magnetic diffusivity at any ν_0 decreases the growth rate until stabilisation. This is expected since only unstable magnetic modes can occur for $\Lambda < 1$. For $\Lambda > 1$, increasing the magnetic diffusivity at fixed ν_0 either stabilises the system if the magnitude of $\nu_0 = \kappa_0$ is beyond the critical diffusion $\nu_0 = \kappa_0 = 2(\Lambda-1)^{3/2}/3\sqrt{3}$ of the hydrodynamic bound (4.61), or has no effect on the growth rate if $\nu_0 < \kappa_0 = 2(\Lambda-1)^{3/2}/3\sqrt{3}$ (for sufficiently large η_0). Indeed, in the latter case, this is because all magnetic modes will have been stabilised such that the most unstable mode is hydrodynamic, so the magnitude of magnetic diffusivity is inconsequential. If we increase the magnetic diffusivity when $\nu_0 > \kappa_0 = 2(\Lambda - 1)^{3/2}/3\sqrt{3} = \nu_c$, the growth rate decreases until the system is stabilised.
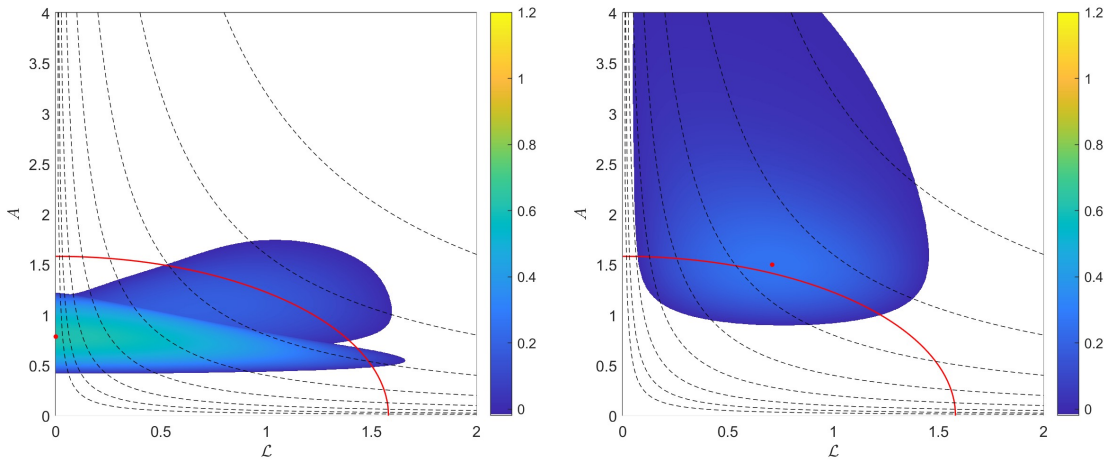
Figure 4.18: $Pr = 1$, $Pm \neq 1$: Growth rate in the $(\mathcal{L}, A)$-space for $\Lambda = 2.5$, with $\nu_0 = 0.2$ and $\eta_0 = 2.0$ ($Pm = 0.1$) in the left panel and with $\nu_0 = 2$ and $\eta_0 = 0.2$ ($Pm = 10$) in the right panel. The red line is the ideal necessary and sufficient boundary (3.25). The dashed black lines represent hyperbolae $A\mathcal{L} = C$, where C incrementally doubles from $C = 0.025$ to $C = 3.2$. The red dot indicates the location of the most unstable mode.
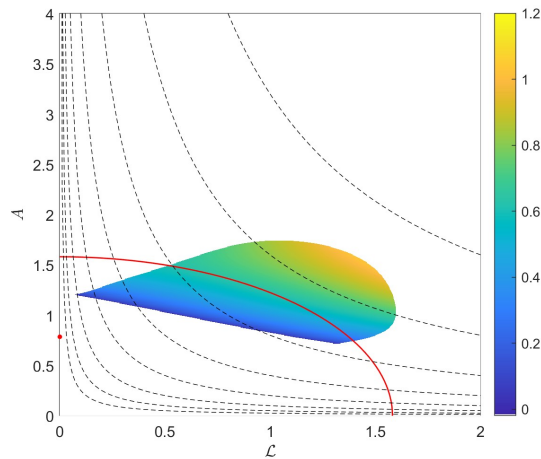
Figure 4.19: $Pr = 1$, $Pm \neq 1$: Frequency of the unstable modes in $(\mathcal{L}, A)$-space for $\Lambda = 2.5$, with $\nu_0 = 0.2$ and $\eta_0 = 2.0$. The red line is the ideal necessary and sufficient boundary (3.25). The dashed black lines represent hyperbolae $A\mathcal{L} = C$, where C incrementally doubles from $C = 0.025$ to $C = 3.2$. The red dot indicates the location of the most unstable mode.
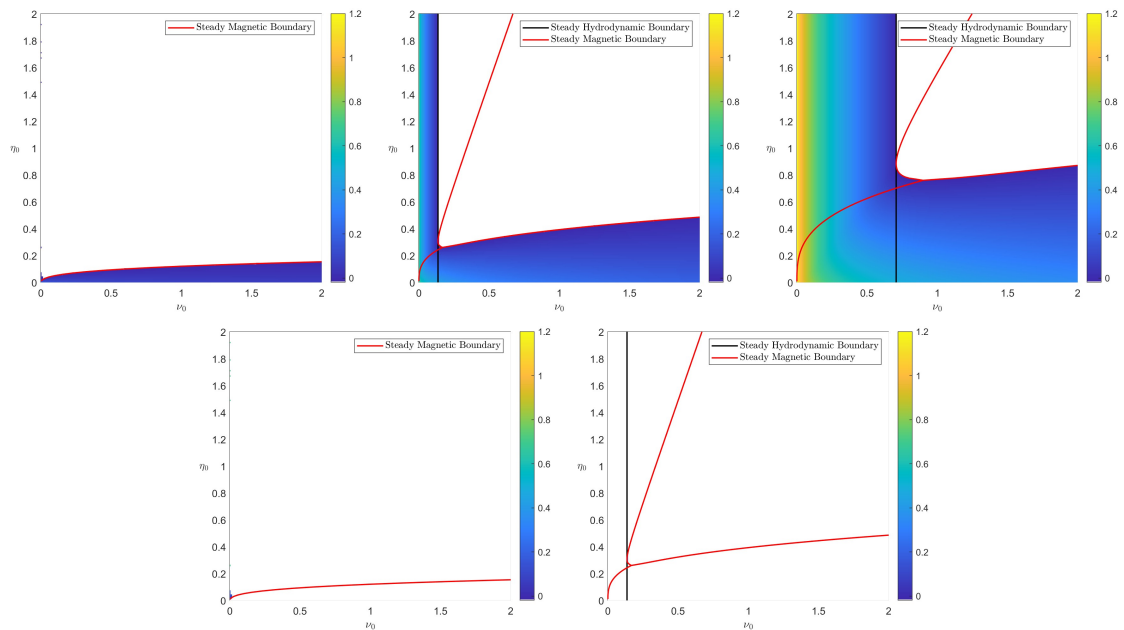
Figure 4.20: $Pr = 1$, $Pm \neq 1$: The maximum growth rate S with corresponding complex part (below) in (ν_0, η_0)-space with $\Lambda = 0.5$ (left), $\Lambda = 1.5$ (centre) and $\Lambda = 2.5$ (right). The black line is the hydrodynamic stability boundary (4.68). The red stability boundaries are equation (4.70). There are no oscillatory modes for $\Lambda = 0.5$. Note that for $\Lambda = 1.5$ and $\Lambda = 2.5$ the oscillatory instabilities are confined to a small region embedded within the red and black bounds.

This implies that for $\nu_0 > \nu_c$ there are no hydrodynamic modes that persist, since the system is stable once the magnetic modes have been stabilised by sufficiently large magnetic diffusivity.

Varying $\nu_0 = \kappa_0$ at fixed η_0 is somewhat more complex than varying η_0 at fixed ν_0. For $\Lambda < 1$, increasing ν_0 from the $\nu_0 = 0$ axis ensures stability given sufficiently large η_0. However, for any value of η_0 the system becomes unstable for sufficiently large ν_0. This can be seen by taking the large η_0 limit of (4.70), yielding $\nu_0 < 64\eta_0^3/\Lambda^3$ for stability. Hence, even for large η_0, the system is unstable provided $\nu_0 > 64\eta_0^3/\Lambda^3$. This behaviour persists for $\Lambda > 1$. However, since the system is now hydrodynamically unstable, there is instability as we increase ν_0 from the $\nu_0 = 0$ axis. Increasing ν_0 then decreases the growth rate until stabilisation at the hydrodynamic bound (4.61) for sufficiently large η_0. The system is then stable until $\nu_0 > 64\eta_0^3/\Lambda^3$, as found for $\Lambda < 1$. However, for $\Lambda > 1$ and sufficiently small magnetic diffusivity, increasing the parameter ν_0 never stabilises the system. The growth rate in the large ν_0 limit remains small due to the competing effects of thermal diffusion and kinematic viscosity on the magnetic modes.

We now discuss figure 4.21 which illustrates the corresponding aspect ratio A and Lehnert number $\mathcal{L}$, $A_{\max}$ and $\mathcal{L}_{\max}$ say, in $(\nu_0 = \kappa_0, \eta_0)$-space that generate the maximum growth rate $S_{\max}$ found in figure 4.20.

First, we comment on the modes close to the hydrodynamic steady bound (4.61) and the magnetohydrodynamic steady bound (4.62). Clearly, modes that are stabilised once the hydrodynamic stability bound (4.61) is surpassed are purely magnetic as the Lehnert number on the stability

boundary (4.62) is non-zero, while the Lehnert number is zero if the modes are stabilised along (4.61).

Figure 4.21 shows, for all Λ, that increasing ν_0 increases $A_{\max}$ indefinitely unless the system is stabilised. However, as we have already discussed, given that ν_0 stabilises the system for a fixed η_0, instability is obtained once again provided ν_0 is sufficiently large (where $A_{\max}$ then increases once again with increasing ν_0). This occurs since large thermal diffusion re-excites the stabilised magnetic modes even in the presence of strong kinematic viscosity. However, as seen in figure 4.20, the growth rate remains small. At fixed ν_0 the aspect ratio increases if the mode is magnetic (see the plot of the Lehnert number) and remains constant if the most unstable mode is hydrodynamic. This is to be expected since if the most unstable mode is hydrodynamic, then magnetic diffusivity of any magnitude will not affect the mode. We can clearly see this for sufficiently large η_0 to the left of the hydrodynamic steady bound (4.61).

For $\Lambda = 0.5$, $\mathcal{L}_{\max}$ remains approximately equal to 0.4, where the ideal maximum growth rate occurs at 0.433. However, for the magnetic instabilities that occur when $\Lambda = 1.5$ and $\Lambda = 2.5$, the Lehnert number approaches approximately 0.5 and 0.7, respectively. This implies that the magnetic field strength that generates the maximum growth rate increases with increasing ν_0 say, since the aspect ratio increases with increasing ν_0. However, interestingly, the Lehnert number approaches some fixed value as we increase ν_0 at fixed η_0 (provided the modes are magnetic). We also see for $\Lambda = 1.5$ and $\Lambda = 2.5$, regions in (ν_0, η_0)-space where the maximum growth rate is hydrodynamic. These regions occur when the kinematic viscosity is sufficiently small and the magnetic diffusivity is large. Note that we restrict $\mathcal{L}$ to be no less than 10^{-4} so that feasible vertical wavenumbers are chosen to fit stellar planetary atmospheres (see vertical lengthscale of the astrophysical bodies in table 2.1).

The magnetic instability in the large $\nu_0 = \kappa_0$ limit, which is illustrated in figures 4.20 and 4.21, requires varying magnitudes of thermal diffusion and magnetic diffusivity to operate (see section 4.4.2 with $Pr = Pm = 1$). In contrast to the double-diffusive instability of the previous section (which required $Pr \neq 1$ and was linked to the GSF instability), we require magnetic field for the instability to operate since imposing $\mathcal{L} = 0$ yields the hydrodynamic system of section 4.3.1, which is stable for $\nu_0 > 2(\Lambda - 1)^{3/2}/3^{3/2}$. Note that, as for the GSF instability, thermal diffusion enables modes with large aspect ratios that would be always stable in the ideal system to become unstable.

The Limit of Strong Kinematic Viscosity and Thermal Diffusion

It is of interest to investigate the magnetic instability in the large $\nu_0 = \kappa_0$ limit ($Pr = 1$) depicted in figures 4.20 and 4.21. Thus, we suppose $\nu_0 \gg 1$, $\eta_0 = O(1)$, $\mathcal{L} = O(1)$ and $A = O(\nu_0^{1/3})$ (where the latter has been numerically determined) in equation (4.66) which reduces to a quadratic as all occurrences of $(S + \nu_0/A^2)$ reduce to ν_0/A^2 (since $S \ll \nu_0/A^2$), yielding the following
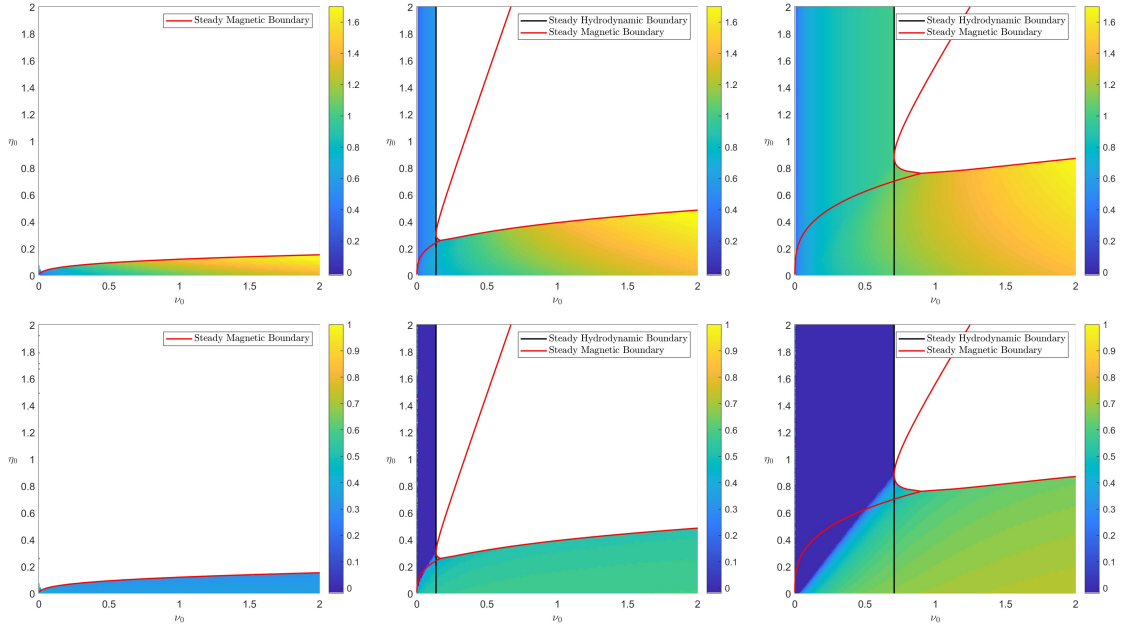
Figure 4.21: $Pr = 1$, $Pm \neq 1$: The value of $A_{\max}$ (top) and $\mathcal{L}_{\max}$ (bottom) in (ν_0, η_0)-space with $\Lambda = 0.5$ (left), $\Lambda = 1.5$ (centre) and $\Lambda = 2.5$ (right). The black line is the hydrodynamic stability boundary (4.68). The red stability boundaries are equation (4.70).

quadratic for $(S + \eta_0/A^2)$:

$$\left(\frac{\nu_0^2}{A^4} + A^2\right)\left(S + \frac{\eta_0}{A^2}\right)^2 + A\mathcal{L}^2\left(\frac{A^3}{\nu_0} + \frac{2\nu_0}{A^3}\right)\left(S + \frac{\eta_0}{A^2}\right) + \mathcal{L}^2(\mathcal{L}^2 - \Lambda) = 0, \qquad (4.72)$$

which can be solved to give

$$S = \frac{A^2\mathcal{L}^2}{2\nu_0}\frac{A^6 + 2\nu_0^2}{A^6 + \nu_0^2}\left(-1 + \sqrt{1 + \frac{4(A^6 + \nu_0^2)\nu_0^2}{(A^6 + 2\nu_0^2)^2\mathcal{L}^2}(\Lambda - \mathcal{L}^2)}\right) - \frac{\eta_0}{A^2}, \qquad (4.73)$$

where we have taken the positive root so that instability is possible. Equation (4.73) therefore implies that $S = O(1/A)$. On inspection of figure 4.21, it might be thought that analytical progress could be made in equation (4.73) by assuming $\mathcal{L}^2 \ll \Lambda$, so that the right hand term inside the square-root is large. However, we numerically determine that $\mathcal{L} = \sqrt{\Lambda}/2 + O(\nu_0^{-1/3})$ in the large ν_0 limit so that the right hand term within the square-root is order unity.

To illustrate the accuracy of the large ν_0 expansion, we plot (4.73) with the exact growth rate (numerically determined from equation (4.66)) against ν_0 for $\Lambda = 2.5, 1.5$ and 0.5 in figure 4.22 with $\eta_0 = 0.05$. Indeed, the expansion is accurate for even relatively small ν_0. We also find that as the Rossby number Λ increases, we require larger ν_0 until the expansion (4.73) accurately describes the growth rate. Note that in all cases, $\mathcal{L}_{\max} \approx \sqrt{\Lambda}/2$.

125
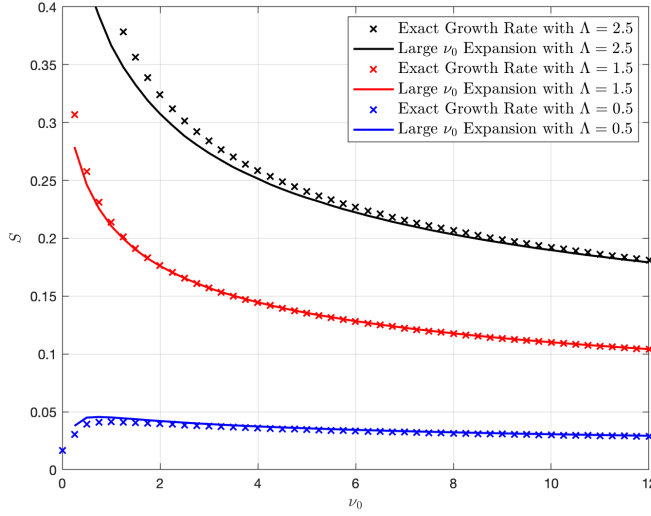
Figure 4.22: $Pr = 1$, $Pm \neq 1$: The large ν_0 expansion (4.73) plotted with the exact solution against ν_0 for $\Lambda = 0.5, 1.5$ and 2.5 with $\eta_0 = 0.05$.

4.4.5 $Pr = Pm \neq 1$

Formulation and Stability Bounds

We now consider the case where $Pr = Pm \neq 1$, and thus by writing κ_0 as η_0, we rewrite equation (4.5):

$$A^2 \left(\left(S + \frac{\nu_0}{A^2} \right) \left(S + \frac{\eta_0}{A^2} \right) + \mathcal{L}^2 \right) - \mathcal{L}^2 \Lambda$$
$$+ (1 - \Lambda) \left(S + \frac{\eta_0}{A^2} \right)^2 + \left(\left(S + \frac{\nu_0}{A^2} \right) \left(S + \frac{\eta_0}{A^2} \right) + \mathcal{L}^2 \right)^2 = 0, \quad (4.74)$$

which has now been reduced to a quartic in S. Thus, we either have four real roots for the growth rate, two real roots and two complex roots or four complex roots.

We can set $S = 0$ in equation (4.74) yielding the criterion for marginal steady instability in terms $A, \mathcal{L}, \nu_0$ and η_0. However, since we are maximising the growth rate over A and $\mathcal{L}$ we can therefore use the previously derived stability criterion (4.50). However, this criterion is only valid if (4.49) predicts $\mathcal{L} > 0$, otherwise the hydrodynamic stability bound (4.34) must be used. Hence, after writing η_0 as ν_0, we may rewrite equation (4.49) as follows:

$$\mathcal{L}^2 = \frac{\Lambda}{4} - \frac{4\eta_0 \nu_0}{\Lambda^2}, \quad (4.75)$$

implying that η_0 or ν_0 cannot become too large. Physically, this is reasonable as we expect large η_0 will suppress magnetic instabilities and simultaneously excite inertial instabilities (since $\kappa_0 = \eta_0$). Equation (4.75) therefore predicts that the magnetic stability bound (4.50) is valid if $\Lambda^3 > 16\eta_0\nu_0$.

In the cases where (4.75) does not predict a positive value for $\mathcal{L}$, we have the hydrodynamic steady stability bound (4.34), which we rewrite for convenience here:

$$\eta_0 = \kappa_0 = \frac{3\sqrt{3}\nu_0^2}{2(\Lambda - 1)^{3/2}}. \quad (4.76)$$

126

In the cases where (4.75) predicts a positive value for $\mathcal{L}$, we have the necessary and sufficient steady stability condition (4.50) which we rewrite as follows:

$$\nu_0 > \frac{\Lambda^3}{64\eta_0} - \frac{1-\Lambda}{\Lambda}\eta_0. \tag{4.77}$$

Recall that the conditions (4.76) and (4.77) apply only to steady instabilities and only apply to one root of (4.74) so that other steady modes may exist $S > 0$. We will address this using contours of the growth rate in (ν_0, η_0)-space.

We now determine a relation between η_0 and Λ at which the stability bound shifts from (4.76) to (4.77). We substitute (4.77) into (4.76) yielding the condition

$$\mathcal{L} > 0 \iff \eta_0^2 > \frac{3\Lambda^4}{64(\Lambda-1)}, \quad \text{or equivalently,} \; \nu_0^2 > \frac{\Lambda^2(\Lambda-1)}{12}. \tag{4.78}$$

Hence, the steady magnetic stability condition (4.77) is valid only if $\eta_0^2 > 3\Lambda/64(\Lambda-1)$, otherwise the hydrodynamic stability bound (4.76) is used. Note that if either of the stability bounds are satisfied (when relevant), then the system is only stable to steady instabilities (i.e., instabilities may still occur with a complex growth rate).

The Maximum Growth Rate as a Function of Aspect Ratio and Lehnert Number

In figures 4.23 and 4.24 we contour the growth rate (calculated numerically from (4.74)) in $(\mathcal{L}, A)$-space for $\Lambda = 1.5$ and $\Lambda = 2.5$, respectively.

In figure 4.23, we again see two regimes; the left hand plot contains inertial and magnetically modified inertial instabilities, while the right hand plot contains purely magnetic instabilities. Interestingly, even with larger values of $\eta_0 = \kappa_0$ in the left hand plot, magnetically modified inertial instabilities still persist. Notably, inertial and magnetically modified instabilities occur for values of A outside of the ideal unstable domain, implying that thermal diffusion plays a significant role in nullifying the stabilising role of the pressure gradient. By comparing the two plots we can see that increasing the magnitude of ν_0 leads to the stabilisation of hydrodynamic modes. The right hand plot shows that magnetic instabilities may still persist with larger ν_0, provided η_0 is sufficiently small. We also note that for all values of ν_0 and κ_0 that allow instability to occur for $\Lambda = 0.5$, we obtain an analogous plot to that seen in the right hand panel, the only difference being that the unstable domain is much smaller owing to the smaller Rossby number.

In figure 4.24 we now have $\Lambda = 2.5$. The plots are very similar to those seen in figure 4.23 for $\Lambda = 1.5$; however, we see that the growth rate of the hydrodynamic modes in the left hand plot is significantly larger. In both cases, the size of the domain containing unstable modes has increased; however, for $\nu_0 = 1.0$ and $\kappa_0 = 0.01$, the unstable domain is completely altered owing to the oscillatory instabilities that can now occur for $\Lambda = 2.5$. To illustrate which of the modes are oscillatory, we provide figure 4.25 which contours the frequency (noting each oscillatory mode has a complex conjugate) in $(\mathcal{L}, A)$-space for $\Lambda = 2.5$ with $\nu_0 = 1.0$ and $\kappa_0 = 0.01$.
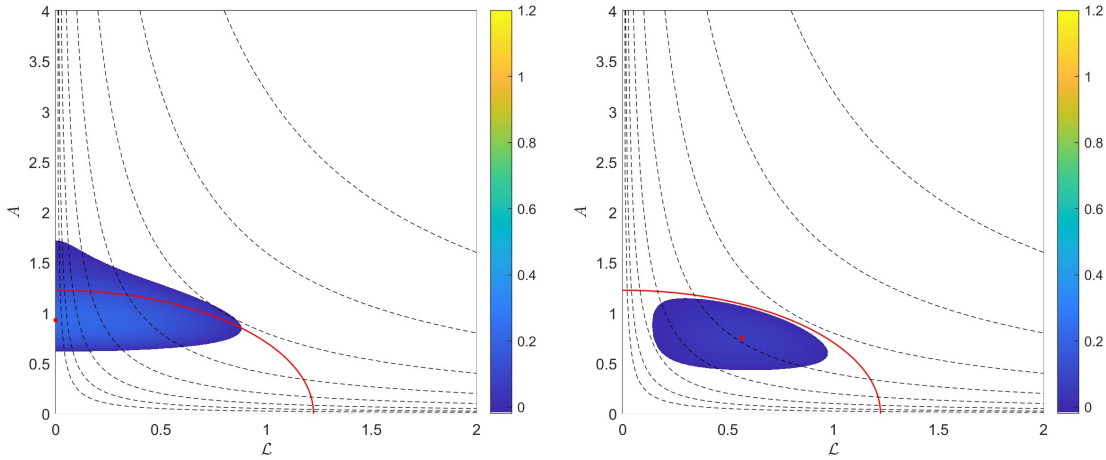
Figure 4.23: $Pr = Pm \neq 1$: Growth rate in the $(\mathcal{L}, A)$-space for $\Lambda = 1.5$, with $\nu_0 = 0.25$ and $\kappa_0 = 1.5$ ($Pr = Pm = 1/6$) in the left panel and with $\nu_0 = 1.0$ and $\kappa_0 = 0.01$ ($Pr = Pm = 100$) in the right panel. The red line is the ideal necessary and sufficient boundary (3.25). The dashed black lines represent hyperbolae $A\mathcal{L} = C$, where C incrementally doubles from $C = 0.025$ to $C = 3.2$. The red dot indicates the location of the most unstable mode.
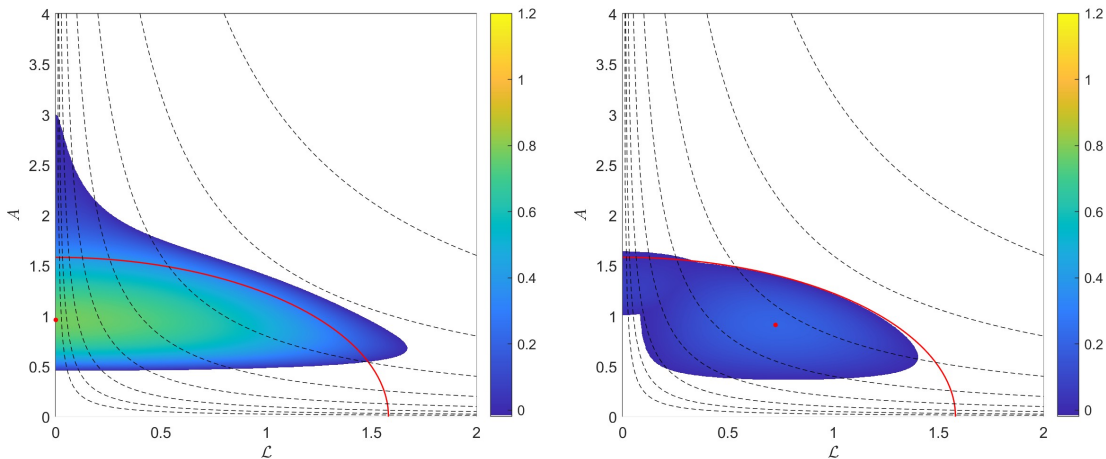
Figure 4.24: $Pr = Pm \neq 1$: Growth rate in the $(\mathcal{L}, A)$-space for $\Lambda = 2.5$, with $\nu_0 = 0.25$ and $\kappa_0 = 1.5$ ($Pr = Pm = 1/6$) in the left panel and with $\nu_0 = 1.0$ and $\kappa_0 = 0.01$ ($Pr = Pm = 100$) in the right panel. The red line is the ideal necessary and sufficient boundary (3.25). The dashed black lines represent hyperbolae $A\mathcal{L} = C$, where C incrementally doubles from $C = 0.025$ to $C = 3.2$. The red dot indicates the location of the most unstable mode.
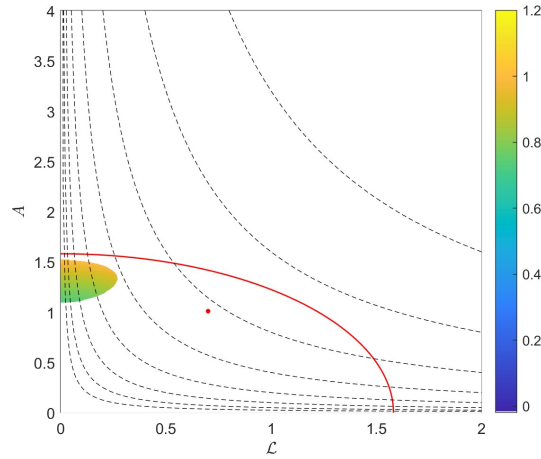
Figure 4.25: $Pr = Pm \neq 1$: Frequency of the unstable modes in $(\mathcal{L}, A)$-space for $\Lambda = 2.5$, with $\nu_0 = 1.0$ and $\kappa_0 = 0.01$. The red line is the ideal necessary and sufficient boundary (3.25). The dashed black lines represent hyperbolae $A\mathcal{L} = C$, where C incrementally doubles from $C = 0.025$ to $C = 3.2$. The red dot indicates the location of the most unstable mode.
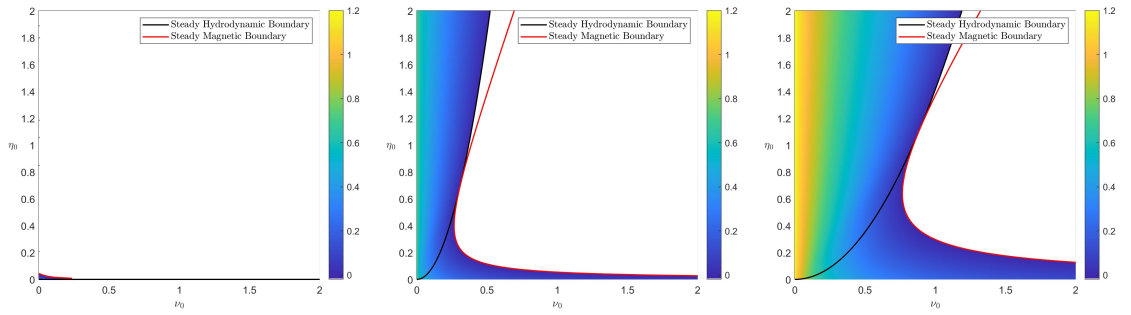
Figure 4.26: $Pr = Pm \neq 1$: The maximum growth rate S in (ν_0, η_0)-space with $\Lambda = 0.5$ (left), $\Lambda = 1.5$ (centre) and $\Lambda = 2.5$ (right). Note that no oscillatory instabilities exist in this system.

The Maximum Growth Rate as a Function of Diffusivities

We now provide contour plots of the maximum growth rate S and the corresponding A and $\mathcal{L}$ at which it occurs in $(\nu_0, \eta_0 = \kappa)$-space for $\Lambda = 0.5$, $\Lambda = 1.5$ and $\Lambda = 2.5$ in figure 4.26 and 4.27, respectively. In the previous sections we have also plotted the corresponding complex part of the growth rare however, in this case there are none.

In this case it is clear that ν_0 always decreases the growth rate, while η_0 always increases the growth rate to the maximum of the inviscid hydrodynamic regime $\Lambda/2$. We would expect this since increasing $\eta_0 = \kappa_0$ dampens magnetic modes and excites inertial modes. It is clear that the maximum occurs in the limit $\eta_0 \gg \nu_0$ (i.e., $Pr = Pm \ll 1$) which is typically the case in planetary atmospheres. In general, we find that sufficiently large $\eta_0 = \kappa_0$ guarantees instability at any value of ν_0. Interestingly, at certain values of ν_0, increasing $\eta_0 = \kappa_0$ first stabilises the system and then generates instability.

We now discuss figure 4.27 that illustrates the corresponding $A = A_{\max}$ and $\mathcal{L} = \mathcal{L}_{\max}$ that generate the maximum growth $S_{\max}$ as found in figure 4.26 in (ν_0, η_0)-space. First, we com-
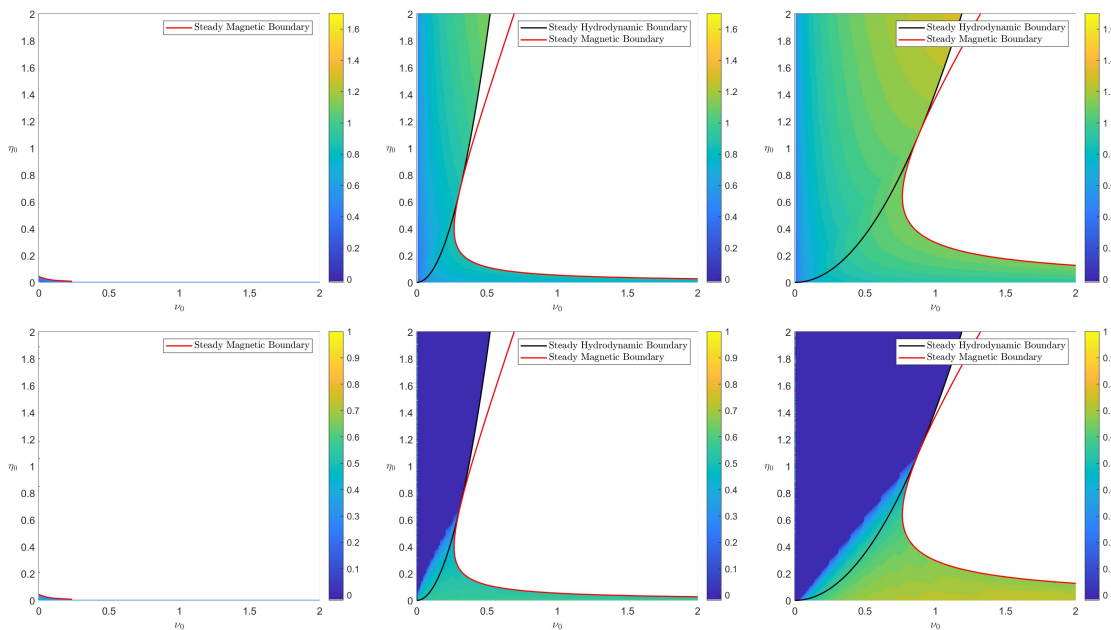
Figure 4.27: $Pr = Pm \neq 1$: The value of $A_{\max}$ (top) and $\mathcal{L}_{\max}$ (bottom) in (ν_0, η_0)-space with $\Lambda = 0.5$ (left), $\Lambda = 1.5$ (centre) and $\Lambda = 2.5$ (right).

ment on the modes close to the hydrodynamic steady bound (4.76) and the magnetohydrodynamic steady bound (4.77). Clearly, modes that are stabilised once the hydrodynamic stability bound (4.76) is surpassed are purely magnetic as the Lehnert number on the stability boundary (4.77) is non-zero, while the Lehnert number is zero if the modes are stabilised along (4.76).

The plots of the Lehnert number shows that increasing $\eta_0 = \kappa_0$ at fixed ν_0 decreases the growth rate of magnetic modes until stabilisation and increases the growth rate of inertial instabilities (as one might expect from increasing thermal diffusion and magnetic diffusivity). Given sufficiently large ν_0, increasing η_0 stabilises all modes; however, for sufficiently large η_0 (hydrodynamic) instability occurs. Indeed, given sufficiently large η_0, the most unstable mode is hydrodynamic, where the effects of increasing η_0 become negligible. Thus, for sufficiently large η_0, we obtain hydrodynamic instabilities analogous to those discussed in section 4.3.2, where we have already discussed the links to the GSF instability.

Figure 4.27 also shows that increasing ν_0 or $\eta_0 = \kappa_0$ increases the value of $A_{\max}$ (so that the vertical wavenumber decreases with increasing ν_0 or η_0). We note that modes with $Pr \ll 1$ have the smallest aspect ratio, which is of interest as Pr is typically small in planetary atmospheres; the maximum growth rate of the hydrodynamic regime also occurs in the large vertical wavenumber (i.e., small aspect ratio) limit (Griffiths, 2008a). Thus, since increasing ν_0 or η_0 decreases the vertical wavenumber, it follows that the magnetic field strength must increase also so that the optimal Lehnert number can remain approximately constant, or even increases slightly.

4.4.6 $Pr \neq Pm \neq 1$

In this section we consider equation (4.5) directly since $Pr \neq Pm \neq 1$.

130

Formulation and Stability Bounds

To restrict the analysis we consider the case where the Prandtl numbers are small and follow the scaling $Pr = Pm^p$ where p is some positive power. Note that $Pr \ll Pm \ll 1$ implies that $\kappa_0 \gg \eta_0 \gg \nu_0$. Formally, we suppose the Prandtl numbers follow the scaling

$$\frac{\nu_0}{\eta_0} = \epsilon \text{ and } \frac{\nu_0}{\kappa_0} = \epsilon^p \text{ with } p > 0, \tag{4.79}$$

where $\epsilon = O(1)$ or smaller. This formulation reduces the system to a 4 parameter problem $(\mathcal{L}, A, \nu_0 \text{ and } \epsilon)$ for the growth rate. It is typical to take scalings with $p = 3/2$, $p = 2$, or $p = 3$; however, we will only consider $p = 3/2$ or $p = 3$ (since there is little difference between the $p = 2$ and $p = 3$ cases).

First, we obtain the relevant steady stability conditions from equations (4.34) and (4.50) where the latter is used if $\mathcal{L} > 0$ in equation (4.49). Writing κ_0 and η_0 as described in (4.79) allows us to rewrite equation (4.49):

$$\mathcal{L}^2 = \frac{\Lambda}{4} - \frac{4\nu_0^2}{\Lambda^2}\epsilon^{2p-3}. \tag{4.80}$$

Note that ϵ is typically small in the solar tachocline as well as the upper atmospheres of Jupiter and Hot Jupiters (see table 2.1). Thus, equation (4.80) implies that $\mathcal{L} > 0$ if $p > \frac{3}{2}$ and $\mathcal{L} < 0$ if $p < \frac{3}{2}$. If $p = 3/2$, then $\mathcal{L} > 0$ if and only if $\Lambda^3 > 16\nu_0^2$. We will be solving for the growth rate for $\epsilon \in [0.01, 1]$ so that $\mathcal{L}$ may not be positive even for $p > \frac{3}{2}$.

In the cases where (4.80) does not predict a positive value for $\mathcal{L}$, the hydrodynamic steady stability bound (4.34) is rewritten as the following necessary and sufficient condition for stability:

$$\frac{2(\Lambda - 1)^{3/2}}{3\sqrt{3}\epsilon^p} < \nu_0, \tag{4.81}$$

implying that instability occurs for $\epsilon \ll 1$ with $p > 0$.

In the cases where (4.80) predicts a positive value for $\mathcal{L}$, the steady magnetic stability bound (4.50) is rewritten as the following necessary and sufficient condition for stability:

$$\nu_0^2 > \frac{\Lambda^4\epsilon^{4-2p}}{64(1 - \Lambda(1 - \epsilon))}. \tag{4.82}$$

In the case where $\epsilon \ll 1$ (which is most relevant in the Solar tachocline as well as the upper atmospheres of Jupiter and Hot Jupiters) equation (4.82) predicts instability for $\Lambda > 1$ since the denominator is guaranteed to be negative. However, if $\Lambda < 1$, then stability is guaranteed if $p < 2$ and instability if $p > 2$. If $p = 2$, then there is stability if and only if $\nu_0^2 < \Lambda^4/64(1 - \Lambda)$. Thus, together, (4.81) and (4.82) form a necessary and sufficient condition for steady instability, where equation (4.80) indicates which bound is appropriate in parameter space. Note that the stability conditions (4.81) and (4.82) apply only to modes with real growth rates. Thus, oscillatory instabilities may still occur while (4.81) or (4.82) are satisfied. Note that equations (4.81) and (4.82) only apply to one root of (4.5) and thus, there may be other steady modes with $S > 0$.

We now determine a relation between ϵ and Λ at which the stability bound shifts from (4.81) to (4.82). We substitute (4.82) into (4.81) giving the condition

$$\mathcal{L} > 0 \iff 4 > \frac{\epsilon\Lambda}{1 - \Lambda + \Lambda\epsilon}. \tag{4.83}$$

Thus, when $\epsilon \ll 1$ we must use the hydrodynamic condition (4.81) since (4.83) is always satisfied. If ϵ is not small however, then the magnetic condition (4.81) may be used if $\Lambda < 1/(1 - \epsilon)$ and $\epsilon > 4(\Lambda - 1)/3\Lambda$ (i.e., the denominator of (4.83) is positive while the inequality is satisfied).

The Maximum Growth Rate as a Function of Aspect Ratio and Lehnert Number

In figures 4.28 and 4.29 we contour the growth rate in $(\mathcal{L}, A)$-space for $\Lambda = 0.5$ and $\Lambda = 1.5$, respectively, for various values of ν_0 and ϵ with $p = 3$. We do not provide plots with $\Lambda = 2.5$ or $p = 3/2$ since there are no significant differences from the $\Lambda = 1.5$ or $p = 3$ cases. Note that in Section 3.3.4 we estimated that $C = A\mathcal{L}$ ranges from $O(10^{-4})$ to $O(10^{-2})$ in the upper atmospheres of Jupiter and Hot Jupiters, while ranging from $O(1)$ to $O(10^2)$ in the solar tachocline.

In figure 4.28 the instabilities are purely magnetic. However, surprisingly, instabilities persist for large values of η_0 (shown in the right hand panel) and occur at values of A far outside of the ideal unstable domain; the instabilities are able to persist owing to the strong thermal diffusion which reduces the stabilising role of the pressure gradient. Interestingly, owing to the values of A at which instability can now occur, the vertical lengthscales of the most unstable modes with $\Lambda = 0.5$ are at least 3 to 4 orders of magnitude larger than those found in the $Pr = Pm = 1$ case.

In figure 4.29 there magnetically modified inertial and purely magnetic instabilities. Notably, both instabilities occur for values of A outside of the ideal unstable domain, implying that thermal diffusion plays a significant role in nullifying the stabilising role of the pressure gradient. By comparing the two plots we can see that increasing the magnitude of ν_0 does not lead to the stabilisation of hydrodynamic modes. Instead, owing to the strong thermal diffusion, hydrodynamic modes and magnetically modified inertial instabilities become more prominent (shown in the right panel of figure 4.29) and occur at larger values of A.

The Maximum Growth Rate as a Function of Diffusivities

In this section we provide contour plots of the maximum growth rate S in (ν_0, ϵ)-space for various Rossby numbers. We first focus on the case $p = 3/2$ and investigate how varying ν_0 and ϵ effects the modes. Then, we consider the case $p = 3$; however, here, owing to the similarities to the $p = 3/2$ case, we focus on how the different scaling alters the nature of the most unstable mode.

We provide contour plots of the maximum growth rate S in (ν_0, ϵ)-space for $\Lambda = 1.5$ and $\Lambda = 2.5$ in figure 4.30 with $Pr = Pm^p$, $p = 3/2$. We determine the growth rate via (4.5) for each $A, \mathcal{L}, \nu_0$ and ϵ at fixed Λ and p.

Clearly, the stability conditions (4.81) and (4.82) bound the unstable domain. The hydrodynamic stability bound (4.81) implies that the last modes to stabilise for sufficiently small ϵ are
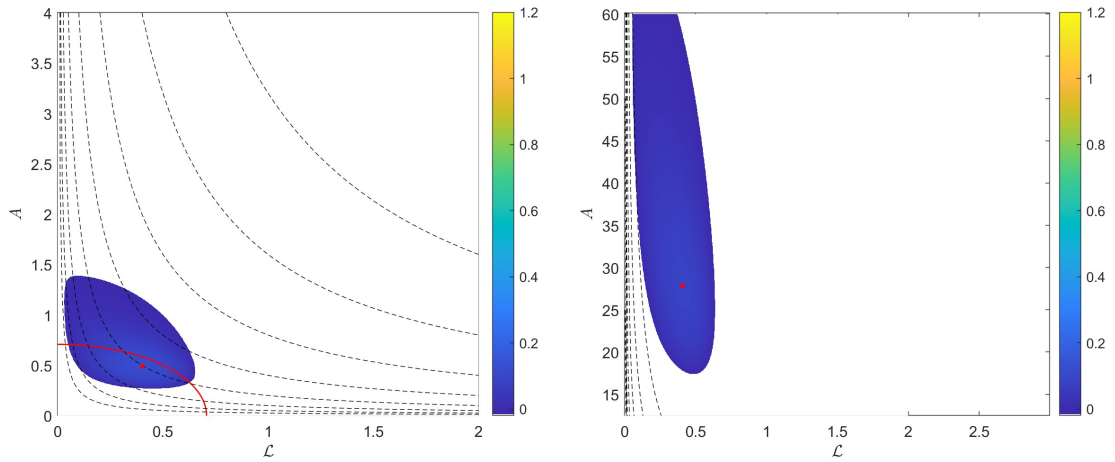
Figure 4.28: $Pr = Pm^3 \ll 1$: Growth rate in the $(\mathcal{L}, A)$-space for $\Lambda = 0.5$ and $p = 3$ with $\nu_0 = 0.01$ and $\epsilon = 0.5$ ($Pr = 0.125, Pm = 0.5$, left panel) and $\nu_0 = 1.0$ and $\epsilon = 0.05$ ($Pr = 1.25 \times 10^{-4}, Pm = 0.05$, right panel). The red line is the ideal necessary and sufficient boundary (3.25). The dashed black lines represent hyperbolae $A\mathcal{L} = C$, where C incrementally doubles from $C = 0.025$ to $C = 3.2$. The red dot indicates the location of the most unstable mode.
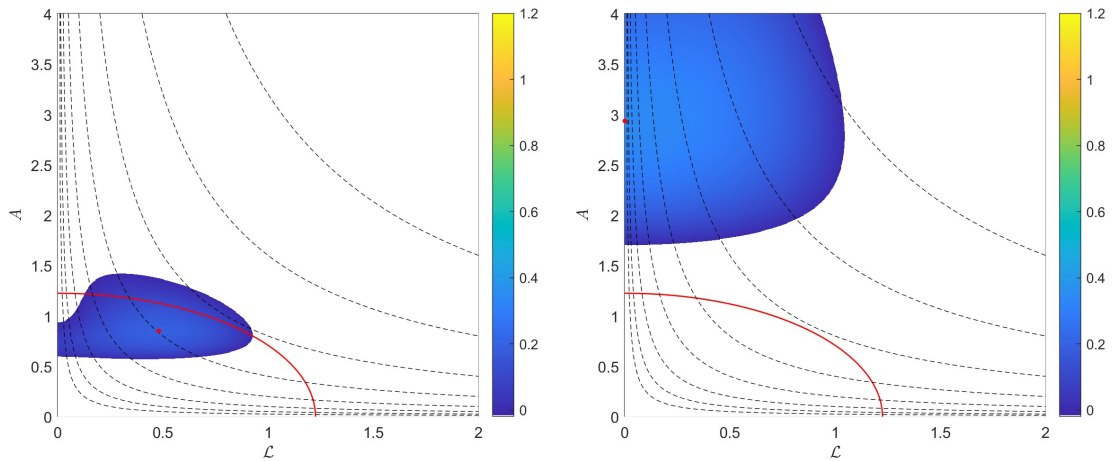
Figure 4.29: $Pr = Pm^3 \ll 1$: Growth rate in the $(\mathcal{L}, A)$-space for $\Lambda = 1.5$ and $p = 3$ with $\nu_0 = 0.2$ and $\epsilon = 0.8$ ($Pr = 0.512, Pm = 0.8$, left panel) and $\nu_0 = 2.0$ and $\epsilon = 0.2$ ($Pr = 8.0 \times 10^{-3}, Pm = 0.2$, right panel). The red line is the ideal necessary and sufficient boundary (3.25). The dashed black lines represent hyperbolae $A\mathcal{L} = C$, where C incrementally doubles from $C = 0.025$ to $C = 3.2$. The red dot indicates the location of the most unstable mode.

133
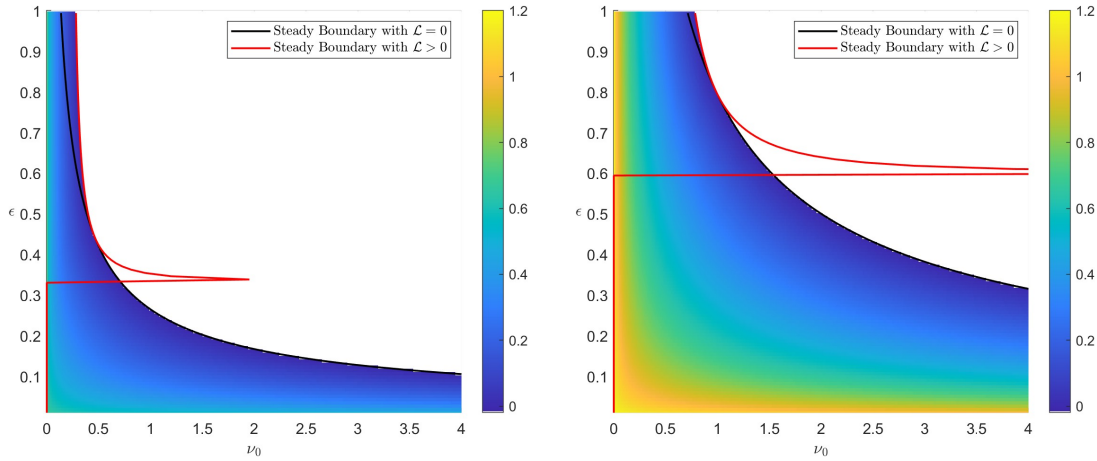
Figure 4.30: $Pr = Pm^{3/2} \ll 1$: The maximum growth rate S in (ν_0, ϵ)-space with $\Lambda = 1.5$ (left) and $\Lambda = 2.5$ (right).

hydrodynamic; this is reasonable since small ϵ yields a larger magnetic diffusivity in relation to kinematic viscosity ν_0.

Figure 4.30 shows that the maximum growth rates occur for either small ϵ or small ν_0. This is expected since the small ϵ limit corresponds to large η_0 and even larger κ_0, implying these instabilities are hydrodynamic in nature, where thermal diffusion allows instability to occur at fixed kinematic viscosity (in comparison to when $Pr = Pm = 1$ say). In the limit of small ν_0 all diffusive parameters become small (as seen in equation (4.79)) allowing large growth rates to occur provided ϵ is not too small.

We also find that increasing ν_0 (at fixed ϵ) and ϵ (at fixed ν_0) decreases the growth rate; however, this occurs much more slowly in the small ϵ and ν_0 limits due to large thermal diffusion that allows modes to remain unstable and small diversities in general, respectively. Note that (4.81) implies instability can be obtained at any ν_0 given sufficiently small ϵ.

It is natural to plot the corresponding $A = A_{\max}$ and $\mathcal{L} = \mathcal{L}_{\max}$ in (ν_0, ϵ)-space that generate the maximum growth rate $S_{\max}$ found in figure 4.30. Thus, we plot $A_{\max}$ and $\mathcal{L}_{\max}$ in (ν_0, ϵ)-space in figure 4.31 for $\Lambda = 1.5$ and $\Lambda = 2.5$. The black line represents the hydrodynamic stability bound (4.81). The red line represents the stability bounds (4.82).

The first row in figure 4.31 clearly shows that for $\Lambda = 1.5$ and $\Lambda = 2.5$, $A_{\max}$ increases with increasing ν_0 and decreasing ϵ. This occurs due the combined effects of increasing kinematic viscosity and thermal diffusion; large magnetic diffusivity ensures the most unstable mode is hydrodynamic. These are analogous to instabilities that occur in section 4.3.2, and link to the GSF instability.

The second row in figure 4.31 clearly shows that for $\Lambda = 1.5$ and $\Lambda = 2.5$, magnetic instabilities may only occur for sufficiently large $\epsilon = \nu_0/\eta_0$ since a smaller magnitude of magnetic diffusivity allows these to occur. Otherwise, the most unstable mode is hydrodynamic in nature within this regime.

134
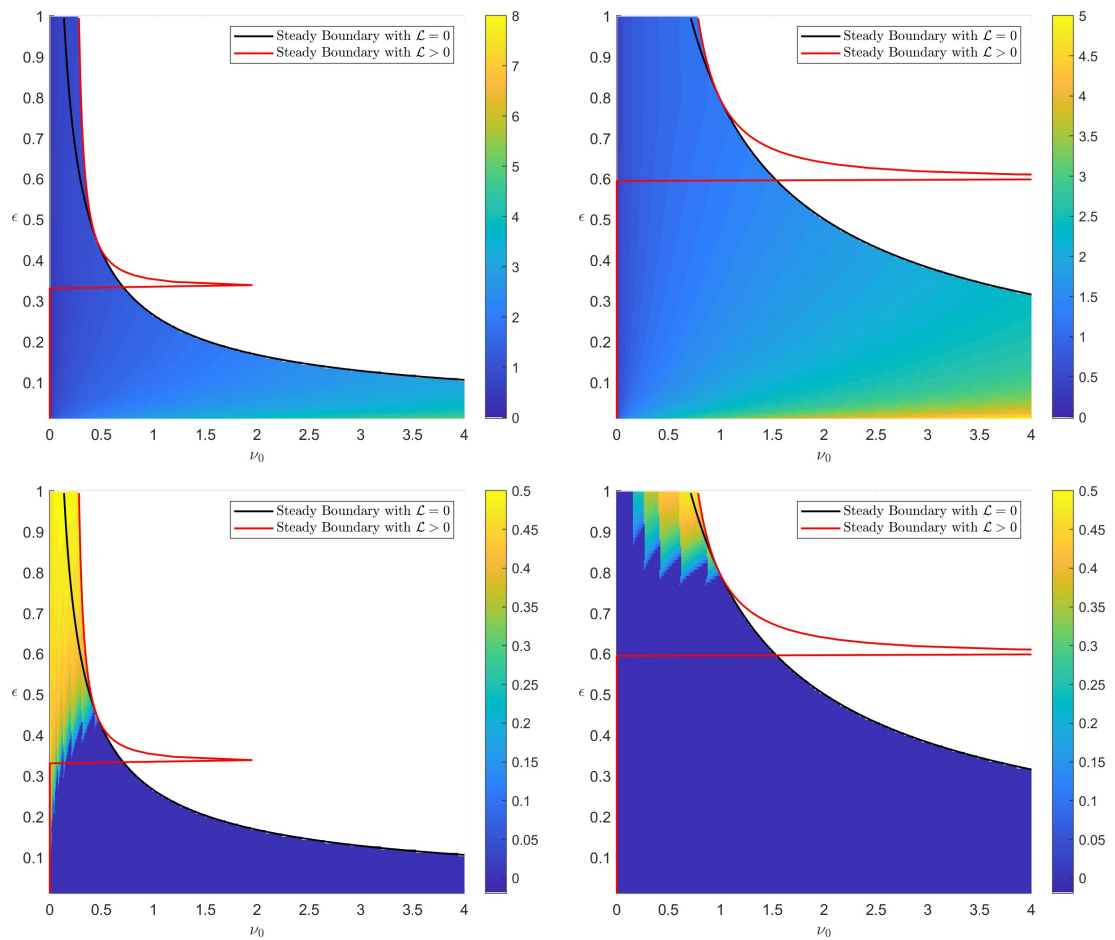
Figure 4.31: $Pr = Pm^{3/2} \ll 1$: The value of $A_{\max}$ (top) and $\mathcal{L}_{\max}$ (bottom) in (ν_0, ϵ)-space with $\Lambda = 1.5$ (left) and $\Lambda = 2.5$ (right).
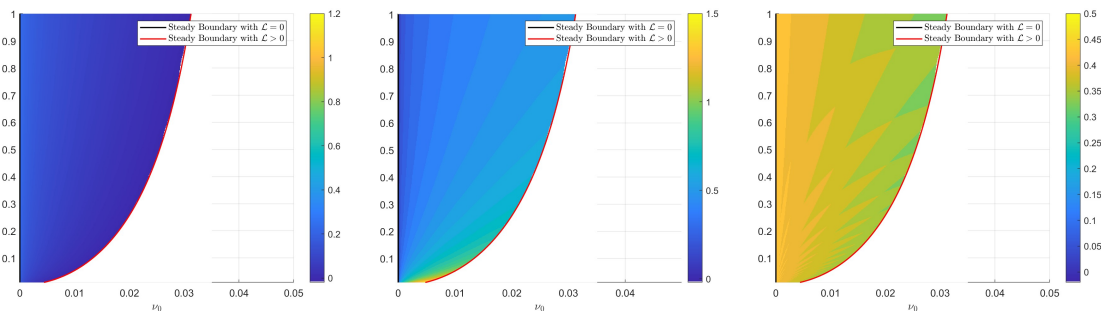
Figure 4.32: $Pr = Pm^{3/2} \ll 1$: The maximum growth rate S (left), corresponding A (centre) and $\mathcal{L}$ (right) in (ν_0, ϵ)-space with $\Lambda = 0.5$.

Here we also provide contour plots of the maximum growth rate S, alongside the corresponding aspect ratio and Lehnert number of the mode, in (ν_0, ϵ)-space for $\Lambda = 0.5$ in figure 4.32 with $Pr = Pm^p$ with $p = 3/2$. Note that the ν_0 domain is on a significantly different scale to that of figures 4.30 and 4.31. This is due to the instabilities being purely magnetic and therefore requiring sufficiently small magnetic diffusivity (i.e., small ν_0 or large ϵ). By contrast, in the hydrodynamically unstable regime, the most unstable modes now occur only in the small ν_0 regime rather than both the small ν_0 and ϵ regimes as in figure 4.30. The aspect ratio again decreases with increasing ϵ as in figure 4.31 for $\Lambda = 1.5$ and $\Lambda = 2.5$. Figure 4.32 also shows that all modes are purely magnetic, where the Lehnert number increases with increasing ϵ and decreases with increasing ν_0.

We now provide contour plots of the maximum growth rate S in (ν_0, ϵ)-space for $\Lambda = 0.5$, $\Lambda = 1.5$ and $\Lambda = 2.5$ in figure 4.33 with $Pr = Pm^p$ with $p = 3$. We also plot the value of A and $\mathcal{L}$ at which the maximum growth rate occurs for in (ν_0, ϵ)-space in figure 4.34 for $\Lambda = 0.5$, $\Lambda = 1.5$ and $\Lambda = 2.5$.

Focusing on the most unstable modes that the new scaling $Pr = Pm^p$ with $p = 3$ (rather than $p = 3/2$), it is clear that the growth rates are generally larger in contrast to the $p = 3/2$ case. The domain of instability is also larger in contrast to figure 4.30, as we would expect, as κ_0 will now be much larger for $p = 3$ for the same ν_0. For $\Lambda = 1.5$ and $\Lambda = 2.5$, the modes are analogous to the previous case with $p = 3/2$ in figures 4.30 and 4.31 which we have already discussed. However, figure 4.34 shows for $\Lambda = 1.5$ that we can now obtain magnetic instabilities for small ν and ϵ, implying the existence of magnetic modified inertial instabilities; this is possible since the magnitude of magnetic diffusivity is not yet sufficient to nullify the effect of magnetic field. The most interesting case is when $\Lambda = 0.5$, where we find that the instability domain is much larger than in figure 4.32 for $p = 3/2$. Instability can even be found at any ν_0 given sufficiently small ϵ; we can see that this is the case from the magnetic stability bound (4.82) with $p = 3$ (as it becomes a hyperbola in this case). This is of clear interest as we expect Rossby numbers $\Lambda < 1$ in the solar tachocline and Jupiter's upper atmosphere, where ϵ is also expected to be small. Importantly, as figure 4.34 suggests, these instabilities are purely magnetic and require quite large aspect ratios, implying that the modes have large vertical wavenumbers and small vertical scales. In contrast to figure 4.32 with $p = 3/2$, instability can now occur at larger ν_0 since κ_0 is even larger than the
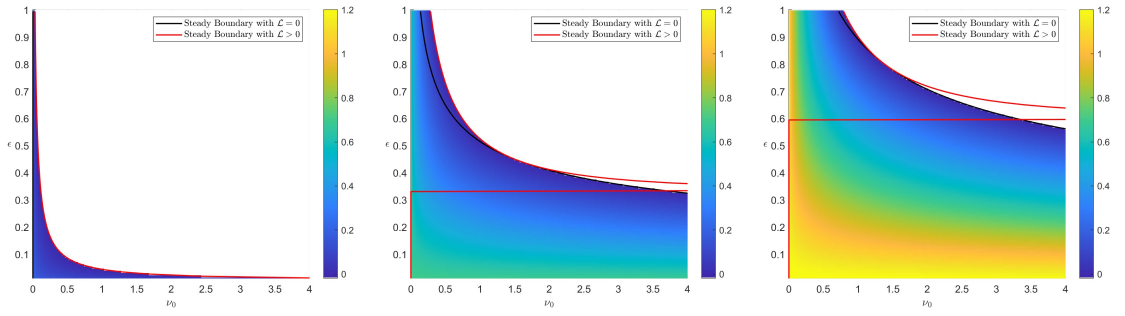
Figure 4.33: $Pr = Pm^3 \ll 1$: The maximum growth rate S in (ν_0, ϵ)-space with $\Lambda = 0.5$ (left), $\Lambda = 1.5$ (centre) and $\Lambda = 2.5$ (right).
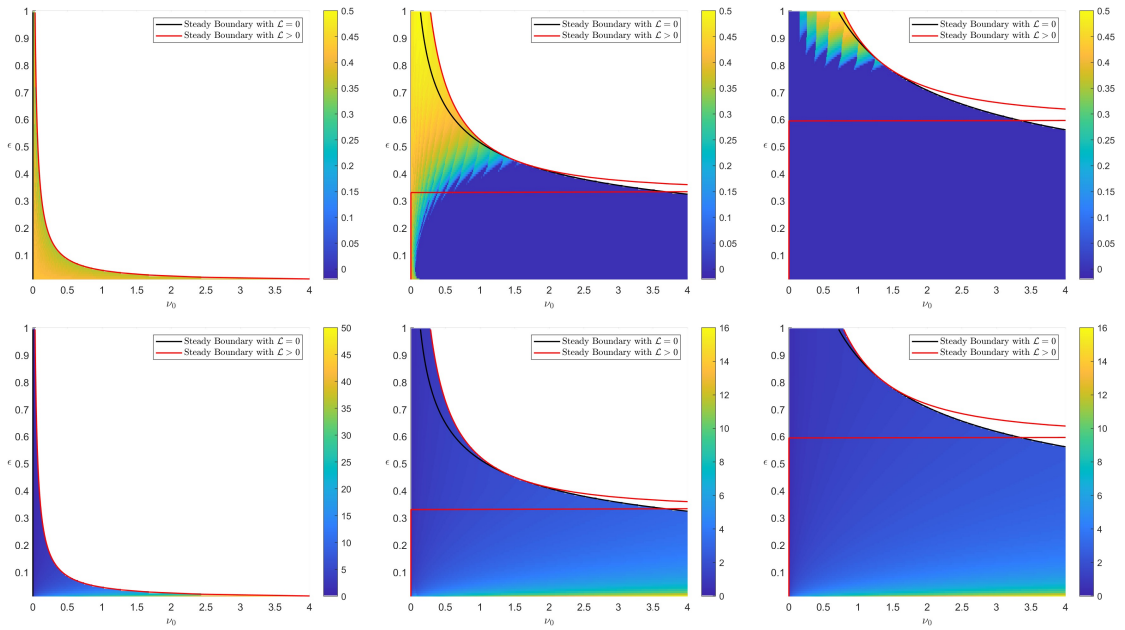
Figure 4.34: $Pr = Pm^3 \ll 1$: The value of $A_{\max}$ (top) and $\mathcal{L}_{\max}$ (bottom) in (ν_0, ϵ)-space with $\Lambda = 0.5$ (left), $\Lambda = 1.5$ (centre) and $\Lambda = 2.5$ (right).

magnitude of the magnetic diffusivity η_0 when $p = 3$. This yields a double-diffusive instability analogous to the magnetic instability found in the large $\nu_0 = \kappa_0$ limit of figures 4.20 and 4.21 where $Pr = 1$ and $Pm \neq 1$. Clearly, as the condition (4.82) suggests, we require $p > 2$ (i.e., $\nu_0 = \epsilon^p \kappa_0$ with $p = 2$) for this instability to operate.

4.5 Conclusions

In this chapter we have extended the system and analysis of Chapter 3 into the diffusive regime. We considered the linear stability of the parallel flow $U(y) = \Lambda_0 y$ with uniform latitudinal shear $U'(y) = \Lambda_0$ on an f-plane in the presence of uniform vertical magnetic field strength $B_3(y) = B_0$, kinematic viscosity ν, thermal conductivity κ and magnetic diffusivity η. We chose this formulation as it is the simplest possible configuration to study the competition between inertial and magnetic modes in the presence of diffusion. Under this formulation the governing equation (2.30)

admits solutions of the form $v \propto \exp(ily)$. The consideration of diffusion stabilises modes that occur at infinite vertical wavenumbers so that the maximum growth rate must must occur at a finite vertical wavenumber.

We analysed the various cases of this chapter via two main routes of analysis. The first addresses what is the most unstable mode of a given astrophysical body (e.g., those seen in 2.1) and what the nature of that mode is; primarily, we do this by providing contours of the maximum growth rate in $(\mathcal{L}, A)$-space at fixed values of Λ, ν_0, κ_0 and η_0. The crucial aspect of these contours is the hyperbolae $C = A\mathcal{L} = |l|Nv_A/f_0^2$, which are independent of vertical wavenumber. We argued that by considering a flow in a latitudinal channel on an astrophysical body, then the mode of interest lies on one of the hyperbolae since we can infer (and fix) values of Λ_0, N and ν from observations. The point along the hyperbola that generates the maximum growth rate yields the chosen vertical lengthscale of the mode.

The second aim is to address the specific role of ν_0, κ_0 and η_0 on the system; we do this by contouring the maximum growth rate as a function of two diffusive parameters (e.g., (ν_0, κ_0)-space with $\nu_0 = \eta_0$), where, at each value of the two diffusive parameters, we have selected the A and $\mathcal{L}$, $A_{\max}$ and $\mathcal{L}_{\max}$ say, that maximise the growth rate. This process isolates the most unstable modes and allows us to determine the role of diffusion on the system. However, it must be noted, it is difficult to interpret these results for given astrophysical bodies since v_A, ν_0, and therefore the cross-stream wavenumber, take fixed values. This consequence arises because the maximisation over A must be interpreted as an optimisation over the vertical wavenumber k, while the maximisation over $\mathcal{L}$ must be interpreted as an optimisation over kv_A, where an optimal magnetic field strength is inferred (since k is already chosen via the optimisation of A) from the quantity kv_A. Thus, since v_A must vary in magnitude, we cannot consider a single astrophysical body.

We derived necessary and sufficient conditions for steady stability in the hydrodynamic and magnetohydrodynamic regimes (see equations (4.34) and (4.50), respectively). In the magnetohydrodynamic regime the conditions complement each other to bound the unstable domain, where the use of each condition depends on whether the modes that are stabilised under the parameter changes (e.g., increasing the kinematic viscosity) are hydrodynamic or magnetohydrodynamic. The conditions are very useful since they are independent of the vertical wavenumber about which there is considerable uncertainty in astrophysical bodies. Indeed, the conditions (4.34) and (4.50) can be used upon estimating the Rossby number $\Lambda = \Lambda_0/f_0$ as well as the diffusive parameters (4.4). The latter requires estimates of the buoyancy frequency N, Coriolis parameter f_0, kinematic viscosity ν, thermal conductivity κ, magnetic diffusivity η and cross-stream wavenumber $l = 2\pi/L$, where L is an observed latitudinal lengthscale. Indeed, by consulting table 2.1, in terms of ordering we find $\nu_0 = O(10^{-10})$, $\kappa_0 = O(10^{-4})$, $\eta_0 = O(10^{-9})$ in the solar tachocline, $\nu_0 = O(10^{-18})$, $\kappa_0 = O(10^{-17})$, $\eta_0 = O(10^{-2})$ in Jupiter's upper atmosphere, and $\nu_0 = O(10^{-14})$, $\kappa_0 = O(10^{-13})$, $\eta_0 = O(10^2)$ typically in Hot Jupiters. Note that the magnitude of η_0 is very sensitive to atmospheric depth in Jupiter (and Hot Jupiters) and could vary by several

orders of magnitude, yielding much smaller values of η_0. Indeed, the magnitude of η reduces from $2.3 \times 10^9 \mathrm{m}^2\mathrm{s}^{-1}$ (the value given in 2.1) at $R = 0.98R_j$ to $1.2 \times 10^5 \mathrm{m}^2\mathrm{s}^{-1}$ at $R = 0.952R_j$ (French *et al.*, 2012).

Following Section 3.3.4 we take $\Lambda = 0.21$ in the solar tachocline, $\Lambda = 0.01$ in Jupiter's upper atmosphere and $\Lambda \in [0.5, 5]$. We find that the hydrodynamic steady bound (4.34) implies stability for the solar tachocline and Jupiter's upper atmosphere since $\Lambda < 1$, while for Hot Jupiters (4.34) the bound implies instability provided Λ is $O(10^{-10})$ larger than 1 (owing to the size of ν_0 and κ_0). The condition for oscillatory stability (4.29) is also violated, implying that Hot Jupiters may be unstable to steady or oscillatory instabilities in the absence of magnetic field. In contrast, if we consider the magnetohydrodynamic stability condition (4.50), steady instability is implied for the solar tachocline and Hot Jupiters (for sufficiently large Λ); instability is also possible by the condition (4.50) in Jupiter's upper atmosphere and Hot Jupiters (with smaller Λ) provided we take η to be sufficiently small. However, under the larger magnetic diffusivity of Jupiter's upper atmosphere at $R = 0.952R_j$ it is likely that these magnetic instabilities are suppressed. Note that in the magnetohydrodynamic regime it is impractical to derive analytical conditions for oscillatory instability using the Routh-Hurwitz criteria; however, the hydrodynamic condition for oscillatory instability (4.29) may still be used in the magnetohydrodynamic regime under certain conditions (see section 4.4.3), but this is not valid for $\Lambda < 1$, which is the case in the solar tachocline and Jupiter's upper atmosphere.

In the magnetohydrodynamic regime we systematically analysed every variation of Pr and Pm being unity or non-unity. We first considered the case $Pr = Pm = 1$ which links to both to the hydrodynamic regime with $Pr = 1$ and the ideal system of Chapter 3 via a simple transformation of the growth rate. Owing to the small values of the diffusive parameters ν_0, κ_0 and η_0, the chosen vertical scale remains close to that predicted by (3.26) and (3.27); however, such small diffusive parameters are unachievable in nonlinear simulations and thus, it is useful to consider stronger diffusive regimes. Indeed, by increasing ν_0 ($= \kappa_0 = \eta_0$ in this case), $A_{\max}$ increased, implying that a larger vertical scale was required; $\mathcal{L}_{\max}$ remained approximately constant. However, for $\Lambda > 2$, $\mathcal{L}_{\max}$ increased (departing from $\mathcal{L} = 0$ — the location of the maximum growth rate for $\Lambda > 2$ in the ideal system of Chapter 3).

The case $Pr \neq 1$ and $Pm = 1$ is a clear extension to the previous case and allowed us to draw links to hydrodynamic section 4.3.2. By making use of the stability bounds (4.29), (4.34) and (4.50), we derived the two conditions for stability (4.64) and (4.65), the first being necessary and sufficient for $2 < \Lambda < 4$ and the latter being necessary and sufficient for $\Lambda > 4$. For $\Lambda < 2$, the stability bound (4.65) may be used as a sufficient condition for stability. Contouring the maximum growth rate in ($\nu_0 = \eta_0$, κ_0)-space highlights a magnetic instability which requires strong thermal diffusion to nullify the stabilising role of stratification at small vertical wavenumbers. This is similar to the hydrodynamic GSF instability (Goldreich & Schubert, 1967; Fricke, 1968), which we discussed in section 4.3.2. However, the instability is significantly modified by magnetic field;

indeed, the growth rate increases at each ν_0 and κ_0 for $\Lambda < 2$ and, under given sufficiently large ν_0, increases the growth rate for $4 > \Lambda > 2$.

We then considered the case $Pr = 1$ and $Pm \neq 1$ in section 4.4.4. Figures 4.20 and 4.21 illustrate the existence of a purely magnetic instability in the large $\nu_0 = \kappa_0$ limit. Equation (4.73) shows that the growth rate scales with $\nu_0^{-1/3}$ with $\nu_0 \gg 1$. It also confirms that the instability is purely magnetic since setting $\mathcal{L} = 0$ in (4.73) implies stability. The $\mathcal{L}$ that generates the maximum growth rate of the instability is found to be uniform such that $\mathcal{L} = \sqrt{\Lambda}/2$; the aspect ratio that generates the maximum growth rate of the instability scales such that $A \sim \nu_0^{1/3}$.

In the case $Pr = Pm \neq 1$, we find instabilities analogous to those found in the hydrodynamic section 4.3.2 in the large $\kappa_0 = \eta_0$ limit. In the large ν_0 limit, the most unstable mode is purely magnetic (the system would be stable for the same ν_0 in section 4.3.2); however, as ν_0 increases, we require decreasing η_0 for instability still to be possible.

Finally, we consider the case $Pr \ll Pm \ll 1$ such that $Pm = \epsilon$ and $Pr = \epsilon^p$ for $p = 3/2$ and $p = 3$ with $\epsilon \ll 1$. Generally, the instability domain is dominated by hydrodynamic instabilities. However, some magnetically modified inertial instabilities are found when $\Lambda = 1.5$ and $p = 3$ in the small ν and ϵ limits, which will be typically the case in the astrophysical bodies we are considering (see table 2.1). Perhaps most interestingly, we find that for $p > 2$ the instability domain for $\Lambda < 1$ (shown for $\Lambda = 0.5$ in figures 4.33 and 4.34) is much larger than when $p < 2$ (which is also implied by the stability bound (4.82)). Indeed, for $p > 2$, it is possible for magnetic instabilities to occur at much larger ν_0; this due to the magnitude of thermal diffusion being much larger than in the $p = 3/2$ case, enabling magnetic instabilities to occur even in the presence of magnetic diffusivity, which would otherwise render the system stable, For both $p < 2$ and $p > 2$, we find that given sufficiently small ν_0, purely magnetic instabilities occur for $\Lambda < 1$. This is relevant to Jupiter's upper atmosphere and the solar tachocline, where it is expected that Rossby numbers $\Lambda < 1$ and $\epsilon = Pm$ to be small.

Chapter 5

Nonlinear Evolution of the Instabilities of a Localised Shear Layer at Mid-latitudes

5.1   Introduction

In this chapter we consider the linear and nonlinear evolution of the localised shear flow $U(y) = U_0 \tanh(y/L)$, with latitudinal scale L on an f-plane. We will also consider uniform vertical magnetic field of strength $B_3(y) = B_0$ and uniform kinematic viscosity ν, thermal diffusion κ and magnetic diffusivity η, such that $Pr = Pm = 1$ (i.e., $\nu = \kappa = \eta$). In contrast to Chapter 3 and 4, we consider a localised shear layer rather than uniform shear flow, so that modes will decay exponentially in the latitudinal direction. Upon linearising, the governing equation (2.30) may still be solved analytically, yielding solutions of the form $v \sim \mathrm{sech}^\alpha(y/L)$; this allows us to investigate the linear regime of the nonlinear evolution of the flow.

Griffiths (2008a) has previously considered the axisymmetric linear stability of the localised shear layer $U(y) = U_0 \tanh(y/L)$ on an f-plane in the absence of magnetic field and diffusion under the hydrostatic approximation. Instability occurs for Rossby numbers $\Lambda > 1$ provided $k > N((\Lambda - 1)f_0 L)^{-1}$ (using our previous notation), with the maximum growth rate occurring as the vertical wavenumber $k \to \infty$. Albeit on an equatorial β-plane with uniform shear $U(y) = \Lambda_0 y$, Griffiths (2003b) considers the hydrodynamic nonlinear evolution of the axisymmetric and hydrostatic system, finding that the absolute vorticity $fQ = f(f - U')$ is redistributed around the initially unstable region (where $fQ < 0$) to stabilise the flow.

We begin the chapter with section 5.2 by deriving a set of nondimensional equations from the nonlinear governing equations (2.14)-(2.18). The nondimensionalisation used is different to that seen in chapters 3 and 4, yielding a new set of nondimensional parameters. Indeed, the magnetic field strength is now governed by the parameter $\mathcal{M}$ rather than the Lehnert number $\mathcal{L}$. We must also consider the nondimensional vertical wavenumber K (defined after perturbing the nondimensional equations). We again consider the Rossby number Λ and diffusive parameters ν_0, κ_0 and η_0 of

Chapter 4 that are defined in a slightly different form to (4.4) owing to the prescribed latitudinal lengthscale L.

In section 5.3 we consider the linear system, briefly investigating the hydrodynamic and magnetohydrodynamic system. The primary purpose of investigating the linear system is to form a basis for the nonlinear evolution; for instance, for each given $\mathcal{M}$, Λ and ν_0 ($Pr = Pm = 1$) we obtain a nondimensional vertical wavenumber K that generates the maximum growth rate. This vertical wavenumber is then used to calculate the vertical domain length $H = 2\pi/K$ which we apply in the numerical method in order to investigate the nonlinear evolution (for the same given values $\mathcal{M}$, Λ and ν_0). We also consider how the linear analysis links to Chapters 3 and 4, finding magnetically modified inertial and magnetorotational instabilities.

In section 5.4 we describe the numerical method used to solve the nonlinear equations. This includes the motivation and explanation for domain choice, numerical scheme, periodicity and numerical checks. We also define the Reynolds and magnetic Reynolds numbers, and describe the energetics of the system, where we find an interesting consequence of the magnetohydrostatic approximation; indeed, the balance between the kinetic and magnetic energy of the basic state can not be defined. Nonetheless, after the onset of the simulation, the energy ratio is defined owing to the non-zero perturbation energies.

In Sections 5.5, 5.6 and 5.7 we provide the results of the numerical solutions, illustrating the nonlinear evolution of the system. We focus on the changes to the mean flow $\overline{U}$ and mean vorticity $\overline{Q}$, which are defined as the vertical average (mean) of $U(y)$ and $Q(y) = f - U'(y)$, from their initial states, and compare the changes at several magnetic field strengths against each other and that of the hydrodynamic regime (when relevant).

In Section 5.5 we illustrate the hydrodynamic nonlinear evolution, each in a weakly nonlinear and strongly nonlinear regime. This, in part, serves as a check against the similar systems found in Griffiths (2003a) and Kloosterziel *et al.* (2007b), as their results suggest and illustrate the latitudinal redistribution of vorticity across the domain, albeit for hydrodynamic flows on the equatorial β-plane and non-hydrostatic flows on the f-plane, respectively. Focusing our analysis on the strongly nonlinear regime, we describe the mean flow and mean vorticity change over the evolution.

In following subsections we compare the hydrodynamic mean flow and mean vorticity change against that of the magnetohydrodynamic regime. In Section 5.6 we consider the magnetohydrodynamic evolution in hydrodynamically unstable regimes at various strengths of magnetic field. In Section 5.7 we consider the magnetohydrodynamic evolution at Rossby numbers at which only magnetohydrodynamic instabilities may occur. The mean flow and mean vorticity changes are shown to be significantly different to those seen in the previous sections.

5.2   Formulation

We derive a set of nondimensional equations from the nonlinear governing equations (2.14)-(2.18). We begin by making an arbitrarily sized perturbation around the basic state $\mathbf{u} = (U(y), 0, 0)$ and $\mathbf{B} = (0, 0, B_0)$ so that equations (2.14)-(2.18) (with $H = 0$ so that the system is magnetohydrostatic) yield the following set of equations

$$\frac{\partial u}{\partial t} = -Q\frac{\partial \psi}{\partial z} + \frac{B_0}{\mu_0 \bar{\rho}}\frac{\partial b_x}{\partial z} + \frac{1}{\mu_0 \bar{\rho}}\mathcal{J}(\phi, b_x) - \mathcal{J}(\psi, u), \tag{5.1a}$$

$$\frac{\partial^3 \psi}{\partial t \partial z^2} = f\frac{\partial u}{\partial z} - \frac{g}{\bar{\rho}}\frac{\partial \rho}{\partial y} + \frac{B_0}{\mu_0 \bar{\rho}}\frac{\partial^3 \phi}{\partial z^3} + \nu\frac{\partial^4 \psi}{\partial z^4} + \frac{\partial}{\partial z}\left(\frac{1}{\mu_0 \bar{\rho}}\mathcal{J}\left(\phi, \frac{\partial \phi}{\partial z}\right) - \mathcal{J}\left(\psi, \frac{\partial \psi}{\partial z}\right)\right), \tag{5.1b}$$

$$\frac{\partial \rho}{\partial t} = \frac{N^2 \bar{\rho}}{g}\frac{\partial \psi}{\partial y} + \kappa\frac{\partial^2 \rho}{\partial z^2} - \mathcal{J}(\psi, \rho), \tag{5.1c}$$

$$\frac{\partial b_x}{\partial t} = -U'\frac{\partial \phi}{\partial z} + B_0\frac{\partial u}{\partial z} + \eta\frac{\partial^2 b_x}{\partial z^2} + \mathcal{J}(\phi, u) - \mathcal{J}(\psi, b_x), \tag{5.1d}$$

$$\frac{\partial^2 \phi}{\partial t \partial z} = B_0\frac{\partial^2 \psi}{\partial z^2} + \eta\frac{\partial^3 \phi}{\partial z^3} + \mathcal{J}\left(\phi, \frac{\partial \psi}{\partial z}\right) - \mathcal{J}\left(\psi, \frac{\partial \phi}{\partial z}\right), \tag{5.1e}$$

where $Q = f - U'$ is the vorticity. Note that we have differentiated (2.15) with respect to z so that we can substitute the magnetohydrostatic balance (2.16) (after differentiation with respect to y) into (2.15) to remove the perturbed pressure from the system of equations. Owing to the incompressibility and solenoidal conditions, we have also introduced the streamfunction ψ and magnetic streamfunction ϕ, which are defined as follows

$$v = -\frac{\partial \psi}{\partial z}, \quad w = \frac{\partial \psi}{\partial y}, \quad b_y = -\frac{\partial \phi}{\partial z}, \quad b_z = \frac{\partial \phi}{\partial y}. \tag{5.2}$$

The introduction of the streamfunctions gives rise to the Jacobian terms

$$\mathcal{J}(\alpha, \beta) = \frac{\partial \alpha}{\partial y}\frac{\partial \beta}{\partial z} - \frac{\partial \alpha}{\partial z}\frac{\partial \beta}{\partial y}, \tag{5.3}$$

which simplify the nonlinear terms of the equations (5.1).

We now nondimensionalise the equations of (5.1). We choose to nondimensionalise on the timescale $1/f_0$ (analogous to Chapters 3 and 4). We also choose to nondimensionalise the cross-stream and vertical scales with the flow lengthscale L and $f_0 L/N$, respectively; the latter is motivated by the parameter $A = |l|N/|k|f_0$ of Chapter 3 and 4, for which stable and unstable modes could occur with $A = O(1)$. Hence, the nondimensional time, latitude and height are given by

$$\hat{t} = f_0 t, \quad \hat{y} = \frac{y}{L}, \quad \hat{z} = \frac{N}{f_0 L}z. \tag{5.4}$$

We choose to nondimensionalise the perturbed horizontal velocities with the flow scale U_0 of the shear layer and the perturbed horizontal fields with $U_0\sqrt{\mu_0 \bar{\rho}}$. These choices lead to the following set of nondimensional variables

$$\{u, v\} = U_0\{\hat{u}, \hat{v}\}, \quad w = \frac{U_0 f_0}{N}\hat{w}, \quad \psi = \frac{U_0 f_0 L}{N}\hat{\psi}, \tag{5.5a}$$

$$\theta = f_0 L U_0 \hat{\theta}, \quad \rho = \frac{\bar{\rho} N U_0}{g}\hat{\rho}, \tag{5.5b}$$

$$\{b_x, b_y\} = U_0\sqrt{\mu_0\bar{\rho}}\{\hat{b}_x, \hat{b}_y\}, \quad b_z = \frac{U_0 f_0\sqrt{\mu_0\bar{\rho}}}{N}\hat{b}_z, \quad \phi = \frac{U_0 f_0 L}{N}\sqrt{\mu_0\bar{\rho}}\hat{\phi}. \tag{5.5c}$$

As a result of the nondimensionalisation (5.4), the velocity of the localised shear layer becomes

$$\hat{U}(\hat{y}) = \frac{U_0}{f_0 L}\tanh\hat{y}, \tag{5.6}$$

where $U = L f_0 \hat{U}$, since L is the chosen latitudinal lengthscale and $1/f_0$ is the chosen timescale.

Hence, the nondimensional parameters (5.4), (5.6) and scalings (5.5) allow us to recast equations (5.1) in the following nondimensional form (after dropping the hats):

$$\frac{\partial u}{\partial t} = -(1 - \Lambda\operatorname{sech}^2 y)\frac{\partial\psi}{\partial z} + \mathcal{M}\frac{\partial b_x}{\partial z} + \nu_0\frac{\partial^2 u}{\partial z^2} + \Lambda\left(\frac{1}{\mu_0\bar{\rho}}\mathcal{J}(\phi, b_x) - \mathcal{J}(\psi, u)\right), \tag{5.7a}$$

$$\frac{\partial^3\psi}{\partial t\partial z^2} = \frac{\partial u}{\partial z} - \frac{\partial\rho}{\partial y} + \mathcal{M}\frac{\partial^3\phi}{\partial z^3} + \nu_0\frac{\partial^4\psi}{\partial z^4} + \Lambda\frac{\partial}{\partial z}\left(\frac{1}{\mu_0\bar{\rho}}\mathcal{J}\left(\phi, \frac{\partial\phi}{\partial z}\right) - \mathcal{J}\left(\psi, \frac{\partial\psi}{\partial z}\right)\right), \tag{5.7b}$$

$$\frac{\partial\rho}{\partial t} = \frac{\partial\psi}{\partial y} + \kappa_0\frac{\partial^2\rho}{\partial z^2} - \Lambda\mathcal{J}(\psi, \rho), \tag{5.7c}$$

$$\frac{\partial b_x}{\partial t} = -\Lambda\operatorname{sech}^2 y\frac{\partial\phi}{\partial z} + \mathcal{M}\frac{\partial u}{\partial z} + \eta_0\frac{\partial^2 b_x}{\partial z^2} + \Lambda\left(\mathcal{J}(\phi, u) - \mathcal{J}(\psi, b_x)\right), \tag{5.7d}$$

$$\frac{\partial^2\phi}{\partial t\partial z} = \mathcal{M}\frac{\partial^2\psi}{\partial z^2} + \eta_0\frac{\partial^3\phi}{\partial z^3} + \Lambda\left(\mathcal{J}\left(\phi, \frac{\partial\psi}{\partial z}\right) - \mathcal{J}\left(\psi, \frac{\partial\phi}{\partial z}\right)\right), \tag{5.7e}$$

where we have also introduced the nondimensional parameters

$$\Lambda = \frac{U_0}{f_0 L}, \quad \mathcal{M} = \frac{N v_A}{f_0^2 L}, \quad \{\nu_0, \kappa_0, \eta_0\} = \frac{N^2}{f_0^3 L^2}\{\nu, \kappa, \eta\}. \tag{5.8}$$

The parameter Λ is analogous to the parameters as seen in Chapters 3 and 4, and can be interpreted as a Rossby number. The parameter $\mathcal{M}$ (not previously seen in this thesis) may be interpreted as a measure of magnetic field strength. The parameters ν_0, κ_0 and η_0 are analogous to the diffusive parameters (4.4) of Chapter 4; however, since here we have a prescribed latitudinal lengthscale L, the parameters ν_0, κ_0 and η_0 are now independent of wavenumbers. Note that the nondimensional velocity of the localised shear layer is $U(y) = \Lambda\tanh y$.

5.3 The Linear System

In this section we investigate the linear stability of the localised shear layer $U(y) = \tanh(y)$ on an f-plane in the presence of a magnetic field of uniform strength B_0 and with $Pr = Pm = 1$. We neglect the nonlinear terms from equations (5.7) and seek normal mode solutions of the form

$$(u, \psi, b_x, \phi, \rho) = Re\left((\overline{u}(Y), \overline{\psi}(Y), \overline{b}_x(Y), \overline{\phi}(Y), \overline{\rho}(Y))e^{iKz+St}\right), \tag{5.9}$$

where the dimensional vertical wavenumber is given by

$$k = \frac{NK}{f_0 L}, \tag{5.10}$$

which results from the factor used to nondimensionalise the vertical coordinate in (5.4).

Thus, with these normal mode solutions, the equations of (5.7) may be combined to yield the following second order equation for the streamfunction ψ (after dropping overbars):

$$\frac{d^2\psi}{dy^2} - K^2\left((S+\nu_0 K^2)^2 + K^2\mathcal{M}^2 + \left(1 + \frac{K^2\mathcal{M}^2}{(S+\nu_0 K^2)^2}\right)^{-1} - \Lambda\operatorname{sech}^2 y\right)\psi = 0. \tag{5.11}$$

The differential equation (5.11) can in fact be solved analytically (cf. Griffiths, 2003a; Park *et al.*, 2020). Note that we are considering one mode only; as noted by Griffiths (2008a) in the hydrodynamic case, taking this solution is not a concern if we are only interested in the most unstable (or lowest frequency). Supposing the streamfunction takes the form $\psi = \operatorname{sech}^\alpha(y)$, where $\alpha > 0$ so that the solutions decay as $|y| \to \infty$, equation (5.11) becomes

$$\alpha\left((\alpha+1)\left(1 - \operatorname{sech}^2 y\right) - 1\right) -$$
$$K^2\left((S+\nu_0 K^2)^2 + K^2\mathcal{M}^2 + \left(1 + \frac{K^2\mathcal{M}^2}{(S+\nu_0 K^2)^2}\right)^{-1} - \Lambda\operatorname{sech}^2 y\right) = 0. \tag{5.12}$$

In order to satisfy equation (5.12) for all latitudes we must choose α such that the coefficients of $\operatorname{sech}^2 y$ vanish. Thus, α must satisfy

$$\alpha(\alpha+1) = \Lambda K^2 \implies 2\alpha = -1 + \sqrt{1 + 4\Lambda K^2}, \tag{5.13}$$

where we have taken the positive sign of the square-root to ensure $\alpha > 0$. We note that α can be interpreted as a localisation parameter, where if α increases the mode becomes more localised since $v = \operatorname{sech}^\alpha y$. Hence, by making use of (5.13), equation (5.12) implies

$$(S+\nu_0 K^2)^4 + (S+\nu_0 K^2)^2\left(2\mathcal{M}^2 K^2 + 1 - \frac{1}{4K^2}\left(1 - \sqrt{1 + 4\Lambda K^2}\right)^2\right) +$$
$$\mathcal{M}^2 K^2\left(\mathcal{M}^2 K^2 - \frac{1}{4K^2}\left(1 - \sqrt{1 + 4\Lambda K^2}\right)^2\right) = 0. \tag{5.14}$$

Equation (5.14) is a quadratic in $(S + \nu_0 K^2)^2$ and thus can be solved analytically, yielding

$$(S+\nu_0 K^2)^2 = \frac{1}{8K^2}\left(1 - \sqrt{1 + 4\Lambda K^2}\right)^2 - \frac{1}{2} - \mathcal{M}^2 K^2 \pm$$
$$\frac{1}{2}\sqrt{\left(1 - \frac{1}{4K^2}\left(1 - \sqrt{1 + 4\Lambda K^2}\right)^2\right)^2 + 4\mathcal{M}^2 K^2}, \tag{5.15}$$

where the negative sign guarantees stability and the positive sign allows the system to be unstable within certain parameter regimes.

Before analysing the magnetohydrodynamic system described by equations (5.14) and (5.15), we first give a brief overview of the hydrodynamic system. This is in part as we have only analysed a uniform shear flow in the thesis thus far and it is important to distinguish the two cases in the simplest regime. The analysis will also us to determine the possible effects of magnetic field on the hydrodynamic system.

5.3.1 The Hydrodynamic System

We first address the hydrodynamic system in the absence of diffusion, for which equation (5.15) reduces to

$$S^2 = \frac{1}{4K^2}\left(1 - \sqrt{1 + 4\Lambda K^2}\right)^2 - 1, \tag{5.16}$$

as found in Griffiths (2008a). By setting $S = 0$ and manipulating, we obtain the following condition for hydrodynamic instability

$$K > \frac{1}{\Lambda - 1} \quad \text{with} \quad \Lambda > 1. \tag{5.17}$$

Note that $\Lambda < 1$ guarantees stability. By differentiating (5.16) with respect to K, we find that the maximum growth rate of the hydrodynamic system is $S_{\max} = \sqrt{\Lambda - 1}$ and occurs in the large K limit (i.e., vanishing vertical scales).

In the presence of diffusion, with $Pr = Pm = 1$, as we have already noted in Chapter 4, we can obtain the growth rate of the diffusive system by considering the transformation $S_I \rightarrow S + \nu_0 K^2$, where S_I is the ideal growth rate given by equation (5.16). Thus, by applying the transformation to (5.16) we obtain the following equation for the growth rate:

$$(S + \nu_0 K^2)^2 = \frac{1}{4K^2}\left(1 - \sqrt{1 + 4\Lambda K^2}\right)^2 - 1. \tag{5.18}$$

Note that (5.18) can also be derived by simply setting $\mathcal{M} = 0$ in (5.15). It is difficult to make analytical progress from (5.18); however, the transformation $S_I \rightarrow S + \nu_0 K^2$ allows us to infer that the maximum growth rate can no longer occur in the large K limit (as we would expect since vertical diffusion will stabilise the small vertical scales) since the transformation dictates we subtract $\nu_0 K^2$ from the inviscid growth rate (which is $\sqrt{\Lambda - 1}$ at its maximum). Hence, the maximum growth rate occurs at some finite K, which is desirable physically and in nonlinear simulations.

5.3.2 The Ideal System

On returning to the magnetohydrodynamic regime we first consider the ideal system. Thus, setting $\nu_0 = 0$ in (5.14) yields the following quadratic for the growth rate squared:

$$S^4 + S^2 \left(2\mathcal{M}^2 K^2 + 1 - \frac{1}{4K^2} \left(1 - \sqrt{1 + 4\Lambda K^2} \right)^2 \right) +$$
$$\mathcal{M}^2 K^2 \left(\mathcal{M}^2 K^2 - \frac{1}{4K^2} \left(1 - \sqrt{1 + 4\Lambda K^2} \right)^2 \right) = 0, \quad (5.19)$$

yielding

$$S^2 = \frac{1}{8K^2} \left(1 - \sqrt{1 + 4\Lambda K^2} \right)^2 - \frac{1}{2} - \mathcal{M}^2 K^2 \pm$$
$$\frac{1}{2} \sqrt{ \left(1 - \frac{1}{4K^2} \left(1 - \sqrt{1 + 4\Lambda K^2} \right)^2 \right)^2 + 4\mathcal{M}^2 K^2 }, \quad (5.20)$$

where the negative sign guarantees stability and the positive sign allows the system to be unstable, provided

$$K^2 < \frac{\Lambda - \mathcal{M}}{\mathcal{M}^2}. \quad (5.21)$$

The stability bound (5.21) can be determined (after some manipulation) by setting $S = 0$ in (5.19) or (5.20). Note that setting $\mathcal{M} = 0$ in (5.21) does not allow us to derive the analogous hydrodynamic stability bound (5.17) owing to a division by $\mathcal{M}^2$ within the bounds derivation. Interestingly, (5.21) implies that given sufficiently small $\mathcal{M}$ with any $\Lambda > 0$, then instability is possible for any vertical wavenumber K. This is in direct contrast to the hydrodynamic system, where $\Lambda > 1$ is a necessary condition for instability; thus, as in Chapters 3 and 4, we have shown that magnetic field can generate instability in the hydrodynamically stable regime. In fact, taking $\mathcal{M}^2 K^2 = O(1) < \Lambda$ with $\mathcal{M} \ll 1$ corresponds to the "thin disc" and "weak field" limits considered by Balbus & Hawley (1991); we have already discussed this interpretation in Chapter 3. Thus, we expect instabilities analogous to the magnetorotational instability for $\Lambda < 1$.

Owing to the various factors of K^2 that occur outside and within square-roots it is difficult to make analytical progress, including determining the maximum growth rate. However, motivated by the results of Chapter 3, where the maximum growth rate occurs with $\mathcal{L} = |k| v_A / f_0 = O(1)$ and $A \ll 1$, with one possible interpretation being that the vertical wavenumber $k \to \infty$ with $k \sim f_0 / v_A$ (so that $\mathcal{L} = O(1)$, we suppose $K \to \infty$ such that $MK = \mathcal{L} = O(1)$ (i.e., weak magnetic field). In this limit, equation (5.20) reduces to

$$S^2 = \frac{\Lambda}{2} - \frac{1}{2} - \mathcal{M}^2 \mathcal{K}^2 \pm \frac{1}{2} \sqrt{(1 - \Lambda)^2 + 4\mathcal{M}^2 \mathcal{K}^2}, \quad (5.22)$$

which is equivalent to equation (3.24) of Chapter 3 upon writing $\mathcal{M}^2 K^2 = \mathcal{L}^2$ and setting $A = 0$ in (3.24). Indeed, differentiating (5.22) with respect to $\mathcal{L} = MK$ and setting the derivative to zero implies that for $\Lambda < 2$, the maximum growth rate is $\Lambda / 2$ and occurs when

$$\mathcal{M}^2 K^2 = \frac{\Lambda}{4} (2 - \Lambda). \quad (5.23)$$
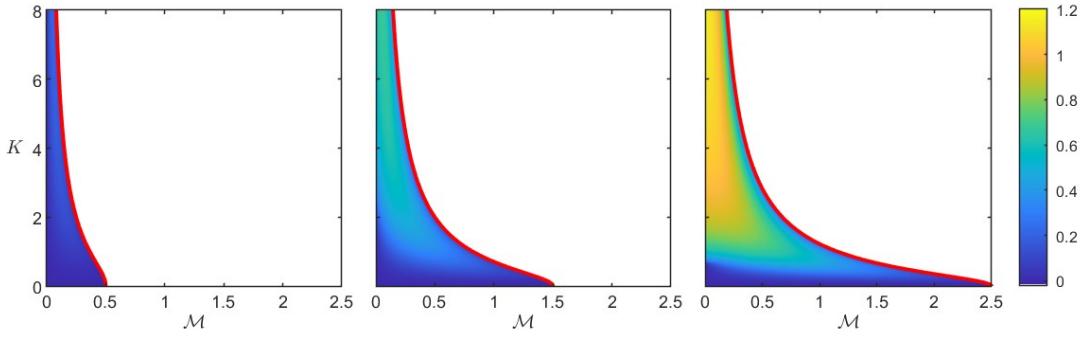
Figure 5.1: The growth rate in $(K, \mathcal{M})$-space for $\nu_0 = 0$ (ideal) with $\Lambda = 0.5$ (left), $\Lambda = 1.5$ (centre) and $\Lambda = 2.5$ (right). The solid red line represents the stability bound (5.21).

For $\Lambda > 2$ the maximum growth rate is $S = \sqrt{\Lambda - 1}$ and occurs when $\mathcal{M} = 0$ (i.e., the maximum growth rate of the hydrodynamic system). This criterion is entirely equivalent to the equations (3.26) and (3.27) of Chapter 3 which give the maximum growth rates and at what points they occur in parameter space for $\Lambda < 2$ and $\Lambda > 2$.

We contour the growth rate in $(K, \mathcal{M})$-space with $\Lambda = 0.5$, 1.5 and 2.5 in figure 5.1. The solid red line represents the necessary and sufficient stability condition (5.21), which is valid for all Rossby numbers Λ with $\mathcal{M} \neq 0$. For $\Lambda = 0.5$, the system is hydrodynamically stable; however, we find for any $\mathcal{M} < \Lambda/2$ that instability can occur for sufficiently small K. Thus, even infinitesimally weak magnetic field strength allows instability to occur in the hydrodynamically stable regime. The maximum growth rate occurs in the large K limit as $\mathcal{M} \to 0$, which is consistent with equation (5.23). Note that this limit corresponds to the "thin disc" and "weak field" limits considered in Balbus & Hawley (1991); the instabilities present are analogous to the magnetorotational instability. For the cases $\Lambda = 1.5$ and $\Lambda = 2$, the system is hydrodynamically unstable for $K > (\Lambda - 1)^{-1}$ ($K = 2$ for $\Lambda = 1.5$ and $K = 2/3$ for $\Lambda = 2.5$) and hydrodynamically stable otherwise. On inspection, it is clear that even weak magnetic field generates instability in the hydrodynamically stable regimes ($K < (\Lambda - 1)^{-1}$). However, in the hydrodynamically unstable regime, the effect of weak magnetic field is less clear; indeed, depending upon the value of K, it seems that weak magnetic field can either reduce or increase the growth rate. In both cases it is clear that the maximum growth rate occurs in the large K limit with sufficiently small $\mathcal{M}$, which is consistent with (5.23).

Figure 5.1 shows that weak magnetic field induces instability within certain parameter regimes, including the hydrodynamically stable regime with $\Lambda < 1$. We consider the weak field regime to categorise the behaviour of the system. For small $\mathcal{M}$, equation (5.20) implies that the roots take the form

$$S_H^2 = \frac{1}{4K^2}\left(1 - \sqrt{1 + 4\Lambda K^2}\right)^2 - 1 -$$
$$\frac{2 - \frac{1}{4K^2}\left(1 - \sqrt{1 + 4\Lambda K^2}\right)^2}{1 - \frac{1}{4K^2}\left(1 - \sqrt{1 + 4\Lambda K^2}\right)^2} K^2 \mathcal{M}^2 + O(\mathcal{M}^4), \quad (5.24)$$

$$S_{\mathcal{M}}^2 = \frac{\frac{1}{4K^2}\left(1 - \sqrt{1 + 4\Lambda K^2}\right)^2}{1 - \frac{1}{4K^2}\left(1 - \sqrt{1 + 4\Lambda K^2}\right)^2} K^2 \mathcal{M}^2 + O(\mathcal{M}^4), \tag{5.25}$$

where S_H is the hydrodynamic root at leading order (unstable if $K > (\Lambda - 1)^{-1}$ with $\Lambda > 1$), while $S_{\mathcal{M}}$ is the magnetic root (unstable if $K < (\Lambda - 1)^{-1}$) and reduces to $S_{\mathcal{M}} = 0$ in the absence of magnetic field.

Clearly, the expansions (5.24) and (5.25) break down when $1 - \left(1 - \sqrt{1 + 4\Lambda K^2}\right)^2 / 4K^2$ is sufficiently close to zero since the leading and first order terms in $\mathcal{M}^2$ become comparable. We address this by supposing $\left(1 - \sqrt{1 + 4\Lambda K^2}\right)^2 / 4K^2 - 1 = \beta\mathcal{M}$ for some constant β of order unity, and substitute into (5.19) to derive the expression

$$S_B^2 = \frac{1}{8K^2}\left(1 - \sqrt{1 + 4\Lambda K^2}\right)^2 - \frac{1}{2} \pm$$
$$\frac{1}{2}\sqrt{\left(\frac{1}{4K^2}\left(1 - \sqrt{1 + \Lambda K^2}\right)^2 - 1\right)^2 + 4K^2\mathcal{M}^2} + O(\mathcal{M}^2), \tag{5.26}$$

or, equivalently

$$S_B^2 = \frac{1}{2}\beta\mathcal{M} + \frac{\mathcal{M}}{2}\sqrt{\beta^2 + K^2} + O(\mathcal{M}^2), \tag{5.27}$$

where S_B^2 is the "breakdown" (or singular) root, which is valid for $\chi = \left(1 - \sqrt{1 + 4\Lambda K^2}\right)^2 / 4K^2 - 1$ sufficiently close to zero. Note that this condition is equivalent to K being sufficiently close to $(\Lambda - 1)^{-1}$, where if $K \to (\Lambda - 1)^{-1}$ from above, $\chi \to 0^+$, while if $K \to (\Lambda - 1)^{-1}$ from below, $\chi \to 0^-$. The positive sign of (5.26) corresponds to unstable modes while the negative sign corresponds only to stable modes. Expressions (5.24), (5.25) and (5.26) describe the entire weak field regime.

Together, the expansions (5.24), (5.25) and (5.26) indicate that if the flow is hydrodynamically stable ($K < (\Lambda - 1)^{-1}$), then the growth rate of the most unstable mode is given by $S_{\mathcal{M}}^2$ (equation (5.25)). Thus, when the flow is hydrodynamically stable, the first order variation in $\mathcal{M}^2$ of equation (5.25) indicates that weak magnetic field is destabilising. However, if the flow is hydrodynamically unstable ($K > (\Lambda - 1)^{-1}$), then the growth rate of the most unstable mode is given by S_H^2 (equation (5.24)). Thus, when the flow is hydrodynamically unstable, the first order variation in $\mathcal{M}^2$ of equation (5.24) indicates that if $\Lambda < 2$, then weak magnetic field increases the growth rate. Similarly, if $\Lambda > 2$, weak magnetic field increases the growth rate provided $K(\Lambda - 2) < \sqrt{2}$ and stabilises if $K(\Lambda - 2) > \sqrt{2}$. Note that we will plot the expansions alongside the exact growth rate against $\mathcal{M}$ at various K to illustrate their accuracy after deriving analogous expansions in the diffusive regime.

We are yet to consider the singular expansion (5.26) in the weak field limit and how it relates to the hydrodynamic and magnetic expansions (5.24) and (5.25). Indeed, we find that when K is not close to $|\Lambda - 1|^{-1}$, the singular expansion (5.26) still describes the exact root (5.20) in the weak field limit. The reason for this can be determined by taking the second order correction of (5.26), which to $O(\mathcal{M}^3)$ gives (5.20) in the small $\mathcal{M}$ limit. However, this does explain why the

singular root (5.26) captures the weak field behaviour of any mode with $K - |\Lambda - 1|^{-1} \neq 0$. To determine how the two roots of (5.26) link to (5.24) and (5.25) in the weak field limit, we consider the large $|\beta|$ limit of (5.26) and compare with the small $|\beta|$ limit of (5.24) and (5.25). Specifically, the positive root of (5.26) yields

$$\frac{S^2}{\mathcal{M}} \to \frac{\beta + |\beta|(1 + 2/\beta^2 + \cdots)}{2} \sim \begin{cases} -1/\beta & \beta < 0, \\ \beta & \beta > 0, \end{cases} \text{ as } |\beta| \to \infty. \tag{5.28}$$

Similarly, the negative root of (5.26) yields

$$\frac{S^2}{\mathcal{M}} \to \frac{\beta - |\beta|(1 + 2/\beta^2 + \cdots)}{2} \sim \begin{cases} \beta & \beta < 0, \\ -1/\beta & \beta > 0, \end{cases} \text{ as } |\beta| \to \infty. \tag{5.29}$$

We also find that the hydrodynamic root (5.24) gives

$$S^2 \sim \beta\mathcal{M} \text{ as } \beta \to 0, \tag{5.30}$$

while the magnetic root (5.25) yields

$$S^2 \sim \frac{\beta\mathcal{M} - 1}{\beta}\mathcal{M} \sim -\frac{\mathcal{M}}{\beta} \text{ as } \beta \to 0. \tag{5.31}$$

Thus, (5.28) shows that the +ve root in (5.26) becomes the hydrodynamic root (5.24) as $\beta \to +\infty$ and the magnetic root (5.25) as $\beta \to -\infty$ (or, the hydrodynamic root (5.24) becomes the magnetic root (5.25) as K increases through $(\Lambda - 1)^{-1}$). Likewise, (5.29) shows that the $-$ve root in (5.26) becomes the magnetic root (5.25) as $\beta \to +\infty$ and the hydrodynamic root (5.24) as $\beta \to -\infty$ (or, the hydrodynamic root (5.24) becomes the magnetic root (5.25) as K decreases through $\Lambda - 1$). So the roots exchange identity as K passes through $\Lambda - 1$. The hydrodynamic mode is not a single entity that can be tracked through parameter space, and neither is the magnetic mode. This has important implications when considering the system; instead of considering a hydrodynamic and a magnetic mode (stable and unstable), we can consider an unstable mode and a stable mode only.

5.3.3 Contours of the Growth rate in $(K, \mathcal{M})$-space

We now return to the diffusive magnetohydrodynamic system described by equation (5.15) and provide contours of the growth rate in $(\mathcal{M}, K)$-space for various Λ and ν_0. The vertical domain length in the nonlinear simulations will be taken to be $H = 2\pi/K_{\max}$, where $K_{\max}$ is the vertical wavenumber at which the growth rate is maximised for given $\mathcal{M}$, Λ and ν_0. When relevant, we will indicate these points in $(K, \mathcal{M})$-space (for given ν_0 and Λ) with red dots so that these may be easily distinguished when referring back from the nonlinear analysis.

We contour the growth rate in $(K, \mathcal{M})$-space for various ν_0 in figures 5.2, 5.3 and 5.4 for $\Lambda = 0.5$, $\Lambda = 1.5$ and $\Lambda = 2.5$, respectively. We can see that the maximum growth rate no longer occurs as $K \to \infty$, owing to vertical diffusion stabilising the small scale modes. The maximum growth rate now occurs at a finite vertical wavenumber K (indicated by the white cross), which is both desirable physically and when considering the nonlinear evolution numerically. In general, as the magnitude of diffusion increases, the most unstable mode occurs at smaller vertical
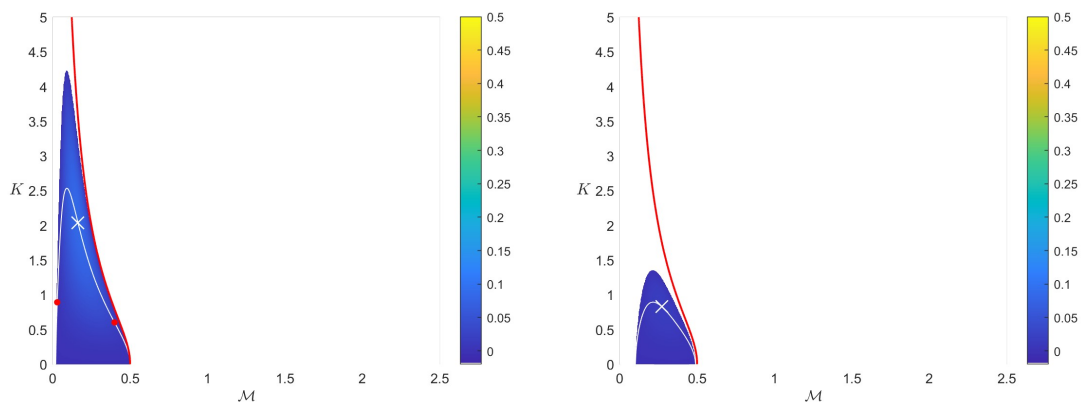
Figure 5.2: The growth rate in $(K, \mathcal{M})$-space for $\Lambda = 0.5$ with $\nu_0 = 0.01$ (left) and $\nu_0 = 0.05$ (right). The solid red line represents the magnetic bound (5.21). The solid white line represents the vertical wavenumber $K_{\max}$ that generates the maximum growth rate for each given $\mathcal{M}$. The white cross represents the maximum growth rate in the entire $(K, \mathcal{M})$ domain. The red dots indicate points that will be relevant in the nonlinear analysis.
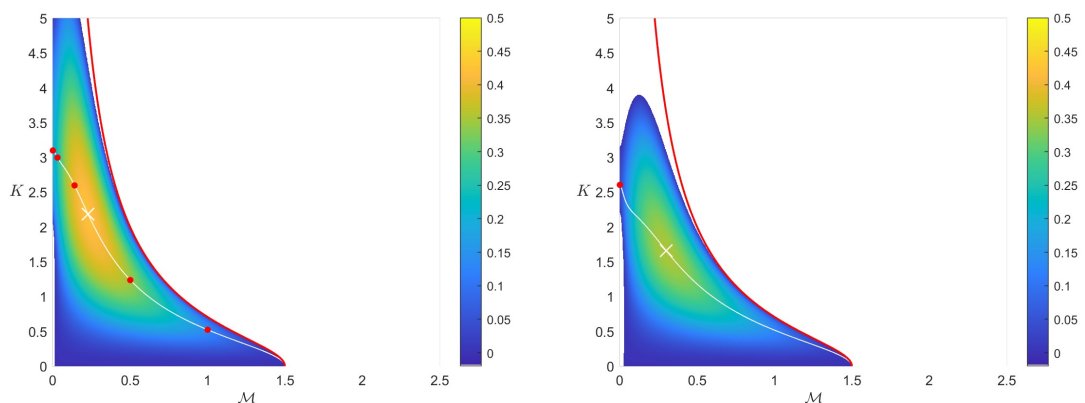
Figure 5.3: The growth rate in $(K, \mathcal{M})$-space for $\Lambda = 1.5$ with $\nu_0 = 0.02$ (left) and $\nu_0 = 0.04$ (right). Other details as in figure 5.2.

wavenumber K and at a larger magnetic field strength $\mathcal{M}$. Indeed, weak magnetic field always increases the growth rate of the hydrodynamic system. The large-scale modes (small K) are somewhat insensitive to increasing diffusion.

5.3.4   Limit of Weak Magnetic Field

In contrast to the ideal case, the effect of weak magnetic field on the hydrodynamic system in figures 5.2, 5.3 and 5.4 is much clearer; however, it is still of interest to investigate the limit of weak magnetic field to confirm the behaviour and determine how the growth rate scales with $\mathcal{M}$ and other parameters. As we have already noted, the diffusive growth rate S can be obtained via the transformation $S_I = S + \nu_0 K^2$, where S_I is the growth rate of the ideal system. Thus, the
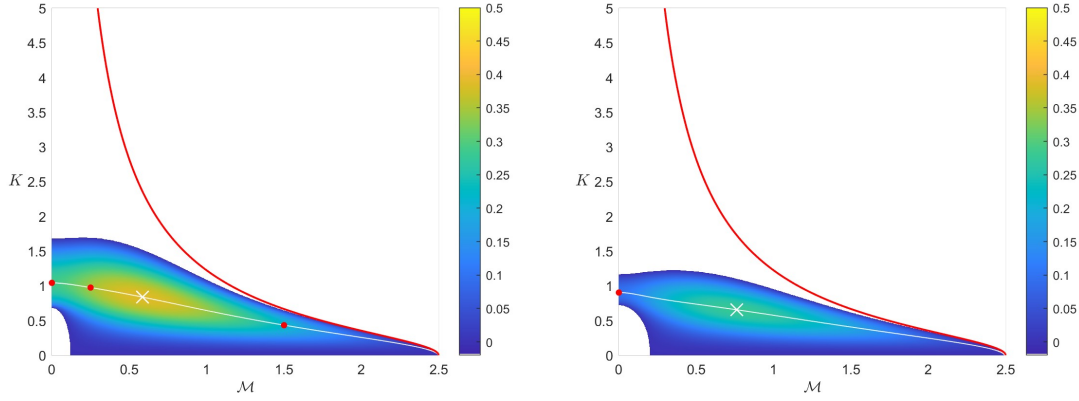
Figure 5.4: The growth rate in $(K, \mathcal{M})$-space for $\Lambda = 2.5$ with $\nu_0 = 0.3$ (left) and $\nu_0 = 0.5$ (right). Other details as in figure 5.2.

ideal weak magnetic field expansions (5.24), (5.25) and (5.26) become

$$S_H + \nu_0 K^2 = \left(\frac{1}{4K^2} \left(1 - \sqrt{1 + 4\Lambda K^2} \right)^2 - 1 \right)^{\frac{1}{2}} +$$

$$\frac{1 - \frac{1}{8K^2} \left(1 - \sqrt{1 + 4\Lambda K^2} \right)^2}{\left(\frac{1}{4K^2} \left(1 - \sqrt{1 + 4\Lambda K^2} \right)^2 - 1 \right)^{\frac{3}{2}}} K^2 \mathcal{M}^2 + O(\mathcal{M}^4), \quad (5.32)$$

$$S_{\mathcal{M}} + \nu_0 K^2 = \frac{\frac{1}{2K} \left(\sqrt{1 + 4\Lambda K^2} - 1 \right)}{\left(1 - \frac{1}{4K^2} \left(1 - \sqrt{1 + 4\Lambda K^2} \right)^2 \right)^{\frac{1}{2}}} K\mathcal{M} + O(\mathcal{M}^3), \quad (5.33)$$

$$S_B + \nu_0 K^2 = \left(\frac{1}{2} \beta \mathcal{M} + \frac{\mathcal{M}}{2} \sqrt{\beta^2 + K^2} \right)^{\frac{1}{2}} + O(\mathcal{M}), \quad (5.34)$$

where S_H is the hydrodynamic root, $S_{\mathcal{M}}$ is the magnetic root and S_B^2 is the "breakdown" (or singular) root which is valid for $\left(1 - \sqrt{1 + 4\Lambda K^2} \right)^2 / 4K^2 - 1$ sufficiently close to zero, which is when the leading and first order terms in $\mathcal{M}^2$ of (5.32) and (5.33) become comparable. Note that this condition is equivalent to K being sufficiently close to $|\Lambda - 1|^{-1}$.

In figure 5.5 we illustrate the accuracy of the expansions (5.32) and (5.33) by plotting them with the exact growth rate (calculated numerically from (5.15)) against the magnetic field strength $\mathcal{M}$ at various ν_0. This also ensures the accuracy of the ideal expansions (5.24) and (5.25) since plots are included with $\nu_0 = 0$. The expansions capture the scale of the growth rate for small $\mathcal{M}$, with the magnetic expansion (5.33) retaining accuracy for much larger $\mathcal{M}$. The expansions (5.32) and (5.33) are plotted for relatively small ν_0 since these values will be used in the following nonlinear analysis. As ν_0 increases, the interval of $\mathcal{M}$ that the expansions accurately describe decreases. For example, at $K = 0.30$ in the right panel of figure 5.4 where $\nu_0 = 0.5$, $\mathcal{M} \approx 0.25$ is required for instability. However, at this value of $\mathcal{M}$ the magnetic expansion (5.32) is no longer accurate as seen in figure 5.5. Note that the singular expansion also accurately describes the growth rate of the unstable modes.
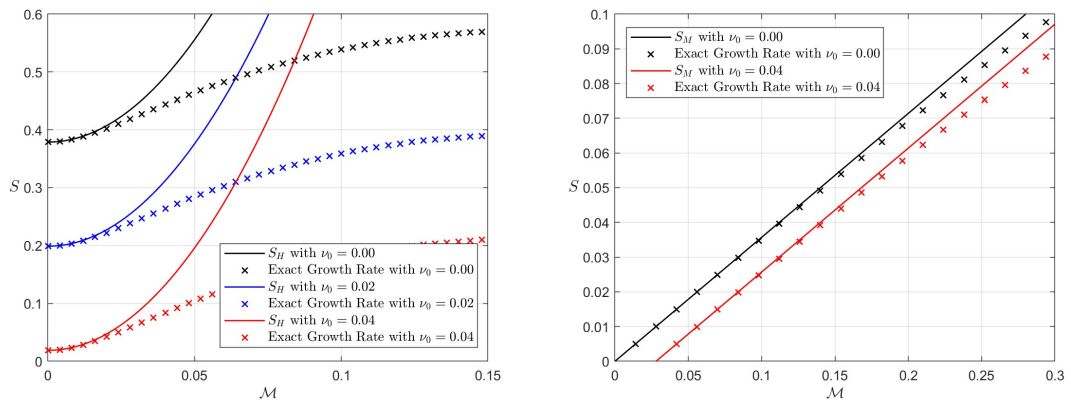
Figure 5.5: The estimated growth rates S_H (left panel) and $S_{\mathcal{M}}$ (right panel) plotted with the exact growth rate against $\mathcal{M}$ for various ν_0.

5.4 Nonlinear Numerical Model

In this and following sections we discuss the nonlinear evolution of the system. Here we lay out the numerical method used to solve the nonlinear equations (5.7).

Owing to the nature of the solutions to the perturbed quantities of the linear system, which are periodic in the vertical and exponentially decaying in the latitudinal direction (since they are proportional to $\operatorname{sech}^\alpha y$ with $\alpha > 0$), we consider a double periodic domain. Assuming periodicity in the latitudinal direction rather than considering another configuration (e.g., a model with latitudinal boundaries) greatly simplifies the numerical scheme. The vertical domain length H is determined for given parameters Λ, $\mathcal{M}$ and ν_0 using the vertical wavenumber K, $K_{\max}$ say, that generates the maximum growth rate of the linear system. Hence, we take the vertical domain length $H = 2\pi/K_{\max}$. One may suspect we could also use the latitudinal domain length L that is motivated by the linear problem (via the parameter α); however, the nonlinear evolution has a tendency to redistribute vorticity and, to a greater extent, the perturbed magnetic field quantities (b_x and ϕ) latitudinally (the later being noted in Hawley & Balbus, 1992; Balbus & Hawley, 1992). Thus, the latitudinal domain lengths L chosen throughout this section are determined by preliminary runs of the simulations, where the perturbed quantities are ensured to have decayed sufficiently by the latitudinal boundary. We determine that the perturbed quantities have decayed sufficiently by numerically comparing their maximum values (which are generally located in the centre of the domain) against the maximum of the quantity at the latitudinal boundary — if the ratio of the minimum to maximum is larger than the tolerance $[O(10^{-5})]$ then a larger domain length is used in a following simulation. A smaller tolerance is not necessary since, in general, the magnetic perturbed quantities only violate the tolerance (at smaller values) near the end of the simulation, where they have no dynamical significance since they decay while redistributing latitudinally. Hence, given L and H, we set the domain to be $y \in [-L/2, L/2]$ and $z \in [-H/2, H/2]$ in all numerical runs. In all simulations, the perturbed quantities are initialised with random "noise"

with initial amplitude 10^{-5}. The numerical resolution taken in each will be sufficient to ensure the evolution is resolved, and will vary from case to case.

Two numerical schemes are employed to treat the nonlinear equations (5.7). The diffusive terms are treated using Crank–Nicolson (CN), while the remaining linear terms and nonlinear terms are treated using three-step Adams–Bashforth (AB3). We initialise the time-stepping with a one-step Euler method, followed by a two-step Adams–Bashforth (AB2). Owing to the use of the CN method we are restricted to a second order scheme; one may therefore argue that the use of AB3 is unnecessary, however, this is implemented to ensure numerical stability provided a sufficiently small timestep is used (Durran, 1991). If AB2 were used to treat the (non-diffusive) linear and nonlinear terms, the scheme would be at best always weakly numerically unstable given any timestep. Indeed, the use of AB3 yields numerical stability, given a sufficiently small timestep, and also allows for the use of a timestep an order of magnitude larger than needed for the AB2 scheme.

5.4.1 Discretisation

Thus, by considering a double Fourier space, where nonlinear terms are calculated in real space (and then transformed back into Fourier space), we apply the above numerical scheme to the equations of (5.7), yielding the following discretisation. The along-stream and cross-stream momentum equations (5.7a) and (5.7b) become

$$\frac{u^{n+1} - u^n}{\Delta t} = \frac{23}{12}\hat{u}^n - \frac{16}{12}\hat{u}^{n-1} + \frac{5}{12}\hat{u}^{n-2} - k_z^2 \nu_0 \left(\frac{1}{2}u^{n+1} + \frac{1}{2}u^n\right), \tag{5.35}$$

$$-k_z^2 \frac{\psi^{n+1} - \psi^n}{\Delta t} = \frac{23}{12}\hat{\psi}^n - \frac{16}{12}\hat{\psi}^{n-1} + \frac{5}{12}\hat{\psi}^{n-2} + k_z^4 \nu_0 \left(\frac{1}{2}\psi^{n+1} + \frac{1}{2}\psi^n\right), \tag{5.36}$$

where

$$\hat{u}^n = -ik_z Q\psi^n + ik_z \mathcal{M}b_x^n + \Lambda(\mathcal{J}^n(\phi, b_x) - \mathcal{J}^n(\psi, u)), \tag{5.37}$$

$$\hat{\psi}^n = ik_z u^n - ik_y \rho^n - ik_z^3 \mathcal{M}\phi^n + k_z^4 \nu_0 \psi^n + ik_z \Lambda(\mathcal{J}^n(\phi, ik_z\phi) - \mathcal{J}^n(\psi, ik_z\psi)), \tag{5.38}$$

and

$$\mathcal{J}^n(\alpha, \beta) = \frac{\partial \alpha^n}{\partial y}\frac{\partial \beta^n}{\partial z} - \frac{\partial \alpha^n}{\partial z}\frac{\partial \beta^n}{\partial y}. \tag{5.39}$$

The thermodynamic equation (5.7c) becomes

$$\frac{\rho^{n+1} - \rho^n}{\Delta t} = \frac{23}{12}\hat{\rho}^n - \frac{16}{12}\hat{\rho}^{n-1} + \frac{5}{12}\hat{\rho}^{n-2} - k_z^2 \kappa_0 \left(\frac{1}{2}\rho^{n+1} + \frac{1}{2}\rho^n\right), \tag{5.40}$$

where

$$\hat{\rho}^n = ik_y \psi^n + \Lambda \mathcal{J}^n(\psi, \rho). \tag{5.41}$$

Finally, the along-stream and cross-stream induction equations (5.7d) and (5.7e) take the form

$$\frac{b_x^{n+1} - b_x^n}{\Delta t} = \frac{23}{12}\hat{b}_x^n - \frac{16}{12}\hat{b}_x^{n-1} + \frac{5}{12}\hat{b}_x^{n-2} - k_z^2 \eta_0 \left(\frac{1}{2}b_x^{n+1} + \frac{1}{2}b_x^n\right), \tag{5.42}$$

$$-k_z^2 \frac{\phi^{n+1} - \phi^n}{\Delta t} = \frac{23}{12} \hat{\phi}^n - \frac{16}{12} \hat{\phi}^{n-1} + \frac{5}{12} \hat{\phi}^{n-2} - ik_z^3 \eta_0 \left(\frac{1}{2} \phi^{n+1} + \frac{1}{2} \phi^n \right), \qquad (5.43)$$

where

$$\hat{b}_x^n = -ik_z \Lambda \operatorname{sech}^2 y \phi^n ik_z \mathcal{M} u^n + \Lambda (\mathcal{J}^n(\phi, u) - \mathcal{J}^n(\psi, b_x)), \qquad (5.44)$$

and

$$\hat{\phi} = -k_z^2 \mathcal{M} \psi^n + \Lambda (\mathcal{J}^n(\phi, ik_z\phi) - \mathcal{J}^n(\psi, ik_z\phi)). \qquad (5.45)$$

5.4.2 Reynolds Numbers

The Reynolds number and the magnetic Reynolds number give an indication of the level of non-linearity throughout the evolution of the flow. For example, given a small Reynolds and magnetic Reynolds number such that instability is still possible, then we expect the evolution to be highly diffusive and weakly nonlinear; for large Reynolds and magnetic Reynolds numbers we expect the evolution to be strongly nonlinear.

The Reynolds number Re is defined as the ratio between advection and kinematic viscosity and is therefore given by

$$Re = \frac{[(\mathbf{u} \cdot \nabla)\mathbf{u}]}{[\nu \nabla^2 \mathbf{u}]}. \qquad (5.46)$$

Typically, the lengthscales of the advection and diffusion terms are assumed to be the same; however, owing to the magnetohydrostatic approximation, we must neglect latitudinal diffusion, so that $\nabla^2 \sim k^2 \sim N^2/f_0^2 L^2$. Hence,

$$Re = \frac{[(\mathbf{u} \cdot \nabla)\mathbf{u}]}{[\nu \nabla^2 \mathbf{u}]} = \frac{U_0^2/L}{\nu N^2 U_0/f_0^2 L^2} = \frac{U_0^2/L}{\nu_0 U_0/f_0} = \frac{\Lambda}{\nu_0}. \qquad (5.47)$$

The Magnetic Reynolds number Rm is defined as ratio between induction and magnetic diffusion and is therefore given by

$$Rm = \frac{[\nabla \times (\mathbf{u} \times \mathbf{B})]}{[\eta \nabla^2 \mathbf{B}]}. \qquad (5.48)$$

Analogous to the derivation of the Reynolds number, here the lengthscales of the induction and diffusion terms differ owing to the magnetohydrostatic approximation, where latitudinal diffusion is neglected so that $\nabla^2 \sim N^2/f_0^2 L^2$. Thus,

$$\mathrm{R}_m = \frac{[\nabla \times (\mathbf{u} \times \mathbf{B})]}{[\eta \nabla^2 \mathbf{B}]} = \frac{U_0^2 \sqrt{\mu_0 \bar{\rho}}/L}{\eta U_0 N^2 \sqrt{\mu_0 \bar{\rho}}/f_0^2 L^2} = \frac{U_0 f_0^2 L}{\eta N^2} = \frac{U_0}{f_0 L} \cdot \frac{f_0^3 L^2}{\eta N^2} = \frac{\Lambda}{\eta_0}. \qquad (5.49)$$

Note that since we are considering the case $Pr = Pm = 1$ only, it follows that $Re = Rm$.

5.4.3 Energetics

In Chapter 2 we derived the dimensional equation (2.20), which governs the rate of change of the total energy in the system for a fixed volume V and closed surface S. We can recast equation (2.20) in nondimensional form by scaling the total energy E by the kinetic energy K_E, where

$K_E \sim \bar{\rho}U_0^2$, so that $E = \bar{\rho}U_0^2\hat{E}$. Hence, after dropping the hats, the rate of change of the total energy of the system (2.20) in nondimensional form is

$$\frac{dE}{dt} = \frac{1}{2}\frac{d}{dt}\int_V \left(|\mathbf{u}|^2 + \rho^2 + |\mathbf{B}|^2\right) dV = -\nu_0 \int_V |\omega|^2 \, dV$$

$$- \kappa_0 \int_V |\nabla\rho|^2 \, dV - \eta_0 \int_V |\mathbf{j}|^2 dV, \quad (5.50)$$

where the nondimensional current, local vorticity and density gradient are given by

$$\mathbf{j} = \frac{U_0 N}{f_0 L}\sqrt{\frac{\bar{\rho}}{\mu_0}}\mathbf{j}, \quad \omega = \frac{U_0 N}{f_0 L}\omega, \quad \nabla\rho = \frac{\bar{\rho}N^2 U_0}{gLf_0}\nabla\rho. \quad (5.51)$$

The volume integrals in (5.50) are surface integrals over y and z due to axisymmetry.

The Basic State Energy Balance

It is important to investigate the ratio of the kinetic and magnetic energy throughout the evolution of the system. We begin by considering the dimensional ratio of initial kinetic energy to initial magnetic energy. The initial kinetic energy in dimensional terms is given by

$$\int_V \bar{\rho}|\mathbf{u}_{\text{initial}}|^2 dV = \bar{\rho}U_0^2 \int_V \tanh^2 y \, dV, \quad (5.52)$$

whereas initial magnetic energy in dimensional terms is given by

$$\int_V \frac{1}{\mu_0}|\mathbf{B}_{\text{initial}}|^2 dV = \frac{1}{\mu_0}\int_V \frac{\bar{\rho}\mu_0 L^2 f_0^4}{N^2}\mathcal{M}^2 \, dV = \bar{\rho}f_0^2 L^2 \delta^2 \mathcal{M}^2 \int_V dV, \quad (5.53)$$

where we have made use of the nondimensional scalings (5.5), nondimensional parameters (5.8) and the definition of the Alfvén velocity $v_A^2 = B_0^2/\bar{\rho}\mu_0$. We have also introduced the parameter $\delta = f_0/N$.

If one were to omit the integrals in equations (5.52) and (5.53), it is clear that the relevant quantity when considering the ratio of kinetic to magnetic energy is

$$\frac{\bar{\rho}U_0^2}{\bar{\rho}f_0^2 L^2 \delta^2 \mathcal{M}^2} = \frac{\Lambda^2}{\delta^2 \mathcal{M}^2}. \quad (5.54)$$

In the absence of the parameter δ, this quantity is fully defined, however owing to the magneto-hydrostatic approximation, δ is infinitesimal (which we noted in section 2.2.3). To see this, we consider the dimensional full vertical momentum equation:

$$\bar{\rho}\left(\frac{Dw}{Dt} + (\mathbf{u}\cdot\nabla)w\right) = -\bar{\rho}\frac{\partial\theta}{\partial z} - \rho g + \mu\nabla^2 w + \frac{1}{\mu_0}(\mathbf{B}\cdot\nabla)b_z, \quad (5.55)$$

where the scaling (5.5) allows us to recast this as

$$\bar{\rho}\left(\frac{U_0 f_0^2}{N}\frac{D\hat{w}}{D\hat{t}} + \frac{U_0^2 f_0}{NL}(\hat{\mathbf{u}}\cdot\nabla)\hat{w}\right) = -\bar{\rho}U_0 N\frac{\partial\hat{\theta}}{\partial\hat{z}} - \bar{\rho}NU_0\hat{\rho} + \mu\frac{NU_0}{f_0 L^2}\frac{\partial^2\hat{w}}{\partial\hat{z}^2} + \frac{\bar{\rho}U_0^2 f_0}{NL}(\hat{\mathbf{B}}\cdot\nabla)\hat{b}_z, \quad (5.56)$$

which, after dividing by $\bar{\rho}U_0 N$ and using the nondimensional parameters (5.8), yields

$$\delta^2\left(\frac{D\hat{w}}{D\hat{t}} + \Lambda(\hat{\mathbf{u}}\cdot\nabla)\hat{w}\right) = -\frac{\partial\hat{\theta}}{\partial\hat{z}} - \hat{\rho} + \delta^2\nu_0\frac{\partial^2\hat{w}}{\partial\hat{z}^2} + \delta^2\Lambda(\hat{\mathbf{B}}\cdot\nabla)\hat{b}_z. \quad (5.57)$$

It is clear from equation (5.57) that taking the magnetohydrostatic approximation is equivalent to taking the limit $\delta \to 0$. Hence, it is not appropriate to consider the initial magnetic energy, which is proportional to δ^2 and is therefore infinitesimal, nor the ratio of initial kinetic energy to initial magnetic energy, which is proportional to $1/\delta^2$ and is therefore infinite.

Although the initial magnetic energy is undefined, it still has a dynamical effect, and it is important to determine how this can occur. Hence, we consider the linear terms that include the parameter $\mathcal{M}$ in the equations (5.7). For instance, $\mathcal{M}\partial_z b_x$ in equation (5.7a) originates from the along-stream Lorentz force $(\mathbf{B} \cdot \nabla)b_x$ (dimensional), where $\mathbf{B} = (b_x, b_y, B_0 + b_z)$. Recasting the terms of the operator $B_0\partial_z$ using the nondimensional scalings (5.5) and parameters (5.8), we obtain

$$B_0 = \frac{f_0^2 L \sqrt{\mu_0 \bar{\rho}}}{N} \mathcal{M} = \delta \cdot L \sqrt{\mu_0 \bar{\rho}} \, \mathcal{M}, \tag{5.58}$$

and

$$\frac{\partial}{\partial z} = \frac{N}{f_0 L} \frac{\partial}{\partial \hat{z}} = \frac{1}{\delta} \cdot \frac{1}{L} \frac{\partial}{\partial \hat{z}}. \tag{5.59}$$

So $B_0 \propto \delta$ is infinitesimal, while $\partial_z \propto \delta^{-1}$ is infinite. However, if one considers the terms of the operator $B_0\partial_z$ together, it is independent of δ. Thus, the dynamical impact of the basic state magnetic field B_0 is felt (via the parameter $\mathcal{M}$) since it is paired with the vertical gradient operator. Note that an analogous argument can be made via $(\mathbf{B}\cdot\nabla)v$ in the cross-stream momentum equation and $(\mathbf{B} \cdot \nabla)\mathbf{u}$ in the horizontal induction equations.

The ratio (5.54) and the equations (5.58) and (5.59) suggest that the quantity $\mathcal{R} = \Lambda/\mathcal{M}$ may provide a gauge of how relevant magnetic field will be during the evolution. This is also implied by the ratio of the advection and Lorentz terms in the momentum equations (5.7a) and (5.7b). Clearly, if Λ is large, the role of magnetic field will be less significant. Note that the importance of the quantity $\mathcal{R} = \Lambda/\mathcal{M}$ depends on whether the system is in a hydrodynamically stable or unstable regime. For example, if $\Lambda < 1$, the system is linearly stable in the absence on magnetic field, implying that magnetic field is crucial for instabilities to occur regardless of its magnitude. However, in the hydrodynamically unstable regime, the ratio $\mathcal{R} = \Lambda/\mathcal{M}$ may provide a gauge as to whether magnetic field will significantly alter the evolution (in contrast to the hydrodynamic evolution).

The Evolution of Kinetic and Magnetic Energy

We now consider the kinetic energy, magnetic energy and their ratio throughout the nonlinear evolution. The kinetic and magnetic energy are given by

$$K_E = \int_V \frac{1}{2} \bar{\rho} |\mathbf{u}|^2 \, dV = \frac{1}{2} \bar{\rho} U_0^2 \int_V (\hat{U}(\hat{y}) + \hat{u}^2)^2 + \hat{v}^2 + \delta^2 \hat{w}^2 \, dV, \tag{5.60}$$

and

$$M_E = \int_V \frac{|\mathbf{B}|^2}{2\mu_0} \, dV = \frac{1}{2} \bar{\rho} U_0^2 \int_V \hat{b}_x^2 + \hat{b}_y^2 + \delta^2 \left(\frac{\mathcal{M}}{\Lambda} + \hat{b}_z\right)^2 \, dV, \tag{5.61}$$

where we have used the nondimensional scalings (5.5) and parameters (5.8). Clearly, under the magnetohydrostatic approximation ($\delta = 0$), the energies (5.60) and (5.61) are neither infinitesimal

nor infinite and are therefore valid. Indeed, with $\delta = 0$, the ratio of kinetic to magnetic energy is given by

$$\frac{K_E}{M_E} = \frac{\int_V (\hat{U}(\hat{y}) + \hat{u})^2 + \hat{v}^2 \, dV}{\int_V \hat{b}_x^2 + \hat{b}_y^2 \, dV}, \tag{5.62}$$

which is clearly quantifiable (and not undefined, as is the ratio of initial kinetic to initial magnetic energy (5.54)).

5.5 Hydrodynamic Nonlinear Evolution

We first review the hydrodynamic nonlinear evolution to ensure the validity of the numerical method and routines through reproducing general mechanisms and results that occur in similar non-hydrostatic studies on the f-plane (e.g., Kloosterziel *et al.*, 2007b) and hydrostatic studies on the equatorial β-plane (e.g., Griffiths, 2003a,b). Thus, we solve equations (5.7) with $\mathcal{M} = 0$, and present results for $\Lambda = 1.5$ and $\Lambda = 2.5$ at various ν_0 in order to illustrate weakly nonlinear and moderately-to-strong nonlinear regimes. Note that in the magnetohydrodynamic regime we will consider the smallest value of ν_0 shown for each Rossby number presented in the hydrodynamic case.

5.5.1 Weakly Nonlinear Regime with $\Lambda = 1.5$

We will begin by presenting the evolution of the weakly nonlinear regime with $\Lambda = 1.5$ and $\mathcal{M} = 0$. We set $\nu_0 = 0.04$ (yielding $Re = 37.5$), and by equation (5.18), gives a nondimensional maximum growth rate $S_{\max} = 0.0413$. Clearly, since the maximum growth rate is $S = 0.7071$ in the absence of diffusion and $Re = 37.5$ we are in a weakly nonlinear regime. Indicated by the leftmost red dot shown in the left panel of figure 5.3, $S_{\max}$ occurs at the vertical wavenumber $K_{\max} = 2.6060$. Thus, the vertical domain for this simulation is chosen to be $H = 2\pi/K_{\max} = 2.4110$. In this simulation we take the latitudinal domain $L = 14$, which is large enough to ensure the perturbed quantities have decayed sufficiently by the latitudinal boundary. Thus, as stated in section 5.4, we take $y \in [-L/2, L/2] = [-7, 7]$ and $z \in [-H/2, H/2] = [-1.2055, 1.2055]$. Also, recall that in all cases we initialise the perturbed quantities with random "noise" and initial amplitude 10^{-5}. In all subsequent cases, we will not repeat the respective domain sizes and initialisation of the perturbed quantities. The grid size is 1024×32. The timestep is $\Delta t = 5.0 \times 10^{-3}$.

Figure 5.6 illustrates the nonlinear evolution (including the linear phase, the nonlinear saturation and the nonlinear equilibrium), including plots of the perturbed along-stream velocity u, streamfunction ψ and density ρ in (y, z)-space at various times t throughout the simulation. The quantities are normalised by the maximum of u, ψ and ρ over the whole evolution, which in this case corresponds to $u = 0.0412$ at $t = 276$; the same procedure is also used for all following analogous figures.

In figure 5.7 we plot the kinetic and potential energy, for numerous vertical modes (integrated over the entire latitudinal domain), of the perturbed quantities, illustrated by the red and cyan lines, respectively, against time t.

Figure 5.8 shows the initial mean flow $\overline{U} = \Lambda \tanh y$ (left panel) and mean vorticity $\overline{Q} = 1 - U' = 1 - \Lambda \operatorname{sech}^2 y$ (right panel) alongside the final mean flow $\overline{U}$ and mean vorticity $\overline{Q}$ against latitude y. Recall that the mean flow and mean vorticity are the vertical averages (means) of $U(y)$ and Q, respectively. Note that, owing to the lack of vertical diffusion, at nonlinear equilibrium the flow U and vorticity Q are homogenized throughout the entire vertical domain, and are equal to final mean flow $\overline{U}$ and mean vorticity $\overline{Q}$.

First, we describe the dynamical process illustrated by the contours of figure 5.6; the description will not be repeated unless the process is significantly different, or, for the magnetohydrodynamic regime, where other perturbed quantities (b_x and ϕ) evolve. The streamfunction ψ in the panels ($\mathbf{b}$) shows an overturning motion in the (y, z)-plane throughout the evolution. The overturning motion lifts up dense fluid and brings down light fluid, giving rise to the density perturbations in the panels ($\mathbf{c}$); the density perturbations grow and decay in the same manner as the streamfunction perturbations, both perturbations reaching their maximum values about the nonlinear saturation, which figure 5.7 implies is approximately $t \in [240, 280]$. The overturning motions also generate latitudinal momentum, displacing fluid which is then deflected by the Coriolis force into the along-stream direction. This leads to the change in the along-stream velocity perturbation u, as shown in the panels ($\mathbf{a}$). Finally, owing to the vertical diffusion, the along-stream velocity perturbation separates into four stable columns (with the centre two being more prominent), which is the nonlinear equilibrium and leads to the change in $\overline{U}$ illustrated in figure 5.8.

Figure 5.7 shows the evolution of the kinetic and potential energy throughout the evolution. There is exponential growth of kinetic and potential energy through the linear phase until nonlinear saturation at approximately $t = 230$. After saturation there is clear decay in the energy of all the modes except the 0th mode of kinetic energy. Once reaching the nonlinear equilibrium (at $t \approx 320$) all the perturbation energy of the system is contained in the 0th mode of kinetic energy since it is comparable in magnitude to the total perturbation energy. Note that the total perturbation energy grows until $t = 276$ at which it is maximum, then decays, and then remains constant once the system has reached nonlinear equilibrium.

Figure 5.8 shows there is very little change to the mean flow $\overline{U}$ and mean vorticity $\overline{Q}$; this is expected as we are in a weakly nonlinear regime (the diffusive growth rate being only 5.8% of the inviscid growth rate). The plots illustrate points that will be relevant throughout the rest of the Chapter. First, we see that the latitudinal shear of $\overline{U}$ has been reduced; this occurs in all of the cases we consider — it is the source of energy for the nonlinear evolution. Hence, for cases with stronger nonlinearity, we may expect a significant reduction of the latitudinal shear and a more notable change to the mean flow. Second, we see that the final minimum value of $\overline{Q}$ is less negative than the initial $\overline{Q}$. This is what allows the evolution to reach an equilibrium state: that is, the vorticity is no longer sufficiently negative to drive an instability. To understand this, recall that the hydrodynamic
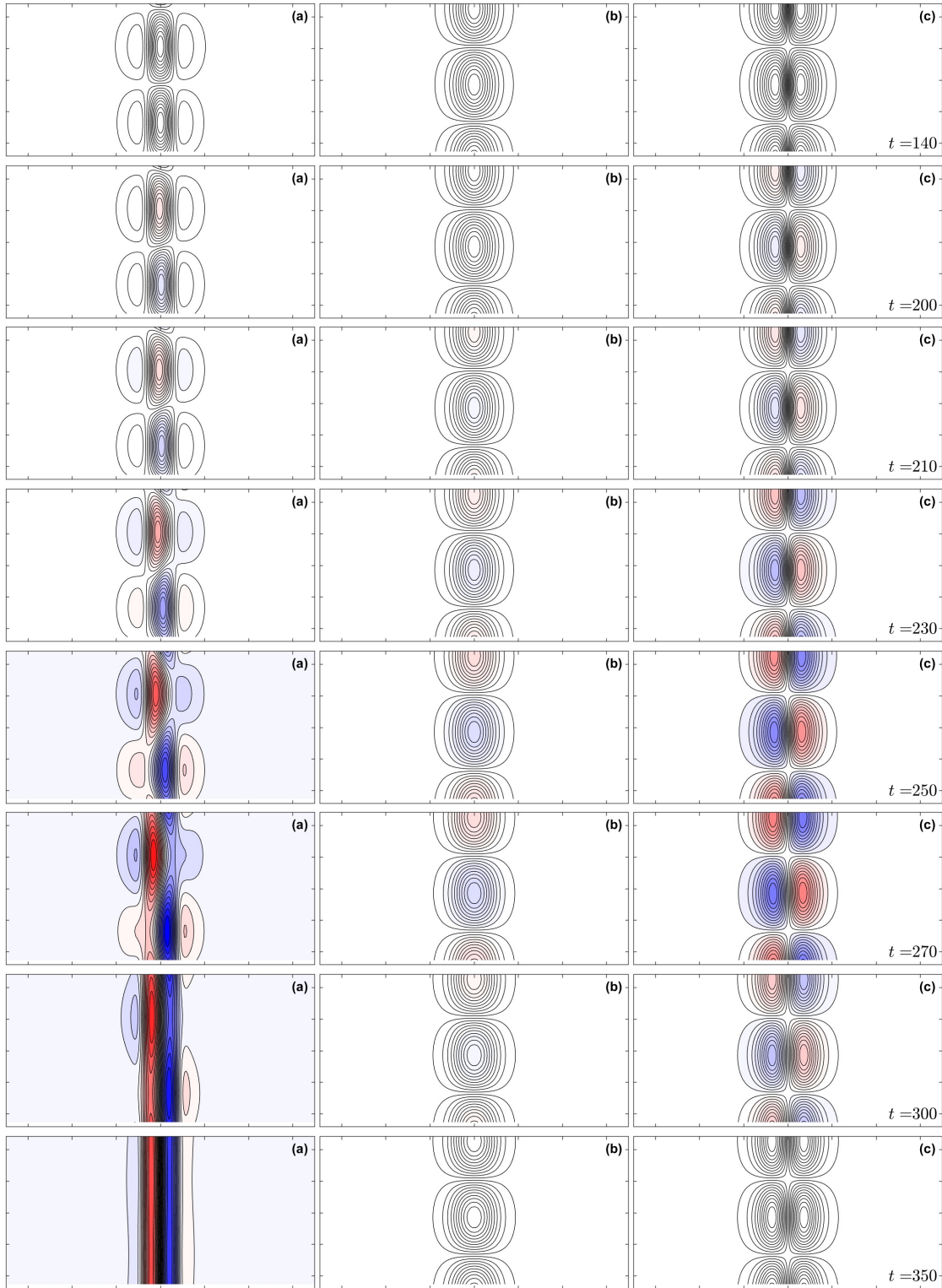
Figure 5.6: Contours in (y, z)-space of (**a**) the perturbed along-stream velocity u, (**b**) the perturbed streamfunction ψ and (**c**) the perturbed density ρ. Each row of panels is at a distinct time t. In this simulation, $\Lambda = 1.5$, $\nu_0 = 0.04$, $L = 14$, $H = 2.4110$, and $(K = 2.6060)$.
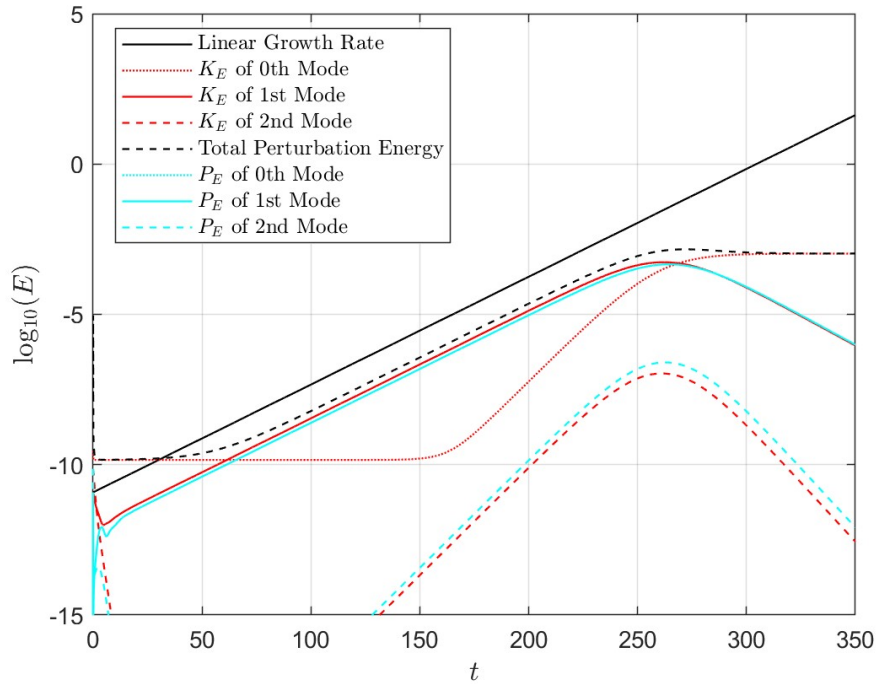
Figure 5.7: Evolution of kinetic and potential energy for the lowest order vertical modes against t corresponding to the dynamical process illustrated in figure 5.6 with $\Lambda = 1.5$ and $\nu_0 = 0.04$.

condition for instability in the absence of diffusion and stratification is that the absolute vorticity $fQ < 0$ (or $\Lambda \operatorname{sech}^2 y > 1$ in terms of our nondimensional parameters). However, in this case, diffusion and stratification act to stabilise the flow so that $fQ < 0$ becomes a necessary but not sufficient condition for instability. Thus, the final $\overline{Q}$ in figure 5.8 is not sufficiently negative to drive instability.
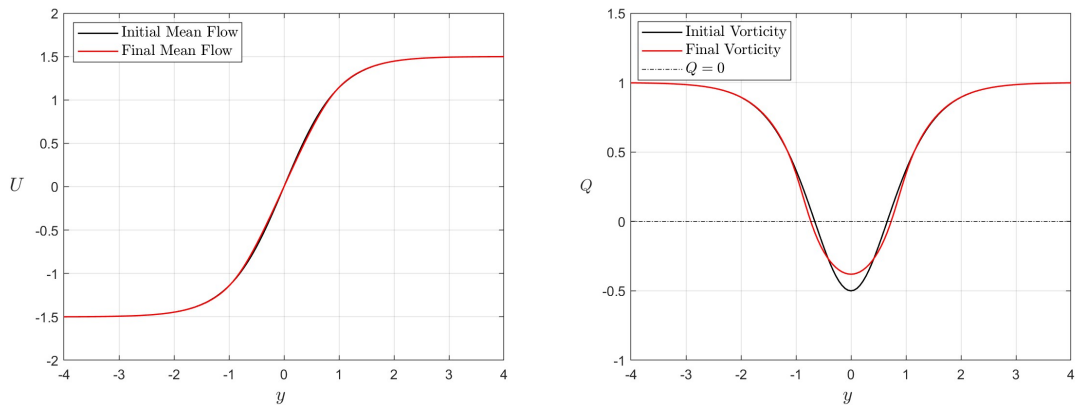
Figure 5.8: The initial (black) and final (red) mean flow $\overline{U}$ (left) and mean vorticity $\overline{Q}$ of the nonlinear evolution (illustrated in figure 5.6) plotted.

5.5.2 Strongly Nonlinear Regime with $\Lambda = 1.5$

We now consider an analogous evolution with significantly stronger nonlinearity than illustrated in figures 5.6, 5.7 and 5.8. We therefore take $\Lambda = 1.5$ and $\nu_0 = 0.02$ ($Re = 75$) and provide figures 5.9, 5.10 and 5.11. Note that the growth rate is 0.1996 (which is approximately 28% of the inviscid growth rate).

In figure 5.9, the perturbed along-stream velocity u, streamfunction ψ and density ρ are contoured in (y, z)-space at various times throughout the evolution. The quantities are normalised by the maximum of u, ψ and ρ over the whole evolution, which (in this case) corresponds to $u = 0.1719$ at $t = 62$. In this case the most unstable mode occurs at $K_{\max} = 3.10$ (shown as the leftmost red dot in the left panel of figure 5.3), yielding $H = 2\pi/K_{\max} = 2.0268$; We also we set $L = 14$. The grid size is 1024×32. The timestep is $\Delta t = 2.0 \times 10^{-3}$.

The dynamical process illustrated in figure 5.9 is, for the most part, analogous to that of figure 5.6. However, it is clear that nonlinear saturation and equilibrium occur much more rapidly, as we expect owing to the larger growth rate. As a result of the more rapid evolution, the latitudinal momentum is much more vigorous and leads to an equilibrium state where the along-stream velocity perturbation has four stable columns, with the outer columns being significantly more prominent than those in figure 5.6.

Figure 5.10 plots, for numerous modes (integrated over the entire latitudinal domain), the kinetic and potential energy of the perturbed quantities against time t. The plot confirms the much more rapid evolution in comparison to that illustrated by figures 5.6, 5.7 and 5.8. Nonlinear saturation now occurs at $t \approx 55$ (rather than $t \approx 230$) and reaches equilibrium at $t \approx 80$ (rather than $t \approx 320$). The total perturbation energy in this case is approximately an order of magnitude larger than in the previous case.

Figure 5.11 shows the initial $\overline{U}$ and $\overline{Q}$ alongside their final values against latitude y. There is a much more notable change to the $\overline{U}$ and $\overline{Q}$ over the evolution in comparison to the weakly nonlinear case. Indeed, the shear of $\overline{U}$ has been reduced more significantly and the minimum value of $\overline{Q}$ is $Q \approx -0.2$ rather than $Q \approx -0.4$. Evidently, in this more nonlinear regime, for the flow to become stable the system requires a less negative minimum $\overline{Q}$. If $\overline{Q}$ were more negative, then fQ would be sufficiently negative to drive an instability.

Vorticity Cusps

Note the "spikes" in the final mean vorticity $\overline{Q}$ at $|y| \approx 1.5$; these are the main limiting factor in being able to reduce ν_0 in order to obtain a larger Reynolds number and more physically realistic system. Indeed, consider figure 5.12, which illustrates the initial and final $\overline{Q}$ against y for an analogous simulation with $\Lambda = 1.5$ and $\nu_0 = 0.01$ (yielding the Reynolds number $Re = 150$). The vorticity spikes are in fact cusps (cf. Griffiths, 2003a) and therefore can not be resolved; increasing the resolution leads only to the code crashing owing to the increasing value of vorticity Q at $|y| \approx 1.6$. It is possible to modify the numerical method and include latitudinal diffusion so
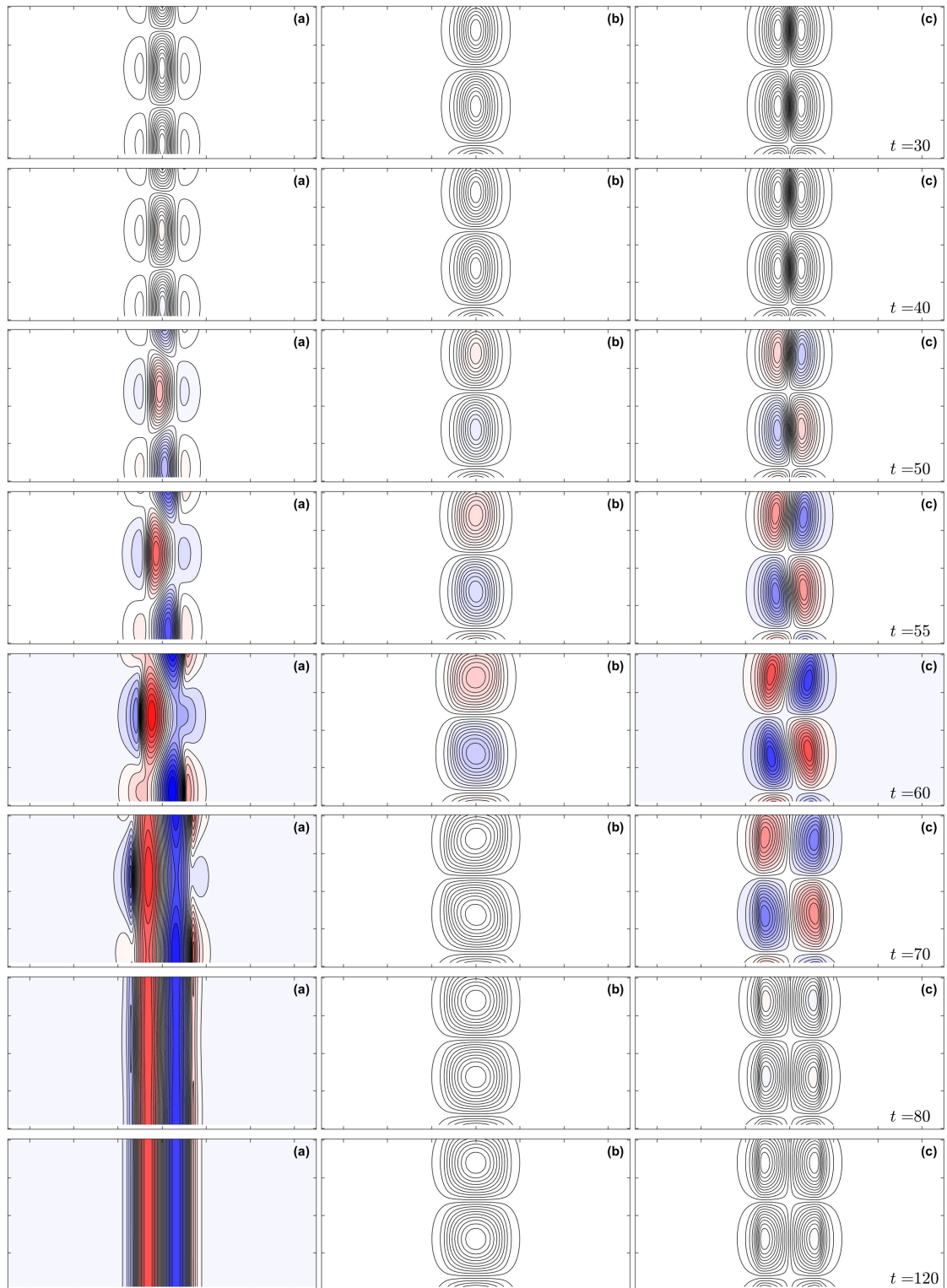
Figure 5.9: Contours in (y, z)-space of (**a**) the perturbed along-stream velocity u, (**b**) the perturbed streamfunction ψ and (**c**) the perturbed density ρ. Each row of panels is at a distinct time t. In this simulation, $\Lambda = 1.5$, $\nu_0 = 0.02$, $L = 14$, and $H = 2.0268$ ($K = 3.10$).
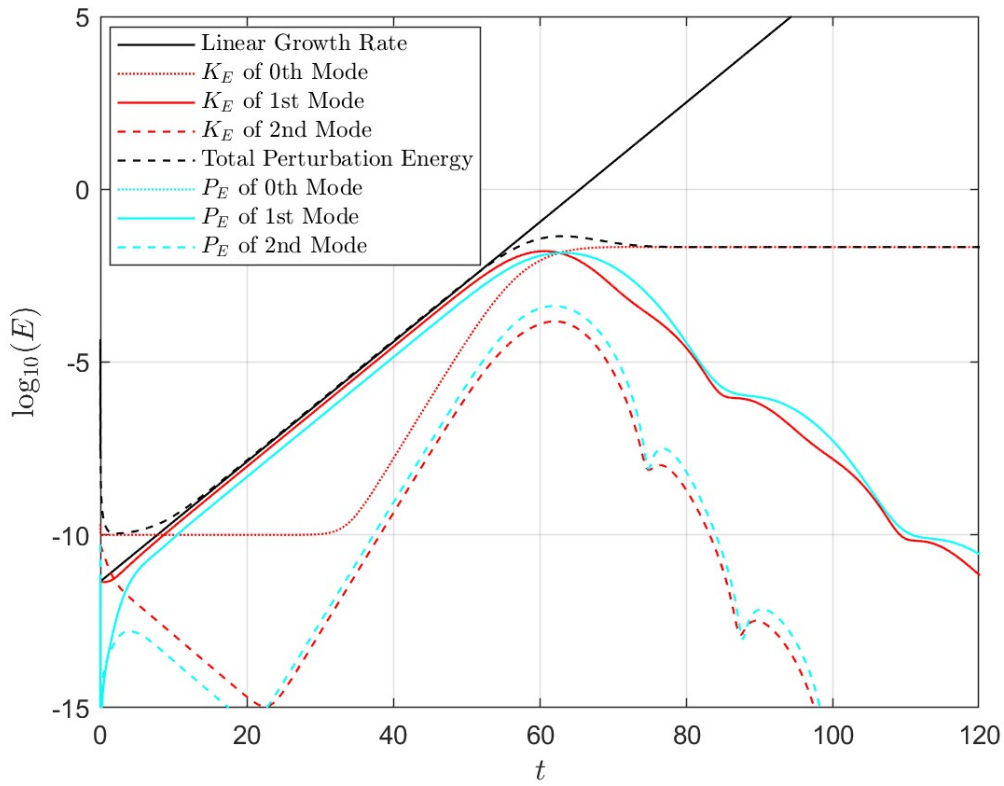
Figure 5.10: Evolution of kinetic and potential energy for the lowest order vertical modes against t corresponding to the dynamical process illustrated in figure 5.9 with $\Lambda = 1.5$ and $\nu_0 = 0.02$.
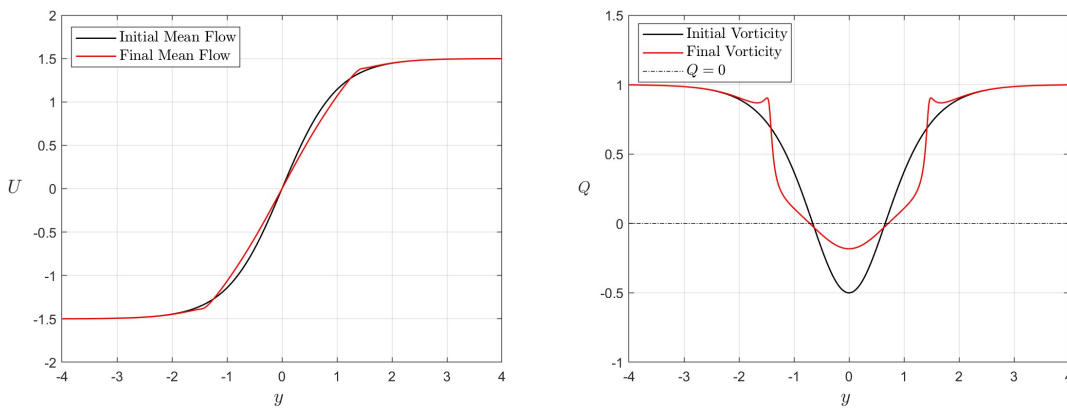
Figure 5.11: The initial (black) and final (red) $\overline{U}$ (left) and $\overline{Q}$ (right) of the nonlinear evolution (illustrated in figure 5.9).
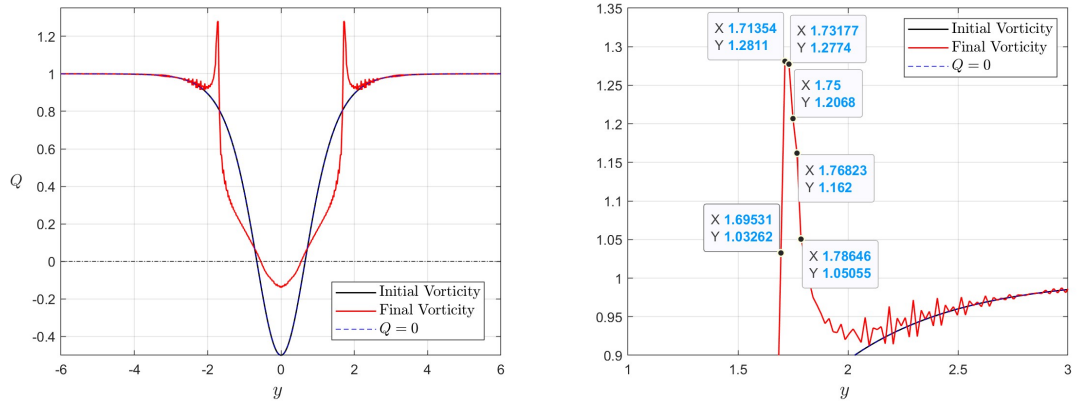
Figure 5.12: The initial and final $\overline{Q}$ against latitude y of a nonlinear evolution with $\Lambda = 1.5$ and $\nu_0 = 0.01$. The right panel is a zoomed in version of the left panel.

that vorticity is dissipated much more rapidly so that cusps can no longer form. However, with the latitudinal diffusion there is no analytical linear solution and it conflicts with the assumptions of the magnetohydrostatic approximation. That is, under the magnetohydrostatic approximation, the Laplacian operators of the diffusive terms take the form

$$\nabla^2 = \frac{1}{L^2}\left(\frac{\partial^2}{\partial y^2} + \frac{1}{\delta^2}\frac{\partial^2}{\partial z^2}\right),\tag{5.63}$$

where $\delta = f_0/N$ as in section 5.4.3. Thus, under the magnetohydrostatic approximation, the latitudinal diffusion is negligible since δ is infinitesimal. If one were to consider latitudinal diffusion, we must prescribe a numerical value to δ contrary to the magnetohydrostatic approximation. However, this would also lead to concern over the neglected terms in the vertical momentum equation (which were justified under the magnetohydrostatic approximation in equation (5.57)) that contained factors of δ. Perhaps this concern could be resolved by taking a small value of δ that is sufficient to suppress the vorticity spikes while containing to neglect the relevant terms in the vertical momentum equation. However, in this thesis, we will simply consider a sufficiently small Reynolds numbers so that the cusps in vorticity do not occur.

5.5.3 Weakly Nonlinear Regime with $\Lambda = 2.5$

We now consider the nonlinear evolution of the system with Rossby number $\Lambda = 2.5$ and $\nu_0 = 0.5$. yielding Reynolds number $Re = 5$ and growth rate 0.2864 (which is approximately 23% of the inviscid growth rate 1.2247). In figure 5.13, u, ψ and ρ are contoured in (y, z)-space at various times throughout the evolution. The quantities are normalised by the maximum of u, ψ and ρ over the whole evolution, which (in this case) corresponds to $u = 0.4269$ at $t = 45$. In this case the most unstable mode occurs at $K_{\max} = 1.0420$ (shown as the leftmost red dot in the right panel of figure 5.4), yielding $H = 6.0299$. The grid size is 1536×64. The timestep is $\Delta t = 1.0 \times 10^{-3}$.

The dynamical process illustrated in figure 5.13 has only minor differences to the evolution shown in figure 5.6 owing to the different Rossby and Reynolds numbers, and thus, we will not
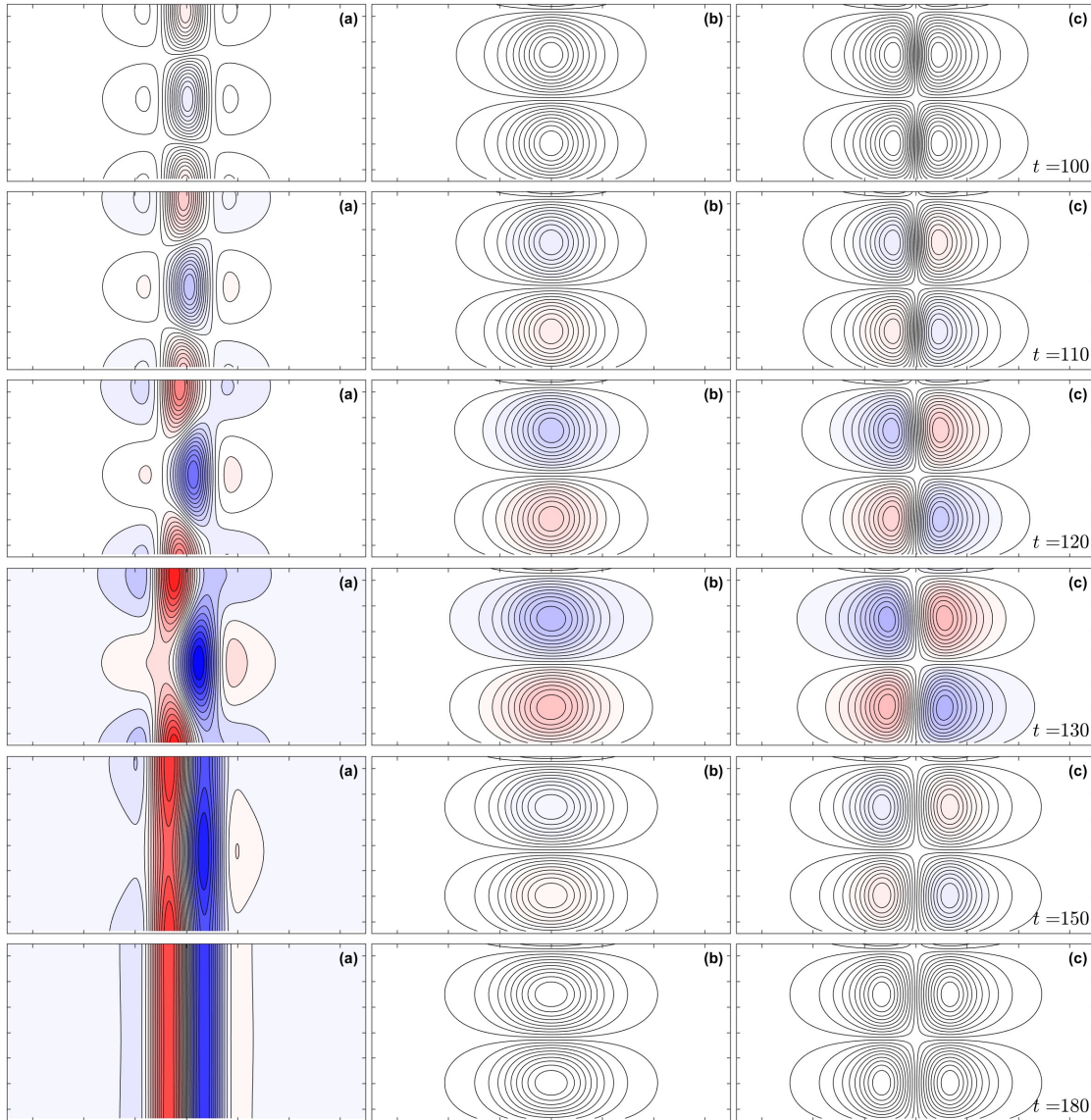
Figure 5.13: Contours in (y, z)-space of (**a**) the perturbed along-stream velocity u, (**b**) the perturbed streamfunction ψ and (**c**) the perturbed density ρ. Each row of panels is at a distinct time t. In this simulation, $\Lambda = 2.5$, $\nu_0 = 0.5$, $L = 14$, and $H = 6.0299$.

provide figures corresponding to this (in the hydrodynamic and magnetohydrodynamic analysis) unless there are significant differences. Figure 5.13 is included to illustrate the similarity in evolution. We also see that the modes fill more of the latitudinal domain; this is to be expected owing to the larger Rossby number, where a larger latitude y is required (in contrast to smaller values of Λ) to reduce the magnitude of shear $U'(y) = \Lambda \operatorname{sech}^2 y$ so that it is no longer sufficient to drive an instability.

Figure 5.14 plots, for numerous modes (integrated over the entire latitudinal domain), the kinetic and potential energy of the perturbed quantities against time t. The plot again illustrates a period of linear growth, nonlinear saturation and equilibrium. However, the nonlinear saturation now occurs much earlier in the evolution in comparison to even figure 5.10 where $\Lambda = 1.5$ and $\nu_0 = 0.02$ ($Re = 75$). The energy of all modes (except the 0th of kinetic energy) also decay much
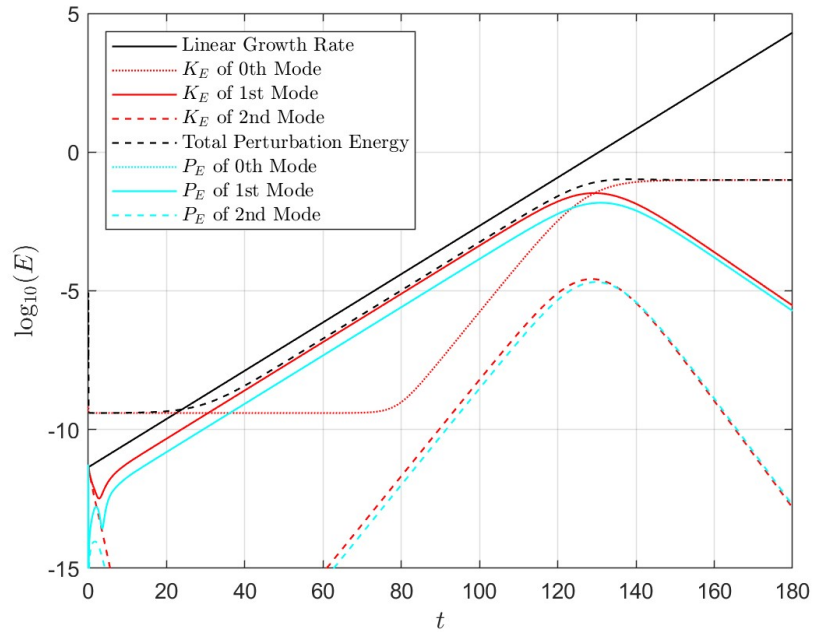
Figure 5.14: Evolution of kinetic and potential energy for the lowest order vertical modes against t corresponding to the dynamical process illustrated in figure 5.13 with $\Lambda = 2.5$ and $\nu_0 = 0.5$.

more rapidly owing to the larger magnitude of diffusion.

Figure 5.15 shows the initial and final $\overline{U}$ and $\overline{Q}$ against latitude y. There is a considerable change to $\overline{U}$ and $\overline{Q}$ over the evolution in comparison to the highly diffusive case with $\Lambda = 1.5$ illustrated in figure 5.8. However, once again, we can see that the shear of $\overline{U}$ has been reduced as well as the minimum value of the final mean vorticity, so that fQ is not sufficiently negative to drive an instability. In comparison to previous cases, the minimum of the final $\overline{Q}$ is much more negative. The shear is not sufficient to drive an instability, as it would be in previous cases, since the magnitude of diffusion is much larger.
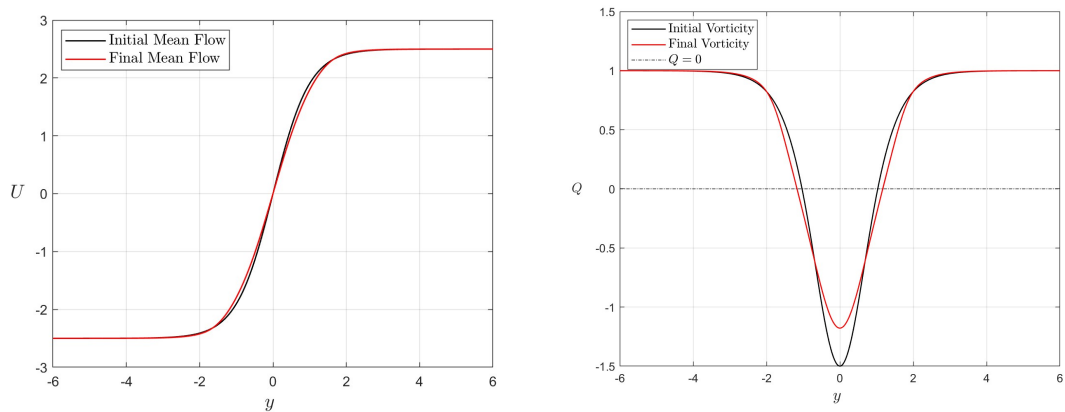
Figure 5.15: The initial (black) and final (red) $\overline{U}$ (left) and $\overline{Q}$ (right) of the nonlinear evolution (illustrated in figure 5.13).
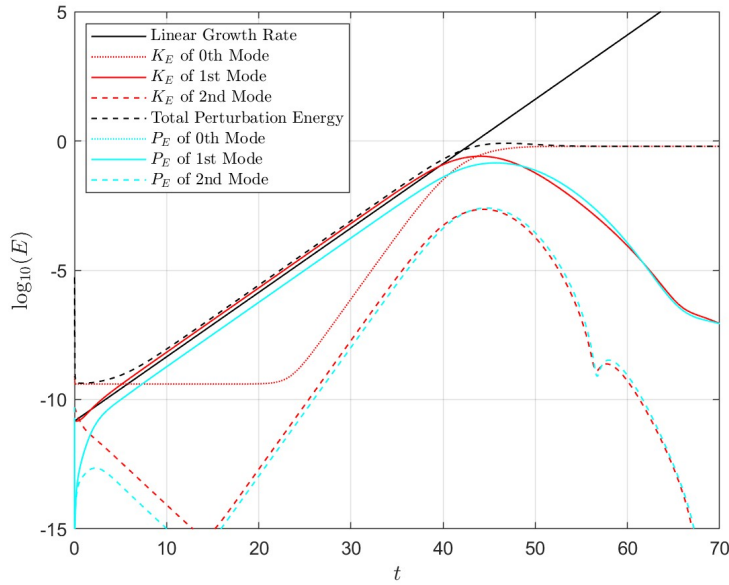
Figure 5.16: Evolution of kinetic and potential energy for the lowest order vertical modes against t with $\Lambda = 2.5$ and $\nu_0 = 0.3$.

5.5.4 Strongly Nonlinear Regime with $\Lambda = 2.5$

We now consider an evolution with significantly stronger nonlinearity than illustrated in figures 5.13, 5.14 and 5.15. We take $\Lambda = 2.5$ and $\nu_0 = 0.3$, yielding $Re = 8.33$ and growth rate 0.2864 (which is approximately 23% of the inviscid growth rate), and provide figures 5.16 and 5.17. We do not contour the perturbed quantities in this case as they are analogous to what we have seen in previous figures. The most unstable mode occurs at $K_{\max} = 1.0420$ (shown as the leftmost red dot in the left panel of figure 5.4), yielding $H = 6.030$; we also set $L = 14$. The maximum of the perturbed quantities is $u = 0.4269$ at $t = 45$. The chosen grid is 1536 in the latitudinal direction and 64 in the vertical direction. The timestep is $\Delta t = 2.0 \times 10^{-3}$.

Figure 5.16 shows, for various modes (integrated over the entire latitudinal domain), the evolution of kinetic and potential energy of the perturbed quantities against time t. The plot shows that there is a much more rapid evolution in comparison to that illustrated by figures 5.13, 5.14 and 5.15. Nonlinear saturation now occurs at $t \approx 40$ (rather than $t \approx 120$) and reaches equilibrium at $t \approx 55$ (rather than $t \approx 150$). The total perturbation energy in this case is approximately an order of magnitude larger than that of the $\Lambda = 2.5$ and $\nu_0 = 0.5$ case.

Figure 5.17 shows the initial and final $\overline{U}$ and $\overline{Q}$ against latitude y. There is a considerable change to the $\overline{U}$ and $\overline{Q}$ over the evolution in comparison to the $\Lambda = 2.5$ and $\nu_0 = 0.5$ case. Indeed, the shear of $\overline{U}$ has been reduced more significantly and the minimum value of the final mean vorticity is $\overline{Q} \approx -0.95$ rather than $\overline{Q} \approx -1.2$. Evidently, in this more nonlinear regime, for the flow to become stable the system requires a less negative minimum $\overline{Q}$. If the $\overline{Q}$ were more negative it would be sufficient to drive an instability.
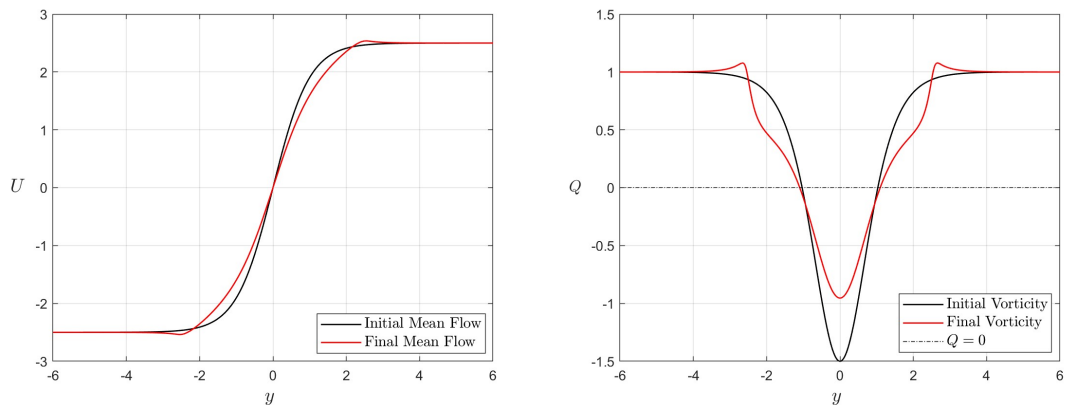
Figure 5.17: The initial (black) and final (red) $\overline{U}$ (left) and $\overline{Q}$ (right) of the nonlinear evolution plotted with $\Lambda = 2.5$ and $\nu_0 = 0.3$.

Thus, we have shown the nonlinear evolution of the system for $\Lambda = 1.5$ with $\nu_0 = 0.04$ and $\nu_0 = 0.02$, and $\Lambda = 2.5$ with $\nu_0 = 0.5$ and $\nu_0 = 0.3$. This illustrated for each Rossby number Λ a weakly nonlinear regime and one with significantly more nonlinearity. We described the general dynamical process of the nonlinear evolution, where latitudinal momentum transfers fluid, which is then deflected by the Coriolis force, driving the along-stream perturbation into two stable columns. We also discussed the mean flow $\overline{U}$ and mean vorticity $\overline{Q}$ changes over the evolution, where we expect more significant changes in the regimes with larger Rossby number or Reynolds number. In general, the evolution reduces the latitudinal shear of $\overline{U}$ and increases the mean vorticity (making it less negative) so that the flow reaches a stable state. In the magnetohydrodynamic regime, we will focus on the case $\Lambda = 1.5$ and $\Lambda = 0.5$ (with a brief discussion given for $\Lambda = 2.5$). For the $\Lambda = 1.5$ case (and $\Lambda = 2.5$) we will focus on the change to $\overline{U}$ and $\overline{Q}$ in comparison to the hydrodynamic mean flow and vorticity change. For $\Lambda = 0.5$ no such comparison can be made since the hydrodynamic system is stable for $\Lambda < 1$.

5.6 Magnetohydrodynamic Nonlinear Evolution in the Hydrodynamically Unstable Regime

In this section we consider the magnetohydrodynamic nonlinear evolution of the system with Rossby number $\Lambda = 1.5$ and $\Lambda = 2.5$, focusing on the case $\Lambda = 1.5$ since the evolutions are largely analogous (as in the hydrodynamic case). For $\Lambda = 1.5$, we will consider $\nu_0 = 0.02$, which is the smallest magnitude of diffusion that we presented in the hydrodynamic section, in order to investigate the regime with largest Reynolds numbers ($Re = Rm = 75$) and most nonlinearity. By the same reasoning we consider $\nu_0 = 0.3$, for $\Lambda = 2.5$.

5.6.1 The Nonlinear Evolution with Weak Magnetic Field and $\Lambda = 1.5$

We will begin by presenting the nonlinear evolution (using the numerical scheme described in section 5.4 to solve the equations (5.7)) in figures 5.18, 5.19, 5.20 and 5.21 with $\Lambda = 1.5$, $\nu_0 = 0.02$ and $\mathcal{M} = 0.03$. The linear growth rate under these parameters is 0.2428; the growth rate in the absence of magnetic field is 0.1996. Thus, we expect magnetic field to have a small dynamical effect. The maximum growth rate is generated at the vertical wavenumber $K_{\max} = 3.0$ (which is indicated by the leftmost red dot not on the axis in the left panel of figure 5.3), yielding $H = 2\pi/K_{\max} = 2.0944$. In this simulation we take the latitudinal domain $L = 16$ which is large enough to ensure the perturbed quantities have decayed sufficiently by the latitudinal boundary. The grid size is 1024×32. The timestep is $\Delta t = 1.0 \times 10^{-2}$.

Figure 5.18 includes plots of u, ψ and ρ, while figure 5.19 includes plots of the perturbed along-stream magnetic field b_x and magnetic streamfunction ψ, both of which are in (y, z)-space at various times t. The quantities are normalised by the maximum of u, ψ, ρ, b_x and ϕ over the whole evolution, which (in this case) corresponds to $u = 0.2848$ at $t = 74$. Note that the choice of larger L is to ensure that magnetic perturbed quantities, which have a tendency to spread over the latitudinal domain (cf. Hawley & Balbus, 1992; Balbus & Hawley, 1992), have decayed sufficiently. For stronger magnetic field significantly larger values of L must be taken.

In figure 5.20 we plot, for various modes (integrated over the entire latitudinal domain), the kinetic, potential and magnetic energy of the perturbed quantities against time t. Figure 5.21 shows the initial (black) and final (blue) magnetohydrodynamic $\overline{U}$ and $\overline{Q}$ alongside the final hydrodynamic (red) mean flow $\overline{U}_H$ and $\overline{Q}_H$.

We describe the dynamical process illustrated in the contours of figure 5.18 and 5.19; this will not be repeated unless the process is significantly different. As in the hydrodynamic case, we see that the streamfunction ψ in the panels (**b**) shows an overturning motion in the (y, z)-plane throughout the evolution. This gives rise to the density perturbations that grow and decay in the same manner as the streamfunction perturbations. The overturning motions lead to the change in u as shown in the panels (**a**). The along-stream velocity perturbation reaches nonlinear equilibrium by separating into stable columns; the nonlinear equilibrium leads to the change in $\overline{U}$ illustrated in figure 5.21. In the magnetohydrodynamic regime we must now also consider the along-stream field and magnetic stream function perturbations that grow until saturation and then viscously decay, as illustrated in panels (**d**) and (**e**) in figure 5.19, respectively. Note that in section 3.4 we already determined that during the linear phase of the evolution, the along-stream field acts to increase the growth rate by increasing the along-stream acceleration via the Lorentz force, while the cross-stream field acts to reduce the growth rate via the cross-stream Lorentz force. Through the nonlinear evolution we see that the magnetic field perturbations continue to increase and decrease the along and cross-stream accelerations in the same manner.

Figure 5.20 shows the evolution of the kinetic, potential and magnetic energy, which grow exponentially until nonlinear saturation at $t \approx 40$. After saturation there is clear decay in the energy of all the modes except the 0th mode of kinetic energy. Once reaching the nonlinear equilibrium
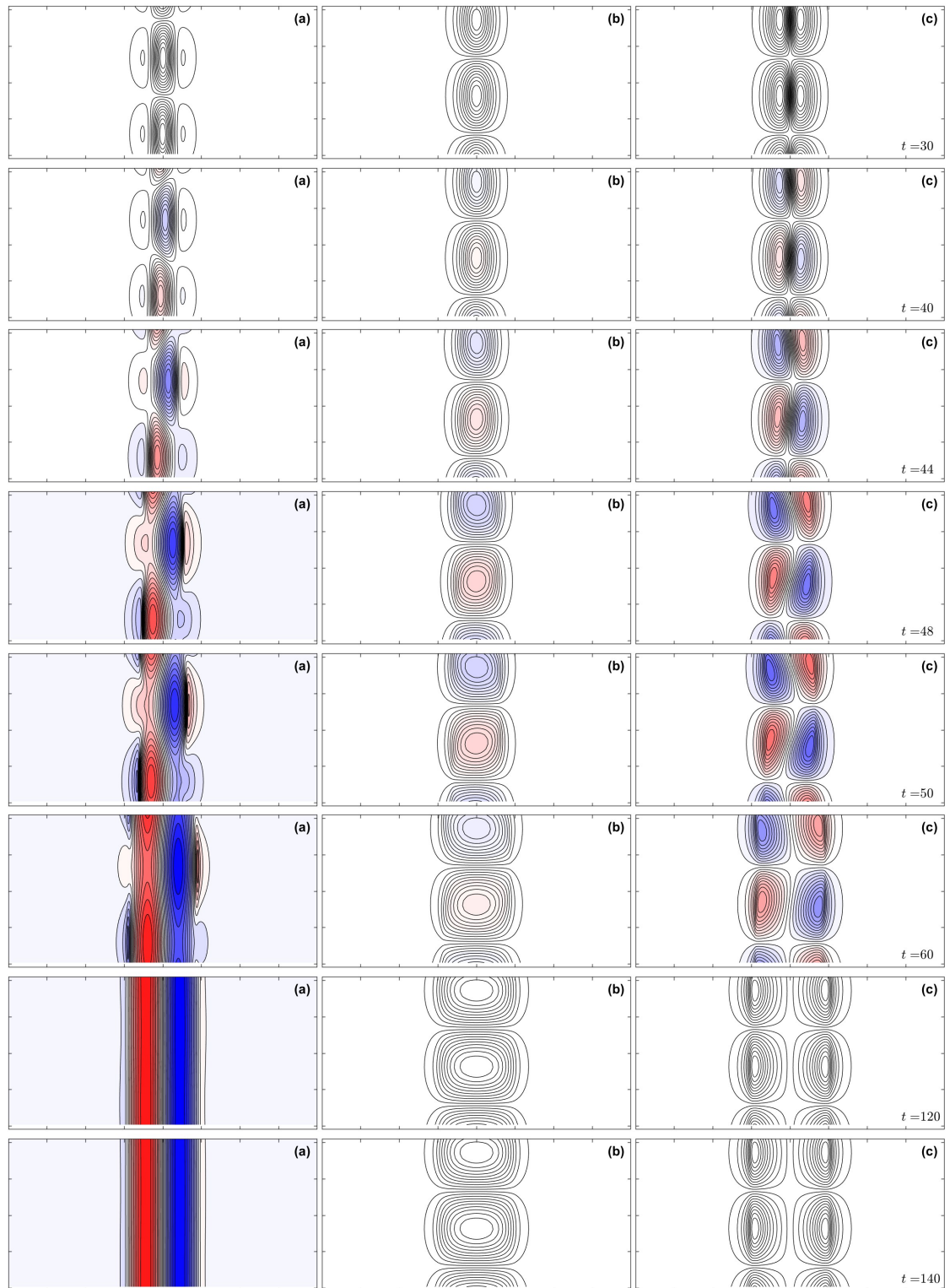
Figure 5.18: Contours in (y, z)-space of (**a**) the perturbed along-stream velocity, (**b**) the perturbed streamfunction ψ and (**c**) the perturbed density ρ. Each row of panels is at a distinct time t. In this simulation, $\Lambda = 1.5$, $\nu_0 = 0.02$, $\mathcal{M} = 0.03$, $L = 16$, and $H = 2.0944$ ($K = 3.0$).
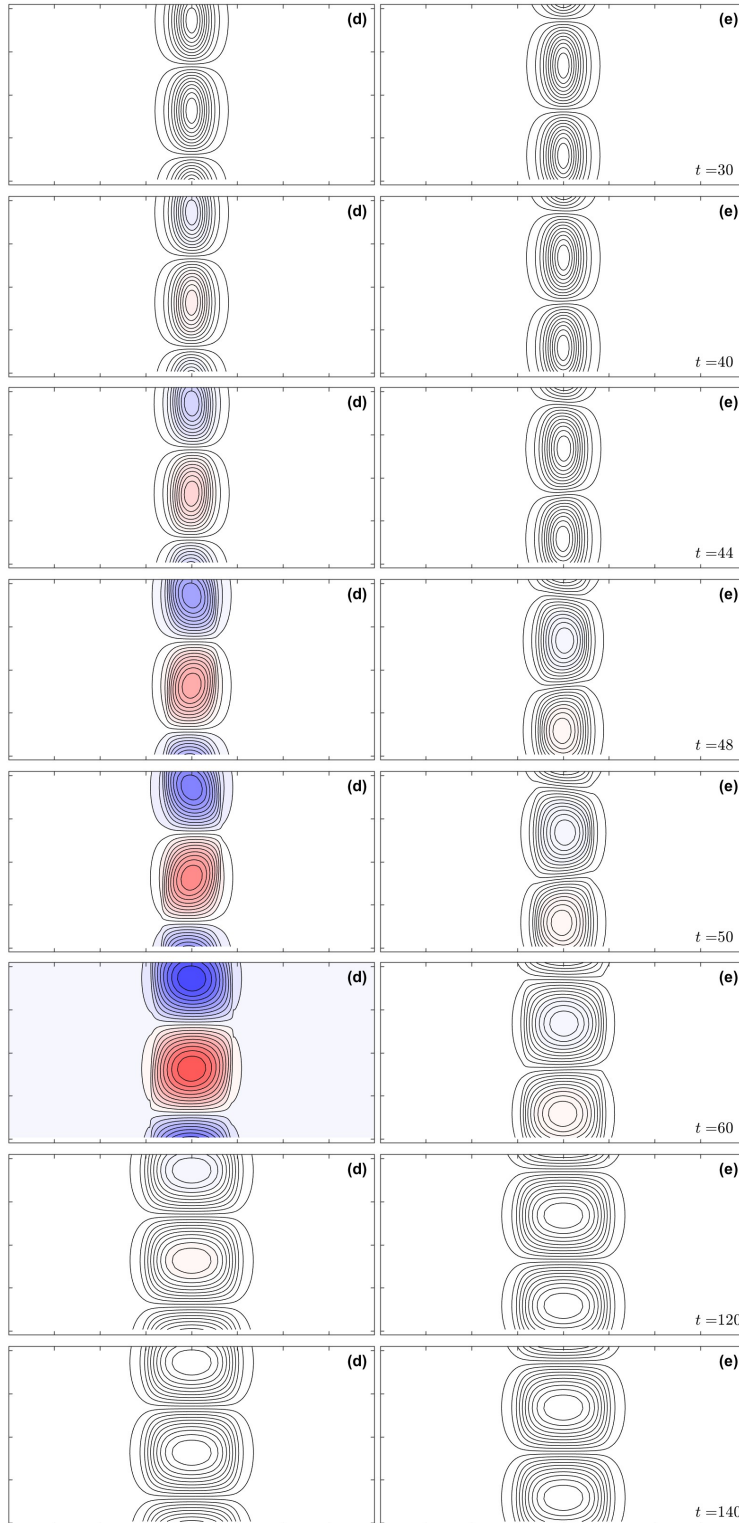
Figure 5.19: Contours in (y, z)-space of (**d**) the perturbed along-stream magnetic field b_x and (**e**) the perturbed magnetic streamfunction ϕ. Each row of panels is at a distinct time t. In this simulation, $\Lambda = 1.5$, $\nu_0 = 0.02$, $\mathcal{M} = 0.03$, $L = 16$, and $H = 2.0944$ ($K = 3.0$).
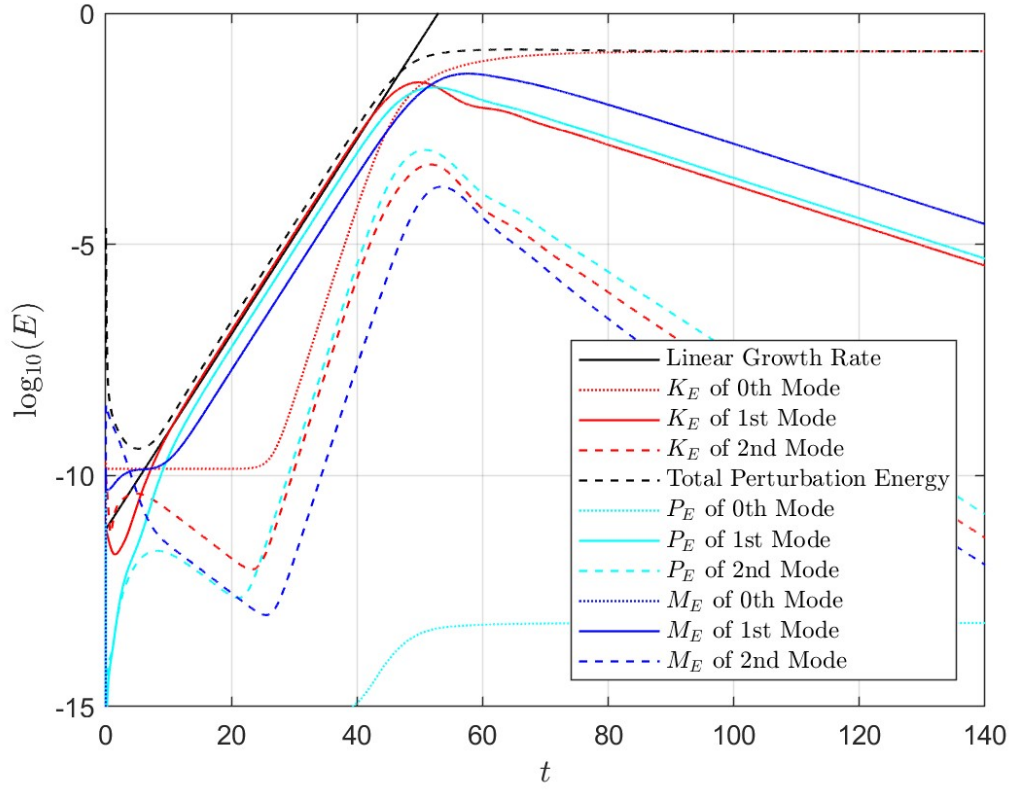
Figure 5.20: Evolution of kinetic, magnetic and potential energy for the lowest order vertical modes against t corresponding to the dynamical process illustrated in figures 5.18 and 5.19 with $\Lambda = 1.5$, $\nu_0 = 0.02$ and $\mathcal{M} = 0.03$.

(at $t \approx 80$) all the perturbation energy of the system is contained in the 0th mode of kinetic energy since it remains comparable to the total perturbation energy. Note that the total perturbation energy grows until $t = 60$ at which it is maximum, decays, and then remains constant once the system has reached nonlinear equilibrium. In contrast to the hydrodynamic case shown in figure 5.10, saturation occurs at $t \approx 40$ rather than $t \approx 55$, and the perturbed quantities in this case take much longer to decay. Indeed, in the hydrodynamic case the 1st mode of kinetic and potential energy have decayed to $E \sim 10^{-10}$, compared to $E \sim 10^{-4.5}$ in this case. Note that at the nonlinear saturation the energy contained in the 1st mode of magnetic energy is larger than that in the 1st mode of kinetic energy; the magnetic energy of the 1st mode is also greater than the kinetic energy of the 1st mode as they both viscously decay.

Figure 5.21 shows that for even this relatively weak magnetic field strength (the ideal system being marginally unstable for $\mathcal{M} = \Lambda/2 = 0.75$), there is a significant alteration to $\overline{U}$ in comparison to the hydrodynamic evolution. Indeed, the minimum of the final mean vorticity is now $\overline{Q} \approx 0$ rather than $\overline{Q} \approx -0.2$. We might expect this, owing to the condition (2.43), which implies that the ideal necessary condition for instability is that anti-cyclonic shear is present somewhere in the system (in dimensional terms, that $U'f > 0$ somewhere in the flow). This necessary condition in nondimensional terms can be re-written as $Q < 1$ (since $1/f = 1/f_0$ is the timescale and
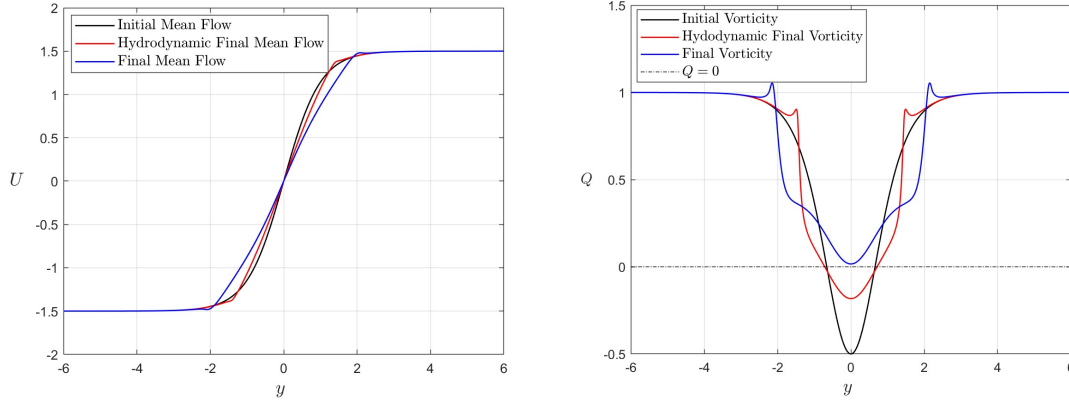
Figure 5.21: The mean flow (left) and vorticity (right) in their initial (black) and final hydrodynamic (red) and magnetohydrodynamic (blue) states of the nonlinear evolution (illustrated in figures 5.18 and 5.19) with $\Lambda = 1.5$, $\nu_0 = 0.02$ and $\mathcal{M} = 0.03$.

$U'f < 0 \implies f^2 - U'f < f^2 \implies fQ < f^2$). Thus, since this is a less stringent condition for instability compared to the hydrodynamic case (where $fQ < 0$ somewhere in the flow is a necessary condition for instability) it is reasonable that a less negative $\overline{Q}$ is required in the magnetohydrodynamic case to ensure the flow is stable. With the necessary condition for instability being $Q < 1$ somewhere in the flow, it is surprising that the final minimum mean vorticity is $\overline{Q} \approx 0$; however, this is sufficient so that instability can no longer occur with the stabilising effects of stratification and diffusion.

5.6.2 The Significance of Weak Magnetic Field

We have just considered the nonlinear evolution of the case with $\Lambda = 1.5$, $\nu_0 = 0.02$ and $\mathcal{M} = 0.03$, where, even with relatively weak magnetic field strength (yielding $\mathcal{R} = \Lambda/\mathcal{M} = 50$), there is a significant change to the final $\overline{U}$ and $\overline{Q}$. Thus, in order to determine what may be classified as weak magnetic field, we consider the nonlinear evolution with $\Lambda = 1.5$, $\nu_0 = 0.02$ for $\mathcal{M} = 0.01$ and $\mathcal{M} = 0.02$ (yielding $\mathcal{R} = 150$ and $\mathcal{R} = 75$). Figure 5.22 shows, for various modes, the kinetic, potential and magnetic energy of the perturbed quantities against time t for $\mathcal{M} = 0.01$ and $\mathcal{M} = 0.02$. Figure 5.21 shows the initial and final $\overline{U}$ and $\overline{Q}$ for $\mathcal{M} = 0$, $\mathcal{M} = 0.01$ and $\mathcal{M} = 0.02$. Evidently, there is much less change to $\overline{U}$ and $\overline{Q}$ for $\mathcal{M} = 0.01$ and $\mathcal{M} = 0.02$ than for $\mathcal{M} = 0.03$ (which is illustrated in figure 5.21). Hence, we argue that $\mathcal{M} = 0.01$ ($\mathcal{R} = 150$) may be classified as weak magnetic field, $\mathcal{M} = 0.03$ ($\mathcal{R} = 75$) is moderate (or, at least, no longer weak) and $\mathcal{M} = 0.02$ is a transitional case. Thus, we suppose that if $\mathcal{R} > 100$, then the magnetic field strength may be classified as weak; figure 5.20 and 5.22 agree with this classification. Indeed, figure 5.22 shows for $\mathcal{M} = 0.01$ (left panel) that after nonlinear saturation the magnetic energy of the 1st mode decays at least an order of magnitude larger than the kinetic energy of the 1st mode. As there is little dynamical effect made by the magnetic field in this case, we can conclude that the effect of magnetic field is determined by the respective magnitude of the peak kinetic and magnetic
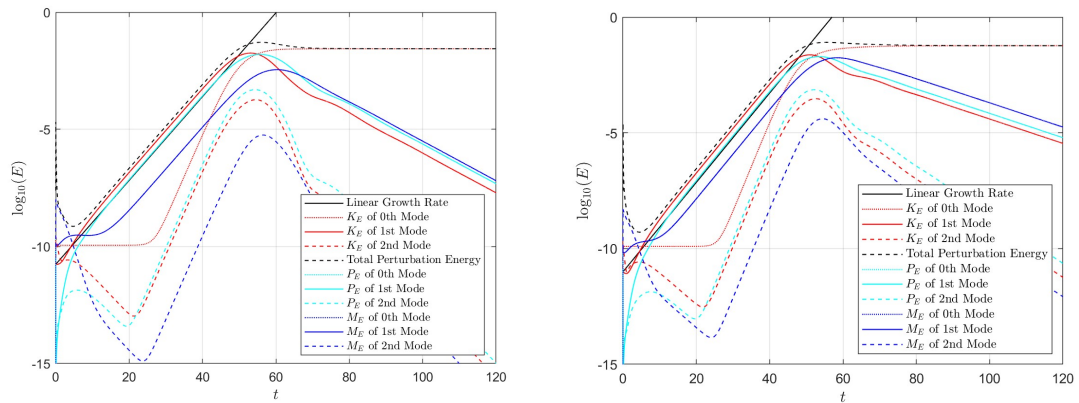
Figure 5.22: Evolution of kinetic, magnetic and potential energy for the lowest order vertical modes against t with $\Lambda = 1.5$, $\nu_0 = 0.02$ for $\mathcal{M} = 0.01$ (left) and $\mathcal{M} = 0.02$ (right).
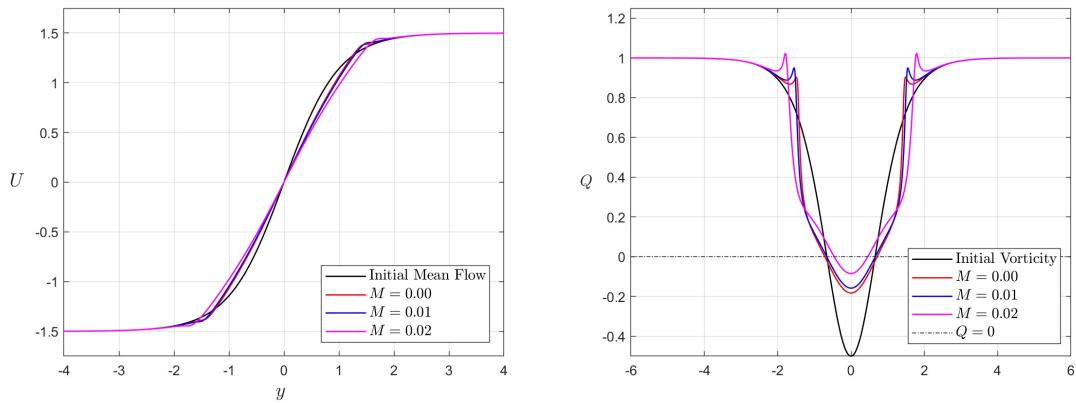
Figure 5.23: The initial (black) and final $\overline{U}$ (left) and $\overline{Q}$ (right) for various $\mathcal{M}$ of the nonlinear evolution with $\Lambda = 1.5$ and $\nu_0 = 0.02$.

energies (both of which occur about nonlinear saturation). Indeed, for $\mathcal{M} = 0.01$, figure 5.22 shows that the peak magnetic energy of the 1st mode is at least an order of magnitude smaller than the peak kinetic energy of the 1st mode, implying there is minimal dynamical effect as a result of the magnetic field, which is certainly the case. For $\mathcal{M} = 0.02$ the right panel of figure 5.22 shows that the peak kinetic and magnetic energy of the 1st mode are comparable, implying that magnetic field may have some dynamical effect (which is indeed the case). Finally, for $\mathcal{M} = 0.03$, figure 5.20 shows that the peak magnetic energy of the 1st mode is larger in magnitude than the peak kinetic energy of the 1st mode, implying that the magnetic field does have a significant dynamic effect, as shown by figure 5.21.

5.6.3 The Nonlinear Evolution of the Most Unstable Mode with $\Lambda = 1.5$

We now consider the nonlinear evolution of the mode with the largest linear growth rate ($S = 0.4218$) for $\Lambda = 1.5$ and $\nu_0 = 0.02$, occurring at $\mathcal{M} = 0.23$ and indicated by the white cross in the figure 5.3. The simulation is run with $H = 2.8862$ (since the maximum growth rate at

$K = 2\pi/H = 2.1770$ for $\Lambda = 1.5$, $\nu_0 = 0.02$ and $\mathcal{M} = 0.23$) and $L = 30$, which is sufficient to ensure all perturbations have decayed by the boundary. The perturbed quantities are normalised by the maximum of u, ψ, ρ, b_x and ϕ over the whole evolution, which (in this case) corresponds to $u = 1.006$ at $t = 37$. The grid size is 1536×32. The timestep is $\Delta t = 5.0 \times 10^{-3}$.

In figures 5.24 and 5.25 we see a similar evolution of the perturbed quantities as in figures 5.18 and 5.19; however, there are also many differences. Indeed, we now see the magnetic, streamfunction and density perturbation viscously decay while spreading over the large latitudinal domain; as before, we continue to see the general growth (until saturation) and decay of the perturbed quantities. At saturation, we also see the central along-stream perturbation be displaced southward rather than northward owing to the difference in phase of the streamfunction in panel (**b**). We also see a much faster nonlinear evolution with equilibrium occurring by $t = 90$ rather than $t = 140$ in figure 5.24 and 5.25. This is confirmed by figure 5.26, which illustrates the growth and decay of the kinetic, potential and magnetic energy over time. Notably, figure 5.26 shows the magnetic energy growing comparably with the kinetic energy, and upon reaching nonlinear saturation, the magnetic energy continues to grow in magnitude beyond that of the kinetic energy (and then continuous to viscously decay, remaining an order of magnitude larger than the kinetic energy throughout); we have already determined that this implies that magnetic field has a strong dynamical role throughout the evolution.

In figure 5.27 we can see that there is a substantial change to $\overline{U}$ and $\overline{Q}$ in comparison to the previous case with $\mathcal{M} = 0.03$ (and the hydrodynamic case). The shear of the mean flow is significantly reduced. It is also clear the minimum of the final $\overline{Q}$ is significantly greater than in the previous MHD or the hydrodynamic case. This is reasonable since presumably, for the most unstable mode of the linear system, a larger $\overline{Q}$ is sufficient for instability. For this case we also see the vorticity redistribute across the latitudinal domain in order to reduce more efficiently the minimum $\overline{Q}$ and stabilise the flow.

5.6.4 The Nonlinear Evolution with Strong Magnetic Field and $\Lambda = 1.5$

Finally, we consider the nonlinear evolution of system with $\Lambda = 1.5$, $\nu_0 = 0.02$ and $\mathcal{M} = 1.0$. The maximum growth rate ($S = 0.1321$) for these parameters occurs at $K_{\max} = 0.5240$ (indicated by the rightmost red dot in the left panel of figure 5.3), yielding $H = 11.9908$. We also take $L = 40$ which is sufficient to ensure all perturbations have decayed by the boundary. The perturbed quantities are normalised by the maximum of u, ψ, ρ, b_x and ϕ over the whole evolution, which (in this case) corresponds to $u = 1.2277$ at $t = 114$. The grid size is 1536×64. The timestep is $\Delta t = 2.5 \times 10^{-3}$.

In figures 5.28 and 5.29 we see a very distinct evolution of the perturbed quantities in comparison to any other case. This becomes evident on inspection of the evolution of energy beyond saturation in figure 5.30, where, instead of viscously decaying, the kinetic, potential and magnetic energies oscillate in magnitude over time, implying Alfvénic behaviour. In figure 5.28 we once
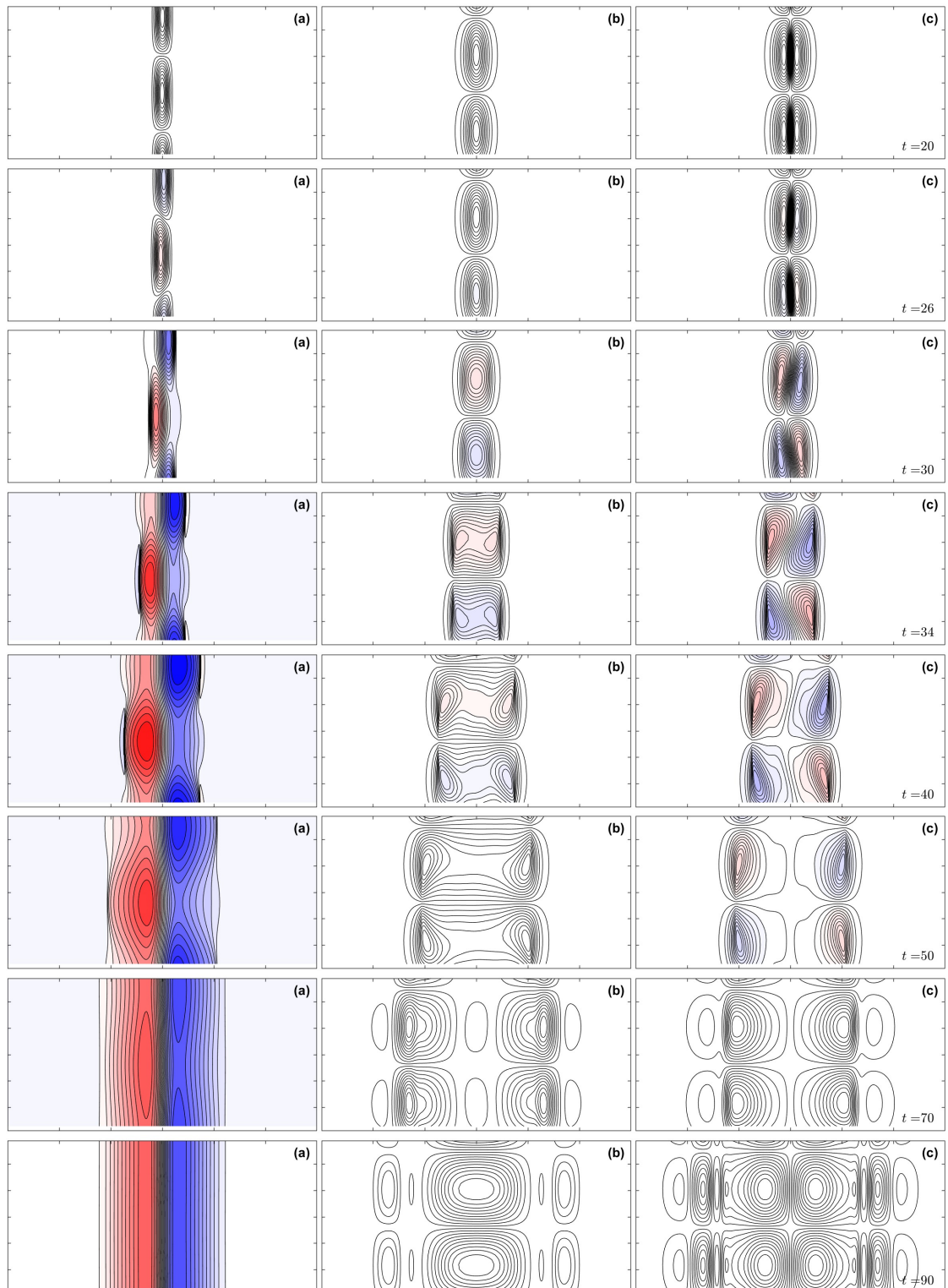
Figure 5.24: Contours in (y, z)-space of (**a**) the perturbed along-stream velocity, (**b**) the perturbed streamfunction ψ and (**c**) the perturbed density ρ. Each row of panels is at a distinct time t. In this simulation, $\Lambda = 1.5$, $\nu_0 = 0.02$, $\mathcal{M} = 0.23$, $L = 30$, and $H = 2.8863$ ($K = 2.1770$).
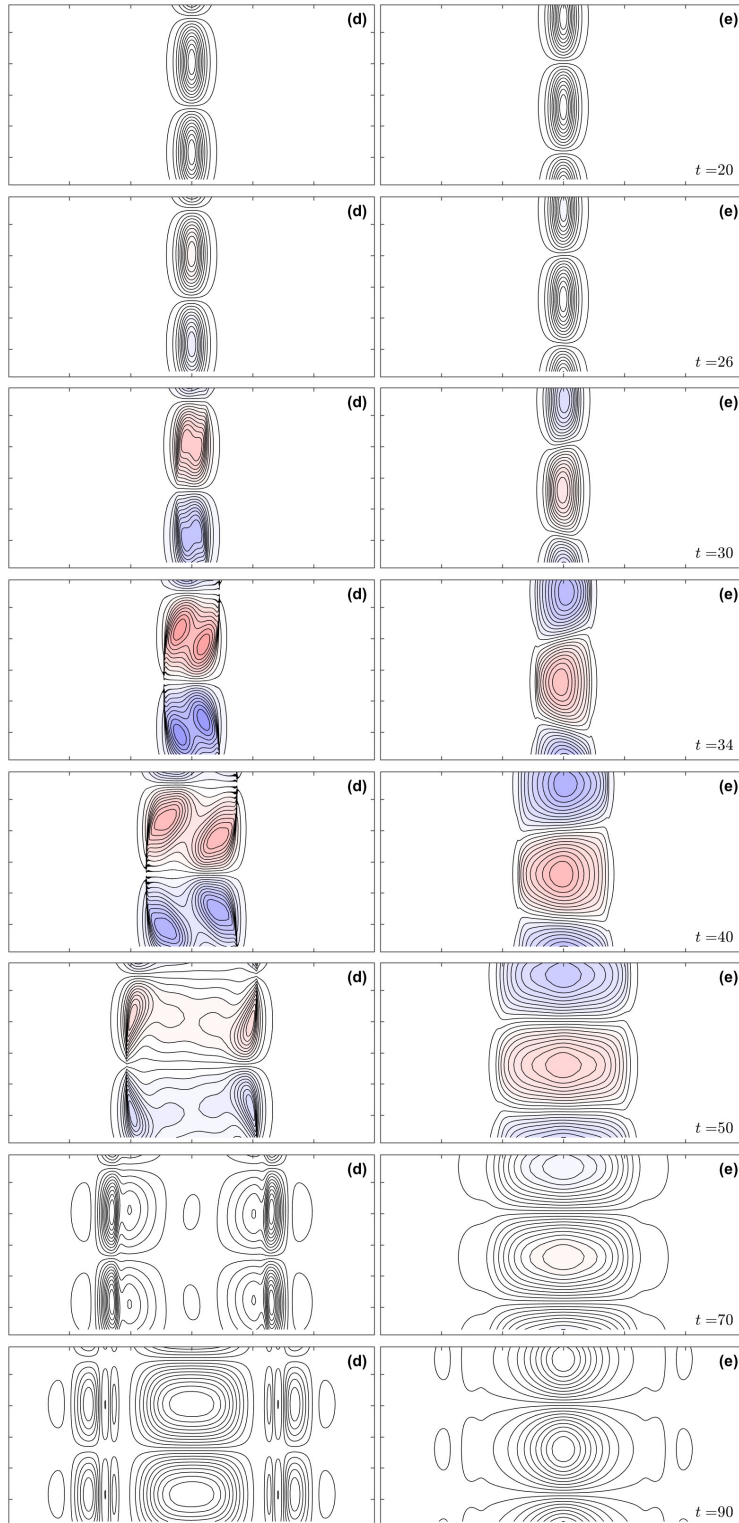
Figure 5.25: Contours in (y, z)-space of ($\mathbf{d}$) the perturbed along-stream magnetic field b_x and ($\mathbf{e}$) the perturbed magnetic streamfunction ϕ. Each row of panels is at a distinct time t. In this simulation, $\Lambda = 1.5$, $\nu_0 = 0.02$, $\mathcal{M} = 0.23$, $L = 30$, and $H = 2.8863$ ($K = 2.1770$).
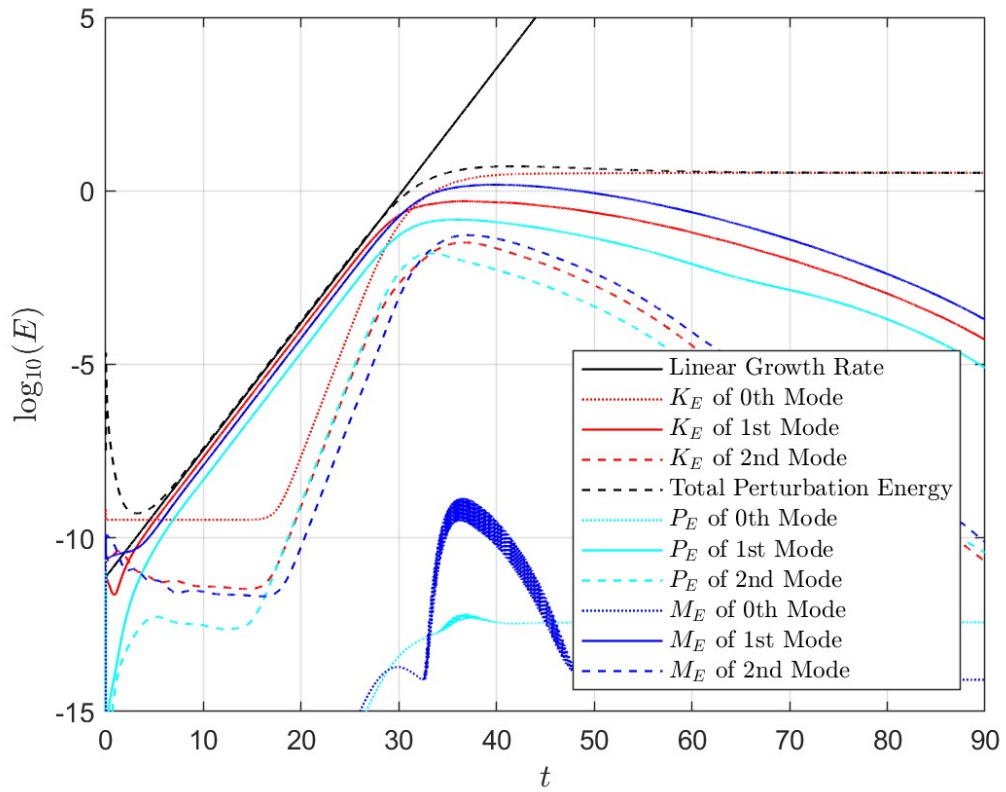
Figure 5.26: Evolution of kinetic, magnetic and potential energy for the lowest order vertical modes against t corresponding to the dynamical process illustrated in figures 5.24 and 5.25 with $\Lambda = 1.5$, $\nu_0 = 0.02$ and $\mathcal{M} = 0.23$.
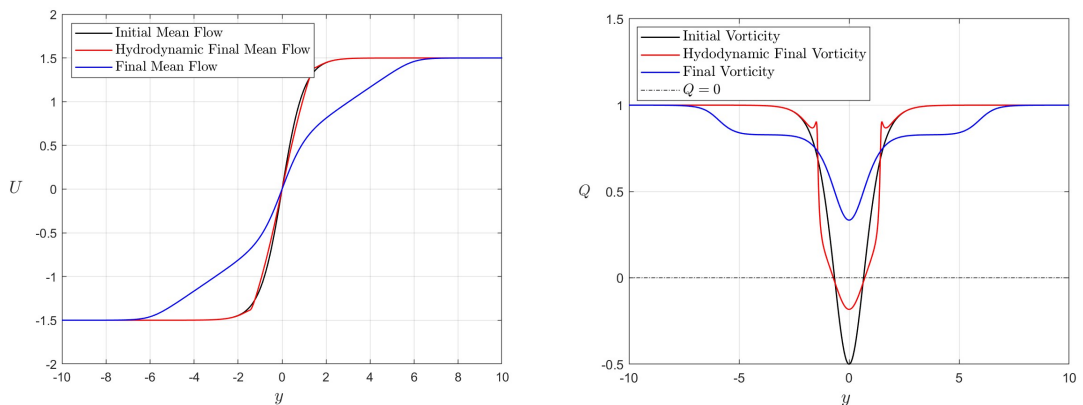
Figure 5.27: The mean flow (left) and vorticity (right) in their initial (black) and final hydrodynamic (red) and magnetohydrodynamic (blue) states of the nonlinear evolution (illustrated in figure 5.24 and 5.25) with $\Lambda = 1.5$, $\nu_0 = 0.02$ and $\mathcal{M} = 0.23$.

again see growth of the streamfunction in panel (**b**) that generates latitudinal momentum and density perturbations, however, the perturbation in u (shown in panel (**a**)) no longer forms a set of stable columns and instead continues to grow and decay from $t \approx 120$. The streamfunction and density perturbations also grow and decay out of phase. The reason we do not see the perturbation in u form into stable columns at $t \approx 120$ is due to the strong magnetic streamfunction perturbation illustrated in panel (**e**) of figure 5.29 that continues to drive latitudinal motion.

In figure 5.31 we can see that there has been little change to $\overline{U}$ and $\overline{Q}$, comparable to that of figure 5.23 which illustrated the mean flow and mean vorticity change with $\mathcal{M} = 0.01$. We might expect this owing to the strong magnetic field inhibiting overturning motions via strong magnetic tension. As a result the minimum $\overline{Q}$ required so that instability can no longer occur is much less than in the previous case since there is diffusion, strong magnetic tension and stratification all acting to stabilise the flow.

5.6.5 Mean Flow and Mean Vorticity Changes at Various $\mathcal{M}$ for $\Lambda = 1.5$

We now summarise the mean flow and mean vorticity changes for various $\mathcal{M}$ with $\Lambda = 1.5$ and $\nu_0 = 0.02$ by plotting them all on a single panel in figures 5.32 and 5.33, respectively. The only mean flow $\overline{U}$ and mean vorticity $\overline{Q}$ plots we have seen before are for the hydrodynamic case and for $\mathcal{M} = 0.23$ (where the most unstable linear mode occurs); this choice has been made as we have already seen the mean flow and mean vorticity changes in those cases and it is of interest to illustrate the changes for other $\mathcal{M}$.

In figure 5.32 we see that the mean flow with largest reduction of shear is not that of $\mathcal{M} = 0.23$ (where the most unstable linear mode occurs), but occurs for $\mathcal{M} = 0.14$ instead. Indeed, figure 5.32 shows that the minimum $\overline{Q}$ for $\mathcal{M} = 0.14$ is also larger than in the $\mathcal{M} = 0.23$ case. This system is harder to stabilise through nonlinear effects for $\mathcal{M} = 0.14$ since the (stabilising) effects of stratification are less significant. This is because the maximum growth rates occur at $K = 2.6020$ and $K = 2.1770$ for $\mathcal{M} = 0.14$ and $\mathcal{M} = 0.23$, respectively, and the effects of stratification are more significant at smaller K (larger aspect ratios). Hence, the minimum $\overline{Q}$ required to stabilise the system is less positive for $\mathcal{M} = 0.23$ than $\mathcal{M} = 0.14$.

Figures 5.32 and 5.33 also illustrate a continuous mean flow and mean vorticity change (alongside the figures for other $\mathcal{M}$ we have already seen) as $\mathcal{M}$ increases. For example, in figure 5.32 there is little change to $\overline{U}$ in the hydrodynamic case (likewise with $\mathcal{M} = 0.01$), then as $\mathcal{M}$ increases the mean flow change becomes more severe (in order to reduce the latitudinal shear) and is maximum at $\mathcal{M} = 0.14$. Finally, as $\mathcal{M}$ increases further, the mean flow change becomes less severe (as stronger latitudinal shear is not sufficient for instability due to other stabilising effects), until the change is almost identical to the hydrodynamic mean flow change at $\mathcal{M} = 1.0$. An analogous argument can be made for $\overline{Q}$.
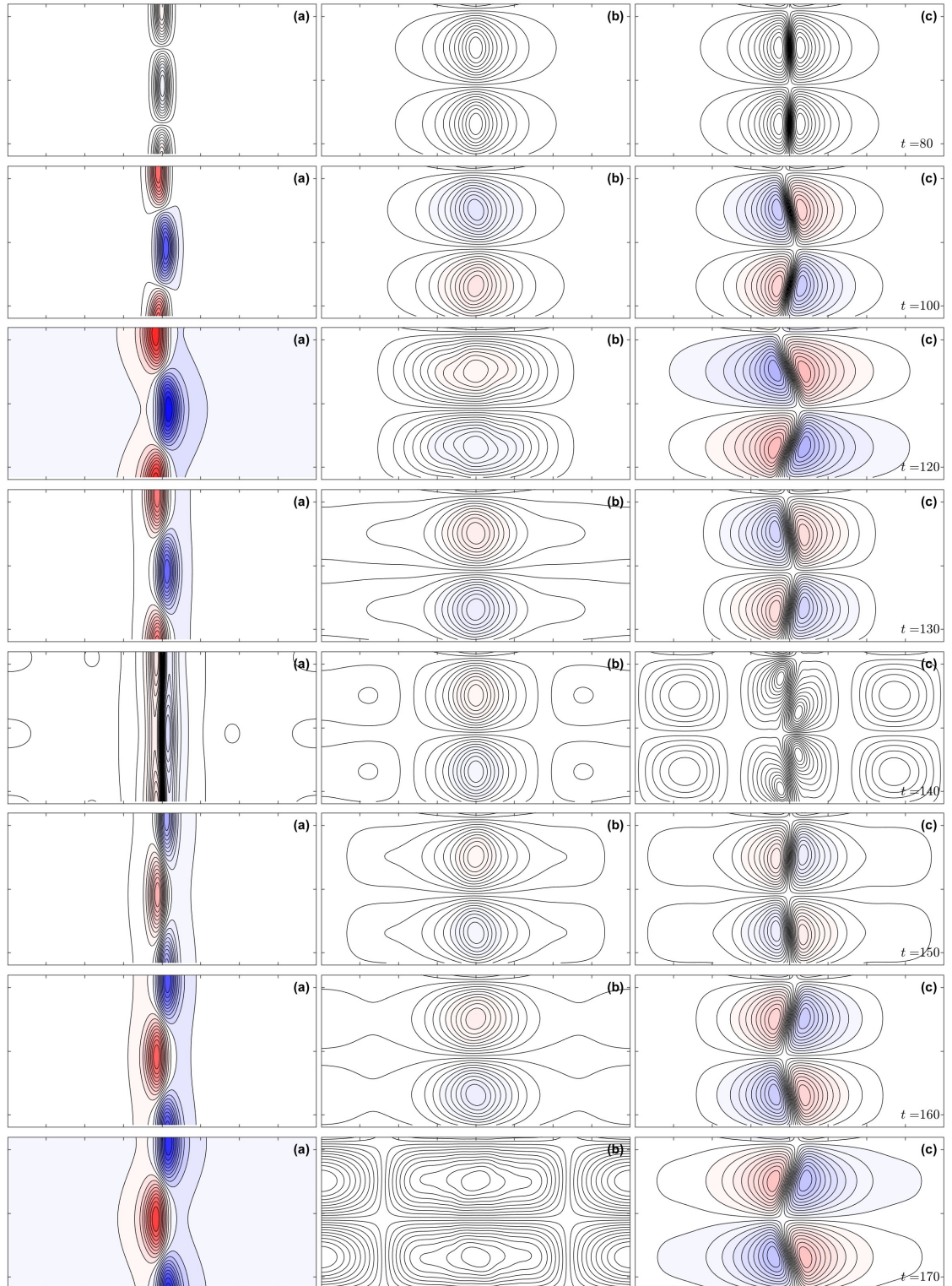
Figure 5.28: Contours in (y, z)-space of (**d**) the perturbed along-stream magnetic field b_x and (**e**) the perturbed magnetic streamfunction ϕ. Each row of panels is at a distinct time t. In this simulation, $\Lambda = 1.5$, $\nu_0 = 0.02$, $\mathcal{M} = 1.0$, $L = 40$, and $H = 11.9908$ ($K = 0.5240$).
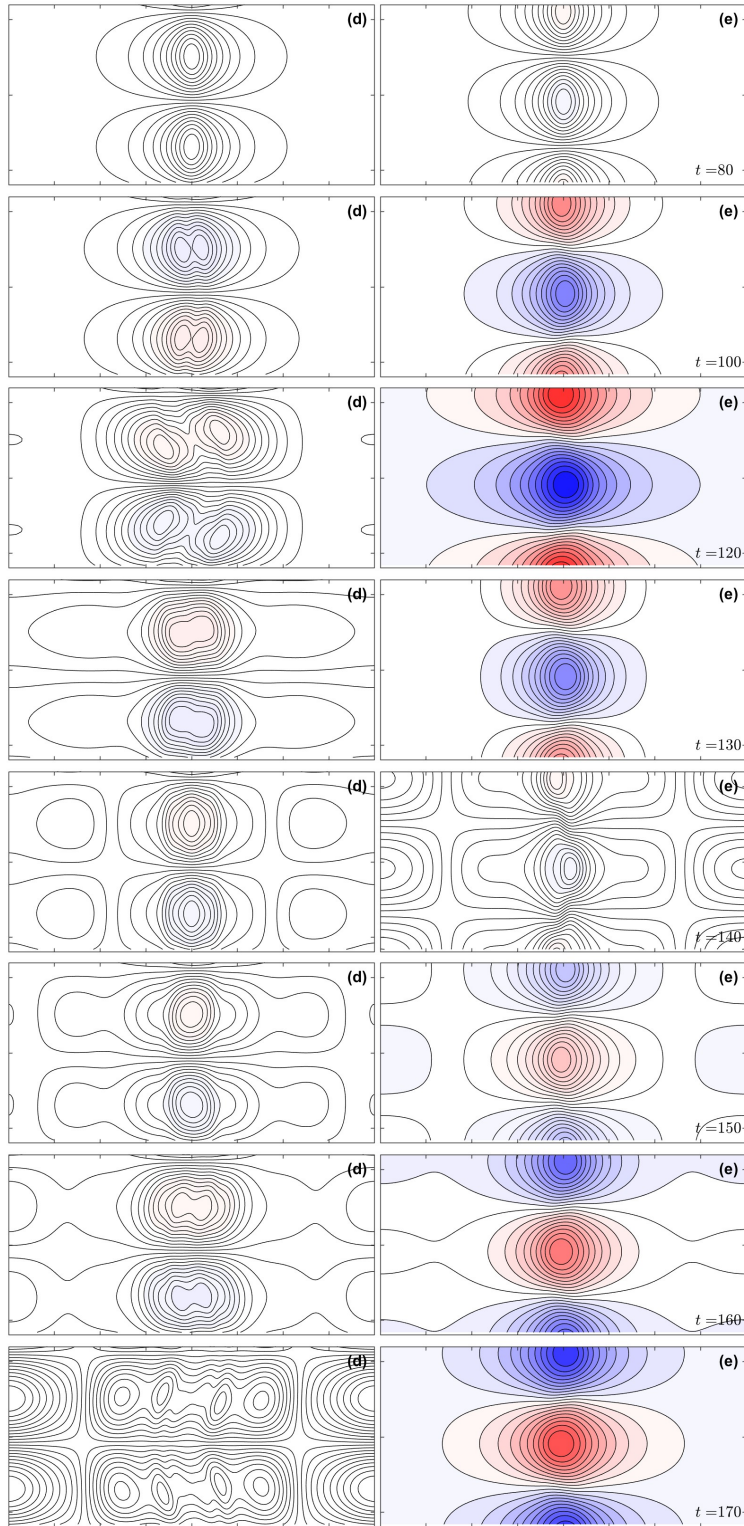
Figure 5.29: Contours in (y, z)-space of (**d**) the perturbed along-stream magnetic field b_x and (**e**) the perturbed magnetic streamfunction ϕ. Each row of panels is at a distinct time t. In this simulation, $\Lambda = 1.5$, $\nu_0 = 0.02$, $\mathcal{M} = 1.0$, $L = 40$, and $H = 11.9908$ ($K = 0.5240$).
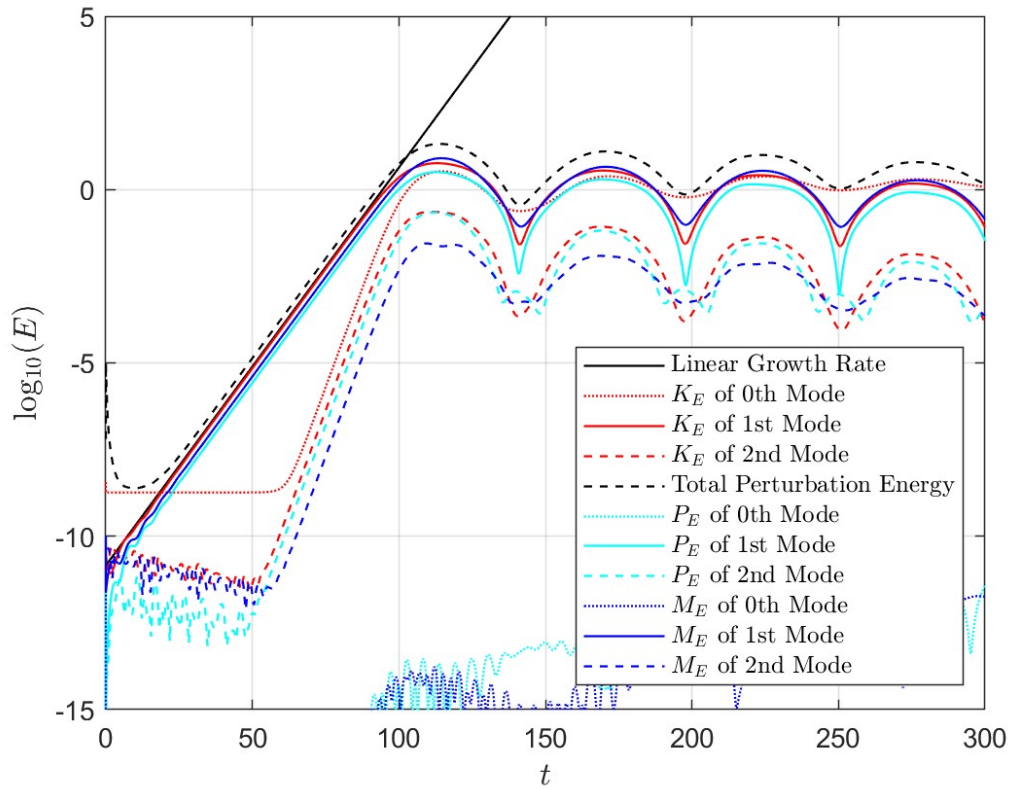
Figure 5.30: Evolution of kinetic, magnetic and potential energy for the lowest order vertical modes against t corresponding to the dynamical process illustrated in figures 5.28 and 5.29 with $\Lambda = 1.5$, $\nu_0 = 0.02$ and $\mathcal{M} = 1.0$.
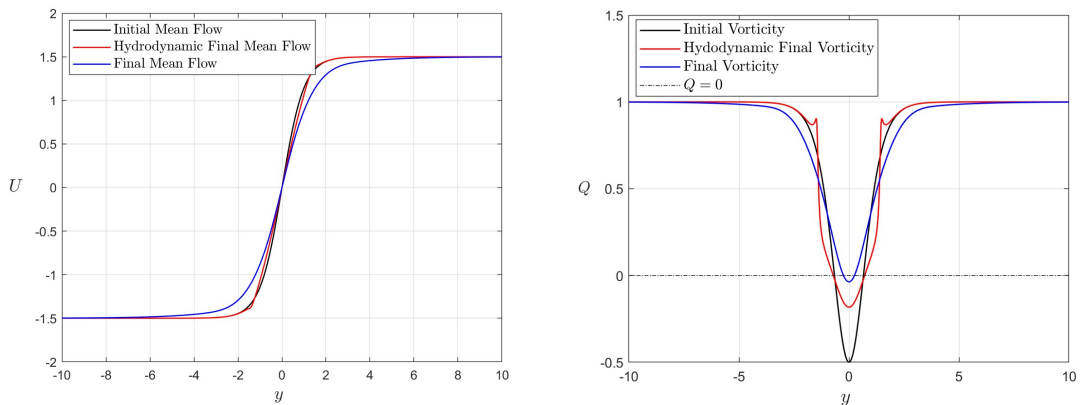
Figure 5.31: The mean flow (left) and vorticity (right) in their initial (black) and final hydrodynamic (red) and magnetohydrodynamic (blue) states of the nonlinear evolution (illustrated in figure 5.28 and 5.29) with $\Lambda = 1.5$, $\nu_0 = 0.02$ and $\mathcal{M} = 1.0$.
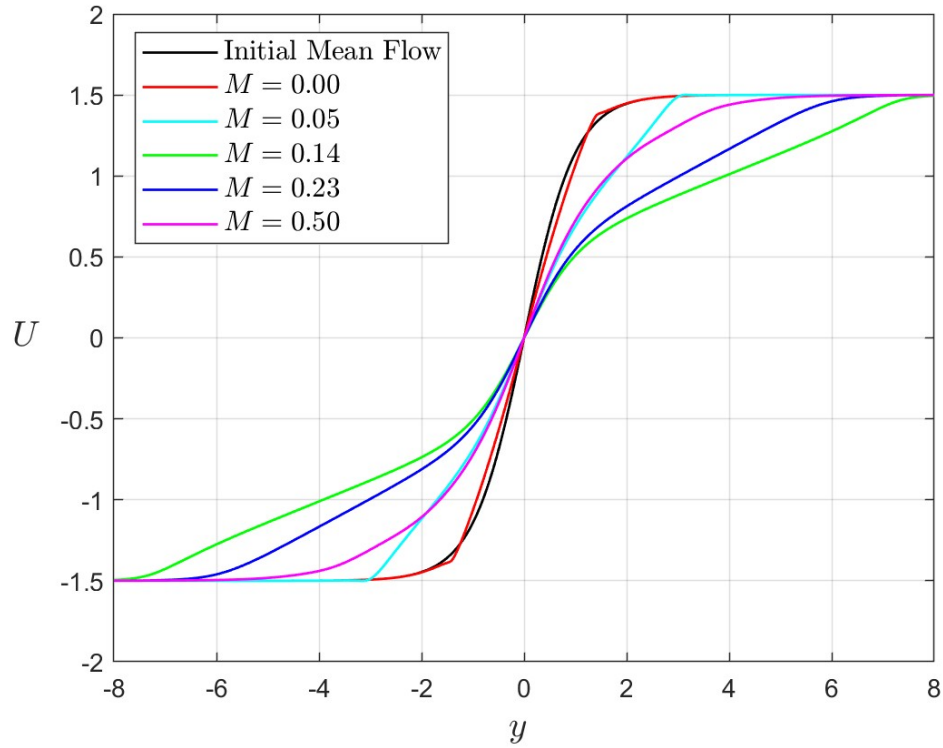
Figure 5.32: The initial (black) and final $\overline{U}$ of the nonlinear evolution for various $\mathcal{M}$ with $\Lambda = 1.5$ and $\nu_0 = 0.02$.
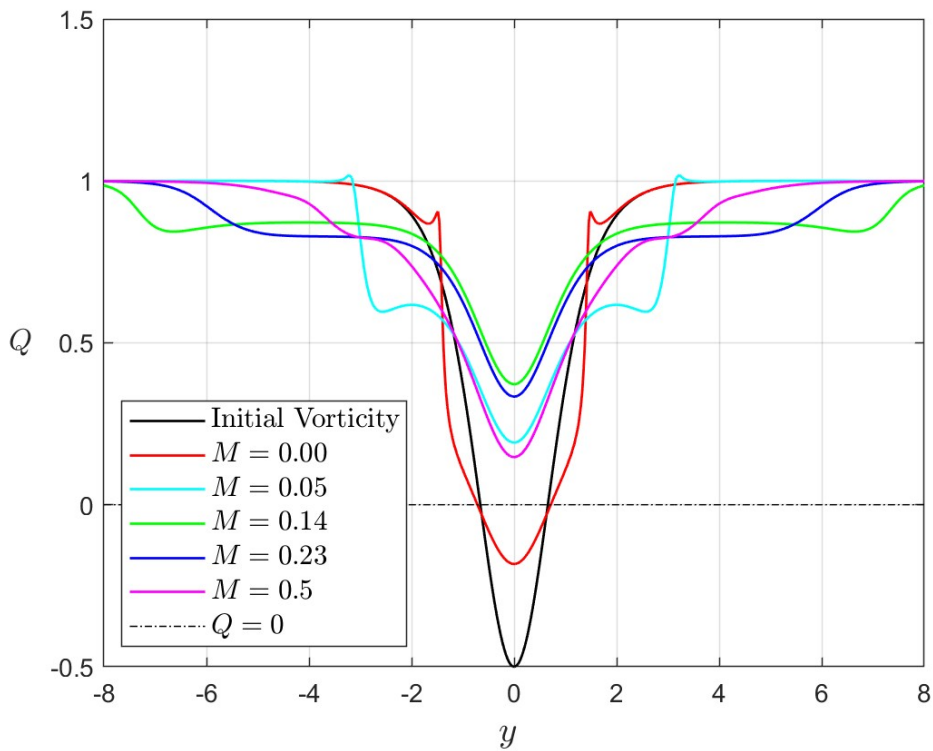
Figure 5.33: The initial (black) and final $\overline{Q}$ of the nonlinear evolution for various $\mathcal{M}$ with $\Lambda = 1.5$ and $\nu_0 = 0.02$.
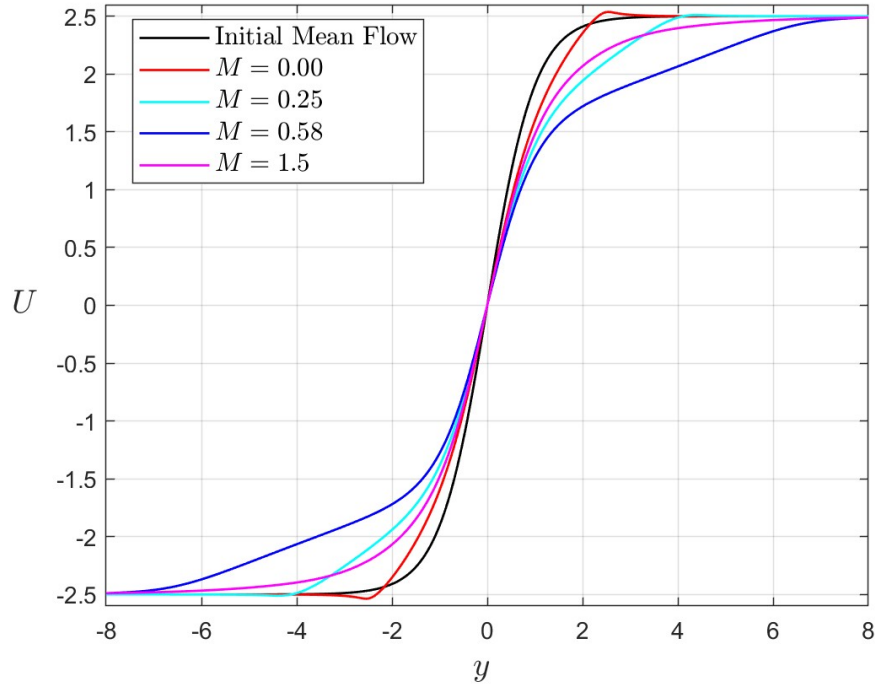
Figure 5.34: The initial (black) and final $\overline{U}$ of the nonlinear evolution for various $\mathcal{M}$ with $\Lambda = 2.5$ and $\nu_0 = 0.30$.

5.6.6 Mean Flow and Mean Vorticity Changes at Various $\mathcal{M}$ for $\Lambda = 2.5$

We now give a brief overview of the $\Lambda = 2.5$ results since the results are largely analogous to the case $\Lambda = 1.5$; the system is just less sensitive to changes in magnetic field strength owing to the larger magnitude of kinetic energy. Thus, we summarise the mean flow and mean vorticity changes for $\Lambda = 2.5$ and $\nu_0 = 0.3$ at various $\mathcal{M}$ in figures 5.34 and 5.35, respectively. First, note that the Reynolds number is much smaller in this case ($Re = 8.33$ for $\Lambda = 2.5$ and $Re = 75$ for $\Lambda = 1.5$) so that evolution is much more diffusive, where less significant changes to $\overline{U}$ and $\overline{Q}$ will occur. However, we still find that the shear of $\overline{U}$ is reduced and the minimum $\overline{Q}$ is increased in order to stabilise the system. We also observe a continuous mean flow and mean vorticity change, as seen for $\Lambda = 1.5$. Indeed, the mean flow and mean vorticity changes are most significant (from the hydrodynamic change) at values of $\mathcal{M}$ at which the maximum growth rate of the linear system occurs ($\mathcal{M} = 0.58$ for $\Lambda = 2.5$ and $\nu_0 = 0.3$). The mean flow and mean vorticity change is least significant (from the hydrodynamic change) for weak and strong magnetic field. Interestingly, the transitional case from weak magnetic field to "non-weak" (i.e., when the peak magnetic and kinetic energy of the 1st mode are comparable) occurs at $\mathcal{M} = 0.25$ yielding $\mathcal{R} = \Lambda/\mathcal{M} = 10$. This does not coincide with the transitional case for $\Lambda = 1.5$, which occurred at $\mathcal{M} = 0.02$ with $\mathcal{R} = 75$. However, if one normalises these quantities with the respective Reynolds number of each case ($Re = 75$ for $\Lambda = 1.5$ and $Re = 8.33$ for $\Lambda = 2.5$), we obtain $\mathcal{R}/Re \approx 1 = O(1)$ in both cases. This critical ratio also holds for larger Rossby numbers Λ.
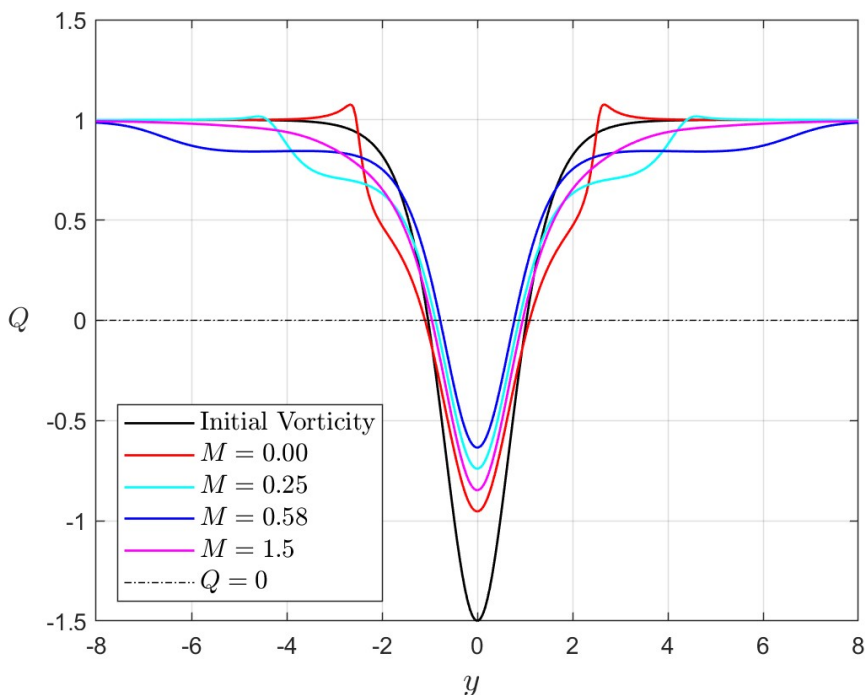
Figure 5.35: The initial (black) and final $\overline{Q}$ of the nonlinear evolution for various $\mathcal{M}$ with $\Lambda = 2.5$ and $\nu_0 = 0.30$.

5.7 Magnetohydrodynamic Nonlinear Evolution in the hydrodynamically stable regime

In this section we consider the magnetohydrodynamic nonlinear evolution of the system with Rossby number $\Lambda = 0.5$, where, in contrast to the previous cases (with $\Lambda = 1.5$ and $\Lambda = 2.5$), linear analysis implies hydrodynamic stability since $\Lambda < 1$. However, the linear analysis also showed that purely magnetic instabilities can occur with $\Lambda < 1$. Thus, we may expect that magnetic field will also play a crucial role in the nonlinear evolution.

5.7.1 The Nonlinear Evolution of the Most Unstable Mode with $\Lambda = 0.5$

We will begin by presenting the nonlinear evolution of the hydrodynamically stable regime with $\Lambda = 0.5$, $\nu_0 = 0.01$ ($Re = Rm = 50$) and $\mathcal{M} = 0.16$, where the most unstable mode occurs (indicated by the white cross in the left panel of figure 5.2). The maximum growth rate $S = 0.0850$ is generated at the vertical wavenumber $K_{\mathrm{max}} = 2.0660$, yielding $H = 3.0412$. We also take $L = 40$ which is sufficient to ensure the perturbed quantities have decayed by the latitudinal boundary. The grid size is 1024×32. The timestep is $\Delta t = 1.0 \times 10^{-2}$.

In figure 5.36 and 5.37 we contour u, ψ, ρ, b_x and ψ in (y, z)-space at various times t. The quantities are normalised by the maximum of u, ψ, ρ, b_x and ϕ over the whole evolution, which (in this case) corresponds to $u = 0.7118$ at $t = 166$. Figure 5.38 illustrates, for numerous vertical modes (integrated over the entire latitudinal domain), the kinetic, potential and magnetic energy
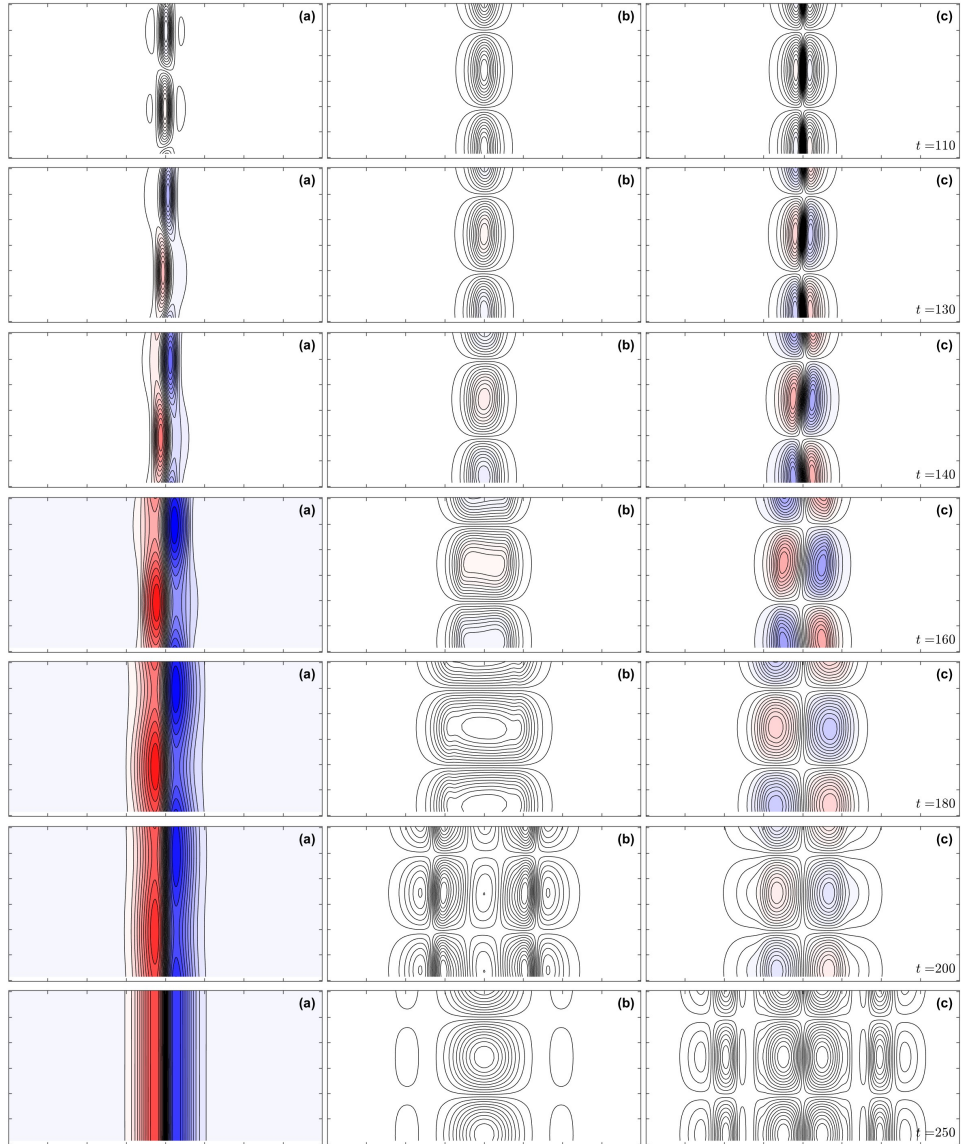
Figure 5.36: Contours in (y, z)-space of (**d**) the perturbed along-stream magnetic field b_x and (**e**) the perturbed magnetic streamfunction ϕ. Each row of panels is at a distinct time t. In this simulation, $\Lambda = 0.5$, $\nu_0 = 0.01$, $\mathcal{M} = 0.16$, $L = 40$, and $H = 3.0412$ ($K = 2.0660$).

of the perturbed quantities against time t. Figure 5.39 shows the initial and final $\overline{U}$ and $\overline{Q}$ against latitude y.

The dynamical process of the evolution is illustrated in figures 5.36 and 5.37. The process is very similar to what we have seen before, with overturning motions driving the along-stream perturbation u into two stable columns, which drive the change to $\overline{U}$. However, noting that $L = 40$ in this case, we can infer that the latitudinal redistribution of the perturbed quantities (and therefore the stable columns) is to a far greater extent than in previous cases.

Figure 5.20 shows the evolution of the kinetic, potential and magnetic energy throughout the evolution. Throughout the whole evolution the magnetic energy of the 1st mode is larger than the kinetic energy of the 1st mode, implying the crucial role of the magnetic field.

Figure 5.21 shows that there is a significant change to $\overline{U}$ and $\overline{Q}$ in comparison to any other
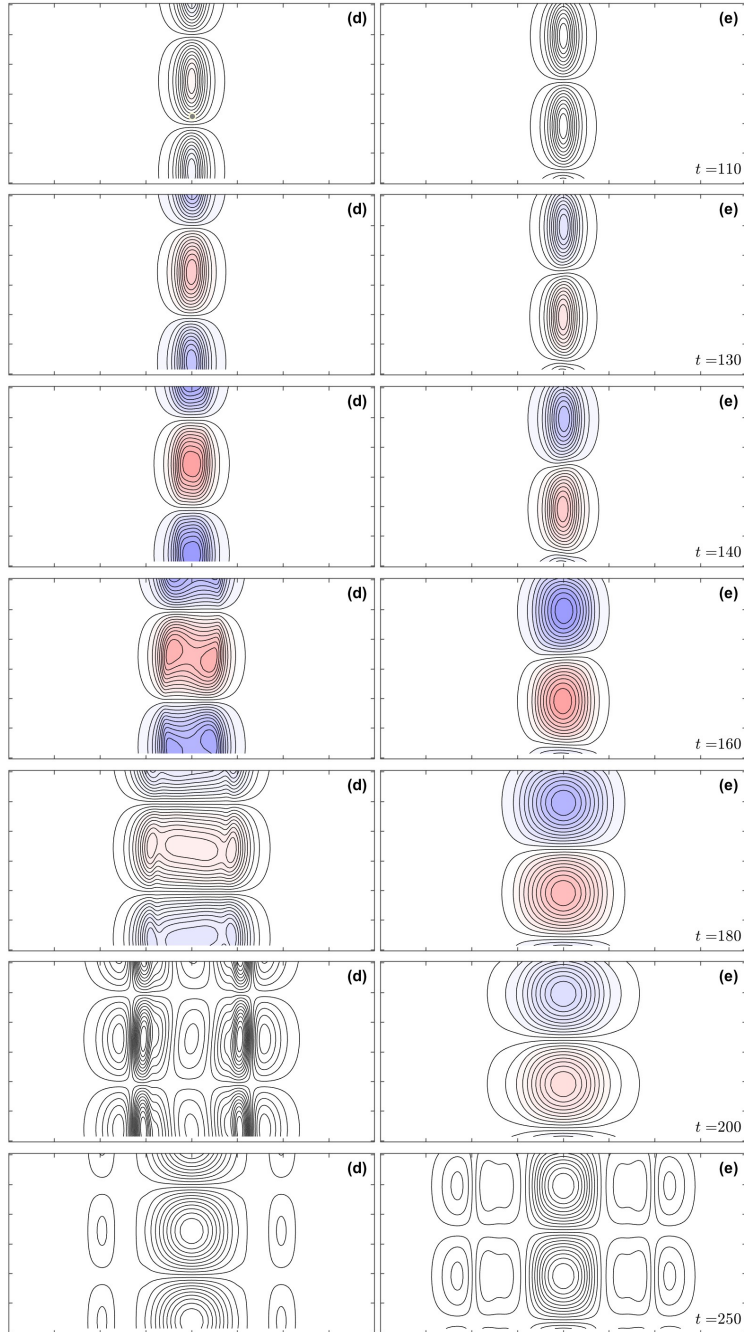
Figure 5.37: Contours in (y, z)-space of (**d**) the perturbed along-stream magnetic field b_x and (**e**) the perturbed magnetic streamfunction ϕ. Each row of panels is at a distinct time t. In this simulation, $\Lambda = 0.5$, $\nu_0 = 0.01$, $\mathcal{M} = 0.16$, $L = 40$, and $H = 3.0412$ ($K = 2.0660$).
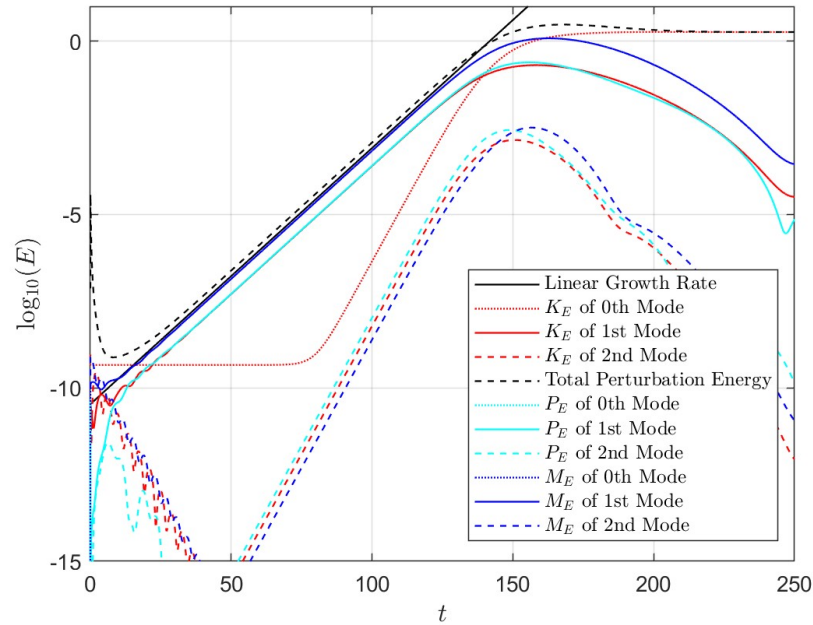
Figure 5.38: Evolution of kinetic, magnetic and potential energy for the lowest order vertical modes against t corresponding to the dynamical process illustrated in figures 5.36 and 5.37 with $\Lambda = 0.5$, $\nu_0 = 0.01$ $\mathcal{M} = 0.16$.

case. Within the central region $|y| < 1$ there is no longer any anti-cyclonic shear present in the mean flow — it is instead cyclonic. The latitudinal shear beyond $|y| = 2$ is non-zero; however, the shear is not as strong as that for the initial mean flow in the central region $|y| < 2$. The right panel of figure 5.21 shows that the minimum mean vorticity $\overline{Q}$ increases significantly with the final maximum $\overline{Q}$ even reaching $\overline{Q} \approx 1.25$. Recall that the ideal necessary condition for linear instability is that $Q < 1$, so that we can presume that $\overline{Q}$ is no longer sufficient to drive instability in the presence of diffusion and stratification.

5.7.2 Mean Flow and Mean Vorticity Changes at Various $\mathcal{M}$ with $\Lambda = 0.5$

Even for the case $\mathcal{M} = 0.16$, where the maximum growth rate occurs, it is surprising to see such a substantial change to $\overline{U}$ and $\overline{Q}$ over the evolution. Thus, in figures 5.40 and 5.41 we illustrate the energy evolution, mean flow and mean vorticity change for $\mathcal{M} = 0.03$, $\mathcal{M} = 0.14$ (for comparison), and $\mathcal{M} = 0.40$. Surprisingly, for $\mathcal{M} = 0.03$, figure 5.41 shows that there still a substantial change to $\overline{U}$ and $\overline{Q}$ (only slightly different to the $\mathcal{M} = 0.14$ case). We can see that the contrast of the mean flow and mean vorticity change between $\mathcal{M} = 0.16$ and $\mathcal{M} = 0.40$ is much more significant; indeed, for $\mathcal{M} = 0.40$, cyclonic shear is no longer required in the central region to stabilise the flow since strong magnetic field contributes towards stabilising the system. Notably, the minimum final mean vorticity for all $\mathcal{M}$ is $\overline{Q} \approx 0.8$, indicating that the same minimum $\overline{Q}$ is required to stabilise flows with $\Lambda = 0.5$ and $\nu_0 = 0.01$. The final minimum mean vorticity for other values of $\mathcal{M}$ does also indicate this, however there is often some variation from $\overline{Q} \approx 0.8$.
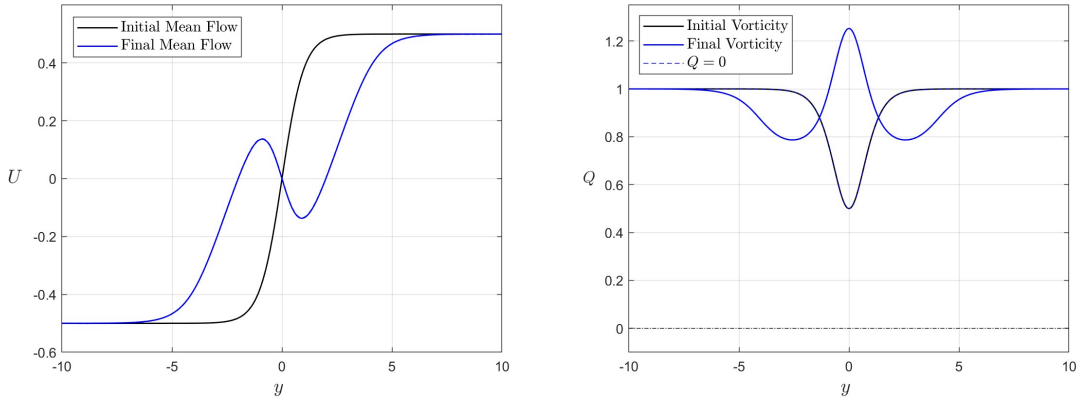
Figure 5.39: The initial (black) and final (blue) $\overline{U}$ (left) and $\overline{Q}$ (right) of the nonlinear evolution (illustrated in figure 5.36 and 5.37) with $\Lambda = 0.5$, $\nu_0 = 0.01$ $\mathcal{M} = 0.16$.
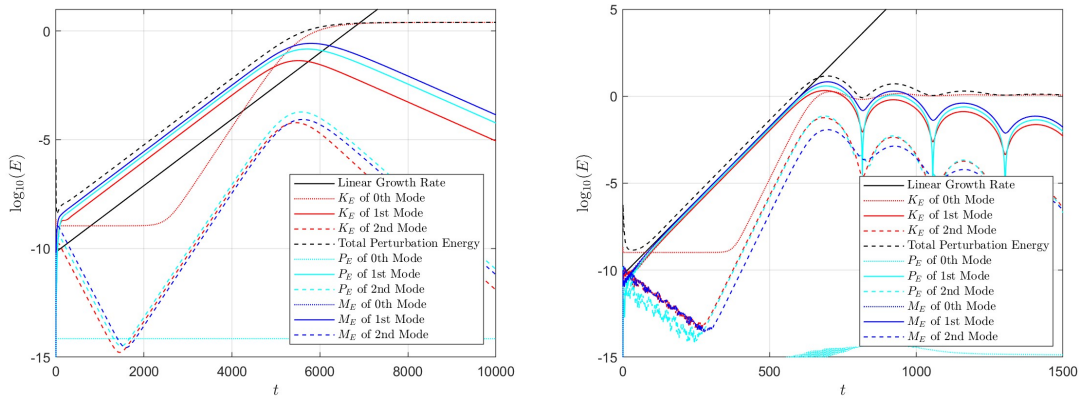
Figure 5.40: Evolution of kinetic, magnetic and potential energy for the lowest order vertical modes against t with $\Lambda = 0.5$ and $\nu_0 = 0.01$ for $\mathcal{M} = 0.03$. (left) and $\mathcal{M} = 0.40$ (right).
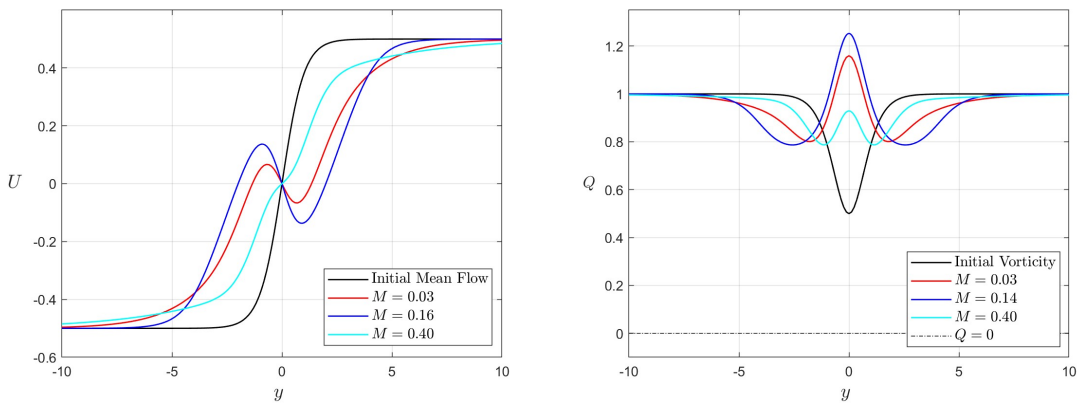
Figure 5.41: The initial (black) and final (blue) $\overline{U}$ (left) and $\overline{Q}$ (right) of the nonlinear evolution for various $\mathcal{M}$ with $\Lambda = 0.5$ and $\nu_0 = 0.01$.

5.8 Conclusions

In this chapter we have considered the linear and nonlinear evolution of a localised shear layer $U(y) = U_0 \tanh(y/L)$ on an f-plane in the presence of uniform vertical magnetic field, and uniform ν, κ and η (with $Pr = Pm = 1$). Although it is not the case that $Pr = Pm = 1$ in the astrophysical bodies of table 2.1, we have discussed important dynamical concepts and interactions that are likely to be applicable for other Prandtl number regimes. It is also a natural extension to hydrodynamic nonlinear studies of similar systems with $Pr = 1$ (e.g., Kloosterziel *et al.*, 2007b; Griffiths, 2003a,b). Also note that the consideration of the localised shear layer $U(y) = U_0 \tanh(y/L)$ is a significant improvement to the model from the uniform shear flow $U(y) = \Lambda_0 y$ considered in Chapters 3 and 4. Physically, astrophysical flows do not extend indefinitely with anti-cyclonic shear ($\Lambda_0 f_0 > 0$). Indeed, the shear layer restricts the flow so that anti-cyclonic shear (which is required for instability) is confined to a finite region.

In Section 5.3 we investigated the linear stability of the system. We initially considered the ideal system, where, in contrast to the unbounded uniform shear flow that we considered in Chapter 3, we found that instability may occur on large vertical scales given sufficiently weak magnetic field strength. We also found that the most unstable mode occurs for the same value of the Lehnert number $\mathcal{L} = K\mathcal{M}$ as in Chapter 3 (given by equations (3.26) and (3.27)). Notably, the maximum growth rate occurs in the large K limit (vanishing vertical scales) and small $\mathcal{M}$ limit such that $K\mathcal{M} = O(1)$, corresponding to the "thin disc" and "weak field" approximations made by Balbus & Hawley (1991). We consider the limit of weak magnetic field on the hydrodynamically stable and unstable modes of (5.19), deriving the expansions (5.24), (5.25) and (5.26). In the hydrodynamically stable regime ($K < (\Lambda - 1)^{-1}$), we find that weak magnetic field always destabilises the system, with the growth rate scaling with $K\mathcal{M}$. This may be applicable to the upper atmosphere of Jupiter were $\Lambda < 1$. In the hydrodynamically unstable regime ($K > (\Lambda - 1)^{-1}$), we find that weak magnetic field increases the growth rate if $K(\Lambda - 2) < \sqrt{2}$ and decreases the growth rate if $K(\Lambda - 2) > \sqrt{2}$. This may be applicable to the upper atmospheres of Hot Jupiters where the Rossby number $\Lambda \in [1, 4]$. We extended this analysis to the diffusive regime with $Pr = Pm = 1$; in this case, we can obtain the diffusive growth rate S via a transformation $S_I \rightarrow S + \nu_0 K^2$, where S_I is the ideal growth rate. We used this transformation to derive the analogous weak field expansions. We also provided numerous contours of the growth rate for $\Lambda = 0.5$, $\Lambda = 1.5$ and $\Lambda = 2.5$ at various magnitudes of diffusion ν_0. The contours were made with the nonlinear analysis in mind, indicating points in $(\mathcal{M}, K)$-space at which we consider the nonlinear evolution of the flow. Diffusion clearly stabilises the modes with large vertical wavenumber (small vertical scales) so that the maximum growth rate now always occurs at finite vertical wavenumber K, yielding a finite vertical scale. In the nonlinear analysis, we use the vertical wavenumber that generates the maximum growth rate at each $\mathcal{M}$ as the vertical domain size.

To investigate the nonlinear analysis of the hyperbolic shear layer, we first developed the nonlinear numerical model used to solve equations (5.7) in Section 5.4. We also discussed the

ratio between the initial kinetic energy of the system (prescribed by the flow $U(y)$) and the initial magnetic energy (prescribed by the uniform vertical field of strength B_0).

In Section 5.5 we investigated the hydrodynamic evolution of the hyperbolic shear layer for Rossby numbers $\Lambda = 1.5$ and $\Lambda = 2.5$ in both highly diffusive and nonlinear regimes. We showed the general evolution of the perturbed along-stream velocity, streamfunction and density in both the hydrodynamic and magnetohydrodynamic regime. The streamfunction perturbation grows, indicating growing density perturbations, latitudinal momentum which is then deflected by the Coriolis force, driving the perturbed along-stream velocity into stable columns and the nonlinear equilibrium. We also focused on the mean flow $\overline{U}$ and mean vorticity $\overline{Q}$ change over the evolution. We found that in order for the system to reach a stable state, the latitudinal shear of the mean flow is reduced and the minimum value of the $\overline{Q}$ is increased. To explain this it is important to recall that the hydrodynamic necessary condition for instability is that $fQ < 0$ somewhere in the flow. The nonlinear evolution stabilises the flow by redistributing the vorticity so that fQ is not sufficiently negative to drive an instability in the presence of diffusion and stratification. This stabilisation mechanism is well understood in the hydrodynamic regime (e.g., Griffiths, 2003a,b; Kloosterziel *et al.*, 2007a); however, this is not necessarily the case for magnetohydrodynamic regime.

In section 5.6 we considered the magnetohydrodynamic evolution of the hyperbolic shear layer for Rossby numbers $\Lambda = 1.5$ and $\Lambda = 2.5$; we focused on the case $\Lambda = 1.5$ with $\nu_0 = 0.02$. We found that the introduction of magnetic field throughout the nonlinear evolution further decreased the latitudinal shear of $\overline{U}$ in comparison with the hydrodynamic evolution. We also found that the evolution further reduces the minimum $\overline{Q}$ further in comparison to the hydrodynamic evolution so that it is either less negative or even positive (in some cases). This is not surprising as one can recall that the necessary magnetohydrodynamic condition for instability is that $U'f > 0$ (anti-cyclonic shear), which is less stringent than the hydrodynamic condition (i.e., $fQ = f^2 - U'f < 0 \implies U'f > 0$). The smallest $\overline{U}$ and $\overline{Q}$ changes occur for relatively small and large $\mathcal{M}$ that generate small growth rates; intermediate values of $\mathcal{M}$ generate the most change to $\overline{U}$ and $\overline{Q}$ over the evolution. The most significant mean flow and vorticity change did not occur for the K and $\mathcal{M}$ that generate the maximum growth rate. Analogous results were found for the case $\Lambda = 2.5$.

Finally, in section 5.6 we considered the magnetohydrodynamic evolution of the hyperbolic shear layer for the Rossby number $\Lambda = 0.5$, noting that the system is hydrodynamically linearly stable for $\Lambda < 1$. In this case even $\mathcal{M}$ that are weakly unstable (linearly) generate a remarkable mean flow and mean vorticity change comparable to those that generate the maximum growth rate in this regime. This differs from $\Lambda = 1.5$ and $\Lambda = 2.5$, where weak magnetic field only lead to slight changes in $\overline{U}$ and $\overline{Q}$ in comparison to the hydrodynamic case. The change to $\overline{U}$ in the central latitudinal regions, which used to exhibit anti-cyclonic latitudinal shear, instead exhibits cyclonic shear. This behaviour is exhibited for all $\mathcal{M}$, with less extreme cyclonic shear for cases with larger $\mathcal{M}$. Physically, the final mean flow, shown in figure 5.39, suggests that the nonlinear evolution of the instability forms tightly packed jets with the north jet travelling westward and southern jet travelling eastward.

Chapter 6

Equatorial Instabilities of Stellar and Planetary Atmospheres

6.1 Introduction

Recently, observations of certain exoplanetary atmospheres, so-called hot Jupiters, have revealed the existence of unexpectedly strong equatorial jets that apparently flow close to the speed of sound (e.g., Showman *et al.*, 2013; Heng & Showman, 2015). The strong equatorial jets compel us to consider the equatorial regime, where inertial instability is most likely to occur in the terrestrial atmosphere (e.g., Hayashi *et al.*, 1998; Knox, 2003). Indeed, Dunkerton (1981) realised that the necessary and sufficient condition for inviscid and axisymmetric stability $fQ > 0$ (where $Q = f - U'$ is the absolute vorticity and $U(y)$ is a parallel shear flow) is easily violated near the equator since the Coriolis parameter f becomes small. To investigate the dynamics of the equatorial atmosphere, Dunkerton (1981) considered the stability of a parallel flow $U(y) = \Lambda_0 y$ with uniform latitudinal shear Λ_0 in the presence of stable stratification with Coriolis parameter $f = \beta y$ (equatorial β-plane approximation), where β is the planetary vorticity gradient. The results of this analysis have already been discussed in section 1.2.2. As Dunkerton predicted, inertial instabilities were later observed in the equatorial atmosphere (e.g., Hayashi *et al.*, 1998; Knox, 2003) and ocean (e.g., Richards & Edwards, 2003; d'Orgeville *et al.*, 2004).

In this chapter we extend the system of Dunkerton (1981) by considering the effect of vertical magnetic field of strength B_0. Thus, we shall consider the linear stability of the uniform parallel flow $U(y) = \Lambda_0 y$ on on equatorial β-plane in the presence of vertical magnetic field of strength B_0 and in the absence of diffusion. We will also consider the jet profile $U(y) = \Lambda_0 y - \delta \beta y^2 / 2$, where δ is a real constant of order unity that governs the width of the jet (cf. Stevens, 1983). The second of these flows ensures that anti-cyclonic shear (which is necessary for instability to occur) is restricted to a finite latitudinal domain so that unstable modes (if they exist) must occur within this region (as in Chapter 5).

In section 6.2 we derive a parabolic cylinder equation for the cross-stream velocity v from the second order equation (2.30), which governs the linear stability of the perturbed quantities. To do

this we introduce the nondimensional variable $Y = (y - y_0)/L$, where y is the latitude, y_0 is the central latitude and L is the latitudinal lengthscale. The equation may be solved analytically, yielding an eigenvalue relation with corresponding eigenfunctions $v \propto H_n(Y) \exp(-Y^2/2)$, where the eigenvalue n is a non-negative integer, and H_n are Hermite polynomials of degree n.

In section 6.3 we first consider the system in the absence of shear, where stability is ensured by equation (2.43) due to the absence of anti-cyclonic shear. We examine the role of weak and strong magnetic field on the system, yielding equatorial magnetically modified inertial and Alfvén waves, respectively.

Following this, we return to the sheared system, where we introduce the nondimensional parameters that will be used throughout the rest of Chapter 6 and Chapter 7: that is, the nondimensional growth rate $S = 2s/\Lambda_0$ (so that $2/\Lambda_0$ is the timescale), re-scaled vertical wavenumber $K = \Lambda_0^2|k|/4N\beta$ and magnetic parameter $M = 8N\beta v_A/\Lambda_0^3$. Under the chosen nondimensionalisation the growth rate becomes a function of K, M and n; however, we take $n = 0$ as that describes the most unstable mode. We contour the frequency and growth rate in (M, K)-space, where, somewhat surprisingly, the system remains unstable in the limit of strong magnetic field. There are two modes only, one that is always stable and one that is always unstable. We investigate both the limit of weak and strong magnetic field analytically, finding that weak magnetic field modifies inertial instabilities as well as generating purely magnetic instabilities in the hydrodynamically stable regime; instability is found to always occur in the presence of strong magnetic field.

In section 6.4 we consider the dynamical balances of the stable and unstable modes of our system. We investigate numerous parameter regimes, including the weak field limits of the hydrodynamically unstable and stable regimes as well as the limit of strong magnetic field. In particular, we categorise magnetically modified inertial instabilities, a "stratified" MRI and the instabilities found in the limit of strong magnetic field.

Finally, in section 6.5 we consider the jet profile $U(y) = \Lambda_0 y - \delta\beta y^2/2$, where instability can occur only in the region $0 < y < \Lambda_0/\delta\beta$, since these are the only latitudes where the flow exhibits anti-cyclonic shear ($U'f > 0$). We now derive stability criteria that depend upon K, M and δ, as well as contouring the growth rate in (M, K)-space. There are no instabilities in the limit of strong magnetic field for this flow. We analytically investigate the role of weak magnetic field and determine the chosen vertical scale in this regime.

6.2 Formulation

In this Chapter we are considering the equatorial atmosphere and therefore apply the equatorial β-plane approximation, where the Coriolis parameter $f = \beta y$ with $\beta > 0$ constant. We also consider uniform magnetic field strength and a flow profile of the form:

$$U(y) = \Lambda_0 y - \frac{\delta}{2}\beta y^2, \tag{6.1}$$

where δ is some dimensionless positive constant that determines the width of the jet (if $\delta \neq 0$). The jet profile (6.1) is considered in extension to the uniform flow so that unstable modes are restricted to the interval $0 < y < \Lambda_0/\delta\beta$ (since cyclonic shear guarantees stability). This latitudinal constraint is of importance as the uniform flow profile $U(y) = \Lambda_0 y$ allows a somewhat non-physical large field instability to occur, which will be discussed in detail later in the chapter. We also recall that we are considering a magnetohydrostatic system, which is most relevant in planetary atmospheres and is subject to the validity condition (2.32). Hence, under this formulation, the eigenvalue constraints and stability results of Chapter 2 imply that the growth rate squared s^2 is real and that the system is stable in the absence of shear.

To proceed, we consider the ideal governing equation (2.33) and define the nondimensional latitude

$$Y = \frac{y - y_0}{L}, \tag{6.2}$$

where y_0 and L are the central latitude and lengthscale of the mode, respectively, and both are at our disposal. Note that under the nondimensional latitude (6.2), the boundary conditions (2.28) become

$$\hat{v}(Y) \to 0 \quad \text{when} \ |Y| \to \infty, \tag{6.3}$$

provided L is real.

The nondimensional latitude (6.2) allows us to recast (2.33) in terms of Y as follows:

$$\frac{N^2}{k^2 L^2}\hat{v}'' + (\beta\Lambda_0(LY + y_0) - s^2 - k^2 v_A^2)\hat{v} - \beta^2(LY + y_0)^2 \left(\delta + \frac{s^2}{k^2 v_A^2 + s^2}\right)\hat{v} = 0, \tag{6.4}$$

which reduces to the normal form of a parabolic cylinder equation which is known to have analytical solutions (e.g., Bender & Orszag, 1978) provided we choose central latitude and lengthscale squared as

$$y_0 = \frac{\Lambda_0}{2\beta}\left(1 + \frac{k^2 v_A^2}{s^2}\right) \bigg/ \left(1 + \delta\left(1 + \frac{k^2 v_A^2}{s^2}\right)\right), \tag{6.5a}$$

$$L^2 = \frac{N}{k\beta}\left(1 + \frac{k^2 v_A^2}{s^2}\right)^{\frac{1}{2}} \bigg/ \left(1 + \delta\left(1 + \frac{k^2 v_A^2}{s^2}\right)\right)^{\frac{1}{2}}. \tag{6.5b}$$

Note that the choice of L^2 ensures that in the absence of magnetic field we obtain the hydrodynamic lengthscales of Stevens (1983) with $\delta \neq 0$, and Dunkerton (1981) with $\delta = 0$. The central latitude and lengthscale in (6.5) reduce equation (6.4) to the normal form of a parabolic cylinder equation:

$$\hat{v}'' + (a - Y^2)\hat{v} = 0, \tag{6.6}$$

where

$$a = \frac{k}{N\beta}\left(1 + \frac{k^2 v_A^2}{s^2}\right)^{\frac{3}{2}}\left(\frac{\Lambda_0^2}{4} - s^2\left(1 + \delta\left(1 + \frac{k^2 v_A^2}{s^2}\right)\right)\right)\left(1 + \delta\left(1 + \frac{k^2 v_A^2}{s^2}\right)\right)^{-\frac{3}{2}}. \tag{6.7}$$

Then, with the boundary conditions (6.3), equation (6.6) has solutions proportional to $\exp(-Y^2/2)$ by (Bender & Orszag, 1978), which always decay as $|Y| \to \infty$. However, to ensure that the solutions decay as $|y| \to \infty$ we require that L^2 has a positive real part since $Y^2 \propto L^{-2}$. Now, since s^2 is real by (2.35), the interior of the square root which defines L^2 in (6.5) must also be real. Thus, for L^2 to have a positive real part we must restrict the eigenvalues such that $k^2 v_A^2/s^2 > -1$ (or equivalently $s^2 > 0$ or $s^2 < -k^2 v_A^2$).

The constraints on the frequency and growth rate ensures the boundary conditions (6.3) continue to decay as $|Y| \to \infty$; hence, by Bender & Orszag (1978), equation (6.6) with boundary conditions (6.3) admit well known eigenfunctions. The eigenfunctions consist of Hermite polynomials $H_n(Y)$ multiplied by a Gaussian of the form $\exp(-Y^2/2)$ with corresponding discrete and non-negative values of n, which satisfy the following eigenvalue relation:

$$\left(1 + \frac{k^2 v_A^2}{s^2}\right)^{\frac{3}{2}} \left(\frac{\Lambda_0^2}{4} - s^2 \left(1 + \delta \left(1 + \frac{k^2 v_A^2}{s^2}\right)\right)\right) =$$

$$(2n+1)\frac{N\beta}{k}\left(1 + \delta \left(1 + \frac{k^2 v_A^2}{s^2}\right)\right)^{\frac{3}{2}}. \quad (6.8)$$

In the absence of magnetic field, equation (6.8) reduces to the eigenvalue relation in Stevens (1983), and for $\delta = 0$, to Dunkerton (1981), where the system is stable provided $|k| > |k_c| = 4N\beta(2n+1)/\Lambda_0^2$. We note that the eigenfunctions are even for even values of n and odd for odd values of n. For example, the $n = 0$ (even) mode has $\hat{v} = H_0(Y)\exp\left(-Y^2/2\right) = \exp\left(-Y^2/2\right)$, while the $n = 1$ (odd) mode has $\hat{v} = H_1(Y)\exp\left(-Y^2/2\right) = Y\exp\left(-Y^2/2\right)$.

6.3 The Equatorial Waves and Instabilities of a Uniform Shear Flow

In this section we will consider the case of uniform shear (i.e., $\delta = 0$) so that the jet profile (6.1) reduces to the parallel flow $U(y) = \Lambda_0 y$. We will discuss the equatorial waves within the system, the instabilities present and their respective dynamical balances. When $\delta = 0$, the eigenvalue relation (6.8) reduces to

$$\frac{|k|}{N\beta}\left(\frac{\Lambda_0^2}{4} - s^2\right)\left(1 + \frac{k^2 v_A^2}{s^2}\right)^{\frac{3}{2}} = 2n + 1. \quad (6.9)$$

The central latitude and lengthscale (6.5) also reduce, yielding

$$y_0 = \frac{\Lambda_0}{2\beta}\left(1 + \frac{k^2 v_A^2}{s^2}\right) \quad \text{and} \quad L^2 = \frac{N}{|k|\beta}\left(1 + \frac{k^2 v_A^2}{s^2}\right)^{\frac{1}{2}}, \quad (6.10)$$

where the eigenfunctions take the form $H_n(Y)\exp(-Y^2/2)$ with $Y = (y - y_0)/L$.

6.3.1 Equatorial Waves

To classify the waves of the system we consider (6.9) in the absence of shear (i.e., $\Lambda_0 = 0$), where stability is ensured by equation (2.43). For convenience we set $s^2 = -\omega^2$, so that ω is the

frequency, and define the nondimensional quantities

$$\phi = \frac{|k|^3 v_A^2}{N\beta} \quad \text{and} \quad \hat{\omega}^2 = \frac{|k|}{N\beta}\omega^2, \tag{6.11}$$

where the chosen timescale is $\sqrt{|k|/N\beta}$, so that $\hat{\omega}$ is the nondimensional frequency. The parameter ϕ may be interpreted as magnetic field strength.

The nondimensional quantities (6.11) allow us to recast equation (6.9) in nondimensional form as

$$\hat{\omega}^2 \left(1 - \frac{\phi}{\hat{\omega}^2}\right)^{\frac{3}{2}} = 2n + 1. \tag{6.12}$$

Recall that we require L^2 to be real so that the solutions of the parabolic cylinder equation (6.6) continue to decay as $|y| \to \infty$. Hence, as $\hat{\omega}^2 > 0$ in the absence of shear, equation (6.12) can only be satisfied if $\hat{\omega}^2 > \phi$ (since one side of (6.12) would be complex, and the other real). Thus, the validity of (6.12) and its subsequent results are confirmed, since $\hat{\omega} > \phi$ implies that $s^2 < -k^2 v_A^2$ is trivially satisfied.

We must also consider the validity of the magnetohydrostatic approximation, where the condition (2.32) in nondimensional terms implies that we require $|\hat{\omega}^2 - \phi| \ll N|k|/\beta$ (where the hydrostatic parameter $N|k|/\beta \gg 1$ in planetary atmospheres) for validity.

It is natural to consider the asymptotic behaviour of $\hat{\omega}^2$ with respect to ϕ, where the parameter ϕ is proportional to v_A^2 which allows us to interpret the small and large ϕ regimes as weak and strong field limits, respectively. The weak and strong field expansions of (6.12) are

$$\hat{\omega}^2 = (2n + 1) + \frac{3}{2}\phi - \frac{3}{8(2n+1)}\phi^2 + O(\phi^3), \tag{6.13}$$

$$\hat{\omega}^2 = \phi + (2n+1)^{\frac{2}{3}}\phi^{\frac{1}{3}} + \frac{1}{3}(2n+1)^{\frac{4}{3}}\phi^{-\frac{1}{3}} + O(\phi^{-1}). \tag{6.14}$$

Note that both expansions satisfy the condition $\hat{\omega}^2 > \phi$. The expansions have been calculated to third order since lower order expansions were relatively inaccurate for $n > 0$, particularly in the large ϕ limit. The lack of accuracy is due to each term of the expansion being dependent on $(2n + 1)^\gamma$ for some γ.

The validity of the magnetohydrostatic approximation in the weak magnetic field expansion (6.13) is trivial since $\hat{\omega}^2 \propto (2n + 1)$ at leading order, so $|\hat{\omega}^2 - \phi| \approx (2n + 1) \ll N|k|/\beta$. The strong field expansion (6.14) can be shown to be valid, provided the magnetic field is sufficiently weak, since $|\hat{\omega}^2 - \phi| \approx ((2n + 1)^2\phi)^{1/3} \approx (|k|^3 v_A^2/(N\beta))^{1/3} \ll N|k|/\beta$.

At leading order, the small and large ϕ expansions (6.13) and (6.14) represent inertia-gravity waves and Alfvén waves, respectively. To demonstrate the accuracy of the expansions, we plot the nondimensional frequency squared $\hat{\omega}^2$ for each expansion against the exact real and non-negative solution of (6.12) in figure 6.1, for the first even mode ($n = 0$) and first odd mode ($n = 1$). The figure shows that the small and large field expansions describe the mode $\hat{\omega}^2$ almost entirely, except for a small interval in ϕ, where $\phi = O(1)$, in which magnetic and inertial effects compete. This interval may be interpreted as an equatorial analogue of the hydromagnetic-inertial waves
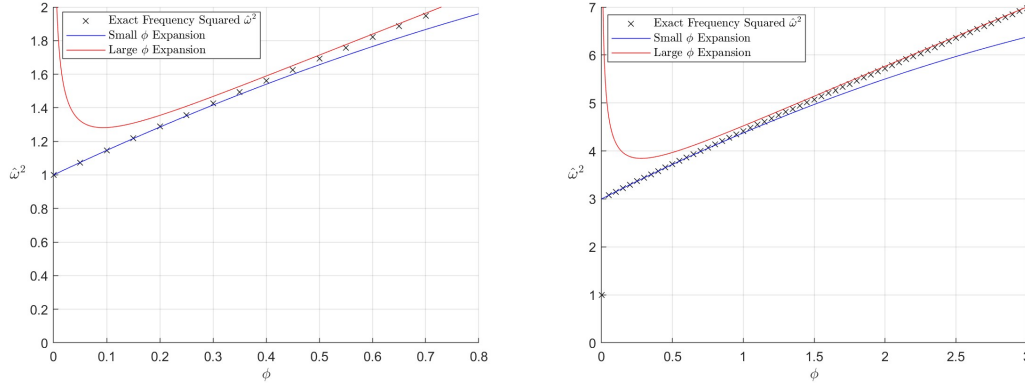
Figure 6.1: Nondimensional frequency squared for equatorial inertia-gravity waves and Alfvén waves, for the $n = 0$ (left) and $n = 1$ (right) modes. The expansions (6.13) and (6.14) are plotted against the magnetic parameter ϕ.

(3.20) found on the f-plane (which were stratified and magnetohydrostatic analogues of (3.19) described by Acheson & Hide, 1973). The figure also indicates that when n increases, the small field expansion describes the mode to a greater degree of accuracy for a larger interval of ϕ. However, the interval of ϕ that is not accurately described by the small and large expansions increases.

6.3.2 Equatorial Instabilities

Formulation

We now consider the case of non-zero shear, where instability is possible since the system can exhibit anti-cyclonic shear. In the following section we will focus our attention to the instabilities present within the system. Recall that s^2 is real, by (2.35), and that the hydrodynamic system is unstable if $|k| > |k_c| = 4N\beta(2n+1)/\Lambda_0^2$ (Dunkerton, 1981).

We define a new set of nondimensional parameters (in contrast to the previous subsection) that includes the shear Λ_0:

$$K = \frac{\Lambda_0^2 |k|}{4N\beta} \ \text{ and } \ M = \frac{8N\beta v_A}{\Lambda_0^3}, \tag{6.15}$$

where we also define the nondimensional growth rate $S = 2s/\Lambda_0$ on the timescale $2/\Lambda_0$. The parameter K can simply be interpreted as a nondimensional vertical wavenumber. However, (6.5b) implies that the natural equatorial latitudinal scale is $(N/\beta|k|)^{1/2}$, which is the so-called radius of deformation L_d (e.g., Gill, 1982). This implies that K can alternatively be interpreted as an inverse equatorial aspect ratio squared that is re-scaled by $\Lambda_0^2/4N^2$ (which is usually large in stellar and planetary atmospheres), since $L_d^{-2} k^{-2} = \beta/N|k| = K\Lambda_0^2/4N^2$. We interpret M as magnetic field strength. The parameter choice (6.15) is not the only reasonable nondimensionalisation for (6.9); however, the parameters are very easily interpreted. Note that the parameter K can never be zero, since we require $k \neq 0$ for the system to be magnetohydrostatic and $\Lambda_0 \neq 0$ by assumption.

The nondimensional parameters (6.15) allow us to recast (6.9) in nondimensional form, yielding

$$K(1 - S^2)\left(1 + \frac{M^2 K^2}{S^2}\right)^{3/2} = (2n + 1).$$ (6.16)

By inspection of equation (6.16), if an unstable mode exists (i.e., $S^2 > 0$), then $S^2 < 1$ (otherwise (6.16) can not be satisfied). Similarly, if the system is stable (i.e., $S^2 < 0$), then the absolute value of S^2 must be greater than $M^2 K^2$ (otherwise the left hand side of (6.16) would be complex, while the right remains real). These constraints on S coincide with the conditions that ensure the lengthscale L is positive. Thus, we do not need to consider if the solutions of (6.16) satisfy the condition on the horizontal lengthscale.

The validity of the magnetohydrostatic approximation must be ensured, so that (2.32) is satisfied; in nondimensional terms we require $|S^2 + M^2 K^2| \ll 4N^2/\Lambda_0^2$ for validity. Hence, there are two cases to consider: the unstable case, where $S^2 = O(1)$ and the stable case, where $S^2 < -M^2 K^2$. The first is trivial since $|S^2 + M^2 K^2|$ can only be larger than order one when M or K is large; thus, provided M and K are not too large the approximation is valid. Note that if one parameter is large while the other is small, then the approximation remains valid provided $MK = O(1)$ or smaller. This also extends to the stable case; however, we must also consider when $S^2 \sim 1/K$ with $K \ll 1$ and $MK = O(1)$. Here, $|S^2 + M^2 K^2| \sim S^2$, in which case $1/K \ll 4N^2/\Lambda_0^2$ for the approximation to be valid. This holds trivially, since we can write $1/K = 4N\beta/\Lambda_0^2|k| = (\beta/N|k|)(4N^2/\Lambda_0^2) \ll 4N^2/\Lambda_0^2$, since $\beta/N|k|$ is the equatorial aspect ratio squared. Hence, the magnetohydrostatic approximation is valid provided that the magnetic field strength is not too large.

The Maximum Growth Rate

To identity the maximum growth rate and where it occurs in (M, K)-space, we differentiate (6.16) with respect to M and K and solve for S^2. This will also allow us to observe how S^2 varies with the parameters M and K. Differentiating (6.16) with respect to K yields

$$\left(1 + \frac{M^2 K^2}{2S^4}(3 - S^2)\right)\frac{\partial S^2}{\partial K} = \frac{1 - S^2}{K}\left(1 + \frac{4M^2 K^2}{S^2}\right),$$ (6.17)

where (6.16) has been used to simplify the expression. Differentiating (6.16) with respect to M yields

$$\frac{\partial S^2}{\partial M} = 6MK^2 S^2 (1 - S^2)\left(2S^4\left(1 + \frac{M^2 K^2}{S^2}\right)^{\frac{1}{2}} + 3M^2 K^2 (1 - S^2)\right)^{-1}.$$ (6.18)

We will first consider unstable modes only so that $0 < S^2 < 1$ by the growth rate bound (2.45). Given that $0 < S^2 < 1$, it follows from equation (6.17) that $\partial S^2/\partial K > 0$ for all M and K. Similarly, given that $0 < S^2 < 1$, then equation (6.18) implies that $\partial S^2/\partial M > 0$ for all M and K. Hence, increasing either M or K when the system is unstable increases the growth rate. Thus, the maximum growth rate will occur in the large K and M limits. Surprisingly, this is in direct

contrast to many magnetohydrodynamic results, where strong magnetic field stabilises unstable systems and produces Alfvén waves.

To determine the maximum growth rate we therefore take the large K and M limits of (6.16) with $0 < S < 1$, yielding $(1-S^2)M^3K^4/S^3 \sim 2n+1$. Thus, since M and K are large, we require $S^2 \to 1$ to balance the equation, and so $S^2 \sim 1 - (2n + 1)/M^3K^4$. Note that this can be derived by considering a single limit (i.e., large K, or large M). Hence, to leading order the maximum growth rate is $S = 1$ ($s^2 = \Lambda_0^2/4$ in dimensional terms); this is also the maximum growth rate of the hydrodynamic system (Dunkerton, 1981; Griffiths, 2003a). The maximum growth rate found is also consistent with (6.17) and (6.18), where $\partial_K S^2 \to 0^+$ and $\partial_M S^2 \to 0^+$ as $S^2 \to 1^-$ in the large K or M limits.

If instead the system is stable then $S^2 < -M^2K^2$. In this case the bracketed term on the left hand side of (6.17) must be positive, however the right hand side of (6.17) can either be negative or positive depending on the sign of $1 + 4M^2K^2/S^2$. Thus, if the system is stable, increasing K increases the frequency if $-4M^2K^2 < S^2$ and decreases the frequency if $-4M^2K^2 > S^2$. If the system is stable, we can also deduce from equation (6.18) that increasing M increases the frequency.

The Growth Rate as a Function of Vertical Wavenumber and Magnetic Field Strength

In order to categorise the system in (M, K)-space we solve (6.16) to provide a plot of the growth rate and for the stable mode, the frequency, given in figure 6.2. Note that the colourbars are on distinct scales.

Figure 6.2 shows that every value in (M, K) space with $M > 0$ has one unstable and one stable mode; however, if $M = 0$, we retain only the hydrodynamic mode, which is unstable if $K > 2n + 1$, and stable otherwise. Thus, if $M > 0$ we can deduce that if $K > 2n + 1$, the hydrodynamic mode is unstable, while the magnetic mode is stable. However, if $K \leq 2n + 1$ the hydrodynamic mode is stable, while the magnetic mode is unstable. We can also conclude that the frequency of the stable hydrodynamic and magnetic modes increase with magnetic field strength, which is consistent with (6.18). Similarly, we can observe that there is instability for all values of K and $M \neq 0$, where, as in the f-plane, weak magnetic field destabilises what would be a hydrodynamically stable system. However, the figure shows that there is no sufficient field strength that stabilises the system. In fact, increasing the magnetic field strength, at any vertical wavenumber K, only increases the growth rate to its maximum value, given by $S^2 = 1$ ($s^2 = \Lambda_0^2/4$), as predicted by (6.18).

The Limit of Strong Field

Motivated by the surprising magnetic behaviour within the system as shown in figure 6.2, where magnetic field of sufficient strength in both the hydrodynamically stable and unstable regimes
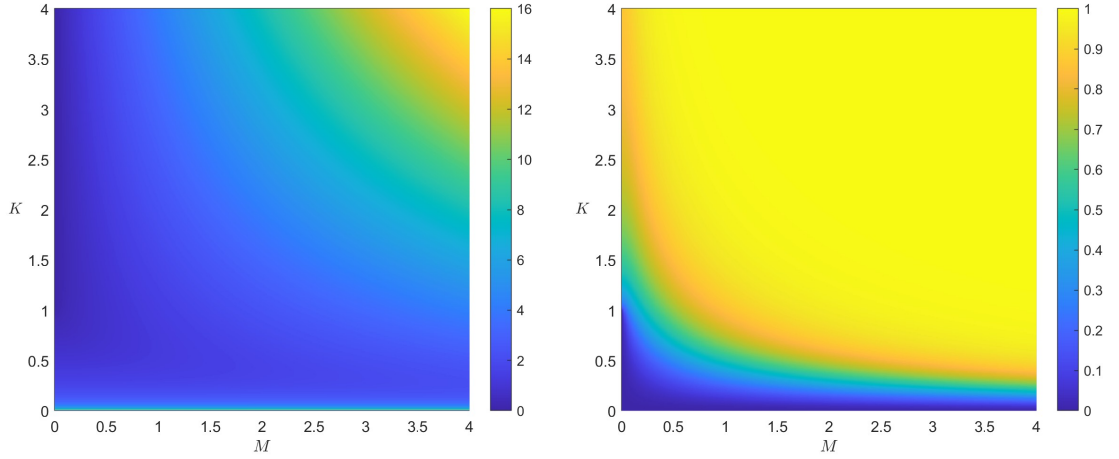
Figure 6.2: The frequency (left) and growth rate S (right) in (M, K) space. Note the distinct colourbars.

yields the maximum growth rate. Thus, we consider the large M limit of (6.16), for which there are two modes, the first being a stable Alfvénic mode:

$$S_+^2 = -K^2 M^2 + O(M). \tag{6.19}$$

The second mode is unstable and given by

$$S_-^2 = 1 + O(M^{-1}), \tag{6.20}$$

which is the maximum growth rate at leading order. In dimensional terms, the frequency of the stable mode (6.19) is $k v_A$, while the growth rate of the unstable mode (6.20) is $\Lambda_0/2$. Clearly, we wish to derive the second order terms of (6.19) and (6.20). To do this, we substitute the leading order terms of (6.19) and (6.20) with a second order term αM^γ (where α and γ are to be determined) into (6.16). Thus, including the second order correction, the stable mode becomes

$$S_+^2 \approx -K^2 M^2 - (2n+1)^{\frac{2}{3}} M^{\frac{2}{3}}, \tag{6.21}$$

while the unstable mode is given by

$$S_-^2 \approx 1 - \frac{(2n+1)}{M^3 K^4}. \tag{6.22}$$

Thus, in the large M limit, the growth rate is the maximum possible (i.e., S^2) as predicted by the growth rate bound (2.45) to $O(M^{-3})$. The stable mode is an Alfvén wave at leading order. Note that the second order correction to the stable mode (6.21) is consistent with the constraint on the eigenvalue since the positive correction ensures that $K^2 M^2 / S^2 < -1$.

Focusing on the unstable mode (6.22), it is clear that the expansion breaks down when $M^3 K^4 = O(1)$ with $M \gg 1$. Thus we investigate the asymptotic behaviour in K while in the large M limit. If $K \gg 1$ we retain the expansion (6.22) with a now smaller second order term. If $M^3 K^4 = O(1)$, equation (6.16) yields the following cubic in S:

$$(2n+1)S^3 + K^4 M^3 S^2 - K^4 M^3 = 0, \tag{6.23}$$

where $S \to 1$ as $M^3 K^4$ increases. Equation (6.23) implies that the maximum growth rate is damped (substituting $S = 1$ leads to a clear contradiction); however, the growth rate is still of order unity. Finally, if $M^3 K^4 \ll 1$, then (6.16) yields

$$S \approx \frac{K^{4/3} M}{(2n + 1)^{1/3}}. \tag{6.24}$$

Hence, (6.22), (6.23) and (6.24) describe the large M limit entirely, where, at leading order, equations (6.22), (6.24) may be derived via (6.23). Clearly, as the vertical wavenumber decreases (limited by the depth of the atmosphere) in the strong field limit, then the maximum growth rate decreases in magnitude and eventually scales with $K^{4/3} M (\ll 1)$; however, the system can never be stabilised.

The Limit of Weak Magnetic Field

It is natural to investigate the small M limit of figure 6.2 in order to categorise the behaviour analytically. In the limit of weak magnetic field ($M \ll 1$) the equation for the growth rate (6.16) yields a perturbation to the hydrodynamic root:

$$S^2 = 1 - \frac{2n + 1}{K} + O(M). \tag{6.25}$$

There is also a small Alfvénic root. Indeed, assuming $S^2 \ll 1$ so that $1 + S^2 \approx 1$ in (6.16), we obtain

$$S^2 = \frac{M^2 K^{8/3}}{(2n + 1)^{2/3} - K^{2/3}} + \cdots . \tag{6.26}$$

In dimensional terms, at large vertical wavenumber this becomes $s^2 \approx -k^2 v_A^2 / \Lambda_0^2$. At small vertical wavenumber, (6.26) implies instability, where terms involving β, stratification N and shear come into play (via K in (6.26)).

As $K \to 2n + 1$, it is clear that the roots (6.25) and (6.26) will break down. In (6.25) the leading-order term vanishes so that higher-order corrections become comparable in magnitude. In (6.26) the leading-order term increases without bound. Because of this, we might anticipate interaction between the modes when the hydrodynamic root (becoming smaller) is of the same size as the Alfvén root (increasing in size from $O(M^2)$). Writing $K = (2n + 1)(1 + \mu M^p)$, where μ measures the departure from $K = 2n + 1$ and $p > 0$ is to be determined, the hydrodynamic root then has $S^2 \propto M^p$ and the Alfvén root has $S^2 \propto M^{2-p}$. So the roots are of the same order of magnitude when $p = 1$ (i.e. K within a distance of $O(M)$ of $2n + 1$), with $S^2 = O(M)$. So we write

$$K = (2n + 1)(1 + \mu M), \quad \hat{\Omega}^2 = \frac{S^2}{M}, \tag{6.27}$$

and recast (6.16) in terms of $\hat{\Omega}(\mu, M)$, rather than $S(K, M)$:

$$(1 + \mu M)\left(1 - M\hat{\Omega}^2\right)\left(1 + \frac{M(2n + 1)^2}{\hat{\Omega}^2}\right)^{3/2} = 1, \tag{6.28}$$

where terms of order M^2 have been neglected. Now, for small M, the $O(1)$ terms cancel, and then terms in $O(M)$ give

$$\mu - \hat{\Omega}^2 + \frac{3(2n+1)^2}{2\hat{\Omega}^2} = 0 \implies \hat{\Omega}^4 - \mu\hat{\Omega}^2 - \frac{3(2n+1)^2}{2} = 0 \implies \hat{\Omega}^2 = \frac{\mu \pm \sqrt{\mu^2 + 6(2n+1)^2}}{2}.$$
(6.29)

This describes the hydrodynamic root and the Alfvén root near the critical vertical wavenumber $K = 2n+1$.

It remains to determine how the two roots of (6.29) link to (6.25) and (6.26). To do this, we consider the large $|\mu|$ limit of (6.29) and compare with the small $|\mu|$ limits of (6.25) and (6.26). Specifically, the positive root of (6.29) yields

$$2\hat{\Omega}^2 \to \mu + |\mu|\left(1 + \frac{3(2n+1)^2}{\mu^2} + \cdots\right) \sim \begin{cases} -3(2n+1)^2/\mu & \mu < 0, \\ 2\mu & \mu > 0, \end{cases} \text{ as } |\mu| \to \infty. \quad (6.30)$$

Similarly, the negative root of (6.29) yields

$$2\hat{\Omega}^2 \to \mu - |\mu|\left(1 + \frac{3(2n+1)^2}{\mu^2} + \cdots\right) \sim \begin{cases} 2\mu & \mu < 0, \\ -3(2n+1)^2/\mu & \mu > 0. \end{cases} \text{ as } |\mu| \to \infty. \quad (6.31)$$

We also find that the hydrodynamic root (6.25) yields

$$S^2 \sim 1 - (1 + \mu M)^{-1} \sim \mu M \implies 2\hat{\Omega}^2 = \frac{2S^2}{M} \sim 2\mu \text{ as } \mu \to 0, \quad (6.32)$$

while the Alfvén root (6.26) yields

$$S^2 \sim \frac{M^2(2n+1)^2}{1 - (1 + \mu M)^{2/3}} \sim -\frac{3M(2n+1)^2}{2\mu} \implies 2\hat{\Omega}^2 = \frac{2S^2}{M} \sim -\frac{3(2n+1)^2}{\mu} \text{ as } \mu \to 0, \quad (6.33)$$

where we have substituted from (6.27) to evaluate (6.25) and (6.26). Thus, (6.30) shows that the +ve root in (6.29) becomes the hydrodynamic root (6.32) as $\mu \to \infty$ and the Alfvén root (6.33) as $\mu \to -\infty$ (or, the hydrodynamic root (6.25) becomes the Alfvén root (6.26) as K decreases through $2n+1$). Likewise, (6.31) shows that the $-$ve root in (6.29) becomes the Alfvén root (6.33) as $\mu \to +\infty$ and the hydrodynamic root (6.32) as $\mu \to -\infty$ (or, the hydrodynamic root (6.25) becomes the Alfvén root (6.26) as K increases through $2n+1$). So the roots exchange identity as K passes through $2n+1$. The hydrodynamic mode is not a single entity that can be tracked through parameter space, and neither is the Alfvén mode.

With the complexities of the weak magnetic field roots categorised, we consider the original nondimensional notation, first adopted in (6.16), to find the next order terms in (6.25) and (6.26). Thus, we substitute (6.25) into (6.16) to find the perturbation to the hydrodynamic root, which is proportional to M^2 when $M \ll 1$. Thus in the limit of weak magnetic field, the hydrodynamic root takes the form

$$S^2 = 1 - \frac{2n+1}{K} + \frac{3(2n+1)K^2}{2((2n+1) - K)}M^2 + O(M^4), \quad (6.34)$$

where, if we are in a hydrodynamically stable regime it follows that the weak magnetic field stabilises the system. However, in a hydrodynamically unstable regime the weak magnetic field destabilises the system.

Similarly, by substituting (6.26) into (6.16), we find the second order term in M^2 for the Alfvén root when $M \ll 1$. Thus, in the limit of weak magnetic field, the Alfvén root takes the form

$$S^2 = \frac{K^{8/3}M^2}{(2n+1)^{2/3} - K^{2/3}} - \frac{2(2n+1)^{2/3}K^{16/3}M^4}{3((2n+1)^{2/3} - K^{2/3})^3} + O(M^6), \qquad (6.35)$$

where, if we are in a hydrodynamiclly stable regime, the weak magnetic field destabilises the system. However, in a hydrodynamiclly unstable regime, the weak magnetic field stabilises the system.

Thus, together, (6.34), (6.35) alongside the singular expansion (6.29) describe the entire system in the limit of weak magnetic field. Thus, in the limit of weak magnetic field, if the system is in a hydrodynamically stable regime $((2n+1) - K > 0)$, equation (6.35) describes the most unstable mode, while if the system is in a hydrodynamically unstable regime, equation (6.34) describes the most unstable mode. The expansions show that weak magnetic field both destabilises the hydrodynamically stable system as well as increasing the growth rate of the hydrodynamically unstable system, justifying the results of figure 6.2.

We now determine the validity of the expansions under the magnetohydrostatic approximation by using the condition (2.32), which, under this nondimensionalisation, is $|S^2 + M^2 K^2| \ll 4N^2/\Lambda_0^2$. The first expansion (6.34) is valid, since at leading order, it implies that $|S^2 + K^2 M^2| \approx |1 - (2n+1)/K| = |1 - (2n+1)4N\beta/\Lambda_0^2|k|| \ll 4N^2/\Lambda_0^2$ since $N|k|/\beta$ is large in planetary atmospheres. The second expansion (6.35) is also valid since $|S^2 + K^2 M^2| \approx |K^2 M^2 (2n+1)^{2/3}/((2n+1)^{2/3} - K^{2/3})| \ll 4N^2/\Lambda_0^2$ as $(2n+1)/K$ is not sufficiently close to 1. The singular expansion (6.29) is by definition of order M and is thus valid provided M is not too large.

6.4 Dynamical Balances

We now categorise the dynamical balances in various limits of the system, giving physical insight into equatorial instabilities present. Further analysis regarding the dynamical balances of various hydrodynamic and magnetohydrodynamic waves is given in Appendix A. Under the assumptions of uniform shear $U'(y) = \Lambda_0$, uniform vertical magnetic field of strength B_0 and Coriolis parameter $f = \beta y$, the second order equation (2.33) has solutions of the form $v \propto \exp(-(y - y_0)^2/2L^2 + ikz + st)$, where v is the perturbed cross-stream velocity. Hence, under these assumptions and by recalling that B_1 does not affect the dynamics of the flow, equations (2.22)-(2.26) reduce to

$$su - Qv = \frac{ikB_0}{\mu_0\bar{\rho}}b_x, \quad sv + fu = -\frac{1}{L}\frac{\partial\theta}{\partial Y} + \frac{ikB_0}{\mu_0\bar{\rho}}b_y, \quad s\theta = \frac{iN^2}{k}w, \quad w - \frac{i}{kL}\frac{\partial v}{\partial Y} = 0, \quad (6.36)$$

$$sb_x = \Lambda_0 b_y + ikB_0 u, \quad sb_y = ikB_0 v, \quad sb_z = ikB_0 w, \quad b_z - \frac{i}{kL}\frac{\partial b_y}{\partial Y} = 0, \qquad (6.37)$$

where we have also made use of the nondimensional parameter Y, given by (6.2), to introduce the cross-stream lengthscale L, as seen in equation (6.5). Note that the solenoidal constraint in (6.37)

can immediately be dropped from the dynamical balance since it is described by cross-stream and vertical induction equations (i.e., the induction equation preserves $\nabla \cdot \mathbf{b} = 0$).

It is now convenient to nondimensionalise equations (6.36) and (6.37) with the nondimensional parameters (6.15), where the chosen timescale $2/\Lambda_0$ yields the nondimensional growth rate $S = 2s/\Lambda_0$. It is also useful to define the nondimensional frequency $\hat{\omega} = -iS$. We choose L and $1/k$ as the cross-stream and vertical lengthscales, respectively, since these are the natural lengthscales in each direction due to the cellular structure of the modes. To nondimensionalise equations (6.36) and (6.37) we must also determine the order of the perturbed quantities. To do this, we nondimensionalise the horizontal velocities with the arbitrary constant V (with dimension of velocity) as we are considering a linear problem. Thus, the appropriate scaling for w is found via the incompressibility condition, given by V/kL. Then, via the thermodynamic equation in (6.36), it follows that the appropriate scaling for the total pressure θ is given by $2N^2V/k^2\Lambda_0 L$. Then, resulting from the nondimensionalisation of the velocities, we choose the following scaling for the horizontal and vertical fields, given by $V\sqrt{\mu_0\bar{\rho}}$ and $V\sqrt{\mu_0\bar{\rho}}/kL$, respectively. Thus, equations (6.36) and (6.37) become

$$Su - (F-2)v = iKMb_x, \;\; Sv + Fu = -K^{-1}C^{-\frac{1}{2}}\frac{\partial\theta}{\partial Y} + iKMb_y, \;\; S\theta = iw, \qquad (6.38)$$

$$w = i\frac{\partial v}{\partial Y}, \;\; Sb_x = 2b_y + iKMu, \;\; Sb_y = iKMv, \;\; Sb_z = iKMw, \qquad (6.39)$$

where F is the resulting nondimensionalisation of the Coriolis term $(2/\Lambda_0) \cdot f = (2/\Lambda_0) \cdot \beta y = 2\beta(LY + y_0)/\Lambda_0$ and C is the nondimensional central latitude $(2\beta/\Lambda_0) \cdot y_0$, given by

$$F = C^{\frac{1}{4}}\left(\frac{Y}{\sqrt{K}} + C^{\frac{3}{4}}\right) \;\; \text{and} \;\; C = 1 + \frac{K^2M^2}{S^2}. \qquad (6.40)$$

Note that we define $\hat{L} = C^{1/4}/\sqrt{K}$ as the nondimensional lengthscale $(2\beta/\Lambda_0) \cdot L$, which results from equation (6.10). This nondimensionalisation allows us to easily investigate various limits of the system, which is now defined by the two parameters K and M. For simplicity, we will consider the dynamical balances of the even mode only, where $n = 0$ and $v \propto \exp(-Y^2/2)$.

Figure 6.3 shows the values that the nondimensional lengthscale $\hat{L}$ and central latitude C (calculated from equation (6.5)) take in the (M, K)-plane for both the stable and unstable mode (as seen in figure 6.2). We find that the lengthscale and central latitude of the stable mode decreases with increasing magnetic field strength. Specifically, in the large field limit, equation (6.21) implies that the central latitude $C \sim K^{-2}M^{-4/3}$, where, as a result, the lengthscale $\hat{L} \sim K^{-1}M^{-1/3}$. We also find that the lengthscale and central latitude of the unstable mode increases with increasing magnetic field strength. Specifically, in the large field limit, equation (6.22) implies that the nondimensional central latitude $C \sim K^2M^2$, so that the lengthscale $\hat{L} \sim M^{1/2}$. We shall address the other asymptotic values of the lengthscale and central latitude on a case by case basis.
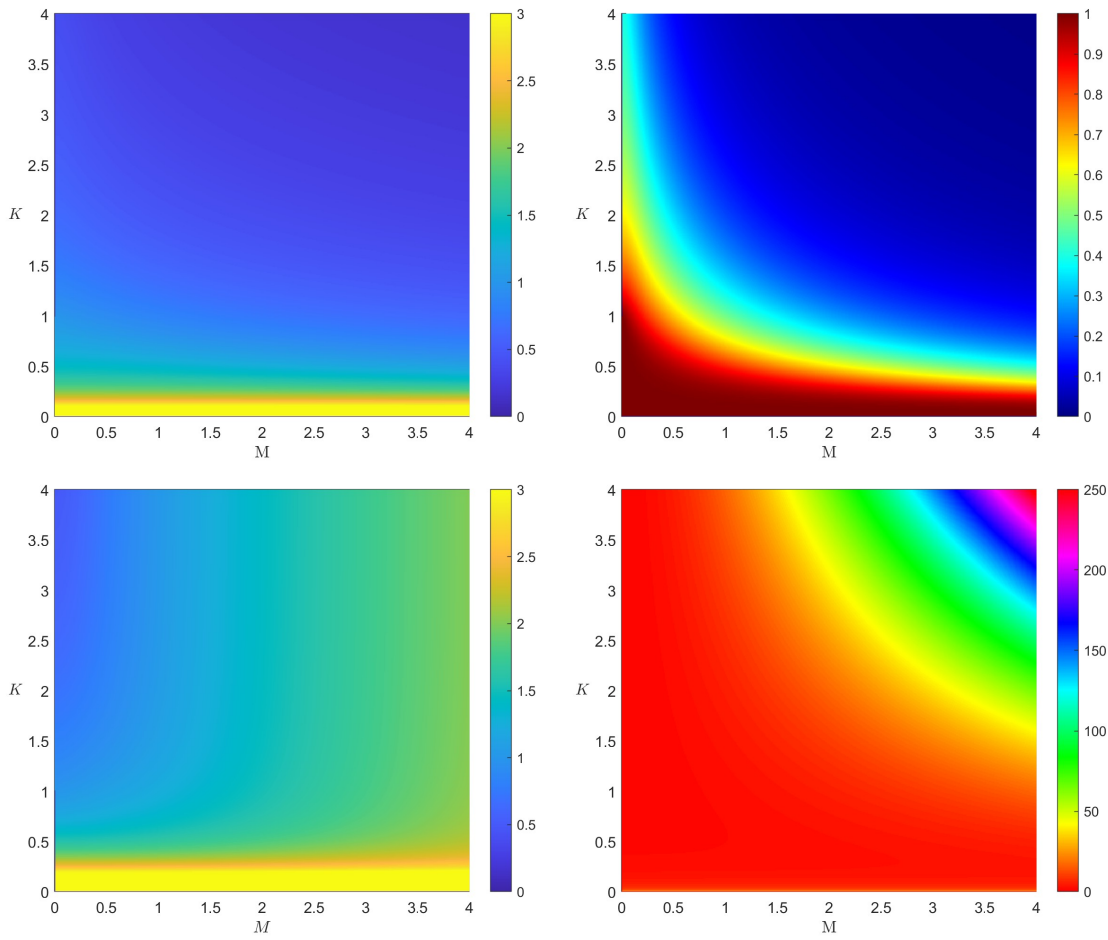
Figure 6.3: Plots for the nondimensional lengthscale $\hat{L} = (2\beta/\Lambda_0) \cdot L = C^{\frac{1}{4}}/\sqrt{K}$ (left panels) and the nondimensional central latitude $C = (2\beta/\Lambda_0) \cdot y_0$ (right panels) for the stable mode (top panels) and the unstable mode (bottom panels).

6.4.1 Equatorial Inertial Instability

We first categorise the dynamical balance of the hydrodynamic regime of Dunkerton (1981), where inertial instability occurs if $K > 2n+1$. If $K < 2n+1$ the system is stable and exhibits equatorial gravity and inertia-gravity waves, the dynamical balance of which are derived in Appendix A. In the hydrodynamic regime, the central latitude $C = 1$, while the lengthscale $\hat{L} = 1/\sqrt{K}$. Thus, $F = 1 + Y/\sqrt{K}$, by which equations (6.38) and (6.39) reduce to

$$Su - \left(\frac{Y}{\sqrt{K}} - 1\right)v = 0, \quad Sv + \left(\frac{Y}{\sqrt{K}} + 1\right)u = \frac{K^{-1}}{S}(Y^2 - 1)v, \qquad (6.41)$$

where we have evaluated the pressure gradient in terms of v via the cross-stream momentum and thermodynamic equations in (6.38). Combining the equations of (6.41) yields the growth rate $S = \sqrt{1 - 1/K}$ for $K > 1$, which is consistent with Dunkerton (1981) and with equation (6.16) with $M = 0$ and $n = 0$. Note that if $K \gg 1$, the pressure gradient can be neglected from the balance (6.41), and gives the growth rate $S = 1$.

To illustrate the dynamical balance (6.41) we plot the cross-stream momentum equation for $K = 1.25$ and $K = 5.0$ in figure 6.4. The equator, the central latitude C (given in equation (6.5)) and latitude $C = 1$ (which is the minimum of the absolute vorticity $fQ = \beta y(\beta y - \Lambda_0)$ in nondimensional form) are represented by a dashed line, dotted line and crosses respectively. We shall retain this convention for all hydrodynamic and magnetohydrodynamic figures. It is important to note that the central latitude of every hydrodynamic mode coincides with the minimum of fQ ($C = 1$). Figure 6.4 shows that increasing K increases the cross-stream acceleration, since the magnitude of the pressure gradient decreases. The maximum growth rate $S = 1$ occurs as $K \to \infty$ since the pressure gradient is then completely negligible and therefore does not damp the cross-stream acceleration.

6.4.2 Magnetohydrodynamic Balances

We now consider the dynamical balances of the magnetohydrodynamic regime, where we shall categorise the various limiting cases seen in figure 6.2. We will address magnetically modified inertial instabilities, and purely magnetic instabilities in the weak and strong magnetic field regimes. The dynamical balance of equatorial magnetic, Alfvén, and magnetically modified inertia-gravity waves are considered in Appendix A.

Magnetically Modified Equatorial Inertial Instabilities

We begin by categorising the dynamic balance of the weak magnetic field limit ($M \ll 1$) in the hydrodynamically unstable regime ($K > 1$) with $K = O(1)$, where an unstable mode is present, as seen in the lower left section of figure 6.2. To isolate the unstable hydrodynamic mode, we assume that $S = O(1)$, which is implied by the leading order hydrodynamic growth rate, as seen
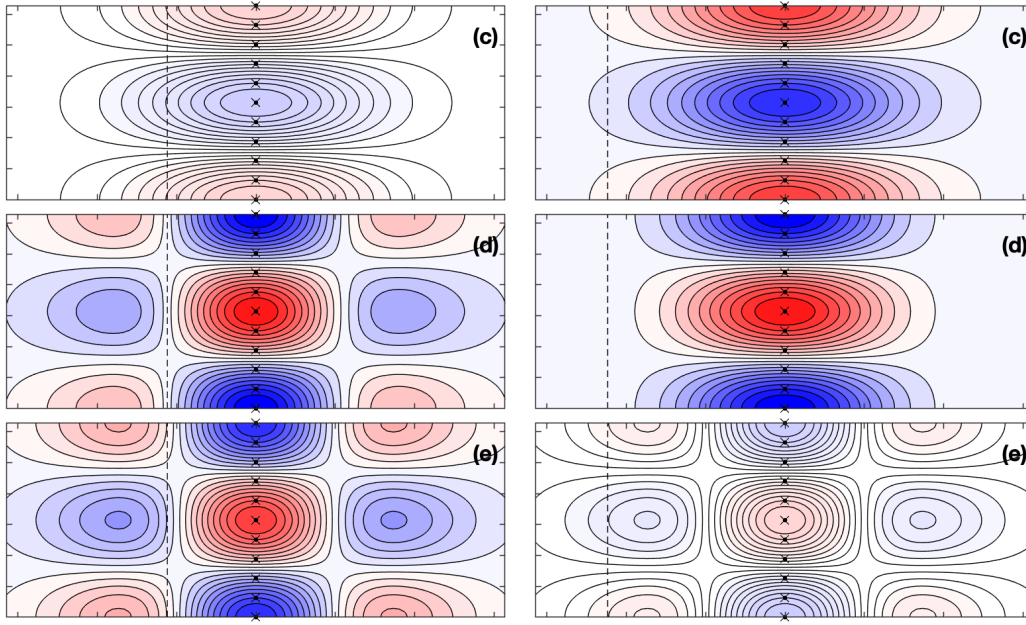
Figure 6.4: The cross-stream momentum equations of the dynamical balance (6.41) plotted for $K = 1.25$ (left) and $K = 5.0$ (right). The panels illustrate equatorial inertial instabilities with growth rates $S = 0.4472$ (left) and $S = 0.8944$ (right), and respective lengthscales $\hat{L} = 0.8944$ and $\hat{L} = 0.4472$ ($C = 1$ in both cases). Plots (c), (d), and (e) show the cross-stream acceleration, Coriolis force and pressure gradient.

in the expansion (6.34). With these assumptions, we can deduce from equations (6.38) and (6.39) that $u \sim \theta \sim v$ and $b_y \sim b_x \sim Mv$. Thus, equations (6.38) and (6.39) reduce to

$$Su - \left(\frac{Y}{\sqrt{K}} - 1\right)v = 0, \quad Sv + \left(\frac{Y}{\sqrt{K}} + 1\right)u = \frac{K^{-1}}{S}(Y^2 - 1)v, \qquad (6.42a)$$

$$Sb_x = 2b_y + iKMu, \quad Sb_y = iKMv, \qquad (6.42b)$$

which are hydrodynamic at leading order and are therefore described by the dynamical balance (6.41). However, the weak magnetic field expansion of the hydrodynamic mode (6.34) implies that weak field increases the growth rate of the hydrodynamically unstable system. Hence, we must include the second order terms in (6.42) to categorise the destabilising mechanism. Note that, if $K \to \infty$, the balance (6.42) would only be altered by neglecting the cross-stream pressure gradient and the $Y/\sqrt{K}$ terms.

To address the destabilising mechanism, we evaluate the Lorentz forces, F and the correction to the pressure gradient in terms of v, using the leading order hydrodynamic growth rate squared $S^2 = 1 - 1/K$ and the balance (6.41). First, it follows from the cross-stream induction equation in (6.39) that the cross-stream Lorentz force $iMKb_y = -M^2K^2v/S$, which is therefore stabilising as it acts to dampen the cross-stream acceleration. Similarly, we can deduce that the $O(M^2)$ contribution from the cross-stream pressure gradient takes the same sign as the leading order term and therefore decreases the growth rate of the system. The along-stream Lorentz force can be

written as

$$iKMb_x = \frac{iKM}{S}(2b_y + iKMu) = -\frac{K^2M^2}{S^2}\left(2 + \frac{1}{Y/\sqrt{K}+1}\left((Y^2-1)/K - S^2\right)\right)v,$$
(6.43)

where, if we use the leading order expansion for the square of the hydrodynamic growth rate, $S^2 = 1 - 1/K$, it follows that

$$iKMb_x = -\frac{K^2M^2}{S^2}\left(1 + \frac{Y}{\sqrt{K}}\right)v.$$
(6.44)

Thus, the along-stream Lorentz force (6.44) acts with the term $(Y/\sqrt{K} - 1)v$ (resulting from the Coriolis and advection terms) when $-\sqrt{K} < Y < \sqrt{K}$ and acts against the term otherwise. Hence, to determine whether the sum of second order contributions from F, the Lorentz force, and the pressure gradient increase or decrease the growth rate we must combine the momentum equations (including their second order corrections) to categorise the role of weak magnetic field. Thus, we expand F as

$$F \approx 1 + \frac{Y}{\sqrt{K}} + \frac{K^2M^2}{S^2}\left(1 + \frac{Y}{4\sqrt{K}}\right),$$
(6.45)

where, by considering all $O(M^2)$ terms in the along-stream momentum equation in (6.38), we obtain a second order correction to the along-stream acceleration, given by

$$Su - \left(\frac{Y}{\sqrt{K}} - 1\right)v = -\frac{3K^2M^2}{4(1-1/K)}\frac{Y}{\sqrt{K}}v.$$
(6.46)

Hence, we can substitute (6.46) into the cross-stream momentum equation via Fu and equate $O(M^2)$ terms to obtain the correction to the cross-stream acceleration, namely

$$(Sv)_{\text{correction}} = -\frac{3K}{2S^3}.$$
(6.47)

Thus, for unstable modes $S^2 > 0$, it follows that the magnetic correction to the hydrodynamic system (6.41) increases the growth rate, since the combination of the M^2 corrections from F, the pressure gradient and cross-stream Lorentz force always act to increase the cross-stream acceleration. We can also note that the correction (6.47) is valid in the hydrodynamically stable regime ($S^2 < 0$) as seen in Appendix A.

To confirm the dynamical balance (6.42) and determine the role of each term, we plot the along-stream momentum, cross-stream momentum and the along-stream induction equations in figure 6.5 with $K = 1.5$ and $M = 0.2$ (so that the effect of magnetic field can be seen). Once again, recall that the equator, the hydrodynamic central latitude and the minimum of fQ are represented by a dashed line, a dotted line and a crossed line, respectively. In contrast to the hydrodynamic case, we see that the central latitude of the mode no longer occurs at the minimum of fQ (and therefore the centre of the hydrodynamic inertially unstable modes); indeed, magnetic field perturbs the mode to higher latitude away from the most unstable hydrodynamic latitude ($C = 1$). In figure 6.5 we see that the along-stream Lorentz force acts with $-(F-2)v$ (the Coriolis and advection term) when $-\sqrt{K} < Y < \sqrt{K}$ and acts with $-(F-2)v$ otherwise, as predicted. We can
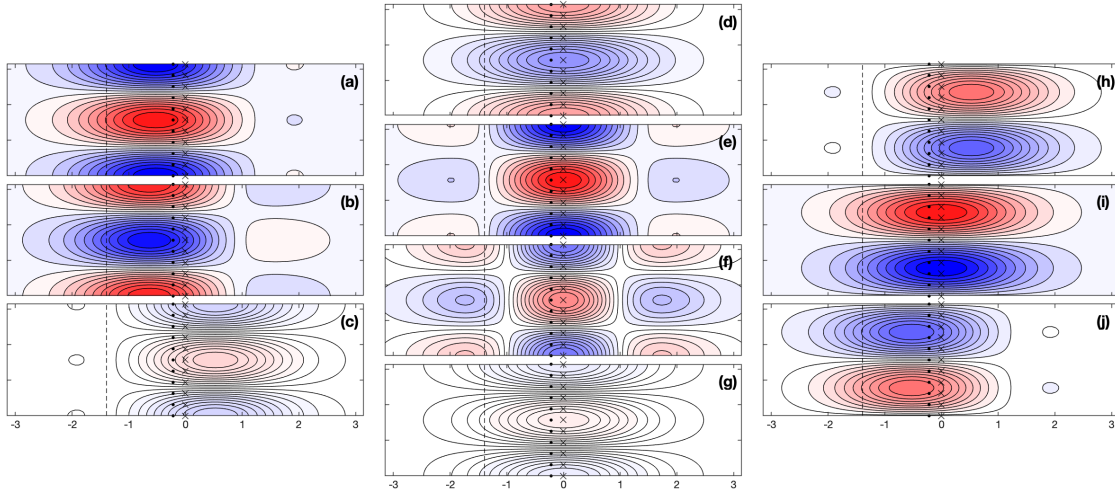
Figure 6.5: The dynamical balance of (6.42) plotted for $K = 1.5$ and $M = 0.2$, illustrating a magnetically modified equatorial inertial instability in the hydrodynamically unstable regime ($K > 1$) with growth rate $S = 0.6956$. The mode has central latitude $C = 1.1860$ and lengthscale $\hat{L} = 0.8521$. Plots (**a**), (**b**) and (**c**) show the along-stream acceleration, advection and Coriolis terms, and Lorentz force. Plots (**d**), (**e**), (**f**) and (**g**) show the cross-stream acceleration, Coriolis force, pressure gradient and Lorentz force. Plots (**h**), (**i**) and (**j**) show the along-stream field generation, advection and tension terms.

also see that the cross-stream Lorentz force acts against the cross-stream acceleration and therefore decreases the growth rate. This is indeed the case, which can be seen when comparing the hydrodynamic growth rate $S = 1 - 1/K = 1/3$ for $K = 1.5$ to the growth rate of the instability in figure 6.5 with $K = 1.5$ and $M = 0.3$, which is $S = 0.6956$.

Weak Magnetic Field Instability in the Hydrodynamically Stable Regime with $K = O(1)$

In this section we discuss the weak magnetic field limit ($M \ll 1$) in the hydrodynamically stable regime ($K < 1$) with $K = O(1)$ and sufficiently far from $K = 2n + 1$ (so we do not have to consider the singular root (6.29)), where an unstable mode is present as seen in the right panel of figure 6.2. To isolate the unstable magnetic mode we assume that $S \ll 1$, which is consistent with the weak magnetic field expansion (6.35). Thus, we can deduce from equations (6.38) and (6.39) that $S \sim M$, so that $b_x \sim u \sim \theta \sim v/S$ and $b_y \sim v$, where C and F retain all terms and are of order unity. Hence, equations (6.38) and (6.39) reduce to

$$Su - (F - 2)v = iKMb_x, \quad Fu = \frac{K^{-1}C^{-\frac{1}{2}}}{S}(Y^2 - 1)v, \quad Sb_x = 2b_y + iKMu, \quad Sb_y = iKMv, \tag{6.48}$$

where we have evaluated the pressure gradient in terms of v via the thermodynamic and incompressibility equations in (6.38). The equations of (6.48) combine to give $S^2 = K^{8/3}M^2/(1 - K^{2/3})$, which is consistent with the weak magnetic field expansion (6.35) with $n = 0$. Thus, in the hydrodynamically stable regime with $K = O(1)$ and $M \ll 1$, we attain geostrophic balance in the cross-stream direction, while retaining all other terms. We can compare (6.48) to the balance
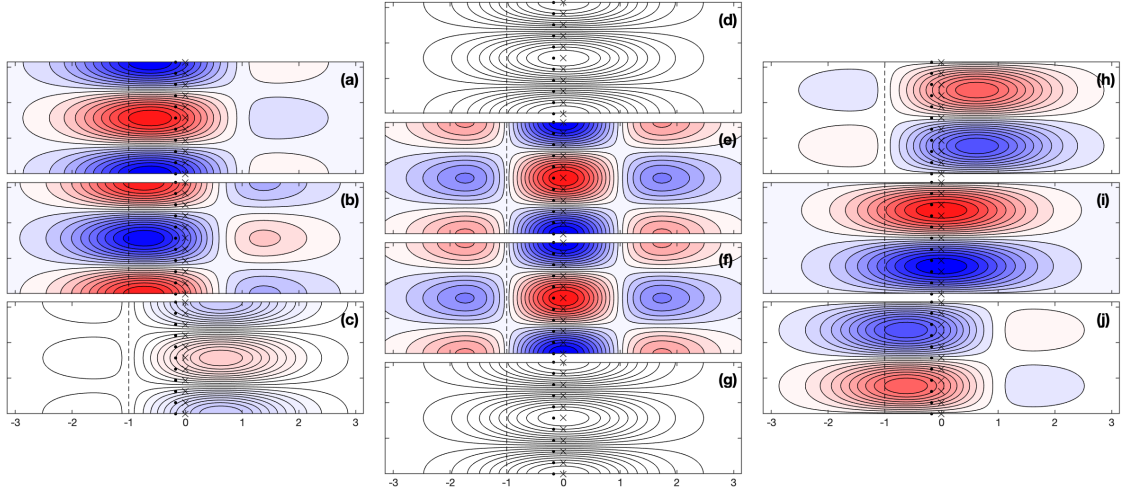
Figure 6.6: The dynamical balance of (6.48) plotted for $K = 0.75$ and $M = 0.01$, illustrating a magnetohydrodynamic equatorial instability in in the hydrodynamically stable regime ($K < 1$) with growth rate $S = 0.0163$. The mode has central latitude $C = 1.2116$ and lengthscale $\hat{L} = 1.2115$. Panel layout as in figure 6.5.

of equatorial inertia-gravity waves (A.29), which is also geostrophic in the cross-stream direction, allowing us to deduce that the along-stream Lorentz force is destabilising the system. Now, to illustrate the dynamical balance and confirm the destabilising mechanism, we plot the terms of (6.48) in figure 6.6. Indeed, by comparing figure 6.6 to figure A.2, we can deduce that the along-stream Lorentz force is indeed destabilising the hydrodynamically stable system. It also follows that the along-stream velocity is stabilising as it dampens the along-stream field generation.

Weak Magnetic Instability in the Hydrodynamically Stable Regime with $K \ll 1$

To extend the previous subsection we categorise the dynamical balance of the weak magnetic field limit ($M \ll 1$) with $K \ll 1$, where an unstable mode is present, as seen in the right panel of figure 6.2. To isolate the unstable magnetic mode we assume that $S \ll 1$, which is implied by the weak magnetic field expansion (6.35). These assumptions allow us to deduce from equations (6.38) and (6.39) that $b_y \sim KMv/S, u \sim v/S$. Then, as the cross-steam momentum equation is in geostrophic balance, the along-stream Lorentz force can not be neglected, otherwise the system would be hydrodynamic and stable. Thus, $b_x \sim Fv/KM$, since Su is small compared to the Coriolis term; we can also deduce that $C \approx M^2/S^2$ (with $S^2 \ll M^2$), so that $F \sim K^2M^2/S^2$. Hence, it follows from the along-stream induction equation that $S \sim MK^{\frac{4}{3}}$, in which $C \sim K^{-2/3}$ and $F \sim K^{-2/3}$, where both terms in F are of comparable order. The growth rate is consistent with (6.35) in the large K limit, which also implies that $S \ll M$. Hence, $b_x \sim K^{-5/3}v/M, u \sim K^{-4/3}v/M$ and $b_y \sim K^{-1/3}v$, so that equations (6.38) and (6.39) reduce to

$$- Fv = iKMb_x, \quad Fu = \frac{K^{-1}}{M}(Y^2 - 1)v, \quad Sb_x = 2b_y + iKMu, \quad Sb_y = iKMv, \quad (6.49)$$

211
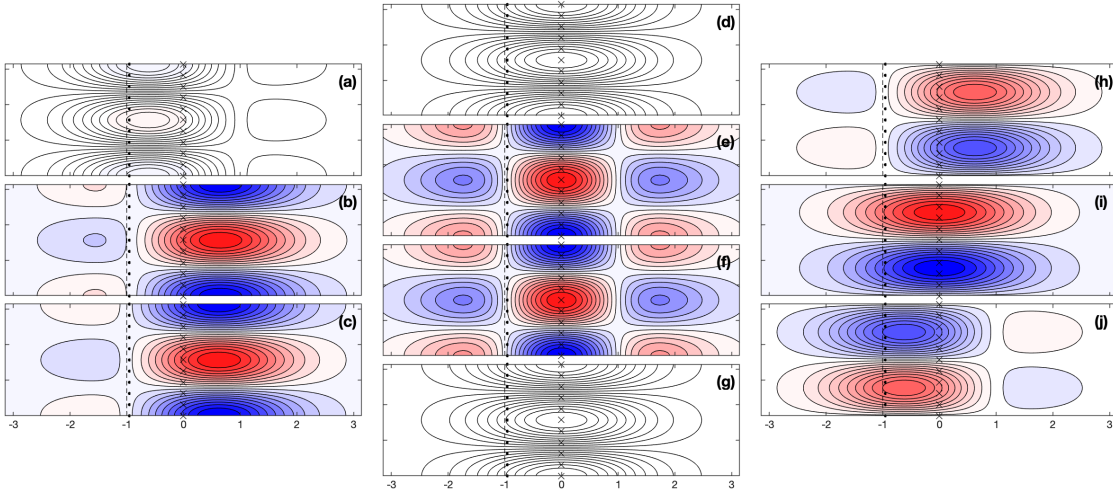
Figure 6.7: The dynamical balance of (6.49) plotted for $K = 0.01$ and $M = 0.01$, illustrating a magnetohydrodynamic equatorial instability in the hydrodynamically stable regime ($K < 1$) with growth rate $S = 2.21 \times 10^{-5}$. The mode has central latitude $C = 21.5443 \approx K^{-2/3}$ and lengthscale $\hat{L} = 21.5443 \approx K^{-2/3}$. Panel layout as in figure 6.5.

where we have evaluated the pressure gradient in terms of v via the thermodynamic and incompressibility equations in (6.38). Equations (6.49) combine to give $S = MK^{4/3}$, which is consistent with the weak magnetic field expansion (6.35) with $n = 0$. Thus, in the hydrodynamically stable regime with $K \ll 1$ and $M \ll 1$ we attain magnetostrophic balance in the along-stream direction and geostrophic balance in the cross-stream direction, while retaining all terms within the induction equations. In figure 6.7 we illustrate the dynamical balance (6.49). Figure 6.7 shows that the instability can be considered to be an equatorial analogue of the stratified MRI, as seen in Chapter 3, where weak magnetic field could destabilise the hydrodynamically stable regime with $K = O(1)$ or $K \ll 1$.

Instability in the Large M limit with $K = O(1)$

Typically, large magnetic field usually renders a system stable due to the Lorentz forces dominating the dynamics of the system and driving Alfvén waves. However, on the equatorial β-plane, large magnetic field does not give stability, but instead further destabilises the unstable hydrodynamic mode as well as the weak magnetic field instability (in the hydrodynamically stable regime), as seen on the right panel of figure 6.2. Thus, to categorise this instability we suppose $M \gg 1$ with $K = O(1)$ and $S = O(1)$, so that $C \approx K^2 M^2 / S^2$, $\hat{L} \approx \sqrt{MS}$ and $F = K^2 M^2 / S^2 + O(M^{1/2})$, from which equations (6.38) and (6.39) imply that $b_y \sim b_x \sim Mv$ and $u \sim v$. Hence, equations (6.38) and (6.39) reduce to

$$-\frac{K^2 M^2}{S^2} v = iKM b_x, \quad \frac{K^2 M^2}{S^2} u = iKM b_y, \quad S b_x = 2b_y + iKMu, \quad S b_y = iKMv, \quad (6.50)$$

since $F \approx K^2 M^2 / S^2$. Equations (6.50) combine to give $S^2 = 1$ as expected. Note that if $K \gg 1$, the dynamical balance (6.50) remains the same, combining to give $S^2 = 1$. Thus, in the limit of
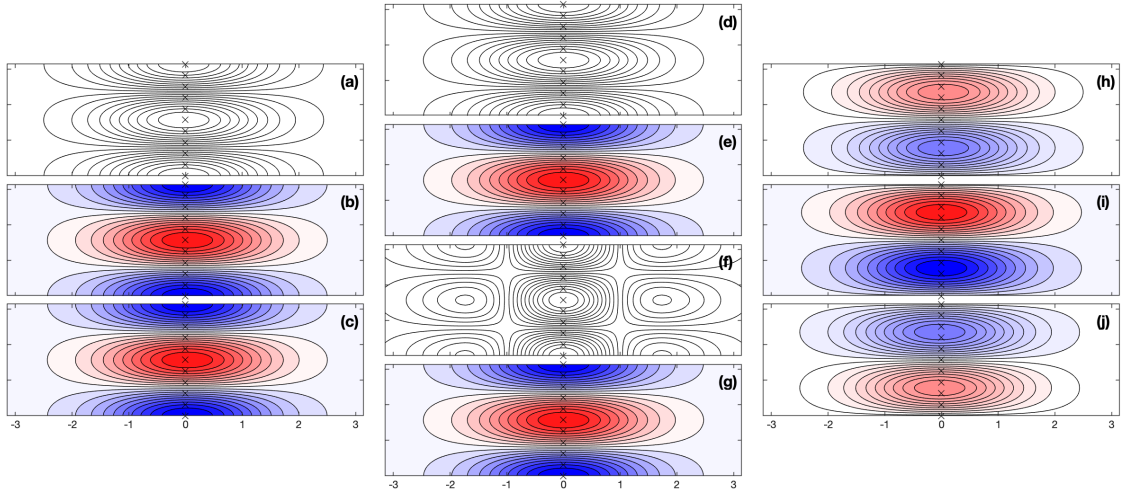
Figure 6.8: The dynamical balance of (6.50) plotted for $K = 1.0$ and $M = 10$, illustrating a magnetic instability in the large M limit with growth rate $S = 0.9995$. The mode has central latitude $C = 101.0985 \approx K^2 M^2/S^2$ and lengthscale $\hat{L} = 3.1709 \approx K^{1/2} M^{1/2}/S^{1/2}$. Panel layout as in figure 6.5.

large magnetic field, the system becomes magnetostrophic in the horizontal directions. This is in direct contrast to equatorial Alfvén waves (A.37), where the Lorentz forces balance and drive horizontal accelerations. This is illustrated in Figure 6.8 for $K = 1.0$ and $M = 10$. Note that increasing K, to $K = 1.5$ for example, does not significantly alter the balance; however, the central latitude moves closer to the equator. Figure 6.8 confirms the balance (6.50) and shows that the central latitude of the mode occurs far from the equator at $C \approx 101$.

Owing to the large magnetic field, the central latitude C occurs $O(M^2)$ from the equator while the lengthscale $\hat{L} \sim M^{1/2}$ (see equations (6.5) and (6.3)). Thus, as the lengthscale is of smaller order than the central latitude, the mode is unaffected by the equator and must therefore occur on an f-plane, where the mode is unstable for any non-zero value of shear. At first glance this conflicts with the results of Chapter 3, where sufficiently strong magnetic field stabilises all modes on the f-plane; however, the instability governed by (6.50) corresponds to a rapidly rotating instability on the f-plane that is hidden by the chosen timescale $1/f_0$ in Chapter 3.

To confirm that the strong magnetic field instability governed by (6.50) corresponds to a rapidly rotating instability on an f-plane, we suppose the shear, the magnetic field strength and the Coriolis parameter are constant (as in chapter 3) so that governing equation (2.30) has solutions of the form $v \propto \exp(-ily)$. Thus, supposing $U' = \Lambda_0, f = f_0$ and $B_3(y) = B_0$ with $v \propto \exp(-ily)$, equation (2.30) reduces to the eigenvalue relation:

$$s^4 + s^2 \left(\frac{l^2 N^2}{k^2} + 2k^2 v_A^2 + f_0 Q_0 \right) + k^2 v_A^2 \left(\frac{l^2 N^2}{k^2} - \Lambda_0 f_0 + k^2 v_A^2 \right) = 0. \tag{6.51}$$

Note that to compare this system with that of Chapter 3, we approximate the wide Hermite modes (with latitudinal lengthscale $L \sim M^{1/2} \gg 1$) locally as a very weak $v \sim \exp(ily)$ mode.

213

The mode of interest has lengthscale proportional to $M^{\frac{1}{2}}$; it follows that the cross-steam wavenumber $l \to 0$ in the large field limit. Hence, the terms that include the cross-stream wavenumbers in equation (6.51) may be neglected, where, upon recasting (6.51) in terms of the nondimensional parameters (6.15), we obtain

$$S^4 + S^2 \left(2K^2M^2 + 4\hat{f}(\hat{f}-1)\right) + K^2M^2 \left(K^2M^2 - 4\hat{f}\right) = 0, \qquad (6.52)$$

where we have also introduced $\hat{f} = f_0/\Lambda_0$. Thus, following the scalings of (6.50) we suppose $\hat{f} \sim M^2 \gg 1$ with $S^2 = O(1)$, where, by considering the $O(M^4)$ terms of (6.52) we obtain

$$S^2 = \frac{K^2M^2}{4\hat{f}^2} \left(4\hat{f} - K^2M^2\right). \qquad (6.53)$$

Equivalently, in dimensional terms, equation (6.53) becomes

$$s^2 = \frac{k^2 v_A^2}{f_0^2} \left(\Lambda_0 f_0 - k^2 v_A^2\right). \qquad (6.54)$$

Recall that the Coriolis parameter $f = \beta y$ was nondimensionalised by $2/\Lambda_0$ and that in the limit of strong field, equation (6.50) implies $2f/\Lambda_0 = F \sim M^2 = 4k^2 v_A^2/\Lambda_0^2$, in which it follows that $f \approx 2k^2 v_A^2/\Lambda_0$. Thus, in the limit of large field, we have shown that (6.50) describes a rapidly rotating system on an f-plane, since substituting $f_0 = 2k^2 v_A^2/\Lambda_0$ into (6.54) gives the maximum growth rate $s^2 = \Lambda_0^2/4$. Hence, by allowing the Coriolis parameter to vary in strength (due to rotation speed or latitude), the instability governed by (6.50) is attainable on an f-plane. We can also note that in the rapidly rotating limit with $f_0 \sim k^2 v_A^2/\Lambda_0$, the f-plane system in Chapter 3 is magnetostrophic in the horizontal directions and retains all terms in the induction equation; indeed, this directly corresponds to the balance (3.60) in section 3.4.

This analogy to the f-plane also allows us to conclude that the sheared cross-stream field $2b_y$ in (6.50) is responsible for the instability. We can conclude this from equations (6.36) and (6.37), where, after supposing $f_0 \sim k^2 v_A^2/\Lambda_0$ and neglecting $\Lambda_0 b_y$ in the along-stream induction equation, we obtain that $s^2 = -k^4 v_A^4/f_0^2$. This dispersion relation describes the hydromagnetic-inertial wave of Acheson & Hide (1973) with the cross-stream wavenumber being set to zero. We can see that this is consistent, since taking (6.50) in the large M limit implies that the lengthscale is $O(M^{1/2})$, so that the cross-stream wavenumber scales with $M^{-1/2}$.

Now, since the lengthscale of the mode is $O(M^{\frac{1}{2}})$ while the central latitude occurs at $O(M^2)$ from the equator (see equation (6.5) and figure 6.3), we must consider the validity of this instability in a planetary atmosphere. To do this, we note that the Coriolis parameter can be written as $f = 2\Omega \sin\theta$, where θ is the azimuthal coordinate and Ω is the angular velocity of the planet. Thus, near the equator, where $\theta \ll 1$, we can expand $f = 2\Omega \sin\theta$ to give

$$f = 2\Omega \left(\theta - \frac{\theta^3}{6} + \ldots\right) = \beta y \left(1 - \frac{y^2}{6a^2} + \ldots\right), \qquad (6.55)$$

since $\beta = 2\Omega/a$ and $y = a\theta$, where a is the planetary radius. Hence, in order to ensure that the second order term of (6.55) is not comparable to the leading order term, we require that the latitude

y of the mode satisfies $y \ll a$. However, (6.50) implies $y \sim \Lambda_0 M^2/2\beta$ and since $\beta = 2\Omega/a$, where Ω is the angular velocity of the planet, we can write the condition $y \ll a$ equivalently as $k^2 v_A^2 \ll \Lambda_0 \Omega$. Thus, the large field instability governed by (6.50) does not violate the equatorial β-plane assumption provided that the vertical wavenumber is sufficiently small (limited by the atmospheric layer and the Boussinesq approximation), or that Λ_0 is sufficiently large (i.e., strong equatorial shear), or the planet is rapidly rotating. However, one must recall that to obtain the dispersion relation (6.54) from (6.52) we required that $f_0 \sim k^2 v_A^2/\Lambda_0$, from which it follows that the dispersion relation may break down if k becomes too small. This is reasonable as large vertical scales may invalidate the magnetohydrostatic approximation and also be physically unattainable in planetary atmospheres.

Note that it is quite likely that the large M instability is violating some assumptions; however, one can just disregard this region of parameter space and remain well within the constraints listed above. This also motivates the jet flow that we will consider in Section 6.5, which does not allow the large M instability to occur.

Instability in the Small K limit with $M = O(1)$

We now address the small K limit with $M = O(1)$, where we expect instability as shown in figure 6.2; however, the growth rate $S \ll 1$, owing to the stabilising effect of stratification when the parameter K is small. These assumptions allow us to deduce from equations (6.38) and (6.39) that $S \sim K^{\frac{4}{3}}$, which is consistent with (6.24). Thus, $b_y \sim u \sim K^{\frac{1}{3}} v$ and $b_x \sim K^{\frac{2}{3}} v$, where, as a result, $C \approx K^2 M^2/S^2$ and the terms of F are comparable. Hence, equations (6.38) and (6.39) reduce to

$$-Fv = iKMb_x, \ \ Fu = \frac{1}{M}(Y^2 - 1)v, \ \ Sb_x = 2b_y + iKMu, \ \ Sb_y = iKMv, \quad (6.56)$$

where we have evaluated the pressure gradient in terms of v via the thermodynamic and incompressibility equations in (6.38). Equations (6.56) combine to give $S = K^{\frac{4}{3}} M$. Hence, with $M = O(1)$ and $K \ll 1$ the system is in magnetostrophic balance in the along-stream direction and geostrophic balance in the cross-stream direction. The dynamical balance (6.56) is clearly similar to the dynamical balance (6.49), where $K \ll 1$ and $M \ll 1$; this implies that finite magnetic field strength with $K \ll 1$ restricts the growth rate to $O(MK^{\frac{4}{3}})$.

Instability in the Large M limit with $K \ll 1$

We now consider the large M limit with $K \ll 1$, where S may be small or of order unity. Then $C = 1 + K^2 M^2/S^2$, from which it follows that $F = C^{1/4} Y/\sqrt{K} + C \sim \max(C^{1/4}/\sqrt{K}, C)$, in which there are three cases to consider regarding the size of K in comparison to M. We find, for all cases, that F must be $O(C)$ as this is always larger or of comparable size to $C^{1/4}/\sqrt{K}$. First, we assume that $1 \gg K^4 M^3$, in which we can deduce from equations (6.38) and (6.39) that

$S \sim MK^{\frac{4}{3}}, C \sim K^2 M^2/S^2, F \sim C, u \sim K^{-4/3}v/M, b_x \sim K^{-5/3}v/M$ and $b_y \sim K^{-1/3}v$. Equations (6.38) and (6.39) then reduce to

$$-Fv = iKMb_x, \quad Fu = \frac{K^{-1}}{M}(Y^2-1)v, \quad Sb_x = 2b_y + iKMu, \quad Sb_y = iKMv, \quad (6.57)$$

where all terms in F are comparable and the pressure gradient has been evaluated in terms of v via the thermodynamic and incompressibility equations in (6.38). Thus, when $K^4 M^3 \ll 1$ we have a weak magnetic instability with growth rate $S \sim MK^{\frac{4}{3}} \ll 1$, which is consistent with equation (6.24). The along-stream momentum equation is in magnetostrophic balance, the cross-stream momentum equation is in geostrophic balance, while the horizontal induction equations are unchanged.

Next, we assume that $K^4 M^3 = O(1)$, from which we can deduce from equations (6.38) and (6.39) that $S \sim MK^{\frac{4}{3}} = O(1), u \sim v, b_x \sim K^{\frac{1}{3}}v$ and $b_y \sim K^{\frac{1}{3}}v$. Equations (6.38) and (6.39) reduce to

$$-Fv = iKMb_x, \quad Fu = \frac{K^{-1}}{M}(Y^2-1)v + iKMb_y \quad Sb_x = 2b_y + iKMu, \quad Sb_y = iKMv, \tag{6.58}$$

where all terms in F are comparable. Thus, when $K^4 M^3 = O(1)$ we have a magnetic instability with growth rate $S \sim M^3/K^4 = O(1)$. The along-stream momentum equation is in magnetostrophic balance while the cross-stream momentum equation and the horizontal induction equations are unchanged.

Finally, we assume that $K^4 M^3 \gg 1$, in which case we can deduce from equations (6.38) and (6.39) that $S \sim 1, u \sim v, b_x \sim KMv$ and $b_y \sim KMv$. Equations (6.38) and (6.39) reduce to

$$-Fv = iKMb_x, \quad Fu = iKMb_y \quad Sb_x = 2b_y + iKMu, \quad Sb_y = iKMv, \quad (6.59)$$

where $F \sim C \approx K^2 M^2/S^2$. Thus when $M^3 K^4 \gg 1$ we have a magnetic instability with a maximum growth rate $S = 1$. The horizontal momentum equations are in magnetostrophic balance while the induction equations remain unchanged.

There is a clear similarity between the various dynamical balances of previous cases and (6.57), (6.58) and (6.59). For example, (6.59) describes the dynamical balance of the large field instability with $K = O(1)$, given by (6.50). Similarly, (6.57) describes the large K dynamical balance with $M = O(1)$, given by (6.56), where, since $M \gg 1$, the order of parameters differ by a factor of M. Hence, by deriving (6.57), (6.58) and (6.59), we have shown that when $K \gg 1$ and $M \gg 1$, there is clear modification in the dynamical balance as the size of K surpasses $M^{-3/4}$. If $K^4 M^3 \gg 1$ the system is unstable with maximum growth rate $S \approx 1$. Then, if $K^4 M^3 \ll 1$, the system is unstable with growth rate $S \sim MK^{\frac{4}{3}}$.

Weak Magnetic Instability in the Hydrodynamic Regime of Neutral Stability

We now categorise the dynamic balance of the weak magnetic field limit ($M \ll 1$) in the neutrally stable hydrodynamic regime stable regime ($K \sim (2n+1)$), where an unstable mode is present,

as seen in figure 6.2. To isolate the unstable mode, we assume that $S \ll 1$, which is implied by the weak magnetic field expansion (6.29). These assumptions allow us to deduce from equations (6.38) and (6.39) that $S \sim M^{1/2}$, from which $C \approx 1$ and $F = 1 + Y/\sqrt{K}$. Hence, $b_y \sim M^{1/2}v$, $u \sim v/S$ and $b_x \sim v$, where equations (6.38) and (6.39) reduce to

$$Su - \left(\frac{Y}{\sqrt{K}} - 1\right)v = 0, \quad \left(\frac{Y}{\sqrt{K}} + 1\right)u = \frac{K^{-1}}{S}(Y^2 - 1)v, \qquad (6.60a)$$

$$Sb_x = 2b_y + iKMu, \quad Sb_y = iKMv, \qquad (6.60b)$$

where we have evaluated the pressure gradient in terms of v via equations (6.38c) and (6.38d). Equations (6.60) denote the hydrodynamic balance (6.41) at leading order; however, the growth rate in the hydrodynamically stable regime attains a similar destabilising mechanism to the balance (6.42) provided $K^{-1} \sim (2n + 1)$.

6.5 Instabilities of Equatorial Jets ($\delta \neq 0$)

We now consider the full flow profile (6.1) with $\delta > 0$ on an equatorial β-plane in the presence of uniform magnetic field of strength B_0. The flow profile $U(y) = \Lambda_0 y - \delta\beta y^2/2$ is an equatorial jet centered at latitude $y = \Lambda_0/\delta\beta$, and contrast to the uniform shear flow ($\delta = 0$), unstable modes are restricted to the interval $0 < y < \Lambda_0/\delta\beta$, which are the only latitudes where anti-cyclonic shear ($U'f > 0$) occurs.

To illustrate the jet profile and the magnetohydrodynamic necessary condition for instability $U'f > 0$, in figure 6.9 we plot $\hat{U} = \beta U(y)/\Lambda_0^2 = \hat{y} - \delta\hat{y}^2/2$, $-\hat{f}\hat{Q} = -fQ/\Lambda_0^2 = \hat{y}(1 - (1+\delta)\hat{y})$, and $\hat{U}'\hat{f} = U'f/\Lambda_0^2 = \hat{y}(1 - \delta\hat{y})$, against the nondimensional latitude $\hat{y} = \beta y/\Lambda_0$ with $\delta = 0.25$. Figure 6.9 shows that the flow profile can be used as a model of a non-symmetric equatorial jet, provided that we only get flow near the off-centre equatorial peak approximately correct; thus, there is clear application to the equatorial jets typically found in the upper atmospheres of Jupiter (Kaspi *et al.*, 2018; Read, 2024) and Hot Jupiters (Showman *et al.*, 2013; Heng & Showman, 2015). However, it is important to note that Jupiter's prominent central equatorial jet is symmetric about the equator, and thus it is more appropriate to model the immediately adjacent jets (so that they are sufficiently close to the equator), which are illustrated in figure 1.2. It is also unlikely that there are regions of $fQ < 0$ which are necessary for inertial instability to occur; however, as we determined in Section 2.5, in the magnetohydrodynamic regime a necessary condition for instability is that $U'f > 0$ (which is less stringent than $fQ < 0$).

Figure 6.9 also shows that $U'f > 0$ for $0 < \hat{y} < 4 (= 1/\delta)$ only, restricting unstable modes to this region. Thus, given the latitudinal decay of the modes, the structure of $\hat{U}$ outside of this region will presumably be somewhat unimportant. Hence, by considering $\hat{U}$ in the region $0 < \hat{y} < 4$, we could model a northern flank of a westward equatorial jet (consistent with a westward jet centred at or near the equator). Westward travelling jets have been recently observed on Hot Jupiters (Armstrong *et al.*, 2016; Dang *et al.*, 2018), where numerical models suggest that strong magnetic
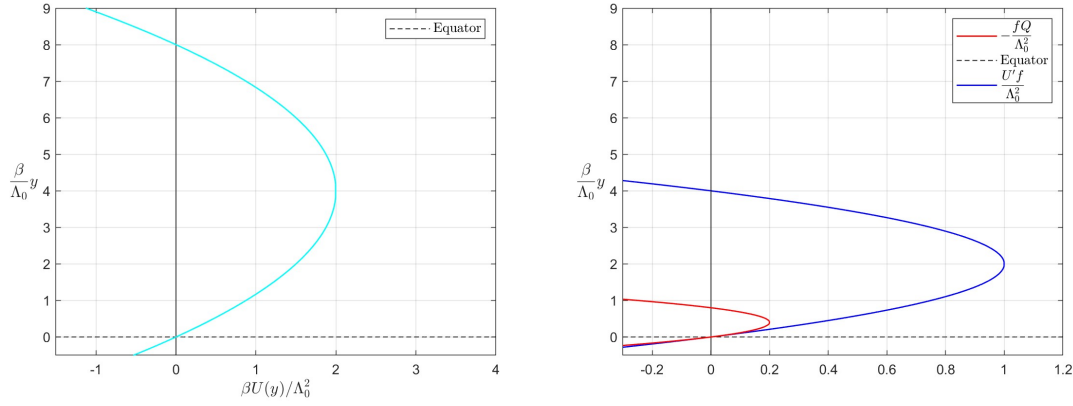
Figure 6.9: The nondimensional flow profile $\hat{U}$ (left), and the quantities $-fQ/\Lambda_0^2$ and $U'f\Lambda_0^2$ (right), plotted against the nondimensional latitude $\hat{y}$ with $\delta = 0.25$.

fields are largely responsible for the atypical westward travelling jets (Rogers & Komacek, 2014; Rogers, 2017; Hindle *et al.*, 2019, 2021).

Note that figure 6.9 also shows that the hydrodynamic necessary condition for instability $fQ < 0$ is only satisfied for $0 < \hat{y} < 0.8 \ (= 1/(1+\delta))$, which is far more stringent than magnetohydrodynamic condition $U'f > 0$ (even close to the equator).

We have already derived the relevant eigenvalue relation (6.8) and corresponding central latitude and lengthscale (6.5), which give eigenfunctions of the form $H_n(Y)\exp(-Y^2/2)$. We can once again consider the previous nondimensional parameters (6.15) used in the $\delta = 0$ analysis. This allows us to recast the eigenvalue relation (6.8) as:

$$\left(1 + \frac{M^2 K^2}{S^2}\right)^{\frac{3}{2}} \left(1 - S^2 \left(1 + \delta\left(1 + \frac{M^2 K^2}{S^2}\right)\right)\right) = \frac{2n+1}{K}\left(1 + \delta\left(1 + \frac{M^2 K^2}{S^2}\right)\right)^{\frac{3}{2}},$$
(6.61)

which reduces to (6.16) when $\delta = 0$. The corresponding nondimensional central latitude C and lengthscale $\hat{L}$ are given by

$$C = \frac{2\beta}{\Lambda_0}y_0 = \left(1 + \frac{M^2 K^2}{S^2}\right)\left(1 + \delta\left(1 + \frac{M^2 K^2}{S^2}\right)\right)^{-1},$$
(6.62a)

$$\hat{L}^2 = \frac{4\beta^2}{\Lambda_0^2}L^2 = \frac{1}{K}\left(1 + \frac{M^2 K^2}{S^2}\right)^{\frac{1}{2}}\left(1 + \delta\left(1 + \frac{M^2 K^2}{S^2}\right)\right)^{-\frac{1}{2}},$$
(6.62b)

using the definition of the central latitude y_0 and lengthscale L from (6.5).

6.5.1 Stability Bounds

First, we obtain the domain of instability by supposing $S \to 0^+$ in (6.61) to obtain the following expression:

$$M^2 = \frac{K - (2n+1)\delta^{\frac{3}{2}}}{\delta K^3}.$$
(6.63)

Equation (6.63) implies that if $M = 0$, then $K = (2n+1)\delta^{\frac{3}{2}}$ is the stability boundary for steady modes. Given $M \ll 1$, the vertical wavenumber $K = (2n+1)\delta^{\frac{3}{2}}$ to $O(M^2)$ instead.
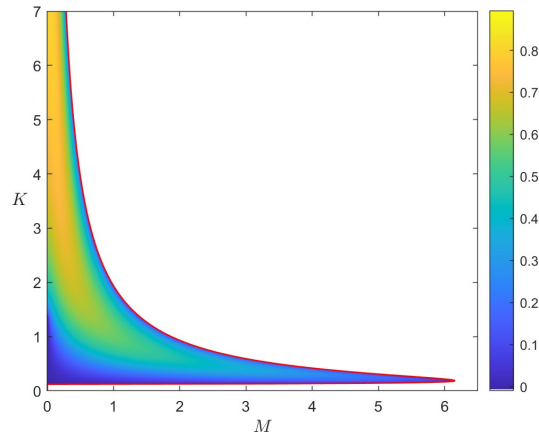
Figure 6.10: The maximum growth rate for $\delta = 0.25$ in (M, K)-space. The maximum growth rate is $S = (1 + \delta)^{-\frac{1}{2}} = 0.8944$ ($s = 0.4472\Lambda_0$) and is found on the $M = 0$ axis as $K \to \infty$.

We can differentiate (6.63) with respect to K to find the maximum M, M_{max} say, for which instability can occur. Indeed, upon setting the derivative to zero we find that M_{max} occurs at $K_c = 3(2n + 1)\delta^{\frac{3}{2}}/2$. Hence, after substituting K_c into equation (6.63), we obtain

$$M_{\text{max}} = \frac{2}{3\sqrt{3}(2n+1)\delta^2} \quad \text{occurring at} \quad K_c = \frac{3(2n+1)\delta^{\frac{3}{2}}}{2}. \tag{6.64}$$

We also find that equation (6.63) is satisfied in the large K limit if and only if $K = 1/M\sqrt{\delta}$. That is, for any K, instability is possible given sufficiently small M.

6.5.2 Growth Rate as a Function of Vertical Wavenumber and Field Strength

We now proceed by solving (6.61) numerically for the maximum growth rate, with $\delta = 0.25$. To solve (6.61) numerically, we square (6.63) and rearrange to form a 12th order polynomial for the growth rate S, which yields 12 roots (some complex). The validity of the roots is then verified by substitution into equation (6.61); roots that do not satisfy the equality (6.61) to a tolerance of $O(10^{-6})$ are neglected. The maximum real part of the valid root is plotted in figure 6.10. We plot the stability boundary (6.63) as a solid red line in order to bound the unstable domain clearly. We also provide plots of the nondimensional central latitude and lengthscale in (M, K)-space with $\delta = 0.25$, given by (6.62), in figure 6.11.

In contrast to the flow profile $U(y) = \Lambda y$, strong magnetic field now stabilises the system. Modes with small K have also been stabilised. Figure 6.10 shows that weak magnetic field allows instability to occur in the hydrodynamically stable regime ($K < (2n + 1)(1 + \delta)^{3/2}$). Weak magnetic field also increases the growth rate of the hydrodynamically unstable system ($K > (2n + 1)(1 + \delta)^{3/2}$) so that the maximum growth rate at fixed K is found at non-zero M. However, the maximum growth rate $S = (1 + \delta)^{-1/2}$ occurs as $K \to 0$ with $M = 0$, which implies that weak magnetic field does not always increase the growth rate.
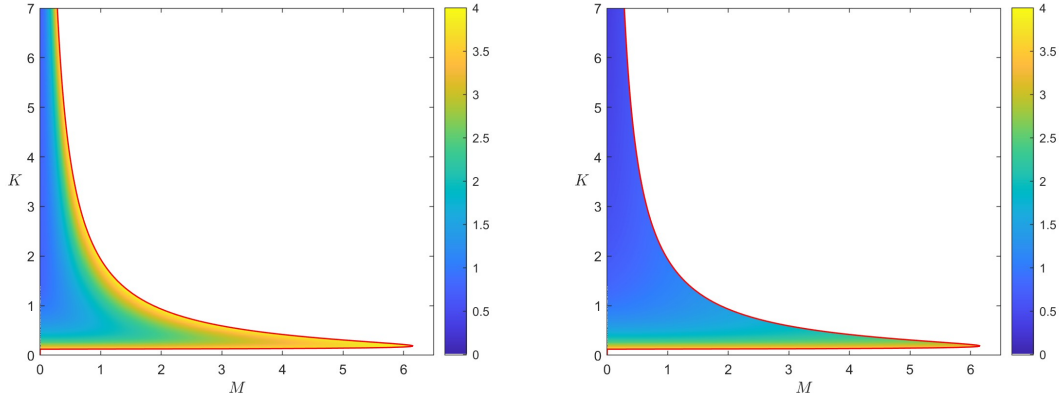
Figure 6.11: The nondimensional central latitude (left) and lengthscale (right) of the most unstable mode plotted in figure 6.10 with $\delta = 0.25$ in (M, K)-space.

Figure 6.11 shows that modes are stabilised when the nondimensional central latitude $C > 4$. This is due to the maximum of $U'f$ occurring at $C = 4$. To see this, we differentiate $U'f = (\Lambda_0 - \delta\beta y)\beta y$ with respect to y, implying that the maximum of $U'f$ occurs at $y = \Lambda_0/2\delta\beta$ which in nondimensional terms yields $\hat{y} = 2\beta y/\Lambda_0 = 1/\delta = 4$ when $\delta = 0.25$. This latitude corresponds to the centre of the anticyclonic region of the domain; that is, $U'f$ is positive for $0 < y < \Lambda_0/2\delta\beta$. We can also recall that the growth rate squared is bounded by the maximum of $U'f$ within the domain (see equation (2.45)). Thus, the latitude $y = \Lambda_0/2\delta\beta$ (corresponding to $C = 4$ for $\delta = 0.25$) is the final latitude to be stabilised in the domain due to the effects of magnetic field, stratification or both. This final latitude at which the modes are stabilised persists regardless the value of the nondimensional lengthscale $\hat{L}$. However, we note that the lengthscale increases monotonically as the vertical wavenumber decreases.

6.5.3 Scale Selection

To determine the value of K, $K_{\max}$ say, at which the maximum growth rate $S_{\max}$ occurs for each value of M. First, we aim to describe the small M limit, where upon inspection of figure 6.10 we can see that the maximum growth rate (which is $O(1)$) occurs as $K \to \infty$. Numerically, it is possible to find a power relationship between M and $K_{\max}$ (close to $A \sim M^{-\frac{2}{3}}$); thus, we suppose that $M, MK \ll 1$ and $S^2 = (1 + \alpha M^\beta)/(1 + \delta)$ for some constants $\alpha, \beta \in R$ of order unity. Under this formulation we may find the value of $K_{\max}$ for small values of M. Indeed, equation (6.61) reduces to

$$-K(\alpha M^\beta + \delta M^2 K^2) = (2n + 1)(1 + \delta)^{\frac{3}{2}}, \qquad (6.65)$$

which allows us to deduce $\beta = 2/3$ since $M^2 K^2 \sim M^\beta$ and $K M^\beta \sim 1$. Equating the terms of (6.65) also allows us to find that $\alpha = -\delta M^{2-\beta} K^2 - (2n + 1)(1 + \delta)^{\frac{3}{2}}/K\tilde{M}^\beta$, which yields the following equation for the growth rate:

$$S^2 = \frac{1}{1 + \delta} - \frac{\delta M^2 K^2}{1 + \delta} - \frac{(2n + 1)(1 + \delta)^{\frac{1}{2}}}{K} + \frac{3}{2}(1 + \delta)^{\frac{1}{2}} M^2 K, \qquad (6.66)$$

220
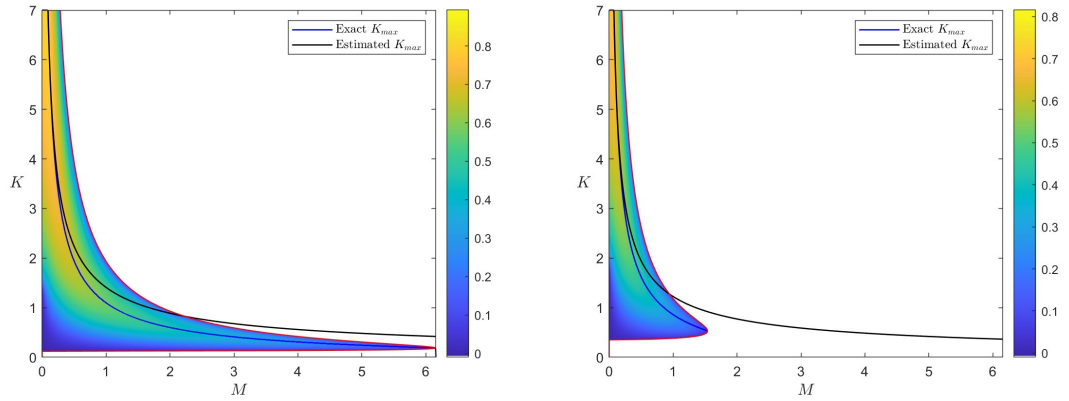
Figure 6.12: Comparison between the small M result (6.68) for $K_{\max}$ and the numerically determined exact result plotted against M with $\delta = 0.25$ (left panel) and $\delta = 0.5$ (right panel). In each case the values are overlayed over contours of the growth rate.

where we have also calculated a second order term ($O(M^{4/3})$) to increase the accuracy of the expansion.

To determine $K_{\max}$, we set $\partial_K S^2 = 0$ starting from (6.66):

$$M^2 = \frac{2(2n+1)(1+\delta)^{\frac{3}{2}}}{K^2(4\delta K - 3(1+\delta)^{\frac{3}{2}})} \approx \frac{(2n+1)(1+\delta)^{\frac{3}{2}}}{2\delta K^3}\left(1 + \frac{3(1+\delta)^{\frac{1}{2}}}{4\delta K}\right), \tag{6.67}$$

where, upon neglecting higher order terms, we obtain

$$K_{\max}^3 = \frac{(2n+1)(1+\delta)^{\frac{3}{2}}}{2\delta M^2}. \tag{6.68}$$

Thus, upon substituting (6.68) into (6.66) we obtain an approximation for the maximum growth rate as a function of $K_{\max}$ (or, equivalently M) and δ only, given by

$$S_{\max}^2 = \frac{1}{1+\delta} - \frac{3}{2}(2n+1)(1+\delta)^{\frac{1}{2}}\frac{1}{K_{\max}} + \frac{3(2n+1)^2(1+\delta)^2}{4\delta}\frac{1}{K_{\max}^2}, \tag{6.69}$$

valid for sufficiently small M.

We now plot the value of the small M result given by $K_{\max}$ in (6.68) with the numerically determined $K_{\max}$ against M to validate the accuracy of the approximation for various δ in figure 6.12. The plots have been overlayed over the instability domain so that $K_{\max}$ can be seen to occur where the growth rate is maximum for each M. Note that the colourbars and axes change for each δ; this is owing to the way δ modifies the unstable domain and maximum growth rate. There is also difficulty numerically determining $K_{\max}$ for $M < 0.01$ since the maximum growth rate as $M \to 0$ occurs as $K \to \infty$. The plots show that as δ increases, the approximation remains valid for a smaller interval of M; this is due to the expression for $K_{\max}^3$ (6.69) becoming smaller as δ increases for $\delta < 2$, conflicting with the weak magnetic field assumption.

We now plot the small M result for the maximum growth rate given by (6.69) against the exact maximum growth rate at each M in figure 6.13 for $\delta = 0.25$ and $\delta = 0.5$. Indeed, equation (6.69) only describes the most unstable mode for a comparatively small interval of M as compared to the
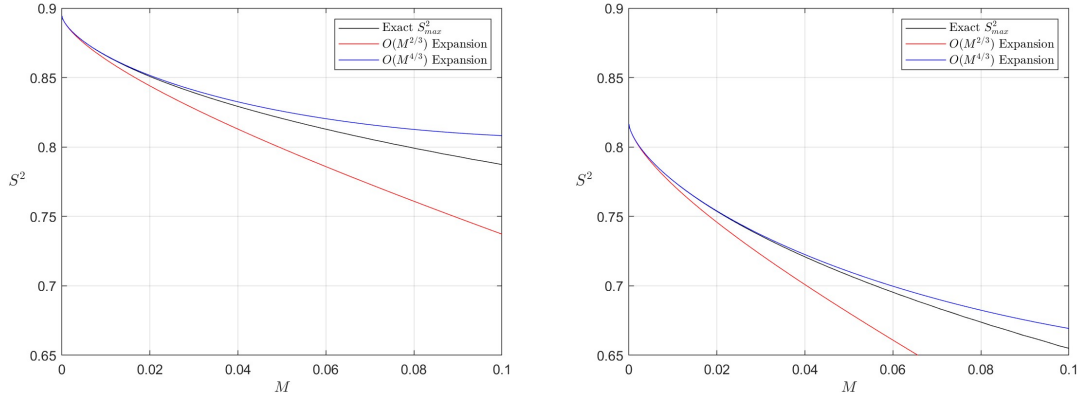
Figure 6.13: The small M result (6.69) for $S^2_{\max}$ and the numerically determined exact value of S^2 plotted against M with $\delta = 0.25$ (left panel) and $\delta = 0.5$ (right panel). Equation (6.69) has been plotted with and without the $O(M^{\frac{4}{3}})$ term to illustrate the increase in accuracy.

interval in which the estimate for $K_{\max}$ remains accurate. This is due to the maximum growth rate occurring as $M \to 0$ and $K \to \infty$; this also creates difficulties comparing the growth rates when M is small. We find that the accuracy of the expansion increases with δ; we may expect this as increasing δ decreases the size of the unstable domain.

6.5.4 The Role of Weak Magnetic Field

In this subsection we focus on the effect of the weak magnetic field on the growth rate rather than the scale selection. This is motivated by the varying role of magnetic field, as seen in figure 6.10.

We first consider the large K limit with $M \ll 1$ of expression (6.61), yielding the following expression for the growth rate at leading order:

$$S^2 = \frac{1 - \delta K^2 M^2}{\delta + 1}, \tag{6.70}$$

provided $M^2 K^2 = O(1)$. We could alternatively derive this by truncating the expansion (6.66). Equation (6.70) implies the system is unstable if $\delta K^2 M^2 < 1$. Thus, for any $K \gg 1$, instability will occur with growth rate (6.70) given sufficiently small M. In the case where $M^2 K^2 \ll 1$, we obtain the maximum growth rate of the hydrodynamic system (i.e., $S^2 = 1/(1 + \delta)$). Equation (6.70) also implies that weak magnetic field reduces the growth rate of the system in the large K limit.

We now consider the case when $A = O(1)$ with $M \ll 1$ and $S = O(1)$ so that we isolate the weak magnetic field effect on the unstable hydrodynamic mode (i.e., for $K > (2n+1)(1+\delta)^{3/2}$). In this limit, equation (6.61) yields the following weak magnetic field expansion:

$$S^2 \approx \frac{K - (2n+1)(1+\delta)^{\frac{3}{2}}}{K(1+\delta)} + \frac{K^2((2n+1)(1+\delta)^{\frac{3}{2}}(3+2\delta) - 2\delta K)}{2(1+\delta)(K - (2n+1)(1+\delta)^{\frac{3}{2}})} M^2. \tag{6.71}$$

Hence, assuming we have hydrodynamic instability, so that the leading order term of (6.71) is positive, it follows that the magnetic correction is positive if

$$(2n+1)(1+\delta)^{\frac{3}{2}}(3+2\delta) > 2\delta K. \tag{6.72}$$

222

Thus, the magnetic field increases the growth rate of the hydrodynamically unstable regime given sufficiently small K. For $\delta = 0.25$ and $n = 0$, the condition (6.72) predicts that for $K < 9.782$ the second order term of (6.71) is positive.

We can also consider the Alfvénic mode in the limit of weak magnetic field by supposing $S \ll 1$ with $K = O(1)$ and $M \ll 1$, in which (6.61) yields

$$S^2 = \frac{(K^{\frac{2}{3}} - (2n+1)^{\frac{2}{3}}\delta)K^2}{(2n+1)^{\frac{2}{3}}(1+\delta) - K^{\frac{2}{3}}}M^2 - \frac{2(2n+1)^{\frac{2}{3}}K^{\frac{16}{3}}}{3((2n+1)^{\frac{2}{3}}(1+\delta) - K^{\frac{2}{3}})^3}M^4. \tag{6.73}$$

Note that (6.73) only describes the growth rate when both the hydrodynamic mode is stable (i.e., $K < (2n+1)(1+\delta)^{3/2}$) and instability is possible (i.e., $K > (2n+1)\delta^{3/2}$). The second order correction in this case is always negative; however, it is only the sign of the leading order term that determines whether the expansion describes the most unstable mode.

The weak magnetic field expansions (6.71) and (6.73) clearly both break down when $K-(2n+1)(1+\delta)^{\frac{3}{2}} = O(M)$. To address this, we suppose that $S^2 = \beta M$ and $K-(2n+1)(1+\delta)^{\frac{3}{2}} = \alpha M$, where α is real and of order unity. Under these assumptions (6.61) yields

$$S^2 = \frac{\alpha \pm |\alpha|\sqrt{1 + 6K^4/\alpha^2}}{2(1+\delta)K}M, \tag{6.74}$$

valid for $A - (2n+1)(1+\delta)^{\frac{3}{2}} = O(M)$. We take the positive mode to describe the growth rate in both the hydrodynamically stable and unstable regimes; we will discuss this further below.

It remains to determine how the two roots of (6.74) link to (6.72) and (6.73). To do this, we consider the large $|\alpha|$ limit of (6.74) and compare with the small $|\alpha|$ limits of (6.72) and (6.73). Specifically, the positive root of (6.74) implies

$$\frac{S^2}{M} \to \frac{\alpha + |\alpha|(1 + 3K^4/\alpha^2 + \cdots)}{2(1+\delta)K} \sim \begin{cases} \alpha/K(1+\delta) & \alpha > 0, \\ 3K^3/2\alpha(1+\delta) & \alpha < 0, \end{cases} \text{ as } |\alpha| \to \infty, \tag{6.75}$$

while the negative root of (6.74) implies

$$\frac{S^2}{M} \to \frac{\alpha - |\alpha|(1 + 3K^4/\alpha^2 + \cdots)}{2(1+\delta)K} \sim \begin{cases} -3K^3/2\alpha(1+\delta) & \alpha > 0, \\ \alpha/K(1+\delta) & \alpha < 0, \end{cases} \text{ as } |\alpha| \to \infty, \tag{6.76}$$

Similarly, the hydrodynamic root (6.72) yields

$$\frac{S^2}{M} \sim \alpha/K(1+\delta) \text{ as } \alpha \to 0, \tag{6.77}$$

while the magnetic root (6.73) yields

$$\frac{S^2}{M} \sim \frac{(K^{\frac{2}{3}} - (2n+1)^{\frac{2}{3}}\delta)K^2}{2\alpha M/3(2n+1)^{\frac{1}{3}}(1+\delta)^{\frac{1}{2}}}M = \frac{3K^3}{2\alpha(1+\delta)} \text{ as } \alpha \to 0, \tag{6.78}$$

where we have substituted $K - (2n+1)(1+\delta)^{\frac{3}{2}} = \alpha M$ to evaluate (6.71) and (6.73). Thus, (6.75) shows that the +ve root in (6.74) becomes the hydrodynamic root (6.72) as $\alpha \to +\infty$ and the magnetic root (6.73) as $\alpha \to -\infty$ (or, the hydrodynamic root (6.72) becomes the magnetic root (6.73) as K decreases through $(2n+1)(1+\delta)^{\frac{3}{2}}$). Likewise, (6.76) shows that the $-$ve root in
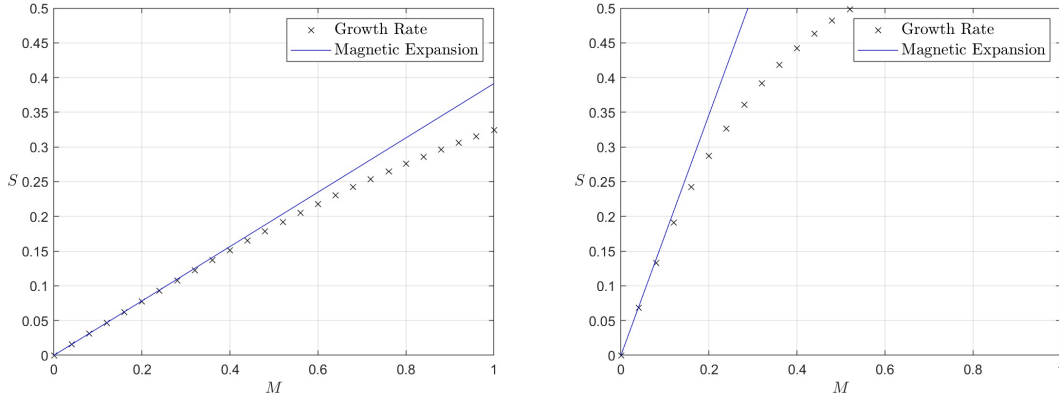
Figure 6.14: The exact growth rate and magnetic expansion (6.73) against M, with $n = 0$ and $\delta = 0.25$ for $K = 0.5$ (left) and $K = 1$ (right).

(6.74) becomes the magnetic root (6.73) as $\alpha \to +\infty$ and the hydrodynamic root (6.72) as $\alpha \to -\infty$ (or, the hydrodynamic root (6.72) becomes the magnetic root (6.73) as K increases through $(2n + 1)(1 + \delta)^{\frac{3}{2}}$). Hence, the roots exchange identity as K passes through $(2n + 1)(1 + \delta)^{\frac{3}{2}}$. The hydrodynamic mode is thus not a single entity that can be tracked through parameter space, and neither is the magnetic mode.

The validity of the weak magnetic field expansions (6.70), (6.72), (6.73) and (6.74) are confirmed by figures 6.14, 6.15 and 6.16, in which the expansions are plotted (where appropriate) with $n = 0$ and $\delta = 0.25$ alongside the exact growth rate against M for various values of K. The hydrodynamic and the purely magnetic expansions (6.72) and (6.73) remain valid for larger M as K moves away from the singular point $K = (2n + 1)(1 + \delta)^{3/2}$ (≈ 1.3875 for $\delta = 0.25$ and $n = 0$). However, the hydrodynamic expansion (6.72) decays in accuracy once the magnetic correction changes sign at $K \approx 9.8$; given sufficiently large K, (6.70) becomes a more accurate approximation for the growth rate. Interestingly, the expansion (6.70), valid for $KM = O(1)$, also describes the hydrodynamic mode at $K = O(1)$ after the hydrodynamic expansion (6.72) becomes invalid at sufficiently large M. Figure 6.16 shows the validity of the singular expansion (6.74), where the positive root has been taken to describe the growth rate of the system. As expected, the hydrodynamic and magnetic expansions become invalid when K is sufficiently close to $(2n + 1)(1 + \delta)^{\frac{3}{2}}$.

6.6 Conclusions

In this chapter we have investigated the linear stability (on an equatorial β-plane where $f = \beta y$) of a uniform shear flow $U(y) = \Lambda_0 y$ as well as a jet profile $U(y) = \Lambda_0 y - \delta\beta y^2/2$ in the presence of stable stratification and uniform vertical magnetic field. In section 6.2 we formulated this problem for both cases (setting $\delta = 0$ yields the uniform shear flow) and derived a parabolic cylinder equation for the perturbed cross-stream velocity by introducing the nondimensional coordinate $Y = (y - y_0)/L$, where y_0 is the central latitude and L is the nondimensional latitudinal
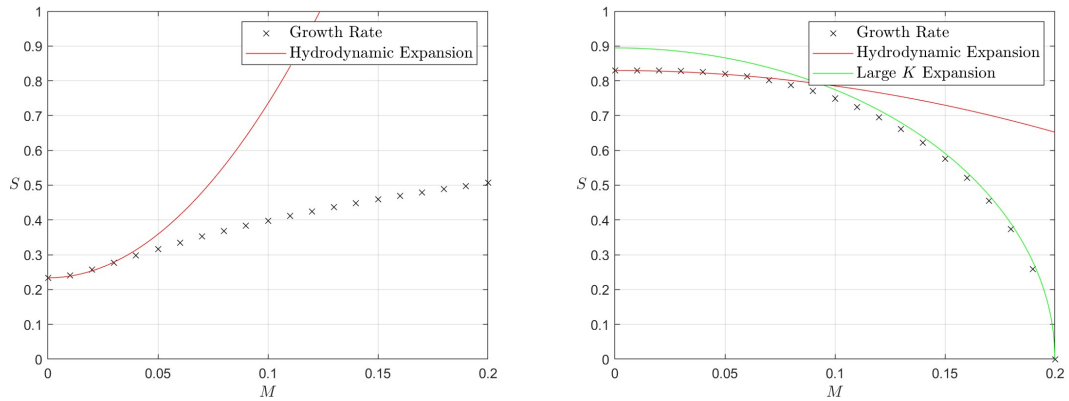
Figure 6.15: The exact growth rate and magnetic expansion (6.72) against M, with $n = 0$ and $\delta = 0.25$ for $K = 1.5$ (left) and $K = 10$ (right). The large K (with $M \ll 1$) expansion (6.70) has also been included in the rightmost plot.
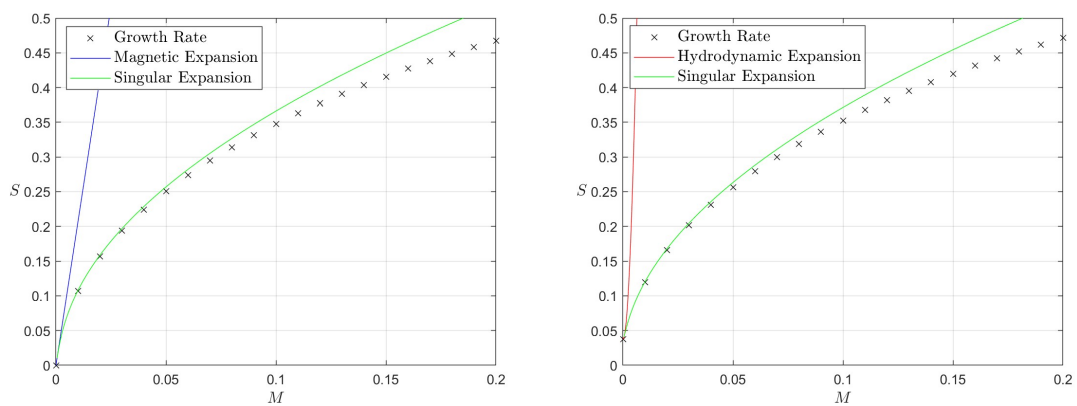
Figure 6.16: The exact growth rate and singular expansion (6.74) against M, with $n = 0$ and $\delta = 0.25$ for $K = 1.39$ (left), $K = 1.4$ (right). The hydrodynamic and magnetic expansions have also been included to illustrate their invalidity when K is sufficiently close to $(2n + 1)(1 + \delta)^{\frac{3}{2}}$.

lengthscale. The parabolic cylinder equation can be solved analytically, yielding an eigenvalue relation with corresponding eigenfunctions $v \propto H_n(Y) \exp(-Y^2/2)$. where the eigenvalue n is a non-negative integer.

In section 6.3 we first discussed the system in the absence of shear, which reduced the system to one stable mode, described entirely by one parameter which depended upon the vertical wavenumber and magnetic field strength. The equatorial waves in the system are categorised as inertial, magneto-inertial or Alfvén waves, depending upon the magnetic field strength. We then continued our analysis by assuming non-zero shear, focusing on the unstable mode present within the system. Indeed, upon the introduction of the nondimensional vertical wavenumber K and magnetic field strength M, we derived an eigenvalue relation that described two modes in (M, K)-space, one of which was always stable while the other was always unstable. We contoured the growth rate in (M, K)-space, finding that weak magnetic field generates instability in the hydrodynamically stable regime ($K < 2n + 1$) and increases the growth rate of the hydrodynamically unstable modes. We also found that the unstable mode attains the maximum growth rate as the vertical wavenumber or magnetic field strength becomes large (provided $KM^3 \gg 1$).

Upon considering the dynamical balances in Section 6.4, we find that the purely magnetic instability is generated owing to the along-stream Lorentz force breaking the hydrodynamic balance and counteracting the stabilising roles of the Coriolis force and stratification. These instabilities can be considered to be equatorial analogues of the instability we classified as a "stratified" MRI in Section 3.4 of Chapter 3. We also find that the growth rate of the hydrodynamic inertial instability is increased by the role of vertical magnetic field as the second order correction from the along-stream Lorentz force always dominates over the stabilising corrections of the Coriolis parameter, cross-stream Lorentz force and pressure gradient. Lastly, we find that instability is present in the strong field limit rather than Alfvénic wavelike behaviour (as one might expect) since the mode traverses away from the equator. This is so that the increasing Lorentz force can be balanced by the increasing Coriolis force generated by being at a higher latitude; this process yields magnetostrophic balance in the horizontal directions at leading order. Recall that we take a balance between the Coriolis, advection, and Lorentz force, to be magnetostrophic. Interestingly, we find an analogous instability on a rapidly rotating f-plane in the limit of large magnetic field provided $f \sim k^2 v_A^2 / \Lambda_0$; the dynamical balance of the rapidly rotating instability on the f-plane has already been discussed in Section 3.4 of Chapter 3.

In Section 6.5 we considered the jet profile $U(y) = \Lambda_0 y - \delta\beta y^2/2$, so that anti-cyclonic shear is present only if $0 < y < \Lambda_0/\delta\beta$; this ensures unstable modes can occur only within this domain and therefore forbids the strong magnetic instability of Section 6.3. Indeed, the maximum value of M for which instability can occur is given by equation (6.64). We contoured the maximum growth rate, where, in contrast to Section 6.3, weak magnetic field either increased the growth rate of modes if K satisfied (6.72) and decreased the growth rate otherwise. Once again, we also found the existence of purely magnetic instabilities in the hydrodynamically stable regime. We

also determined the vertical scale chosen by the modes, given by equation (6.68), in the limit of weak magnetic field.

For the uniform shear flow we find a clear application of the results of Section 6.3 in the flanks of the strong equatorial jets present on Hot Jupiters. The results of Section 6.5 are applicable to eastward traveling jets (close to the equator) in the northern hemisphere on Jupiter or Hot Jupiters. Note that westward jets are required for the uniform shear flow so that anti-cyclonic shear is present within the system. Interestingly, numerous hydrodynamic simulations and observations suggest that Hot Jupiters exhibit eastward travelling jets; however, in recent years, there has also been evidence for westward travelling jets. For example, Hindle *et al.* (2019) suggest that the jets may be reversed given a sufficiently large magnetic field strength. In terms of our nondimensional parameters, table 2.1 implies that M ranges from $O(10^{-6})$ to $O(1)$ on Hot Jupiters and ranges from $M = O(1)$ to $M = O(10^4)$ in Jupiter's upper atmosphere, so that all of the results of this chapter may be applicable.

If we first consider the applicability of the results to Hot Jupiters, figure 6.2 suggests vanishing vertical scales are always preferred in the absence of diffusion (regardless of magnetic field strength). Interestingly, the strong field instabilities, which occur at large latitudes (since instability is no longer possible at the equator), link to the large latitudinal lengthscales of the equatorial jets that are inferred from observations and simulated in global numerical models (e.g., Rogers & Komacek, 2014; Rogers, 2017). Thus, since instabilities (and therefore the development of turbulence) are not able to occur close to the equator, it is possible for stable jets to form.

We now consider Section 6.5, where strong magnetic field instabilities can no longer occur since anti-cyclonic shear is only present close to the equator. Owing to the values of M that can be taken on Hot Jupiters, figure 6.10 suggests that instabilities can only occur with $K > 1$. This implies vertical lengthscales of $O(10^6\text{m})$ or smaller. Since M ranges from $O(10^{-6})$ to $O(1)$ on Hot Jupiters, the results regarding the limit of weak magnetic field may be important. Indeed, magnetic field may increase or decrease the growth rate in comparison to the hydrodynamic regime; figure 6.11 also suggests that increasing M increases the central latitude and lengthscale of the unstable mode. By assuming a jet width of $60°$ on Hot Jupiters, and equating this with the width $0 < y < 2\Lambda_0/\delta\beta$ (i.e., the two roots of $U(y) = 0$), the parameter values in table 2.1 suggest that δ may range from $O(10^{-1})$ to $O(10^2)$ on Hot Jupiters. Thus, the results shown with $\delta = 0.25$ are physically viable. For large values of δ, figure 6.12 suggests that instability will only be able to occur for small values of M; indeed, the stability bound (6.63) implies instability can only occur for $M = M_{\max} < 2/3\sqrt{3}\delta^2$ (for $n = 0$), yielding $M_{\max} = O(10^{-5})$ for $\delta = O(10^2)$.

The results of Section 6.5 are also applicable to Jupiter's upper atmosphere, provided we consider the jets adjacent to Jupiters prominent central equatorial jet (since we are modelling an off-centered equatorial jet), which are illustrated in figure 1.2. Estimating the value of δ as before, table 2.1 suggest that δ may range from $O(10^{-2})$ to $O(10^{-3})$, yielding $M_{\max}$ from $O(10^3)$ to $O(10^5)$. Thus, for the large values of M possible in Jupiter's upper atmosphere (for which figure 6.10 with $\delta = 0.25$ implies stability), instability is still possible. However, owing to the large

values of M and small δ, if these instabilities occur, they will likely be confined to the "tip" of the unstable region illustrated in figure 6.10 (e.g., at $M = 5$, $K = 0.2$). Indeed, the stability bound (6.63) implies that the instabilities will occur at K from $O(10^{-3})$ to $O(10^{-1})$ (calculated numerically and depending on the value of M and δ). The instabilities would therefore be purely magnetic (i.e., they occur in the hydrodynamically stable regime $K < (2n + 1)(1 + \delta)^{3/2}$) and yield vertical lengthscales of order 10^6m or smaller.

In the following chapter we consider the role of kinematic viscosity ν, thermal diffusion κ and magnetic diffusivity η on the stability of the jet profile $U(y) = \Lambda_0 y - \delta\beta y^2/2$ on the equatorial β-plane in the presence of stable stratification and uniform vertical magnetic field.

Chapter 7

Diffusive scale selection on the equatorial β-plane

7.1 Introduction

In this chapter we extend equatorial β-plane linear analysis of Chapter 6 by incorporating the effects of uniform kinematic viscosity ν, thermal diffusion κ and magnetic diffusivity η. However, we restrict our attention to the jet profile $U(y) = \Lambda_0 y - \delta\beta y^2/2$, which is more physically appropriate than the unbounded shear flow $U(y) = \Lambda_0 y$. The jet profile, which is illustrated in figure 6.9, prevents the occurrence of the strong magnetic instabilities (which violated the assumptions of the equatorial β-plane approximation) since anti-cyclonic shear, which is required for instability to occur, is now restricted to a bounded latitudinal domain. Figure 6.9 shows that the flow profile can be used as a model of a non-symmetric equatorial jet so that there is clear application to the equatorial jets found in the upper atmospheres of Jupiter (Kaspi *et al.*, 2018; Read, 2024) and Hot Jupiters (Showman *et al.*, 2013; Heng & Showman, 2015). However, it is important to note that Jupiter's prominent central equatorial jet is symmetric about the equator, and thus it is more appropriate to model the immediately adjacent jets (so that they are sufficiently close to the equator).

Under this formulation we are able to derive a parabolic cylinder equation for the cross-stream velocity v from the second order differential equation (2.30). We again introduce the nondimensional variable $Y = (y - y_0)/L$, where y is the latitude, y_0 is the central latitude and L is the latitudinal lengthscale. Thus, in Section 7.2, we solve the parabolic cylinder equation analytically, and introduce our nondimensional parameters, many of which are used in Chapter 6.

Throughout this chapter we will consider a number of different constraints on the Prandtl numbers (e.g., $Pr \neq 1$ and $Pm = 1$) in both the hydrodynamic and magnetohydrodynamic regimes. To investigate each regime, we contour the maximum growth rate as a function of magnetic field and vertical wavenumber and, by selecting the vertical wavenumber K that maximises the growth rate S, contour both K and S as a function diffusive parameters.

We expect diffusion to be a key element of the linear instability scale selection problem. Indeed, in the ideal analysis of Section 6.5, we found that the most unstable mode has vanishing vertical scales. For sufficiently strong magnetic field these were stabilised; however, diffusion is likely to affect the scale selection of all unstable modes. We also note that many numerical models run with anomalously large diffusion, and thus it is very interesting to understand if they artificially suppress instabilities that might otherwise occur.

In Chapter 1 we have already discussed a number of diffusive hydrodynamic systems that are relevant to this chapter. Dunkerton (1981) and Griffiths (2003a) considered the linear stability of a zonal flow $U(y) = \Lambda_0 y$ on an equatorial β-plane with uniform vertical stratification and $Pr = \nu/\kappa = 1$ under the hydrostatic approximation. Dunkerton (1981) derived the marginally stable shear $\Lambda_0 = 2\sqrt{5}\nu^{1/5}(N\beta/4)^{2/5}$ and the vertical wavenumber at which it occurs. Griffiths (2003a) extended this analysis by deriving an asymptotic expansion for the vertical wavenumber that generates the maximum growth rate in terms of a diffusive parameter. Dunkerton (1982) also considered the regime $Pr \neq 1$, where several steady and oscillatory stability conditions were derived. We will review and extend upon this analysis in Section 7.2 for $Pr = 1$ and $Pr \neq 1$, again deriving stability bounds and vertical wavenumbers that generate the maximum growth rate (which are now also dependent on the jet width δ). We also contour the maximum growth rate as function of ν and κ, linking to the GSF instability (Goldreich & Schubert, 1967; Fricke, 1968), where strong thermal diffusion damps the stabilising effect of stratification, and allows instability to occur at smaller vertical wavenumbers.

In the magnetohydrodynamic regime, we consider the cases $Pr = Pm = 1$, $Pr \neq 1$ and $Pm = 1$, $Pr = 1$ and $Pm \neq 1$, $Pr = Pm \neq 1$ and $Pr \ll Pm \ll 1$. The case $Pr = Pm = 1$ can be described by a transformation from the ideal system of Chapter 6, allowing us to easily investigate the limit of weak magnetic field from previously derived asymptotic expansions. For more complex Prandtl number regimes we find multiple double diffusive instabilities, one of which links to the hydrodynamic GSF instability even while magnetic field still has a significant dynamical effect. In the case $Pr = Pm \neq 1$, we find that increasing the magnitude of κ and η does not stabilise magnetically modified inertial instabilities; instead, the magnitude of magnetic field strength required for the same dynamical effect increases, resulting in stabilisation at larger values of M. Finally, we consider $Pr \neq 1$ and $Pr \neq 1$, investigating the regimes $Pr \ll Pm \ll 1$ (such that $Pr = Pm^p$ for $p = 1.5$ and $p = 3$) and $Pr = 0.3$ with $Pm \ll 1$. The first Prandtl number regime is found in many astrophysical bodies, including the Solar tachocline and Jupiter's interior (and, perhaps, Hot Jupiters); the second is the Prandtl number regime in Jupiter's upper atmosphere (see table 2.1), which could also apply to the upper atmospheres of Hot Jupiters. In both cases, the most unstable modes are hydrodynamic, where increasing magnetic field strength decreases the growth rate of the instabilities; these are categorised as magnetically modified inertial instabilities. Purely magnetic instabilities also occur as well as magnetic instabilities that occur at small vertical wavenumbers that would otherwise be stable in the ideal system owing to thermal diffusion damping the stabilising role of the pressure gradient.

7.2 Formulation

We consider the flow profile

$$U(y) = \Lambda_0 y - \frac{\delta}{2}\beta y^2, \tag{7.1}$$

with shear $\Lambda_0 > 0$ and $\delta > 0$. The flow profile is a jet centered in the northern hemisphere at $y = \Lambda_0/\delta\beta$. The flow will be considered on an equatorial β-plane ($f = \beta y$) in the presence of uniform vertical magnetic field B_0. Given sufficiently large $|y|$, the flow profile (7.1) guarantees cyclonic shear and therefore stability.

With this formulation, the magnetohydrostatic governing equation (2.27) will have coefficients that depend on y; however, (2.27) may still be solved analytically in an analogous manner to equation (6.8) by transforming (2.27) into a parabolic cylinder equation. Hence, we introduce the nondimensional coordinate

$$Y = \frac{y - y_0}{L}, \tag{7.2}$$

where y_0 and L are the central latitude and lengthscale of the mode, which are both at our disposal. Specifically, we choose the following central latitude and lengthscale squared:

$$y_0 = \frac{\Lambda_0}{2\beta}\left(1 + \frac{k^2 v_A^2}{(s+\eta k^2)^2}\right)\bigg/\left(1 + \delta\left(1 + \frac{k^2 v_A^2}{(s+\eta k^2)^2}\right)\right), \tag{7.3}$$

and

$$L^2 = \frac{N}{k\beta}\left(\frac{(s+\eta k^2)(s+\nu k^2) + k^2 v_A^2}{(s+\kappa k^2)(s+\eta k^2)}\right)^{\frac{1}{2}}\bigg/\left(1 + \delta\left(1 + \frac{k^2 v_A^2}{(s+\eta k^2)^2}\right)\right)^{\frac{1}{2}}, \tag{7.4}$$

where the choice of L^2 ensures that we obtain the hydrodynamic lengthscale of Dunkerton (1981) in the absence of field. Note that all parameters have been previously defined; however, in particular, recall that k is the vertical wavenumber.

Using the nondimensional coordinate (7.2) the boundary conditions (2.28) become

$$v(Y) \to 0 \quad \text{when} \quad y \to \pm\infty. \tag{7.5}$$

By recasting (2.27) into the normal form of a parabolic cylinder equation, we obtain

$$\frac{N\beta}{k}\left(\frac{(s+\eta k^2)(s+\nu k^2) + k^2 v_A^2}{(s+\kappa k^2)(s+\eta k^2)}\right)^{\frac{1}{2}}\left(1 + \delta\left(1 + \frac{k^2 v_A^2}{(s+\eta k^2)^2}\right)\right)^{\frac{3}{2}}(v'' - Y^2 v) +$$
$$\frac{\Lambda_0^2}{4}\left(1 + \frac{k^2 v_A^2}{(s+\eta k^2)^2}\right)^2 - \left(s + \nu k^2 + \frac{k^2 v_A^2}{s+\eta k^2}\right)^2\left(1 + \delta\left(1 + \frac{k^2 v_A^2}{(s+\eta k^2)^2}\right)\right) v = 0. \tag{7.6}$$

With the boundary conditions (7.5), equation (7.6) has solutions proportional to $\exp(-Y^2/2)$ by Bender & Orszag (1978). To ensure that the solutions decay as $y \to \pm\infty$ we require that L^2 has a positive real part since $Y^2 \propto L^{-2}$; to ensure this, we must restrict the values that s can take, according to the definition of L^2 in (7.4). Although it is possible to consider both waves and instabilities, in this chapter, we will focus entirely on instabilities, where s has positive real part with either zero or non-zero imaginary part (the latter in complex conjugate pairs). Now, if s is real

and positive, then the interior of the square roots in (7.4) must be positive so that L^2 has positive real part (provided $\delta > 0$). However, if s has an imaginary part it becomes significantly more difficult to derive a condition. Thus, we consider the values of L^2 on a case by case basis. Hence, given L^2 has positive real part, the boundary conditions (7.5) are satisfied as $y \to \pm\infty$, and thus, by Bender & Orszag (1978), equation (7.6) admits well-known eigenfunctions. The eigenfunctions consist of Hermite polynomials $H_n(Y)$ multiplied by a Gaussian of the form $\exp(-Y^2/2)$, with corresponding discrete and non-negative eigenvalues n, which satisfy the following relation for the growth rate s:

$$
\frac{\Lambda_0^2}{4}\left(1 + \frac{k^2 v_A^2}{(s+\eta k^2)^2}\right)^2 - \left(s + \nu k^2 + \frac{k^2 v_A^2}{s+\eta k^2}\right)^2 \left(1 + \delta\left(1 + \frac{k^2 v_A^2}{(s+\eta k^2)^2}\right)\right) =
$$
$$
(2n+1)\frac{N\beta}{k}\left(\frac{(s+\eta k^2)(s+\nu k^2) + k^2 v_A^2}{(s+\kappa k^2)(s+\eta k^2)}\right)^{\frac{1}{2}} \left(1 + \delta\left(1 + \frac{k^2 v_A^2}{(s+\eta k^2)^2}\right)\right)^{\frac{3}{2}}. \quad (7.7)
$$

In the absence of magnetic field and diffusion, equation (6.8) reduces to (1.2) of Dunkerton (1981) with $\delta = 0$, where the system is stable provided $|k| > |k_c| = 4N\beta(2n+1)/\Lambda_0^2$. Dunkerton (1981) and Griffiths (2003a) consider (7.7) in the absence of magnetic field with $\delta = 0$ and $Pr = 1$. We note that the eigenfunctions take an even or odd form, which depends upon the eigenvalue n. For example, the $n = 0$ (even) mode has $\hat{v} = H_0(Y)\exp\left(-Y^2/2\right) = \exp\left(-Y^2/2\right)$, while the $n = 1$ (odd) mode has $\hat{v} = H_1(Y)\exp\left(-Y^2/2\right) = Y\exp\left(-Y^2/2\right)$. The even and odd relationship continues for all following n.

We once again use the nondimensional parameters found in Chapter 6, allowing us to easily compare results to the ideal regime. Hence, we reintroduce the parameters (6.15):

$$
K = \frac{\Lambda_0^2 k}{4N\beta}, \quad \text{and} \quad M = \frac{8N\beta v_A}{\Lambda_0^3}, \quad (7.8)
$$

with nondimensional growth rate $S = 2s/\Lambda_0$, where $2/\Lambda_0$ is the timescale. Reiterating Chapter 6, K is the nondimensional vertical wavenumber and M is a measure of the field strength. Note that the parameter K can never be zero as we require $k \neq 0$ for the system to be magnetohydrostatic and $\Lambda_0 \neq 0$ by assumption.

To nondimensionalise the diffusive coefficients we require a quantity with some dimension of length. This leaves us with a few non-obvious choices, such as the Rossby parameter β, the vertical wavenumber or the Alfvén wave speed. Naturally, we do not want to nondimensionalise using the vertical wavenumber as this would lead to complicated interpretations of parameters. If we choose the Alfvén wave speed we obtain the following nondimensional parameters: $\{\tilde{\nu}, \tilde{\kappa}, \tilde{\eta}\} = \Lambda_0\{\nu, \kappa, \eta\}/2v_A^2$. However, in this case, there is no smooth comparison to the hydrodynamic system. As a consequence of this choice of nondimensionalisation, instabilities can still occur as $K \to \infty$ even in the presence of vertical diffusion. This is reasonable mathematically as our system is magnetohydrostatic and stably stratified; however, physically, modes do not exist on infinitesimally small vertical lengthscales.

Hence, we choose the following nondimensional diffusive parameters:

$$\nu_0 = \frac{32N^2\beta^2\nu}{\Lambda_0^5}, \quad \kappa_0 = \frac{32N^2\beta^2\kappa}{\Lambda_0^5} \quad \text{and} \quad \eta_0 = \frac{32N^2\beta^2\eta}{\Lambda_0^5}. \tag{7.9}$$

This choice allows us to maximise the growth rate over the vertical wavenumber K only since we may argue that all other parameters are fixed as they can be inferred from observations. For example, in the case of Hot Jupiters, we can estimate the angular velocity, buoyancy frequency, and field strength together with the speed and lengthscale of equatorial jets, yielding a single numerical value for M, ν_0, κ_0 and η_0. Thus, for a given class of astrophysical objects, say Hot Jupiters, where $\beta, N, \Lambda_0, v_A, \nu, \kappa$ and η are fixed (estimated from observations) we find the maximum growth rate alongside its corresponding vertical wavenumber.

Recasting (7.7) in terms of the nondimensional parameters (7.8) and (7.9), we obtain

$$\left(1 + \frac{M^2K^2}{(S+\eta_0K^2)^2}\right)^2 - \left(S + \nu_0K^2 + \frac{M^2K^2}{S+\eta_0K^2}\right)^2 \left(1 + \delta\left(1 + \frac{M^2K^2}{(S+\eta_0K^2)^2}\right)\right) =$$
$$\frac{(2n+1)}{K}\left(\frac{S+\nu_0K^2}{S+\kappa_0K^2} + \frac{M^2K^2}{(S+\kappa_0K^2)(S+\eta_0K^2)}\right)^{\frac{1}{2}} \left(1 + \delta\left(1 + \frac{M^2K^2}{(S+\eta_0K^2)^2}\right)\right)^{\frac{3}{2}}. \tag{7.10}$$

We also have the nondimensional central latitude and lengthscale, given by

$$\frac{2\beta}{\Lambda_0}y_0 = \hat{y}_0 = \left(1 + \frac{M^2K^2}{(S+\eta_0K^2)^2}\right) \Big/ \left(1 + \delta\left(1 + \frac{M^2K^2}{(S+\eta_0K^2)^2}\right)\right), \tag{7.11}$$

and

$$\hat{L} = \frac{1}{\sqrt{K}}\left(\frac{S+\nu_0K^2}{S+\kappa_0K^2} + \frac{M^2K^2}{(S+\eta_0K^2)(S+\kappa_0K^2)}\right)^{\frac{1}{4}} \Big/ \left(1 + \delta\left(1 + \frac{M^2K^2}{(S+\eta_0K^2)^2}\right)\right)^{\frac{1}{4}}. \tag{7.12}$$

7.3 Hydrodynamic Regime

First we consider the hydrodynamic system and investigate under what conditions the system is unstable, determine the vertical wavenumber at which the growth rate is maximum and consider the effects of kinematic viscosity ν_0 and thermal conductivity κ_0. Setting $M = 0$ in equation (7.10) gives the following equation for the growth rate:

$$K(1 - (S + \nu_0K^2)^2(1+\delta)) = (2n+1)\left(\frac{S+\nu_0K^2}{S+\kappa_0K^2}\right)^{\frac{1}{2}}(1+\delta)^{\frac{3}{2}}. \tag{7.13}$$

Equation (7.13) with $\delta = 0$ and $Pr = 1$ is found in Dunkerton (1981), Griffiths (2003a) and Griffiths (2003b). Griffiths (2003a) derived conditions for instability and the vertical wavenumber that generates the maximum growth rate by introducing the nondimensional variable $\epsilon = (2\nu N^2\beta^2/\Lambda^5)^{1/3} = (\nu_0/16)^{1/3}$. The system is unstable provided $\epsilon < 5^{-5/6} \approx 0.26$, while the most unstable mode occurs at $k \approx N\beta/\Lambda^2\epsilon = (N\beta/2\nu\Lambda)^{1/3}$. Note that Griffiths (2003a,b) also considered the nonlinear regime. Dunkerton (1982) considered the case $Pr \neq 1$, deriving

marginal stability criteria for both oscillatory and steady instabilities. We will derive this stability criteria with $\delta \neq 0$ and form a basis for our magnetohydrodynamic results. In general, equation (7.13) does not allow us to obtain an analytical expression for the growth rate and must be solved numerically. However, in the case where the Prandtl number is unity we may obtain an analytical expression for the growth rate.

7.3.1 $Pr = 1$

Assuming the Prandtl number is unity, equation (7.13) gives the following expression for the growth rate:

$$S = \left(\frac{K - (2n+1)(1+\delta)^{\frac{3}{2}}}{K(1+\delta)} \right)^{\frac{1}{2}} - \nu_0 K^2. \tag{7.14}$$

Thus, by taking $Pr = 1$, we can see there has been a significant simplification of equation (7.13); indeed, the other modes of (7.13) are only present given distinct magnitudes of ν_0 and κ_0. Equation (7.14) may be obtained via a transformation from the inviscid system, transforming the inviscid growth rate from S to $S+\nu_0 K^2$. Equation (7.14) implies that $K > (2n+1)(1+\delta)^{3/2}$ is a necessary condition for instability. Equation (7.14) implies that modes with large vertical wavenumbers ($K \gg 1$) are stabilised since the diffusive term becomes large. This is in contrast to the ideal case where the most unstable mode is found at infinite vertical wavenumber and where stability occurs only if $K < (2n+1)(1+\delta)^{3/2}$. Indeed, we find that unstable modes with $\nu_0 \neq 0$ become stable for $K < (2n+1)(1+\delta)^{3/2}$ owing to the diffusive term dampening the instabilities (which is always the case since $\partial_{\nu_0} S < 0$ for all K, n and δ). Thus, with $\nu_0 \neq 0$, instability (and therefore the maximum growth rate) must occur in a finite and bounded region of K. This can be seen by setting $S = 0$ in (7.14), where we find that the system is unstable if $K - (2n+1)(1+\delta)^{3/2} - \nu_0^2 K^5 (1+\delta) > 0$. This is a quintic in K, where, for example, if $n = 0, \delta = 0.25$ and $\nu_0 = 0.05$, then the system is unstable if $3.7665 > K > 1.4153$. However, in the absence of diffusion the system is unstable if $K > (2n+1)(1+\delta)^{3/2} (= 1.3975$ with $n = 0$ and $\delta = 0.25$). Thus, the introduction of diffusion restricts instability to a finite region of K.

It is of interest to find the vertical wavenumber, $K_{\max}$ say, for which the maximum growth rate occurs at fixed δ and ν_0. Thus, we differentiate equation (7.14) with respect to K and set the derivative to zero, giving

$$\frac{\partial S}{\partial K} = \frac{1}{2K_{\max}^2} (2n+1)(1+\delta)^{\frac{1}{2}} \left(\frac{K_{\max} - (2n+1)(1+\delta)^{\frac{3}{2}}}{K_{\max}(1+\delta)} \right)^{-\frac{1}{2}} - 2\nu_0 K_{\max} = 0 \tag{7.15}$$

Hence, after squaring (7.15), it follows that $K_{\max}$ satisfies the following cubic polynomial in $K_{\max}^2$:

$$16\nu_0^2 K_{\max}^6 - 16\nu_0^2 (2n+1)(1+\delta)^{3/2} K_{\max}^4 - (2n+1)^2 (1+\delta)^2 = 0. \tag{7.16}$$

The polynomial (7.16) does not allow us to derive a corresponding $S_{\max} = S(K_{\max})$ for each $K_{\max}$ since the expression cannot be solved analytically for $K_{\max}$. However, provided $\nu_0 \ll 1$

(which is typically the case in planetary atmospheres) we may approximate $K^2_{\max}$, by expanding in terms of ν_0:

$$K^2_{\max} = \frac{(2n+1)^{2/3}(1+\delta)^{2/3}}{16^{1/3}}\nu_0^{-2/3} + \frac{(2n+1)(1+\delta)^{3/2}}{3} + O(\nu_0^{2/3}). \qquad (7.17)$$

On taking $n = \delta = 0$, equation (7.17) is analogous to the power series in ϵ of the vertical wavenumber as found in Griffiths (2003b). Thus, we extend the analysis of the uniform shear layer to that of an equatorial jet, which amounts to a transformation of $\nu_0 \to (1+\delta)^{-1}\nu_0$, or equivalently, $\epsilon \to (1+\delta)^{-1/3}\epsilon$ as in Griffiths (2003b).

Hence, provided $\nu_0 \ll 1$, the dimensional vertical wavenumber that generates the maximum growth rate satisfies

$$k^2_{\max} \approx \left(\frac{(2n+1)(1+\delta)N\beta}{2\nu\Lambda_0}\right)^{2/3} + \frac{16(2n+1)(1+\delta)^{3/2}N^2\beta^2}{3\Lambda_0^2} + \cdots, \qquad (7.18)$$

which implies we may expect $k_{\max} = O(10^{-2}\mathrm{m}^{-1})$ for a typical Hot Jupiter. Griffiths (2003b) notes that the leading order term, with $n = \delta = 0$, of equation (7.18) allows us to conclude that stratification and the β effect encourage smaller vertical scales, whereas diffusion and cross-equatorial shear encourage larger vertical scales. It is also noted that $k_{\max}$ is relatively insensitive to the magnitude of diffusion since $K_{\max} \propto \nu^{-1/3}$. Equation (7.18) also implies that as the jet width δ increases, the vertical lengthscale decreases and vice versa. We also find that $K_{\max} \propto (1+\delta)^{1/3}$, and thus is relatively insensitive to jet width.

Next, by substituting (7.17) into (7.14), we can also derive the corresponding maximum growth rate $S_{\max} = S(K_{\max})$ when $\nu_0 \ll 1$, in terms of δ and ν_0 only:

$$S_{\max} \approx \frac{1}{(1+\delta)^{1/2}} - 4^{-2/3}(2n+1)^{2/3}\left(4^{-5/6} + (1+\delta)^{2/3}\right)\nu_0^{1/3}. \qquad (7.19)$$

Thus, in the small ν_0 limit, the maximum growth rate is $O(\nu_0^{1/3})$ less than that of the ideal system. Increasing δ increases the magnitude of the diffusive correction, and therefore decreases the growth rate.

Next, we derive the marginal ν_m at arbitrary K and Λ, for which no instability may occur if surpassed. We set $S = 0$ in equation (7.14):

$$\nu_m^2 = \frac{K - (2n+1)(1+\delta)^{\frac{3}{2}}}{K^5(1+\delta)}. \qquad (7.20)$$

In a similar manner, we can derive the critical diffusion (in terms of n and δ only) for which no instability may occur if $\nu_0 > \nu_c$ for any K at fixed δ. To do this, we simultaneously consider equation (7.15) alongside (7.20), which allows us to find the critical value of K, K_c say, where the final unstable mode occurs, given by

$$K_c = \frac{5}{4}(2n+1)(1+\delta)^{3/2}. \qquad (7.21)$$

Then, by substituting (7.21) into (7.20) for K, we obtain the absolute critical diffusion in terms of δ and n only:

$$\nu_c = \frac{4^2}{(2n+1)^2\sqrt{5^5(1+\delta)^7}}. \tag{7.22}$$

We find for $\delta = n = 0$, that $\nu_c = 0.2862$, which is analogous to the results of Dunkerton (1981) and Griffiths (2003a). With $\delta \neq 0$ and $n = 0$, we find that the critical diffusion decreases for increasing jet width; for example, with $\delta = 0.25$, the critical diffusion is $\nu_c = 0.1311$ — approximately half in comparison to the analogous case with $\delta = 0$. We also note that since the critical diffusion remains $O(1)$ for any physically reasonable value of δ, then, by equations (7.17) and (7.21) the vertical wavenumber K also remains $O(1)$.

Now, we determine an estimate for the bounded region in K where instability is possible for arbitrary ν_0 and Λ. To do this, we consider the small ν and large K limits of equation (7.20). The first trivially implies that $K \approx (2n+1)(1+\delta)^{3/2}$. We obtain second order terms by writing K as a power series in ν we obtain the following lower bound in K:

$$K = (2n+1)(1+\delta)^{3/2} + (2n+1)^5(1+\delta)^{17/2}\nu_0^2 + O(\nu_0^4). \tag{7.23}$$

Hence, as we would expect, weak diffusion increases the lower bound in K, where the correction becomes larger for larger jet profiles. To find the upper bound in K, we consider the large K limit of equation (7.20) which yields $K \approx \nu_0^{-1/2}(1+\delta)^{-1/4}$. Then, once again, to find second order terms, we write K as a power series in ν_0, yielding the following upper bound in K:

$$K = \frac{1}{\nu_0^{1/2}(1+\delta)^{1/4}} - \frac{(2n+1)(1+\delta)^{3/2}}{4} + O(\nu_0^{1/2}). \tag{7.24}$$

Thus, combining the lower bound (7.23) and upper bound (7.24), we obtain the following approximate interval of unstable vertical wavenumbers K:

$$(2n+1)(1+\delta)^{3/2} + (2n+1)^5(1+\delta)^{17/2}\nu_0^2 < K < \frac{1}{\nu_0^{1/2}(1+\delta)^{1/4}} - \frac{(2n+1)(1+\delta)^{3/2}}{4}. \tag{7.25}$$

Hence, with increasing ν_0 and jet width δ, the interval of unstable vertical wavenumbers decreases. Note that equation (7.25) is an approximation, since it is derived in the small ν_0 limit; indeed, equating the leading order terms of (7.25) yields a critical ν_c which is $5^{5/2}/16 \approx 3.49$ times larger than (7.22). However, the parameter ν_0 is typically small in planetary atmospheres, and thus (7.25) will give an accurate interval of unstable vertical wavenumbers.

Figure 7.1 shows contours of the growth rate S in (K, ν_0)-space for $\delta = 0.25$, obtained by solving (7.14). This illustrates the bounded region in K for which instability may occur, provided $\nu_0 < \nu_c$, alongside the maximum growth rate and where it occurs. We can see that both of the bounds on K as well as the estimate for $K_{\max}$ are reasonably accurate for all ν_0 for which instability can occur. Clearly, increasing ν_0 decreases the growth rate monotonically; the value of K that generates the maximum growth rate also decreases with increasing ν_0 and reduces the size of the interval of unstable vertical wavenumbers. Note that the critical diffusion given by (7.22) is clearly accurate in this case ($\nu_c = 0.1311$ for $\delta = 0.25$ and $n = 0$).
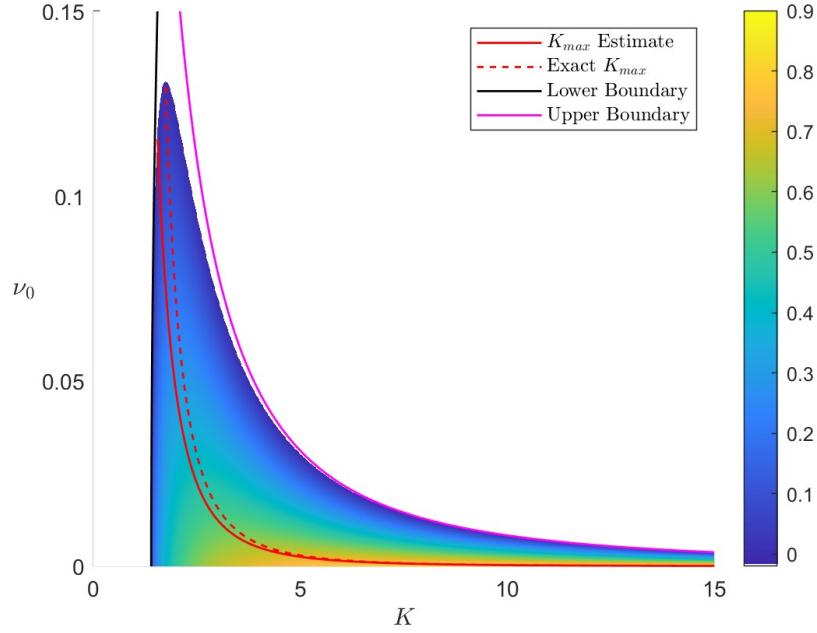
Figure 7.1: $Pr = 1$: The growth rate S contoured in (K, ν_0)-space. The black stability boundary is the approximate lower bound on K for which instability occurs, given by equation (7.23). The magenta stability boundary is the approximate upper bound for which instability can occur, given by equation (7.24). The solid red line is the approximate value of $K_{\max}$ given by (7.17), while the dashed line is the exact value of K that generates the maximum growth rate for each ν_0.

7.3.2 $Pr \neq 1$

It is possible to write equation (7.13) as a quintic in S, however it is desirable to mirror the results of Dunkerton (1982) which considers (7.13) directly. We recast equation (7.13) here for convenience:

$$K(1 - (S + \nu_0 K^2)^2 (1 + \delta)) = (2n + 1) \left(\frac{S + \nu_0 K^2}{S + \kappa_0 K^2} \right)^{\frac{1}{2}} (1 + \delta)^{\frac{3}{2}}. \qquad (7.26)$$

As noted by Dunkerton (1982), it is possible for oscillatory instabilities to occur in the system, the stability criteria of which is rather cumbersome to derive.

Thus, we will consider steady stability criteria only; however, incidentally, since the steady and oscillatory modes share a boundary, one of the steady stability conditions bound the unstable oscillatory modes. To determine the boundary, we follow Dunkerton (1982), and set the imaginary part of $S = S_r + iS_i$ to zero with $S_r \neq 0$ (i.e., an unstable steady mode transitions into an unstable complex conjugate pair on the boundary) so that we can write $S = S_r$ and recast (7.26):

$$\frac{2n + 1}{K} \left(\frac{S_r + \nu_0 K^2}{S_r + \kappa_0 K^2} \right)^{\frac{1}{2}} (1 + \delta)^{\frac{1}{2}} + (S_r + \nu_0 K^2)^2 = \frac{1}{1 + \delta}. \qquad (7.27)$$

We then differentiate (7.27) with respect to K and S_r, set the derivatives to zero, and obtain

$$(2n+1)\frac{S_r(\nu_0-\kappa_0)}{(S_r+\kappa_0K^2)^2}\left(\frac{S_r+\nu_0K^2}{S_r+\kappa_0K^2}\right)^{-1/2}(1+\delta)^{1/2}$$
$$=\frac{2n+1}{K^2}\left(\frac{S_r+\nu_0K^2}{S_r+\kappa_0K^2}\right)^{1/2}(1+\delta)^{1/2}-4\nu_0K(S_r+\nu_0K^2)=0,\quad(7.28)$$

and

$$(2n+1)\frac{K^2(\kappa_0-\nu_0)}{(S_r+\kappa_0K^2)^2}\left(\frac{S_r+\nu_0K^2}{S_r+\kappa_0K^2}\right)^{-1/2}(1+\delta)^{1/2}+4K(S_r+\nu_0K^2)=0,\qquad(7.29)$$

respectively. Noticeably, the right hand term of (7.28) and (7.29) are equal after multiplying (7.29) by $-\nu_0$. Thus, multiplying (7.29) by $-\nu_0$ and then subtracting from (7.28), yields

$$\frac{S_r(\nu_0-\kappa_0)}{(S_r+\kappa_0K^2)^2}-\frac{1}{K^2}\left(\frac{S_r+\nu_0K^2}{S_r+\kappa_0K^2}\right)+\frac{K^2(\nu_0-\kappa_0)}{(S_r+\kappa_0K^2)^2}=0,\qquad(7.30)$$

where we have also multiplied by $(S_r+\nu_0K^2)/(2n+1)(1+\delta)^{1/2}(S_r+\kappa_0K^2)$. Then, after some manipulation, we find that the growth rate S_r on the bound satisfies

$$S_r=K^2(\nu_0-2\kappa_0),\qquad(7.31)$$

which is analogous to the result of Dunkerton (1982), valid for $Pr>2$. Thus, since $S_r\neq0$, equation (7.31) implies that $\nu_0>2\kappa_0$ on the bound. We expect this since oscillatory instabilities do not occur given sufficiently large κ_0. Thus, the growth rate on the bound increases with increasing K and ν_0, while decreases for increasing κ_0 (subject to the constraint $Pr>2$).

Next, by substituting (7.31) into (7.29), we find that the vertical wavenumber K on the bound satisfies

$$K=\frac{5}{2\sqrt{2}}(2n+1)(1+\delta)^{\frac{3}{2}}.\qquad(7.32)$$

This is again analogous to the results of Dunkerton (1982); however, owing to the variable jet width prescribed by the parameter δ, here we find that a larger vertical wavenumbers (smaller vertical lengthscales) are required to stabilise the oscillatory instabilities. Finally, by substituting (7.31) and (7.32) into (7.27) we obtain the following sufficient condition for steady stability:

$$\kappa_0<\nu_0-\frac{4}{(2n+1)^2\sqrt{5^5(1+\delta)^7}},\qquad(7.33)$$

valid for $\nu_0<2\kappa_0$ and $\nu_0<4/5^{5/2}(2n+1)^2(1+\delta)^{7/2}$. Note that this is also a necessary condition for oscillatory instability, since (7.33) describes the boundary between the steady and oscillatory modes. Together these imply the bound (7.33) is valid if $4/5^{5/2}(2n+1)^2(1+\delta)^{7/2}<\nu_0<8/5^{5/2}(2n+1)^2(1+\delta)^{7/2}$.

It is also of interest to derive stability bounds for steady modes that do not coincide with unstable oscillatory modes. To do this, we differentiate (7.26) with respect to K and then set $S=\partial S/\partial K=0$, yielding the following expression for the vertical wavenumber on the steady stability bound:

$$K^4=\frac{1}{5\nu_0^2(1+\delta)}.\qquad(7.34)$$

Equation (7.34) implies that the vertical wavenumber required to stabilise the system increases with decreasing ν_0 and δ. We can substitute (7.34) into (7.26) with $S = 0$ in order to obtain the following necessary condition for steady stability:

$$\kappa_0 < \frac{5^{5/2}}{4^2}(2n + 1)^2(1 + \delta)^{7/2}\nu_0^2. \tag{7.35}$$

The stability bound (7.35) cannot be maximised with respect to ν_0. However, this implies that for any given ν_0, instability is possible for sufficiently large κ_0. Likewise, at any κ_0 sufficiently large, increasing the magnitude of ν_0 will eventually stabilise the steady modes. Note that instability may still occur given sufficiently small ν_0 while (7.35) is satisfied since the condition is on a single mode only (i.e., the steady mode that becomes oscillatory is still unstable). However, this can be resolved by considering (7.33) and (7.35) to determine which of the bounds is appropriate.

Thus, by setting (7.33) equal to (7.35) we obtain a quadratic in ν_0 with a single (double root) solution, implying that (7.35) is necessary and sufficient condition for steady stability if

$$\nu_0^2 > \frac{4^3}{5^5(2n + 1)^4(1 + \delta)^7}. \tag{7.36}$$

If (7.36) is not satisfied, then (7.33) is the appropriate necessary and sufficient condition for steady stability.

Thus, provided (7.36) is satisfied, the condition (7.35) requires no additional assumption and the stability bound is independent of the vertical wavenumber. Thus, given some astrophysical body, the parameters ν_0, κ_0 and δ may be estimated so that (7.35) may imply that the system is stable.

Owing to (7.35) being a condition on a single steady mode only, equation (7.36) also implies it is possible for instability to occur regardless of the value of κ_0 if ν_0 is sufficiently small. Thus, equation (7.36) also implies that instability occurs for any κ_0 if

$$\nu_0^2 < \frac{4^3}{5^5(2n + 1)^4(1 + \delta)^7}. \tag{7.37}$$

Interestingly, taking $n = 0$ and $\delta = 0.25$ implies instability will occur for any κ_0 if $\nu_0 < 0.065536$. Thus, given anti-cyclonic shear, we expect instability in the upper atmospheres of Jupiter and Hot Jupiters since table 2.1 suggests ν_0 is at most $O(10^{-4})$. Note the solar tachocline exhibits cyclonic latitudinal shear only at the equator.

We now solve (7.26) numerically for the maximum growth rate (and its corresponding frequency) by selecting the vertical wavenumber K, K_{max} say, which generates the maximum growth rate $S_{\mathrm{max}} = S(K_{\mathrm{max}})$ at each ν_0 and κ_0, with $\delta = 0.25$. We do this by determining the growth rate from (7.26) at each K, ν_0 and κ_0 (with $\delta = 0.25$), and then select the K that generates the maximum growth rate for each ν_0 and κ_0. Thus, in figure 7.2 we contour the maximum growth rate S (and its corresponding frequency) in (ν_0, κ_0)-space for $\delta = 0.25$. In figure 7.3 we contour the K_{max} that generates the maximum growth rate of figure 7.2 in (ν_0, κ_0)-space for $\delta = 0.25$. Note that the white regions of figure 7.2 indicate stability, so that the conditions (7.33) and (7.35)
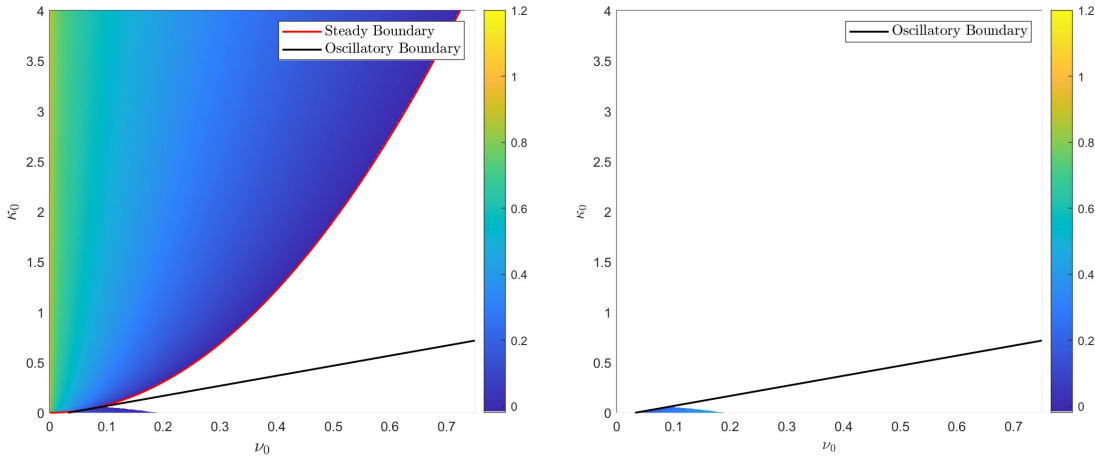
Figure 7.2: The maximum growth rate S (left) and corresponding frequency (right) in (ν_0, κ_0)-space with $\delta = 0.25$. The red stability boundary is given by equation (7.35). The black oscillatory stability boundary is given by equation (7.33).

on κ_0 indeed hold depending on (7.36), which corresponds to the region between the red and black bounds.

Figure 7.2 shows that increasing ν_0 always decreases the maximum growth rate. The maximum growth rates occur in the limit $Pr \ll 1$, and thus, since this is typically the case in stellar and planetary atmospheres, if instabilities occur, we may expect them to be steady. Interestingly, for $\nu_0 \approx 0.1$ to $\nu_0 \approx 0.2$, increasing κ_0 from zero stabilises the system and then generates instability at larger κ_0. This is owing to the oscillatory instabilities that can occur only for sufficiently weak thermal diffusivity where buoyancy effects are still felt. Note that sufficiently large κ_0 guarantees instability at any value of ν_0, and increases the maximum growth rate to that of the inviscid hydrodynamic regime $S = (1 + \delta)^{-1}$. Stability is also guaranteed at any value of κ_0 given sufficiently large ν_0.

Figure 7.3 shows that increasing ν_0 or κ_0 decreases the value of $K_{\max}$. Modes with $Pr \ll 1$ have the largest vertical wavenumbers, and correspond to the modes with the largest growth rate, as shown in figure 7.2. The large κ_0 limit also shows that instability may occur within the stable regime of the inviscid system. That is, instability may now occur for $K < K_{\text{cutoff}} = (2n + 1)(1 + \delta)^{3/2}$. For example, taking $\delta = 0.25$, $n = 0$, $\nu_0 = 1.5$ and $\kappa_0 = 4$ yields $K_{\max} \approx 1 < K_{\text{cutoff}} = 1.40$. Thus, instability can occur at smaller values of K which are stable in the ideal regime ($K < K_{\text{cutoff}}$). This is because the pressure gradient (whose strength increases with decreasing K) is damped by an increasing rate of thermal diffusion. We can compare these instabilities to the Goldreich–Schubert–Fricke (GSF) instability (Goldreich & Schubert, 1967; Fricke, 1968), where thermal diffusion counteracts the stabilising effect of the pressure gradient and allows instability to occur at smaller K (which would otherwise by stable in the absence of diffusion). We also found an analogous instability in both the hydrodynamic and magnetohydrodynamic analysis of Chapter 4.
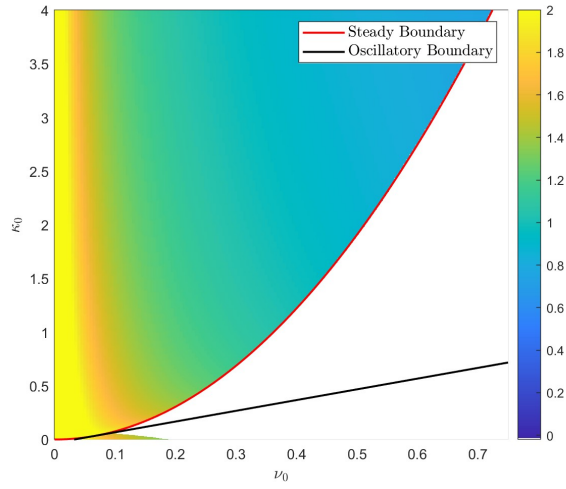
Figure 7.3: The value of $K_{\max}$ that generates the maximum growth rate $S_{\max}$ (as seen in figure 7.2) in (ν_0, κ_0)-space with $\delta = 0.25$. The red stability boundary is given by equation (7.35). The black oscillatory stability boundary is given by equation (7.33).

7.4 Magnetohydrodynamic Regime

We now investigate the magnetohydrodynamic regime, where we consider the cases $Pr = Pm = 1$, $Pr \neq 1$ and $Pm = 1$, $Pr = 1$ and $Pm \neq 0$ as well as $Pr \neq 0$ and $Pm \neq 0$ with $Pr \ll Pm \ll 1$.

Note that in contrast to Chapter 4, where numerous stability criteria could be derived *a priori*, there is little to be done here owing to the complexity of the equation for the growth rate (7.10). However, with some restriction on the Prandtl numbers (e.g., $Pr = 1$, $Pm \neq 1$), it is possible to make analytical progress; in particular, by considering the asymptotic limits of various parameters.

7.4.1 $Pr = 1$ & $Pm = 1$

We first consider the simplest possible choice of Prandtl numbers, where both are unity. In this case, we write κ_0 and η_0 as ν_0 which allows us to recast equation (7.10) as

$$
K \left(1 + \frac{M^2 K^2}{(S + \nu_0 K^2)^2} \right)^{\frac{3}{2}} \left(1 - (S + \nu_0 K^2)^2 \left(1 + \delta \left(1 + \frac{M^2 K^2}{(S + \nu_0 K^2)^2} \right) \right) \right) =
$$
$$
(2n + 1) \left(1 + \delta \left(1 + \frac{M^2 K^2}{(S + \nu_0 K^2)^2} \right) \right)^{\frac{3}{2}}. \quad (7.38)
$$

Equation (7.38) reduces to (6.61) in the absence of diffusion. However, we can also obtain equation (7.38) from (6.61) via the transformation of the growth rate $S_I = S + \nu_0 K^2$, where S_I is the growth rate of the ideal system. That is, for each point in (M, K)-space we may obtain the growth rate when $\nu_0 \neq 0$ by subtracting $\nu_0 K^2$ from the growth rate in the absence of diffusion. This transformation allows us to use numerous results from the inviscid case such as the weak field expansions (6.71), (6.73) and (6.74). The transformation also implies that weakly unstable modes within the ideal instability domain, given by (6.61), will be stabilised as ν_0 increases. Thus, the
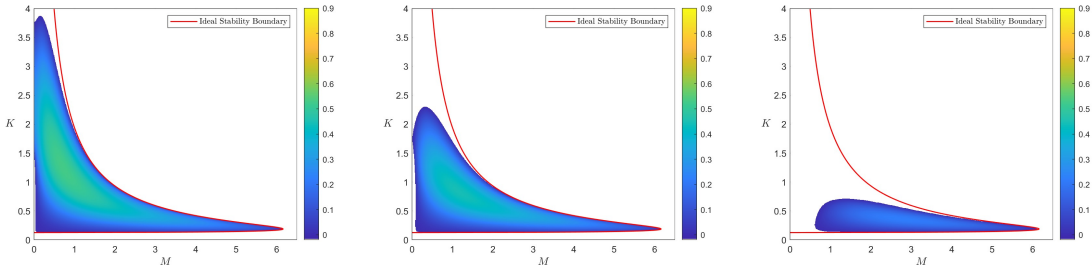
Figure 7.4: $Pr = Pm = 1$: The most unstable mode with $\delta = 0.25$ in (M, K)-space for $\nu_0 = 0.05$ (left), $\nu_0 = 0.131$ (centre) and $\nu_0 = 1$ (right). The system is stabilised at $\nu_0 = 4.358$. The red line represents the ideal stability boundary $M^2 = (K - \delta^{3/2})/\delta K^3$.

sufficient and necessary condition for stability in the ideal case (i.e., equation (6.63)) becomes a sufficient condition only.

We proceed by solving equation (7.38) numerically, leading to figure 7.4 for the growth rate in (M, K)-space with $\delta = 0.25$ for $\nu_0 = 0.05, 0.131$ and 1. To do this, we square (7.38), solve the resulting 10th degree polynomial in S, and verify the roots using (7.38). Note that all unstable modes are steady instabilities. Figure 7.4 shows that even weak diffusion stabilises the modes with large vertical wavenumber ($K \gg 1$) as well as those in the weak field limit of the hydrodynamically stable regime. This results in the maximum growth rate being found with K and M both being of order unity. We can thus conclude that weak magnetic field increases the growth rate of the hydrodynamically unstable regime as well as generating instability in the hydrodynamically stable regime, provided it is sufficiently large. Increasing the magnitude of diffusion reduces the growth rate of all modes, and reduces the maximum K for which instability can occur; in contrast, the interval of magnetic field at which instability can occur is somewhat insensitive to increasing ν_0. All hydrodynamic instabilities are stabilised once $\nu_0 > 0.131$ for $\delta = 0.25$ (to 3 significant figures). Thus, all instabilities are purely magnetic for $\nu_0 > 0.131$. Increasing the magnitude of diffusion further continues to reduce the instability domain until all modes are stabilised at $\nu_0 = 4.358$.

Weak Field Expansions

Figure 7.4 shows that weak magnetic field induces instability within certain parameter regimes, including the entire unstable domain for $\nu_0 > 0.131$ since this is hydrodynamically stable. Following the ideal analysis, we consider the weak field regime in order to categorise the behaviour of the system. To investigate the small M regime, we can transform the ideal weak field expansions (6.71), (6.73) and (6.74) by writing S as $S + \nu_0 K^2$ or, alternatively, consider the small M regime of equation (7.38). Indeed, in the weak field limit ($M \ll 1$) with $K = O(1)$ and $S = O(1)$, the

transformation yields the hydrodynamic mode with a magnetic correction:

$$S = \left(\frac{K - (2n+1)(1+\delta)^{\frac{3}{2}}}{K(1+\delta)} \right)^{\frac{1}{2}} - \nu_0 K^2 +$$

$$\frac{K^{\frac{5}{2}}((2n+1)(1+\delta)^{\frac{3}{2}}(3+2\delta) - 2\delta K)}{4(1+\delta)^{\frac{1}{2}}(K - (2n+1)(1+\delta)^{\frac{3}{2}})^{\frac{3}{2}}} M^2 + O(M^4). \quad (7.39)$$

Hence, if $\nu_0 K^2 = O(1)$, hydrodynamic instability is governed by the leading order term of (7.39). The magnetic correction of (7.39) acts in the same way as in the ideal case, increasing the growth rate when $(2n+1)(1+\delta)^{3/2}(3+2\delta) > 2\delta K$ and reducing the growth rate otherwise. With $\nu_0 K^2 = O(1)$, we may stabilise the hydrodynamic mode; however, in certain cases where $(K - (2n+1)(1+\delta)^{3/2})(K(1+\delta))^{-1} \sim \nu_0^2 K^4$, instability may be possible given some small M (that is sufficiently large), as seen in right panel of figure 7.4, owing to the positive contribution from the second order term (provided $(2n+1)(1+\delta)^{3/2}(3+2\delta) > 2\delta K$).

In the weak field limit ($M \ll 1$) with $K = O(1)$ we also have an unstable Alfvénic mode, provided ν_0 is sufficiently small, given by

$$S = \left(\frac{K^{\frac{2}{3}} - (2n+1)^{\frac{2}{3}}\delta}{(2n+1)^{\frac{2}{3}}(1+\delta) - K^{\frac{2}{3}}} \right)^{\frac{1}{2}} KM - \nu_0 K^2, \quad (7.40)$$

which describes the most unstable mode provided $K < (2n+1)(1+\delta)^{\frac{3}{2}}$ (provided it is not stabilised by diffusion). These modes can be seen in the bottom left of the panels in figure 7.4 with $\nu_0 = 0.05$ and $\nu_0 = 0.131$.

The weak field expansions (7.39) and (7.40) may both break down when $K - (2n+1)(1+\delta)^{\frac{3}{2}} = O(M)$. To address this, we suppose that $S^2 = \alpha M$ and $K - (2n+1)(1+\delta)^{\frac{3}{2}} = \alpha M$, where α is real and of order unity and substitute into (7.38) to derive the expression for the growth rate:

$$S = \left[\frac{\alpha \pm |\alpha|(1 + 6K^4)^{\frac{1}{2}}}{2(1+\delta)K} \right]^{\frac{1}{2}} M^{\frac{1}{2}} - \nu_0 K^2, \quad (7.41)$$

valid for $K - (2n+1)(1+\delta)^{\frac{3}{2}} = O(M)$. We require the positive sign to describe the unstable mode.

To ensure the validity of the weak field expansions (7.39), (7.40) and (7.41), in figures 7.5, 7.6 and 7.7, we plot the expansions (where appropriate) with $n = 0$ and $\delta = 0.25$ alongside the exact growth rate against M for various values of K and ν_0. The hydrodynamic and the purely magnetic expansions (7.39) and (7.40) remain valid for larger M as K moves away from the singular point $K = (2n+1)(1+\delta)^{3/2}$ (≈ 1.3875 for $\delta = 0.25$ and $n = 0$). The expansions (7.39) and (7.40) both decay in accuracy as ν_0 increases since $\nu_0 K^2$ is becoming large. However, they still remain accurate given $\nu_0 K^2$ sufficiently small; for example, if K is decreased (so that $\nu_0 K^2 = O(1)$ or smaller) in the final plot of figure 7.6 then (7.40) would once again describe the growth rate. Figure 7.7 shows the validity of the singular expansion (6.74), in which the positive root has been taken to describe the growth rate of the system. As expected, the hydrodynamic and magnetic expansions are invalid when K is sufficiently close to $(2n+1)(1+\delta)^{\frac{3}{2}}$.
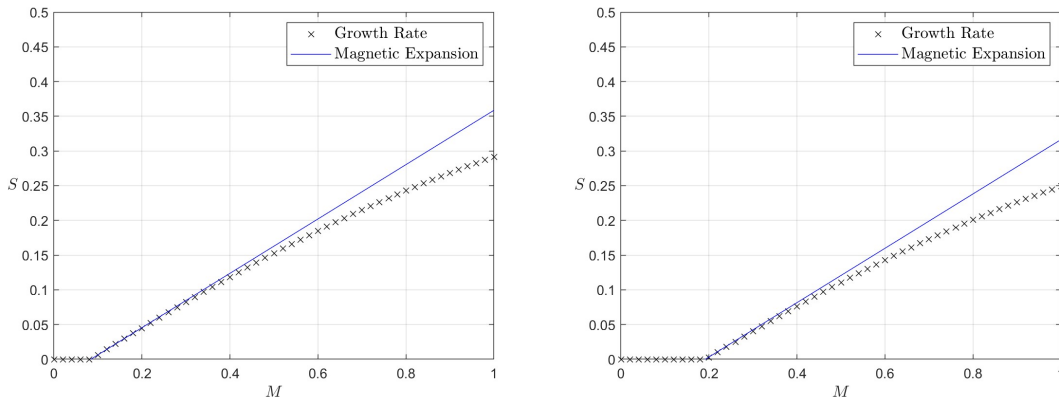
Figure 7.5: The exact growth rate and magnetic expansion (7.40) against M with $n = 0$, $\delta = 0.25$ and $K = 0.5$ for $\nu_0 = 0.131$ (left) and $\nu_0 = 0.30$ (right).
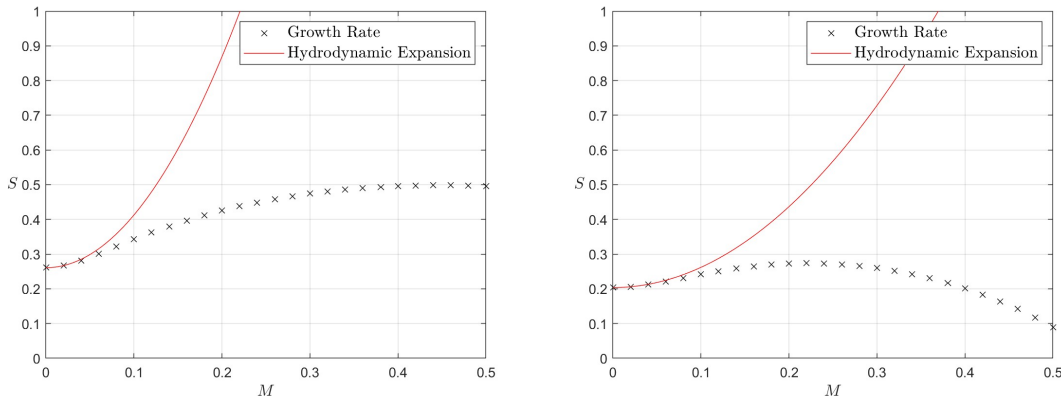
Figure 7.6: The exact growth rate and magnetic expansion (7.39) against M for $n = 0$, $\delta = 0.25$, $\nu_0 = 0.05$ with $K = 1.8$ (left) and $K = 3.0$ (right).
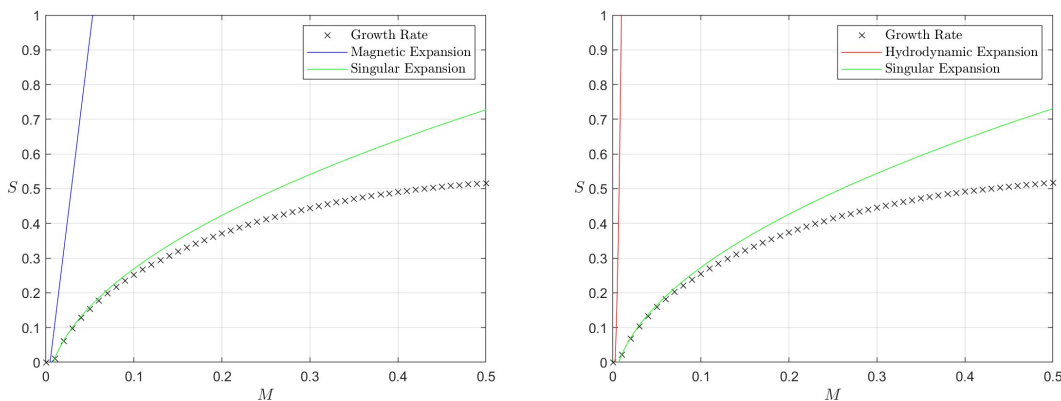
Figure 7.7: The exact growth rate and singular expansion (7.41) against M with $n = 0$, $\delta = 0.25$ and $\nu_0 = 0.05$ for $K = 1.39$ (left) and $K = 1.4$ (right). The hydrodynamic and magnetic expansions have also been included to show their invalidity as we approach $K = (2n+1)(1+\delta)^{\frac{3}{2}}$, indicated by their inability to accurately describe the growth rate at any M.

7.4.2 $Pr \neq 1$ & $Pm = 1$

In this section we consider the case $Pr \neq 1$ and $Pm = 1$, which allows us to make useful analogies to the hydrodynamic case described by (7.26) where $Pr \neq 1$.

Writing η_0 as ν_0 in (7.10) yields the following equation for the growth rate S:

$$\left(1 + \frac{M^2 K^2}{(S + \nu_0 K^2)^2}\right)^{\frac{3}{2}} \left(1 - (S + \nu_0 K^2)^2 \left(1 + \delta \left(1 + \frac{M^2 K^2}{(S + \nu_0 K^2)^2}\right)\right)\right) =$$
$$\frac{(2n+1)}{K} \left(\frac{S + \nu_0 K^2}{S + \kappa_0 K^2}\right)^{\frac{1}{2}} \left(1 + \delta \left(1 + \frac{M^2 K^2}{(S + \nu_0 K^2)^2}\right)\right)^{\frac{3}{2}}. \quad (7.42)$$

It is difficult to make analytical progress from (7.42) in general; however, using numerical results as motivation, it is possible to make progress in various limiting cases.

We first solve (7.42) numerically in order to contour the maximum growth rate in (M, K)-space in figure 7.8 with $\delta = 0.25$ and $\nu_0 = \eta_0 = 0.05$ with $\kappa_0 = 0.01$ (left panel) and $\kappa_0 = 10$ (right panel). Figure 7.9 also illustrates the corresponding complex part of the maximum growth rates (as shown in figure 7.8) in (M, K)-space. Note that the case with $\nu_0 = 0.05$ and $\kappa_0 = 10$ has no oscillatory instabilities, while for the case with $\nu_0 = 0.05$ and $\kappa_0 = 0.01$, oscillatory instabilities occur at dispersed points in parameter space, at both small and large M.

Figure 7.8 shows that increasing κ_0 increases the size of the instability domain (in M and K) and the magnitude of the maximum growth rate. Note that the maximum growth rate occurs at $M = O(1)$ for $Pr = 5$ and at $M = 0$ for $Pr = 5 \times 10^{-3}$. We can see that with increasing κ_0, instability can now occur at larger and smaller vertical wavenumbers. Interestingly, the smaller wavenumbers are stable in the ideal system (for $M = 0$ and $M > 0$), which is implied by the condition for stability (6.63). We have already discussed the unstable modes for $M = 0$ in Section 7.3, linking them to the GSF instability. However, as magnetic field already allows instabilities to occur for $K < (2n+1)(1+\delta)^{3/2}$, even relatively weak thermal diffusion allows instability to occur for smaller K in comparison to the hydrodynamic system (even with significantly stronger thermal diffusion). Thus, the instabilities which occur at small K for large κ_0 are purely magnetic and enabled by thermal diffusion. Notably, instability may also occur at larger M since the combination of the cross-stream pressure gradient and cross-stream Lorentz force (which are both stabilising) is no longer sufficient to stabilise the system.

The Limit of Strong Thermal Diffusion

Motivated by the interesting consequences of strong thermal diffusion in figure 7.8, we investigate the large κ_0 limit of equation (7.42). Indeed, we must consider the asymptotic behaviour of the growth rate S and vertical wavenumber K since they also vary with κ_0, as seen in figure 7.8. First, we address when the vertical wavenumber and growth rate are order unity. Thus, with $S = O(1), K = O(1)$ and $\kappa_0 \gg 1$, equation (7.42) reduces to

$$S = \left(\frac{1 - \delta M^2 K^2}{1 + \delta}\right)^{\frac{1}{2}} - \nu_0 K^2, \quad (7.43)$$
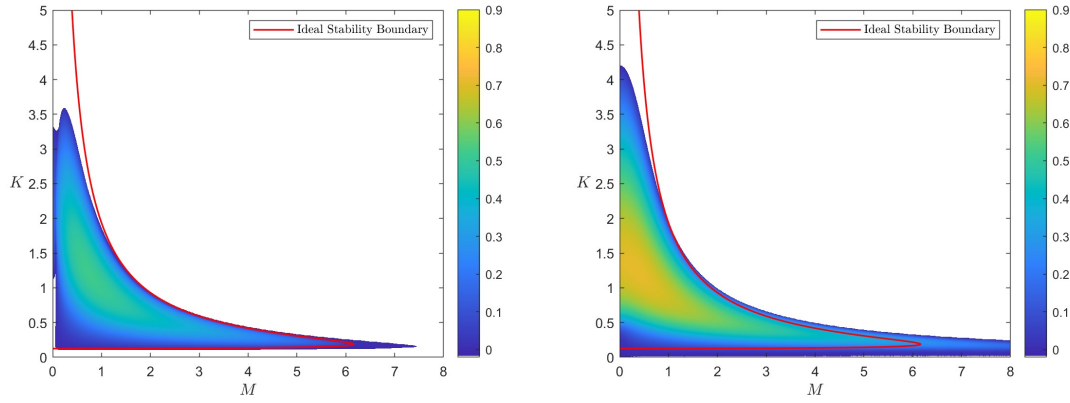
Figure 7.8: $Pr \neq 1$, $Pm = 1$: The maximum growth rate in (M, K)-space for $\delta = 0.25$ and $\nu_0 = 0.05$ with $\kappa_0 = 0.01$ ($Pr = 5$, left panel) and $\kappa_0 = 10$ ($Pr = 5 \times 10^{-3}$, right panel). The maximum growth rates are 0.512 and 0.708, respectively. The solid red line represents the ideal stability boundary (6.63).
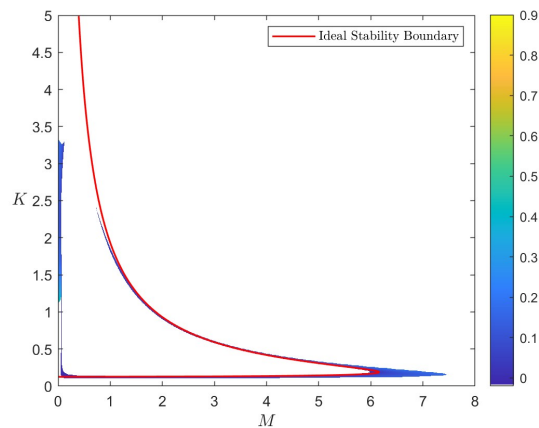
Figure 7.9: $Pr \neq 1$, $Pm = 1$: The corresponding frequency of the maximum growth rate (illustrated in figure 7.8) in (M, K)-space for $\delta = 0.25$, $\nu_0 = 0.05$ and $\kappa_0 = 0.01$. The case with $\nu_0 = 0.05$ and $\kappa_0 = 10$ (right panel of figure 7.8) has no oscillatory instabilities. The solid red line represents the ideal stability boundary (6.63).
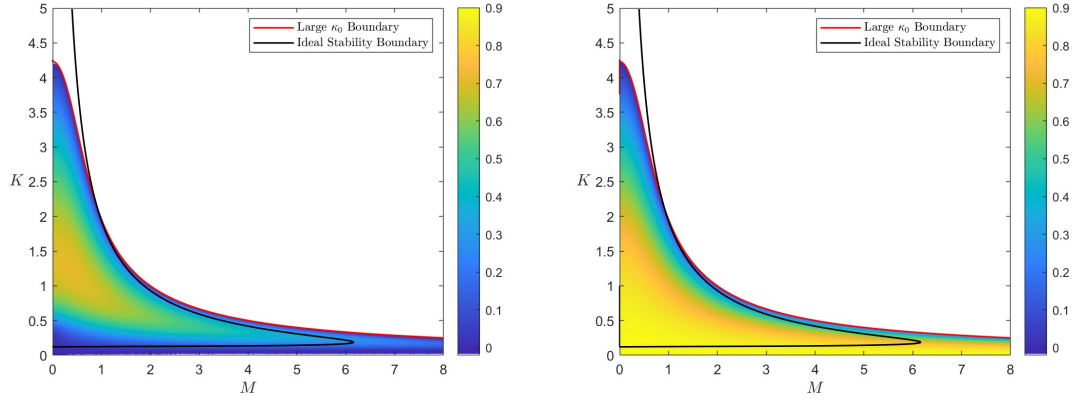
Figure 7.10: $Pr \neq 1$, $Pm = 1$: The maximum growth rate for $\delta = 0.25$ in (M, K)-space with $\kappa_0 = 10$ and $\nu_0 = \eta_0 = 0.05$ as numerically calculated from (7.10) (left) and (7.43) (right). Equation (7.44) gives the red line where $S = 0$ is predicted to be zero. The solid black line is the ideal stability bound (6.63).

which implies stability when

$$\nu_0^2 > \frac{1 - \delta M^2 K^2}{K^4(1 + \delta)}. \tag{7.44}$$

Equation (7.44) is a cubic in K^2 which allows us to calculate the maximum value of K for which instability can occur, given by

$$K^2 = \frac{-\delta M^2 + \sqrt{\delta^2 M^4 + 8\nu_0^2(1 + \delta)}}{4\nu_0^2(1 + \delta)}. \tag{7.45}$$

To illustrate the accuracy of the expansion (7.43) we contour the estimated growth rate alongside the exact growth rate in (M, K)-space in figure 7.10 for $\delta = 0.25$, $\nu_0 = \eta_0 = 0.05$ and $\kappa_0 = 10$. The large κ_0 stability boundary (7.44) is accurate even for $\kappa = O(1)$ and smaller; however, as κ_0 decreases, the bound becomes a sufficient condition for stability only. The contours suggest that (7.43) is accurate for $K > 1.5 = O(1)$ and some smaller K provided M is sufficiently large.

The approximation for the growth rate (7.43) increases in accuracy with increasing κ_0; however, as figure 7.10 suggests, (7.43) can not address the small K regime. To do so, we consider the asymptotic behaviour of the growth rate S and vertical wavenumber K in this regime by supposing $S \sim \kappa_0^{-\beta}$ and $K \sim \kappa_0^{-\gamma}$ for some $\beta, \gamma > 0$ and of order unity with $\kappa_0 \gg 1$. We find via dominant balance that $\beta = 1$ and $\gamma = -1/2$, so that equation (7.42) reduces to

$$S \approx \frac{K^4}{(2n + 1)^2 \delta^3} \kappa_0. \tag{7.46}$$

Equation (7.46) describes the small K regime when κ_0 is large (i.e., the bottom of the left panel in figure 7.10), predicting the growth rate scales with κ_0^{-1} (since $K \sim \kappa_0^{-1/2}$).

The Growth Rate in (ν_0, κ_0)-space

In this subsection we suppose that the magnetic field strength M is prescribed (from observations) which is a reasonable assumption when considering astrophysical bodies such as those given in table 2.1. Indeed, for each ν_0 and κ_0, there is a vertical wavenumber, $K_{\max}$ say, that generates the maximum growth rate (e.g., in the left panel of figure 7.8 where $\nu_0 = 0.05$ and $\kappa_0 = 0.01$, the growth rate is maximum at $M = 4.0$ when $K = K_{\max}$). Therefore, for a given M, we will be contouring the maximum growth rate, its frequency (if relevant), and $K_{\max}$ in (ν_0, κ_0)-space with $\delta = 0.25$. To do this, we numerically determine the growth rate for each ν_0, κ_0 and K for the given M and δ from equation (7.42); we then select the vertical wavenumber, $K_{\max}$ say, that maximises the growth rate at each ν_0 and κ_0. We will repeat this procedure and analysis in following subsections for different Prandtl number constraints (e.g., $Pr = 1$ and $Pm \neq 1$).

Figure 7.11 shows the maximum growth rate, its frequency, and $K_{\max}$ in (ν_0, κ_0)-space for $\delta = 0.25$ with $M = 0.40$ (left panels) and $M = 4.0$ (right panels). In both cases, we can see that increasing the magnitude of ν_0 (and η_0 since $Pm = 1$) decreases the growth rate, while increasing the magnitude of κ_0 increases the growth rate. Oscillatory instabilities occur with $Pr > 1$, for sufficiently large ν_0.

Comparing with the hydrodynamic case, illustrated in figures 7.2 and 7.3, we can see that for $M \neq 0$, the range of ν_0 and κ_0 for which instability can occur is much larger; indeed, the ν_0 (and η_0) required to stabilise the system is much larger for any given κ_0 (e.g., at $\kappa_0 = 1$ the hydrodynamic system requires $\nu_0 \approx 0.3$ for stability, whereas, even for $M = 0.40$, $\nu_0 \approx 0.8$ is required). We also see that the instabilities occur at vertical wavenumbers that would otherwise be stable in the ideal regime (i.e., instability occurs at $K < 0.1$ for either value of M). Indeed, the ideal bound for stability $M^2 < (K - \delta^{3/2})/\delta K^3$ implies that instability occurs for $0.1251 < K < 4.9363$ when $M = 0.40$ and for $0.1348 < K < 0.4188$ when $M = 4.0$. Thus, the instabilities are enabled by large κ_0 since it reduces the stabilising role of the pressure gradient, and therefore allows instability to occur at smaller vertical wavenumbers.

We now compare the system for the two different values of M in figure 7.11 ($M = 0.40$ and $M = 4.0$). First, for $M = 4.0$, we see a much larger instability domain; however, the maximum growth rate is significantly larger for $M = 0.40$. We might expect this, since increasing M while remaining at $K_{\max}$ in figure 7.8 implies that there will be both stronger Lorentz forces (due to increasing M) and pressure gradients (owing to decreasing K). This is in agreement with the value of $K_{\max}$ when $M = 4.0$, which is much smaller in comparison to the $M = 0.40$ case. Notably, we also see a much larger domain for which oscillatory instability can occur for $M = 4.0$.

7.4.3 $Pr = 1$ & $Pm \neq 1$

In this section we will consider the system with $Pr = 1$ and $Pm \neq 1$. In certain parameter regimes the results of this section will be applicable to Jupiter's upper atmosphere, where we expect large magnitudes of magnetic diffusivity. Indeed, estimating the magnitude of the diffusive
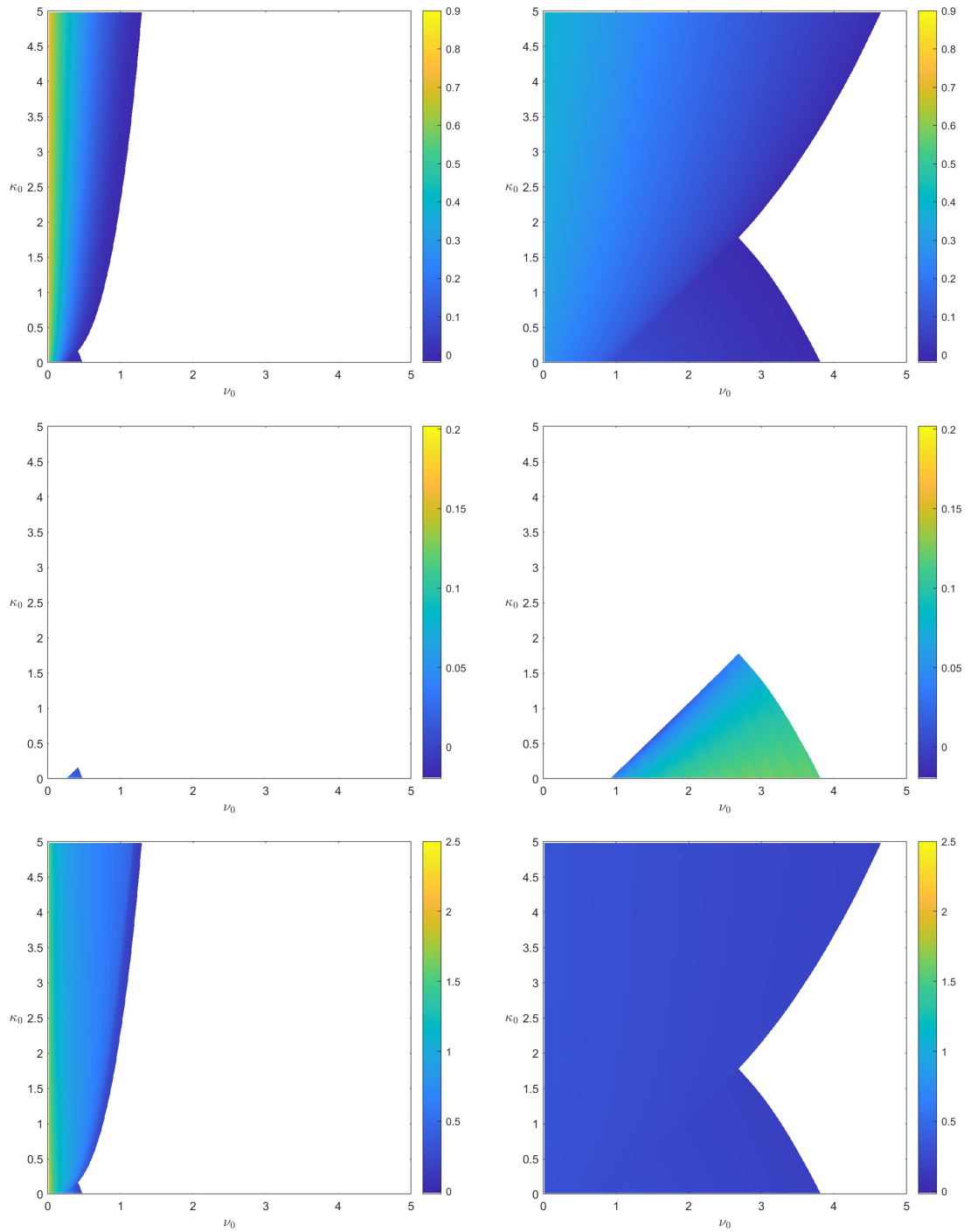
Figure 7.11: $Pr \neq 1$, $Pm = 1$: The maximum growth rate $S_{\mathrm{max}}(K_{\mathrm{max}})$ (top panels), corresponding frequency (centre panels) and the value of K_{max} (bottom panels) in (ν_0, κ_0)-space for $M = 0.4$ (left column) and $M = 4.0$ (right column) with $\delta = 0.25$.

parameters in Jupiter's upper atmosphere using the values from table 2.1 yields $Pr = 0.3 \, (\approx 1)$ with $Pm = O(10^{-16})$ and $\nu_0 = O(10^{-8})$.

Thus, writing κ_0 as ν_0, equation (7.10) reduces to

$$\left(1 + \frac{M^2 K^2}{(S + \eta_0 K^2)^2}\right)^2 - \left(S + \nu_0 K^2 + \frac{M^2 K^2}{S + \eta_0 K^2}\right)^2 \left(1 + \delta\left(1 + \frac{M^2 K^2}{(S + \eta_0 K^2)^2}\right)\right) =$$

$$\frac{(2n+1)}{K}\left(1 + \frac{M^2 K^2}{(S + \nu_0 K^2)(S + \eta_0 K^2)}\right)^{\frac{1}{2}} \left(1 + \delta\left(1 + \frac{M^2 K^2}{(S + \eta_0 K^2)^2}\right)\right)^{\frac{3}{2}}. \quad (7.47)$$

Once again we first contour the maximum growth rate in (M, K)-space in figures 7.12 and 7.14 for $\delta = 0.25$. In figures 7.13 and 7.15 we also contour the corresponding frequencies of the maximum growth rates (as shown in figures 7.12 and 7.14) in (M, K)-space.

In figure 7.12 we contour the maximum growth rate at fixed $\eta_0 = 0.05$ for $\nu_0 = 0.01$ and $\nu_0 = 5$. Increasing ν_0 reduces the growth rate of the most unstable mode and stabilises both the hydrodynamically unstable modes and the magnetically modified instabilities which occur there, so that all unstable modes become purely magnetic. Increasing the magnitude of ν_0 further reduces the size of the unstable region (seen in the right panel); however, instability persists as $\nu_0 = \kappa_0 \to \infty$, with the unstable modes occurring only in the small K limit. These modes can be stabilised only with sufficiently strong magnetic diffusivity, where the required magnitude of η_0 decreases with increasing ν_0. Figure 7.14 shows contours of the maximum growth rate at fixed $\nu_0 = \kappa_0 = 0.05$ for $\eta_0 = 0.5$ and $\eta_0 = 2.5$. With increasing η_0, the growth rate of the magnetic modes decreases, stabilising the purely magnetic modes. The hydrodynamic modes are unaffected by increasing η_0; however, instability can now occur for larger M (as seen about $(M, K) = (0.5, 2.5)$ in the right panel). The instabilities at larger M can now occur since the effect of weak magnetic field on the hydrodynamically unstable modes is damped, for which stronger magnetic field is required to have the same dynamical effect. Thus, in turn, stronger magnetic field is required in order to stabilise the magnetically modified inertial instabilities. As η_0 increases, say to $O(10^{-8})$ as expected in Jupiter's upper atmosphere, the magnetically modified instabilities may occur even for $M = O(10^3)$; however, magnetic field has no dynamical effect until $M = O(10)$. This is interesting as table 2.1 suggests $M = O(1)$–$O(10^2)$ in Jupiter's upper atmosphere. Finally, the purely magnetic instabilities (occurring for K that are hydrodynamically stable) are stabilised for $\eta_0 > 4.86$.

The Growth Rate in (ν_0, η_0)-space

In this subsection we once again suppose that the magnetic field strength M is prescribed (from observations). Figure 7.16 shows the maximum growth rate, its frequency, and $K_{\max}$ in (ν_0, η_0)-space for $\delta = 0.25$ with $M = 0.40$ and $M = 4.0$.

Clearly, for any fixed $\nu_0 = \kappa_0$, the system is stabilised for sufficiently large η_0, whereas, for any fixed η_0, instability will occur for sufficiently large κ_0. This is of particular interest as it implies magnetic instabilities can persist even in the presence of strong magnetic diffusivity (which
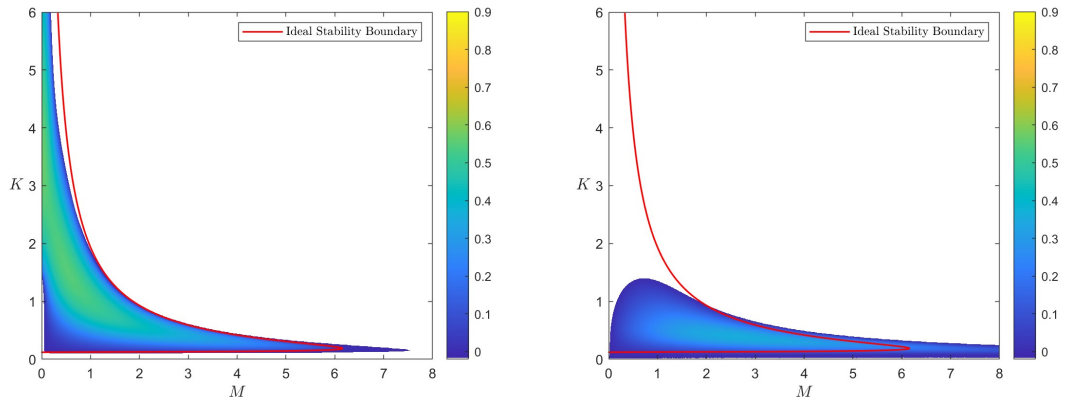
Figure 7.12: $Pr = 1$, $Pm \neq 1$: The maximum growth rate for $\delta = 0.25$ in (M, K)-space with $\eta_0 = 0.05$ for $\nu_0 = \kappa_0 = 0.01$ ($Pm = 0.2$, left panel) and $\nu_0 = \kappa_0 = 5$ ($Pm = 100$, right panel). The solid red line is the ideal stability boundary (6.63).
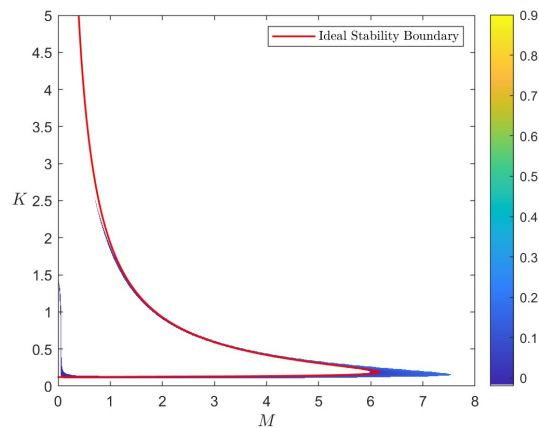
Figure 7.13: $Pr = 1$, $Pm \neq 1$: The corresponding frequency of the maximum growth rate (illustrated in figure 7.12) in (M, K)-space for $\delta = 0.25$, $\nu_0 = 0.01$ and $\eta_0 = 0.05$. The case with $\nu_0 = 5.0$ and $\eta_0 = 0.05$ (right panel of figure 7.12) has no oscillatory instabilities. The solid red line is the ideal stability boundary (6.63).
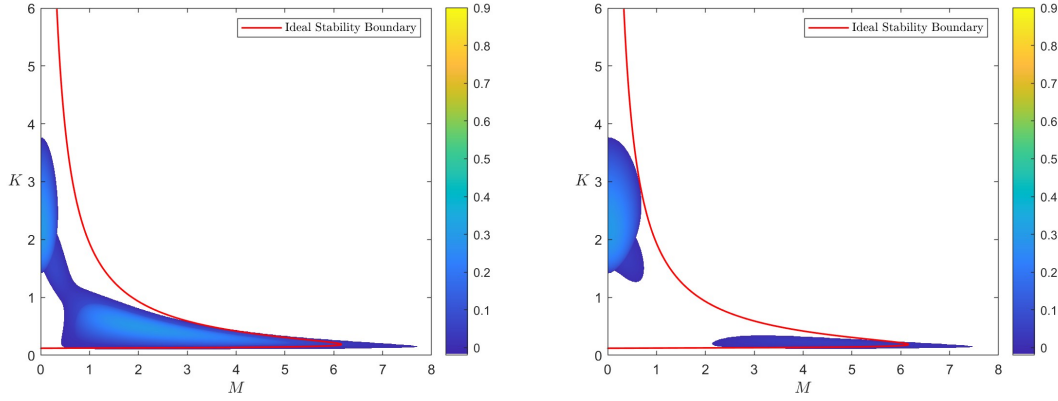
Figure 7.14: $Pr = 1$, $Pm \neq 1$: The maximum growth rate for $\delta = 0.25$ in (M, K)-space with $\nu_0 = \kappa_0 = 0.05$ for $\eta_0 = 0.5$ ($Pm = 0.1$, left panel) and $\eta_0 = 2.5$ ($Pm = 0.025$, right panel). The maximum growth rates are 0.6095 and 0.2982, respectively. Note that when $\eta_0 = 4.86$ the magnetic instabilities found at $M > 1$ are stabilised. The solid red line is the ideal stability boundary (6.63).
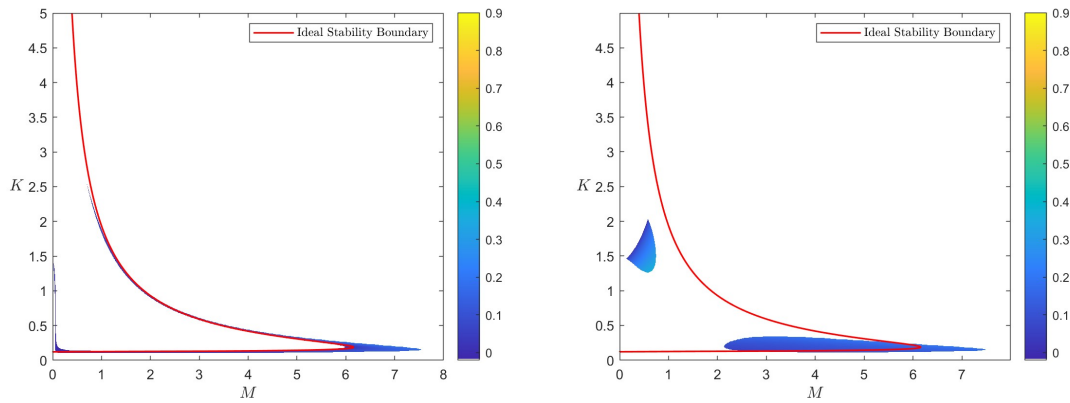
Figure 7.15: $Pr = 1$, $Pm \neq 1$: The corresponding frequency of the maximum growth rate (illustrated in figure 7.14) for $\delta = 0.25$ in (M, K)-space with $\nu_0 = \kappa_0 = 0.05$ for $\eta_0 = 0.5$ ($Pm = 0.1$, left panel) and $\eta_0 = 2.5$ ($Pm = 0.025$, right panel). The solid red line is the ideal stability boundary (6.63).

is the case in Jupiter's upper atmosphere) provided there is sufficiently strong thermal diffusion. Interestingly, we also see that at some fixed η_0, increasing ν_0 from zero initially gives oscillatory instabilities, then stability, followed by steady stability given sufficiently large κ_0. This is due to increasing thermal diffusion first stabilising oscillatory modes (damping vertical oscillations) and then generating steady instabilities (since increasing κ_0 reduces the stabilising role of the pressure gradient).

We now compare the system for the two different values of M in figure 7.16 ($M = 0.40$, $M = 4.0$). First, for $M = 4.0$, we see a much larger instability domain; the maximum growth rate is also significantly larger for $M = 4.0$. We might expect this, since increasing M allows magnetic instabilities to persist even in the presence of strong magnetic diffusivity. The bulk of the values of K_{max} are similar in both cases, ranging from $K = 0.15$ to $K = 0.35$, implying a preferred vertical scale. Looking back to figures 7.12 and 7.14 we can see that this is indeed the case, with magnetic instabilities primarily occurring at $K = O(10^{-1})$. We also see a much larger domain for which oscillatory instability can occur for $M = 4.0$.

7.4.4 $Pr = Pm \neq 1$

In the section we consider the case $Pr = Pm \neq 1$. Since no simplification can be made, by writing η_0 as κ_0, we recast equation (7.38) for convenience, yielding

$$\left(1 + \frac{M^2 K^2}{(S + \kappa_0 K^2)^2}\right)^2 - \left(S + \nu_0 K^2 + \frac{M^2 K^2}{S + \kappa_0 K^2}\right)^2 \left(1 + \delta\left(1 + \frac{M^2 K^2}{(S + \kappa_0 K^2)^2}\right)\right) =$$

$$\frac{(2n+1)}{K}\left(\frac{S + \nu_0 K^2}{S + \kappa_0 K^2} + \frac{M^2 K^2}{(S + \kappa_0 K^2)^2}\right)^{\frac{1}{2}} \left(1 + \delta\left(1 + \frac{M^2 K^2}{(S + \kappa_0 K^2)^2}\right)\right)^{\frac{3}{2}}. \quad (7.48)$$

In figures 7.17 and 7.18 we contour the maximum growth rate in (M, K)-space for $\delta = 0.25$. In figure 7.17 we contour the maximum growth rate at fixed $\kappa_0 = \eta_0 = 0.05$ for $\nu_0 = 0.01$ and $\nu_0 = 10$.

Figure 7.17 shows that increasing ν_0 (with $\kappa_0 = \eta_0$ fixed) stabilises modes at large vertical numbers, eventually stabilising all modes in the hydrodynamically unstable regime so that only purely magnetic instabilities exist (as seen in the right panel of figure 7.17). The growth rate of the remaining modes generally decreases; however, the growth rates of the magnetic modes that remain (in the right panel) are largely unaffected since they occur at small vertical wavenumbers (i.e., $K = O(10^{-1})$). Figure 7.18 shows that increasing $\kappa_0(= \eta_0)$ (with ν_0 fixed) reduces the growth rate of purely magnetic modes, while increasing the growth rate of hydrodynamic instabilities. Indeed, owing to increasing magnitudes of κ_0 and η_0, the most unstable mode occurs at $M = 0$ (in the right panel) rather than at $M \neq 0$ (in the left panel). In general, the unstable domain illustrated in the right panel of figure 7.18 is somewhat more complex than previous cases, however there are some similarities to the right panel of figure 7.14. Indeed, in both cases there are purely magnetic instabilities for $M > 1$ and magnetically modified inertial instabilities for $M < 1$. The unstable domain containing the magnetically modified inertial instabilities expands
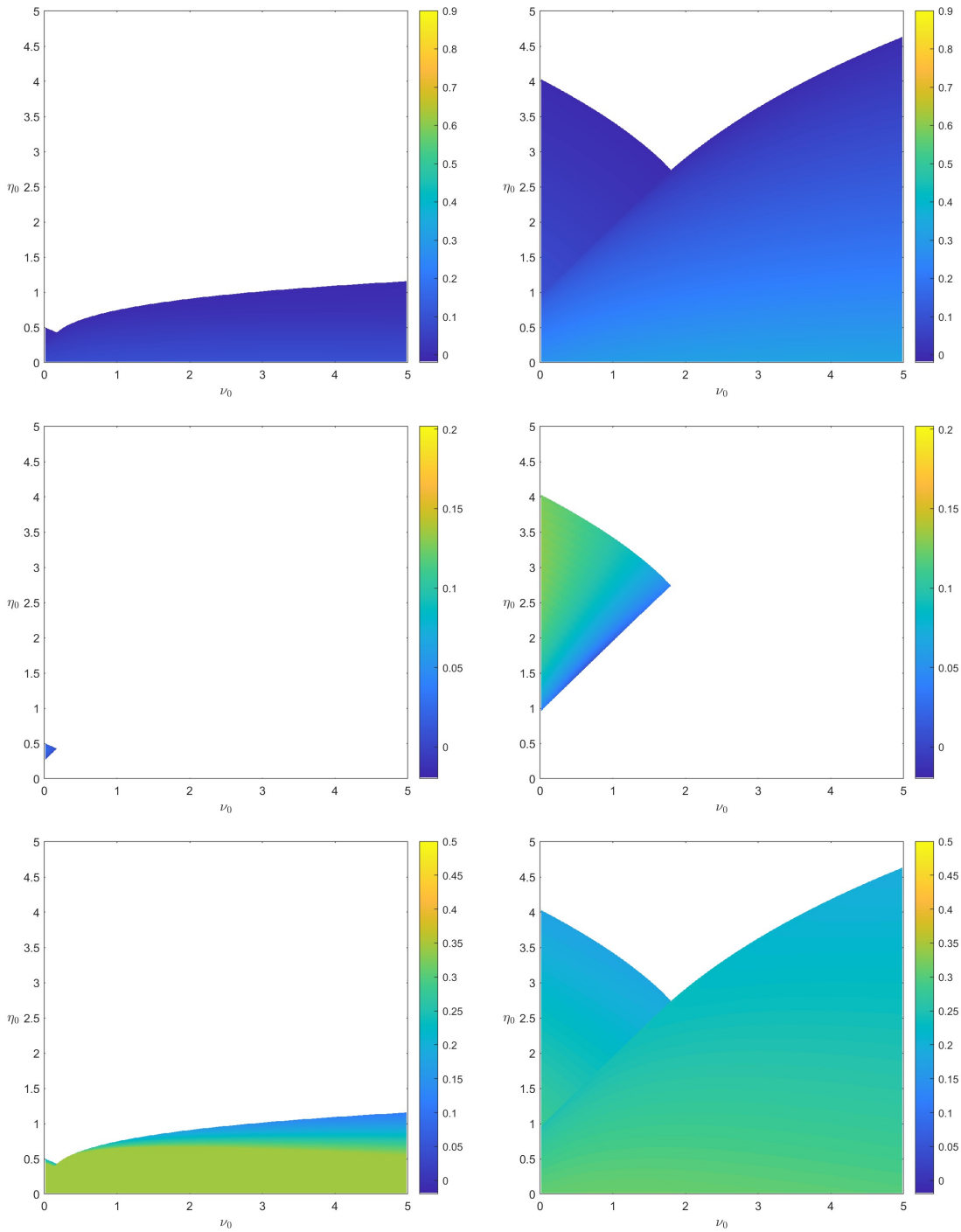
Figure 7.16: $Pr = 1$, $Pm \neq 1$: The maximum growth rate $S_{\max}(K_{\max})$ (top panels), corresponding frequency (centre panels) and the value of $K_{\max}$ (bottom panels) in (ν_0, η_0)-space for $M = 0.4$ (left column) and $M = 4.0$ (right column) with $\delta = 0.25$. Note the distinct colourbars.
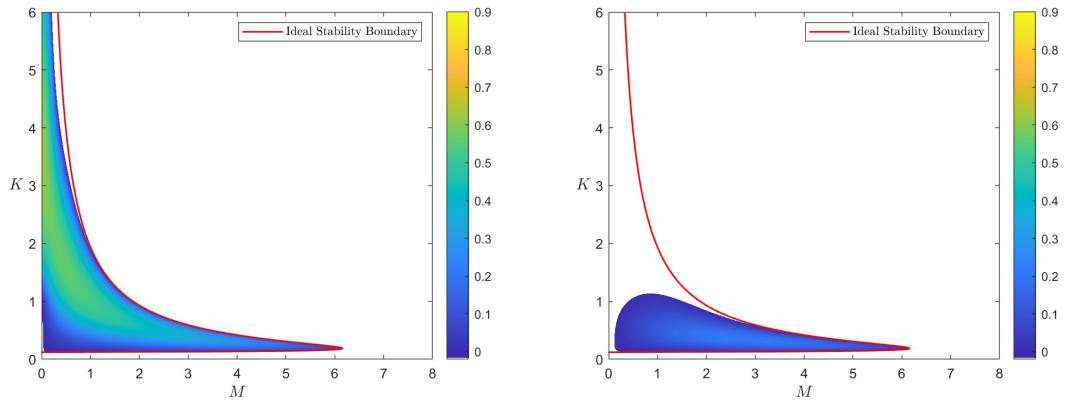
Figure 7.17: $Pr = Pm \neq 1$: The maximum growth rate in (M, K)-space for $\delta = 0.25$ with $\kappa_0 = \eta_0 = 0.05$ and $\nu_0 = 0.01$ ($Pr = Pm = 0.2$, left panel) and $\nu_0 = 10$ ($Pr = Pm = 200$, right panel). The maximum growth rates are 0.621 and 0.213, respectively. The solid red line is the ideal stability boundary (6.63).
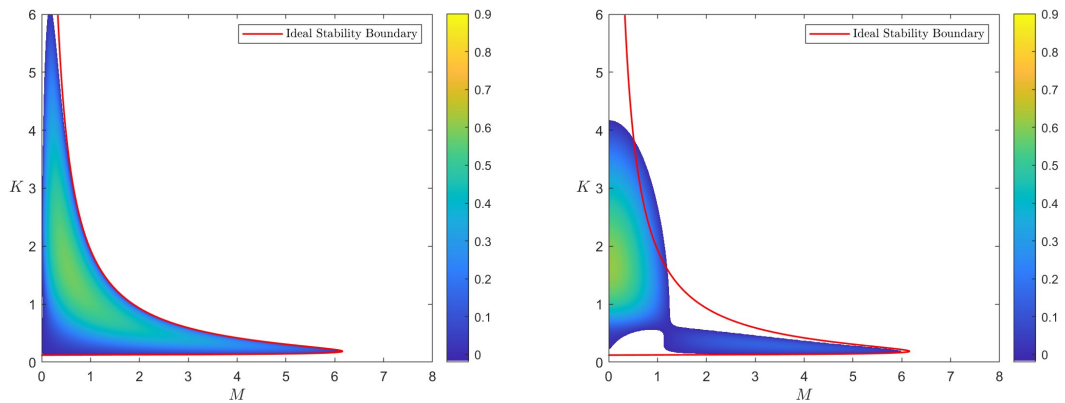
Figure 7.18: $Pr = Pm \neq 1$: The maximum growth rate in (M, K)-space for $\delta = 0.25$ with $\nu_0 = 0.05$ and $\kappa_0 = 0.01$ ($Pr = Pm = 5$, left panel) and $\kappa_0 = 2$ ($Pr = Pm = 0.025$, right panel). The maximum growth rates are 0.579 and 0.613, respectively. The solid red line is the ideal stability boundary (6.63).

with increasing $\kappa_0 = \eta_0$ (with the purely magnetic instabilities being stabilised at $\kappa_0 = 4.61$). This is analogous to what was discussed regarding figure 7.14, where magnetic field of larger magnitude is required for the same dynamic effect. However, since $Pr = Pm$ the maximum growth rate also increases (since κ_0 is also increasing), tending toward $1/\sqrt{1 + \delta}$ in the limit of large κ_0.

The Growth Rate in (ν_0, κ_0)-space

In this subsection we suppose M is prescribed (from observations) and, as before, we contour the maximum growth rate and $K_{\max}$ in (ν_0, κ_0)-space in figure 7.16 for $\delta = 0.25$ with $M = 0.30$ (left panels) and $M = 3.0$ (right panels). There are no oscillatory instabilities under these Prandtl number constraints.

For any fixed $\kappa_0 = \eta_0$, the system is stabilised given sufficiently large ν_0 (in particular for large η_0). However, for any fixed ν_0, the effect of increasing $\kappa_0 = \eta_0$ is less clear. Indeed, for $M = 0.30$, at any fixed ν_0, instability will occur given sufficiently large κ_0; owing to the increasing magnitude of η_0 the instabilities are hydrodynamic in nature even in the presence of moderate magnetic field strength. In contrast, for $M = 3.0$, at any fixed ν_0, stability is guaranteed given sufficiently large $\kappa_0 = \eta_0$. The instabilities that occur for sufficiently small $\kappa_0 = \eta_0$ are purely magnetic in nature and occur at vertical wavenumbers $K \sim O(10^{-1})$. The system at these vertical wavenumbers would otherwise be stable in the ideal regime. Indeed, the ideal bound for stability $M^2 < (K - \delta^{3/2})/\delta K^3$ implies that instability occurs for $0.1299 < K < 0.5921$ when $M = 3.0$; figure 7.19 suggests instability can now occur at vertical wavenumbers $K < 0.1299$ for $M = 3.0$. As previously discussed, instabilities may occur at smaller vertical wavenumbers since thermal diffusion reduces the stabilising role of the pressure gradient.

We now compare the system for the two different values of M in figure 7.19 ($M = 0.30$, $M = 3.0$). First, for $M = 3.0$, we see a much larger instability domain; however, the maximum growth rate is significantly larger for $M = 0.3$, occurring in $Pr = Pm \ll 1$ regime. The maximum growth rates occur for $Pr = Pm \gg 1$ for $M = 4.0$. This might be expected, since unstable modes with $M = 4.0$ are purely magnetic (occurring in the hydrodynamically stable regime) and will therefore prefer small magnitudes of η_0. For $M = 0.3$ the most unstable modes are hydrodynamic in nature and therefore are not affected by large η_0. The values of K_{max} in the lower right of region of the unstable domain for $M = 0.3$ are similar to those for $M = 3.0$, ranging from $K = 0.15$ to $K = 0.35$, implying a preferred vertical scale. Looking back to figures 7.17 and 7.18 we can see that this is indeed the case, with magnetic instabilities primarily occurring at $K = O(10^{-1})$.

7.4.5 $Pr \neq 1$, $Pm \neq 1$

In this section we consider equation (7.38) directly since $Pr \neq 1$ and $Pm \neq 1$. However, owing to the complexity of the diffusive parameter space (i.e., ν_0, κ_0 and η_0 may all vary independently of one another) we will consider the two cases $Pr \ll Pm \ll 1$ and $Pr = 0.3$ with $Pm \ll 1$. The first Prandtl number regime is found in many astrophysical bodies, including the Solar tachocline and Jupiter's interior (and, perhaps, Hot Jupiters); the second is the Prandtl number regime in Jupiter's upper atmosphere (see table 2.1), which could also apply to the upper atmospheres of Hot Jupiters. Recall that we argue that the flow profile $U(y) = \Lambda_0 y - \delta \beta y^2/2$ can model the jets adjacent to Jupiter's prominent central equatorial jet (since the central jet is symmetric about the equator).

$Pr \ll Pm \ll 1$

To restrict the analysis we consider the case where the Prandtl numbers are small and follow the scaling $Pr = Pm^p$ where p is some positive power. Formally, we suppose the Prandtl numbers
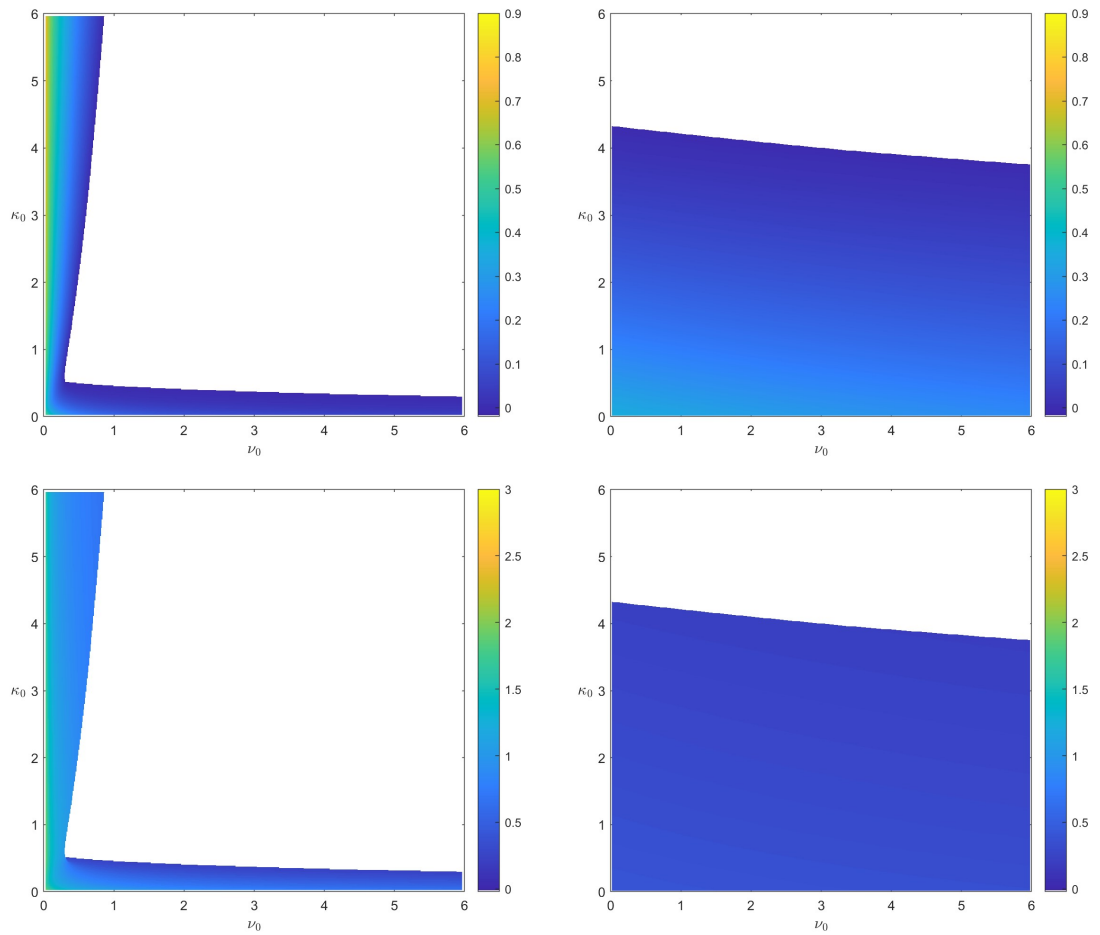
Figure 7.19: $Pr = Pm \neq 1$: The maximum growth rate $S_{\max}(K_{\max})$ (top panels) and the value of $K_{\max}$ (bottom panels) in (ν_0, κ_0)-space for $M = 0.30$ (left panels) and $M = 3.0$ (right panels) with $\delta = 0.25$. Note the distinct colourbars.

follow the scaling

$$\frac{\nu_0}{\eta_0} = \epsilon \quad \text{and} \quad \frac{\nu_0}{\kappa_0} = \epsilon^p \quad \text{with} \quad p > 0, \tag{7.49}$$

where $\epsilon = O(1)$ or smaller. This formulation reduces the system to a 4 parameter problem $(M, K, \nu_0$ and $\delta)$ for the growth rate.

Under this formulation equation (7.38) only simplifies slightly; we therefore solve (7.38) numerically and contour the growth rate in (M, K)-space in figures 7.20 and 7.21 with $\delta = 0.25$ for various values of p, ϵ and ν_0.

In general, the figures show that increasing ν_0 ($= \epsilon\eta_0 = \epsilon^p\kappa_0$) at fixed ϵ and p reduces the interval of K for which instability can occur, decreases the maximum growth rate, and stabilises the system at sufficient magnitude. We also see that decreasing ϵ at fixed ν_0 and p increases the maximum growth rate of the system, which in every case occurs at $M = 0$, owing to the increasing magnitude of κ_0; however, the growth rate of the magnetic modes also increases significantly. This is surprising as decreasing ϵ at fixed ν_0 implies that the magnitude of η_0 also increases, so that one might expect the growth rate of magnetic modes to decrease. Presumably this damping is offset by a more rapidly increasing magnitude of κ_0 since $\kappa_0 = \nu_0/\epsilon^p$ rather than $\eta_0 = \nu_0/\epsilon$.

Figures 7.20 and 7.21 show that instabilities may occur at vertical wavenumbers that would otherwise be stable in the ideal regime owing to large κ_0 reducing the stabilising effects of the pressure gradient at small K. We also see instability occur at values of M that would otherwise be stable in the ideal regime, once again owing to the increasing magnitude of κ_0. We already determined that instability can occur at larger M since stronger cross-stream Lorentz forces are no longer alone sufficient to stabilise the system in the absence of the pressure gradient.

In terms of the effects of increasing the parameter p we must compare figure 7.20 to figure 7.21. We can see, by comparing each panel, that increasing p from 2 to 3 at fixed ν_0 and ϵ allows instability to occur at smaller vertical wavenumbers, while the maximum vertical wavenumber for which instability can occur remains the same. We also see that the range of M at which instability occurs also increases with increasing p, as well as the maximum growth rate of the system.

Application to Jupiter's Upper Atmosphere

We now briefly consider the Prandtl number regime in Jupiter's upper atmosphere. Using the values from table 2.1 we obtain $Pr = 0.3$ and $Pm = 10^{-16}$ with $\nu_0 = 10^{-8}$. Table 2.1 also implies that the parameter $M = O(1)$–$O(10^2)$.

In figure 7.22 we contour the growth rate in (M, K)-space with $\delta = 0.25$, $\nu_0 = 10^{-8}$, $\kappa_0 = 3.33 \times 10^{-8}$ (so that $Pr = 0.3$) and $\eta_0 = 10^2$. We are using a smaller value of η_0 than suggested by table 2.1 so that the instability domain is more easily illustrated.

Surprisingly, the instability domain is significantly different to all previous cases that we have seen throughout this chapter. However, many concepts we have already discussed are relevant here. Indeed, owing to the large magnitude of η_0, larger magnitudes of magnetic field strength are required to modify the hydrodynamic inertial instabilities significantly, in turn, delaying stabilisation. If we were instead to plot figure 7.22 with $\eta_0 = 10^{-6}$ (as table 2.1 suggests), then instability
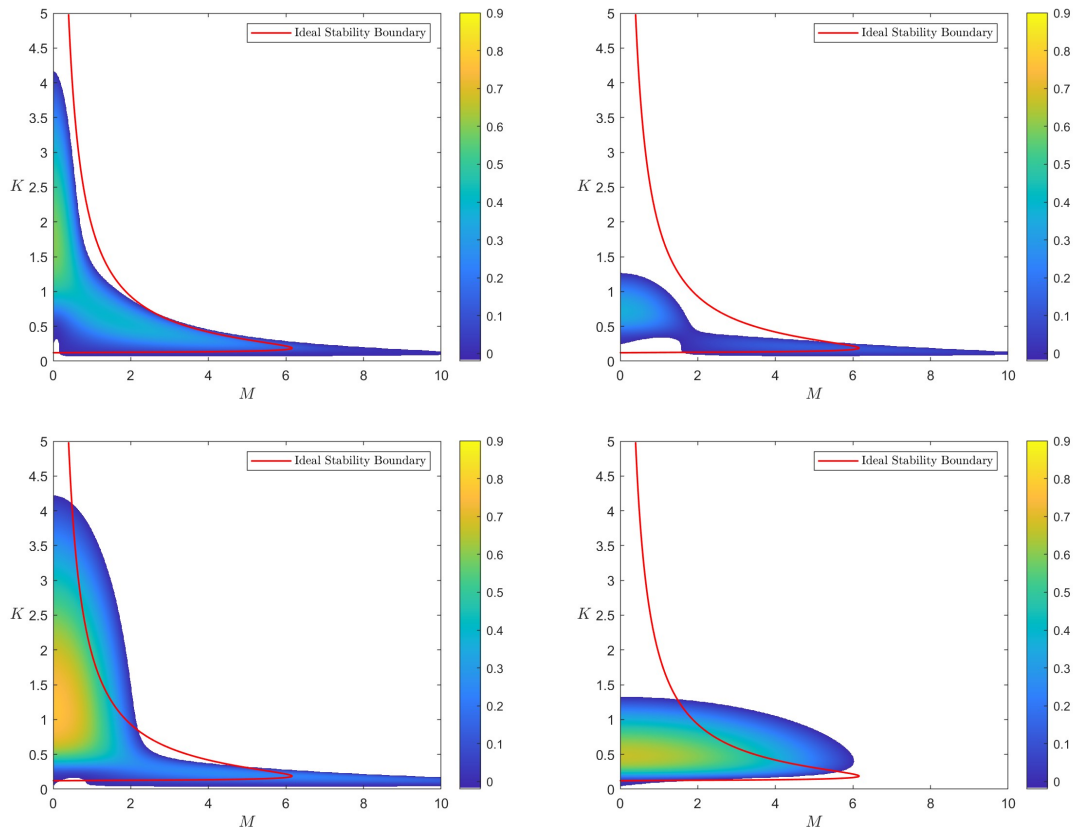
Figure 7.20: $Pr \ll Pm \ll 1$: The maximum growth rate in (M, K)-space for $p = 2$ ($Pr = Pm^p = \epsilon^p$) and $\delta = 0.25$ with $\nu_0 = 0.05$ (left panels) and $\nu_0 = 0.5$ (right panels), $\epsilon = 0.1$ (top panels, $Pr = 0.01$, $Pm = 0.1$) and $\epsilon = 0.01$ (bottom panels, $Pr = 10^{-4}$. $Pm = 0.1$). The maximum growth rates for the top row are 0.598 and 0.359. For the second row the maximum growth rates are 0.766 and 0.665. The solid red line is the ideal stability boundary (6.63).
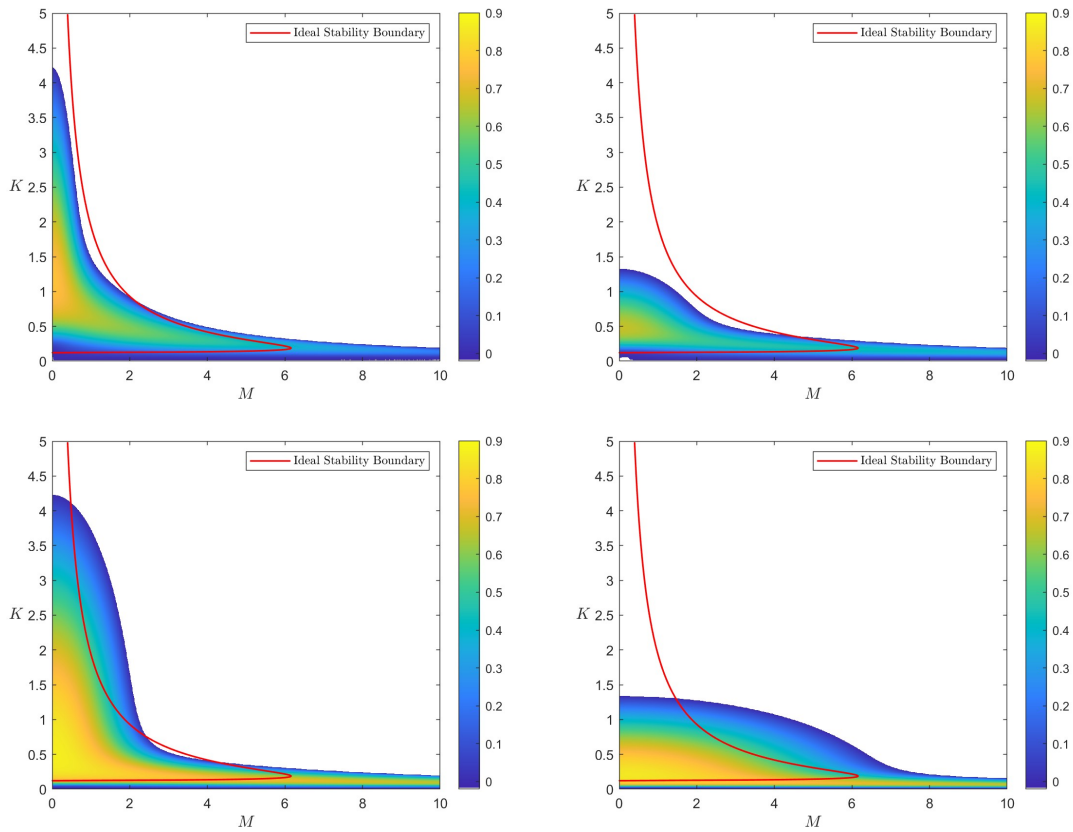
Figure 7.21: $Pr \ll Pm \ll 1$: The maximum growth rate in (M, K)-space for $p = 2$ ($Pr = Pm^p = \epsilon^p$) and $\delta = 0.25$ with $\nu_0 = 0.05$ (left panels) and $\nu_0 = 0.5$ (right panels), $\epsilon = 0.1$ (top panels, $Pr = 10^{-3}$, $Pm = 0.1$) and $\epsilon = 0.01$ (bottom panels, $Pr = 10^{-6}$. $Pm = 0.1$). The maximum growth rates for the top row are 0.766 and 0.665. For the second row the maximum growth rates are 0.871 and 0.854. The solid red line is the ideal stability boundary (6.63).
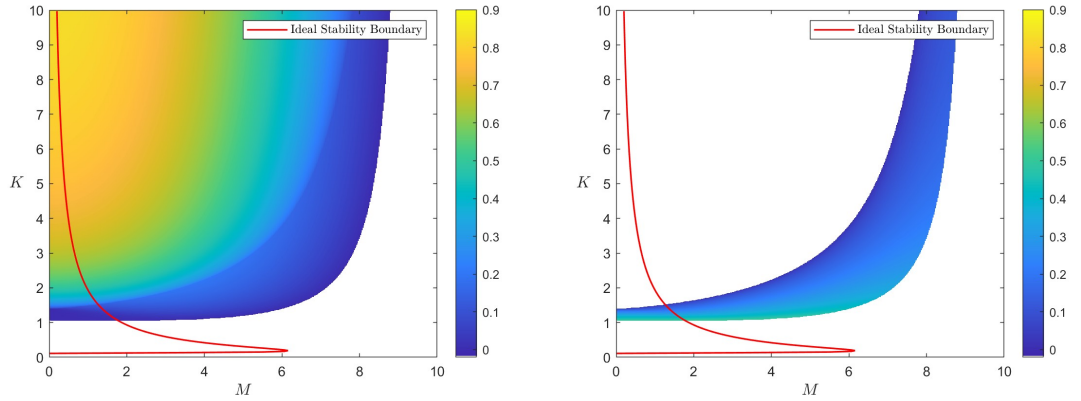
Figure 7.22: $Pr = 0.3$, $Pm = 10^{-10}$: The maximum growth rate (left panel) and its corresponding frequency (right panel) in (M, K)-space for $\delta = 0.25$ with $\nu_0 = 10^{-8}$, $\kappa_0 = 3.33 \times 10^{-8}$ and $\eta_0 = 10^2$. The solid red line is the ideal stability boundary (6.63).

may still occur for $M = O(10^3)$; indeed, the resulting unstable domain is much larger than that illustrated in figure 7.22. Instability being able to occur at $M = O(10^3)$ is crucial in application to Jupiter's upper atmosphere since table 2.1 implies $M = O(1)$–$M(10^2)$ (depending on the value of Λ_0); thus, instabilities in Jupiter's upper atmosphere, if they occur, may be categorised as magnetically modified inertial instabilities. There is also a large region in (M, K)-space for which oscillatory instability may occur; this region becomes larger with increasing M; it is therefore possible that oscillatory instabilities occur in Jupiter's upper atmosphere.

7.5 Conclusions

In this chapter we have extended the system and analysis of Chapter 6 into the diffusive regime. We considered the linear stability of the jet profile $U(y) = \Lambda_0 y - \delta \beta y^2/2$ on an equatorial β-plane in the presence of uniform vertical magnetic field strength B_0, kinematic viscosity ν, thermal conductivity κ and magnetic diffusivity η. Although this flow profile is not the simplest possible choice available to study the effects of diffusion on an equatorial β-plane, it confines any anticyclonic shear to the region $0 < y < \Lambda_0/\delta\beta$, where instability is confined to this region. This also ensures the non-equatorial strong magnetic field instability of Chapter 6 cannot occur. This formulation allowed for the derivation of a parabolic cylinder equation for the perturbed cross-stream velocity by introducing the nondimensional coordinate $Y = (y - y_0)/L$, where y_0 is the central latitude and L is the nondimensional latitudinal lengthscale. The parabolic cylinder equation can be solved analytically, yielding an eigenvalue relation with corresponding eigenfunctions $v \propto H_n(Y) \exp(-Y^2/2)$. where the eigenvalue n is a non-negative integer. Note that we considered only $n = 0$ since this is the most unstable mode. We then introduced the nondimensional growth rate S (with timescale $2/\Lambda_0$), vertical wavenumber K, magnetic field strength M, kinematic viscosity ν_0, thermal diffusion κ_0 and magnetic diffusivity η_0. We argued that given some astrophysical body, one could infer values for M, ν_0, κ_0, η_0, and δ, reducing the system to a one

parameter problem for the growth rate S. Thus, given these parameters, a vertical wavenumber K is selected in order to maximise the growth rate S and imply a vertical scale of the instability.

It is important to note that the results of this chapter are very applicable to the upper atmospheres of Jupiter and Hot Jupiters (as well as stellar interiors), which we will now discuss. Table 2.1 allows us to estimate the nondimensional parameters in the upper atmospheres of Jupiter and Hot Jupiters. Table 2.1 yields $\nu_0 = 10^{-8}$, $\kappa_0 = 3.33 \times 10^{-8}$, $\eta_0 = 10^8$ and $M = O(1)$–$O(10^2)$ in Jupiter's upper atmosphere. Taking the same values for ν, κ and η in the upper atmospheres of Hot Jupiters yields $\nu_0 = 10^{-17}$–10^{-12}, $\kappa_0 = 3.33 \times 10^{-17}$–$3.33 \times 10^{-12}$, $\eta_0 = 10^{-1}$–10^4 and $M = O(10^{-8})$–$O(1)$; however, the values of ν_0, κ_0 and η_0 may be significantly different in reality, perhaps satisfying $Pr \ll Pm \ll 1$. The significant ranges in the estimated nondimensional parameters for Hot Jupiters are due to their sensitivity to the shear Λ_0 (powers of 5 in the diffusive parameters and 3 in the magnetic parameter); indeed, the shear Λ_0 may vary by multiple orders of magnitudes on Hot Jupiters owing to their inferred extreme equatorial jets.

We first considered the hydrodynamic regime, in which the jet profile extends slightly upon the studies of Dunkerton (1981, 1982) and Griffiths (2003a) where a flow profile with uniform shear was considered. For $Pr = 1$, we drew links to Dunkerton (1981) and Griffiths (2003a), focusing on how the jet width, governed by the parameter δ, affects the results. Exploiting the small ν_0 limit, which table 2.1 suggests is the parameter regime in the solar tachocline, and upper atmosphere's of Jupiter and Hot Jupiters, we derive a bound on the vertical wavenumber K (and therefore vertical lengthscale). For $Pr \neq 1$, we derived a steady and an oscillatory stability bound on the system, which reduce to those found in Dunkerton (1982) with $\delta = 0$. Combining these bounds allowed us to derive a necessary and sufficient condition for stability. Finally, we found that strong thermal diffusion allows instabilities to occur at vertical wavenumbers that would otherwise be stable in the ideal regime. This is due to thermal diffusion reducing the stabilising role of the pressure gradient (the strength of which increases with decreasing K). We discuss links to the GSF instability (Goldreich & Schubert, 1967; Fricke, 1968).

In the magnetohydrodynamic regime we systematically analysed every variation of the Prandtl number and magnetic Prandtl number being unity or non-unity. We first considered the case $Pr = Pm = 1$ which links to both the hydrodynamic regime with $Pr = 1$ and the ideal system of Chapter 6 via a simple transformation of the growth rate. This regime does not directly apply to those in astrophysical bodies; however, we can infer numerous important results. First, owing to the presumably small values of the nondimensional diffusive parameters in the upper atmospheres of Jupiter and Hot Jupiters (excluding η_0), the most unstable modes of the system will occur close to the vertical wavenumber of the hydrodynamic regime, as predicted by (7.17), yielding $K = 315$ and $K = 6789$ for Jupiter and Hot Jupiters, respectively. For Jupiter, this yields a vertical lengthscale of $O(10^2\mathrm{m})$, giving a lower bound on the vertical lengthscale of possible instabilities in the upper atmosphere. For Hot Jupiters the corresponding vertical lengthscale is $O(10\mathrm{km})$ (although we obtain vertical lengthscales of $O(10^2\mathrm{m})$ for smaller shears). It is reasonable to expect vertical lengthscales numerous orders of magnitude larger in these atmospheres; however,

on inspection of figure 7.4, it is clear that increasing the magnetic field strength decreases the preferred vertical wavenumber (and therefore vertical lengthscale). Taking $M = O(1)$–$O(10^2)$ in Jupiter's upper atmosphere yields vertical lengthscales of $O(10^3 \text{km})$. Taking $M = O(10^{-8})$ in the upper atmospheres of Hot Jupiters again yields vertical lengthscales of $O(10 \text{km})$; however, taking $M = O(10^{-2})$ yields vertical lengthscales of $O(10^3 \text{km})$ (using the estimate (6.68) of Chapter 6 for the vertical wavenumber in the limit of weak magnetic field). We also note that increasing ν_0 decreases the preferred vertical wavenumber and the maximum growth rate, where the critical diffusion for stabilisation over all M and K is $\nu_0 = 4.358$.

As we have already noted numerical models run with anomalously large diffusion, and thus it is very interesting to understand if they artificially suppress instabilities that might otherwise occur. For simplicity, we take the critical diffusion $\nu_0 = 4.358$ (with $Pr = Pm = 1$) and compare this to values found in numerical models. For example, Rogers & Komacek (2014) present global magnetohydrodynamic simulations of Hot Jupiters, and take $\nu = \kappa = \eta = 5.0 \times 10^6 \text{m}^2\text{s}^{-1}$ (although stronger magnetic diffusivity is also considered). Thus, by taking $N \approx 5 \times 10^{-4}\text{s}^{-1}$, $\beta = 4 \times 10^{-13}\text{m}^{-1}\text{s}^{-1}$, $\Lambda_0 = 3 \times 10^{-5}\text{s}^{-1}$, we obtain $\nu_0 \approx 30$. Hence, these instabilities are likely to be artificially suppressed in planetary scale numerical simulations. This is an important finding, since throughout this thesis, we have been identifying classes of instabilities that will not be resolved in large-scale models, but will have implications for modifying jet strengths, redistributing momentum, and vertical mixing (due to overturning in cells).

The case $Pr \neq 1$ and $Pm = 1$ allowed us to draw links to hydrodynamic analysis of section 7.3, where strong thermal diffusion allows instability to occur at small K that would otherwise be stable in the ideal regime. We contoured the maximum growth rate in (M, K)-space, where taking $M = O(1)$–$O(10^2)$ in Jupiter's upper atmosphere yields larger vertical lengthscales of $O(10^3 \text{km})$–$O(10^4 \text{km})$, or stability given sufficiently large M. With increasing κ_0 allows instabilities to occur at larger values of M (in contrast to the ideal regime or $Pr = Pm = 1$) since the combination of the cross-stream pressure gradient and cross-stream Lorentz force (which are both stabilising) are no longer sufficient to stabilise the system. This is in fact the reason why instability can occur only at larger values of M given smaller values of K in the ideal regime. Further, by contouring the maximum growth rate in (ν_0, κ_0)-space at fixed M, we can conclude that the vertical wavenumber that generates the maximum growth rate decreases with increasing M or increasing ν_0 (or decreasing κ_0).

In the case $Pr = 1$ and $Pm \neq 1$, figure 7.14 shows the existence of purely magnetic instabilities that persist in the large $\nu_0 = \kappa_0$ limit provided η_0 is sufficiently small; once again, these may occur at values of M that would otherwise be stable in the ideal regime. This, along with the previous case ($Pr \neq 1$, $Pm = 1$), allows us to conclude that increasing magnitudes of κ_0 allow instability to occur at smaller vertical wavenumbers and larger values of M (both of which would imply stability in the ideal regime). We also find that increasing η_0 at fixed $\nu_0 = \kappa_0$ stabilises all purely magnetic instabilities; however, inertial instabilities modified by magnetic field can not be stabilised. Instead, increasing magnetic diffusion can only damp the effect of magnetic field

on the inertial modes; thus, larger magnetic field strength is required to modify the hydrodynamic instability and, in turn, stabilise the instabilities. In terms of scale selection in Jupiter's upper atmosphere (and Hot Jupiters), where $M = O(1)$–$O(10^2)$ and η_0 is large, we may expect instabilities (if they occur) to have vertical lengthscales significantly smaller than $O(10^3 \text{km})$. The instabilities are not purely magnetic as those are stabilised by large η_0 and instead can be categorised as magnetically modified inertial instabilities, which occur at larger vertical wavenumbers.

In the case $Pr = Pm \neq 1$, we find instabilities analogous to those found in the hydrodynamic analysis of section 7.3 for a finite range of $\kappa_0 = \eta_0$ with $M \neq 0$; κ_0 cannot be so small that the stabilising role of the pressure gradient is not damped at smaller vertical wavenumbers, while η_0 can not be so large as to stabilise instabilities at $M \neq 0$. In the large ν_0 limit, the most unstable mode is purely magnetic (the system would be stable for the same ν_0 hydrodynamically, as seen in section 7.3); however, as ν_0 increases, we require decreasing η_0 for instability still to be possible.

Finally, we consider two cases with $Pr \neq Pm \neq 1$. The first considers the regime $Pr \ll Pm \ll 1$ such that $Pm = \epsilon$ and $Pr = \epsilon^p$ for $p = 3/2$ and $p = 3$ with $\epsilon \ll 1$, which is the case in many astrophysical bodies, including the solar tachocline, stellar interiors and, perhaps, Hot Jupiters. We also consider the case $Pr = 0.3$ and $Pm \ll 1$, which is applicable to Jupiter's upper atmosphere (as suggested by table 2.1), and perhaps the upper atmospheres of Hot Jupiters. In the case $Pr \ll Pm \ll 1$, generally, the most unstable mode of the system is always hydrodynamic; however, in certain cases, instabilities with similar growth rates may also occur with $M \neq 0$. Specifically, in the bottom left panel of figure 7.21 where $Pr = 10^{-6}$, $Pm = 0.1$ ($p = 3$), there are unstable modes with growth rates of comparable magnitude to the hydrodynamic mode, even for $M = O(1)$–$O(10)$. These unstable modes also occur at vertical wavenumbers that would otherwise be stable in the ideal regime. Thus, purely magnetic instabilities may occur in stellar interiors, where we expect M is larger than $O(1)$, with vertical lengthscales of $O(10^4 \text{km})$.

In the case $Pr = 0.3$ and $Pm \ll 1$, which is the Prandtl number regime in Jupiter's upper atmosphere, we contour the growth rate in (M, K)-space in figure 7.22 for $\eta_0 = 10^2$ (rather than $\eta_0 = 10^8$ for illustration purposes). Owing to the large η_0, all purely magnetic instabilities (i.e., those that occur in the hydrodynamically stable regime) are stabilised, so that all instabilities may be categorised as inertial or magnetically modified inertial instabilities. However, once again, owing to large η_0, the dynamical effect of magnetic field is damped in comparison to the ideal regime. Thus, much larger magnetic field strength is required so that the modes may be categorised as magnetically modified inertial instabilities, and, consequently, much larger M is required for stabilisation. We estimate $M = O(1)$–$O(10^2)$ in Jupiter's upper atmosphere, so that instability may occur at all magnetic field strengths (noting that $\eta_0 = 10^8$ allows instability to occur for even $M = O(10^3)$). The preferred vertical lengthscale is largely unaffected by increasing magnetic field, and owing to the large η_0 and small ν_0, the vertical wavenumber takes values close to that predicted by expression (6.68), yielding vertical lengthscales of $O(10^3 \text{km})$; however, since this estimate concerned the ideal regime, we may expect kinematic viscosity to increase the vertical lengthscale by an order of magnitude or more.

Chapter 8

Conclusions

In this chapter we will summarise the main results of the thesis and their application to the solar tachocline as well as to the upper atmospheres of Jupiter and Hot Jupiters. We will also discuss possible extensions and future work that builds upon the results of the thesis. We will not provide a detailed conclusion since each chapter contains its own conclusion and discussion therein.

8.1 Summary

Inertial instabilities (which are planetary analogous of centrifugal instabilities) are well understood in the terrestrial atmosphere (e.g., Dunkerton, 1981, 1982, 1983, 1993; Griffiths, 2003a,b, 2008a; Kloosterziel *et al.*, 2007a; Kloosterziel & Carnevale, 2008; Kloosterziel *et al.*, 2015) and it is thus natural to investigate if they may be realised in stellar and planetary atmospheres, which, in general are electrically conducting and can therefore host large-scale magnetic fields. It is already well understood that magnetic field has a significant dynamical effect on electrically conducting fluid flows; for example, even weak axial magnetic field allows instabilities to occur in accretion discs (i.e., the MRI) which have centrifugally (inertially) stable flow profiles, and have been the focus of many studies (e.g., Kuiper, 1941; Balbus & Hawley, 1991; Menou *et al.*, 2004). However, we extended these studies by considering the (axisymmetric) linear and nonlinear evolution of a number of parallel flows (dependent on latitude) in the presence of vertical magnetic field in a planetary configuration, where background rotation (f-plane or equatorial β-plane), uniform vertical density stratification, uniform diffusion, and the magnetohydrostatic (thin layer) approximation are considered. The magnetohydrostatic approximation makes the analysis distinct from previous studies, and allows us to investigate the large scale dynamics of stellar and planetary atmospheres.

In Chapter 1 we introduced the astrophysical bodies relevant to this research, inertial instability and its analogies with centrifugal instability and the magnetorotational instability.

In Chapter 2 we derived the equations of motions in Cartesian geometry, which were used throughout the entire thesis. We linearised about the basic state $\mathbf{u} = U(y)\mathbf{e_x}$ and $\mathbf{B} = (0, 0, B_3(y))$, deriving a second order ordinary differential equation (ODE) that forms the basis for all linear

results in the thesis. A condition on the validity of the magnetohydrostatic approximation was derived from the ODE since it does not extend trivially from the hydrostatic approximation. Finally, we derived a series of growth rate bounds and stability criteria for an ideal fluid; namely, we showed that necessary conditions for linear hydrodynamic and magnetohydrodynamic instability are that $fQ < 0$ and $U'f > 0$, respectively.

In Chapter 3 we considered the ideal linear stability of the parallel flow $U(y) = \Lambda_0 y$, with uniform latitudinal shear Λ_0, on an f-plane in the presence of uniform vertical magnetic field strength. With our interest primarily on the unstable modes, we derived stability criteria, the maximum growth rate (and the corresponding values of magnetic field strength and aspect ratio at which it occurs), and analogies to the magnetorotational instability of Balbus & Hawley (1991). We also considered the dynamical balances of our system in numerous parameter regimes.

In Chapter 4 we extended the linear analysis of Chapter 3 by considering the effects of uniform kinematic viscosity, thermal diffusion and magnetic diffusivity. In the hydrodynamic and magnetohydrodynamic regimes, we derived several sufficient and necessary conditions for stability, and investigated the instability domain for various Prandtl and magnetic Prandtl numbers. We investigated regimes physically relevant to the solar tachocline, and the upper atmospheres of Jupiter and Hot Jupiters. We found a number of double-diffusive instabilities, and discussed links to the Goldreich-Schubert-Fricke (GSF) instability (Goldreich & Schubert, 1967; Fricke, 1968).

In Chapter 5 we considered the linear and nonlinear evolution of the hyperbolic shear layer $U(y) = U_0 \tanh(y/L)$ on an f-plane in the presence of a uniform vertical magnetic field and uniform diffusion with $Pr = Pm = 1$. We focused on the nonlinear evolution and the resulting change to the mean flow and vorticity. The regime $Pr = Pm = 1$ is not physically relevant in astrophysical bodies; however, the regime illustrates several ideas and mechanisms. Indeed, we investigate the significance of diffusion and magnetic field on the nonlinear evolution, the latitudinal redistribution of momentum, and the evolution that we might expect in hydrodynamically stable and unstable flows.

In Chapter 6 we investigated the ideal linear stability of the parallel flow $U(y) = \Lambda_0 y$ with uniform latitudinal shear Λ_0 on an equatorial β-plane in the presence of a uniform vertical magnetic field. We derive a parabolic cylinder equation which can be solved analytically to yield an eigenvalue relation. We discussed inertial and hydromagnetic waves and investigated the unstable domain, deriving asymptotic expansions that concern the weak and strong field limits. We then considered the dynamical balances of equatorial magnetically modified inertial instabilities and stratified equatorial magnetic instabilities analogous to the MRI. We then considered the jet profile $U(y) = \Lambda_0 y - \delta y^2/2$, for some constant δ, so that the shear is no longer uniform and unbounded; there are significant changes to the unstable domain since anti-cyclonic shear may now only occur in some bounded latitudinal region.

Chapter 7 extended the linear analysis of the jet profile in Chapter 6 to the diffusive regime, where the effects of kinematic viscosity, thermal diffusion and magnetic diffusivity were considered. We followed a similar systematic analysis to that of Chapter 4. The hydrodynamic regime

is closely related to that studied by Dunkerton (1982) and Griffiths (2003a, 2008a). Once again, a number of double-diffusive instabilities occur.

8.2 Discussion of Results

In the linear analysis of Chapters 3 and 6, we found that even weak magnetic field can modify inertial instabilities and generate purely magnetic instabilities in the inertially stable regime. The effect of magnetic field on inertial instabilities crucially depends upon the magnitudes of the along-stream Lorentz force, the cross-stream Lorentz force and the cross-stream pressure gradient; in both chapters we obtain a condition governing whether weak magnetic field increases or decreases the growth rate. In chapter 3, instabilities can persist even with strong magnetic field since the stabilising effect is offset by smaller vertical wavenumbers being chosen (however this is limited by the aspect ratio and the depth of the atmosphere). Similarly, in Chapter 6, we find that the equatorial instabilities of a uniform shear flow persist with strong magnetic field by traversing to a higher latitude; however, for the equatorial jet profile, sufficiently strong magnetic field stabilises all instabilities. Importantly, the analysis of both chapters showed that inertial instabilities could still occur in the presence of magnetic field and therefore in stellar and planetary atmospheres; purely magnetic instabilities were also possible. Indeed, we found that in the limit of large vertical wavenumber (vanishing vertical scales) and weak magnetic field strength that the purely magnetic instabilities were analogous to the magnetorotational instability (Balbus & Hawley, 1991), where the two limits correspond to the "thin disc" and "weak field" assumptions of Balbus & Hawley (1991). This is an interesting analogy and demonstrates the close links between inertial instabilities of planetary and stellar atmospheres and centrifugal instabilities in accretion discs.

In any hydrodynamic or magnetohydrodynamic study it is natural to consider the effects of diffusion, which both makes the mathematical model more physically appropriate and provides a basis to consider the nonlinear evolution of the system. One hydrodynamic instability that can result owing to varying magnitudes of kinematic viscosity and thermal diffusion is the Goldreich–Schubert–Fricke (GSF) instability (Goldreich & Schubert, 1967; Fricke, 1968). Strong thermal diffusion allows inertial instabilities to occur (even in the presence of strong viscosity) since it damps the stabilising role of the pressure gradient. This allows modes at vertical wavenumbers that would otherwise be stable in the absence of diffusion (owing to strong pressure gradients) to become unstable. However, in Chapters 4 and 7 with $Pr < 1$ and $Pm = 1$, we show that magnetically modified inertial instabilities that share a similar mechanism to the GSF instability occur on both the f-plane and equatorial β-plane owing to distinct magnitudes ν and κ. We also find another double-diffusive instability owing to distinct magnitudes of thermal diffusion and magnetic diffusivity. Indeed, with $Pr = 1$ and $Pm > 1$, the instability operates in much the same way to that of the GSF instability, where strong thermal diffusion allows instability to occur at vertical wavenumbers that would otherwise be rendered stable owing to the strong pressure

gradients. However, in this case, the instability is purely magnetic (rather than magnetically modified) and may even occur in hydrodynamically stable regimes (where magnetic field is crucial for instability) provided the magnitude of magnetic diffusivity is not too large.

In Chapter 5 we investigated the nonlinear evolution of magnetically modified inertial instabilities (which occur with Rossby number $\Lambda > 1$) by considering a localised shear layer $U(y) \sim \tanh y$ on an f-plane in the presence of uniform vertical field and diffusion with $Pr = Pm = 1$. The nonlinear evolution, as in the hydrodynamic case, redistributed vorticity (and therefore momentum) latitudinally in order to reduce the latitudinal shear of the mean flow and, in turn, stabilise the flow. The key to stabilisation (and a nonlinear equilibrium) relies on the minimum vorticity $Q = f - U'$ of the system; indeed, if the vorticity Q is sufficiently less than f (i.e., $Q = f - U' < f$) instability will occur. Note that this is equivalent to requiring sufficiently positive shear U' for instability. These (equivalent) conditions are less stringent criteria than in the hydrodynamic case, which requires Q to be sufficiently less than zero for instability to occur. Thus, in the magnetohydrodynamic evolution the vorticity is redistributed to a greater extent in order to increase the minimum vorticity, reduce the shear of the basic flow and therefore stabilise the system. The most significant changes to the mean flow and vorticity occur at magnetic field strengths of similar magnitude to that which generated the maximum growth rate of the linear system. For weak and strong magnetic field there is comparable change to the mean flow as in the hydrodynamic case. We also investigated the nonlinear evolution of the hydrodynamically stable regime (Rossby number $\Lambda < 1$), where even weak magnetic field generated a very significant change to the mean flow and vorticity, resulting in the formation of coinciding eastward and westward jets.

8.3 Applications to Astrophysical Bodies

The results of this thesis are applicable to the solar tachocline, and the upper atmospheres of Jupiter and Hot Jupiters. Table 2.1 gives the relevant parameters in each region of the astrophysical bodies.

8.3.1 Applications to the Solar Tachocline

We will first discuss applications to the solar tachocline, which plays a role in the transport of energy, mass and magnetic field throughout the Sun (Gough, 2007, Chapter 1), and is thought to be partly responsible for the solar dynamo. Observations imply that the angular velocity decreases with increasing radius at latitudes larger than $30°$. Thus, there is no anti-cyclonic shear present near the equator, implying that Chapters 3, 4 and 5 will be most relevant since they are concerned with mid-latitudes. We also expect that the Rossby number $\Lambda < 1$ so that the mid-latitudes of the solar tachocline are hydrodynamically stable.

The ideal analysis of Chapter 3 suggests purely magnetic instabilities analogous to the MRI are possible in this region, where even the strong stratification may be overcome by small vertical scales. However, strong magnetic field (10^3–10^5G, Gough, 2007) may render the regions stable

if the vertical wavenumber is not sufficiently small to yield a Lehnert number of order unity (or smaller), limited by the maximum aspect ratio at which instability can occur. Strong thermal diffusion may allow instabilities to occur even with large vertical lengthscales owing to the suppression of the effects of stratification. This is the case in the solar tachocline, where $Pr = O(10^{-6})$ and $Pm = O(10^{-1})$. Indeed, we found that this Prandtl number regime (i.e., $Pr \ll Pm \ll 1$, or approximately $Pr = O(10^{-6})$, $Pm = 1$) allows magnetic instabilities to persist.

We discussed the nonlinear evolution of hydrodynamically stable regimes ($\Lambda < 1$) at mid-latitudes in Chapter 5 (albeit with $Pr = Pm = 1$). Table 2.1 suggests $\mathcal{M} = O(10)$ (a relatively strong magnetic field), so that the system will either be stable or, if instabilities do occur, they will drive only a moderate to small latitudinal redistribution of the vorticity (and therefore mean flow). The nonlinear evolution tended to redistribute magnetic energy latitudinally also. In many cases the nonlinear evolution of the instabilities gave rise to Alfvén waves.

8.3.2 Applications to Jupiter's Upper Atmosphere

Jupiter exhibits rapid rotation and an approximately axisymmetric surface layer with retrograde and prograde jets, which exhibit strong latitudinal shear and are thought to extend to $0.96R_j$ before rapidly decaying to $\approx 1\%$ of their surface amplitude (Kaspi *et al.*, 2018), where $R_j = 69911\text{km}$ is the radius of Jupiter. The upper atmosphere is also strongly stratified and, owing to the large scale magnetic field generated in the electrically conducting dynamo region, is weakly magnetised (even with low levels of conductivity). Owing to the rapid rotation, we are once again concerned with a Rossby number $\Lambda < 1$. However, in contrast to the solar tachocline, there is anti-cyclonic shear close to the equator so that instabilities may still occur. Thus, we will discuss results related to mid-latitudes (f-plane) and the equator (equatorial β-plane).

We first discuss instabilities that may occur at mid-latitudes. As the Rossby number $\Lambda < 1$ we expect these regions to be hydrodynamically stable; however, purely magnetic instabilities may occur as shown in the ideal analysis of Chapter 3. As discussed in section 3.3.4 by taking an appropriate latitudinal lengthscale, vertical lengthscales of $O(10^4\text{m})$–$O(10^5\text{m})$ (which are physically reasonable) yield the maximum growth rate of the system, and may be considered to be analogous to the MRI of Balbus & Hawley (1991). However, owing to strong magnetic diffusivity, and relatively weak kinematic viscosity and thermal diffusion such that $Pr = 0.30$ and $Pm \ll 1$, the instabilities can either be stabilised or modified. Assuming $Pr = 1$ is an appropriate approximation, section 4.4.4 predicts that purely magnetic instabilities may persist with vertical lengthscales an order of magnitude larger (i.e., $O(10^5\text{m})$–$O(10^6\text{m})$); the magnitude of thermal diffusion is sufficient to nullify pressure gradients that would otherwise stabilise the flows at these vertical lengthscales.

The nonlinear hydrodynamically stable ($\Lambda < 1$) analysis of Chapter 5 gives insight into the evolution of these magnetorotational instabilities. Table 2.1 yields $\mathcal{M} \sim O(10^{-1})$ or smaller, which, as we discovered, resulting instabilities drive very significant latitudinal redistribution of the vorticity. This led to a significant change to the mean flow, not only reducing the anti-cyclonic

shear of the $U(y) = U_0 \tanh(y/L)$ profile, but driving the shear to become cyclonic for $y \in [-L, L]$ which is about the minimum of fQ, $y = 0$.

We now discuss equatorial instabilities that may occur in Jupiter's upper atmosphere. We restrict our discussion of the ideal system to the more physically appropriate jet profile $U(y) = \Lambda_0 y - \delta y^2/2$, which was investigated in section 6.5, and illustrated in 1.2. However, it is important to note that Jupiter's prominent central equatorial jet is symmetric about the equator, and thus it is more appropriate to model the immediately adjacent jets (so that they are sufficiently close to the equator). It is also unlikely that there are regions of $fQ < 0$ in the equatorial atmosphere owing to the structure of the prominent central equatorial jet; however, as we determined in Section 2.5, in the magnetohydrodynamic regime a necessary condition for instability is that $U'f > 0$ (which is less stringent than $fQ < 0$).

The most unstable mode occurred at large vertical wavenumber and weak magnetic field strength (relating once again to the "thin disc" and weak field assumptions of Balbus & Hawley, 1991). However, the parameters given in table 2.1 suggest the equatorial magnetic field strength parameter is $M = O(1)$–$O(10)$, for which purely magnetic instabilities may only occur with $K \approx O(10^{-1})$. This yields a more physically appropriate finite vertical lengthscale $H \approx O(10^5)$. Further to this, upon considering the effects of diffusion (in chapter 7) it is clear that the maximum growth rate no longer occurs at large vertical wavenumbers; all instabilities now occur with vertical lengthscales $H = O(10^4)$–$O(10^5)$ even in the absence of diffusion. Owing to the large values of η in Jupiter's upper atmosphere, it is unlikely that the purely magnetic instabilities will persist. However, the magnetic diffusivity does vary by multiple orders of magnitude in the upper atmosphere alone (i.e., η decreases from $1.0R_j$ to $0.95R_j$), perhaps sufficiently so that magnetic instabilities may still occur. If, instead, the magnitude of magnetic diffusivity makes the effective magnetic field strength negligible or weak, inertial or magnetically modified inertial instabilities may occur provided $fQ < 0$. The thesis does not contain analysis of the nonlinear evolution of the flow on the equatorial β-plane. However, if the instabilities are inertially driven we may presume from the results of Chapter 5 and Griffiths (2003a,b), that the vorticity will be redistributed poleward so that fQ is no longer sufficiently negative to drive instability and, in turn, reducing the anti-cyclonic shear present in the jet. Chapter 5 suggests the evolution of purely magnetic instabilities is less clear, but redistributes vorticity to the same effect.

8.3.3 Applications to the Upper Atmospheres of Hot Jupiters

Observations of Hot Jupiters imply the existence of strong equatorial jets, some of which flow close to the speed of sound (Showman *et al.*, 2013; Heng & Showman, 2015). This has important implications as flows on Hot Jupiters are therefore likely to be compressible; hence, modelling these flows as Boussinesq (and thus incompressible) is not ideal. However, the system is still less idealised than other studies (e.g., the shallow water models of Showman & Polvani, 2011).

The equatorial jets are inferred to reach mid-latitudes upwards of $30°$; it is therefore justifiable to model the flanks of these jets with a uniform shear flow $U(y) = \Lambda_0 y$ at mid-latitudes as is the

case in Chapters 3 and 4. Owing to the strong shear and slow rotation, the Rossby numbers on Hot Jupiters lie in the range $1 < \Lambda < 5$; we must therefore consider the inertially unstable regime (i.e., $\Lambda > 1$) at mid-latitudes.

The ideal linear analysis of Chapter 3 suggests the most unstable modes at mid-latitudes may be classified as strongly inertial in nature (given $\Lambda > 2$) or magnetically modified inertial instabilities (given $1 < \Lambda < 2$). The first yields vertical lengthscales $H = O(10^5 \text{m})$ and maximum growth rates $s_h \approx \sqrt{\Lambda_0 - f_0}$, while the second yields vertical lengthscales $H = O(10^4 \text{m})$ and maximum growth rates $s_m \approx \Lambda_0/2$. Assuming the diffusive parameters take similar values to those in Jupiter's upper atmosphere, we discuss the regime $Pr = 1$ and $Pm \ll 1$. Chapter 4 suggests that in this regime the magnetically modified inertial instabilities will no longer occur owing to large values of η and will instead become hydrodynamic (inertial) in nature. As a result, the instabilities are predicted to occur with scales heights $H = O(10^6 \text{m})$.

In terms of the nonlinear analysis, Chapter 5 suggests the instabilities, if they occur, depend crucially on the parameter $\mathcal{M}$, which is expected to be $O(10^{-3}) - O(1)$. Given the large Rossby numbers, magnetic field weaker than $\mathcal{M} = O(1)$ yields an evolution similar to the hydrodynamic system. That is, the latitudinal shear of the profile is reduced and the vorticity (and therefore momentum) is redistributed latitudinally. However, given $\mathcal{M} = O(1)$, changes to the mean flow and vorticity are much more significant since less anti-cyclonic shear is required for instability to occur.

We may also consider equatorial jets that are more confined to the equatorial atmosphere. In Chapters 6 and 7 the magnetic parameter M is expected to be $O(10^{-4}) - O(1)$, where the large interval arises from the sensitivity of the parameter M to the latitudinal shear Λ_0. We restrict our discussion of the ideal system to the more physically appropriate jet profile $U(y) = \Lambda_0 y - \delta y^2/2$, which was investigated in section 6.5. In this system, the most unstable mode occurred at large vertical wavenumber and weak magnetic field strength (relating once again to the "thin disc" and weak field assumptions of Balbus & Hawley, 1991). However, M is not necessarily small, so purely magnetic instabilities may occur with $K \approx O(10^{-1})$. This yields vertical lengthscales $H \approx O(10^7 \text{m})$–$O(10^8 \text{m})$ which are not physically appropriate; thus, instabilities are restricted by the atmospheric layer, implying they may no longer occur for $K < O(1)$ and by extension for $M > 1$. Taking the diffusive parameters for ν, κ and η from Jupiter, we once again expect that instabilities, if they occur, are dominated by inertial modes. However, chapter 7 implies that given sufficiently large κ or small η, then purely magnetic instabilities may occur as well as magnetically modified inertial modes.

8.4 Further Work

There are many possible extensions of the results in this thesis. We first discuss specific extensions highly relevant to the thesis, followed by more broad generalisations.

First, it is possible to extend the linear and nonlinear analysis of the hyperbolic shear flow in Chapter 5 by considering varying constraints on the Prandtl numbers (e.g., $Pr \neq Pm \neq 1$) rather than restricting to the case $Pr = Pm = 1$. This will allow us to consider ratios of Pr and Pm that are similar in magnitude to those found in astrophysical bodies, including the solar tachocline and the upper atmospheres of Jupiter and Hot Jupiters (found in table 2.1).

In Chapter 6 and Chapter 7 we considered the linear stability analysis of an eastward jet on an equatorial β-plane in the presence of uniform vertical magnetic field strength and uniform diffusion. It would be natural to consider the nonlinear evolution of this flow, as we did for the hyperbolic shear layer on the f-plane in Chapter 5. The analysis would be a natural extension to hydrodynamic studies of the nonlinear evolution of inertial instability on a an equatorial β-plane (Griffiths, 2003a,b). Physically, the analysis would be very applicable to the strong equatorial jets of Hot Jupiters.

There are also more broad extensions of this work. For example, one could consider a Coriolis parameter f, parallel flow U and vertical magnetic field B all arbitrarily dependent on the latitude y. This would be a natural extension to the hydrodynamic investigation of inertial instability made by Griffiths (2008a), who considered a Coriolis parameter and parallel flow both dependent on latitude. For example, in the absence of diffusion, analytical progress may be made by exploiting the tendency of the modes to prefer infinitesimally small scales (i.e., infinite vertical wavenumber).

We may also consider asymmetric perturbations about the basic state, extending the hydrodynamic analysis of Dunkerton (1983) and Griffiths (2008a). As a result, more complex field geometry may also be important (we found that the along-stream magnetic field in the basic state had no dynamical effect owing to the lack of field line curvature). It would also be natural to consider a non-magnetohydrostatic system, relating to many studies of geophysical flows (Clark & Haynes, 1996; Kloosterziel et al., 2007a,b). This will also give insight into the validity of the traditional approximation close to the equator, which has been discussed in application to the Earth's ocean by Kloosterziel et al. (2017). Finally, one could consider more complex flows that depend on height as well as latitude, yielding both latitudinal and vertical shear. Indeed, we have already seen a number of examples in Chapter 1, when discussing the hydrodynamic "diffusive destabilisation" in McIntyre (1970) and the magnetohydrodynamic stability results of Menou et al. (2004).

Appendix A

Derivations, Waves, and Other Results

A.1 The Analogies of Centrifugal and Inertial Instability

We initially derive the condition for instability in an inviscid and axisymmetric rotating flow, via a parcel argument in cylindrical geometry, with radial coordinate R and azimuthal coordinate θ. We consider a basic flow $V(R)$ in the azimuthal direction, where the pressure P opposes centrifugal effects, such that $\partial_R P = V^2/R$. Then, since $\partial_\theta = 0$ in an axisymmetric system, the azimuthal momentum equation gives that

$$\frac{Du_\theta}{Dt} + \frac{u_\theta u_R}{R} = -\frac{1}{R}\frac{\partial \tilde{p}}{\partial \theta} = 0, \tag{A.1}$$

where $\tilde{p}$ is the perturbed value of the pressure, u_R is radial velocity and u_θ is the azimuthal velocity. Here, we note that equation (A.1) corresponds to the conservation of angular momentum as it allows us to derive that

$$\frac{Du_\theta}{Dt} + \frac{u_\theta u_R}{R} = \frac{\partial u_\theta}{\partial t} + \frac{u_R}{R}\left(R\frac{\partial u_\theta}{dR} + u_\theta\right) = \frac{1}{R}\left(\frac{\partial(Ru_\theta)}{\partial t} + u_R\frac{\partial(Ru_\theta)}{dR}\right) = \frac{1}{R}\left(\frac{D(Ru_\theta)}{Dt}\right) = 0. \tag{A.2}$$

We must also consider the radial momentum equation

$$\frac{Du_R}{Dt} = -\frac{\partial \tilde{p}}{\partial R} + \frac{\tilde{V}^2}{R}, \tag{A.3}$$

where $\tilde{V}$ is the perturbed value of the azimuthal velocity. Thus, we consider a parcel that is displaced from R_0 to $R_0 + \delta R(t)$ such that it experiences a radial acceleration, while assuming that the parcel pressure gradient remains unchanged under the perturbation, so that

$$\frac{\partial \tilde{p}}{\partial R}(R_0 + \delta R) = \frac{dP}{dR}(R_0 + \delta R). \tag{A.4}$$

The final term of $(A.2)$ allows us to derive that $(R\tilde{V})|_{R_0+\delta R} = (RV)|_{R_0}$ for angular momentum to be conserved. Hence, using the expression for the conservation of angular momentum and equation $(A.4)$, it follows that $(A.3)$ becomes

$$\delta\ddot{R} = -\left.\frac{V^2}{R}\right|_{R_0+\delta R} + \left.\frac{(R\tilde{V})^2}{R^3}\right|_{R_0+\delta R} \approx \frac{1}{R_0^3}\left((RV)^2|_{R_0} - (RV)^2|_{R_0+\delta R}\right), \tag{A.5}$$

273

where we have approximated $R_0 + \delta R$ as R_0 in the denominator of both terms. Hence, by approximating the azimuthal flow $V(R)$ at $R_0 + \delta R$, via a Taylor expansion, equation (A.5) becomes

$$\delta \ddot{R} = -\frac{1}{R_0^3} \left.\frac{d(RV)^2}{dR}\right|_{R_0} \delta R. \tag{A.6}$$

Thus, we write (A.6) as

$$\delta \ddot{R} + \Phi_0 \delta R = 0, \tag{A.7}$$

where Φ_0 is (1.1) evaluated at $R = R_0$ (after using $V(R) = R\Omega(R)$), so that

$$\Phi_0 = \frac{1}{R_0^3} \left.\frac{d(RV)^2}{dR}\right|_{R_0} = \Phi(R_0). \tag{A.8}$$

Thus, the condition for inviscid axisymmetric instability is that $\Phi_0 < 0$. We note that the condition (A.7) is valid at any R_0, thus, it can be written in terms of R, giving (1.1).

It is useful to show that $fQ < 0$ is the Cartesian equivalent of the condition (1.1) since we will be considering planetary atmospheres under a Cartesian coordinate system. Hence, we derive the condition on fQ for instability in an inviscid and axisymmetric rotating flow with along-stream coordinate x and cross-stream coordinate y. We consider a basic flow $U(y)$ in the along-stream direction, where the pressure P satisfies $\partial_y P = -fU$, where $f(y)$ is the Coriolis parameter. Then, since $\partial_x = 0$ in an axisymmetric system, the along-stream momentum equation gives

$$\frac{Du}{Dt} - fv = -\frac{\partial \tilde{p}}{\partial x} = 0 \implies \frac{D}{Dt}\left(u - \int_0^y f(y)dy\right) = 0, \tag{A.9}$$

where u is the along-stream velocity, v is the cross-stream velocity and $\tilde{p}$ is the perturbed value of the pressure. Equation (A.9) corresponds to the conservation of angular momentum. The cross-stream momentum equation implies that

$$\frac{Dv}{Dt} = -\frac{\partial \tilde{p}}{\partial y} - f\tilde{u}, \tag{A.10}$$

where $\tilde{u}$ is the perturbed value of the along-stream velocity. Thus, we consider a parcel that is displaced from y_0 to $y_0 + \delta y(t)$ such that it experiences a cross-stream acceleration, while assuming that the parcel pressure gradient remains unchanged under the perturbation, so that

$$\frac{\partial \tilde{p}}{\partial y}(y_0 + \delta y) = \frac{dP}{dy}(y_0 + \delta y). \tag{A.11}$$

Considering the along-stream momentum equation (A.9) under the displacement allows us to derive that $\tilde{u}|_{y_0+\delta y} \approx U|_{y_0} + f|_{y_0}\delta y$ for angular momentum to be conserved. Hence, using the expression for the conservation of angular momentum and equation (A.11), it follows that (A.10) becomes

$$\delta \ddot{y} = f|_{y_0+\delta y}\left(U|_{y_0+\delta y} - \tilde{u}|_{y_0+\delta y}\right) = f|_{y_0+\delta y}\left(U|_{y_0+\delta y} - U|_{y_0} - f|_{y_0}\delta y\right). \tag{A.12}$$

Hence, by approximating the zonal flow $U(y)$ and Coriolis parameter $f(y)$ at $y = y_0 + \delta y$, via Taylor expansions, it follows that (A.12) becomes

$$\delta \ddot{y} \approx f|_{y_0}\left(\left.\frac{dU}{dy}\right|_{y_0} - f|_{y_0}\right)\delta y, \tag{A.13}$$

Thus, we write (A.13) as

$$\delta \ddot{y} + (fQ)_0 \delta y = 0, \tag{A.14}$$

where

$$(fQ)_0 = f|_{y_0} \left(f - \frac{dU}{dy} \right) \bigg|_{y_0}. \tag{A.15}$$

Thus, the condition for inviscid axisymmetric instability is that $(fQ)_0 < 0$, which is valid at any y_0, so the condition (A.14) can be written in terms of y. Hence, the condition on fQ is the Cartesian equivalent of the Rayleigh criterion (1.1).

A.2 Energetics

In this section we consider the evolution of energy of the system governed by the equations (2.14) to (2.18). To do this, it is convenient to write the momentum equations (2.14) to (2.17) in vector notation, given by

$$\frac{D\mathbf{u}}{Dt} + \mathbf{f} \times \mathbf{u} = -\frac{1}{\bar{\rho}}\nabla p - \frac{g\rho}{\bar{\rho}}\mathbf{e}_z + \nu\nabla^2\mathbf{u} + \frac{1}{\bar{\rho}}\,\mathbf{j} \times \mathbf{B}, \tag{A.16}$$

where $\mathbf{f} = (0, 0, f)$, p is the gas pressure and $\mathbf{j} = \mu_0^{-1}\nabla \times \mathbf{B}$ is the current. We have not absorbed the magnetic pressure into the pressure gradient for convenience. Note that the system is axisymmetric and magnetohydrostatic so that all x derivatives are zero and the vertical momentum equation reduces to the magnetohydrostatic balance.

A.2.1 Kinetic and Potential Energy

We begin by deriving the rate of change of the kinetic and potential energy of the system. To do this, we first consider the rate of change of kinetic energy, given by

$$\frac{\partial}{\partial t}\left(\frac{1}{2}\bar{\rho}|\mathbf{u}|^2\right) = \bar{\rho}\mathbf{u} \cdot \frac{\partial\mathbf{u}}{\partial t} = -\mathbf{u} \cdot \nabla\left(p + \frac{1}{2}\bar{\rho}|\mathbf{u}|^2\right) - g\rho w + \mu\mathbf{u} \cdot \nabla^2\mathbf{u} + \mathbf{u} \cdot \mathbf{j} \times \mathbf{B}, \tag{A.17}$$

where we have used equation (A.16). The rotational term $\mathbf{f} \times \mathbf{u}$ and $\mathbf{u} \times (\nabla \times \mathbf{u})$ (which results from the advection term) vanish owing to the dot product with $\mathbf{u}$. In order to determine the rate of change of potential energy we must introduce a t derivative of a function of ρ. Thus, by making use of (2.17), we obtain

$$\frac{D\rho}{Dt} + w\frac{d\rho_0(z)}{dz} = \kappa\nabla^2\rho \implies g\rho w = \frac{g^2}{N^2\bar{\rho}}\frac{D}{Dt}\left(\frac{\rho^2}{2}\right) - \frac{g^2\kappa}{\bar{\rho}N^2}\rho\nabla^2\rho, \tag{A.18}$$

using (2.13). Hence, by substituting (A.18) into (A.17) we obtain

$$\frac{\partial}{\partial t}\left(\frac{1}{2}\bar{\rho}|\mathbf{u}|^2 + \frac{1}{2}\frac{g^2}{\bar{\rho}N^2}\rho^2\right) = -\nabla \cdot \left(\left[p + \frac{1}{2}\frac{g^2}{N^2}\rho^2 + \frac{1}{2}\bar{\rho}|\mathbf{u}|^2\right]\mathbf{u}\right)$$
$$+ \frac{g^2\kappa}{\bar{\rho}N^2}\rho\nabla^2\rho + \mu\mathbf{u} \cdot \nabla^2\mathbf{u} + \mathbf{u} \cdot \mathbf{j} \times \mathbf{B}, \tag{A.19}$$

after making use of a vector identity and the incompressibility condition. Integrating over a fixed volume V with a stationary rigid boundary S, where $\mathbf{u} \cdot \mathbf{n} = 0$, yields

$$\frac{d}{dt} \int_V \left(\frac{1}{2} \bar{\rho} |\mathbf{u}|^2 + \frac{1}{2} \frac{g^2}{\bar{\rho} N^2} \rho^2 \right) dV = \frac{g^2 \kappa}{\bar{\rho} N^2} \int_V \rho \nabla^2 \rho \, dV$$
$$+ \mu \int_V \mathbf{u} \cdot \nabla^2 \mathbf{u} \, dV + \int_V \mathbf{u} \cdot \mathbf{j} \times \mathbf{B} \, dV. \quad \text{(A.20)}$$

We can make useful analytical progress from (A.20) by noting that

$$\int_V \mathbf{u} \cdot \nabla^2 \mathbf{u} \, dV = -\int_V \mathbf{u} \cdot \nabla \times \omega \, dV = \int_V \nabla \cdot (\mathbf{u} \times \omega) - |\omega|^2 \, dV = -\int_V |\omega|^2 \, dV, \quad \text{(A.21)}$$

via standard vector identities, the divergence theorem, $\mathbf{u} \cdot \mathbf{n} = 0$ and where $\omega = \nabla \times \mathbf{u}$ is the vorticity. We can also write $\rho \nabla^2 \rho = \nabla^2 (\rho^2/2) - |\nabla \rho|^2$, so that we can write

$$\int_V \rho \nabla^2 \rho \, dV = \int_V \nabla \cdot \nabla \left(\frac{1}{2} \rho^2 \right) - |\nabla \rho|^2 \, dV = -\int_V |\nabla \rho|^2 \, dV, \quad \text{(A.22)}$$

by the divergence theorem and that $\mathbf{n} \cdot \nabla(\rho^2/2)$ is zero on the surface S, since there is no heat flux.

Hence, by making use of (A.21) and (A.22), (A.20) becomes

$$\frac{d}{dt} \int_V \left(\frac{1}{2} \bar{\rho} |\mathbf{u}|^2 + \frac{1}{2} \frac{g^2}{\bar{\rho} N^2} \rho^2 \right) dV = -\mu \int_V |\omega|^2 \, dV$$
$$- \frac{g^2 \kappa}{\bar{\rho} N^2} \int_V |\nabla \rho|^2 \, dV + \int_V \mathbf{u} \cdot \mathbf{j} \times \mathbf{B} \, dV. \quad \text{(A.23)}$$

Equation (A.23) governs the rate of change of kinetic and magnetic energy in the system. The three terms on the right hand side of (A.23) denote the dissipation through the flow vorticity, the loss in potential energy due to thermal diffusion distributing the flow density, and the rate of gain of kinetic energy due to the rate of working of the Lorentz force, respectively.

A.2.2 Magnetic Energy

We now proceed to determine the rate of change of magnetic energy in the system. Indeed, the rate of energy of magnetic field in a fixed volume V is given by

$$\frac{d}{dt} \left(\frac{1}{2\mu_0} \int_V |\mathbf{B}|^2 dV \right) = \frac{1}{\mu_0} \int_V \mathbf{B} \cdot \frac{\partial \mathbf{B}}{\partial t} \, dV = -\frac{1}{\mu_0} \int_V \mathbf{B} \cdot \nabla \times \mathbf{E} \, dV, \quad \text{(A.24)}$$

where we have used Faraday's Law. To make useful analytical progress we note that by a standard vector identity, followed by Ampere's law and then Ohm's law (as well as a second vector identity), we obtain

$$\mathbf{B} \cdot \nabla \times \mathbf{E} = \nabla \cdot (\mathbf{E} \times \mathbf{B}) + \mathbf{E} \cdot \nabla \times \mathbf{B}$$
$$= \nabla \cdot (\mathbf{E} \times \mathbf{B}) + \mu_0 \mathbf{E} \cdot \mathbf{j} = \nabla \cdot (\mathbf{E} \times \mathbf{B}) + \frac{\mu_0}{\sigma} |\mathbf{j}|^2 + \mu_0 \mathbf{u} \cdot (\mathbf{j} \times \mathbf{B}). \quad \text{(A.25)}$$

Hence, by substituting (A.25) into (A.24) and using the divergence theorem, it follows that

$$\frac{d}{dt} \left(\frac{1}{2\mu_0} \int_V |\mathbf{B}|^2 dV \right) = -\frac{1}{\sigma} \int_V |\mathbf{j}|^2 dV - \int_V \mathbf{u} \cdot (\mathbf{j} \times \mathbf{B}) \, dV - \int_S \mathbf{P} \cdot d\mathbf{S}, \quad \text{(A.26)}$$

where $\mathbf{P} = (\mathbf{E} \times \mathbf{B})/\mu_0$ is the Poynting vector. The three terms on the right hand side denote, respectively, the dissipation through electric currents (Joule dissipation), the rate of loss of magnetic energy due to the rate of working of the Lorentz force, and the rate at which magnetic energy flows out through the surface S.

A.2.3   Total Energy

Here we derive the rate of change of the total energy E in the system. Indeed, by combining the expressions (A.23) and (A.26) for the rate of change of kinetic, potential and magnetic energies, we obtain the rate of change of total energy, given by

$$
\frac{dE}{dt} = \frac{d}{dt} \int_V \left(\frac{1}{2}\bar{\rho}|\mathbf{u}|^2 + \frac{1}{2}\frac{g^2}{\bar{\rho}N^2}\rho^2 + \frac{1}{2\mu_0}|\mathbf{B}|^2 \right) dV = -\mu \int_V |\omega|^2 \, dV
$$
$$
- \frac{g^2\kappa}{\bar{\rho}N^2} \int_V |\nabla\rho|^2 \, dV - \frac{1}{\sigma} \int_V |\mathbf{j}|^2 dV - \int_S \mathbf{P} \cdot d\mathbf{S}. \quad \text{(A.27)}
$$

Thus, the magnetic energy lost owing to the rate of working of the Lorentz force in (A.26) is balanced by the rate of kinetic energy gained from the working of the Lorentz force on the flow in (A.23). Note that since the system is axisymmetric, the volume and surface integrals in equation (A.27) can be equivalently written as surface and line integrals, respectively.

A.3   Hydrodynamic Equatorial Waves

In Chapter 6 we discussed the dynamical balances in various limits of the system, focusing on the equatorial instabilities present. Here we discusses the dynamical balances of hydrodynamic equatorial gravity and inertia-gravity waves.

A.3.1   Equatorial Gravity Waves

We now consider the dynamical balance of equatorial gravity waves, which occur in the small K limit. Thus, assuming that $K \ll 1$, it follows from (6.41) that $u \sim v$ and that the frequency $\hat{\omega} = -iS \sim 1/\sqrt{K}$, so that (6.41) reduces to

$$
Su - \frac{Y}{\sqrt{K}}v = 0, \quad Sv + \frac{Y}{\sqrt{K}}u = \frac{K^{-1}}{S}(Y^2 - 1)v, \quad \text{(A.28)}
$$

since $|Y|/\sqrt{K} \gg 1$. To illustrate the dynamical balance (A.28) we plot the terms of the horizontal momentum equations in figure A.1 for $K = 0.1$. The equator, the central latitude C (given in equation (6.5)) and latitude $C = 1$ (which is the minimum of the absolute vorticity $fQ = \beta y(\beta y - \Lambda_0)$ in nondimensional form) are represented by a dashed line, dotted line and crosses respectively. We shall retain this convention for all hydrodynamic and magnetohydrodynamic figures. It is important to note that the central latitude of every hydrodynamic mode coincides with the minimum of fQ ($C = 1$).
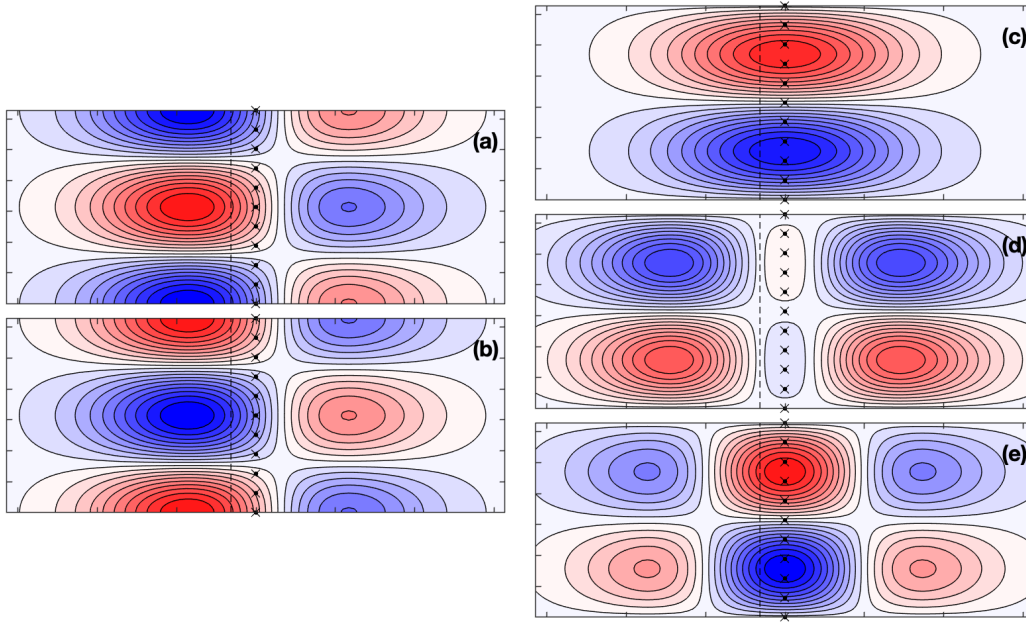
Figure A.1: The dynamical balance of (A.28) plotted for $K = 0.1$, illustrating a hydrodynamic equatorial gravity wave with frequency $\hat{\omega} = 3.0$. The mode has central latitude $C = 1$ and length-scale $\hat{L} = 3.1623$. Plot (**a**) shows the along-stream acceleration. Plot (**b**) shows the combination of the advection and Coriolis terms. Plots (**c**), (**d**), and (**e**) show the cross-stream acceleration, Coriolis force and pressure gradient.

A.3.2   Equatorial Inertia-gravity Waves

We next consider the dynamical balance of equatorial inertia-gravity waves, which occur when $K < 1$ and $K = O(1)$. We retain the hydrodynamic balance (6.41) with $\hat{\omega}^2 = -S^2 = -1 + 1/K$; however, as $K \to 1^-$ there is a special case as we approach neutral stability ($S^2 \to 0^-$). Thus, supposing $S \ll 1$, it follows that (6.41) reduces to

$$Su - (Y - 1)\,v = 0, \quad (Y + 1)\,u = \frac{1}{S}(Y^2 - 1)v, \tag{A.29}$$

where $u \sim v/S$. Hence, as we approach neutral stability, there is geostrophic balance in the cross-stream direction as there is no longer any cross-stream acceleration. The two equations in (A.29) are equivalent, so one must retain the second order term Sv along with the factors of K to yield the balance (6.41) and the frequency squared $\hat{\omega}^2 = -S^2 = 1/K - 1 \ll 1$. To illustrate the neutral stability limit as well as typical inertia-gravity waves we once again plot the horizontal momentum equations in figure A.2 for $K = 0.75$, which illustrates the dynamical balance of typical equatorial inertial waves with $K = O(1)$. However, we can also compare figure A.2 to figure A.1, where it is evident that as K increases, we approach geostrophic balance in the cross-stream direction, as predicted by (A.29). The frequency of the wave also decreases as K increases.
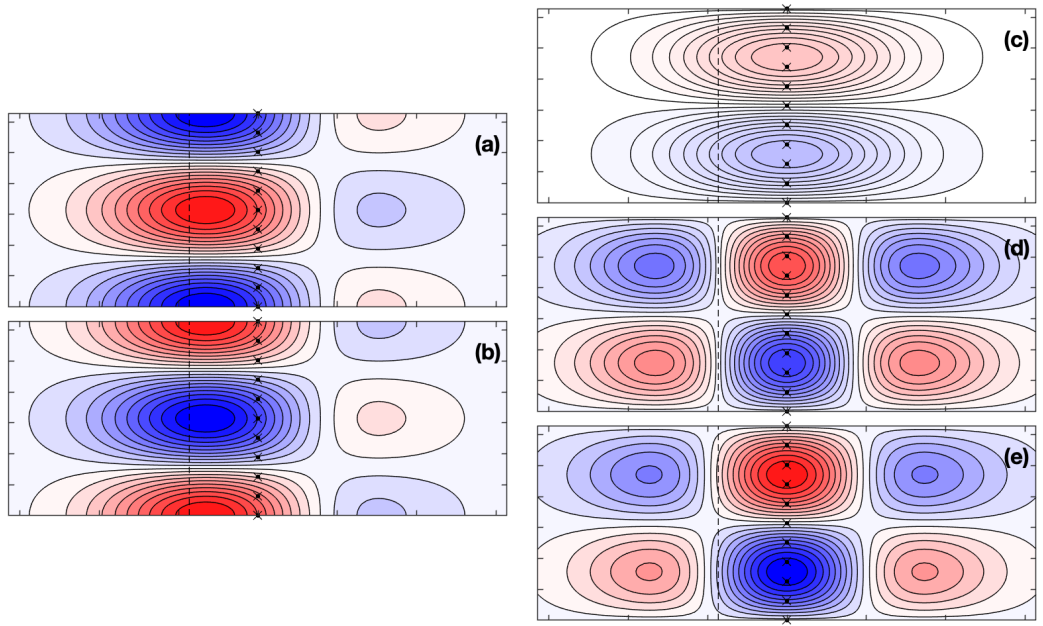
Figure A.2: The dynamical balance of (A.29) plotted for $K = 0.75$, illustrating a hydrodynamic equatorial inertia-gravity wave with frequency $\hat{\omega} = 0.5774$. The mode has central latitude $C = 1$ and lengthscale $\hat{L} = 1.1547$. Plot (**a**) shows the along-stream acceleration. Plot (**b**) shows the combination of the advection and Coriolis terms. Plots (**c**), (**d**), and (**e**) show the cross-stream acceleration, Coriolis force and pressure gradient.

A.4   Magnetohydrodynamic Equatorial Waves

In Chapter 6 we discussed the dynamical balances in various limits of the system, focusing on the magnetohydrodynamic equatorial instabilities present. Here we discusses the dynamical balance of equatorial magnetic, Alfvén, and magnetically modified inertia-gravity waves.

A.4.1   Magnetohydrodynamic Balances

We now consider the dynamical balances of the magnetohydrodynamic regime, where we shall systematically categorise the various limiting cases as seen in figure 6.2. First, we will address equatorial waves, including magnetic and magnetically modified waves. Secondly, we will address the magnetically modified equatorial instabilities as well as purely magnetic instabilities in the weak and strong magnetic field regimes.

A.4.2   Magnetically Modified Equatorial Inertia-gravity Waves

We first discuss magnetically modified equatorial waves, which occur in the hydrodynamically stable regime ($K < 1$) with $K = O(1)$ in the limit of weak magnetic field ($M \ll 1$). To isolate the hydrodynamic mode we assume that $S = O(1)$, which is implied by the leading order term of the hydrodynamic expansion (6.34). This yields $C = 1$ and $\hat{L} = 1/\sqrt{K}$ at leading order.

These assumptions allow us to deduce from equations (6.38) and (6.39) that $u \sim \theta \sim v$ and $b_y \sim b_x \sim Mv$. Thus, equations (6.38) and (6.39) reduce to

$$Su - \left(\frac{Y}{\sqrt{K}} - 1\right)v = 0, \quad Sv + \left(\frac{Y}{\sqrt{K}} + 1\right)u = \frac{K^{-1}}{S}(Y^2 - 1)v, \tag{A.30a}$$

$$Sb_x = 2b_y + iKMu, \quad Sb_y = iKMv, \tag{A.30b}$$

which represent the hydrodynamic dynamical balance (6.41). However, the weak magnetic field expansion of the hydrodynamic mode (6.34) implies that weak field increases the frequency of the hydrodynamically stable system. Hence, to categorise the stabilising mechanism of magnetic field, we must include the second order terms in (A.30). Note that, if $K \to 0$, the balance would be that of equatorial gravity waves at leading order. We also note that the balance (A.30) describes hydrodynamic unstable modes ($K < 1$) in the limit of weak magnetic field ($M \ll 1$).

Now, to address the stabilising mechanism, we must evaluate the Lorentz forces, F, and the correction to the pressure gradient in terms of v, using the leading order hydrodynamic frequency squared $\hat{\omega}^2 = -S^2 = -1 + 1/K$, and the balance (6.41). First, it follows from the cross-stream induction equation in (6.39) that the cross-stream Lorentz force $iMKb_y = -M^2K^2v/S$, which is always stabilising as it always acts to increase the cross-stream acceleration when $S^2 < 0$. Similarly, we can deduce that the $O(M^2)$ contribution from the cross-stream pressure gradient takes the same sign as the leading order term and therefore increases the frequency of the system. The along-stream Lorentz force can be written as

$$iKMb_x = \frac{iKM}{S}(2b_y + iKMu) = -\frac{K^2M^2}{S^2}\left(2 + \frac{1}{Y/\sqrt{K} + 1}\left((Y^2 - 1)/K - S^2\right)\right)v, \tag{A.31}$$

where, if we use the leading order expansion for the square of the hydrodynamic growth rate, $S^2 = 1 - 1/K$, it follows that

$$iKMb_x = -\frac{K^2M^2}{S^2}\left(1 + \frac{Y}{\sqrt{K}}\right)v. \tag{A.32}$$

Thus, the along-stream Lorentz force (A.32) acts against the term $(Y/\sqrt{K} - 1)v$ (resulting from the Coriolis and advection terms) when $-\sqrt{K} < Y < \sqrt{K}$ and acts with the term otherwise. Hence, to determine whether the sum of second order contributions from F, the Lorentz force, and the pressure gradient increase or decrease the frequency we must combine the momentum equations (including their second order corrections) to categorise the role of weak magnetic field. Thus, we expand F as

$$F \approx 1 + \frac{Y}{\sqrt{K}} + \frac{K^2M^2}{S^2}\left(1 + \frac{Y}{4\sqrt{K}}\right), \tag{A.33}$$

where, by considering all $O(M^2)$ terms in the along-stream momentum equation in (6.38), we obtain a second order correction to the along-stream acceleration, given by

$$Su - \left(\frac{Y}{\sqrt{K}} - 1\right)v = -\frac{3K^2M^2}{4(1 - 1/K)}\frac{Y}{\sqrt{K}}v. \tag{A.34}$$

280

Hence, we can substitute (A.34) into the cross-stream momentum equation via Fu and equate $O(M^2)$ terms to obtain the correction to the cross-stream acceleration, namely

$$(Sv)_{\text{correction}} = -\frac{3K}{2S^3}. \tag{A.35}$$

Thus, considering stable modes so that $S^2 < 0$, it follows that the magnetic correction to the hydrodynamic system (6.41) increases the frequency, since the combination of the M^2 corrections from F, the pressure gradient and cross-stream Lorentz force always act to increase the cross-stream acceleration. We can also note that the correction (A.35) is valid in the hydrodynamically unstable regime ($S^2 > 0$); however, we will discuss the instability in a later subsection.

To confirm the dynamical balance and determine the role of each term, we plot the along-stream momentum, cross-stream momentum and the component of the along-stream induction equations in figure A.3 with $K = 0.75$ and $M = 0.3$ (so that the effect of magnetic field can be seen). Once again, recall that the equator, the hydrodynamic central latitude and the minimum of fQ are represented by a dashed line, a dotted line and a crossed line, respectively. In contrast to the hydrodynamic case, we see that the central latitude of the mode no longer necessarily occurs at the minimum of fQ ($C = 1$). In figure A.3 we see that the along-stream Lorentz force acts against $-(F - 2)v$ (the Coriolis and advection term) when $-\sqrt{K} < Y < \sqrt{K}$ and acts with $-(F - 2)v$ otherwise, as predicted. We can also see that the cross-stream Lorentz force acts to drive the cross-stream acceleration and therefore increasing the frequency. This is indeed the case, which can be seen when comparing the hydrodynamic frequency $\hat{\omega} = 0.5774$ to the frequency of figure A.3 with $M = 0.3$, which is $\hat{\omega} = 0.775$.

A.4.3 Magnetic Equatorial Waves

We now address the hydrodynamically unstable regime ($K > 1$), where the introduction of weak magnetic field allows for the existence of a magnetic equatorial wave. To isolate the magnetic mode we suppose $S \ll 1$ with $M \ll 1$ and $K = O(1)$. These assumptions allows us to deduce from equations (6.38) and (6.39) that $u \sim b_x \sim v/M$ and $b_y \sim v$. The Coriolis term F, central latitude C and lengthscale $\hat{L}$ do not simplify in this case since $S \sim M$, as implied by the weak magnetic field expansion (6.35); note that we do not assume this at onset. In this limit equations (6.38) and (6.39) reduce to

$$Su - (F - 2)\,v = iKMb_x, \;\; Fu = \frac{K^{-1}C^{-1/2}}{S}(Y^2 - 1)v, \;\; Sb_x = 2b_y + iKMu, \;\; Sb_y = iKMv, \tag{A.36}$$

where we have evaluated the pressure gradient in terms of v via the thermodynamic and incompressibility equation in (6.38). The equations of (A.36) can be combined to give the growth rate squared $S^2 = K^{8/3}M^2/(1 - K^{2/3})$ which is consistent with the weak magnetic field expansion (6.35) with $n = 0$. Thus, in the hydrodynamically unstable regime with $K = O(1)$ and $M \ll 1$ we attain geostrophic balance in the cross-stream direction, while retaining all other terms. Thus, to confirm the dynamical balance and determine the role of each term, we plot the along-stream momentum, cross-stream momentum and the along-stream induction equations in figure A.4.
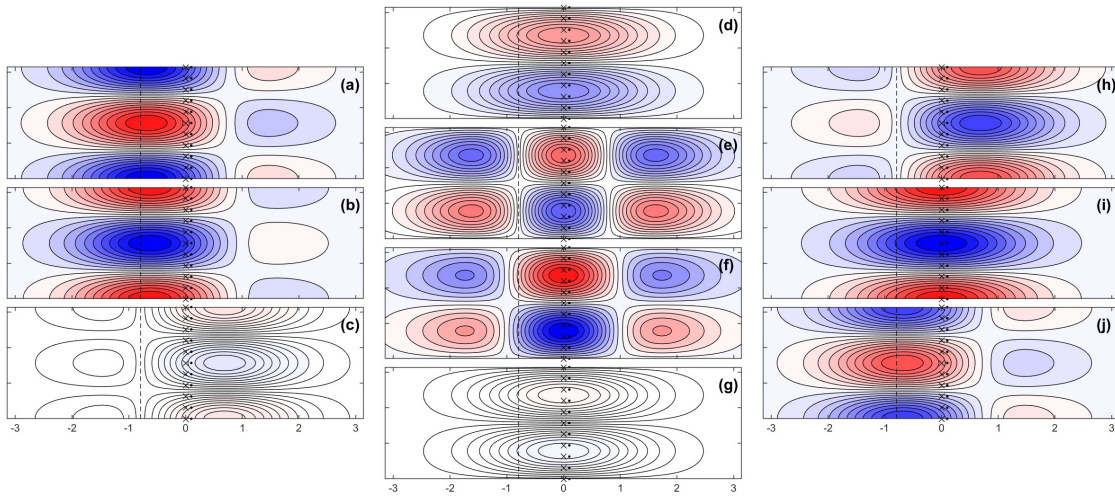
Figure A.3: The dynamical balance of (A.30) plotted for $K = 0.75$ and $M = 0.3$, illustrating a magnetically modified equatorial wave in the hydrodynamically stable regime ($K < 1$) with frequency $\hat{\omega} = 0.775$. The mode has central latitude $C = 0.8853$ and lengthscale $\hat{L} = 1.1201$. Plots (**a**), (**b**) and (**c**) show the along-stream acceleration, advection and Coriolis terms, and Lorentz force. Plots (**d**), (**e**), (**f**) and (**g**) show the cross-stream acceleration, Coriolis force, pressure gradient and Lorentz force. Plots (**h**), (**i**) and (**j**) show the along-stream field generation, advection and tension terms.
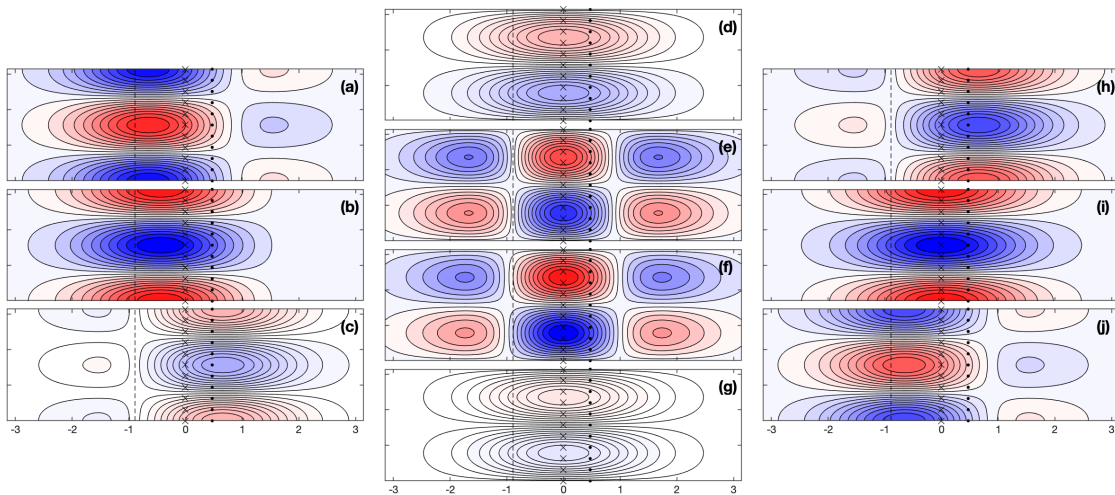
Figure A.4: The dynamical balance of (A.36) plotted for $K = 1.5$ and $M = 0.2$, illustrating a magnetohydrodynamic equatorial wave in the hydrodynamically unstable regime ($K > 1$) with frequency $\hat{\omega} = 0.5101$. The mode has central latitude $C = 0.6541$ and lengthscale $\hat{L} = 0.7343$. Plots (**a**), (**b**) and (**c**) show the along-stream acceleration, advection and Coriolis terms, and Lorentz force. Plots (**d**), (**e**), (**f**) and (**g**) show the cross-stream acceleration, Coriolis force, pressure gradient and Lorentz force. Plots (**h**), (**i**) and (**j**) show the along-stream field generation, advection and tension terms.
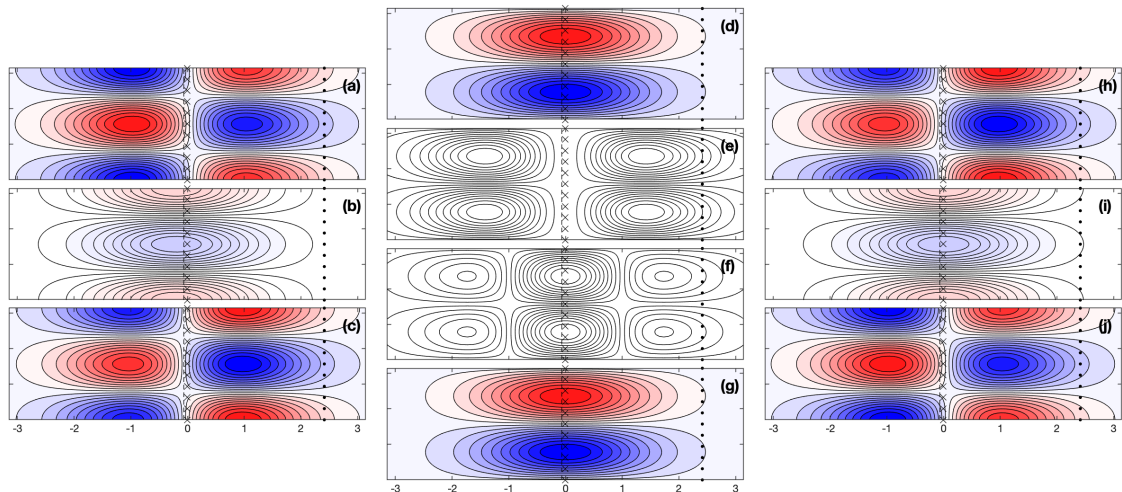
Figure A.5: The dynamical balance of (A.37) plotted for $K = 1.0$ and $M = 15$, illustrating an equatorial Alfvénic wave with frequency $\hat{\omega} = 15.2026$. The mode has central latitude $C = 0.0265$ and lengthscale $\hat{L} = 0.4034$. Plots (**a**), (**b**) and (**c**) show the along-stream acceleration, advection and Coriolis terms, and Lorentz force. Plots (**d**), (**e**), (**f**) and (**g**) show the cross-stream acceleration, Coriolis force, pressure gradient and Lorentz force. Plots (**h**), (**i**) and (**j**) show the along-stream field generation, advection and tension terms.

A.4.4 Equatorial Alfvén Waves

We now address the stable mode of the large M limit, where we expect Alfvénic behaviour. To isolate the Alfvénic mode we suppose $S^2 \to -\infty$ with $M \to \infty$ and $K = O(1)$. These assumptions allows us to deduce from equations (6.38) and (6.39) that $S^2 \sim -M^2$, where, as a result, C and F are small, with $u \sim b_x \sim b_y \sim v$ and $\theta \sim v/S$. Hence, equations (6.38) and (6.39) reduce to

$$Su = iKMb_x, \quad Sv = iKMb_y, \quad Sb_x = iKMu, \quad Sb_y = iKMv, \tag{A.37}$$

which combine to give $S^2 = -K^2M^2$, which is consistent with Alfvén waves. To illustrate the dynamical balance (A.37) we plot the along-stream momentum, cross-stream momentum and the components of along-stream induction equations in figure A.5. Clearly, the momentum equations are in Alfvénic balance, while the along-stream field is driven primarily by the magnetic stretching generated by the along-stream velocity. The figure shows that the central latitude and the lengthscale of the mode are very small, which is consistent with (6.3), where the lengthscale and the central latitude are $O(M^{-\frac{1}{3}})$ and $O(M^{-\frac{4}{3}})$, respectively. Hence, the Alfvénic mode is locked around the equator where the perturbed along-stream velocity takes the form $u \propto Y \exp(-Y^2)$.

References

ACHESON, D.J. & HIDE, R. (1973). Hydromagnetics of rotating fluids. *Reports on Progress in Physics*, **36**, 159–221. 23, 43, 44, 45, 47, 49, 51, 82, 198, 214

ADAM, J.A. (1980). Eigenvalue bounds in magnetoatmospheric shear flow. *Journal of Physics A: Mathematical and General*, **13**, 3325. 14

AFANASYEV, Y.D. & PELTIER, W.R. (1998). Three-dimensional instability of anticyclonic swirling flow in rotating fluid: laboratory experiments and related theoretical predictions. *Physics of Fluids*, **10**, 3194–3202. 14

ARMSTRONG, D.J., DE MOOIJ, E., BARSTOW, J. *et al.* (2016). Variability in the atmosphere of the hot giant planet HAT-p-7 b. *Nature Astronomy*, **1**, 1–7. 4, 217

BALBUS, S.A. & HAWLEY, J.F. (1991). A powerful local shear instability in weakly magnetized disks. I-Linear analysis. II-Nonlinear evolution. *The Astrophysical Journal*, **376**, 214–233. 1, 15, 16, 17, 19, 20, 21, 22, 23, 26, 38, 39, 43, 44, 52, 53, 54, 60, 61, 71, 82, 147, 148, 191, 265, 266, 267, 269, 270, 271

BALBUS, S.A. & HAWLEY, J.F. (1992). A powerful local shear instability in weakly magnetized disks. IV. Nonaxisymmetric perturbations. *Astrophysical Journal*, **400**, 610–621. 20, 153, 170

BARKER, A.J., JONES, C.A. & TOBIAS, S.M. (2019). Angular momentum transport by the GSF instability: non-linear simulations at the equator. *Monthly Notices of the Royal Astronomical Society*, **487**, 1777–1794. 11, 12

BARKER, A.J., JONES, C.A. & TOBIAS, S.M. (2020). Angular momentum transport, layering, and zonal jet formation by the GSF instability: non-linear simulations at a general latitude. *Monthly Notices of the Royal Astronomical Society*, **495**, 1468–1490. 12

BENDER, C.M. & ORSZAG, S.A. (1978). *Advanced mathematical methods for scientists and engineers*. McGraw-Hill. 195, 196, 231, 232

BERRIER, J.C. & SELLWOOD, J.A. (2015). Smoothing rotation curves and mass profiles. *The Astrophysical Journal*, **799**, 213. 4

BOUSSINESQ, J. (1903). *Théorie analytique de la chaleur: mise en harmonie avec la thermodynamique et avec la théorie mécanique de la lumière*, vol. 2. Gauthier-Villars. 27

BOWKER, J.A., HUGHES, D.W. & KERSALÉ, E. (2014). Incorporating velocity shear into the magneto-Boussinesq approximation. *Geophysical & Astrophysical Fluid Dynamics*, **108**, 553–567. 28

CALLY, P.S. (1983). Complex eigenvalue bounds in magnetoatmospheric shear flow. I. *Geophysical & Astrophysical Fluid Dynamics*, **23**, 43–55. 14

CARNEVALE, G.F., KLOOSTERZIEL, R.C. & ORLANDI, P. (2016). Equilibration of centrifugally unstable vortices: A review. *European Journal of Mechanics-B/Fluids*, **55**, 246–258. 13

CAULEY, P.W., SHKOLNIK, E.L., LLAMA, J. & LANZA, A.F. (2019). Magnetic field strengths of hot Jupiters from signals of star-planet interactions. *Nature Astronomy*, **3**, 1128–1134. 4, 41

CHANDRASEKHAR, S. (1960). The stability of non-dissipative Couette flow in hydromagnetics. *Proceedings of the National Academy of Sciences of the United States of America*, **46**, 253–7. 15, 16, 19, 21, 22, 26, 36, 38, 39

CHANDRASEKHAR, S. (1961). Hydrodynamic and Hydromagnetic Stability, 652 pp., Clarendon. 28

CHARNEY, J.G. (1947). The dynamics of long waves in a baroclinic westerly current. In *The Atmosphere—A Challenge*, 223–250, Springer. 5

CHRISTENSEN, U.R., WICHT, J. & DIETRICH, W. (2020). Mechanisms for limiting the depth of zonal winds in the gas giant planets. *The Astrophysical Journal*, **890**, 61. 3

CHRISTENSEN-DALSGAARD, J. (2002). Helioseismology. *Reviews of Modern Physics*, **74**, 1073. 40

CHRISTENSEN-DALSGAARD, J. & THOMPSON, M.J. (2007). Observational results and issues concerning the tachocline. In D.W. Hughes, R. Rosner & N.O. Weiss, eds., *The Solar Tachocline*, 53–86, Cambridge University Press. 40

CLARK, P.D. & HAYNES, P.H. (1996). Inertial instability on an asymmetric low-latitude flow. *Quarterly Journal of the Royal Meteorological Society*, **122**, 151–182. 12, 272

CONNERNEY, J.E.P. (1993). Magnetic fields of the outer planets. *Journal of Geophysical Research: Planets*, **98**, 18659–18679. 3

CONNERNEY, J.E.P., KOTSIAROS, S. *et al.* (2018). A new model of Jupiter's magnetic field from Juno's first nine orbits. *Geophysical Research Letters*, **45**, 2590–2596. 40

CONNERNEY, J.E.P., TIMMINS, S. *et al.* (2022). A new model of Jupiter's magnetic field at the completion of Juno's Prime Mission. *Journal of Geophysical Research: Planets*, **127**, e2021JE007055. 3

COOPER, C.S. & SHOWMAN, A.P. (2005). Dynamic meteorology at the photosphere of hd 209458b. *The Astrophysical Journal*, **629**, L45. 4

CORREIA, A.C.M., LASKAR, J. & DE SURGY, O.N. (2003). Long-term evolution of the spin of Venus: I. theory. *Icarus*, **163**, 1–23. 4

DANG, L., COWAN, N.B., SCHWARTZ, J.C. *et al.* (2018). Detection of a westward hotspot offset in the atmosphere of hot gas giant CoRoT-2b. *Nature Astronomy*, **2**, 220–227. 4, 217

DEBRAS, F. & CHABRIER, G. (2019). New models of Jupiter in the context of Juno and Galileo. *The Astrophysical Journal*, **872**, 100. 3, 40

DEEG, H.J. & ALONSO, R. (2018). Transit photometry as an exoplanet discovery method. *arXiv preprint arXiv:1803.07867*. 41

DELUCA, E.E. & GILMAN, P.A. (1986). Dynamo theory for the interface between the convection zone and the radiative interior of a star: Part I model equations and exact solutions. *Geophysical & Astrophysical Fluid Dynamics*, **37**, 85–127. 30

DEMORY, B. & SEAGER, S. (2011). Lack of inflated radii for Kepler giant planet candidates receiving modest stellar irradiation. *The Astrophysical Journal Supplement Series*, **197**, 12. 4, 41

D'ORGEVILLE, M., HUA, B.L., SCHOPP, R. & BUNGE, L. (2004). Extended deep equatorial layering as a possible imprint of inertial instability. *Geophysical Research Letters*, **31**. 7, 21, 193

DRAZIN, P.G. & REID, W.H. (2004). *Hydrodynamic stability*. Cambridge University Press. 5

DUNKERTON, T.J. (1981). On the Inertial Stability of the Equatorial Middle Atmosphere. *Journal of the Atmospheric Sciences*, **38**, 2354–2364. 6, 7, 9, 10, 12, 21, 23, 32, 35, 39, 52, 54, 56, 65, 85, 193, 195, 196, 198, 200, 207, 230, 231, 232, 233, 236, 262, 265

DUNKERTON, T.J. (1982). The double-diffusive modes of symmetric instability on an equatorial *beta*-plane. *Journal of the Atmospheric Sciences*, **39**, 1653–1657. 7, 21, 23, 24, 32, 85, 92, 96, 230, 233, 237, 238, 262, 265, 267

DUNKERTON, T.J. (1983). A nonsymmetric equatorial inertial instability. *Journal of the Atmospheric Sciences*, **40**, 807–813. 12, 21, 265, 272

DUNKERTON, T.J. (1993). Inertial instability of nonparallel flow on an equatorial β-plane. *Journal of Atmospheric Sciences*, **50**, 2744–2758. 12, 265

DURRAN, D.R. (1991). The third-order Adams-Bashforth method: An attractive alternative to leapfrog time differencing. *Monthly weather review*, **119**, 702–720. 154

DYMOTT, R.W., BARKER, A.J., JONES, C.A. & TOBIAS, S.M. (2023). Linear and non-linear properties of the Goldreich–Schubert–Fricke instability in stellar interiors with arbitrary local radial and latitudinal differential rotation. *Monthly Notices of the Royal Astronomical Society*, **524**, 2857–2882. 12

EADY, E.T. (1949). Long waves and cyclone waves. *Tellus*, **1**, 33–52. 5

ESPINOZA, N., RABUS, M. *et al.* (2017). K2-113: a dense hot-Jupiter transiting a solar analogue. *Monthly Notices of the Royal Astronomical Society*, **471**, 4374–4380. 41

FRENCH, M., BECKER, A., LORENZEN, W., NETTELMANN, N., BETHKENHAGEN, M., WICHT, J. & REDMER, R. (2012). Ab initio simulations for material properties along the Jupiter adiabat. *The Astrophysical Journal Supplement Series*, **202**, 5. 3, 40, 139

FRICKE, K. (1968). Instabilität stationärer rotation in sternen. *Zeitschrift fur Astrophysik*, **68**, 317. 11, 17, 18, 23, 86, 102, 114, 118, 139, 230, 240, 262, 266, 267

GALLAIRE, F. & CHOMAZ, J. (2003). Three-dimensional instability of isolated vortices. *Physics of Fluids*, **15**, 2113–2126. 14

GAMMIE, C.F. & BALBUS, S.A. (1994). Quasi-global, linear analysis of a magnetized disc. *Monthly Notices of the Royal Astronomical Society*, **270**, 138–152. 17

GASTINE, T. & WICHT, J. (2021). Stable stratification promotes multiple zonal jets in a turbulent jovian dynamo model. *Icarus*, **368**, 114514. 3, 40

GERKEMA, T., ZIMMERMAN, J.T.F., MAAS, L.R.M. & VAN HAREN, H. (2008). Geophysical and astrophysical fluid dynamics beyond the traditional approximation. *Reviews of Geophysics*, **46**. 31

GILL, A.E. (1982). *Atmosphere-ocean dynamics*, vol. 30. Academic press. 198

GILMAN, P.A. (2000). Magnetohydrodynamic "shallow water" equations for the solar Tachocline. *The Astrophysical Journal Letters*, **544**, L79. 30

GOLDREICH, P. & SCHUBERT, G. (1967). Differential rotation in stars. *The Astrophysical Journal*, **150**, 571. 11, 17, 18, 23, 86, 102, 114, 118, 139, 230, 240, 262, 266, 267

GOUGH, D. (2007). An introduction to the solar tachocline. In D.W. Hughes, R. Rosner & N.O. Weiss, eds., *The Solar Tachocline*, 3–30, Cambridge University Press. 2, 40, 268

GRIESSMEIER, J.M., STADELMANN, A. *et al.* (2004). The effect of tidal locking on the magnetospheric and atmospheric evolution of "hot Jupiters". *Astronomy & Astrophysics*, **425**, 753–762. 4

GRIFFITHS, S.D. (2003a). The nonlinear evolution of zonally symmetric equatorial inertial instability. *Journal of Fluid Mechanics*, **474**, 245–273. 8, 10, 21, 23, 24, 32, 39, 56, 93, 142, 145, 158, 162, 191, 192, 200, 230, 232, 233, 236, 262, 265, 267, 270, 272

GRIFFITHS, S.D. (2003b). Nonlinear vertical scale selection in equatorial inertial instability. *Journal of the Atmospheric Sciences*, **60**, 977–990. 8, 9, 12, 13, 21, 23, 32, 141, 158, 191, 192, 233, 235, 265, 270, 272

GRIFFITHS, S.D. (2008a). The limiting form of inertial instability in geophysical flows. *Journal of Fluid Mechanics*, **605**, 115–143. 9, 12, 21, 24, 26, 31, 32, 35, 37, 39, 52, 54, 65, 101, 117, 130, 141, 145, 146, 265, 267, 272

GRIFFITHS, S.D. (2008b). Weakly diffusive vertical scale selection for the inertial instability of an arbitrary shear flow. *Journal of Fluid Mechanics*, **594**, 265–268. 85

GUILLOT, T., STEVENSON, D.J., HUBBARD, W.B. & SAUMON, D. (2004). The interior of Jupiter. In F. Bagenal, T.E. Dowling & W.B. McKinnon, eds., *Jupiter. The Planet, Satellites and Magnetosphere*, vol. 1, 35–57, Cambridge University Press. 3

HARVEY, V.L. & KNOX, J.A. (2019). Beware of inertial instability masquerading as gravity waves in stratospheric temperature perturbations. *Geophysical Research Letters*, **46**, 1740–1745. 7

HATZES, A.P. (2016). The radial velocity method for the detection of exoplanets. *Methods of detecting exoplanets: 1st advanced school on exoplanetary science*, 3–86. 41

HAWLEY, J.F. & BALBUS, S.A. (1991). A powerful local shear instability in weakly magnetized disks. II. Nonlinear evolution. *The Astrophysical Journal*, **376**, 223. 17

HAWLEY, J.F. & BALBUS, S.A. (1992). A powerful local shear instability in weakly magnetized disks. III-Long-term evolution in a shearing sheet. *The Astrophysical Journal*, **400**, 595–609. 17, 153, 170

HAYASHI, H., SHIOTANI, M. & GILLE, J.C. (1998). Vertically stacked temperature disturbances near the equatorial stratopause as seen in cryogenic limb array etalon spectrometer data. *Journal of Geophysical Research: Atmospheres*, **103**, 19469–19483. 7, 8, 9, 21, 28, 39, 40, 193

HENG, K. & SHOWMAN, A.P. (2015). Atmospheric dynamics of hot exoplanets. *Annual Review of Earth and Planetary Sciences*, **43**, 509–540. 1, 4, 41, 82, 193, 217, 229, 270

HINDLE, A.W., BUSHBY, P.J. & ROGERS, T.M. (2019). Shallow-water magnetohydrodynamics for westward hotspots on hot Jupiters. *The Astrophysical Journal Letters*, **872**, L27. 4, 218, 227

HINDLE, A.W., BUSHBY, P.J. & ROGERS, T.M. (2021). The magnetic mechanism for hotspot reversals in hot Jupiter atmospheres. *The Astrophysical Journal*, **922**, 176. 4, 218

HITCHMAN, M.H., LEOVY, C.B., GILLE, J.C. & BAILEY, P.L. (1987). Quasi-stationary zonally asymmetric circulations in the equatorial lower mesosphere. *Journal of the atmospheric sciences*, **44**, 2219–2236. 8, 28, 39

HOSKINS, B.J. (1974). The role of potential vorticity in symmetric stability and instability. *Quarterly Journal of the Royal Meteorological Society*, **100**, 480–482. 10

HOWARD, L.N. (1961). Note on a paper of John W. Miles. *Journal of Fluid Mechanics*, **10**, 509–512. 14

HOWARD, L.N. & GUPTA, A.S. (1962). On the hydrodynamic and hydromagnetic stability of swirling flows. *Journal of Fluid Mechanics*, **14**, 463–476. 19

HUGHES, D.W. & TOBIAS, S.M. (2001). On the instability of magnetohydrodynamic shear flows. *Proceedings of the Royal Society of London. Series A: Mathematical, Physical and Engineering Sciences*, **457**, 1365–1384. 14

HUGHES, D.W., ROSNER, R. & WEISS, N.O. (2007). *The Solar Tachocline*. Cambridge University Press. 2, 40

HUNT, J.C.R. (1966). On the stability of parallel flows with parallel magnetic fields. *Proceedings of the Royal Society of London. Series A. Mathematical and Physical Sciences*, **293**, 342–358. 14

HURWITZ, A. (1895). Ueber die Bedingungen, unter welchen eine Gleichung nur Wurzeln mit negativen reellen Theilen besitzt. *Mathematische Annalen*, **46**, 273–284. 104, 113

IESS, L., FOLKNER, W.M. *et al.* (2018). Measurement of Jupiter's asymmetric gravity field. *Nature*, **555**, 220–222. 3

KASPI, Y., GALANTI, E. *et al.* (2018). Jupiter's atmospheric jet streams extend thousands of kilometres deep. *Nature*, **555**, 223–226. 3, 40, 217, 229, 269

KENT, A. (1968). Stability of laminar magnetofluid flow along a parallel magnetic field. *Journal of Plasma Physics*, **2**, 543–556. 14

KLOOSTERZIEL, R.C. (1990). *Barotropic vortices in a rotating fluid*. Ph.D. thesis, Rijksuniversiteit Utrecht. 14

KLOOSTERZIEL, R.C. & CARNEVALE, G.F. (2008). Vertical scale selection in inertial instability. *Journal of Fluid Mechanics*, **594**, 249–269. 10, 85, 86, 88, 92, 93, 94, 265

KLOOSTERZIEL, R.C. & VAN HEIJST, G.J.F. (1991). An experimental study of unstable barotropic vortices in a rotating fluid. *Journal of Fluid Mechanics*, **223**, 1–24. 13

KLOOSTERZIEL, R.C., CARNEVALE, G.F. & ORLANDI, P. (2007a). Inertial instability in rotating and stratified fluids: barotropic vortices. *Journal of Fluid Mechanics*, **583**, 379–412. 13, 192, 265, 272

KLOOSTERZIEL, R.C., ORLANDI, P. & CARNEVALE, G.F. (2007b). Saturation of inertial instability in rotating planar shear flows. *Journal of Fluid Mechanics*, **583**, 413–422. 11, 13, 142, 158, 191, 272

KLOOSTERZIEL, R.C., ORLANDI, P. & CARNEVALE, G.F. (2015). Saturation of equatorial inertial instability. *Journal of Fluid Mechanics*, **767**, 562–594. 11, 265

KLOOSTERZIEL, R.C., CARNEVALE, G.F. & ORLANDI, P. (2017). Equatorial inertial instability with full Coriolis force. *Journal of Fluid Mechanics*, **825**, 69–108. 10, 272

KNOBLOCH, E. (1992). On the stability of magnetized accretion discs. *Monthly Notices of the Royal Astronomical Society*, **255**, 25P–28P. 17

KNOX, J.A. (2003). Inertial Instability. *In Encyclopedia of Atmospheric Sciences*, 1004–1013. 7, 8, 10, 21, 193

KOLL, D.D.B. & KOMACEK, T.D. (2018). Atmospheric circulations of hot Jupiters as planetary heat engines. *The Astrophysical Journal*, **853**, 133. 41

KUIPER, G.P. (1941). On the Interpretation of beta Lyrae and Other Close Binaries. *The Astrophysical Journal*, **93**, 133. 1, 15, 21, 265

KUO, H.L. (1949). Dynamic instability of two-dimensional nondivergent flow in a barotropic atmosphere. *Journal of Atmospheric sciences*, **6**, 105–122. 5

KUSHNER, P.J., MCINTYRE, M.E. & SHEPHERD, T.G. (1998). Coupled Kelvin-Wave and Mirage-Wave Instabilities in Semigeostrophic Dynamics. *Journal of Physical Oceanography*, **28**, 513–518. 14

LYNDEN-BELL, D. & PRINGLE, J.E. (1974). The evolution of viscous discs and the origin of the nebular variables. *Monthly Notices of the Royal Astronomical Society*, **168**, 603–637. 1, 15

MAMATSASHVILI, G., STEFANI, F., HOLLERBACH, R. & RÜDIGER, G. (2019). Two types of axisymmetric helical magnetorotational instability in rotating flows with positive shear. *Physical Review Fluids*, **4**, 103905. 19

MANDUSHEV, G., O'DONOVAN, F.T. *et al.* (2007). Tres-4: A transiting hot Jupiter of very low density. *The Astrophysical Journal*, **667**, L195. 4, 41

MAYOR, M. & QUELOZ, D. (1995). A Jupiter-mass companion to a solar-type star. *Nature*, **378**, 355–359. 4

McIntyre, M.E. (1970). Diffusive destabilisation of the baroclinic circular vortex. *Geophysical and Astrophysical Fluid Dynamics*, **1**, 19–57. 272

Menou, K., Balbus, S.A. & Spruit, H.C. (2004). Local axisymmetric diffusive stability of weakly magnetized, differentially rotating, stratified fluids. *The Astrophysical Journal*, **607**, 564. 17, 18, 21, 23, 43, 86, 90, 91, 92, 114, 118, 265, 272

Michael, D.H. (1954). The stability of an incompressible electrically conducting fluid rotating about an axis when current flows parallel to the axis. *Mathematika*, **1**, 45–50. 18, 34

Ogilvie, G.I. (2007). Instabilities, angular momentum transport and magnetohydrodynamic turbulence. *The Solar Tachocline (ed. D. W. Hughes, R. Rosner, & N. O. Weiss)*, 299. 18

Ooyama, K. (1966). On the Stability of the Baroclinic Circular Vortex: a Sufficient Criterion for Instability. *Journal of the Atmospheric Sciences*, **23**, 43–53. 6

Orlandi, P. & Carnevale, G.F. (1999). Evolution of isolated vortices in a rotating fluid of finite depth. *Journal of Fluid Mechanics*, **381**, 239–269. 13, 14

Parfrey, K.P. & Menou, K. (2007). The origin of solar activity in the tachocline. *The Astrophysical Journal*, **667**, L207. 18

Park, J., Prat, V. & Mathis, S. (2020). Horizontal shear instabilities in rotating stellar radiation zones-I. Inflectional and inertial instabilities and the effects of thermal diffusion. *Astronomy & Astrophysics*, **635**, A133. 145

Potylitsin, P.G. & Peltier, W.R. (1998). Stratification effects on the stability of columnar vortices on the f-plane. *Journal of Fluid Mechanics*, **355**, 45–79. 21

Priest, E.R. (2012). *Solar magnetohydrodynamics*, vol. 21. Springer Science & Business Media. 25, 26

Proctor, M.R.E. & Weiss, N.O. (1982). Magnetoconvection. *Reports on Progress in Physics*, **45**, 1317. 28

Rapp, M., Dörnbrack, A. & Preusse, P. (2018). Large midlatitude stratospheric temperature variability caused by inertial instability: A potential source of bias for gravity wave climatologies. *Geophysical Research Letters*, **45**, 10–682. 7, 8

Rauscher, E. & Menou, K. (2010). Three-dimensional modeling of hot Jupiter atmospheric flows. *The Astrophysical Journal*, **714**, 1334. 4

Rayleigh, L. (1880). On the stability, or instability, of certain fluid motions. *Proc. London Math. Soc.*, **9**, 57–70. 5

RAYLEIGH, L. (1917). On the Dynamics of Revolving Fluids. *Proceedings of the Royal Society of London. Series A, Containing Papers of a Mathematical and Physical Character*, **93**, 148–154. 6, 13, 15, 26

READ, P.L. (2024). The Dynamics of Jupiter's and Saturn's Weather Layers: A Synthesis After Cassini and Juno. *Annual Review of Fluid Mechanics*, **56**, 271–293. 3, 217, 229

RICHARDS, K.J. & EDWARDS, N.R. (2003). Lateral mixing in the equatorial pacific: The importance of inertial instability. *Geophysical Research Letters*, **30**. 7, 21, 193

ROGERS, T.M. (2017). Constraints on the magnetic field strength of HAT-P-7 b and other hot giant exoplanets. *Nature Astronomy*, **1**, 1–4. 4, 218, 227

ROGERS, T.M. & KOMACEK, T.D. (2014). Magnetic effects in hot Jupiter atmospheres. *The Astrophysical Journal*, **794**, 132. 4, 100, 218, 227, 263

ROUTH, E.J. (1877). *A Treatise on the Stability of a Given State of Motion: Particularly Steady Motion. Being the Essay to which the Adams Prize was Adjudged in 1877, in the University of Cambridge*. Macmillan and Company. 104, 113

RÜDIGER, G., GELLERT, M., HOLLERBACH, R., SCHULTZ, M. & STEFANI, F. (2018). Stability and instability of hydromagnetic Taylor-Couette flows. *Physics reports*, **741**, 1–89. 20

SALMON, R. (1998). *Lectures on geophysical fluid dynamics*. Oxford University Press. 25, 27, 28

SCHOU, J., ANTIA, H.M. *et al.* (1998). Helioseismic studies of differential rotation in the solar envelope by the solar oscillations investigation using the Michelson Doppler Imager. *The Astrophysical Journal*, **505**, 390. 18, 40

SHAKURA, N.I. & SUNYAEV, R.A. (1973). Black holes in binary systems. Observational appearance. *Astronomy and Astrophysics, Vol. 24, p. 337-355*, **24**, 337–355. 15, 21

SHEN, C.Y. & EVANS, T.E. (2002). Inertial instability and sea spirals. *Geophysical Research Letters*, **29**, 39–1. 21

SHOWMAN, A.P. & GUILLOT, T. (2002). Atmospheric circulation and tides of "51 Pegasus b-like" planets. *Astronomy & Astrophysics*, **385**, 166–180. 4

SHOWMAN, A.P. & POLVANI, L.M. (2011). Equatorial superrotation on tidally locked exoplanets. *The Astrophysical Journal*, **738**, 71. 270

SHOWMAN, A.P., WORDSWORTH, R.D., MERLIS, T.M. & KASPI, Y. (2013). Atmospheric circulation of terrestrial exoplanets. *Comparative Climatology of Terrestrial Planets*, **1**, 277–326. 1, 4, 41, 193, 217, 229, 270

SMITH, A.K. & RIESE, M. (1999). Cryogenic Infrared Spectrometers and Telescopes for the Atmosphere (CRISTA) observations of tracer transport by inertially unstable circulations. *Journal of Geophysical Research: Atmospheres*, **104**, 19171–19182. 8, 28, 39

SPIEGEL, E.A. & VERONIS, G. (1960). On the Boussinesq approximation for a compressible fluid. *The Astrophysical Journal*, **131**, 442. 27

SPIEGEL, E.A. & WEISS, N.O. (1982). Magnetic buoyancy and the Boussinesq approximation. *Geophysical & Astrophysical Fluid Dynamics*, **22**, 219–234. 28

SPITZER, L. (2006). *Physics of fully ionized gases*. Courier Corporation. 15

STEFANI, F., GUNDRUM, T. *et al.* (2006). Experimental evidence for magnetorotational instability in a Taylor-Couette flow under the influence of a helical magnetic field. *Physical review letters*, **97**, 184502. 21

STEVENS, D.E. (1983). On symmetric stability and instability of zonal mean flows near the equator. *Journal of the Atmospheric Sciences*, **40**, 882–893. 65, 193, 195, 196

SYNGE, J.L. (1933). The stability of heterogeneous liquids. *Trans. R. Soc. Canada*, **27**, 1. 6, 13

TAYLER, R.J. (1957). Hydromagnetic instabilities of an ideally conducting fluid. *Proceedings of the Physical Society. Section B*, **70**, 31–48. 20

TAYLOR, G.I. (1923). VIII. Stability of a viscous liquid contained between two rotating cylinders. *Philosophical Transactions of the Royal Society of London. Series A, Containing Papers of a Mathematical or Physical Character*, **223**, 289–343. 13, 15

TOLLEFSON, J., WONG, M.H., *et al.* (2017). Changes in Jupiter's Zonal Wind Profile preceding and during the Juno mission. *Icarus*, **296**, 163–178. 3, 40

TRITTON, D.J. (2012). *Physical fluid dynamics*. Springer Science & Business Media. 31

TSAI, S., DOBBS-DIXON, I. & GU, P. (2014). Three-dimensional structures of equatorial waves and the resulting super-rotation in the atmosphere of a tidally locked hot jupiter. *The Astrophysical Journal*, **793**, 141. 41

VALLIS, G.K. (2017). *Atmospheric and oceanic fluid dynamics*. Cambridge University Press. 25, 28, 29, 31, 43

VANDAKUROV, Y.V. (1972). Theory for the Stability of a Star with a Toroidal Magnetic Field. *Soviet Astronomy*, **16**, 265. 19, 20, 34

VASAVADA, A.R. & SHOWMAN, A.P. (2005). Jovian atmospheric dynamics: An update after Galileo and Cassini. *Reports on Progress in Physics*, **68**, 1935. 3, 56

VELIKHOV, E.P. (1959). Stability of an ideally conducting liquid flowing between cylinders rotating in a magnetic field. *Sov. Phys. JETP*, **36**, 995–998. 16, 19, 22, 38

VERONIS, G. (1968). Effect of a stabilizing gradient of solute on thermal convection. *Journal of Fluid Mechanics*, **34**, 315–336. 31

WATSON, M. (1980). Shear instability of differential rotation in stars. *Geophysical & Astrophysical Fluid Dynamics*, **16**, 285–298. 5

WILCZYŃSKI, F., HUGHES, D.W. & KERSALÉ, E. (2022). Magnetic buoyancy instability and the anelastic approximation: regime of validity and relationship with compressible and Boussinesq descriptions. *Journal of Fluid Mechanics*, **942**, A46. 28

WINN, J.N., FABRYCKY, D., ALBRECHT, S. & JOHNSON, J.A. (2010). Hot stars with hot Jupiters have high obliquities. *The Astrophysical Journal Letters*, **718**, L145. 4, 41

YADAV, R.K. & THORNGREN, D.P. (2017). Estimating the magnetic field strength in hot Jupiters. *The Astrophysical Journal Letters*, **849**, L12. 4, 41

YAVNEH, I., MCWILLIAMS, J.C. & MOLEMAKER, M.J. (2001). Non-axisymmetric instability of centrifugally stable stratified Taylor–Couette flow. *Journal of Fluid Mechanics*, **448**, 1–21. 14